Dissertation

SUBMITTED TO THE

Combined Faculty of Natural Sciences and Mathematics

of Heidelberg University, Germany

FOR THE DEGREE OF

Doctor of Natural Sciences

Put forward by

Dominik Lentrodt

Born in: Munich, Germany

Oral examination: October 13th, 2021

Ab initio approaches to x-ray cavity QED

From multi-mode theory to nonlinear dynamics of Mössbauer nuclei

Referees:

apl. Prof. Dr. Jörg Evers

Prof. Dr. Maurits W. Haverkort

Zusammenfassung

In dieser Arbeit werden theoretische Ansätze zur Untersuchung von Quantenelektrodynamik in Röntgenkavitäten entwickelt. Zuerst wird gezeigt, wie Jaynes-Cummings-artige wenig-Moden Modelle für offene Resonatoren aus fundamentalen Grundprinzipien hergeleitet werden können, was eine offene Frage in der quantenoptischen Literatur darstellte. Die resultierende ab initio wenig-Moden Theorie wird auf den Fall von Röntgenkavitäten angewendet, wodurch ein vorheriges phänomenologisches Modell verallgemeinert wird. Zudem wird ein zweiter orthogonaler Ansatz entwickelt, der die numerisch effiziente Beschreibung komplexer Kavitätengeometrien ermöglicht. Es wird gezeigt, dass man dadurch Mastergleichungen für Kernensembles direkt herleiten kann, wobei Greensche Funktionen zur Enkodierung der Kavitätenumgebung genutzt werden. Dieser Ansatz stellt eine ab initio Quantentheorie für das System dar, die frühere Diskrepanzen auflöst und erlaubt, Kavitäten-modifizierte Kernniveauschemata ohne die Notwendigkeit einer Fitting-Prozedur semi-analytisch auszurechnen. Auf der Grundlage der beiden entwickelten Theorien werden mehr-Moden Effekte, die aus großen Verlusten in undichten Resonatoren resultieren, untersucht. Ein allgemeines Kriterium zur Identifizierung und Klassifizierung solcher mehr-Moden Effekte wird eingeführt, wodurch demonstriert wird, dass diese für bereits beobachtete Signaturen in Experimenten mit Röntgenkavitäten verantwortlich sind und zur künstlichen Modifizierung von Kernquantensystemen eingesetzt werden können. Weitere interessante Eigenschaften in der Form von Spitzen in nuklearen Fano-Interferenztrajektorien von Röntgenkavitäten mit überlappenden Moden werden aufgezeigt. Zu guter Letzt werden die gewonnenen Einblicke zur Untersuchung der nichtlinearen Anregungsdynamik von Mössbauerkernen in der Präsenz starker treibender Röntgenfelder benutzt. Die Realisierbarkeit der Inversion von Kernensembles und die Möglichkeit, fokussierte Pulse in Kombination mit Röntgenkavitäten zur Erhöhung der Intensität zu nutzen, wird analysiert.

Abstract

In this thesis, a theoretical framework for x-ray cavity QED with Mössbauer nuclei is developed. First, it is shown how Jaynes-Cummings-like few-mode models for open resonators can be derived from first principles, which has been an open question in the quantum optics literature. The resulting ab initio few-mode theory is applied to the x-ray cavity case, generalizing a previous phenomenological model. In addition, a second orthogonal approach is developed to enable the numerically efficient treatment of complex cavity geometries. It is shown that one can thereby directly derive a nuclear ensemble Master equation using Green's functions to encode the cavity environment. This approach provides an ab initio quantum theory for the system, which resolves previous discrepancies and allows to semi-analytically calculate cavity-modified nuclear level schemes without the need for a fitting procedure. On the basis of the two developed theories, multi-mode effects resulting from large losses in leaky resonators are investigated. A general criterion is introduced to identify and classify such multi-mode effects, which demonstrates that they are responsible for previously observed signatures in x-ray cavity experiments and can be harnessed to artificially tune nuclear quantum systems. Further interesting cusp features in nuclear Fano interference trajectories of x-ray cavities with overlapping modes are reported. Finally, the gained insights are employed to investigate nonlinear excitation dynamics of Mössbauer nuclei in the presence of strong x-ray driving fields. The feasibility of inverting nuclear ensembles at upcoming facilities and the possibility of using focused pulses in combination with x-ray cavities for intensity boosting is analyzed.

Within the framework of this thesis, the following articles were published in refereed journals:

[LE20] ***Ab Initio Few-Mode Theory for Quantum Potential Scattering Problems***
D. Lentrodt and J. Evers
Physical Review X **10**, 011008 (2020)

[Len20] ***Ab Initio Quantum Models for Thin-film X-ray Cavity QED***
D. Lentrodt, K. P. Heeg, C. H. Keitel, and J. Evers
Physical Review Research **2**, 023396 (2020)

[Hee21] ***Coherent X-ray-optical Control of Nuclear Excitons***
K. P. Heeg, A. Kaldun, C. Strohm, C. Ott, R. Subramanian, D. Lentrodt, J. Haber, H.-C. Wille, S. Goerttler, R. Rüffer, C. H. Keitel, R. Röhlsberger, T. Pfeifer, and J. Evers
Nature **590**, 401 (2021)

The following articles are available as preprints:

[Len21] ***Classifying and Harnessing Multi-mode Light-matter Interaction in Lossy Resonators***
D. Lentrodt, O. Diekmann, C. H. Keitel, S. Rotter, and J. Evers
arXiv:2107.11775 [quant-ph]

The following articles are currently in preparation:

[Le21p] ***Nonlinear Excitation of Mössbauer Nuclei in Thin-film Cavities by Focussed X-ray Pulses***
D. Lentrodt, C. H. Keitel, J. Evers, et al.
in preparation

Declarations on usage of the material in this document and the involvement of the thesis author are given at the start of each chapter.

Outside the scope of this thesis, the following articles were published:

[Hee17] ***Spectral Narrowing of X-ray Pulses for Precision Spectroscopy with Nuclear Resonances***
K. P. Heeg, A. Kaldun, C. Strohm, C. Ott, R. Subramanian, D. Lentrodt, J. Haber, H.-C. Wille, S. Goerttler, R. Rüffer, C. H. Keitel, R. Röhlsberger, T. Pfeifer, and J. Evers
Science **357**, 375-378 (2017)

Contents

Chapter 1

Introduction

"I don't like it, and I'm sorry I ever had anything to do with it."
– Erwin Schrödinger on the Probability Interpretation of Quantum Mechanics

Whether we like it or not, quantum mechanics has long been a cornerstone of our understanding of the physical world and has enabled a wide range of technologies from the laser [ST58; Hak70; Sie86] to superconductors [MO33; BCS57; BM88]. In recent decades, experiments have progressed from merely using quantum systems to controlling them, as has been recognized in the 2012 Nobel Prize awarded to Haroche&Wineland [Har13; Win13]. At present, we are witnessing the emergence of new quantum technologies [Fey82; DM03] such as quantum computers [Lad10; Pre18], quantum metrology [GLM11; Pez18; Bra18] and quantum simulators [Hau12; GAN14; Mar16], which often harness the entanglement between quantum systems — the aspect of the theory despised by Schrödinger, which is reflected in the above quote and which led him to contrive his famous thought experiment involving a possibly dead cat [Sch35].

An important class of quantum mechanical systems is given by qubits [Lad10], that is quantum objects which feature two possible quantum states and superpositions thereof. A simple example of a qubit is an atomic transition with a ground state and an excited state. These and other quantum objects can in turn be interrogated and controlled by light fields [Chu91; Ash97], which is the subject of quantum optics [SZ97; HR06; Mey21a], and such control is an important ingredient in the establishment of practically useful devices.

Many of the above-mentioned quantum technologies have been a result of a search for the best qubits that nature provides. Multiple candidates including superconducting qubits [Kra19; Kja20], photons [KLM01; Kok07], atoms [Blo08; SWM10] and ions [CZ00; BW08a; Bru19], quantum dots [Han07], solid state defects [Web10] and more [BAN11; Xia13] are currently part of a race to build a fully functional and programmable quantum computer with as many qubits as possible [Gib20]. Recent milestones include reports of a quantum computational advantage over classical computers, also called "quantum supremacy", with superconducting qubits [Aru19] and with photons [Zho20]. In quantum sensing, various systems are employed to precisely measure quantities such as electric and magnetic fields [DRC17]. In quantum metrology, transitions in special atoms and ions are used to build the most accurate clocks [Lud15]. Besides enabling new experiments and potentially the access to new physics [Saf18], some of the associated technologies have now already entered the business world [Gib19] to hopefully provide an immediate technological benefit to humankind in the near future [Bro19].

Nevertheless, the fundamental search for new quantum systems is ongoing. A particularly interesting class of qubits, whose utility as a quantum system has only been started to be investigated recently [BEK06; Pál08; Ada13; KK17b], is given by atomic nuclei. Due to their different nature compared to processes in the electron shell, nuclear transitions often feature unique properties and span themselves a huge parameter space (see [Wen16] and references therein). A particularly interesting example is given by an isomeric excited state transition in ^{229}Th [KR76]. Motivated by its low lying transition energy and long half-life (see Fig. 1.1), this nucleus is currently being investigated intensively as a candidate to build a nuclear clock [Wen16; Sei19; Pei21]. Another special class of transitions — the one investigated in this thesis — is found in Mössbauer nuclei.

When seen as a type of qubit, Mössbauer transitions are not only an exotic candidate, but also feature unique and extreme properties. Due to the Mössbauer effect [Mös58; Mös62], which enables recoilless emission with the emitted photon's momentum being absorbed by the entire lattice of a solid state body [Mös62; HT99], these transitions feature extremely narrow linewidths, typically in the neV range and below [Röh05b]. This property forms the basis for a broad range of applications in classical Mössbauer spectroscopy [Ger94; Röh05b; KK12; YL21; RC21]. For example, shifts of the narrow line and splittings induced by magnetic and electric fields allow a precise determination of their chemical environment, rendering Mössbauer nuclei an important tool in geoscience [McC21], archae-

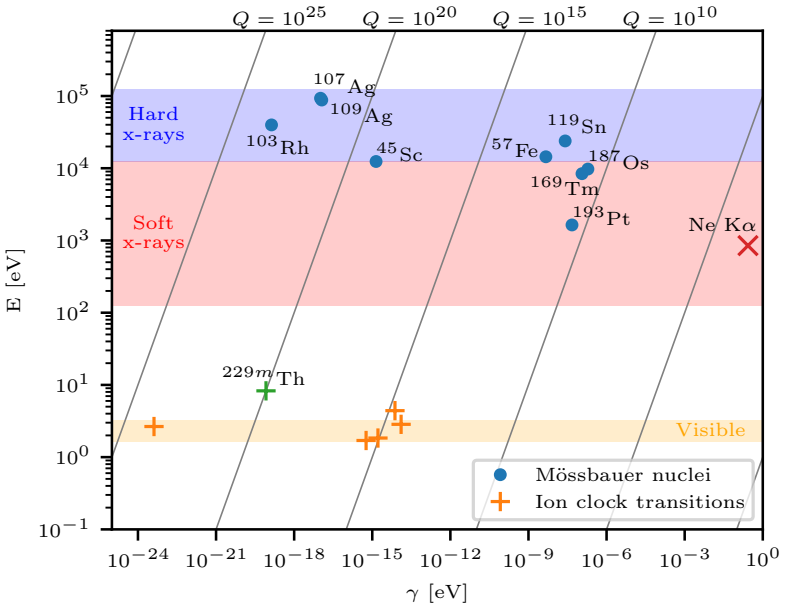

Figure 1.1: Energy-linewidth map of qubits mentioned in the introduction of this thesis, featuring Mössbauer nuclei (data from [Röh05b]), some ion clock transitions (data from [Lud15]), the isomeric transition in ^{229m}Th (data from [Wen16; Sei19]), and an inner-shell transition in K-shell photo-ionized neon (data from [Roh12]). The nucleus which is used for most practical investigations in this thesis is ^{57}Fe. Q-factors ($Q = E/\gamma$) are indicated as diagonal grid lines. Conventional energy ranges of the electromagnetic spectrum are shaded for visual guidance. This plot was inspired by similar figures in [Wen16; RE21].

ology [WK04], battery development [Lip21], for the investigation of biomolecules [Sch21], magnetism [KO21] and atomic diffusion [Yos21], and in thin-film physics [Röh05b]. To illustrate the broad importance of the Mössbauer effect in the sciences, the famous Pound-Rebka experiment [PR59; PR60] provides a good example, since its measurement of the gravitational red shift of Mössbauer photons is considered to have started an era of precision tests of general relativity [Hen96]. More recently, a miniaturized Mössbauer spectrometer has even featured on the Mars Exploration Rover [KK12], providing evidence for water on the planet [Kli04].

From the qubit perspective, the narrow linewidth corresponds to an incredibly low decoherence. If quantified by the quality factor Q given as the ratio of linewidth and transition energy, Mössbauer nuclei lie in the region of the best optical clock transitions [Lud15; Wen16; RE21], with values ranging from $Q \sim 10^{10}$ to 10^{24} (see Fig. 1.1). Another advantage is that due to solid state arrangement, the natural linewidth is closely realized practically without the need for cooling or a vacuum to prevent Doppler broadening or atom collisions in a gas [Smi86; Röh05b; YL21]. As a consequence, the astonishing properties of the nuclear transitions are also accessible robustly. These features further enable the appearance of pronounced collective effects, such as nuclear forward scattering [Bür92] and superradiance [Bal86; Bür99; Ada09].

Besides their extreme linewidths, Mössbauer transitions lie in a completely different energy range than the qubits that are usually considered. The latter are typically found at optical or microwave frequencies [WM08; Lad10]. In particular, quantum optics enabled by laser technology at optical photon energies has provided an extensive toolkit to control quantum systems in these energy ranges [Ash97; Har13; Win13], which is an important basis for many of the quantum technologies mentioned above.

Instead, Mössbauer transitions are typically in the hard x-ray regime corresponding to very high photon energies around and above 10 keV (see Fig. 1.1 for examples). In this context, the narrow linewidth of the nuclei becomes a challenge, since it imposes demanding conditions on the sources to significantly excite the transitions [BS97; JPK12; HKE16; RE21]. Compared to optical lasers, the available sources in the x-ray regime have long been inferior with regards to coherence [Pfe10] and spectral intensity [PMR16], which hinders the direct transfer of concepts from the optical to the x-ray domain. However, recent decades have seen a tremendous development in this direction. With the advent of fourth generation synchrotrons [Eri16; Liu16; Sch18b] and x-ray free electron lasers

(XFELs) [MT10; PMR16] — including LCLS in the USA [Emm10; Bos16], SACLA in Japan [Ish12; YTI15], the EuXFEL in Germany [Tsc17] and more [Mil17; Kan17] — highly coherent and bright x-ray sources are now available. Motivated by this "source-driven revolution" [SR08], it is an excellent time to start exploring nuclear quantum optics to fully exploit these new facilities even beyond their original science cases [KK17b; Eve20]. Future prospects include self-seeded XFELs [Fel97; Sal01], the operation of which has recently been demonstrated at PAL XFEL in South Korea [Nam21], and XFEL oscillators [KSR08; Ada19], which are particularly promising with regards to addressing narrow nuclear lines [Ada19; RE21].

From a different perspective, the high transition energy also provides another motivation for pursuing a quantum optics with Mössbauer nuclei. X-rays have a broad range of applications [ANM01; Bos16; Min18], with their short wavelength enabling imaging beyond the optical diffraction limit [SC95; GC07; Cha11] and their energy allowing spectroscopic access to important systems and processes [Fri07; You10; Ber12]. While traditionally mainly the classical properties of x-ray light are exploited, the investigation of nonlinear x-ray processes [EM71; Yod98; Ada03; Dou11; Glo12; Tam14] and quantum optical concepts at these energies [Ada13; Ada19] constitutes a recent frontier. For example, on the quantum optics side using higher-order photon correlations to extract interference information from incoherent light has been introduced as a way to enhance x-ray imaging [Cla17; Sch18a] and various other avenues are being pursued [Sof19; RES14; Ada13]. Besides the practical motivation and the broad range of potential applications, x-rays also offer some advantages with regards to implementing quantum optical schemes. For example, due to the high photon energy, the x-ray range boasts efficient detectors for counting experiments [BRM97; Bar00; Bar06; Chu18].

In this context, Mössbauer nuclei can be seen as a particular platform to implement an x-ray quantum optics [Ada13]. Again due to their unique properties, nuclei offer an interesting alternative to electronic resonances at x-ray energies. As an example, let us compare to an inner-shell transition in neon, which has recently been used to implement an x-ray laser [Roh12]. The lasing transition at 0.849 keV has a radiative linewidth of 0.27 eV [Roh12], with the excited state lifetime of 2.4 fs being dominated by Auger decay [Roh12]. The resulting quality factor is on the order of $Q \sim 10^3$. While such transitions have the advantage of larger cross-sections resulting in the feasibility of population inversion [Roh12] at current source intensities, they thus feature much lower coherence than Mössbauer transitions (see also Fig. 1.1) and often compete with unwanted processes in the electron shell. Mössbauer nuclei can also provide interesting quantum optical multi-level schemes beyond the simple qubit case, which can lead to phenomena such as quantum beats [TH78] and which are otherwise difficult to realize at x-ray energies [Cou02; Röh12; KK17b], or in certain cases even across the frequency spectrum [Hee13]. Electronic and nuclear transitions can therefore be regarded as complementary, implementing contrasting regimes of light-matter interactions at x-ray energies. Their different properties are in turn reflected in their different potential uses, with Mössbauer nuclei traditionally leaning towards precision spectroscopy applications [PR60; LA15] and the implementation of coherent collective interactions [TH78; HT99; Röh10].

In the last decade, the field of x-ray quantum optics with Mössbauer nuclei has sparked considerable interest and already a number of effects have been demonstrated. Besides the long successful history of classical Mössbauer spectroscopy [Smi86; GBT11; YL21] and efforts to implement a nuclear γ-ray laser [BS97; Ode10], the investigation of quantum optical effects was particularly sparked by the advent of modern x-ray facilities [SR08], starting with synchrotrons [Rub74; GVB94; RC21]. The observation of quantum beats [TH78], the demonstration of storing nuclear excitations by switching the direction of magnetic fields [Shv96], related approaches to coherent control of Mössbauer spectra [Vag90; KKR99], and the realization of accelerated spontaneous emission via the Purcell effect [Röh05a] constituted first practical steps in this direction. Subsequently, a milestone was the discovery of the collective Lamb shift with an ensemble of Mössbauer nuclei [Röh10]. The latter also kickstarted the field of nuclear quantum optics with thin-film x-ray cavities, implementing a counterpart to the successful field of optical cavity QED [Wal06; HR06; Rit13; RR15] and providing the option of artificially modifying nuclear level schemes through the cavity environment [HE13; HE15]. Since then, a number of quantum optical phenomena have been demonstrated in this platform, including electromagnetically induced transparency (EIT) without a control field [Röh12], spontaneously generated coherences (SGC) [Hee13], Fano resonances [Hee15a], slow light [Hee15b], collective strong coupling [Hab16a] and coherence oscillations between two nuclear ensembles [Hab17]. Additional setups have been proposed theoretically [KP16; LP17]. More recently, the option of using such thin-film cavities with electronic x-ray resonances instead of Mössbauer nuclei has also been considered, with already conducted experiments demonstrating spectral control of an inner-shell transition [Hab19]

and modification of core-hole lifetimes [Hua21]. Further theoretical proposals in this direction have been suggested [Gu21a; Gu21b] and a novel setup where spontaneously generated x-rays are generated inside a waveguide by electron impact has recently been introduced [VS21].

Besides nuclear x-ray cavity QED, concepts from quantum optics have also been utilized in nuclear forward scattering. In particular using mechanical motion on the (sub-)nanometer length and nanosecond time scale, which can be induced by piezo-electric transducers [Hel91; Sch02], has been a valuable tool. With radioactive sources, such setups have been used for time-domain shaping of γ-ray waveforms [SVK13; Vag14; SVG20]. Single photon entanglement [PKE09], nuclear quantum memories [Zha19] and coherent control schemes based on magnetic switching [LPK12; KLP14; WL18], extending the earlier experiment by Shvyd'ko [Shv96], have been proposed theoretically. In synchrotron experiments, spectral narrowing of x-ray pulses [Hee17] and coherent control of nuclear dynamics using x-ray double pulses [Hee21] were demonstrated, with the latter breaking previous records of interferometric phase stability from experiments in the extreme-ultraviolet domain [Lab12]. Similar control techniques have recently been implemented using magnons instead of mechanical motion [Boc21]. Beyond x-ray double pulses, visible pump/nuclear resonance probe experiments have also been developed [Sak17] and practically applied in the investigation of spin-crossover complexes [Sak17].

In the context of overcoming the source limitations imposed by the narrow linewidth in order to implement nonlinear effects, particularly the x-ray cavity setup has been seen as promising. After investigations in the 1990s demonstrating the difficulty of implementing a Mössbauer γ-ray laser [BS97], an estimate in relation to the cavity EIT effect found that observation of a nuclear Kerr nonlinearity could be feasible at XFEL sources [Röh12], promising new possibilities at the upcoming facilities. With regards to inverting nuclear ensembles, after an early investigation of exciting nuclear $E1$ transitions by x-ray sources [BEK06], the inversion of Mössbauer ensembles was calculated for forward scattering [JPK12] and in thin-film cavities [HKE16], with the latter including a potential detection scheme. On the practical side, a recent experiment [Chu18] at the x-ray free electron laser SACLA in Japan demonstrated nuclear resonance scattering with multiple excitations per shot, opening the door to an entirely new era of nuclear x-ray quantum optics.

On the theory side, the nuclear resonant scattering processes in all of the above-mentioned experiments are very well understood within semi-classical theory [VB86; HT99; SBH99; Shv99; Stu00; Stu04; Röh05b], which has had a long history [AK64; KAP67; HT68; HT69] since the discovery of the Mössbauer effect in 1958 [Mös58; Mös62]. Semi-classical theory is applicable due to the low driving intensities at synchrotron sources, which imply that previous and current experiments lie in the linear scattering regime. Much of the more recent work related to x-ray cavity QED has additionally relied on a quantum optical model [HE13; HE15], which allows to interpret the experimental signatures in terms of quantum optical level schemes and which has been tremendously important for providing insight into the underlying processes of recent experiments [Hee13; HE15; Hee15a; Hee15b; Hab16a; Hab17; Hab19]. The model also allows one to go beyond the semi-classical formalisms in order to explore the non-linear regime [Hee14; HKE16], establishing a route to describe upcoming experiments at XFELs.

Perspective

At this stage, one can see that nuclear quantum optics with Mössbauer nuclei and thin-film x-ray cavity QED are promising experimental platforms with exciting developments to be expected in the near future. Interestingly, one can observe that there are multiple distinct motivations for the subject with regards to immediate scientific progress. For the sake of clarity, we devote this perspective section to delineate different motivations in the field which this thesis connects to.

Note that the categories outlined below can be overlapping and are not intended to be exclusive, since unexpected motivations and applications are an important part of science. Instead, this perspective is intended to provide a guide to the current motivation structure of the field and to illustrate in which ways quantum optical effects or concepts can be useful.

(a) **Advancing current applications.**—The first and most immediate motivation is to advance existing applications of Mössbauer spectroscopy and x-ray science using quantum optical concepts, such as coherent control and interference phenomena. Importantly, this motivation category can reside in the realm of currently accessible phenomena, which do not require so far unobserved nonlinearities or quantum correlation effects. In this context, in particular the coherent control and interference setups discussed above, such as [Vag14; Sak17; Hee21], provide

interesting techniques for pulse shaping and novel spectroscopy schemes. Potential applications range from boosting of resonant count rate [Hee17] to multidimensional Mössbauer spectroscopy [Sak17; HE20], and even nuclear Ramsey spectroscopy [Hee21] and quantum memories [Zha19] have been envisioned.

(b) **An extreme platform for quantum optics.**—Second, one can use nuclei and x-rays as a platform to observe quantum effects, which may be elusive in other energy ranges or with other qubits. As motivated above, the extreme properties of Mössbauer nuclei can unlock entirely new regimes of light-matter interactions. A prime example is the collective Lamb shift experiment in [Röh10], since this effect was indeed first observed using Mössbauer nuclei in an x-ray cavity, and only later realized with atomic ensembles in the optical regime [Kea12]. Most experiments in x-ray cavity QED implementing interesting quantum optical level schemes [Röh10; Röh12; Hee13; Hee15a; Hee15b; Hab16a; Hab17; Hab19] mainly fall into this motivation category as well. Note that also in this case, the regimes currently accessible at synchrotron facilities can be perfectly sufficient, since many relevant effects are observable through linear scattering signatures if complemented by an appropriate quantum optical model for interpretation [HE13; HE15; Hee14; Hab16b].

(c) **Unlocking new phenomena.**—Third, a central motivation which underpins the field is the striving to realize nuclear quantum optics phenomena that cannot be described by the semi-classical theories of nuclear resonance scattering [HT99; Shv99; Stu00; Stu04; Röh05b]. As already discussed, possible effects include nonlinearities and quantum correlations as they are well studied at optical frequencies [Boy03; CVL14; HSP10], providing modified goals related to the long-sought nuclear γ-laser [BS97]. While in particular the observation of EIT [Röh12], slow light [Hee15b] and strong coupling [Hab16a] are indicators that such effects should be achievable with Mössbauer ensembles at higher source intensities [KK17b; RE21], to my knowledge no experimental signatures beyond the semi-classical have been reported with x-rays from Mössbauer nuclei so far. Even a recent experiment at an x-ray free electron laser featuring multi-photon excitation [Chu18] was well described by semi-classical theory for the time-dependent intensity, supplemented by independent photon statistics to understand the arrival times of each separate photon.

Each of these motivations is aimed at advancing in a different direction. Nevertheless, we see that all of them benefit from a quantum optical perspective, either by extracting ideas for novel setups (a), interpretations with regards to observed effects (b), or by attempting to directly implement novel quantum optical effects and requiring a predictive theory beyond the semi-classical sector (c). The development of a quantum theory for nuclear resonance scattering is therefore an important task to support these efforts and to understand upcoming experiments at XFEL facilities.

This thesis in a nutshell

The central topic of this thesis is to develop an improved theoretical description of x-ray cavity QED with Mössbauer nuclei. A main motivation is that the previous quantum optical model [HE13; HE15] — which we refer to as pXCQED (**p**henomenological **x**-ray **c**avity **q**uantum **e**lectro**d**ynamics) model for brevity — features open problems which prevent progress with regards to the above motivations. In particular, the phenomenological character of the model has raised questions with regards to the interpretation of discrepancies [HE15] and most importantly its predictiveness in higher intensity regimes (see Chapter 2 for a detailed background). For this reason, the goal of this thesis is to develop a well-understood ab initio theory.

Interestingly, as a first obstacle one encounters that the ab initio origin of few-mode models for resonator QED is a general open question in theoretical quantum optics (see Chapter 3 for an outline). Before tackling the x-ray case, this problem is resolved in Chapters 4 and 5 by constructing ab initio versions of such models, which we refer to as ab initio few-mode theories [LE20].

In Chapter 6, this formalism is applied to the x-ray cavity case, resolving the open questions with regards to the structure of the pXCQED model. However, one finds that numerical difficulties of the approach prevent practical applications [Len20].

To make further progress, an orthogonal approach to describe Mössbauer ensembles in the cavity environment is developed in Chapters 7 to 9. This second method [Len20] allows to directly predict the quantum optical level schemes which were previously obtained from the pXCQED model. In

addition, it enables a straightforward numerical implementation for general thin-film cavity geometries without the need for a fitting procedure. It is shown that the resulting practical insights fully resolve the previous questions, providing an ab initio quantum optical theory to describe x-ray cavity QED.

As an application, multi-mode effects resulting from strong loss processes in these x-ray cavities [Len21] are investigated in Chapter 10. One finds that the previously observed collective Lamb shift [Röh10] can be attributed to multi-mode effects, and that the latter can be harnessed to control the properties of the artificial nuclear quantum system by tuning the cavity environment. A general criterion to identify and classify multi-mode effects in lossy resonators is further introduced, which may be of relevance also in other platforms such as nanophotonics.

In Chapter 11, cusp and loop signatures in Fano interference trajectories are reported, which are also a consequence of spectral overlap between multiple cavity modes.

In Chapters 12 and 13, the developed theories are employed to explore nonlinear excitation dynamics of Mössbauer nuclei in thin-film cavities, linking back to the original motivations outlined above. We particularly study the feasibility of inverting nuclear ensembles in x-ray cavities using focused x-ray pulses as they are available at current facilities.

Chapter 14 is a standalone chapter introducing a data analysis technique for multi-dimensional Mössbauer spectra, which was employed in a recent experiment [Hee21].

Chapter 15 provides a summary of the results of this thesis and an outlook with regards to future developments.

In addition to the above overview, a detailed outline of the each chapter is given in the following, including technical progress descriptions.

Detailed thesis outline

In Chapter 2, a background on the field of x-ray cavity QED with Mössbauer nuclei and thin-film cavities is provided. The general setup, typical observables and important features are described. After summarizing recent experiments with relation to quantum optics, a detailed review of theoretical approaches to the subject is given, with a particular focus on providing a bird's eye view of connections between the different formulations. Within semi-classical theory, three separate methods are identified, which can be traced back to different variants of two central approximations. In the context of x-ray cavity QED, the aforementioned pXCQED model by Heeg&Evers [HE13; HE15] is summarized. The latter is based on introducing cavity modes interacting with the nuclear ensemble and a Master equation for the nuclei alone is obtained by adiabatically eliminating the cavity modes, which results in an effective few-level scheme for the nuclei. A central goal of this thesis is to develop an ab initio version of this quantum optical model, such that the background chapter provides a basis for subsequent results.

On the way to such an ab initio theory, one encounters the problem that various aspects of few-mode models for open resonators were previously not understood within general quantum optics theory. In particular, the origin of the underlying Hamiltonian — which is not only used in the pXCQED model, but also a common tool across the field of resonator QED — was not known. In Chapters 4 and 5, an ab initio few-mode theory is developed to resolve this problem and associated open questions. Since these chapters are independent of x-ray cavity QED, an additional detailed background on few-mode theories in quantum optics is given in Chapter 3. The structure of Jaynes-Cummings type few-mode models [JC63] is outlined and their importance in resonator QED is discussed. As a perspective and to illustrate the conceptual gap in the theory, the few-mode approach is compared to alternative matter-continuum interaction formulations. We further introduce the seminal input-output formalism and Gardiner-Collett system-bath Hamiltonian [GC85] as a way to describe leakage from the resonator and to compute spectral observables in scattering experiments. A detailed discussion is presented, outlining open problems, the physical limitations of few-mode theory and why understanding their origin is important practically. Recent progress and alternative approaches are further surveyed.

In Chapter 4, a method to derive general few-mode Hamiltonians from fundamental continuum Hamiltonians is presented. The result answers the question of how Jaynes-Cummings type few-mode models can be derived from first principles, resolving the aforementioned open problems. In addition, an exact equivalence between standard scattering theory applied to the continuum Hamiltonian and the input-output formalism applied to the few-mode case is shown, introducing a background scattering term. On the technical side, these results are based on an exact operator basis transformation constructed by a Feshbach projection — a method originating in nuclear and atomic physics [Fes58; Dom83] — onto a chosen set of discrete modes. The projection scheme ensures canonical commu-

tation relations of the mode operators and the resulting few-mode Hamiltonian is of the standard Gardiner-Collett form. In the regime of high resonator loss, where resonances spectrally overlap, modifications including cross-mode decay terms and frequency-dependent system-bath couplings are found to be necessary [HVH02; VH03]. The basis transformation is performed for the examples of the canonically quantized Schrödinger and resonator Maxwell equations.

In Chapter 5, the ab initio few-mode approach is considered in the presence of quantum systems interacting with the resonator field. It is shown that the exact ab initio few-mode Hamiltonian can be used to tremendously simplify the matter-continuum interaction via a few-mode approximation. We present a few-mode expansion scheme which allows to systematically select the relevant system modes of the resonator to approximate the field-matter interaction while keeping the free field dynamics exact. This approach provides a new perspective on few-mode models as a systematic truncation of an ab initio interaction Hamiltonian. The technique is illustrated for simple resonator examples in different light-matter and cavity-bath coupling regimes. The relevance of the approach with regards to current experimental regimes is discussed in detail. We further provide an afterword section to discuss recent progress related to and building on the presented results.

In Chapter 6, the focus returns to the investigation of x-ray cavity QED with Mössbauer nuclei by applying the ab initio few-mode method to the thin-film x-ray cavity geometry. The resulting model provides a direct generalization of the pXCQED model [Hee15b; HE15]. Differences between the ab initio and the phenomenological version are discussed. A simple x-ray cavity is investigated as an example and the approach is benchmarked with semi-classical theory, finding essentially perfect agreement. The resulting effective nuclear level scheme is calculated from the cavity geometry. As a downside, the approach is difficult to implement practically, since there is currently no numerical scheme to calculate the required few-mode matrix elements in the projection scheme beyond the simplest cavity geometries. Nevertheless, the ab initio technique provides a detailed understanding of the origin and necessary modifications of the x-ray cavity description.

Based on this understanding and recognizing the numerical difficulties in the ab initio few-mode theory, a second orthogonal approach to x-ray cavity QED with Mössbauer nuclei is developed in Chapter 7. The central realization is that due to the typically ultra-weak light-nucleus couplings, the few-mode approach can be circumvented. Instead, one can directly derive a nuclear many-body Master equation and effective few-level scheme via a Born-Markov approximation. This method avoids the detour of introducing a modal basis and subsequently eliminating the cavity modes by directly tracing out the cavity field acting as an environment for the nuclei. The approach is implemented by well-known techniques [DKW00; SB08] using the classical electromagnetic Green's function to describe the cavity mediated interactions between the nuclei, which further has the advantage that material absorption is included rigorously. The desired effective level scheme is then obtained by introducing a spin-wave basis and a single parallel wave vector approximation. Conveniently, the relevant Green's function is available analytically for the thin-film geometry [Tom95]. As a consequence, this approach provides a numerically efficient ab initio Master equation whose couplings can be straightforwardly computed even for complex thin-layer cavity geometries, eliminating the need for a phenomenological fitting procedure as it is used in the pXCQED model.

The practical power of the Green's function approach is demonstrated in Chapter 8, where cavity geometries featuring the EIT phenomenon [Röh12; HE15] are considered. A first ab initio calculation of the associated level scheme parameters is presented, resulting in an unambiguous interpretation of the effect. In addition, the origin of previous discrepancies [HE15] is identified as a non-negligible layer thickness of the nuclear ensemble.

In Chapter 9, we further show how effective transition dipole moments, which are the central parameter in the theory, can be calculated for multi-pole transitions from standard nuclear resonance scattering parameters.

In Chapter 10, a combination of the developed ab initio theories is employed to investigate multi-mode light-matter interaction in lossy resonators. A general technique to identify and classify multi-mode effects on two-level systems is presented, which is again independent of the x-ray case and applicable across resonator QED. In particular, a simple and practical criterion for the appearance of multi-mode effects is introduced, using the Lamb shift as a diagnostic observable. The criterion further allows to distinguish off-resonant and two types of resonant multi-mode effects. The method is based on connecting few-mode theory in the form of a recently developed model version [Med21] of the ab initio few-mode theory to Mittag-Leffler pole expansions of the Green's function, as they are used in quasi-mode theory [Lal18]. As an application, it is shown that the resulting multi-mode effects can be harnessed for controlling the properties of an artificial quantum system in a lossy resonator by

designing a sign inversion of the collective Lamb shift in nuclear x-ray quantum optics. The results further provide insight on the previous collective Lamb shift measurement [Röh10] as an off-resonant multi-mode effect.

In Chapter 11, the effect of multiple resonator modes on Fano interference is investigated. In particular, cusp and loop features in Fano q-parameter trajectories are reported, which appear in the regime of spectrally overlapping modes of x-ray double cavities.

In Chapter 12, the feasibility of nonlinear excitation of Mössbauer ensembles in thin-film cavities by focused x-ray pulses from current XFEL facilities is investigated. The Green's function Master equation is employed to construct a systematic approximation hierarchy applicable during ultra-short pulses. The resulting nonlinear equations of motion are solved semi-analytically using the pulse area theorem [MH67]. Moreover, a Fourier-transform based algorithm to account for the beam divergence of tightly focused x-ray pulses is introduced, enabling practical calculations. On this basis, the feasibility of inverting nuclear ensembles at current facilities is estimated and the role of the cavity is analyzed. We find that thin-film cavities can act as an excitation booster at low beam divergences, but new geometries or alternative approaches may be required if tightly focused beams are to be utilized. Our results provide an improvement over a previous calculation within the pXCQED model [HKE16] and indeed feature quantitative differences, both in the collimated case and for higher beam divergences.

In Chapter 13, solution methods for the nuclear ensemble Master equation are discussed. We show that the latter can be solved using existing software packages [Sha18] for relatively large spin numbers. Additionally, we introduce a symbolic algorithm to implement a cumulant expansion method for permutation symmetric models to further extend the capabilities. We discuss that due to a single parallel wave vector approximation, the ensemble Master equation and these solution methods may only provide limited insight in the highly excited sector and give an outlook with regards to possible alternative approaches.

Chapter 14 investigates the experimental aspect of how to statistically analyze two-dimensional Mössbauer spectra. We apply Bayesian methods to introduce a metric which evaluates the goodness of fit of theoretical models given an experimental data set. The approach was utilized for the data analysis of a recent experiment implementing coherent control of nuclei with x-ray double pulses [Hee21]. This chapter is largely disconnected from the x-ray cavity QED theme of the remaining chapters and presented separately, including a brief introduction.

Chapter 2

Background - Nuclear resonant scattering

In this background chapter, we provide an overview of the basic setting considered in this thesis and in particular review previous theoretical approaches. Open problems are outlined to set the stage for subsequent chapters.

2.1 Experimental system

2.1.1 Mössbauer nuclei

As motivated in Chapter 1, one focus of this thesis is the topic of Mössbauer nuclei as an exotic and extreme kind of qubit. Their unique features particularly include high-lying transition energies in the x-ray regime and ultra-narrow linewidths (see Fig. 1.1). The latter is partially owed to typically small transition moments of nuclei [Röh05b], resulting from their small size. More importantly, the ultra-narrow lines are enabled by an effect discovered by Rudolf Mössbauer in the 1950s [Mös58; KK12], which is named after him. The Mössbauer effect results in recoilless emission and scattering of x-rays from certain nuclear transitions. The underlying physical mechanism is that for Mössbauer nuclei, the recoil can be absorbed by the large mass of the entire lattice [Mös62]. In quantum mechanical terms, there is a finite probability that the emission or scattering process does not produce a phonon excitation [HT99]. The resulting spectrum is known as a zero phonon line, a phenomenon which is also encountered in solid state systems featuring resonances other than Mössbauer nuclei [SH88]. As a consequence, a significant fraction of the photons and nuclei, quantified by the Lamb-Mössbauer factor [Röh05b], participate in an elastic scattering process with conserved photon energy.

The Mössbauer effect then results in the bare nuclear transition being accessible without a significant line broadening from recoil. Interestingly, Mössbauer transitions are often not electric dipole, but instead $M1$ or higher order electric transitions [Röh05b]. A typical example is given in Fig. 2.1, where the transition scheme of the archetype Mössbauer nucleus ^{57}Fe is shown, which has been the workhorse of Mössbauer science [YL21], especially in experiments with relation to quantum optics [RE21]. The transition data including transition energy ω_{nuc}, full line width γ_{nuc} and radiative line width γ_{rad} are indicated on the plot (note that we frequently adopt natural units in this thesis, see Appendix A).

In the presence of magnetization, the two levels feature hyperfine splitting and six transitions can be observed [Röh05b] (see Fig. 2.1). Depending on the host material, other level schemes can also be realized, for example, via quadrupole splittings in the presence of electric field gradients at the nuclear position [Röh05b]. These properties can, however, only be tuned to a limited extent in practice. For instance, the direction of the magnetic field can often be chosen or even switched dynamically for certain materials [Shv99] using external magnets, but the field magnitude is mostly determined by the intrinsic magnetization. As a consequence, the number of realizable level schemes is limited and additional design options are desired. Such tunability can be provided by thin-film x-ray cavities, as we review in the following.

2.1.2 Nuclear excitons and thin-film x-ray cavities

Another implication of the solid state lattice and the high coherence of Mössbauer transitions is the appearance of collective and interference effects. Instead of exciting a single nucleus independently of the others, x-ray sources typically create coherent superpositions delocalized across the Mössbauer ensemble. As a result, one is dealing with a quantum many-body system. For weak x-ray intensities [Röh05b] or in the single photon case with radioactive sources [Vag14], the resulting quantum state

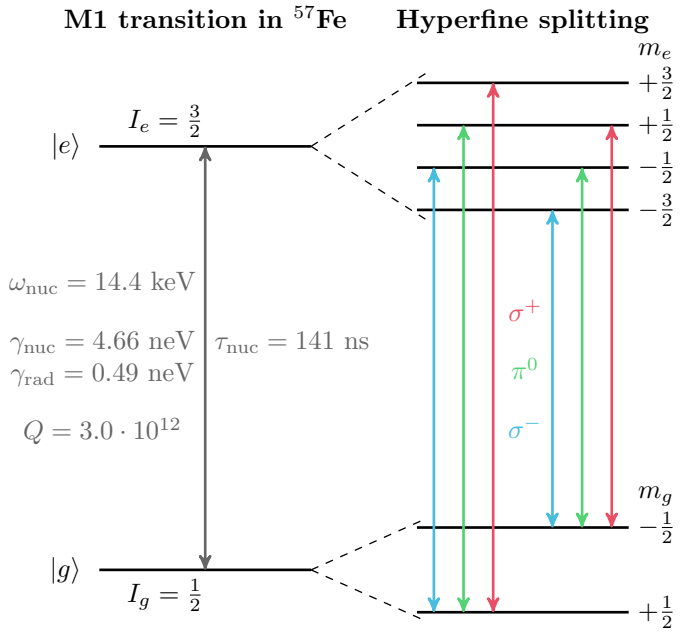

Figure 2.1: Level scheme of the Mössbauer nucleus ^{57}Fe, which features an $M1$ transition at an energy of $\omega_{\mathrm{nuc}} = 14.4$ keV (see [Röh05b] for transition data). The associated linewidth is $\gamma_{\mathrm{nuc}} = 4.66$ neV, with a radiative part $\gamma_{\mathrm{rad}} = \gamma_{\mathrm{nuc}}/(1+\alpha) = 0.49$ neV and the remaining decay proceeding via an internal conversion channel (α is the internal conversion coefficient). $Q = \omega_{\mathrm{nuc}}/\gamma_{\mathrm{nuc}}$ is the quality factor of the transition (see also Fig. 1.1). The hyperfine splitting of each level (not to scale) and the polarization for each transition (π^0 corresponds to linear polarization and $\sigma^{\pm}$ to right/left circular polarization, respectively) are indicated. This figure was inspired by a similar illustrations in [Hee14; Röh05b].

is a nuclear exciton such as [TH78; HT99; Hee14]

$$|\Psi\rangle = \frac{1}{\sqrt{N}} \sum_{n=1}^{N} e^{i\mathbf{k}\cdot\mathbf{r}_{\mathrm{nuc}}^{(n)}} |g_1 g_2 \dots e_n \dots g_N\rangle \,. \tag{2.1}$$

The phase information stored in this delocalized state then results in directional emission — such as in nuclear forward scattering [Bür92], where x-rays impinge on a solid state foil containing Mössbauer resonances at vertical incidence. As the name indicates, most of the scattered radiation is found in the forward direction in this geometry.

Further examples of nuclear excitons are encountered in a thin-film x-ray cavity geometry, which is schematically depicted in Fig. 2.2. There, Mössbauer ensembles are embedded in a stack of layers with typical thicknesses on the nanometer scale [Röh05b; Hee14; Hab16b]. The electronic refractive index of the cavity materials then results in off-resonant scattering of photons in addition to the effect of the nuclear resonances [Par54].

However, the electronic refractive index at x-ray energies is typically close to unity and can be written as [ANM01]

$$n_{\mathrm{el}} = 1 - \delta + i\beta \,, \tag{2.2}$$

where δ, β are small positive numbers (see Fig. 2.3). Consequently, x-ray cavities are usually used at grazing incidence geometry [Par54; Röh05b; Hee14] in order to achieve significant refraction at the layer boundaries.

From the perspective of the nuclear ensembles, the grazing incidence beam excites a nuclear exciton similar to the state described by Eq. (2.1) [HE13]. Below the first Bragg peak [Röh05b], the stored phase information again ensures highly directional emission with a reflection and a transmission channel. The incidence angle can then be used to select different exciton states in the nuclear ensemble.

Typical observables in this setup are depicted in Fig. 2.2. A pure cavity property is given by the off-resonant reflection spectrum as a function of incidence angle, which is also known as the rocking curve and can experimentally be obtained at synchrotron facilities [Röh05b]. The reflection channel is

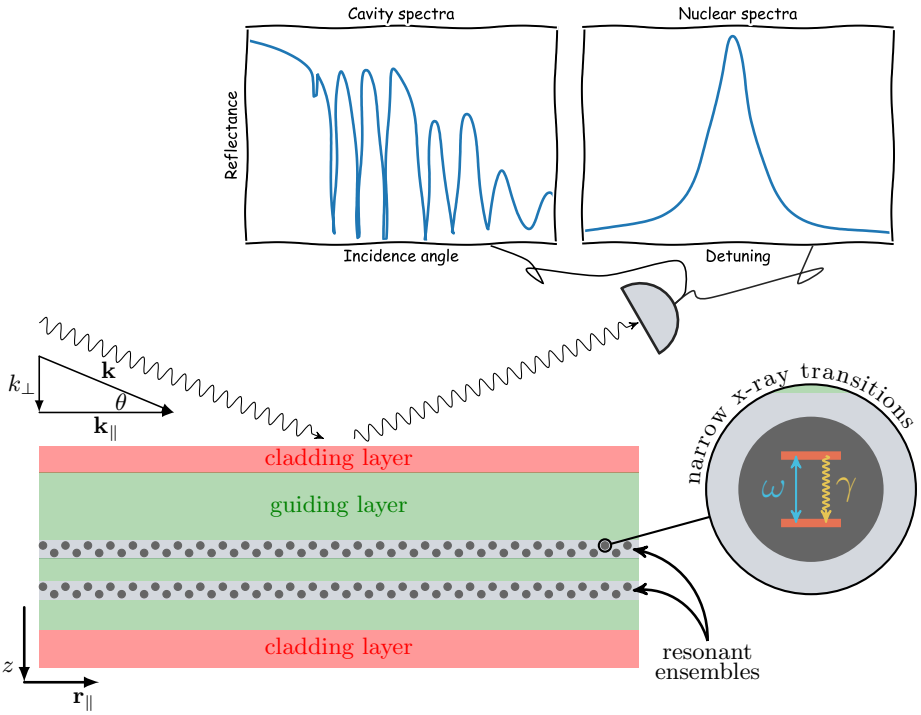

Figure 2.2: Sketch of a typical setting in thin-film x-ray cavity QED. A side-on view of a thin-film layer cavity, typically consisting of cladding layers (red) and a guiding layer (green) doped with thin resonant layers (gray), is shown. In the example in the figure, the resonant layers contain atoms or nuclei (black) featuring ultra-narrow transitions in the hard x-ray range, such as those provided by Mössbauer nuclei (see zoom, for the example of ^{57}Fe, $\hbar\omega \approx 14.4$ keV and $\gamma \approx 4.7$ neV). The system is probed spectroscopically at grazing incidence (wave vector $\mathbf{k}$ with parallel component $\mathbf{k}_\parallel$, perpendicular component $k_\perp$ and incidence angle θ) by x-radiation. Typical observables include off-resonant cavity reflection spectra as a function of incidence angle and resonant nuclear spectra (sketched plots). Figure reproduced from [Len20] (© 2020 American Physical Society).

typically preferred in experiments due to the practical constraint that a substrate is usually required for the thin-film sample preparation [Röh05b], although other setups are possible (see e.g. [VS21]).

With regards to quantum optics, the most interesting observable is the nuclear reflection spectrum around the transition energy of the Mössbauer nuclei, which is typically obtained experimentally by heterodyne detection schemes [Röh05b] using an analyzer to scan the energy detuning (see also Chapter 14 for details). The cavity in turn features sharp resonances visible in the rocking curve, but has a constant response on the energy scale of the nuclear line width [Röh05b; HE13].

While such cavities have practical applications in classical Mössbauer spectroscopy [Röh97; Röh05b], their central use considered within this thesis is to implement a counterpart to optical cavity QED [Wal06; Har07]. By confining the electromagnetic field through scattering at the layer boundaries, such cavities provide an environment to mediate and modify the interaction between nuclear ensembles. The cavity can thus act to implement novel nuclear level schemes and many-body interactions [RE21]. This idea of an x-ray cavity QED has been one of the major platforms of nuclear x-ray quantum optics, as we review in Sec. 2.1.3.

We also note that compared to optical cavities [Vah03], the thin-film x-ray implementation usually features rather bad resonators, due to the strong absorption and large leakage at x-ray energies. This results in the cavity resonances featuring overlapping modes (see Fig. 2.4 for an illustration). Such spectral overlap between the cavity resonances and strong resonator losses will be a central issue with regards to the theory development in this thesis (see particularly Chapter 10 for an effect that derives from these properties).

2.1.3 Nuclear x-ray quantum optics and cavity QED

In relation to nuclear quantum optics, there have been two main lines of research. The first encompasses pulse shaping and coherent control techniques using mechanical motion [Hel91; SVK13; Vag14;

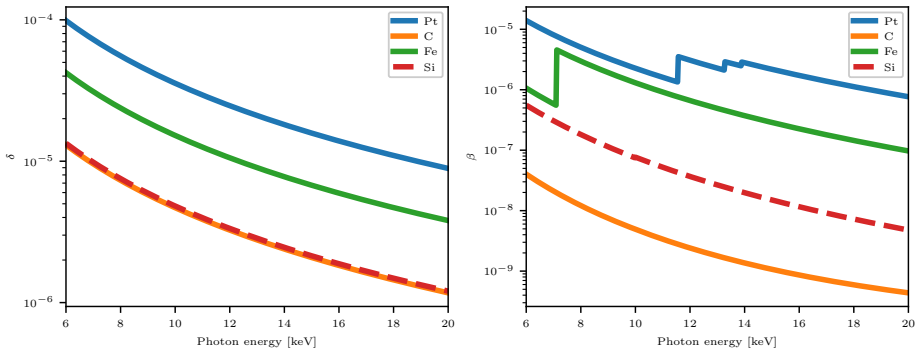

Figure 2.3: Electronic refractive indices of typical materials (see legend) used in x-ray cavities. The refractive index is parametrized by $n_{\mathrm{el}} = 1 - \delta + i\beta$. Materials data calculated using [Hee19].

SVG20; Zha19; Hee17; Hee21], magnetic fields [Shv96; LPK12; WL18] or more recently magnons [Boc21]. These experiments and theoretical proposals have in particular enabled the control of γ-ray photons [Vag14] and nuclear excitation [Hee21], which is an important step towards implementing tools and spectroscopy schemes as they are used at lower frequencies [Win13; DSM16; Ber19].

The second line of research is x-ray cavity QED, which we focus on in this thesis. The idea is to use the cavities described in the previous section to artificially modify the properties of Mössbauer ensembles, in close analogy to optical cavity QED [Wal06; Har07].

There are two central effects at play. First of all, as one is dealing with many-body excitations of the Mössbauer ensemble, various collective effects appear as they are also studied at lower frequencies [FHM73; Gar90; Scu09; GRK17]. In addition, the cavity modifies the electromagnetic environment of the nuclei and their interaction, which leads to modified ensemble properties similar to optical cavity QED [Wal06; HR06; Mey21b]. For example, cavities typically increase the coupling of a contained emitter to the light field. The latter in turn results in a line broadening and the associated decay speedup known as the Purcell effect, which was originally discovered at radio frequencies [Pur46].

X-ray cavity QED has developed as a platform to use these effects for the manipulation of Mössbauer ensembles. An analogous phenomenon to the Purcell effect with collective excitations of Mössbauer nuclei in a thin-film cavity was reported in [Röh05a], providing a first hint that such schemes can also be implemented at x-ray energies. However, besides porting concepts from lower frequencies to a new domain, the extreme properties of Mössbauer nuclei have enabled the observation of new effects in this platform at an early stage. In particular, the discovery of the collective Lamb shift [Röh10] was a milestone demonstrating that the setup can provide novel insights, since the effect was only measured two years later using atomic ensembles [Kea12].

Subsequently, a number of quantum optical concepts were implemented. The demonstration of electromagnetically induced transparency [Röh12] showed that nuclear multi-level schemes can be realized beyond what is available via natural hyperfine splittings. A particularly interesting aspect is that EIT typically requires additional control fields for the coupling of levels, which are not available at x-ray energies [FIM05]. In the setup in [Röh12], these control fields are simulated by the x-ray cavity coupling two ensembles, such that no additional x-ray field is necessary.

Soon after, another interesting phenomenon which had been elusive at lower energies and difficult to implement using atomic ensembles was experimentally observed in this system. In [Hee13], it was shown that x-ray cavities can be used to realize so called spontaneously generated coherences (SGC) between excited states of magnetized Mössbauer ensembles, featuring direct interference signatures in the reflection spectrum. Multiple different configurations were considered, demonstrating the potential of the platform for implementing a broad range of quantum optical level schemes.

In subsequent years, Fano resonances [Hee15a] in the frequency domain and slow light [Hee15b] in the time domain were observed using similar setups, implementing novel spectroscopy methods such as interferometric phase detection [Hee15a]. Another interesting step forward was the observation of strong coupling reported in [Hab17], where an optical lattice of many Mössbauer ensemble layers was used. A double cavity structure was further introduced in [Hab17] to implement strong coupling between two Mössbauer ensembles and to observe the associated time-domain phenomenon of Rabi oscillations. Such collective strong coupling schemes are promising with regards to implementing nonlinear quantum optics at higher source intensities [KK17b; RE21].

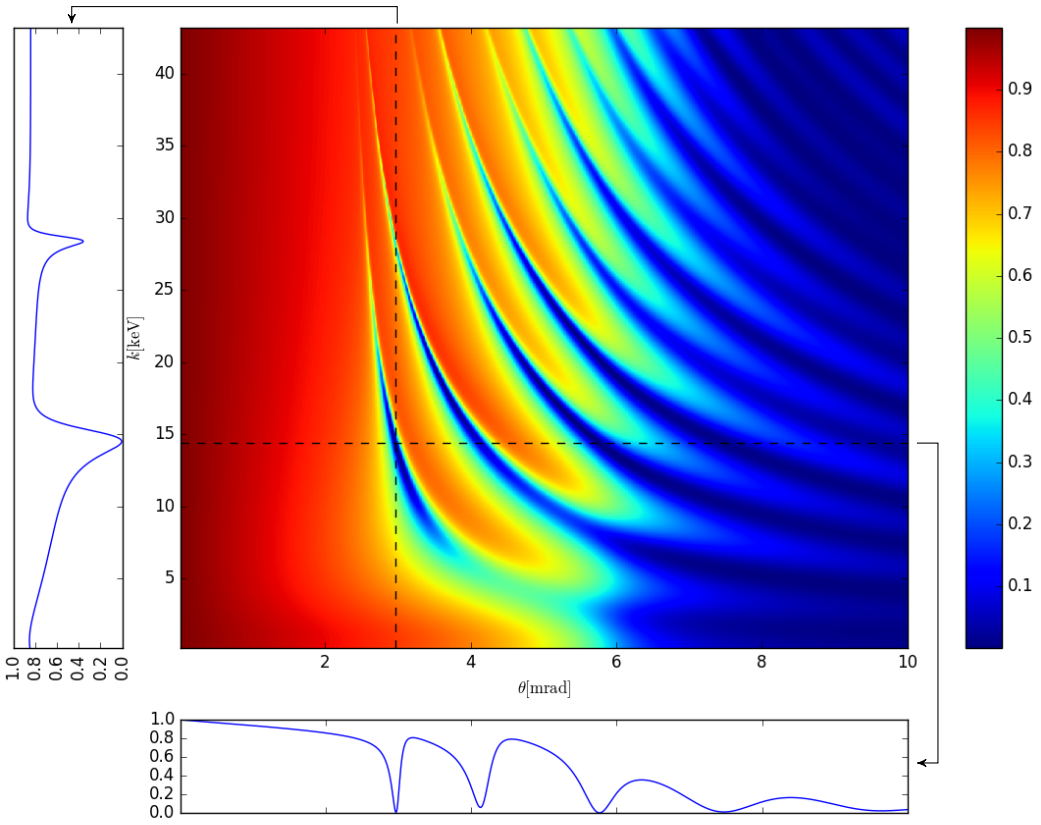

Figure 2.4: Typical x-ray cavity spectrum at grazing incidence. Colour plot: Off-resonant reflectance, that is without the effect of nuclear transitions, as a function of incidence angle θ and energy. Lower panel: Rocking curve corresponding to constant energy $k = 14.4$ keV. Left panel: Spectrum corresponding to constant angle θ equal to the first rocking curve minimum. The example cavity here is a Pt(2.6 nm)/C(7.9 nm)/Fe(1.5 nm)/C(9.3 nm)/Pt(∞) (top to bottom) layer system. The reflectance has been calculated using Parratt's formalism with constant refractive indices at 14.4 keV and serves mainly as an illustration of the typical mode structure of such cavities at grazing incidence.

Note that all of the above experiments made use of the Mössbauer transition in ^{57}Fe, such that there is much more to be explored. For example, an experiment measuring the collective Lamb shift with the ^{119}Sn Mössbauer nucleus was conducted recently [Vel21]. Beyond nuclei, thin-film x-ray cavity QED setups were recently implemented with electronic resonances. Two experiments reported the control of inner-shell transition spectra [Hab19] and core-hole lifetimes [Hua21], providing further promising applications featuring other qubits than Mössbauer transitions. A related waveguide geometry was recently used to manipulate x-rays created by electron impact [VS21]. These developments suggest that x-ray cavity QED may develop into a broadly used tool across x-ray physics in the future.

We note that the above timeline focuses on experimental development. In addition, there have been a number of theoretical suggestions of quantum optical level and control schemes in x-ray cavities [KP16; Hua17; Len20; Gu21a; Gu21b; Len21].

The progress in implementing quantum optical level schemes has in particular been supported by a quantum optical model for thin-film x-ray cavities with Mössbauer ensembles [HE13; HE15], which we refer to as the pXCQED (**p**henomenological **x**-ray **c**avity **q**uantum **e**lectro**d**ynamics) model. This model has been crucial for the interpretation of experimental results, since the semi-classical scattering theory employed in traditional Mössbauer spectroscopy is not able to predict the cavity-modified collective level scheme (see also Sections 2.2 and 2.3 for details). In early experiments [Röh05a; Röh10; Röh12] prior to this model, the quantum optical features contained in experimental signatures were interpreted by comparing spectra with standard results from quantum optical models and phenomenologically identifying central features, such as a pronounced spectral dip in the EIT case [Röh12]. The pXCQED model instead allows to predict such effective level schemes from an

underlying Master equation, offering a clear interpretation of the quantum optical processes.

Interestingly, however, the pXCQED model takes a completely orthogonal approach to the scattering problem. While the resulting spectra agree well with semi-classical scattering theory, there are also open problems and shortcomings. Since a main goal of this thesis is to improve the pXCQED model and to understands its link to the semi-classical theory, the remainder of this chapter is devoted to providing an overview of the different theoretical approaches to nuclear resonance scattering.

Note that one central motivation of this thesis are upcoming experiments at new x-ray facilities and higher source intensities. In this context, a recent experiment at the XFEL SACLA in Japan [Chu18] investigated the time-dependent scattering of multi-photon excitations from a nuclear ensemble. This investigation opens the door to a new generation of nuclear resonance scattering experiments and much of the theory development in this thesis is motivated by this future direction. The following review of existing theory approach also provides a perspective with regard to which approximations may break down in these upcoming experimental regimes.

2.2 Semi-classical theories

The nuclear resonance scattering community has largely employed semi-classical theories, which have been very successful in describing the experiments up to now. Initially derived in terms of diagrammatic scattering theory [AK64; KAP67; HT68; HT69] (see also [VB86; HT99; Smi99] and references therein), there are now standard formulations using effective wave equations [Röh05b; Shv99], whose solution is implemented in software packages [Shv00; Stu00; Hee19] and well-tested experimentally. Depending on the details, at least three distinct methods are in use. In this section, we summarize each of them and outline which approximations render the theory semi-classical.

We note that instead of going into technical details, we focus on the conceptual side of the theory. In particular, we are interested in the semi-classical aspect which all three approaches have in common. We further focus on coherent elastic scattering and do not provide details on practical aspects relevant for Mössbauer spectroscopy [Röh05b; YL21].

2.2.1 Scattering theory

The historically earliest techniques to describe nuclear resonant scattering and Mössbauer spectroscopy experiments are variants of semi-classical scattering theory [AK64; HT69; BW80] (see [HT99; Stu04] for reviews), which is nowadays also the most frequently used method [Röh05b] and has been implemented in the established software package CONUSS [Stu00]. More recently, the software package PYNUSS [Hee19] has provided a re-implementation in the PYTHON language, which also adds various features related to quantum optics and has recently been employed for evaluation of experimental data [Hee17; Hee20; Heu21] and for theoretical considerations [Len20; HE20; Len21; AP21].

The semi-classical scattering theory provides a rather complete account of resonant scattering processes in the linear regime [Stu04]. In particular, it is suitable for describing many experiments, since it allows to include various practical considerations and experimental imperfections [Röh05b], such as parameter distributions in realistic samples. Here, we will not go into detail on these practical aspects. Instead, we will give a very brief summary which focuses on the conceptual basis of the formalism.

There are two central conceptual steps in deriving the semi-classical scattering theory:

(a) Translating the nuclear resonances into a frequency-dependent linear refractive index.

(b) Solving the resulting effective Maxwell equations.

The first step (a) includes solving the nuclear eigenproblem for the given configuration of hyperfine fields and splittings. In a scattering setup, the second step (b) can often be done semi-analytically using Parratt's formalism [Par54] or the extended layer formalism [Röh05b]. In the following, we first illustrate the typical form of the nuclear refractive index. We then summarize the two approaches to solving the resulting Maxwell equations.

Nuclear refractive index

For the general case, the refractive index of the material including the nuclear resonance is given by [Röh05b]

$$\mathbf{n}(\omega) = \mathbf{n}_{\text{electronic}}(\omega) + \frac{\mathbf{f}_{\text{nuclear}}(\omega)}{k_0}\,, \tag{2.3}$$

where $\mathbf{f}_{\text{nuclear}}$ is the nuclear forward scattering matrix [Röh05b]. The latter can be expressed in term of the coherent forward scattering length of the nuclei $\mathbf{N}(\omega)$ via [Röh05b]

$$\mathbf{f}_{\text{nuclear}}(\omega) = \frac{2\pi}{k_0}\sum_i \rho_i \mathbf{N}_i(\omega)\,, \tag{2.4}$$

where the sum runs over all nuclear species i and ρ_i are their number densities [Röh05b].

For a general electric 2^L-pole transition [Röh05b], the coherent forward scattering length is given by [Röh05b]

$$\mathbf{N}(\omega) = \frac{4\pi f_R}{k_0}\sum_{M=-L}^{L} \mathbf{Y}^\dagger_{LM}(\mathbf{k}_0)\mathbf{Y}_{LM}(\mathbf{k}_0)F_{LM}(\omega)\,, \tag{2.5}$$

were $\mathbf{Y}_{LM}(\mathbf{k}_0)$ are the vector spherical harmonics [Röh05b] and f_R is the Debye-Waller or the Lamb-Mössbauer factor [Röh05b] in the respective relaxation speed limits. The energy dependence of the resonances is given by [Röh05b]

$$F_{\text{LM}}(\omega) = \sum_{\alpha,\eta} \frac{p_\alpha p_\alpha(\eta)\Gamma_x(\alpha M\eta;\, L)}{E(\eta) - E(\alpha) - \hbar\omega - i\Gamma(\eta)/2}\,, \tag{2.6}$$

where the parameters are as described in [Röh05b], that is α runs over all initial (ground) states, η runs over all excited states, p_α is the probability that the initial state α is occupied, $p_\alpha(\eta)$ is the probability that the excited state η is *not* occupied, $E(\alpha)$ and $E(\eta)$ are the energies of the ground and excited state, respectively, $\Gamma_x(\alpha M\eta;\, L)$ is the partial resonance width of the transition and $\Gamma(\eta)$ is the full resonance width.

For the special case of a single ground state with $p_\alpha = p_\alpha(\eta) = 1$ and for an unpolarized sample without hyperfine splittings, the above form can be simplified to a scalar refractive index, which reads [Röh05b; Hee14]

$$n(\omega) = n_{\text{electronic}} - \frac{\pi}{2}\frac{f_{\text{LM}}\rho_n}{k_0^3}\frac{2I_e+1}{2I_g+1}\frac{\gamma}{1+\alpha}\frac{1}{\Delta + i\gamma/2}\,, \tag{2.7}$$

where $\Delta = \omega - \omega_{\text{nuc}}$ is the detuning to the nuclear transition frequency ω_{nuc}. We thus see that the semi-classical linear refractive index corresponding to a nuclear transition is given by a Lorentzian resonance line on top of an electronic background $n_{\text{electronic}}$, which is approximately constant on the scale of the natural linewidth γ. The nuclear resonance amplitude is determined by transition and material properties, including the aforementioned Lamb-Mössbauer factor f_{LM}, the wave number k_0 of the nuclear transition, the internal conversion coefficient α, the spin of the nuclear excited/ground state $I_{e/g}$, and the detuning of the driving field from the transition $\Delta = \omega - \omega_{\text{nuc}}$ [Hee14]. For the case of the archetype Mössbauer transition in ^{57}Fe, these values are $\omega_{\text{nuc}} = 14.4$ keV, $\gamma = 4.66$ neV, $k_0 = 73.04$ nm^{-1}, $\rho_N = 83.2$ nm^{-1}, $f_{\text{LM}} \approx 0.8$, $\alpha = 8.56$, $I_e = 3/2$ and $I_g = 1/2$ [Hee14; Röh05b].

As a historical note, the origin of such semi-classical formulas for the refractive index can be traced back to the early days of quantum mechanics [BW80]. The central concept of linear semi-classical scattering theory was already captured in the Kramers-Heisenberg formula [KH25], which was extended by Weisskopf to account for the finite lifetimes of states [Wei33]. While originally derived from the correspondence principle, Dirac showed its relation to quantum mechanical radiation theory [Dir27b] by the use of perturbative scattering theory [Dir27a; Bor26] for the light-matter interaction. In the classical electromagnetism literature, similar formulas were found using the Lorentz oscillator model [BW80], which gives a frequency dependent polarizability, in combination with the Clausius-Mossotti [Mos50; Cla79; BW80] or the Lorenz-Lorentz relation [Lor80; Lor81; BW80], which relates the polarizability of an atom to the dielectric permittivity or refractive index, respectively.

In general quantum optics, the topic has been revisited in a number of contexts, such as for quantum and cooperative phenomena [Fle99; FY99; YF97; GRK17]. Importantly, it has been recognized

that linear dispersion theory is valid at strong coupling [Zhu90]. A quantum optical perspective on which approximations enter the derivation of the linear semi-classical refractive index for the resonant transitions is given in Sec. 2.2.4 and in Chapter 7.

In nuclear resonance scattering, similar results were derived using diagrammatic perturbation theory [HT69] and the Maxwell-Bloch like approach [Shv99], which allowed to include aspects such as cooperative phenomena, nuclear motion and dynamical scattering[HT99]. The effect of cavities was included with the introduction of the layer formalism [Röh99a; Röh05b]. For a complete account of the historical development of the theory we refer to the numerous reviews [HT99; Smi99], books [Röh05b; GVB94] on nuclear resonant scattering, as well as [Hee14]. The Maxwell-Bloch approach is also revisited in Secs. 2.2.2 and 2.2.3.

Effective wave equation and scattering

The refractive index formulas given above can then be used as an input for Maxwell's wave equation, which is given in frequency space by [Jac75]

$$\nabla \times \nabla \times \mathbf{E}(\mathbf{r},\omega) = \frac{\omega^2}{c^2}\boldsymbol{\varepsilon}(\mathbf{r},\omega)\mathbf{E}(\mathbf{r},\omega)\,, \tag{2.8}$$

where the dielectric permittivity is

$$\boldsymbol{\varepsilon}(\mathbf{r},\omega) = \mathbf{n}^2(\mathbf{r},\omega)\,. \tag{2.9}$$

This effective wave equation defines the light-propagation of an incident field which scatters from the resonant nuclei and the off-resonant dielectrics.

Observables are then given by solutions of the wave equation. In experiments at modern x-ray facilities, one is usually interested in scattering observables, that is a collimated incident beam from the source hits the target and scattered photons are observed in the far-field [Röh05b]. This information is usually captured by the scattering matrix $S_{mm'}(\mathbf{k},\mathbf{k}')$ [New82] between incident wave vector $\mathbf{k}$ and final wave vector $\mathbf{k}'$, with the indices m, m' capturing additional degrees of freedom such as polarization.

For the case of elastic scattering, which is what the refractive index in Sec. 2.2.1 describes, energy is conserved in the scattering process [New82]. For the case of a two-dimensional cavity, the translation invariance in the cavity plane further implies that the part of the wave vector parallel to the surface is conserved [Röh05b; Len20]. For a highly collimated incident beam, the field is additionally well described by a single incident wave vector $\mathbf{k}$. In the resulting single channel scenario [Röh05b], the scattering process is fully captured by a set of energy dependent reflection and transmission coefficients.

For the typical layered cavity structures used for x-ray cavity QED with Mössbauer nuclei (see Sec. 2.1.2), Fig. 2.5 illustrates the resulting scattering problem. The field in each layer is given by a downward and an upward traveling wave, with the amplitudes being given by the energy dependent reflection and transmission coefficients.

The latter can then be calculated by solving the boundary conditions at each interface, to ensure that the resulting field is a solution of the wave equation Eq. (2.8). This problem can be solved elegantly using Fresnel coefficients and a recursive algorithm, as we explain in the following section.

Parratt's formalism Here we summarise the results of Parratt's formalism [Par54; Hee14], which is a convenient algorithm to solve the scattering problem depicted in Fig. 2.5. It provides a recursive method to calculate the cavity reflection coefficient $R = r'_{01}$ of such a system from the Fresnel reflection coefficients $r_{m,m+1}$ and transmission coefficients $t_{m,m+1}$ at each boundary between two layers of refractive indices n_m and n_{m+1}. The recursive formula is [Hee14]

$$r'_{m-1,m} = \frac{r_{m-1,m} + r'_{m,m+1}e^{2i\phi_m}}{1 + r_{m-1,m}r'_{m,m+1}e^{2i\phi_m}}\,, \tag{2.10}$$

which can be obtained from summing up all possible scattering paths between the layers [Hee14], as depicted in Fig. 2.6. We use unprimed symbols for the Fresnel coefficients at a single interface and primed symbols for the reflection or transmission coefficient of a combined system.

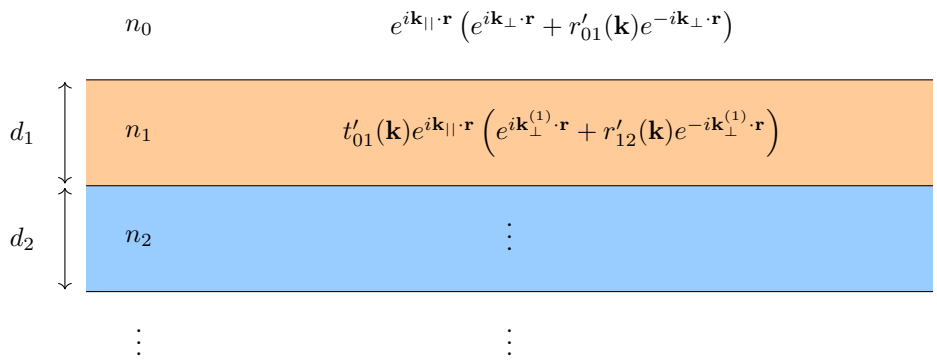

Figure 2.5: Wave fields in the different layers of a schematic x-ray cavity when the incoming beam amplitude is normalized to unity. The prefactor of the outgoing wave in the topmost layer is the energy dependent reflection coefficient r'_{01}, which is typically measured in spectroscopic experiments. The layers have thicknesses $d_1, d_2, \ldots d_{n-1}$ with refractive indices $n_1, n_2, \ldots n_{n-1}$. The topmost layer, which will usually be the vacuum with unit refractive index, is infinite and has refractive index n_0. Similarly, the lowest layer is usually given by an infinitely thick substrate of refractive index n_n.

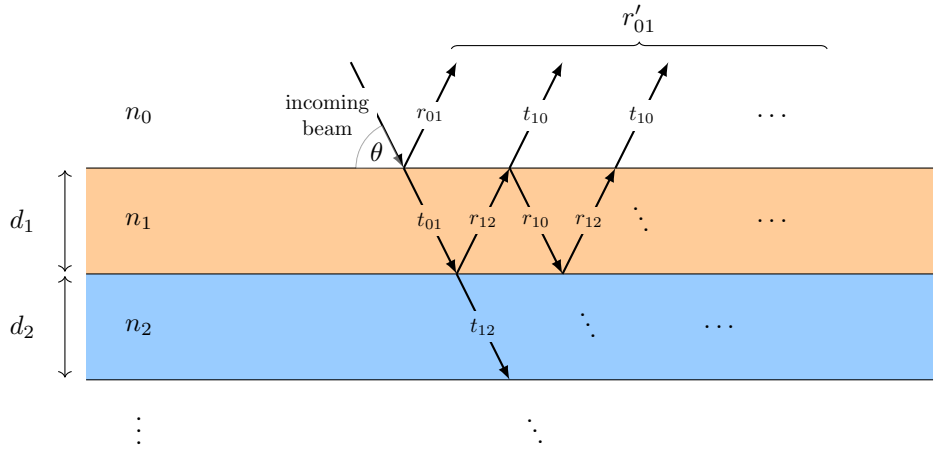

Figure 2.6: Illustration of Parratt's method [Par54], which uses the Fresnel reflection (r) and transmission (t) coefficients at each boundary to recursively calculate the total reflection r'_{01}. The algorithm solves the wave problem illustrated in Fig. 2.5 by summing up all possible paths between the interfaces. This figure was inspired by a similar illustration in [Hee14].

For M layers, that is when the lowest infinitely thick layer has refractive index n_M, one gets the starting condition of the recursion as [Hee14]

$$r'_{M-1,M} = r_{M-1,M}. \tag{2.11}$$

The phase accumulated from propagation through a layer is

$$\phi_m = k_z^{(m)} d_m \tag{2.12}$$

where $k_z^{(m)}$ is the perpendicular component of the wave vector in layer m. Since by Maxwell's equations the parallel component of the wave vector is conserved, the former can be written as [Hee14]

$$k_z^{(m)} = k^2\sqrt{n_m^2 - \cos^2(\theta)}. \tag{2.13}$$

The Fresnel reflection coefficients are in general polarization dependent. However, at grazing incidence the coefficients for s- and p-polarization are approximately equal [Par54], and read [Hee14]

$$r_{m,m+1} = \frac{k_z^{(m)} - k_z^{(m+1)}}{k_z^{(m)} + k_z^{(m+1)}}. \tag{2.14}$$

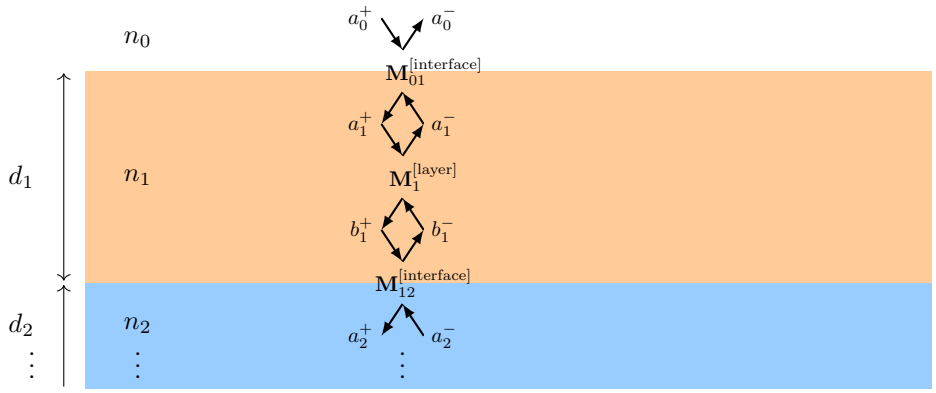

Figure 2.7: Illustration of the transfer matrix method [MS08] described in the text. The wave amplitudes at each interface and at the top and bottom of a layer are related via the corresponding transfer matrices. The connected structure of the amplitudes illustrates the multiplicative property of transfer matrices.

For a full solution without the grazing incidence approximation, we refer to Chapter 7.

Since these formulas fully apply for frequency dependent refractive indices, the nuclear resonances simply enter as part of their corresponding layer according to the nuclear refractive index [e.g. Eq. (2.7)].

Transfer matrix and layer formalism The layer formalism [Röh99a; Röh05b] is a method that extends Parratt's formalism, mainly to include cross-polarization scattering induced by hyperfine splitting of the Mössbauer nuclei.

The formalism can be seen as a way of expressing the recursive Parratt algorithm outlined above in terms of transfer matrices of the individual layers, which can be multiplied to obtain the transfer matrix of a stack of layers. For given reflection and transmission coefficients of a system, its transfer matrix is defined as [MS08]

$$\mathbf{M}'_{ij} = \begin{pmatrix} t'_{ji} - \frac{r'_{ij}}{t'_{ij}} r'_{ji} & \frac{r'_{ji}}{t'_{ij}} \\ -\frac{r'_{ij}}{t'_{ij}} & \frac{1}{t'_{ij}} \end{pmatrix} . \tag{2.15}$$

For scattering at a layer interface, using the properties of the Fresnel coefficients [Hee14] allows to simplify the expression to

$$\mathbf{M}_{ij}^{[\text{interface}]} = \begin{pmatrix} \frac{1}{t_{ij}} & \frac{r_{ij}}{t_{ij}} \\ \frac{r_{ij}}{t_{ij}} & \frac{1}{t_{ij}} \end{pmatrix} . \tag{2.16}$$

For propagation through layer i, the transfer matrix simply encodes the accumulated phase ϕ_i as

$$\mathbf{M}_i^{[\text{layer}]} = \begin{pmatrix} e^{i\phi_i} & 0 \\ 0 & e^{-i\phi_i} \end{pmatrix} . \tag{2.17}$$

One can then calculate the transfer matrix of the full system as a product of the interface and layer transfer matrices

$$\mathbf{M}'_{ij} = \mathbf{M}_{i,i+1}^{[\text{interface}]} \prod_{l=i+1}^{j} \left(\mathbf{M}_{l-1}^{[\text{layer}]} \mathbf{M}_{l-1,l}^{[\text{interface}]} \right) \tag{2.18}$$

$$= \mathbf{M}_{i,i+1}^{[\text{interface}]} \dots \mathbf{M}_{j-2}^{[\text{layer}]} \mathbf{M}_{j-2,j-1}^{[\text{interface}]} \mathbf{M}_{j-1}^{[\text{layer}]} \mathbf{M}_{j-1,j}^{[\text{interface}]} . \tag{2.19}$$

Transmission and reflection coefficients of the full layer stack can then be extracted from the combined transfer matrix $\mathbf{M}'_{ij}$ by solving Eq. (2.15). In terms of the elements of the transfer matrix defined by

$$\mathbf{M}'_{ij} = \begin{pmatrix} m_{ij}^{00} & m_{ij}^{01} \\ m_{ij}^{10} & m_{ij}^{11} \end{pmatrix} , \tag{2.20}$$

the solution reads

$$r'_{ij} = -\frac{m^{10}_{ij}}{m^{11}_{ij}}\,, \tag{2.21}$$

$$r'_{ji} = \frac{m^{01}_{ij}}{m^{11}_{ij}}\,, \tag{2.22}$$

$$t'_{ij} = \frac{1}{m^{11}_{ij}}\,, \tag{2.23}$$

$$t'_{ji} = m^{00}_{ij} - \frac{m^{01}_{ij} m^{10}_{ij}}{m^{11}_{ij}}\,. \tag{2.24}$$

The multiplicative combination property Eq. (2.18) can also be understood by noting that the transfer matrix relates field amplitudes on one side of the system to field amplitudes on the other side [MS08], as illustrated in Fig. 2.7. That is if the field is of the form

$$\mathbf{E}(\mathbf{r}) = \begin{cases} e^{i\mathbf{k}_{||}\cdot\mathbf{r}} \left(a^+_{\text{bot}} e^{i\mathbf{k}_\perp\cdot\mathbf{r}} + a^-_{\text{bot}} e^{-i\mathbf{k}_\perp\cdot\mathbf{r}}\right) & \text{for } \mathbf{r} \text{ below system} \\ e^{i\mathbf{k}_{||}\cdot\mathbf{r}} \left(a^+_{\text{top}} e^{i\mathbf{k}_\perp\cdot\mathbf{r}} + a^-_{\text{top}} e^{-i\mathbf{k}_\perp\cdot\mathbf{r}}\right) & \text{for } \mathbf{r} \text{ above system} \end{cases}, \tag{2.25}$$

similarly to the ansatz in Fig. 2.5, the transfer matrix relates [MS08]

$$\begin{pmatrix} a^+_{\text{bot}} \\ a^-_{\text{bot}} \end{pmatrix} = \mathbf{M}'_{\text{top,bot}} \begin{pmatrix} a^+_{\text{top}} \\ a^-_{\text{top}} \end{pmatrix} \tag{2.26}$$

Here, the $a^\pm$ amplitude coefficients are chosen to correspond to waves traveling in positive (negative) direction, respectively.

A related quantity is the scattering matrix defined by

$$\begin{pmatrix} a^-_{\text{top}} \\ a^+_{\text{bot}} \end{pmatrix} = \mathbf{S}'_{\text{top,bot}} \begin{pmatrix} a^+_{\text{top}} \\ a^-_{\text{bot}} \end{pmatrix}\,, \tag{2.27}$$

which instead relates the waves traveling towards the system to the waves traveling away from the system. As such, it is directly related to the reflection and transmission coefficients via [MS08]

$$\mathbf{S}'_{ij} = \begin{pmatrix} r'_{ij} & t'_{ij} \\ t'_{ji} & r'_{ji} \end{pmatrix}\,. \tag{2.28}$$

The scattering matrix thus contains the physical observables that we are interested in when performing scattering experiments, while the transfer matrix is useful due to the multiplicative combination property Eq. (2.18). Note that the scattering matrix is not usually not unitary for x-ray cavities, due to the material absorption which is encoded in the imaginary part of the refractive index.

The transfer matrix method was originally invented by Abelès [Abe50] and its application to x-ray cavities in the form of the layer formalism is detailed in [Röh99b; Röh05b], where in particular the polarization scattering problem and multi-channel cases in combination with the nuclear resonance problem are included.

The layer formalism, including various practical aspects relevant for experiments, has been implemented in the software package CONUSS [SG94; Stu00], which has since been tested extensively and found to be in excellent agreement with experiment. Recently, the program was re-implemented in python as the software package PYNUSS [Hee19]. The latter offers largely identical functionalities compared to CONUSS, however, with significant extensions regarding quantum optical applications. We use PYNUSS for much of the work in this thesis.

2.2.2 Shvyd'ko's time-and-space picture

A second semi-classical approach is the time-and-space picture developed by Shvyd'ko [Shv99], which has also been implemented in the software package MOTIF [Shv00]. An application to the layered cavity geometry is further found in PYNUSS [Hee19].

Compared to the layer formalism, the time-and-space picture has many common features. The central difference is that the effective Maxwell equation is replaced by an integro-differential equation [Shv99] in the time-domain

$$\frac{\partial \mathbf{E}(z,t)}{\partial z} = -\int_{-\infty}^{t} dt' \mathbf{K}(t,t') \cdot \mathbf{E}(z,t') \,, \tag{2.29}$$

where we have restricted the problem to a single propagation direction z. The integral kernel $\mathbf{K}(t,t')$ is a matrix in the polarization degrees of freedom and in general has a complicated form [Shv99], which we do not define here in detail. Compared to the layer formalism, this extended wave equation for the resonant scattering allows to include the effects of inelastic scattering and time-dependent Hamiltonians. The former is encoded in an ensemble average containing time-dependent nucleus positions [Shv99] and the latter is included via an ensemble average of the time-dependent nuclear current matrix elements [Shv99].

The relation between the approaches can be understood by considering the special case of *elastic scattering* [Shv99; Röh05b]. In this case, the frequency domain version of the integral kernel [Shv99]

$$\mathbf{K}(\omega,\omega') := \int dt \int dt' \mathbf{K}(t,t') e^{i\omega t} e^{-i\omega' t'} \,, \tag{2.30}$$

is energy conserving, such that [Shv99]

$$\mathbf{K}_{\text{elastic}}(\omega,\omega') = \tilde{\mathbf{K}}_{\text{elastic}}(\omega) 2\pi\delta(\omega-\omega') \,. \tag{2.31}$$

Consequently, the effective wave equation Eq. (2.29) in the frequency domain simplifies to [Shv99]

$$\frac{\partial \mathbf{E}(z,\omega)}{\partial z} = -\tilde{\mathbf{K}}_{\text{elastic}}(\omega) \cdot \mathbf{E}(z,\omega) \,. \tag{2.32}$$

We see that in this special case, the time-and-space picture wave equation has the same form as the effective wave equation Eq. (2.8) in the layer formalism, if we replace $\nabla \times \nabla \times \rightarrow -\frac{\partial}{\partial z}$ (which is a consequence of the slowly-varying envelope approximation and restriction to a single propagation dimension in [Shv99]) and identify

$$\tilde{\mathbf{K}}_{\text{elastic}}(\omega) \rightarrow \frac{\omega^2}{c^2} \boldsymbol{\varepsilon}(\mathbf{r},\omega) \,. \tag{2.33}$$

From a quantum optical perspective, the layer formalism and Shvyd'ko's time-and-space picture are therefore conceptually analogous in that they both describe *semi-classical linear* scattering (for further discussion see Sec. 2.2.4 and Chapter 7) via an effective wave equation encoding the nuclear resonances in a response function. The main generalization introduced by the time-and-space picture is that it allows to describe inelastic scattering and time-dependent hyperfine Hamiltonians.

2.2.3 Maxwell-Bloch equations

With the advent of modern x-ray sources [RES14; Bos16; RE21], the theoretical interest in the community has shifted to go beyond the limitations of the semi-classical linear methods outlined above. A natural first step to describe dynamics at higher x-ray intensities is to remove the linear approximation while still considering semi-classical dynamics. In the quantum optics community, this approach is implemented as the *Maxwell-Bloch equations* [SZ97].

In the context of nuclear x-ray transitions, this approach was already employed by Shvyd'ko [Shv96; Shv99] in the context of the time-and-space picture described in the previous section. However, the linear approximation was incorporated there via assuming the nuclear populations to be in the ground state [Shv99].

Beyond the linear approximation, a Maxwell-Bloch type approach was used by Bürvenich et al. [BEK06] to investigate the feasibility of inducing Rabi oscillations of nuclear $E1$ transitions by x-ray free electron lasers, which was a foundational suggestion for the field of nuclear quantum optics [KK17b; RE21]. Particularly in nuclear forward scattering, the Maxwell-Bloch equations have since been used for a number of investigations [LPK11; JPK12; LPK12; LPK13; KLP14; KP16; LKP16; WL18; Zha19]. Here, we briefly summarize the approach, following the presentation in [Lia13].

The Maxwell-Bloch treatment considers two coupled equations of motion, one for the quantum system in question — the nuclei in our case — and one for the electromagnetic field propagation.

The dynamics for a single nucleus with a single nuclear transition are given by the Master equation in the interaction picture [Lia13]

$$\dot{\rho} = -i[\hat{H}_{\mathrm{nuc}},\, \rho] + \mathcal{L}[\rho]\,, \tag{2.34}$$

where the nucleus-field interaction is given by

$$\hat{H}_{\mathrm{nuc}} = \Omega(t)\hat{\sigma}^{-} + h.c.\,, \tag{2.35}$$

where the driving term is given by $\Omega(t) = \mathbf{d}\cdot\tilde{\mathbf{E}}(\mathbf{r}_{\mathrm{nuc}}, t)$, $\mathbf{d}$ is the dipole moment of the transition and $\tilde{\mathbf{E}}(\mathbf{r}_{\mathrm{nuc}}, t)$ is the electric field in the interaction picture. The spontaneous decay Lindblad term — including both radiative emission and internal conversion in the line width γ — can be written as

$$\mathcal{L}[\rho] = \frac{\gamma}{2}(2\hat{\sigma}^{-}\rho\hat{\sigma}^{+} - \{\hat{\sigma}^{+}\hat{\sigma}^{-},\, \rho\})\,. \tag{2.36}$$

The optical Bloch equations are then given by writing out the Master equation for the matrix elements $\rho_{ab} = \langle a|\,\rho\,|b\rangle$ between the ground and excited state, $|g\rangle$ and$|e\rangle$, respectively, as [SZ97]

$$\dot{\rho}_{gg} = -i\Omega\rho_{eg} + i\Omega^{*}\rho_{ge} + \gamma\rho_{ee}\,, \tag{2.37}$$

$$\dot{\rho}_{ge} = i\Omega(\rho_{gg} - \rho_{ee}) - \frac{\gamma}{2}\rho_{ge}\,, \tag{2.38}$$

$$\dot{\rho}_{eg} = i\Omega^{*}(\rho_{ee} - \rho_{gg}) - \frac{\gamma}{2}\rho_{eg}\,, \tag{2.39}$$

$$\dot{\rho}_{ee} = i\Omega\rho_{eg} - i\Omega^{*}\rho_{ge} - \gamma\rho_{ee}\,. \tag{2.40}$$

Restricting to one propagation dimension z and within certain approximations, including the slowly-varying envelope approximation, the corresponding Maxwell wave equation is [Lia13]

$$\frac{1}{c}\partial_t\tilde{\mathbf{E}}(z,t) + \partial_z\tilde{\mathbf{E}}(z,t) = i\frac{2\pi}{\varepsilon_0\lambda}n\mathbf{d}\rho_{eg}(z,t)\,, \tag{2.41}$$

where λ is the wavelength of the transition and n the nuclear number density.

Variants of this type of approach have been used to study various aspects of nuclear resonant scattering, in particular time-dependent problems in nuclear forward scattering featuring magnetic switching [LPK12; KLP14], building on the early work by Shvyd'ko [Shv96]. However, in particular due to the optical Bloch equation featuring only a single nucleus and neglecting collective effects, there have been doubts whether the Maxwell-Bloch equations actually capture the nuclear dynamics correctly. For example, a heuristic collective enhancement factor was introduced in [JPK12] to calculate nuclear inversion in forward scattering setups. Furthermore, it is not clear whether the semi-classical character of the theory is appropriate at high excitation due to the high coherence of the nuclear transitions and the resulting many-body interactions.

Consequently, there are a number of open questions with respect to the application of Maxwell-Bloch equations in nuclear resonant scattering, some of which we will address in Part IV of this thesis.

2.2.4 Common features and approximation hierarchy

As we have seen, there are a number of related semi-classical approaches to nuclear resonant scattering. In this section, we discuss their relation from a conceptual perspective by starting from a basic cornerstone of quantum optics theory: the light-matter interaction Hamiltonian in the dipole approximation. As we will see, the layer formalism, time-and-space picture and Maxwell-Bloch equation approaches can all be understood as the application of two central approximations of this Hamiltonian: the *semi-classical* and the *linear* approximation. Additional approximations are often employed to simplify the problem, such as the rotating-wave, slowly-varying envelope or Born-Markov approximation, but can in principle be circumvented straightforwardly. We again focus on the conceptual side here, in order to highlight the connection between the different theories, and do not provide detailed derivations.

The basic dipole coupling Hamiltonian

The basic dipole interaction Hamiltonian is given by [SZ97; CTDRG08; Ste19]

$$\hat{H} = \hat{H}_{\text{field}} + \frac{\hbar\omega_{\text{nuc}}}{2}\hat{\sigma}^z - [\mathbf{d}^*\hat{\sigma}^+ + \mathbf{d}\hat{\sigma}^-]\cdot\hat{\mathbf{E}}(\mathbf{r}_{\text{nuc}})\,, \tag{2.42}$$

where the free field Hamiltonian is typically of the form [GL91]

$$\hat{H}_{\text{field}} = \frac{1}{2}\int d^3\mathbf{r}\left[\varepsilon_0|\hat{\mathbf{E}}(\mathbf{r})|^2 + \frac{1}{\mu_0}|\hat{\mathbf{B}}(\mathbf{r})|^2\right]\,. \tag{2.43}$$

This light-matter coupling Hamiltonian is a standard tool used in quantum optics and rather generally describes a single two-level system coupling to the electromagnetic field. The approximations which are necessary to obtain this Hamiltonian are usually well valid for nuclear $E1$ transitions, most notably including the dipole approximation [SZ97] to express the nuclear charge dynamics in a certain energy range as a single two-level system. However, even for $M1$ or higher-order electric multi-pole transitions, a similar form can be derived [Ste19; AP21] (see also Chapter 9).

Note that the simple Hamiltonian above is of course missing various processes which practically occur in nuclear resonant scattering. Most notably, we ignore internal conversion and interaction with the phonon sector leading to the Lamb-Mössbauer factor. However, a look at this most basic Hamiltonian is instructive to uncover the conceptual structure of the various semi-classical theories from a quantum optical perspective. For elastic scattering, the missing processes can also be added straightforwardly, as we discuss in Chapters 7 and 9. In the following, the Hamiltonian Eq. (2.42) is used to identify the central approximations in the semi-classical theory.

Equations of motion

The dynamics of the operators for this Hamiltonian can be expressed by the Heisenberg equations of motion [BP02; CDG97]. For the nuclear lowering operator, we have

$$\dot{\hat{\sigma}}^-(t) = -i\omega_{\text{nuc}}\hat{\sigma}^-(t) - \frac{i}{\hbar}\hat{\sigma}^z(t)\mathbf{d}\cdot\hat{\mathbf{E}}(\mathbf{r}_{\text{nuc}},t)\,. \tag{2.44}$$

For the field operators, we can express the equations of motion in wave equation like form as [SZ97; Shv99; Len20]

$$\nabla\times\nabla\times\hat{\mathbf{E}}(\mathbf{r},t) + \frac{\partial^2}{\partial t^2}\hat{\mathbf{E}}(\mathbf{r},t) = \frac{\omega_{\text{nuc}}^2}{\varepsilon_0\hbar}\delta(\mathbf{r}-\mathbf{r}_{\text{nuc}})[\mathbf{d}^*\hat{\sigma}^+(t) + \mathbf{d}\hat{\sigma}^-(t)] \tag{2.45}$$

where we assumed weak coupling on the scale of the transition frequency (see Chapter 7 for details), as is well justified for most nuclear transitions of interest.

Semi-classical approximation

Taking the expectation values of the operator equations of motion Eq. (2.44), (2.45), we obtain

$$\frac{d}{dt}\langle\hat{\sigma}^-\rangle = -i\omega_{\text{nuc}}\langle\hat{\sigma}^-\rangle(t) - \frac{i}{\hbar}\mathbf{d}\cdot\langle\hat{\sigma}^z\hat{\mathbf{E}}(\mathbf{r}_{\text{nuc}})\rangle\,, \tag{2.46}$$

$$\nabla\times\nabla\times\langle\hat{\mathbf{E}}(\mathbf{r})\rangle + \frac{\partial^2}{\partial t^2}\langle\hat{\mathbf{E}}(\mathbf{r})\rangle = \frac{\omega_{\text{nuc}}^2}{\varepsilon_0\hbar}\delta(\mathbf{r}-\mathbf{r}_{\text{nuc}})[\mathbf{d}^*\langle\hat{\sigma}^-\rangle^* + \mathbf{d}\langle\hat{\sigma}^-\rangle]\,, \tag{2.47}$$

where we have omitted the time-dependencies for brevity.

As a first feature, we note that these equations are not actually closed. Instead the single operator expectation values $\langle\hat{\mathbf{E}}(\mathbf{r})\rangle$, $\langle\hat{\sigma}^-\rangle$ couple to the second-order operator correlation $\langle\hat{\sigma}^z\hat{\mathbf{E}}(\mathbf{r}_{\text{nuc}})\rangle$. If the equations of motion of the latter are computed, one finds coupling to even higher orders. The resulting infinite ladder of coupled correlation functions is known as the BBGKY hierarchy [Bon98].

The first central approximation used in nuclear resonant scattering theory is then the *semi-classical approximation*, also known as mean-field theory, which amounts to factorizing second-order operator correlations, such as [Bon98; SZ97]

$$\langle\hat{\sigma}^z\hat{\mathbf{E}}(\mathbf{r}_{\text{nuc}})\rangle \approx \langle\hat{\sigma}^z\rangle\langle\hat{\mathbf{E}}(\mathbf{r}_{\text{nuc}})\rangle\,. \tag{2.48}$$

Upon inclusion of the equation

$$\frac{d}{dt}\langle\hat{\sigma}^z\rangle = \frac{2i}{\hbar}\mathbf{d}^* \cdot \langle\hat{\mathbf{E}}(\mathbf{r}_{\mathrm{nuc}})\rangle\langle\hat{\sigma}^-\rangle^* - \frac{2i}{\hbar}\mathbf{d} \cdot \langle\hat{\mathbf{E}}(\mathbf{r}_{\mathrm{nuc}})\rangle^*\langle\hat{\sigma}^-\rangle\,, \tag{2.49}$$

the above set of equations is then closed.

Noting that $\langle\hat{\sigma}^-\rangle = \rho_{eg}$ and similarly for the other operators, we recognize that the Maxwell-Bloch equations in Sec. 2.2.3 have an essentially identical form to the above equations, where the presentation in Sec. 2.2.3 featured some additional approximations — such as the slowly-varying envelope approximation to simplify the wave equation, the rotating-wave approximation to condense the source term and a reduction to a single propagation direction. In addition, spontaneous emission as a process resulting from quantum noise is included via a Lindblad-type decay term.

Linear approximation

In the low-excitation regime, one can simplify the situation even further. If one introduces the *linear approximation* [WV06; FKS10; Len20]

$$\langle\hat{\sigma}^z\rangle \approx -1\,, \tag{2.50}$$

the semi-classical treatment becomes a linear set of coupled differential equations. The latter can then be solved via Fourier transforms to obtain a frequency domain solution similar to Eq. (2.8), as it is used in the layer formalism. The linear approximation can also be seen independently of mean-field theory as approximating

$$\langle\hat{\sigma}^z\hat{\mathbf{E}}(\mathbf{r}_{\mathrm{nuc}})\rangle \approx -\langle\hat{\mathbf{E}}(\mathbf{r}_{\mathrm{nuc}})\rangle\,. \tag{2.51}$$

Another closely analogous implementation is the Holstein-Primakoff approximation at linear order [De 14; DBJR18]. We note that the latter has recently been employed in the context of x-ray cavity QED in [AP21], extending previous treatments based on Eq. (2.51) [Len20; KCP20] to account for parameter distributions and potentially allowing to describe few-photon correlations.

Summary of approximations

We thus see that the three approaches in nuclear resonant scattering theory can be understood by a simple hierarchy of approximations. All of them include the semi-classical approximation, ignoring the quantum character of the light field and light-nucleus correlations. The time-and-space picture [Shv99] and scattering theory in the form of the layer formalism [Röh05b] additionally employ the linear approximation, which reduces the nonlinear coupled Maxwell-Bloch equations to a single linear effective wave equation.

We again note that the above presentation is not intended to give a rigorous and detailed derivation of each approach. In practice, various additional approximations are used for convenient simplification. Other physical processes, such as spontaneous decay via internal conversion, may also be included in the equations of motion. For example, the time-and-space picture [Shv99] allows for inelastic scattering by considering the nuclear position as a time-dependent degree of freedom entering in an ensemble average.

That said, the semi-classical and linear approximations are the key conceptual steps to make the problem tractable in the first place. They are also the central limitations of the existing approaches to nuclear resonance scattering, since quantum optical phenomena involve nonlinear dynamics and quantum correlations. Within the above framework, one can gain insight into how to potentially go beyond these approximations, which is one of the main topics of this thesis.

2.3 The quantum optical pXCQED model

Motivated by experiments which pointed out quantum effects in the x-ray cavities doped with Mössbauer nuclei [Röh10; Röh12; Hee13] (see Sec. 2.1.3), a quantum optical model for the system was developed by Heeg&Evers in [HE13], which we refer to as pXCQED (**p**henomenological **x**-ray **c**avity **q**uantum **e**lectro**d**ynamics) model. The approach allows to interpret linear scattering spectra in terms of quantum optical level schemes and further opened the door to investigate the nonlinear and quantum correlated regime [HKE16; Hee14]. With regards to the former aspect, the model has been

tremendously successful in describing experiments at synchrotron facilities [Hee13; Hee14; Hee15a; Hee15b; Hab16a; Hab16b; Hab17; Hab19].

In this section, we summarize the pXCQED model, focusing on its structure and central features. The model was originally developed for a single cavity mode and nuclear layer in [HE13], and extended to multiple cavity modes and nuclear ensembles in [HE15]. For simplicity and illustration purposes, we consider the simplest possible case in the following. That is we neglect polarization and consider only one cavity mode interacting with a single nuclear ensemble without hyperfine splitting. This setup demonstrates the working principle of the theory and lays a foundation for the generalizations to be developed in Chapter 6 and Part II. For a more detailed summary of the multi-mode version of the model, we refer to Sec. 6.2.

2.3.1 Mode-nuclei Master equation

In brief, the model can be written as a master equation for the nuclei coupling to the cavity as [HE13]

$$\dot{\rho} = -i[H_{\mathrm{M}} + H_{\mathrm{N}}, \rho] + \mathcal{L}_{\mathrm{M}}[\rho] + \mathcal{L}_{\mathrm{SE}}[\rho]\,, \tag{2.52}$$

where ρ is the combined density matrix of the nuclei and cavity modes. Each of the terms in the Hamiltonian and their physical meaning is explained separately in the following.

Cavity Hamiltonian

The cavity Hamiltonian H_M is [HE13]

$$H_{\mathrm{M}} = \omega_{\mathrm{C}}(\theta)\hat{a}^\dagger\hat{a} + i\sqrt{2\kappa_R}\left(a_{\mathrm{in}}e^{-i\omega t}\hat{a}^\dagger - h.c.\right), \tag{2.53}$$

where $a^\dagger$ (a) is the cavity mode creation (annihilation) operator, defined by the commutation relation $[a, a^\dagger] = 1$. $\omega_C(\theta)$ is the resonance frequency of the cavity mode as a function of the incidence angle θ such that the first term in H_M is the free evolution of the cavity mode. The second term is a classical driving term, where a_{in} is the driving strength, ω the driving frequency and $\sqrt{2\kappa_R}$ the coupling strength between the external driving field and the cavity mode. Such a term can be obtained from a a system-bath coupling term $i\sqrt{2\kappa_R}\left(ba^\dagger - h.c.\right)$ if the external mode b is in a coherent state [Bet16].

In the interaction picture where the driving becomes time independent, the Hamiltonian then reads [HE13]

$$H_{\mathrm{M}}^{(I)} = \Delta_{\mathrm{C}}(\theta)\hat{a}^\dagger\hat{a} + i\sqrt{2\kappa_R}\left(a_{\mathrm{in}}\hat{a}^\dagger - h.c.\right), \tag{2.54}$$

with $\Delta_C(\theta) = \omega_C(\theta) - \omega$. The functionality of the cavity detuning with incidence angle is given by [HE13]

$$\Delta_{\mathrm{C}}(\theta) = \sqrt{\omega^2\cos^2(\theta) + \omega_0^2\sin^2(\theta_0)} - 1 \tag{2.55}$$

$$\approx \delta_{\mathrm{C}}\Delta\theta, \tag{2.56}$$

where the approximation applies in grazing incidence. θ_0 is the resonance angle at frequency ω_0, $\Delta\theta = \theta - \theta_0$ and $\delta_{\mathrm{C}} = -\omega\theta_0$.

Cavity mode losses

Spontaneous emission from a cavity mode to the surrounding environment is included via the Linblad term [HE13]

$$\mathcal{L}_{\mathrm{M}}[\rho] = -\kappa\mathcal{L}[\rho, \hat{a}^\dagger, \hat{a}]$$

for the mode operator [HE13], where κ is the overall decay rate from the mode and the Linblad operator is defined by [Lin76; BP02]

$$\mathcal{L}[\rho, \mathcal{O}^\dagger, \mathcal{O}] = \mathcal{O}^\dagger\mathcal{O}\rho + \rho\mathcal{O}^\dagger\mathcal{O} - 2\mathcal{O}\rho\mathcal{O}^\dagger.$$

Nuclear Hamiltonian

The nuclear Hamiltonian H_N including the free evolution and the mode-nucleus coupling is [HE13]

$$H_{\mathrm{N}} = \omega_g \sum_n |g_n\rangle \langle g_n| + \omega_e \sum_n |e_n\rangle \langle e_n| + \sum_{n \in \mathrm{nuclei}} (g_n \hat{\sigma}_n^+ \hat{a} + h.c.), \tag{2.57}$$

with $|g\rangle$ ($|e\rangle$) being the ground (excited) state of the nucleus and ω_g (ω_e) the corresponding frequency. $\hat{\sigma}_n^+$ is the raising operator for the $|g_n\rangle \rightarrow |e_n\rangle$ transition of nucleus n. g_n is the coupling constant between the cavity mode and the transition, which typically includes a phase ϕ_n along the ensemble induced by the pane wave excitation, such that $g_n = ge^{i\phi_n}$ [HE13]. The sum over each nucleus within the ensemble encodes the collective character of the induced excitations [HKE16].

The interaction picture version of the above Hamiltonian is [HE13]

$$H_{\mathrm{N}}^{(I)} = -\Delta \sum_n \hat{\sigma}_n^+ \hat{\sigma}_n^- + \sum_n (g_n \hat{\sigma}_n^+ \hat{a} + h.c.) \tag{2.58}$$

where $\Delta = \omega - \omega_0$ and $\omega_0 = \omega_e - \omega_g$ is the transition frequency, that is 14.4 keV for the example of ^{57}Fe [Röh05b].

Nuclear decay

The nuclear decay via spontaneous emission and internal conversion is accounted for by the Lindblad term [HE13]

$$\mathcal{L}_{\mathrm{SE}}[\rho] = -\frac{\gamma}{2} \sum_n \mathcal{L}[\rho, \hat{\sigma}_n^+, \hat{\sigma}_n^-] \tag{2.59}$$

where γ is the natural linewidth for the transition, which takes a value of 4.7 neV for the example of ^{57}Fe [Röh05b]. Note that it includes both radiative spontaneous emission and internal conversion processes [HE13].

2.3.2 Nuclei-only Master equation

So far, we have outlined the model presented in [HE13] including both the nuclei and the cavity modes in the Master equation. Conveniently, the modes can usually be adiabatically eliminated, resulting in a Master equation for the nuclei alone [HE13], which we summarize in the following.

Adiabatic elimination of the cavity modes

Within the above model, the Heisenberg equation of motion for the cavity mode reads [HE13]

$$\dot{\hat{a}} = i[H_{\mathrm{M}}^{(I)} + H_{\mathrm{N}}^{(I)}, \hat{a}] - \kappa \hat{a}. \tag{2.60}$$

Adiabatic elimination of the cavity mode is then achieved by setting $\frac{d}{dt}\hat{a} = 0$ in the interaction picture. This step assumes that the cavity mode is in a steady state, which is a valid approximation if both

- the cavity lifetime set by $1/\kappa$ is much smaller than the pulse length of the driving field, such that the pulse is approximately constant on the scale of the cavity dynamics [HE13],
- and κ is much larger than g, which means that the cavity dynamics are governed by fast dissipation on the timescale of the nuclear dynamics [HE13].

The second of these criteria is also known as the bad cavity regime and both approximations are typically valid for nuclear resonance scattering experiments [HE13].

Performing the adiabatic elimination yields the mode operator in terms of the nuclear operators and driving field [HE13] as

$$\hat{a} \approx \frac{\sqrt{2\kappa_R} a_{\mathrm{in}} - i \sum_n g_n^* \hat{\sigma}_n^-}{\kappa + i\Delta_{\mathrm{C}}(\theta)}. \tag{2.61}$$

The Master equation

Substituting into the full Master equation Eq. (2.52) and absorbing the coupling phase into an operator rotation [Hee14], one then obtains effective equations of motion for the nuclei [Hee14]

$$\frac{\mathrm{d}}{\mathrm{d}t}\rho^{(\mathrm{nuc})} = -i[H_{\mathrm{eff}}, \rho] + \mathcal{L}_{\mathrm{eff}}[\rho] \tag{2.62}$$

with [Hee14]

$$H_{\mathrm{eff}} = -\Delta \sum_n \hat{\sigma}_n^+ \hat{\sigma}_n^- - g^2 \delta_{\mathrm{LS}} \sum_{n,m} \hat{\sigma}_n^+ \hat{\sigma}_m^- + \sum_n (\Omega a_{\mathrm{in}} g \hat{\sigma}_n^+ + h.c.) \tag{2.63}$$

and [HE13]

$$\mathcal{L}_{\mathrm{eff}}[\rho] = -\zeta_S g^2 \sum_{n,m} \mathcal{L}[\rho, \hat{\sigma}_n^+, \hat{\sigma}_m^-] + \mathcal{L}_{\mathrm{SE}}[\rho]. \tag{2.64}$$

The quantum optical parameters in the above effective equations of motions are defined as [HE13]

$$\Omega = \frac{\sqrt{2\kappa_R}}{\kappa + i\Delta_{\mathrm{C}}}, \tag{2.65}$$

$$\delta_{LS} = -\frac{\Delta_{\mathrm{C}}}{\kappa^2 + \Delta_{\mathrm{C}}^2} = \mathrm{Im}\left[\frac{1}{\kappa + i\Delta_{\mathrm{C}}}\right], \tag{2.66}$$

and

$$\zeta_S = \frac{\kappa}{\kappa^2 + \Delta_{\mathrm{C}}^2} = \mathrm{Re}\left[\frac{1}{\kappa + i\Delta_{\mathrm{C}}}\right]. \tag{2.67}$$

This nuclei-only Master equation is useful, since it features fewer degrees of freedom than with the modes included. Consequently, its quantum dynamics can be tackled in the linear [HE13] and nonlinear regime [HKE16] (see also Part IV).

2.3.3 Spectroscopic observables

Since the Hamiltonian describing the cavity mode and external driving in the pXCQED model is of so-called Gardiner-Collett form [GC85] one can use input-output relations (see also Chapters 3 and 4 for details) to relate the outgoing field to the cavity field via [HE13]

$$\hat{a}_{\mathrm{out}} = -\hat{a}_{\mathrm{in}} + \sqrt{2\kappa_R}\hat{a}. \tag{2.68}$$

Substitution of Eq. (2.61) results in an expression for the reflection coefficient in terms of the nuclear operator expectation, which reads [HE13]

$$R = \frac{\langle \hat{a}_{\mathrm{out}} \rangle}{a_{\mathrm{in}}} = \underbrace{\frac{2\kappa_R}{\kappa + i\Delta_{\mathrm{C}}(\theta)} - 1}_{\text{pure cavity, } R_{\mathrm{C}}} \underbrace{- \frac{i}{a_{\mathrm{in}}} \frac{\sqrt{2\kappa_R}}{\kappa + i\Delta_{\mathrm{C}}(\theta)} \sum_n g_n^* \langle \hat{\sigma}_n^- \rangle}_{\text{nuclear contribution, } R_{\mathrm{N}}}. \tag{2.69}$$

The reflection coefficient of a nuclear ensemble in an x-ray cavity can then be calculated directly, if the nuclear dynamics given by $\langle \hat{\sigma}_n^- \rangle$ are known.

The latter can be obtained by solving the Master equation Eq. (2.62). For example, in the linear regime — that is for small driving strength a_{in} (see also Chapter 12) — the solution for the expectation value of the nuclear ensemble coherences $\langle \hat{\sigma}_n^- \rangle$ can be obtained analytically, resulting in [HE13]

$$R = \underbrace{\frac{2\kappa_R}{\kappa + i\Delta_{\mathrm{C}}(\theta)} - 1}_{\text{pure cavity, } R_{\mathrm{C}}} \underbrace{- i \frac{|g|^2 \Omega^2}{\Delta - |g|^2 \delta_{\mathrm{LS}} + i\left(\frac{\gamma}{2} + |g|^2 \zeta_{\mathrm{S}}\right)}}_{\text{nuclear contribution, } R_{\mathrm{N}}}. \tag{2.70}$$

We see that the nuclear contribution is a Lorentzian resonance on the cavity background with cavity Lamb shift [HE13] (see also Chapter 10)

$$\Delta_{\mathrm{LS}} = |g|^2 \delta_{\mathrm{LS}} \tag{2.71}$$

and superradiance [HE13]

$$\gamma_S = 2|g|^2 \zeta_{\mathrm{S}}\,. \tag{2.72}$$

For $\Delta_{\mathrm{C}} \neq 0$, the combined lineshape further results in an asymmetric Fano curve [HE13] due to phase-dependent interference between the nuclear line and cavity background (see also Chapter 11).

2.3.4 Generalizations and nonlinear effects

For simplicity, we have considered a simple special case of the model here. The fully general version developed in [HE13; HE15] includes polarization, magnetic hyperfine splitting, multiple cavity modes and multiple nuclear ensemble. Further generalizations have been considered, including coupled modes in separate cavities [Hab17], optical lattices of many resonant layers [Hab16a], and the effect of transition edges for electronic transitions [Hab19]. Time-dependent observables beyond simple energy reflection spectra have also been investigated [Hee15b] .

Beyond these considerations of the precise setup and cavity geometry, one exciting prospect is the possibility of nonlinear effects [Hee14] in such systems, which can in principle be described using the pXCQED model. Indeed, a recent method [Hee14; HKE16] allowed to solve the Master equation Eq. (2.62) beyond the linear approximation via a mapping to the Dicke model [Dic54]. The case of nonlinear excitation is discussed in more detail in Part IV of this thesis.

2.3.5 Practical application

Parameter fitting

The power of the pXCQED model lies in the quantum optical interpretation of the nuclear spectra, which has already led to numerous experimental applications [Hee13; Hee15a; Hee15b; Hab16a; Hab17; Hab19] (compare Sec. 2.1.3). The model has been verified in this context and found to be in excellent agreement with experiment and simulation [Stu00; Hee19].

The way the model was used in these works is by setting up the appropriate Master equation for the system under consideration, including the relevant physical processes, and subsequently fitting the model parameters to linear scattering observables [HE13; HE15]. The latter can either be obtained from experiment or from the semi-classical scattering theory summarized in Sec. 2.2.1.

For example, in the simple single mode single ensemble case considered above, the constants κ, κ_R, g and δ_C form a complete set of quantum optical parameters to model the system [HE13]. Beyond the low excitation regime, the number of coherently interacting nuclei N also constitutes an important quantity [HKE16]. The latter has to be estimated through other methods, since it is not encoded in the linear observables [HKE16], where only the number density turns out to be relevant [Len20] (see also Chapter 7).

Heuristic extensions

Particularly in the multi-mode multi-ensemble case, the fitting procedure can be rather tricky, since a large number of parameters have to be determined from limited data [HE15]. Nevertheless and rather interestingly, it was found that even the most general model was unable to explain certain experimental observations [Hee14; Hee15a; HE15].

A particular effect that could not be explained at first is an unforeseen shift in the collective Lamb shift signature. According to Eq. (2.66), the pXCQED model predicts zero Lamb shift at the cavity resonance where $\Delta_C = 0$, corresponding to an incidence angle of minimum cavity reflectance. In [Röh10], however, a non-zero Lamb shift was found in this configuration, which has since been verified in other cavities [Hee14; Hee15a].

To include this effect in the theoretical model, a heuristic dispersion phase ϕ_C was added, introducing an asymmetry of the cavity resonance line [HE15]. This phase essentially shifts the energy of the cavity mode relative to the associated minimum in the reflection curve [HE15], such that a non-zero collective Lamb shift is allowed at the latter.

In the multi-mode case [HE15], it was found that further heuristic extensions are necessary. In particular, an envelope function $R_\mathrm{envelope}(\theta)$ was introduced in [HE15] to account for the reflection from the topmost cladding layer of the cavity.

Both of these heuristic extensions are implemented by a modified form of the cavity reflection coefficient compared to Eq. (2.69), which reads [HE15]

$$R_\mathrm{C}(\theta) = R_\mathrm{envelope}(\theta)\left(\frac{2\kappa_R}{\kappa + i\Delta_\mathrm{C}(\theta)} - e^{i\phi_\mathrm{C}}\right) . \tag{2.73}$$

2.4 Open problems

Despite the various existing theory approaches to nuclear resonance scattering, there are a number of open problems connected to the nonlinear quantum optics frontier. The semi-classical scattering theories commonly employed for modeling current experiments cannot be applied in the nonlinear regime, since they are based on the linear approximation and the resulting effective wave equations. The semi-classical approach without a linear approximation in the form of the Maxwell-Bloch equations is in principle not limited to low excitation, but nevertheless expected to be unsuitable in the nonlinear regime due to collective effects featuring in nuclear ensembles [JPK12; HKE16].

Consequently, the main focus with regards to interpreting quantum optical effects [Hee13; Hee15a; Hee15b; Hab16a; Hab17; Hab19] and describing nonlinear quantum dynamics [HKE16] of nuclear ensembles in x-ray cavities has been on the pXCQED model. Compared to the semi-classical approaches, its unique feature is that it is based on a many-body Master equation, which captures collectivity and coherent interactions across the nuclear ensemble. The resulting excitation and decay dynamics have already been solved approximately in [HKE16], providing first predictions for expected inversion fractions at current and upcoming XFEL sources.

However, there are different concerns casting doubts on the validity of the pXCQED model at higher excitation, which we briefly summarize in the following.

- In particular, the necessity of heuristic extensions to capture various effects [HE15; Hee14] has raised questions. The origin of the dispersion phase and envelope reflection term is currently unknown and their implications for the predictive power of the model at higher intensities is unclear.

- Beyond these explicit factors, the phenomenological character of the model means that its microscopic origin and implicit approximations are not understood. One example is that the structure of the assumed Hamiltonian indicates that only a single parallel wave vector of the cavity field participates in the dynamics. While this approximation is natural at low excitation, where the parallel wave vector is a conserved quantity, the implications of this approximation at higher intensities have not been discussed (see Chapter 13 for details).

- Even with heuristic extensions, the model features discrepancies in the case of EIT cavities [HE15], which are currently unresolved and may result in a different interpretation of the underlying level scheme.

- Besides questions with regards to nonlinear dynamics, the fitting procedure has also hindered a straightforward and numerically efficient calculation of nuclear level schemes in general x-ray cavity structures. In particular, in the presence of multiple ensembles and modes [HE15], the fitting procedure is rather intricate and requires careful tuning of parameter ranges. Consequently, progress in the direction of inverse designing desired nuclear level schemes [LKE16; BB20] has been prevented up to now.

Thesis outline from a theory perspective

A detailed thesis outline has already been given in Chapter 1. In the following, we provide a second brief outline from a nuclear resonance scattering theory perspective.

As a main result, the origin of the pXCQED model is fully explained in Chapters 6 and 7. Our approach provides a numerically efficient way to calculate nuclear level schemes, and applications in inverse design are already being explored on this basis [Die21]. Chapter 8 further resolves the previously encountered discrepancies for EIT cavities. Chapters 10 and 11 investigate novel multi-mode effects on nuclear ensembles, which result from the high leakage of thin-film x-ray cavities and are connected to the heuristic dispersion phase discussed above.

In the context of nonlinear dynamics, our approach provides a well-understood Master equation upgrading and extending the reach of the pXCQED model. On this basis, we provide a new estimation of ensemble excitation fractions at current x-ray facilities in Chapter 12. Potential approaches to solving the resulting Master equations on the longer time scales of nuclear dynamics are discussed in Chapter 13.

Part I

Ab initio few-mode theory

Chapter 3

Background - Few-mode theories in quantum optics

As outlined in Chapter 1, this part of the thesis addresses the problem of how to derive Jaynes-Cummings type few-mode models for open resonators from first principles, which had been an open question in quantum optics. The theory is outlined in Chapters 4 and 5. Applications to x-ray cavity QED are presented in Chapter 6.

The method to be developed is motivated by open questions in x-ray cavity QED as outlined in Sec. 2.4, but has broader implications for quantum optics and relations to the theory of light-matter interactions in general. To understand our results, theoretical background for different perspectives on the problem is required, which goes beyond the nuclear resonance scattering background given in Chapter 2. To this end, we will briefly survey a few standard approaches in the theory of light-matter interactions and their connections in the following. The chapter is partially based on [LE20], but provides a different point of view within the framework of this thesis and takes into account recent progress.

3.1 Goal of this chapter

The aim of this chapter is two-fold. First of all, we provide a background on common theoretical methods in cavity QED. In particular, we give an overview of Jaynes-Cummings type models, which are a cornerstone of light-matter interaction theory, in Sec. 3.2. We further introduce the seminal input-output formalism in Sec. 3.3, which provides access to spectroscopic observables.

A second goal of this chapter is to provide a particular perspective on these standard methods, in order to clarify the open problem outlined in Chapter 1. At its core, the central question we will address in Chapters 4 to 6 is how to relate Jaynes-Cummings like few-mode models [JC63] to the fundamental light-continuum interaction Hamiltonian for open resonator QED. The associated theory problem is illustrated in Fig. 3.1 and will be explained in detail in this chapter.

In this context, this background chapter provides a comparative perspective on few-mode and continuum approaches to light-matter interactions. In particular, we discuss why matter-continuum models are difficult to solve in certain regimes in Sec. 3.2.2. We then illustrate why few-mode theory is useful and why it is typically employed phenomenologically in Sec. 3.3.1.

A brief summary of open problems in few-mode theory and the current discussion in the literature is given in Sec. 3.4. We further provide a motivation for why an understanding of the connection between the two sides in Fig. 3.1 is important with regards to current experimental regimes in Sec. 3.5. Recent progress and alternative approaches to the underlying physics are discussed in Sec. 3.6.

3.2 Jaynes-Cummings type few-mode models

3.2.1 The basic model and its generalizations

The Jaynes-Cummings model [JC63] is a seminal tool in the theory of light-matter interactions. In its most basic form, it describes the coupling of a two-level system to a single mode of the quantized electromagnetic field. The Hamiltonian reads [SZ97; HR06]

$$\hat{H}_{\mathrm{JC}} = \omega_{\mathrm{a}} \frac{\hat{\sigma}^z}{2} + \omega_{\mathrm{mode}} \hat{a}^\dagger \hat{a} + g \hat{\sigma}^+ \hat{a} + g^* \hat{\sigma}^- \hat{a}^\dagger \,, \tag{3.1}$$

where g is the coupling constant between the bosonic field mode $\hat{a}$ and the two-level system. ω_{a} is the two-level system's transition frequency, where the subscript "a" stands for atom. For details on the operators involved see Appendix A.2.

Already in this simple form, the Jaynes-Cummings model is able to describe various phenomena from weak to strong light-matter coupling, such as vacuum Rabi oscillations of an initially excited atom [Aga85; Aga12] and the non-linearity of multi-excitation states [Fin08].

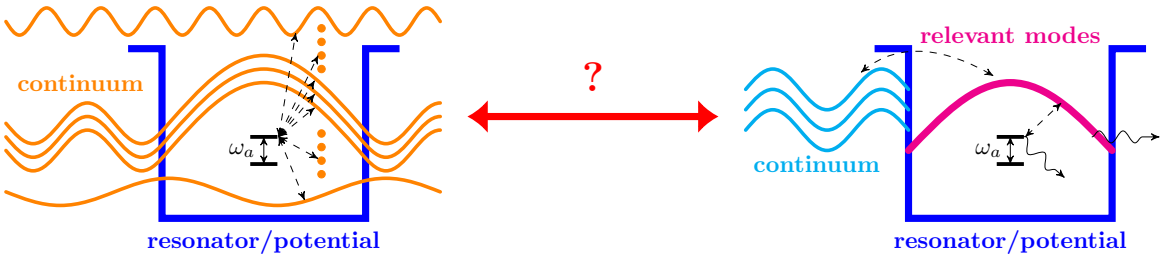

Figure 3.1: Illustration of an open problem in resonator QED. The left hand side schematically depicts the typical structure of light-matter interaction theories, where a quantum level system couples to a continuum of the electromagnetic field (details see text), which may be structured by a resonator. The right hand side depicts a typical Jaynes-Cummings like model approach to the same system (details see text), where the level system only couples to a few relevant modes, which in turn couple to an external continuum bath. The open problem, which we address in this part of the thesis, is how the two sides relate to each other. This figure was inspired by related figures in [LE20], which also feature in Chapters 4 and 5.

Variations and extensions of the model allow to include other effects. For example, including external semi-classical fields allows to describe driven Rabi oscillations [SZ97]. Multiple modes of the electromagnetic field can also be included straightforwardly [SZ97], giving a Hamiltonian such as

$$\hat{H}_{\mathrm{JC,driven,multi}} = \omega_{\mathrm{a}} \frac{\hat{\sigma}^z}{2} + \sum_\lambda \omega_\lambda \hat{a}_\lambda^\dagger \hat{a}_\lambda + \sum_\lambda (g_\lambda \hat{\sigma}^+ \hat{a}_\lambda + h.c.) + \sum_\lambda (\Omega_{\mathrm{drive},\lambda} \hat{a}_\lambda + h.c.)\,. \tag{3.2}$$

In the context of resonator QED, an important class of processes are losses from the modes and from the two-level system, which are usually accounted for in a Master equation framework [SZ97; BP02; Car93]. An example for a typical Lindblad term for leakage from the modes is

$$\mathcal{L}_{\mathrm{cav}}[\rho] = \sum_\lambda \kappa_\lambda \left(2\hat{a}_\lambda \rho \hat{a}_\lambda^\dagger - \{\hat{a}_\lambda^\dagger \hat{a}_\lambda, \rho\} \right) , \tag{3.3}$$

where $\{\cdot,\cdot\}$ denotes the anti-commutator. The resulting Master equation

$$\dot{\rho} = -i \left[\hat{H}_{\mathrm{JC}}, \rho \right] + \mathcal{L}_{\mathrm{cav}}[\rho] \tag{3.4}$$

is then one of the simplest possible descriptions of a two-level system interacting with the light field. This class of Hamiltonians features in most modern quantum optics textbooks (e.g. [SZ97; WM08; Car93; HR06]) and has found a multitude of practical applications.

In many scenarios, one may find that the assumptions or approximations entering the above model are no longer valid. At large coupling strengths, for example, counter-rotating coupling terms beyond the rotating wave approximation are required, leading to the quantum Rabi model [Rab36; Bra11; Ros17] (see [FK19; FD19] for recent reviews). For multiple atoms or many-body systems, generalized Hamiltonians such as the Tavis-Cummings [TC69] and the Dicke model [Dic54; Kir19; Gar11] are often considered. Here, we will not go into detail in this direction and we mainly mention these examples to illustrate the importance of few-mode models in quantum optics theory.

A central aspect to note is that, especially in resonator QED, the above model Hamiltonians are usually employed in a phenomenological way. That is, a model including all necessary physical processes is set up and its parameters are subsequently fit to data. For the case of a perfectly closed cavity, the Hamiltonian is usually motivated via boundary conditions at perfectly reflecting mirrors, canonical quantization and the minimal coupling prescription [SZ97]. Practically, however, resonators feature losses to their surroundings, which are encoded in Lindblad terms such as Eq. (3.3). In the presence of such losses, the electromagnetic field is non-zero in and around the resonator, such that no boundary conditions can be imposed. The latter then results in the phenomenological nature of the model, which has been tremendously successful for good resonators, but can become problematic in other regimes.

For example, within x-ray cavity QED, we are mainly interested in the application to nuclear quantum systems and the thin-film geometry, where the relevant physical processes are given by the pXCQED model [HE13; HE15]. The latter is essentially a many-body version of the Jaynes-Cummings form (closely related to the Dicke model [HKE16]) and also employs a fitting procedure

to semi-classical data to fix the parameters (see Chapter 2 and Chapter 6 for details). However, due to the extreme regimes of the nuclear x-ray quantum optics platform, certain issues were identified [HE15; Hee15a] which are not commonly encountered at optical energies. As we show in Chapter 6, these problems are directly linked to the phenomenological character of the Jaynes-Cummings description and a first principles derivation is required for their resolution.

3.2.2 Few-mode versus continuum coupling

Interestingly, Jaynes-Cummings like few-mode descriptions are not the only class of Hamiltonians one encounters in the theory of light-matter interactions. In the following, we describe continuum Hamiltonians as they are commonly used for the quantized description of the light-field and contrast the two approaches. This perspective is intended to illustrate the open problem depicted in Fig. 3.1.

Continuum interaction Hamiltonians

In first principles theory, the electromagnetic field features a continuum of modes over the frequency spectrum. The basic quantum optics Hamiltonian of the free field is usually written as [SZ97; CDG97]

$$\hat{H}_{\text{field}} = \sum_p \int d^3\mathbf{k}\, \omega(\mathbf{k}) \hat{c}_p^\dagger(\mathbf{k}) \hat{c}_p(\mathbf{k}) \tag{3.5}$$

and can be understood as a non-relativistic limit of the full QED Hamiltonian, involving multiple approximations which are usually applicable in quantum optics, unless extreme coupling regimes [FK19; FD19], field strengths [Di 12] or other complications [SN21] are considered.

The interaction with an atom can also be described on various levels of detail. One of the most basic Hamiltonians, involving the two-level, rotating-wave and various other approximations for the interaction [SZ97] and omitting polarization as well as spatial degrees of freedom on the field side, is given by

$$\hat{H}_{\text{light-matter}} = \omega_{\text{a}} \frac{\hat{\sigma}^z}{2} + \int d\omega\, \omega \hat{c}^\dagger(\omega)\hat{c}(\omega) + \int d\omega \left[g(\omega)\hat{c}(\omega)\hat{\sigma}^+ + h.c. \right] \tag{3.6}$$

For the case of dielectric resonators, similar Hamiltonians can be derived [Kri14], where the central difference compared to free space is the magnitude and frequency structure of the coupling $g(\omega)$. In the absence of absorption, the underlying theory was given by Glauber&Lewenstein [GL91] and is of the precise form of the above continuum Hamiltonian. For more complex media featuring effects such as absorption, a common approach is macroscopic QED (see [SB08] and references therein), whose Hamiltonian can also be reduced to a similar form [BW08b; Med21].

We see that while this model features a closely related operator structure to the Jaynes-Cummings Hamiltonian Eq. (3.1), the central difference is the coupling to a continuum of modes. As an important consequence, radiative loss processes are already included in this Hamiltonian and do not have to be added in a phenomenological fashion. However, the continuum aspect complicates the solution of the associated quantum dynamics, as we discuss in the following.

Master equations and Wigner-Weisskopf theory

To gain further insight, we briefly review a standard approach to solve the dynamics of the matter-continuum Hamiltonian: Markovian Master equations and the related Wigner-Weisskopf theory.

At weak light-matter coupling, one can conveniently eliminate the electromagnetic continuum completely by tracing it out within a Born-Markov approximation [SZ97; BP02]. For the case of our simple two-level system given by Eq. (3.6) and when the field is in the vacuum state, the resulting Master equation for spontaneous emission reads [BP02]

$$\dot{\rho} = -i \left[\hat{H}_{\text{atom}}, \rho \right] + \mathcal{L}_{\text{SE}}[\rho] \,, \tag{3.7}$$

$$\mathcal{L}_{\text{SE}}[\rho] = \frac{\gamma}{2} (2\hat{\sigma}^- \rho \hat{\sigma}^+ - \{\hat{\sigma}^+\hat{\sigma}^-,\, \rho\}) \,, \tag{3.8}$$

The Born-Markov approximation requires the light-matter interaction to be weak, such that perturbation theory applies, and that the environment does not feature memory effects. A detailed discussion

of its applicability can be found elsewhere [BP02]. For our purposes, it is sufficient to note that the approximation breaks down at strong light-matter coupling [BP02; Gar97a].

We see that within the Born-Markov approximation, an excited two-level system will only decay radiatively while evolving under its free Hamiltonian $\hat{H}_{\text{atom}}$. These dynamics therefore indeed do not feature strong coupling effects such as vacuum Rabi oscillations [Aga85; Kri14].

An approach featuring similar approximations is Wigner-Weisskopf theory. There, the specific scenario of the decay of the excited state of the two-level system is investigated. Since the derivation is rather instructive, we will briefly summarize it in the following to illustrate its limitations and breakdown at strong coupling [Gar97b]. We closely follow the presentation in [Kri14; MPT17].

We firstly note that due to the rotating wave approximation, the light-matter Hamiltonian Eq. (3.6) only couples the states $|n_\omega\rangle_{\text{ph}} |g\rangle_{\text{a}}$ to $|(n-1)_\omega\rangle_{\text{ph}} |e\rangle_{\text{a}}$, such that the total excitation number is conserved [MPT17]. Here, $|n_\omega\rangle_{\text{ph}}$ is a photonic state with photon number n at frequency ω and $|g\rangle_{\text{a}}$ ($|e\rangle_{\text{a}}$) is the ground state (excited state) of the atom.

When the initial state is the fully excited atom with the photon field in the vacuum state, we are then restricted to the single excitation subspace. An ansatz for the corresponding time-dependent wave function is [Kri14]

$$|\Psi(t)\rangle = c(t) |0\rangle_{\text{ph}} |e\rangle_{\text{a}} + \int d\omega c_\omega(t) |1_\omega\rangle_{\text{ph}} |g\rangle_{\text{a}} \,. \tag{3.9}$$

Evaluating the Schrödinger equation $\hat{H} |\Psi(t)\rangle = i\partial_t |\Psi(t)\rangle$ gives the coefficient equations of motion

$$i\dot{c}(t) = \frac{\omega_{\text{a}}}{2} c(t) + \int d\omega g(\omega) c_\omega(t) \,, \tag{3.10}$$

$$i\dot{c}_\omega(t) = \left[\omega - \frac{\omega_{\text{a}}}{2}\right] c_\omega(t) + g^*(\omega) c(t) \,. \tag{3.11}$$

Formally solving the second equation and substituting, this coupled system of equations can be reduced to the integro-differential equation [Kri14]

$$\dot{\tilde{c}}(t) = -\int d\omega |g(\omega)|^2 \int_{t_0}^{t} dt' \tilde{c}(t') e^{i(\omega_a - \omega)(t-t')} \,, \tag{3.12}$$

where $\tilde{c}(t) = c(t) e^{i\frac{\omega_{\text{a}}}{2} t}$.

While this equation may seem simple enough to tackle numerically, its solution practically involves multiple complications. The seminal approach by Wigner and Weisskopf [Wei33; SZ97; MPT17] assumed that the frequency integral can be simplified by evaluating the coupling constant at the resonant frequency of the atom. The idea behind this approach is that at weak coupling, the atom selects a narrow frequency window where the environment response is approximately constant. The equation then simplifies to [MPT17]

$$\dot{\tilde{c}}(t) = -|g(\omega_{\text{a}})|^2 \int d\omega \int_{t_0}^{t} dt' \tilde{c}(t') e^{i(\omega_a - \omega)(t-t')} \,. \tag{3.13}$$

The frequency integral typically runs from zero to infinity, but can approximately be extended at the lower end to negative infinity [MPT17]. Using the Fourier resolution of the Dirac δ-function (see Appendix A.3), we then obtain the simple decay equation

$$\dot{c}(t) = \left[-i\frac{\omega_{\text{a}}}{2} - 2\pi |g(\omega_{\text{a}})|^2\right] c(t) \,. \tag{3.14}$$

Within Wigner-Weisskopf theory, the excited state therefore also simply decays in addition to its free phase oscillation. Noting that the evolution of the reduced density matrix of the atom can also be obtained by tracing out the photon states in the Wigner-Weisskopf ansatz Eq. (3.9), this behavior can be seen as analogous to the Lindblad term Eq. (3.8) with a decay constant

$$\gamma = 2\pi |g(\omega_{\text{a}})|^2 \,. \tag{3.15}$$

We note that within our simple model consideration, the constant factors found in textbook presentations [SZ97] are contained in $g(\omega)$. The similarity between the Lindblad Master equation and the Wigner-Weisskopf result is no coincidence, since approximating the frequency integral and extending its integration range closely relates to the Born and Markov approximations [MPT17].

We note that Eq. (3.12) can also be addressed beyond the Wigner-Weisskopf approximation by using Laplace transforms [Kri14], which allow to access the strong coupling and multi-mode strong coupling regimes [Kri14]. Due to the divergence of the Wigner-Weisskopf frequency integral, Gaussian cutoffs are required in this approach [Kri14]. The divergence problem has also been resolved by fully accounting for counter-rotating terms and gauge invariance [MPT17]. While these works show that matter-continuum coupling models can be tackled theoretically, we also see that already the simplest possible case of a single two-level atom coupled to a single continuum constitutes a non-trivial problem. In the following section, we discuss how few-mode models enter the stage in this context.

Why is the few-mode approach useful?

As outlined in the previous section, the matter-continuum coupling dynamics can be solved analytically at weak coupling within the Born-Markov approximation. This observation raises the question of why the Jaynes-Cummings type few-mode models are so commonly used?

One of the central reasons, as also discussed in the previous section, is that matter-continuum dynamics are a difficult problem beyond weak coupling. Quantum mechanics intrinsically suffers from the issue of the Hilbert space growing quickly with the degrees of freedom number [Tho13]. In the case of a continuum, one additionally faces the problem that the degrees of freedom number is already infinite and furthermore continuous, similarly to what is encountered in quantum field theory [CDG97]. For strong light-matter coupling in resonators, one additionally faces the problem that perturbation theories such as Born-Markov master equations have their limitations [Gar97b; Gar97a].

In order to make such problems numerically tractable, one therefore not only has to deal with the quickly growing Hilbert space (e.g. via suitable truncation schemes), but also has to account for the continuum (e.g. via discretization). In recent years, progress has been made to tackle these issues directly, e.g. using matrix product operators [Str18; Gri20] or methods from quantum field theory [SBD16]. As we saw in the previous section, certain cases[1] can also be solved analytically [Kri14] or via suitable perturbation expansions [MPT17].

However, even the most advanced schemes are eventually limited by numerical constraints. Especially when the quantum system itself is theoretically demanding already — such as for many-body systems coupled to the light field (see e.g. [Kir19; SBD16] and references therein) — simplifications of the underlying Hamiltonian are paramount.

In this context, few-mode models are tremendously useful, since they provide a complexity reduction of the continuum coupling. The central idea is that, especially in the case of resonator QED, the quantum system often does not couple strongly to the whole continuum, but only to a few degrees of freedom related to the cavity resonances [Gar97b]. One can then extract these few relevant modes to include them explicitly in the description and trace out the remaining weakly coupled continuum within the Master equation treatment [GC85; BP02].

From this perspective, the gap between the two sides in Fig. 3.1 can be seen as a missing algorithm to extract a few-mode description from the continuum theory. Such a method, which we refer to as an ab initio few-mode theory, is presented in Chapters 4 and 5.

3.3 Input-output theory

In the previous section, we mainly focused on the few-mode mode idea in Jaynes-Cummings type models. In this section, we provide additional background on the treatment of the resonator openness within few-mode models, which is related to a seminal system-bath model developed by Gardiner&Collett [GC85]. In particular, we provide intuition on the role of the so-called input-output formalism [GC85] (see [GZ04; WM08] for textbook references).

3.3.1 The Gardiner-Collett Hamiltonian

In Sec. 3.2.1, we introduced loss processes from the cavity via the phenomenological Lindblad term Eq. (3.3). Instead of directly modeling loss-terms on the Master equation level, one can instead

[1] We note that the methods referenced here are selected as recent illustrative examples in the specific context of light-matter interactions, the general literature on open system approaches to non-Markovian and strongly coupled dynamics is too vast to be surveyed within this thesis and we refer to extensive textbook treatments [BP02] and reviews [Bre16; dA17] on the topic.

explicitly introduce a bath Hamiltonian which the few modes in the Jaynes-Cummings model couple to. The most frequently used form is the Gardiner-Collett Hamiltonian [GZ04]

$$\hat{H} = \hat{H}_{\mathrm{JC}} + \int d\omega\, \omega \hat{b}^\dagger(\omega)\hat{b}(\omega) + \sum_\lambda \int d\omega\, W_\lambda(\omega)[\hat{b}(\omega)\hat{a}_\lambda^\dagger + h.c.] \tag{3.16}$$

or generalizations thereof (see [VH03; CC06; Zha13] and references therein). The central feature of this Hamiltonian is the bilinear coupling between the system modes and bosonic bath modes, which reduces to a Lindblad term of the form of Eq. (3.3) within the Born-Markov approximation and when the bath is in the vacuum state [GC85; GZ04; BP02].

The physical interpretation of this model is that the modes in the Jaynes-Cummings Hamiltonian, which are tightly confined by the resonator, can leak to the surrounding which approximates free space far from the resonator. The above coupling Hamiltonian is then one of the simplest ways to model the leakage of excitations from the resonator modes to the bath.

We note that similar system-bath Hamiltonians are found across the theory of open quantum systems and often share the bilinear coupling form [BP02]. An example of particular importance is the two-level system coupling to the electromagnetic field, which we have discussed in Sec. 3.2.2. However, we emphasize that there is a qualitative difference between such light-matter coupling Hamiltonians and Gardiner-Collett system-bath models. In the former case, the Hamiltonian can be derived from the minimal coupling prescription [CTDRG08] and the simplified models which are often used in practice, such as Eq. (3.6), can be obtained by a series of systematic approximations [SZ97; CDG97]. The Gardiner-Collett Hamiltonian for resonator QED, however, is a phenomenological model where the coupling constants are usually fitted to data. Until very recently [HVH02; VH03; VH04], no systematic prescription to derive such a Hamiltonian in its system-bath form had been known. Chapters 4 and 5 also address this problem, extending the work in [VH03].

3.3.2 Input-output relations and spectroscopic observables

Importantly, having a description which includes the bath explicitly allows one to access bath observables, such as scattering or spectroscopic quantities. By formally solving the operator equations of motion of the system-bath Hamiltonian, one can obtain so-called *input-output* relations [GZ04].

For the case of the Hamiltonian Eq. (3.16), the input-output relation in the Markov approximation reads [GC85]

$$\hat{b}_{\mathrm{out}}(t) - \hat{b}_{\mathrm{in}}(t) = -i\sum_\lambda \sqrt{\kappa_\lambda}\hat{a}_\lambda(t)\,, \tag{3.17}$$

where the system-bath couplings are assumed constant over the relevant frequency range [GC85]

$$W_\lambda(\omega) \approx \sqrt{\kappa_\lambda} \tag{3.18}$$

and the input (output) operator is an interaction picture operator at a time in the past t_0 (future t_1), defined as [GC85; VH03; LE20]

$$\hat{b}_{\mathrm{in/out}}(t) = \int \frac{d\omega}{2\pi}\, e^{-i\omega(t-t_{0/1})}\, \hat{b}_m(\omega, t_{0/1})\,. \tag{3.19}$$

For scattering calculations, one usually considers the distant past $t_0 \to -\infty$ (future $t_1 \to \infty$).

Such input-output relations are tremendously useful and have found a broad application basis [GZ04; WM08] with various extensions to system-bath Hamiltonians beyond the Gardiner-Collett form. From a physical perspective, they can be understood as a kind of scattering relation that supplements solution methods for the system dynamics. Once one knows the dynamics of the system operators ($\hat{a}_\lambda$ in the above example), one can readily obtain scattering observables from the input-output relation.

For example, when one uses a Master equation such as in the open Jaynes-Cummings model given by Eq. (3.4), one can straightforwardly solve the dynamics of the system operators. However, in Master equations such as Eq. (3.4), the bath is traced out and thus there is no direct information on its dynamics. Input-output relations can then be used to obtain the bath dynamics from the Master equation solution.

One can obtain many spectroscopic observables by taking appropriate expectation values of the input and output operators. For example, the intensity reflection coefficient can be evaluated as [Hee14]

$$R = \frac{\langle \hat{b}^\dagger_{\mathrm{out}}(t)\hat{b}_{\mathrm{out}}(t)\rangle}{\langle \hat{b}^\dagger_{\mathrm{in}}(t)\hat{b}_{\mathrm{in}}(t)\rangle}\,, \tag{3.20}$$

which semi-classically can often be reduced to (see [Hee14] and references therein)

$$R \approx \left| \frac{\langle \hat{b}_{\mathrm{out}}(t)\rangle}{\langle \hat{b}_{\mathrm{in}}(t)\rangle} \right|^2 . \tag{3.21}$$

Beyond such simple intensity scattering quantities, generalizations of input-output theory have also been used to evaluate few-photon scattering matrices [XF15; XF17; Tri18; Can15]. Various other generalizations, such as to ultra-strong coupling featuring counter-rotating terms [CC06; CBC05; BO14; De 14] and to non-Markovian dynamics [Zha13; Dió12], have been developed. Input-output relations can also be obtained for real space fields (see e.g. [Kha05; Med21]) instead of for mode models. The central idea of input-output theory, which is to access scattering observables in the bath via the dynamics of the localized system, is therefore an important concept in the theory of quantum optics [GZ04; WM08; Mey21b].

We note that the distinction between reflection, transmission and other scattering channels is fixed by the system-bath coupling constants κ_λ, which are usually determined phenomenologically again, by fitting to experimental or semi-classical theory data (see e.g. [HE15; Day08]). As explained in Sec. 3.3.1, this procedure is necessary due to the unknown origin of the Gardiner-Collett Hamiltonian for cavity QED. As a consequence, it is often also unclear which degrees of freedom the bath operators $\hat{b}(\omega)$ correspond to. While the fitting procedure works well in most cases, it can fail in more complex scenarios such as in x-ray cavity QED (see Sec. 2.4), where heuristic extensions were required [HE15]. Beyond x-ray cavity QED, this problem has been discussed intensively in various contexts [BR88; DN00b; DN00a; DN01; VH03; VH04; HVH02; Kha05; HRK18].

In relation to the open problem depicted in Fig. 3.1, the associated question is how the method for calculating scattering observables on each side relate to each other, which we resolve in Chapter 4.

3.4 Summary of open problems in few-mode theory

As illustrated in this background chapter, there are several open questions related to few-mode models. The central question is that it is not known how to derive few-mode Hamiltonians from fundamental light-matter interaction theory, which typically feature a continuum, as schematically depicted in Fig. 3.1. In the following, we briefly summarize open problems identified in this chapter, which are a result from this conceptual gap in the theory.

- First, the lack of a fundamental derivation of the Gardiner-Collett Hamiltonian causes the approximation hierarchy in quantum optics to be disrupted.
- Second, since this Hamiltonian is the basis for few-mode light-matter interaction models, there are doubts on their applicability in certain physical regimes, as we discuss in more detail in Sec. 3.5, and appropriate extensions are required.
- Third, there is generally no algorithm to calculate the parameters in such models from the resonator geometry. Instead, phenomenological fitting procedures are employed.
- Fourth, the role of the input-output formalism applied to few-mode models is unclear, since the associated bath modes are determined heuristically.
- Within x-ray cavity QED with Mössbauer nuclei, some concrete discrepancies between few-mode models and semi-classical scattering theory have been identified, resulting in a practical need for extensions.

Addressing these open problems is the central goal of Chapters 4 to 6, where we partially or fully resolve each of these questions.

We note that the above does not constitute an exhaustive list of open problems in few-mode theory for resonator QED. Various other issues which we do not address in this thesis, for example related to cavity-modified chemical processes [Fli17; Gal19; MM21] and gauge ambiguities [DS19; Tay20; SN21], are currently being investigated extensively.

3.5 Physical limitations and motivation

As discussed in this background chapter, few-mode theory and the input-output formalism have a variety of applications, forming a toolbox in particular for resonator QED [GZ04; Car99; Ber94; Har13; Rit13]. Models such as the Jaynes-Cummings model [JC63], the quantum Rabi model [Rab36; Bra11; Ros17], the Dicke model [Dic54; Kil80; SBD16; Kir19] and related models from many-body physics [TC69; ZKR19; Dha18], which all employ the few-mode concept, are indispensable methods in quantum physics.

However, the conceptual and technical questions summarized in Sec. 3.4 have practical implications, limiting the applicability of few-mode and input-output models. The validity of the approach has particularly been debated in the bad cavity and overlapping modes regimes [BR88; DN00b; DN01] as well as in the presence of absorption [Kha05]. This regime is of particular current importance due to its realization in nanophotonic systems such as plasmonic cavities [Tam13; Sto18; Sav12], which often feature large leakage and absorption [Koe10] (see also [Fra19; Med21] and references therein). Recently, limitations of few-mode theory in extreme coupling strength regimes [BO13; BO14; FK19] have also been discussed extensively.

Another practical implication of the phenomenological character of few-mode models is that, as explained in Sec. 3.2, there is currently no method to calculate their parameters, such as coupling strengths and decay rates, from the resonator geometry. Instead, fitting procedures have to be employed, which inhibit design possibilities. Additionally, fitting can introduce ambiguity with regards to the the underlying physics and degrees of freedom, such that applications in more general settings [Sea02; Gar04] are sparse.

Interestingly, similar tools are also employed in a variety of other fields related to scattering theory, such as mesoscopic [Dat97; BB00; RG17], atomic [Bur65; Smi66], photonic [Joa08; RG17] and nuclear [MW69; MRW10] physics. These fields often feature similar regimes, in particular the overlapping modes regime appears in laser systems [Pet79; HVH02; Tür05; Tür08], photonics [EG18; MA19; Özd19] and other platforms with significant leakage [Sto18; FDBM18]. On the methodological sides, chaotic scattering theory [Bee97], nuclear physics [MRW10], mesoscopic physics [RG17; Dat97] and non-Hermitian photonics [Dit00; Moi11; Rot09; RG17] often employ similar concepts as few-mode and input-output theory in quantum optics. However, there is no clear relation between the languages in the different fields.

From a general theory perspective, a main motivation for Chapters 4 to 6 is to extend few-mode theory in this direction, to enable applications in the above-mentioned physical regimes.

In a more narrow sense, we are again motivated by x-ray cavity QED [Röh10; Röh12; HE13], which features highly leaky and absorptive resonators, as outlined in Chapter 2. Most interestingly, x-ray cavity QED has historically employed semi-classical scattering formalisms, as we discussed in detail in Sec. 2.2, which do not feature the limitations of few-mode theory. On the other hand, recent formulations using quantum optical descriptions in the form of the pXCQED model [HE13; HE15] have hinted at the breakdown of few-mode models for these resonators, which are precisely due to the regime of high resonator losses (see Chapters 6 and 10). X-ray cavity QED with Mössbauer nuclei is therefore located right at the interface where the open questions identified in this chapter become relevant.

3.6 Recent progress and alternative approaches

While few-mode models are an important method in quantum optics theory, they are not the only way to approach resonator QED. Due to the increasing interest in the physical regimes where few-mode models are suspected to break down, much progress in developing alternative methods has been made recently, which we discuss in the following.

One option is to tackle the matter-continuum coupling directly and to solve the dynamics of the resulting Hamiltonian. As already outlined in Sec. 3.2, recent works have shown how the spontaneous

emission problem in resonators can be solved beyond the Wigner-Weisskopf and rotating-wave approximations [Kri14; MPT17; MPT16; MT16]. More general numerical schemes using matrix product operators have been developed to solve non-Markovian dynamics in structured environments [Str18; Gri20]. However, due to the detailed and numerically expensive treatment of the bath dynamics, these approaches are often limited when describing complex quantum matter inside the resonator, such as many-body systems, calling for complementary approaches.

With regards to generalizations, rigorous descriptions for absorptive systems can be obtained using the framework of macroscopic QED [GW96] (see also [SB08] and references therein). While the macroscopic QED Hamiltonian features an electromagnetic continuum, its resulting Markovian Master equations [DKW02] have also had much success, most recently in the field of atomic waveguide QED [AG17a; AG17b; MAG20].

Besides few-mode theory, various approaches to simplifying the light-matter Hamiltonian have been developed, some of which are based on similar ideas as the few-mode concept. In general wave mechanics and scattering theory, a variety of modal bases has been used for different purposes. Quasi-modes [Gam28; FL61; Chi98; DBK99; LR99; DN00b; Tür05; KH14; Alp17; HRK18; Lal18; Zsc18] have been an ubiquitous tool in classical wave scattering theory. The related constant flux states [TSC06] have particularly found applications in laser theory [Tür08; CS16] and circuit QED [MPT16]. Temporal coupled-mode theory [Hau84; FSJ03] is an important method, for example, to describe light-scattering in nanostructures [FR18; Joa08]. In addition, various methods from the theory of chaotic scattering [MRW10; Dit00; Rot09; ZD10] employ similar concepts.

With regards to quantum optics theory, quasi-modes have recently been quantized [HRK18; Fra19] and the resulting formalism has already been applied to quantum optics problems [Fra20b; Fra20a; Fra21]. This approach is promising due to its connection to a large toolbox in classical electromagnetism that is associated with quasi-modes [Chi98; Lal18; KH14] and since it rigorously includes absorption. However, from a quantum optics perspective, the quantized quasi-modes are rather unusual degrees of freedom, since they are associated with the poles of the electromagnetic response in the complex plane and thus constitute a non-Hermitian basis. The associated quantum mechanical degrees of freedom thus pose technical challenges [HRK18; Fra19]. Consequently, these methods do not necessarily connect to the toolbox associated with quantum optical few-mode theory [GZ04; SZ97; Car93] and can be seen as complementary. It will be interesting to see how the different Hermitian and non-Hermitian modal bases connect to each other in the future, an issue which we partially discuss in Chapter 10. At this stage, it appears that despite the different starting points and bases, the resulting multi-mode Master equations are rather similar, featuring the necessity of mode cross-coupling terms as a central common insight [HVH02; VH03; LE20; Fra20b; Med21].

Besides the progress with regards to quantization, much recent attention has been devoted to the question of how to use quasi-modes in scattering theory, which is a challenging problem due to their divergent behavior in the far-field. Recent progress includes [Alp17; Bin20; ZM20; Ben21b], which feature interesting relations to input-output theory (see also the afterword Sec. 5.6 for a discussion).

A related approach which also makes use of the pole structure in the complex plane is pseudo-mode theory [Gar97b; Gar97a]. Originally developed as a method to solve non-perturbative decay in the single excitation subspace [Gar97b] of models similar to Eq. (3.6), it has recently been extended [PGP20] and connected to a general theorem on the equivalence of correlation function dynamics between continuum and few-mode Hamiltonians [Tam18] in general open quantum systems theory (see also the afterword Sec. 5.6 for a discussion).

In direct relation to ab initio system-bath Hamiltonians, the results in Chapters 4 and 5 build on previous progress. In particular, a Gardiner-Collett Hamiltonian with an infinite number of modes was derived in [VH03; VH04] and used in the context of random lasers [HVH02; ZD10], forming a direct basis for the ab initio few-mode method to be developed.

We note that the above summary constitutes a rough overview of the current state at the time of writing of this thesis. Since the theory development in this field has been rather active in the last few years, some of the mentioned works were published in parallel or after submission of the manuscript that this part of the thesis summarizes. For context, we additionally devote an afterword in Sec. 5.6 to this recent progress, where we also discuss few works not mentioned above.

Chapter 4

Non-interacting theories: Few-mode Hamiltonians and scattering

This chapter is based on the following publication:

Ab Initio Few-Mode Theory for Quantum Potential Scattering Problems
D. Lentrodt and J. Evers
Physical Review X **10**, 011008 (2020)

4.1 Outline

In this chapter, we address the non-interacting side of the open questions in few-mode theory discussed in Chapter 3 (see particularly Fig. 3.1). That is, we show how to construct an ab initio few-mode basis transformation and how to use the input-output formalism for exact scattering calculations. Fig. 4.1 provides an overview of the results presented in this chapter and explains its structure. The corresponding results for interacting quantum theories are then given in Chapter 5.

The left hand side of Fig. 4.1 represents established ab initio methods, for example based on the canonical quantization of a wave equation. While we mainly consider the Schrödinger equation and a special case of Maxwell's equation for a dielectric medium as particular examples of quantum scattering problems in this thesis, Fig. 4.1 depicts the more general concept illustrated by a model potential (blue) with a schematic normal mode (orange). The normal mode basis is convenient, since it diagonalizes the Hamiltonian, which is obtained from the canonical quantization procedure. In Sec. 4.2.1, this approach is reviewed for the Schrödinger equation. The normal modes then obtain associated operators $\hat{c}$ (Sec. 4.2.2). The equations of motion for these operators can be solved using standard scattering theory, to obtain the scattering matrix (Sec. 4.3). Throughout the chapter, we will denote this approach as the *normal mode approach* (NMA). On the right hand side, the *few-mode approach* (FMA) is depicted, on which we focus here. It is usually employed in the form of phenomenological models, featuring a small number of discrete system modes coupled to an external bath with coupling constant W and complex energy shift / loss rate Γ. The input-output formalism is then used to calculate the scattering between the bath modes via the system modes.

The chapter is organized as follows. As our first result, we project the full problem into a system-bath representation in Sec. 4.2.3 and use it to derive an ab initio few-mode Hamiltonian for the Schrödinger field in Sec. 4.2. As our main result for non-interacting systems, in Sec. 4.4, we rigorously reconstruct the full scattering matrix from the ab initio few-mode Hamiltonian obtained in Sec. 4.2 using a suitable input-output formalism. We in particular show in Sec. 4.4.2 that the equivalence to the full scattering solution obtained from the NMA can only be established if a so-called background scattering term is included, which translates the bath modes scattering on the system into the asymptotically free modes. Our results thus not only connect the Hamiltonians on each side, which govern the dynamical equations of the system, but also the methods for computing scattering observables. This promotes the FMA and the input-output formalism to a rigorous theory and allows the two pictures to be used as equivalent approaches, which each have their advantages in practical situations. In Sec. 4.5, we present corresponding results for the dielectric Maxwell equations, which form the basis for major fields of application of input-output models such as cavity QED. These

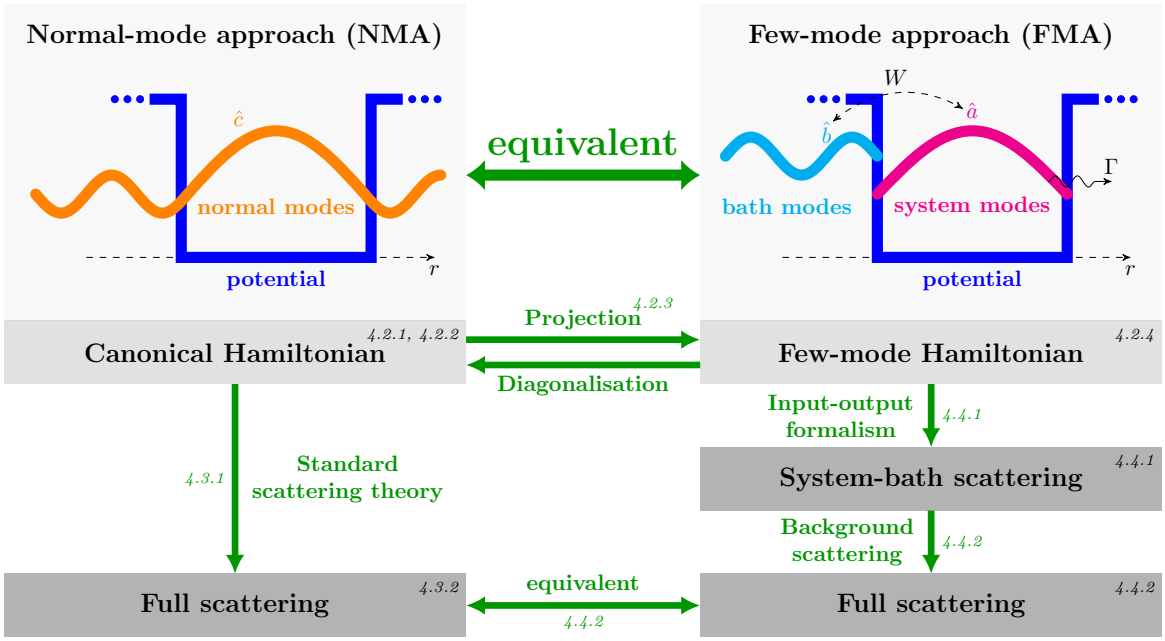

Figure 4.1: Schematic of the theoretical connections on non-interacting theories presented in this chapter. The left hand side represents the normal-mode approach (NMA) to quantum potential scattering, where one can rigorously obtain a Hamiltonian from canonical quantization. The latter is conveniently expressed in terms of normal mode operators $\hat{c}$ (top left picture). The right hand side represents the few-mode approach (FMA), usually employed in terms of phenomenological models. There, a discrete set of system modes is coupled to a continuum of bath modes (top right picture), corresponding to operators $\hat{a}$ and $\hat{b}$, respectively, with coupling constant W and loss rate Γ. We show that the Hamiltonians on each side can be connected by a basis transformation. A common method to calculate scattering observables in the FMA, known as the input-output formalism, can further be connected to standard scattering theory by inclusion of a background scattering contribution. Having shown that the Hamiltonians as well as the methods for calculating scattering observables can be rigorously connected, allows the normal-mode and the few-mode approaches to quantized potential scattering theory to be regarded as equivalent. Corresponding section numbers are indicated in the diagram as a structural overview.

results are brought into a practical context in Sec. 4.6 by comparing to what is usually done in corresponding phenomenological approaches. For illustration and proof-of-concept purposes, Sec. 4.7 discusses a Fabry-Perot cavity with variable mirror quality and a double barrier tunneling potential as example systems to illustrate the results on non-interacting systems.

4.2 Ab initio few-mode Hamiltonians

In order to link the FMA to the NMA, we begin by establishing a direct connection between the typical Hamiltonians in the two fields (see Section 4.2 labels in Fig. 4.1). On the NMA side, this is a diagonal normal modes Hamiltonian which can be obtained from the canonical quantization of a wave equation [CDG97; YI99]. On the FMA side, a *system* and a *bath* appear as coupled degrees of freedom [GZ04] (see Fig. 4.1). Via a suitable basis transformation [Dom83; VH03], we show that the two descriptions are equivalent for an arbitrary number of system modes. Based on this equivalence, we promote the few-mode input-output model to an ab initio theory in Sec. 4.4.

Our technique can be applied to a general class of wave equations. In this Section, we demonstrate its working principle on the Schrödinger equation

$$H\psi(r,t) = i\frac{\partial}{\partial t}\psi(r,t)\,, \tag{4.1}$$

where $\psi(r,t)$ is the wave function, $H = H_0 + V(r)$ is the first quantized Hamiltonian, $V(r)$ is a real-valued potential that vanishes at large $|r|$ and $H_0 = K = -\frac{1}{2}\frac{\partial^2}{\partial r^2}$ is the free kinetic energy operator. For simplicity, we work with $\hbar = m = 1$ and restrict ourselves to one dimension, the technique is however not limited to this setting.

4.2.1 Canonical quantization

Second quantization (see Appendix B.1 for details) of Eq. (4.1) yields the Hamiltonian

$$\hat{H} = \int dr\; \hat{\psi}^\dagger(r,t)\, H\, \hat{\psi}(r,t)\,, \tag{4.2}$$

where $\hat{\psi}(r,t)$, $\hat{\psi}^\dagger(r,t)$ are now operators with bosonic commutation relations

$$[\hat{\psi}(r,t),\, \hat{\psi}^\dagger(r',t)] = \delta(r-r')\,. \tag{4.3}$$

4.2.2 Normal mode basis and Fock space

It is useful to write the second quantized Hamiltonian in terms of normal mode creation and annihilation operators. To this end the field operator can be expanded in a normal mode basis

$$\hat{\psi}(r,t) = \sum_m \int dE(k)\; \phi_m(r,k)\, \hat{c}_m(k,t)\,. \tag{4.4}$$

Here, the normal mode $\phi_m(r,k)$ is defined as an eigenstate of the time-independent Schrödinger equation

$$H\,\phi_m(r,k) = E(k)\,\phi_m(r,k) \tag{4.5}$$

with energy $E(k)$ and further quantum numbers denoted by the index m.

With appropriate mode normalization (see Appendix B.2) the second quantized Hamiltonian is

$$\hat{H} = \sum_m \int dE(k)\; E(k)\, \hat{c}_m^\dagger(k,t)\hat{c}_m(k,t)\,. \tag{4.6}$$

The normal mode operators $\hat{c}_m(k,t)$ satisfy the canonical ladder operator commutation relations, for example,

$$[\hat{c}_m(k,t),\, \hat{c}_{m'}^\dagger(k',t)] = \delta_{mm'}\,\delta(E(k)-E(k'))\,. \tag{4.7}$$

We note that in the normal mode basis, the Hamiltonian is diagonal. The normal modes generally form a continuum, since they include scattering states, and are also known as modes-of-the-universe in the context of electromagnetic radiation [LSL73].

4.2.3 System-and-bath representation

To obtain a system-bath representation of the Hamiltonian [VH03], we would like to split the normal mode operators into a discrete set of system operators $\hat{a}_\lambda$ and a continuum of bath operators $\hat{b}_m(k)$ via a basis transformation of the form

$$\hat{c}_m(k) = \sum_{\lambda\in\Lambda_Q} \alpha^*_{\lambda m}(k)\, \hat{a}_\lambda + \sum_{m'} \int dE(k')\, \beta^*_{mm'}(k,k')\, \hat{b}_{m'}(k')\,, \tag{4.8}$$

where $\alpha^*_{\lambda m}(k)$ and $\beta^*_{mm'}(k,k')$ are expansion coefficients. This separation of the Hilbert space into two parts gives a Hamiltonian with couplings between the system and the bath modes, thus a non-diagonal Hamiltonian. A similar basis transformation with infinite number of system modes has been obtained by Viviescas&Hackenbroich [VH03]. Our method extends their approach, such that the discrete set of system modes denoted by Λ_Q can be chosen to contain only few or even a single mode, and does not need to span a region in position space as a basis. This way effective few-mode theories capturing the relevant resonant dynamics can be formulated (see Chapter 5 for details).

However, constructing such a few-mode basis is non-trivial. For Eq. (4.8) to be a consistent basis transformation, the system and bath together have to span the original Hilbert space. To connect to quantum noise theory [GZ04], we would also like $\hat{a}_\lambda$ and $\hat{b}_m(k)$ to be bosonic operators, which places a restriction on their commutation relations, and the Hamiltonian to be of so-called Gardiner-Collett form [GC85; GZ04]. In the following, we show that all of these conditions can be ensured by using Feshbach projections [Fes58; Fes62; Fes67; Dom83] to select a certain set of system states corresponding to the second quantized system operators $\hat{a}_\lambda$.

Feshbach projection for states

The idea of the Feshbach projection formalism [Fes58; Fes62; Fes67] is to reformulate the Schrödinger equation Eq. (4.1), which describes the wave propagation in the full Hilbert space, in terms of wave equations in two subspaces, which are then coupled to each other. In this spirit we follow Domcke [Dom83] to first express the eigenstates of the Schrödinger equation in terms of the subspace eigenstates.

We start by defining projection operators Q, P such that

$$P^2 = P,\ Q^2 = Q,\ P + Q = 1\,. \tag{4.9}$$

Q will correspond to the system subspace and P to the bath subspace, which together span the full Hilbert space. However, we note that in the few-mode case, Q and P itself generally do not correspond to disjunct regions in position space. Specifically, the Q-space projector is defined by choosing a set of system modes $\Lambda_Q = \{|\chi_\lambda\rangle\}$, which are discrete normalized states that span the Q-space such that

$$Q = \sum_{\lambda\in\Lambda_Q} |\chi_\lambda\rangle\langle\chi_\lambda|\,. \tag{4.10}$$

We further require[3] that these states be eigenstates of the projected Q-space Hamiltonian $H_{QQ} = QHQ$, that is

$$H_{QQ}\,|\chi_\lambda\rangle = E_\lambda\,|\chi_\lambda\rangle\,. \tag{4.11}$$

Analogously, we can define the bath modes $\left|\tilde{\psi}_m(k)\right\rangle$ as eigenstates of the P-space Hamiltonian

$$H_{PP}\left|\tilde{\psi}_m(k)\right\rangle = E(k)\left|\tilde{\psi}_m(k)\right\rangle\,. \tag{4.12}$$

These states form a continuum and can only be determined uniquely after choosing appropriate boundary conditions [New82; Dom83], which will become relevant in the context of scattering in Sec. 4.3.

We note that the hermicity of the subspace Hamiltonians implies certain orthogonality conditions for their eigenstates (see Appendix B.2 for details), which will become relevant in the context of quantization in Sec. 4.2.3.

[3] This requirement is imposed to obtain a Hamiltonian in the second quantized case, where the system states do not couple to each other directly. It does not restrict the generality since Q and H_{QQ} commute.

We can now write the eigenstates in full space as an expansion over the subspace eigenstates

$$|\phi_m(k)\rangle = Q\ |\phi_m(k)\rangle + P\ |\phi_m(k)\rangle \tag{4.13}$$

$$= \sum_{\lambda\in\Lambda_Q} \alpha_{\lambda m}(k)\ |\chi_\lambda\rangle + \sum_{m'} \int dE(k')\, \beta_{mm'}(k,k')\ \left|\tilde{\psi}_{m'}(k')\right\rangle . \tag{4.14}$$

This can be interpreted as a system-bath expansion of the normal mode states. Importantly, the coefficients

$$\alpha_{\lambda m}(k) = \langle\chi_\lambda|\phi_m(k)\rangle\ , \tag{4.15a}$$

$$\beta_{mm'}(k,k') = \left\langle\tilde{\psi}_{m'}(k')\middle|\phi_m(k)\right\rangle \tag{4.15b}$$

can be calculated without direct knowledge of the normal mode functions $\phi_m(r,k)$ by so-called separable expansions (see Appendix B.3 for details), which can have computational advantages [Dom83].

Feshbach projection for operators

The separation of the dynamics into two coupled subspaces can alternatively be formulated in Fock space by introducing operators $\hat{a}_\lambda$ and $\hat{b}_m(k)$ corresponding to the system modes $|\chi_\lambda\rangle$ and bath modes $\left|\tilde{\psi}_m(k)\right\rangle$, respectively. It can be shown (see Appendix B.4) that analogously to Eq. (4.14), the normal mode operators relate to these system-bath operators via

$$\hat{c}_m(k) = \sum_{\lambda\in\Lambda_Q} \alpha^*_{\lambda m}(k)\, \hat{a}_\lambda + \sum_{m'} \int dE(k')\, \beta^*_{mm'}(k,k')\, \hat{b}_{m'}(k')\,, \tag{4.16}$$

which is the operator system-bath expansion Eq. (4.8), with the coefficients now given by Eqs. (4.15). In addition, the operators $\hat{a}_\lambda$ and $\hat{b}_m(k)$ fulfill the desired commutation relations [VH03] (see Appendix B.4 for details), that is they are each bosonic degrees of freedom and the system commutes with the bath. It has previously been unclear whether the latter holds in the bad cavity regime and alternative models have been suggested [DN01]. Now, the condition can be ensured constructively using the Feshbach projection method, even in the few-mode case.

4.2.4 Ab initio few-mode Hamiltonian

Applying the system-bath expansion Eq. (4.16) to the second quantized Hamiltonian Eq. (4.6) and using Appendices B.4, B.5 we obtain

$$\hat{H} = \sum_{\lambda\in\Lambda_Q} E_\lambda \hat{a}^\dagger_\lambda \hat{a}_\lambda + \sum_m \int dE(k)\, E(k)\, \hat{b}^\dagger_m(k)\hat{b}_m(k) + \sum_{\lambda\in\Lambda_Q}\sum_m \int dE(k)\ \left[W_{\lambda m}(k)\, \hat{a}^\dagger_\lambda \hat{b}_m(k) + \text{h.c.}\right] , \tag{4.17}$$

with the coupling constants

$$W_{\lambda m}(k) := \left\langle\chi_\lambda\middle|\, H\, \middle|\tilde{\psi}_m(k)\right\rangle . \tag{4.18}$$

We have thus derived an ab initio few-mode Hamiltonian of Gardiner-Collett form for the Schrödinger equation. We note that the few-mode Hamiltonian exactly captures the system's dynamics, equivalently to the Hamiltonian in its normal mode representation Eq. (4.6), even though the system modes are discrete and their number is finite. This feature opens new theoretical possibilities when interactions such as atoms are present inside the cavity, as we investigate in detail in Chapter 5.

We note that Eq. (4.17) generalizes the Hamiltonian derived by Viviescas&Hackenbroich [VH03] from an infinite to an arbitrary number of system modes and to a general class of wave equations. More importantly, as we will show in the following sections, an ab initio input-output formalism can now be used to reconstruct the scattering information, which for Viviescas&Hackenbroich's Hamiltonian [VH03] is hindered by the appearance of divergent series in the infinite mode case (see Appendix B.6). Due to the non-trivial behavior of this limit, which has already been noted in [Dom83], the few-mode Hamiltonians proposed here are better suited to achieve this task.

For completeness, we further note that the inverse of the presented basis transformation constitutes a Fano diagonalization [Fan61] of the system-bath Hamiltonian. A similar basis transformation has been investigated in [DBG01] in relation to pseudo-modes theory [Gar97b; Gar97a], and in an early paper [BR88] considering an approximate treatment.

4.3 Quantum potential scattering

In practice, system-bath Hamiltonians are most commonly used as phenomenological models for quantum mechanical systems [GZ04; Yur04]. Their great value arises since scattering observables can be calculated using the famous input-output formalism [GZ04; Yur04], which is a standard tool in quantum optics. Despite its success, the input-output formalism only addresses the scattering problem from the perspective of a model Hamiltonian, which the inventors called a "simplified representation of reality" [GZ04]. In the previous section, we showed how to rigorously derive few-mode system-bath Hamiltonians from canonical quantization, and thereby eliminated the need for the ad hoc assumption of a model Hamiltonian. With this ab initio version of the Hamiltonian at hand, we now have the tools to connect the input-output formalism to scattering theory.

To set a foundation for comparison, in this section, we first derive scattering theory results in the first and second quantized setting as a reference (see also Sec. 4.3 labels in Fig. 4.1).

4.3.1 First quantized potential scattering theory

Standard scattering theory

For a wave equation such as the time-dependent Schrödinger equation Eq. (4.1), the scattering problem is given by the question of how an incoming wave-packet defined in the infinite past evolves into an outgoing wave-packet in the infinite future [New82]. For elastic scattering this information can be encoded in the on-shell scattering matrix $S_{mm'}(k)$, which is defined by the linear relation between states $\left|\phi_m^{(+)}(k)\right\rangle$ and $\left|\phi_m^{(-)}(k)\right\rangle$ [New82]

$$\left|\phi_m^{(+)}(k)\right\rangle = \sum_{m'} \left|\phi_{m'}^{(-)}(k)\right\rangle S_{m'm}(k)\,. \tag{4.19}$$

The states $\left|\phi_m^{(\pm)}(k)\right\rangle$ are the normal modes defined in Eq. (4.5) as eigenstates of the Hamiltonian. The $(\pm)$ corresponds to a choice of boundary conditions. As usual in scattering theory, $(+)$ is the state with a controlled incoming free state, and $(-)$ is the state with a controlled outgoing free state [New82].

Another useful scattering quantity is the transition operator T defined by

$$\left|\phi_m^{(+)}(k)\right\rangle = \left|k_m\right\rangle + G_0^{(+)}\,T\,\left|k_m\right\rangle \tag{4.20}$$

where $G_0^{(+)}$ is the free propagator given via the free Hamiltonian H_0 as

$$G_0^{(+)} = \left(E(k) - H_0 + i\eta\right)^{-1}\,, \tag{4.21}$$

and $|k_m\rangle$ is an eigenstate of H_0 with $H_0\,|k_m\rangle = E(k)\,|k_m\rangle$. The operator T thus quantifies transitions between a full eigenstate and a free eigenstate. It is linked to the on-shell scattering matrix defined above via [New82]

$$S_{mm'}(k) = \delta_{mm'} - 2\pi i\,T_{mm'}(k) \tag{4.22}$$

with $T_{mm'}(k) = \langle k_m|\,T\,|k_{m'}\rangle$.

The scattering properties can thus be obtained by solving the eigenproblem for the full Hamiltonian and computing their transition probabilities to freely propagating states.

Potential scattering via projection operators

Domcke showed [Dom83] that instead of using the eigenstates in full space, the scattering matrix can also be calculated from the system and bath states that we used in Sec. 4.2. Details on the calculation are summarized in Appendix B.7. Here we will focus on the definitions and interpretation of the results relevant to our work. The relation between the different states and scattering matrices used below is illustrated in the left part of Fig. 4.2.

We first define a transition operator T_{res} by considering the bath modes as "free" states. Analogously to Eq. (4.20), omitting matrix subscripts for brevity, we can write

$$P\left|\phi^{(+)}(k)\right\rangle = \left|\tilde{\psi}^{(+)}(k)\right\rangle + \tilde{G}^{(+)}\,T_{\text{res}}\,\left|\tilde{\psi}^{(+)}(k)\right\rangle\,, \tag{4.23}$$

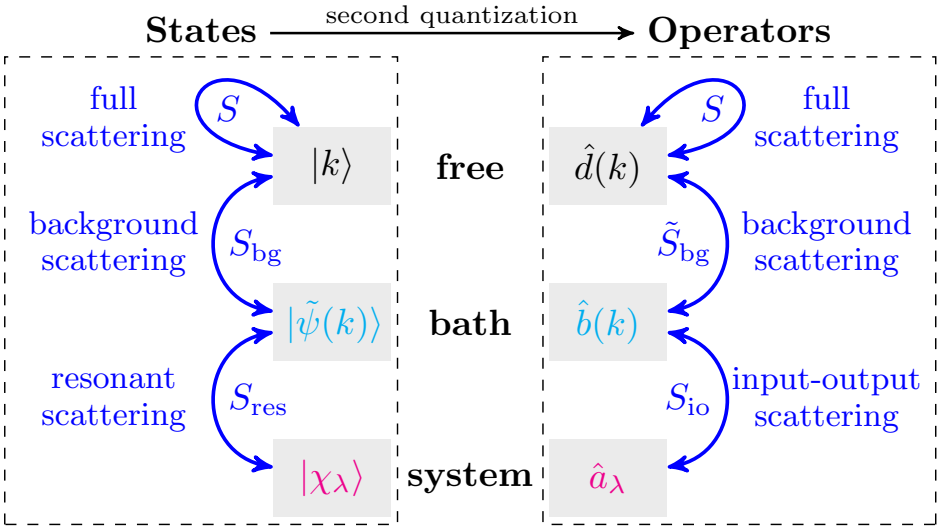

Figure 4.2: Schematic of the different degrees of freedom and scattering connections in the Feshbach projection formalism for potential scattering problems. The full scattering matrix S can be used to relate asymptotically free states or operators to each other. The background scattering S_{bg} arises from a basis transformation of the free states into the bath states. The bath states scatter via S_{res} on the system states, which span part of the region where the scattering potential $V(r)$ is non-zero. Similarly on the operator level, the scattering between bath operators that are coupled to the system is given by the input-output scattering matrix S_{io}. To obtain the full scattering matrix, a background scattering contribution $\tilde{S}_{\mathrm{bg}}$ has to be applied.

where $\tilde{G}^{(+)}$ is the Green function for P-space propagation

$$\tilde{G}^{(+)} = (E(k) - H_{PP} + i\epsilon)^{-1} \,. \tag{4.24}$$

We can then quantify the scattering between bath states by a scattering matrix

$$S_{\mathrm{res}}(k) \equiv \mathbb{I} - 2\pi i \, T_{\mathrm{res}}(k) \,, \tag{4.25}$$

where $T_{\mathrm{res}}(k)$ is the matrix element of T_{res} on the basis of retarded bath states.

However the bath states are not necessarily free states. Therefore there is a residual scattering contained in the asymptotic structure of the bath states, which can be described by a transition operator for transitions from a bath state to a free state

$$\left|\tilde{\psi}^{(+)}(k)\right\rangle = |k\rangle + G_0^{(+)} \, T_{\mathrm{bg}} \, |k\rangle \,. \tag{4.26}$$

The background scattering matrix S_{bg} is again defined as the corresponding on-shell scattering matrix

$$S_{\mathrm{bg}}(k) \equiv \mathbb{I} - 2\pi i \, T_{\mathrm{bg}}(k) \,, \tag{4.27}$$

where $T_{\mathrm{bg}}(k)$ is the matrix element of T_{bg} on the basis of free states. The effect of $S_{\mathrm{bg}}(k)$ can thus be interpreted as an asymptotic basis transformation between bath states and free states.

The full scattering matrix S is then decomposed into the resonant scattering matrix S_{res} and the background scattering matrix S_{bg} via [Dom83]

$$S(k) = S_{\mathrm{bg}}(k) \, S_{\mathrm{res}}(k) \,. \tag{4.28}$$

In terms of the system and bath states these matrices read (see Appendix B.7)

$$S_{\mathrm{res}}(k) = \mathbb{I} - 2\pi i \, \left\langle \tilde{\psi}^{(+)}(k) \right| H_{PQ} G_{QQ} H_{QP} \left| \tilde{\psi}^{(+)}(k) \right\rangle \,, \tag{4.29}$$

$$S_{\mathrm{bg}}(k) = \mathbb{I} - 2\pi i \, \langle k | \, (H_{PP} - K) \left| \tilde{\psi}^{(+)}(k) \right\rangle \,. \tag{4.30}$$

We note that unlike in the quasi-modes approach [Chi98; KH14; Alp17; Lal18], the "resonant" part in the Feshbach projection formalism does not necessarily correspond to the resonances of the wave

equation, that is the poles of the scattering matrix. However by choosing the system states appropriately, certain resonances can be selected, such that their poles appear in S_{res}, and the remaining poles appear in S_{bg}. This behavior has been investigated partially in [Dom83] and we demonstrate its significance for extracting few-mode dynamics in Sec. 4.7. In the context of interacting theories the concept further becomes a powerful tool to construct effective few-mode expansions, which we show in Chapter 5.

We further note that from the viewpoint of the entire scattering problem, both S_{res} and S_{bg} are unphysical on their own, since their properties depend on the arbitrary choice of the system states. However, they individually may provide accurate approximations of the full scattering matrix in the vicinity of their corresponding resonances (see also Sec. 4.7), such that the choice of system states becomes a resource allowing the extraction of relevant properties of the whole system.

4.3.2 Second quantized potential scattering theory

In the second quantized setting, one investigates the dynamics of operators defined by the Hamiltonian and its corresponding Heisenberg equations of motion. That is, the quantization procedure promotes the wave equation to a non-relativistic quantum field theory, such that correlation functions can be computed and interactions can be considered.

For potential scattering we can define asymptotically free operators by expanding the quantum field in a free mode basis instead of in its normal mode basis. If $\phi_m^{(\mathrm{free})}(r,k) = \left\langle r \middle| k_m \right\rangle$ are the field distribution of the free eigenstates, then the free state expansion of the field operator reads

$$\hat{\psi}(r,t) = \sum_m \int dE(k)\, \phi_m^{(\mathrm{free})}(r,k)\, \hat{d}_m(k,t)\,, \tag{4.31}$$

where $\hat{d}_m(k,t)$ are the free bosonic operators satisfying canonical commutation relations.

One can solve the Heisenberg equations of motion for these operators (see Appendix B.8 for details) to obtain a scattering relation

$$\hat{d}_m^{(\mathrm{out})}(k) = \sum_{m'} S_{mm'}(k)\, \hat{d}_{m'}^{(\mathrm{in})}(k)\,, \tag{4.32}$$

where the asymptotically free in [out] operators are interaction picture operators in the infinite past [future], that are defined via adiabatically switching on [off] of the potential in the corresponding time limits (see Appendix B.8 for details).

In the case of potential scattering, the operator scattering matrix can be shown to be exactly the first quantized scattering matrix Eq. (4.19) [GL91]. This correspondence between the solution to the wave equation and its second quantized analogue is also required for consistency, since on average the result from the wave equation should be obtained, that is $\langle \hat{d}_{\mathrm{out}}(k) \rangle = S \langle \hat{d}_{\mathrm{in}}(k) \rangle$.

For clarity, we emphasize that the scattering matrices employed here relate different asymptotic *operators*. The relation of this formulation to scattering between initial and final states of the quantum field has, for example, been noted in [FKS10; XF15; Tri18] in the context of few-photon transport.

4.4 Few-mode scattering

We now show how to rigorously reconstruct the full scattering information from the ab initio few-mode Hamiltonian derived in Sec. 4.2 using the input-output formalism. We further show the equivalence of the input-output formalism result to that of standard scattering theory (see Sec. 4.4 labels in Fig 4.1). The applicability of the input-output formalism is thus not limited to the good cavity regime, but applies to a general class of quantum scattering problems and in extreme regimes.

4.4.1 Ab initio input-output formalism

We now apply the input-output formalism [GC85; GZ04; VH03] to our ab initio few-mode Hamiltonian Eq. (4.17). This constitutes solving the Heisenberg equations of motion for the Hamiltonian Eq. (4.17),

which are

$$\frac{d}{dt}\hat{a}_\lambda(t) = -iE_\lambda\,\hat{a}_\lambda(t) - i\sum_m \int dE(k)\,W_{\lambda m}(k)\,\hat{b}_m(k,t)\,, \tag{4.33}$$

$$\frac{d}{dt}\hat{b}_m(k,t) = -iE(k)\,\hat{b}_m(k,t) - i\sum_{\lambda\in\Lambda_Q} W^*_{\lambda m}(k)\,\hat{a}_\lambda(t)\,. \tag{4.34}$$

We can solve Eq. (4.34) formally in terms of the initial time t_0 and final time t_1 as

$$\hat{b}_m(k,t) = e^{-iE(k)(t-t_0)}\,\hat{b}_m(k,t_0) - i\sum_{\lambda\in\Lambda_Q} W^*_{\lambda m}(k)\int_{t_0}^{t} dt' e^{-iE(k)(t-t')}\,\hat{a}_\lambda(t') \tag{4.35}$$

and

$$\hat{b}_m(k,t) = e^{-iE(k)(t-t_1)}\,\hat{b}_m(k,t_1) + i\sum_{\lambda\in\Lambda_Q} W^*_{\lambda m}(k)\int_{t}^{t_1} dt' e^{-iE(k)(t-t')}\,\hat{a}_\lambda(t')\,, \tag{4.36}$$

respectively. As usual in quantum noise theory [GC85; VH03] and in analogy with the quantum field theory definition (see Sec. 4.3.2) we define the in- and out- operators

$$\hat{b}^{(\mathrm{in})}_m(k) = e^{iE(k)t_0}\,\hat{b}_m(k,t_0)\,, \tag{4.37a}$$

$$\hat{b}^{(\mathrm{out})}_m(k) = e^{iE(k)t_1}\,\hat{b}_m(k,t_1)\,, \tag{4.37b}$$

respectively. Taking initial [final] times to negative [positive] infinity gives the input-output relation

$$\hat{b}^{(\mathrm{out})}_m(k) - \hat{b}^{(\mathrm{in})}_m(k) = -i\sum_{\lambda\in\Lambda_Q} W^*_{\lambda m}(k)\,\hat{a}_\lambda(k)\,, \tag{4.38}$$

where the Fourier transform of $\hat{a}_\lambda(t)$ is defined by

$$\hat{a}_\lambda(k) = \int_{-\infty}^{\infty} dt' e^{iE(k)t'}\,\hat{a}_\lambda(t')\,. \tag{4.39}$$

Substituting the formal solution Eq. (4.35) into Eq. (4.33) and inverting the resulting matrix equation gives

$$\hat{a}_\lambda(k) = 2\pi\sum_{\lambda'\in\Lambda_Q}\sum_m D^{-1}_{\lambda\lambda'}(k)\,W_{\lambda' m}(k)\,\hat{b}^{(\mathrm{in})}_m(k)\,, \tag{4.40}$$

where we defined D^{-1} as the inverse of the matrix of

$$D_{\lambda\lambda'}(k) = (E(k) - E_\lambda)\delta_{\lambda\lambda'} + \Gamma_{\lambda\lambda'}(k). \tag{4.41}$$

The decay matrix (see also Fig. 4.1) is given by

$$\Gamma_{\lambda\lambda'}(k) = -\sum_m \int dE(k')\frac{W_{\lambda m}(k')W^*_{\lambda' m}(k')}{E(k) - E(k') + i\epsilon} \tag{4.42}$$

$$=: -\Delta_{\lambda\lambda'}(k) + i\gamma_{\lambda\lambda'}(k)\,, \tag{4.43}$$

where we have defined the real and imaginary parts of $\Gamma_{\lambda\lambda'}(k)$ as $\Delta_{\lambda\lambda'}(k)$ and $\gamma_{\lambda\lambda'}(k)$. In the latter equation, the limit $\epsilon \to 0^+$ is implied. For $\lambda \neq \lambda'$, the complex decay matrix $\Gamma_{\lambda\lambda'}(k)$ describes couplings between the system modes, whereas the diagonal parts correspond to frequency shifts $\Delta_{\lambda\lambda}$ and loss rates $\gamma_{\lambda\lambda}$.

We note that to obtain this expression, the Fourier transform integrals have been regularized (see Appendix B.9 for details), analogously to what is usually done in time-independent scattering theory [New82]. We further note that a Markov approximation is not necessary in this derivation [VH03].

Upon substitution of Eq. (4.40) into Eq. (4.38) we can read off the scattering matrix

$$S_{\mathrm{io}}(k) = \delta_{mm'} - 2\pi i\sum_{\lambda,\lambda'} W^*_{\lambda m}(k)D^{-1}_{\lambda\lambda'}(k)W_{\lambda' m'}(k), \tag{4.44}$$

such that

$$\hat{b}^{(\mathrm{out})}(k) = S_{\mathrm{io}}(k)\,\hat{b}^{(\mathrm{in})}(k). \tag{4.45}$$

The subscript 'io' stands for 'input-output' to indicate that this scattering matrix has been obtained by solving the quantum statistical operator equations of motion of the ab initio few-mode Hamiltonian using the input-output formalism of quantum noise theory [GC85; GZ04].

4.4.2 Equivalence to standard scattering theory

We now show that the above calculation is equivalent to the full quantum scattering calculation, only expressed in a different basis. The relation is best understood by analogy to the state case (see Fig. 4.2).

Firstly we recognize that, using the definition of the coupling constants Eq. (4.18) as well as the completeness relations of the subspace eigenstates and Eq. (4.11), the decay matrix Eq. (4.42) can be written as

$$\Gamma_{\lambda\lambda'}(k) = -\langle\chi_\lambda| H_{QP}\tilde{G}^{(+)}H_{PQ}\,|\chi_{\lambda'}\rangle\ . \tag{4.46}$$

We have now chosen the bath states fulfilling retarded boundary conditions $\left|\tilde{\psi}^{(+)}(k)\right\rangle$ [New82; Dom83], since by writing Eq. (4.40) in terms of the incoming operator, we have decided to solve an initial value scattering problem.

From Eq. (4.41), the D-matrix therefore consists of the matrix elements

$$D_{\lambda\lambda'}(k) = \langle\chi_\lambda|\, E(k) - H_{QQ} - H_{QP}\tilde{G}^{(+)}H_{PQ}\,|\chi_{\lambda'}\rangle\ . \tag{4.47}$$

Noting that the effective Q-space Hamiltonian is

$$H_{\text{eff}} = H_{QQ} + H_{QP}\tilde{G}^{(+)}H_{PQ}\,, \tag{4.48}$$

we see that the inverse of the D-matrix coincides with the matrix elements

$$D^{-1}_{\lambda\lambda'}(k) = \langle\chi_\lambda|\, G_{QQ}\,|\chi_{\lambda'}\rangle \tag{4.49}$$

of the Q-space propagator $G_{QQ} = [E(k) - H_{\text{eff}}]^{-1}$.

Substituting into Eq. (4.44), again using the definition of the coupling constants Eq. (4.18) and the completeness relations of the subspace eigenstates, we find that

$$S_{\text{io}}(k) = \mathbb{I} - 2\pi i\,\left\langle\tilde{\psi}^{(+)}(k)\right| H_{PQ}G_{QQ}H_{QP}\left|\tilde{\psi}^{(+)}(k)\right\rangle = S_{\text{res}}(k)\,. \tag{4.50}$$

Thus the expression for the input-output scattering matrix $S_{\text{io}}(k)$ coincides with the scattering matrix $S_{\text{res}}(k)$ in Eq. (4.29) obtained from potential scattering theory using the Feshbach projection formalism [Dom83].

From our interpretation of the resonant scattering matrix in Sec. 4.3.1, it is to be expected that $S_{\text{io}}(k)$ is not the full scattering matrix. The ab initio few-mode Hamiltonian Eq. (4.17) only contains information about the dynamics of the system and bath modes, which interact via the coupling terms. Despite capturing these dynamics exactly, it does not contain information about the structure of the bath modes. In addition, the bath operators are not asymptotically free. Therefore analogously to the first quantized potential scattering case in Sec. 4.3.1, an asymptotic basis transformation is needed to translate from the bath operators in Eq. (4.45) to the asymptotically free operators in Eq. (4.32), as schematically shown in Fig. 4.2. We further know from Eq. (4.28) that this transformation can be expressed as the background scattering matrix $S_{\text{bg}}(k)$. Therefore, the full scattering matrix can be calculated from the input-output result by

$$S(k) = S_{\text{bg}}(k)S_{\text{io}}(k)\,. \tag{4.51}$$

To summarize, the background scattering contribution translates the bath mode scattering from the input-output formalism into free-state scattering as usually observed in spectroscopic experiments.

We have thus clarified the relation of our ab initio FMA to the NMA and conventional quantum scattering theory. The two approaches are equivalent if care is taken to compute the scattering between asymptotically free operators in both cases. Figures 4.1 and 4.2 illustrate the equivalence and the relation between the different operators.

4.5 Application to Maxwell's equations

While so far we have presented the construction of ab initio few-mode Hamiltonians on the example of the Schrödinger equation, our technique is in fact quite general. The essential requirements are that

the Hilbert space of the quantum system can be separated into two orthogonal subspaces and that each subspace is spanned by a set of orthonormal modes. In the Schrödinger case, these conditions were ensured by the hermicity of the corresponding operators. One can thus envision an application of the formalism to a variety of quantized scattering problems. One such problem with practical relevance in quantum optics and cavity QED is the scattering of light from dielectric materials, described by Maxwell's equations. Since this field is a main application of system-bath theory and the input-output formalism as a phenomenological model, the question arises if our ab initio FMA can be applied to this setting as well.

In the following, we analyze this question for the simplest possible case of a linear, isotropic, non-absorbing dielectric medium in one dimension, with only a single polarization considered. We show that within the rotating wave approximation (RWA), the correspondence between the input-output formalism and the potential scattering approach can be established.

Our assumptions allow us to write the wave equation for a component $A(r,t)$ of the vector potential as [VH04]

$$\frac{\partial^2}{\partial r^2} A(r,t) = \varepsilon(r) \frac{\partial^2}{\partial t^2} A(r,t)\,, \tag{4.52}$$

where $\varepsilon(r)$ is the dielectric function and again $c = 1$. The applicability of this scalar Helmholtz equation to physical scenarios has been discussed in [RG17]. This problem is closely related to our treatment of the Schrödinger equation, since the corresponding time-independent equation for the normal modes $f_m(r,k)$ [VH03],

$$\frac{\partial^2}{\partial r^2} f_m(r,\omega) + \varepsilon(r)\omega^2 f_m(r,\omega) = 0\,, \tag{4.53}$$

can be written as a Schrödinger equation with an energy-dependent potential [Chi98; RG17]

$$\tilde{V}(r,\omega) = \frac{1-\varepsilon(r)}{2}\,\omega^2\,. \tag{4.54}$$

The normal modes of this wave equation are still orthogonal, but under a modified inner-product [VH03; RG17]

$$\langle x|y\rangle = \int dr\, \varepsilon(r)\, x^*(r)\, y(r)\,. \tag{4.55}$$

The Maxwell wave equation can be quantized canonically [GL91] (see Appendix B.10.1 for details), similarly to the Schrödinger case in Sec. 4.2.1. However due to the double time-derivative, the Hamiltonian now contains coordinate operators $\hat{q}$ and momentum operators $\hat{p}$ [GL91; VH03], such that the corresponding commutation relations differ [GL91; VH03].

The separation into system and bath operators via a Feshbach projection can also be performed analogously to the Schrödinger case (see Appendix B.10.2 for details). The resulting few-mode Hamiltonian is of the form [VH03]

$$\begin{aligned}\hat{H} = &\sum_{\lambda\in\Lambda_Q} \omega_\lambda \hat{a}_\lambda^\dagger \hat{a}_\lambda + \sum_m \int d\omega\, \omega\, \hat{b}_m^\dagger(\omega)\hat{b}_m(\omega) \\ &+ \sum_{\lambda,m} \int d\omega\, \left[\mathcal{W}_{\lambda m}(\omega)\, \hat{a}_\lambda^\dagger\, \hat{b}_m(\omega) + \mathcal{V}_{\lambda m}(\omega)\, \hat{a}_\lambda\, \hat{b}_m(\omega) + h.c.\right]\,.\end{aligned} \tag{4.56}$$

We note the appearance of counter-rotating terms in the system-bath coupling [VH03], which are also a result of the second time-derivative in the Maxwell wave equation.

4.5.1 Scattering in the rotating wave approximation

We proceed with the analysis by applying the rotating wave approximation, which simplifies the Hamiltonian Eq. (4.56) to

$$\hat{H}_{\text{rot}} = \sum_{\lambda\in\Lambda_Q} \omega_\lambda \hat{a}_\lambda^\dagger \hat{a}_\lambda + \sum_m \int d\omega\, \omega\, \hat{b}_m^\dagger(\omega)\hat{b}_m(\omega) + \sum_{\lambda,m} \int d\omega\, \left[\mathcal{W}_{\lambda m}(\omega)\, \hat{a}_\lambda^\dagger\, \hat{b}_m(\omega) + h.c.\right]\,. \tag{4.57}$$

One can solve the equations of motion for this Hamiltonian analogously to Sec. 4.4.1. The resulting scattering matrix is

$$S_{\mathrm{io}}^{(\mathrm{rot})}(\omega) = \delta_{mm'} - 2\pi i \sum_{\lambda,\lambda'} \mathcal{W}^*_{\lambda m}(\omega)\mathcal{D}^{-1}_{\lambda\lambda'}(\omega)\mathcal{W}_{\lambda' m'}(\omega)\,, \tag{4.58}$$

with

$$\mathcal{D}_{\lambda\lambda'}(\omega) = (\omega - \omega_\lambda)\delta_{\lambda\lambda'} + \Gamma'_{\lambda\lambda'}(\omega) \tag{4.59}$$

and

$$\Gamma'_{\lambda\lambda'}(\omega) = -\sum_m \int d\omega' \, \frac{\mathcal{W}_{\lambda m}(\omega')\,\mathcal{W}^*_{\lambda' m}(\omega')}{\omega - \omega' + i\epsilon}\,. \tag{4.60}$$

In order to compare to scattering theory, we substitute the definition of the coupling constants $\mathcal{W}$ and translate to the Schrödinger normalization and energy labeling by (see Appendix B.10.1)

$$\mathcal{W}_{\lambda m}(\omega) = \frac{1}{2\sqrt{\omega_\lambda \omega}}\tilde{W}_{\lambda m}(\omega) = \frac{1}{\sqrt[4]{2E_\lambda}} W_{\lambda m}(k)\,, \tag{4.61}$$

where $W_{\lambda m}(k)$ are the coupling constants corresponding to the scattering normalization. The scattering matrix then reads

$$S_{\mathrm{io}}^{(\mathrm{rot})}(k) = \delta_{mm'} - 2\pi i \sum_{\lambda,\lambda'} W^*_{\lambda m}(k)(D^{-1}_{\mathrm{rot}}(k))_{\lambda\lambda'} W_{\lambda' m'}(k)\,, \tag{4.62}$$

with

$$(D_{\mathrm{rot}}(k))_{\lambda\lambda'} = 2\sqrt{E_\lambda}(\sqrt{E(k)} - \sqrt{E_\lambda})\delta_{\lambda\lambda'} + \Gamma^{(\mathrm{rot})}_{\lambda\lambda'}(k)$$

and

$$\Gamma^{(\mathrm{rot})}_{\lambda\lambda'}(k) = -\sum_m \int \frac{dE(k')}{2\sqrt{E(k')}} \frac{W_{\lambda m}(k')W^*_{\lambda' m}(k')}{\sqrt{E(k)} - \sqrt{E(k')} + i\epsilon}\,. \tag{4.63}$$

We now see that these integrals are different to the ones encountered in scattering theory, due to the square-rooted energy dependence. However, since these expressions were derived under the assumption that the rotating wave approximation holds, we should also approximate $2\sqrt{E_\lambda} \approx \sqrt{E_\lambda} + \sqrt{E(k)}$ and $2\sqrt{E(k')} \approx \sqrt{E(k)} + \sqrt{E(k')}$ in the relevant energy ranges of above expressions. Substitution of these approximations shows that

$$D_{\mathrm{rot}}(k) \approx D(k)\,, \tag{4.64}$$

such that from comparing Eq. (4.62) with Eq. (4.44) we get

$$S_{\mathrm{io}}^{(\mathrm{rot})}(k) \approx S_{\mathrm{res}}(k)\,. \tag{4.65}$$

This means that if the rotating wave approximation applies and is carried through consistently, the correspondence between the input-output operator scattering and the resonant state scattering matrix still holds. We note that it is in fact crucial to perform the above second step within the rotating wave approximation, in order to obtain the correct pole structure of the system propagator yielding a converging multi-mode expansion (see also Chapter 5 and Appendix B.13).

We further note that a similar correspondence can be established within the slowly-varying envelope approximation as outlined in Appendix B.11, an approximation which only modifies the time-dependence of the system and still yields the exact steady-state response.

As a result, we find that within these approximations, our formalism can be applied straightforwardly to the scalar Helmholtz wave equation in the same way as for the Schrödinger equation, if a modified inner product and an energy-dependent potential are considered.

4.5.2 Scattering beyond the rotating wave approximation

Going beyond these approximations, we note that the input-output formalism does not require neglecting the counter-rotating terms [CC06]. Without RWA, an additional linear equation for the

conjugated operators has to be considered, which couples to the original equations via the counter-rotating terms. The input-output calculation can thus in principle be performed analogously.

From the discussion in Sec. 4.3 and Fig. 4.2 it is clear that this will yield an input-output scattering matrix describing scattering between bath operators, which has to be multiplied by a background term to obtain the full scattering between asymptotically free operators. The key difficulty now is to relate the contour integrals appearing in the operator scattering calculation (such as Eq. (4.63)) to the matrix elements in the state scattering calculation (such as Eq. (4.29)). In the case of the Schrödinger equation, a correspondence between the state scattering and the operator scattering has been shown in Sec. 4.4.2, using the relation of the contour integrals to the bath Green function. In the Maxwell case, this correspondence is obscured due to the rooted energy dependence in the contour integrals. The origin of this can be understood since for Maxwell's equations, the field satisfying the wave equation has mixed operator contributions $A(r,t) \sim \hat{b}\tilde{\psi} + \hat{b}^\dagger\tilde{\psi}^*$, while for the Schrödinger equation $\psi(r,t) \sim \hat{b}\tilde{\psi}$. We note that conceptually the lack of such a correspondence makes no difference and the input-output scattering matrix can still be calculated if the contour integrals are evaluated correctly. Only now it is not clear if $S_{\mathrm{io}}(k) = S_{\mathrm{res}}(k)$ can be invoked to simplify the calculation.

As a result, we conclude that even beyond the rotating wave approximation our formalism can be applied to calculate ab initio input-output scattering matrices, however the precise form of the corresponding background scattering matrix on the operator scattering level remains to be determined (see also Fig. 4.2).

4.6 Practical aspects

Before turning to an example calculation, we conclude our analysis with practical remarks, in particular focusing on applications in cavity QED. Applying the ab initio FMA discussed here in essence entails two parts. The first part is the calculation of the quantum optical parameters and coupling constants entering the Hamiltonian and the input-output relations. The second part is the solution of the equations of motion resulting from the Hamiltonian. Regarding the second part, it is important to note that the Hamiltonian and the input-output relations obtained from our FMA are quite similar in structure to that of the well-established phenomenological models. This is of great advantage, since it means that the solution methods established for phenomenological models can also be applied to our approach, once the coupling constants are evaluated.

Nevertheless, there are certain differences to standard phenomenological models, which we discuss in the following. The model input-output relation is usually written in the form [GZ04]

$$\hat{b}^{(\mathrm{out})}(t) - \hat{b}^{(\mathrm{in})}(t) = -i \sum_\lambda \sqrt{\kappa_\lambda}\, \hat{a}_\lambda(t)\,, \tag{4.66}$$

or alternatively in terms of the corresponding Fourier transforms

$$\hat{b}^{(\mathrm{out})}(\omega) - \hat{b}^{(\mathrm{in})}(\omega) = -i \sum_\lambda \sqrt{\kappa_\lambda}\, \hat{a}_\lambda(\omega)\,, \tag{4.67}$$

from which a spectrum can be computed. Here, κ_λ is the coupling constant between the cavity mode λ and the external bath mode considered.

The corresponding input-output relation derived within our approach reads (compare Eq. (4.38))

$$\hat{b}_m^{(\mathrm{out})}(\omega) - \hat{b}_m^{(\mathrm{in})}(\omega) = -i \sum_\lambda \mathcal{W}^*_{\lambda m}(\omega)\, \hat{a}_\lambda(\omega)\,. \tag{4.68}$$

This expression is similar in structure to Eq. (4.67), only now the cavity-bath coupling is frequency dependent. It is important to note that this frequency dependence also includes the possibility that the couplings change considerably within the spectral width of a single resonance, which cannot be captured by fitting a phenomenological Lorentzian mode to the response of the system. An example for this will be shown in Sec. 4.7.

Next, we turn to the equations of motion for the cavity modes. Including a loss constant γ, a typical equation of motion within a phenomenological model reads

$$\frac{d}{dt}\hat{a}_\lambda(t) = -i\omega_\lambda\, \hat{a}_\lambda(t) - i\sqrt{\kappa_\lambda}\, \hat{b}^{(\mathrm{in})}(t) - \gamma_\lambda\, \hat{a}_\lambda(t)\,. \tag{4.69}$$

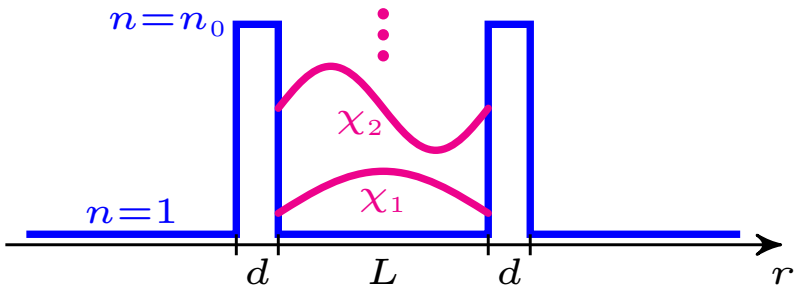

Figure 4.3: Model potential with two barriers. In the Maxwell case, this corresponds to the Ley-Loudon model for a two-sided Fabry-Perot cavity [LL87], and the solid blue curve shows the spatial refractive index distribution. For simplicity, in the calculation, the thin-mirror limit $d \to 0$ is considered, with $n_0 \to \infty$ such that $\eta = n_0^2 d$ remains finite [LL87; VH04]. In the cavity, the first two perfect-cavity modes χ_1, χ_2 are shown as magenta curves. For the Schrödinger case, the solid blue curve indicates the potential energy, which defines a tunneling problem.

This can again be expressed in Fourier space as

$$-i\omega\hat{a}_\lambda(\omega) = -i\omega_\lambda\,\hat{a}_\lambda(\omega) - i\sqrt{\kappa_\lambda}\,\hat{b}^{(\mathrm{in})}(\omega) - \gamma_\lambda\,\hat{a}_\lambda(\omega)\,, \tag{4.70}$$

so that spectroscopic quantities such as reflection or transmission spectra can be obtained by substituting Eq. (4.70) into Eq. (4.67). When atoms or other quantum systems are present inside the cavity, additional terms are added to describe cavity-atom interactions (see also Chapter 5).

The corresponding Langevin equation in our ab initio few-mode theory reads (compare Eqs. (4.40, 4.60))

$$-i\omega\hat{a}_\lambda(\omega) = -i\omega_\lambda\,\hat{a}_\lambda(\omega) - 2\pi i\sum_m \mathcal{W}_{\lambda m}(\omega)\,\hat{b}_m^{(\mathrm{in})}(\omega) - \sum_{\lambda'}[\gamma_{\lambda\lambda'}(\omega) + i\Delta_{\lambda\lambda'}(\omega)]\,\hat{a}_{\lambda'}(\omega)\,. \tag{4.71}$$

Comparing this with Eq. (4.70), we again find frequency dependent decay and coupling constants. Additionally, next to the loss rates $\gamma_{\lambda\lambda}$, an imaginary contribution $\Delta_{\lambda\lambda}$ appears, which induces a frequency shift. Furthermore, both the loss and the frequency shift parameters are now matrices, such that cross-mode coupling terms with $\lambda \neq \lambda'$ are present. Such cross-mode terms bear the potential for qualitatively different phenomena, for example, spontaneously generated coherences [FS05; Kif10; Hee13].

Also the frequency dependence of the coupling constants may lead to qualitative differences to phenomenological models, since in the time-domain, it implies non-Markovian dynamics. For example, the input-ouput relation in the time domain can be obtained by Fourier transforming Eq. (4.68) and reads [VH03]

$$\hat{b}_m^{(\mathrm{out})}(t) - \hat{b}_m^{(\mathrm{in})}(t) = -i\sum_\lambda \mathcal{W}^*_{\lambda m}(t) * \hat{a}_\lambda(t)\,, \tag{4.72}$$

where $\mathcal{W}^*_{\lambda m}(t) = \int \frac{d\omega}{2\pi}\, e^{-i\omega t}\mathcal{W}^*_{\lambda m}(\omega)$ and $*$ denotes a convolution. The output field thus depends on the history of the cavity mode operators. A similar connection is obtained when writing the Langevin equation in the time domain. We note that such non-Markovian input-output relations have been studied in detail in [Dió12; Zha13].

We therefore see that our ab initio few-mode theory can be employed as a tool to calculate cavity spectra analogously to the phenomenological approach, and the computational simplicity of the phenomenological models is not destroyed by the ab initio method. In particular for spectral observables, including frequency dependent couplings does not incur significant additional complexity. The main task to apply the formalism will thus lie in calculating the frequency dependent coupling and decay constants from the cavity geometry by employing the projection operator equations in Sec. 4.2. After this calculation, the complete tool box of the input-output formalism and system-bath theory can be applied and the various approximation schemes that are available for few-mode systems can be employed. For details on how these statements generalize in the presence of interactions refer to Chapter 5.

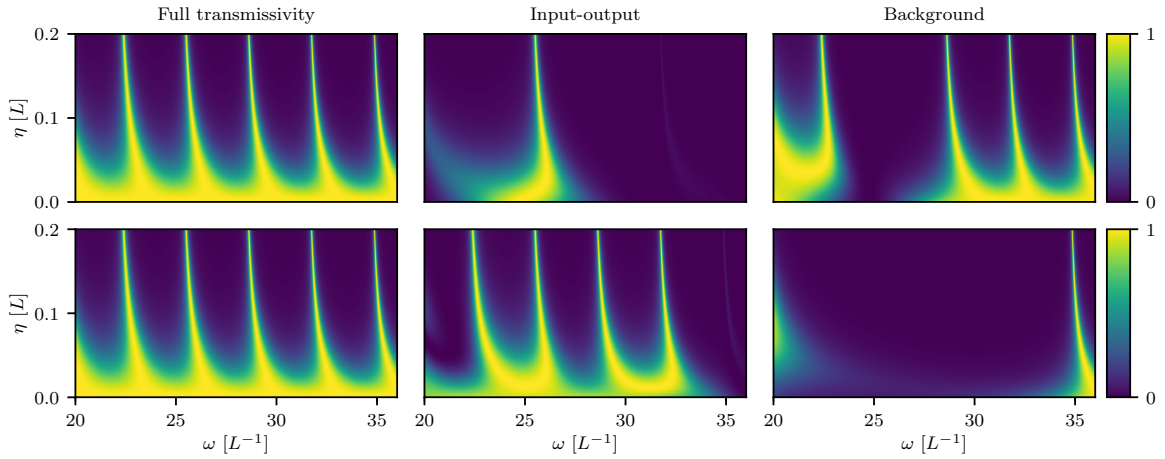

Figure 4.4: Transmission spectra for a Fabry-Perot cavity as a function of the mirror quality η. The top row shows the case in which the system comprises the single mode $\lambda = 8$. The bottom row shows corresponding results with the system consisting of the modes $\lambda \in \{7, 8, 9, 10\}$. In both cases, the left column illustrates the full transmissivity of the system. The middle and right columns show the input-output (S_{io}) and the background (S_{bg}) contributions, respectively. The full result can either be obtained from standard methods such as a transfer matrix formalism also known as Parratt's formalism [Par54; Röh05b], or as a product of the input-output and background scattering matrices.

4.7 Example: Double barrier potential

To illustrate our formalism for non-interacting theories and as a proof-of-concept, we perform explicit calculations for the example of a one-dimensional potential featuring two barriers, see Fig. 4.3. Because our derivation in the Maxwell case works analogously to the Schrödinger case, it is tempting to assume that the two wave equations will give similar results. Below, we show that this is not the case, because they lead to different potentials in the respective Hamiltonians, and thus to different scattering properties. In each case, we demonstrate how our few-mode formalism enables the extraction of relevant resonant dynamics.

4.7.1 Maxwell case: Fabry-Perot cavity

In the Maxwell case, the two-barrier potential is realized using a spatially varying index-of-refraction distribution, and corresponds to a two-sided Fabry-Perot cavity with a semi-transparent mirror at each end. For simplicity, we consider the thin-mirror limit $d \to 0$ with $n_0 \to \infty$ such that $\eta = n_0^2 d$ remains finite, which is known as the Ley-Loudon model [LL87; VH04]. This model is one of the simplest cavity geometries with tunable sharp resonances. The mirror quality can be characterized by $\eta = n_0^2 d$, which relates to the energy dependent mirror reflectivity via $r(\omega) = i\omega\eta/(2 - i\omega\eta)$ [LL87; VH04]. Within this model, the potential in the Maxwell case thus becomes

$$\tilde{V}(r, \omega) = -\big[\eta_1 \delta(r - L/2) + \eta_2 \delta(r + L/2)\big]\omega^2/2\,. \tag{4.73}$$

For this system a natural choice of cavity modes are the "perfect cavity modes", that is eigenstates in the cavity region with Dirichlet boundary conditions at the mirrors given by

$$\chi_\lambda(r) = \sqrt{\frac{2}{L}} \sin(\omega_\lambda r), \quad 0 \le r \le L. \tag{4.74}$$

The eigenfrequencies are $\omega_\lambda = \lambda\pi/L$ and L is the cavity length.

Based on these states, we numerically evaluate the input-output scattering matrix S_{io} and the corresponding background scattering matrix S_{bg} in the rotating wave approximation. Due to the cavity being open on both sides, this is a two channel problem featuring transmission as well as reflection. Each part in the relation $S = S_{\mathrm{bg}} S_{\mathrm{io}}$ thus is a 2×2 matrix.

In Fig. 4.4, we show transmission spectra for the cavity as a function of the mirror quality, and compare it to the individual resonant input-output (S_{io}) and background (S_{bg}) contributions. In all cases, the full transmissivity coincides with the product of the resonant and the background

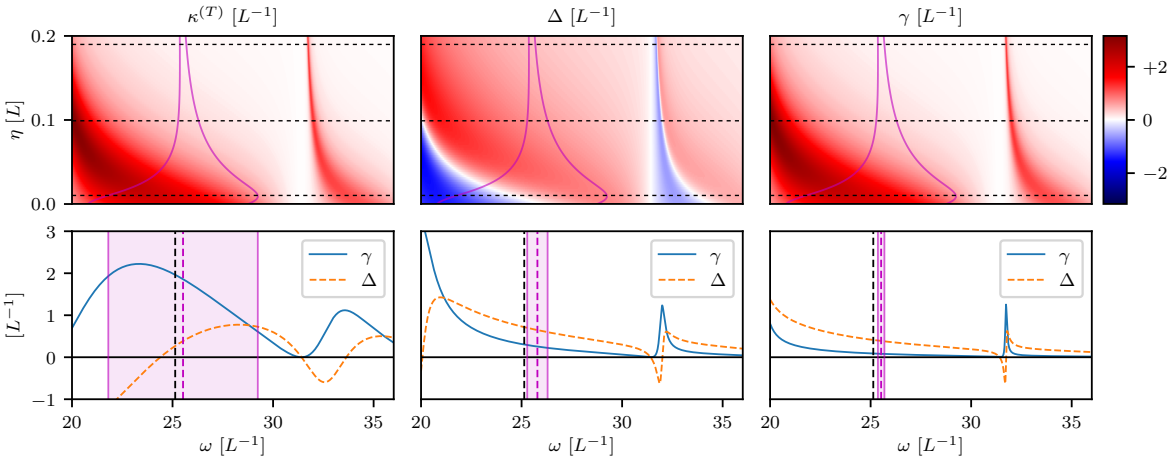

Figure 4.5: Quantum optical parameters calculated via the ab initio few-mode theory. The upper row shows the transmission coupling strength $\kappa^{(T)} = 2\pi|\mathcal{W}|^2$, the mode frequency shift Δ and the resonance width γ as a function of frequency and mirror quality η. The parameters are as in the upper row of Fig. 4.4, with the system comprising the single mode $\lambda = 8$. The magenta curves indicate the width of the resonance as function of η. The lower row shows cuts through the upper panels at fixed $\eta = 0.01, 0.1, 0.19$ (left to right, corresponding to the transition from a bad to a good cavity) indicated as dotted lines in the upper panel. The respective widths of the modes are indicated as shaded magenta regions, defined as twice the value of γ. The vertical dashed lines indicate the bare center frequency of the mode (black) as well as the actual center frequency (magenta).

contributions, as has been shown in Sec. 4.4.2. The upper row illustrates the case in which the system space comprises a single mode with $\lambda = 8$. The lower row shows corresponding results with four resonant modes as the system part ($\lambda \in \{7, 8, 9, 10\}$). As expected, for a good cavity with high η, well-resolved transmission resonances are obtained, which naturally split into the resonant and the background contributions. Each mode that is included in the few-mode Hamiltonian removes a resonance peak from the background and adds it to the input-output scattering matrix. This means that in the vicinity of the included resonances, one can expect that the input-output result alone gives a good representation of the scattering behavior. But towards the bad-cavity limit ($\eta \to 0$), the modes start to overlap, and the separation into resonant and background part becomes non-trivial. As a result, the background part is crucial, and more modes are required for the input-output matrix to capture the resonance behavior in the same frequency range. Also, the position of the mode resonance systematically shifts with the quality factor η, which is a consequence of the imaginary contribution δ found in the ab initio equations. Furthermore, the resonant modes become asymmetric with respect to their central frequencies, and are no longer of Lorentzian shape. This asymmetry can be understood since the width of the resonances decreases for this cavity with increasing energy. As a result there is more overlap of any particular resonance with its lower energy neighbor than with its higher energy neighbor, which also leads to the formation of two distinct pairs of modes in the case of multiple system modes in the lower row of Fig. 4.4.

Next, we study the quantum optical parameters extracted from our ab initio approach. Fig. 4.5 shows the transmission coupling strength $\kappa^{(T)}$ entering the input-output relation, the mode frequency shift Δ and the decay rate γ as a function of frequency and mirror quality η. All plots correspond to the upper panel of Fig. 4.4, with a single mode as the system subspace. In the upper panels of Fig. 4.5, the solid purple curve indicates the spectral width of the mode as function of η. The lower panels show three cuts through the plots in the upper panel, for different values of η. In these lower panels, the purple shaded area indicates the spectral width of the mode, which grows towards lower η. As expected, for a high-quality cavity, the system parameters calculated using the ab initio method are approximately constant over the spectral width of the resonance. Thus we again find that a phenomenological approach with constant parameters is well-suited to model the cavity dynamics. However, towards the bad-cavity limit, the system parameters significantly change within the spectral width of the mode, rendering a modeling using fixed phenomenological rates difficult. Finally, the vertical lines in the lower panel indicate the difference of the actual mode frequency from the "bare" mode frequency, that is the effect of the imaginary part Δ.

From these results, we conclude that our formalism can indeed be used to extract the resonant

dynamics of the system, by choosing the relevant modes that participate in the dynamics. We further conclude that the input-output formalism is not limited to the good cavity regime, however has to be applied with care when the cavity features overlapping modes, since background scattering and frequency dependence of the quantum parameters become sizable and cannot be neglected.

4.7.2 Schrödinger case: Tunneling problem

In the Schrödinger case, the double-barrier potential structure shown in Fig. 4.3 defines a tunneling problem, and can be written as

$$V(r) = \xi_1 \delta(r - L/2) + \xi_2 \delta(r + L/2)\,. \tag{4.75}$$

We note that this potential has prefactors independent of the energy, while the corresponding potential Eq. (4.73) for the Maxwell case is proportional to ω^2, and thus energy dependent. This gives rise to crucial differences between the Schrödinger and the Maxwell wave equation, which we discuss below.

Fig. 4.6 compares the transmissivity in the Schrödinger case and the Maxwell case, for the parameters $\xi_1 = \xi_2 = 10L^{-1}$ and $\eta_1 = \eta_2 = 0.5L$. The three rows correspond to a system space containing one mode (top row: $\lambda = 1$), two modes (middle row, $\lambda \in \{1, 2\}$), or the many-mode limit (bottom row, $\lambda \in \{1, \ldots, 100\}$).

The Schrödinger transmissivity features sharp resonances at low energies, which can be understood by noting that at low energies it is less likely for a particle to tunnel through or overcome the confining barriers (see Fig. 4.3). With increasing energy, these resonances become broader and start to overlap. Furthermore, the baseline of the transmissivity resonances rises with increasing energy.

In the Maxwell case, the transmissivity spectrum at low energies is entirely different. This is due to the prefactor ω^2 in the potential, which vanishes at low energies. As a consequence, the modes become broader and the baseline of the transmissivity resonances raises towards lower energies. In contrast, towards higher energies, the potential $\sim \omega^2$ is highly confining and features sharp resonances. On a qualitative level, the frequency dependence of the Maxwell resonances thus appears reversed as compared to the Schrödinger case.

Next, we investigate the behavior of the few-mode input-output results further in both cases, by comparing the input-output and background transmissivity separately for different system mode numbers (see Fig. 4.6). As expected, we observe that for each additional system mode, a resonance peak gets transferred from the background to the input-output spectrum. For the case where a single mode with $\lambda = 1$ is included, the Schrödinger and Maxwell equations show very different behavior. In the Schrödinger case the corresponding resonance is sharp and isolated, such that the input-output transmissivity reproduces the full result in the energy range of the resonance peak, even without having to include the background contribution. In the Maxwell case, however, these modes are broad and overlap, such that the background contribution is crucial. It is important to note that this difference is a consequence of the ω^2-dependence of the Maxwell potential, and not of the single-mode approximation. This can be seen from the top panel of Fig. 4.4, where the single mode $\lambda = 8$ is well-represented by the input-output part alone for the Maxwell case. As a result of the ω^2 dependence, the "perfect" system modes Eq. (4.74) for barriers of infinite height do not represent the $\lambda = 1$ case of shallow potential barriers well.

We further note that the transmissivity maxima in the Maxwell case of Fig. 4.6 lie between the ones for the Schrödinger equation, despite the identical geometry. On the level of wave equations, this can also be explained by the energy dependence of the potential causing the complex poles of the scattering matrix to shift. In the quantized few-mode Hamiltonian approach, the shift can alternatively be understood as radiative corrections to the bare system states, which we chose to be the perfect cavity states Eq. (4.74). These corrections arise from the system-bath coupling and are expressed as the complex decay matrix. The shifting effect can thus also be seen in Fig. 4.5, where the mode frequency shift Δ remains larger than the mode width for large η.

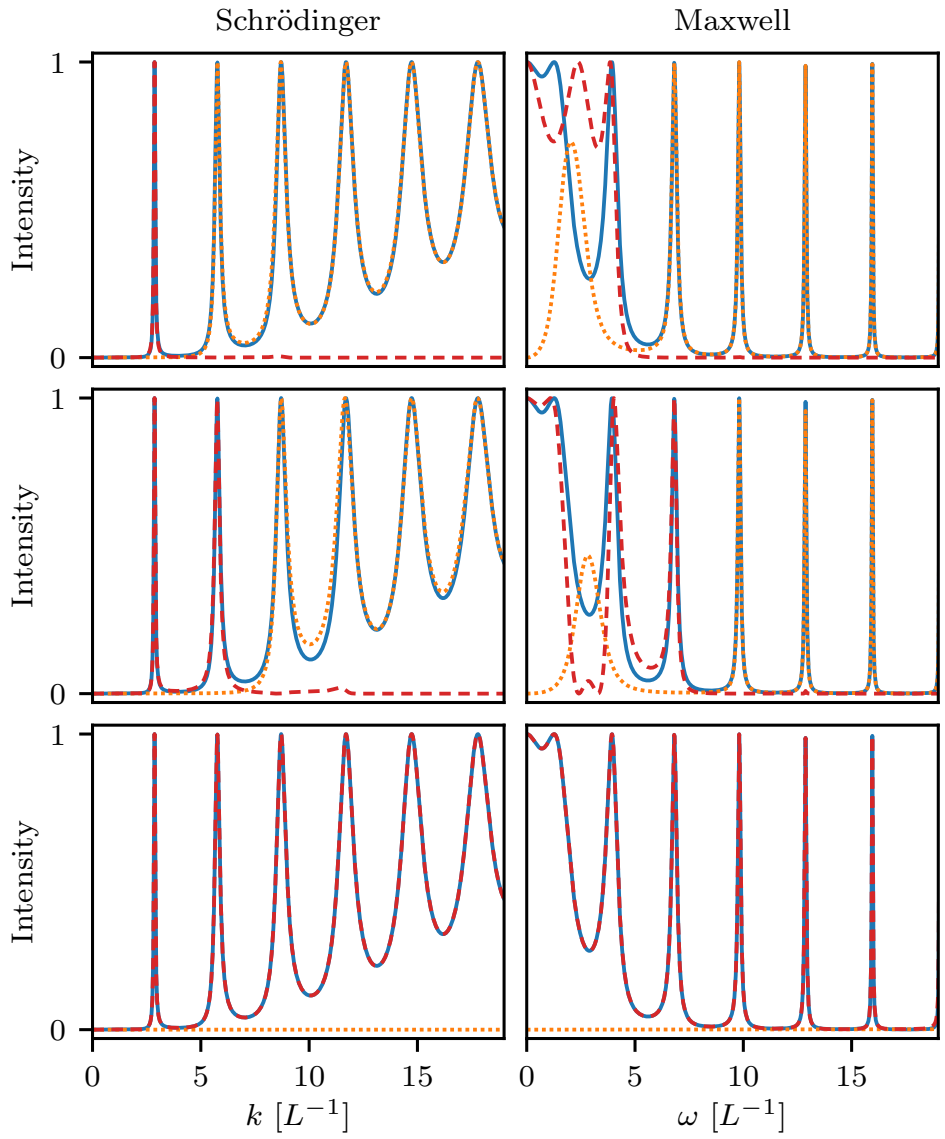

Figure 4.6: Transmission spectra for a Schrödinger (left column) and a Maxwell (right column) Fabry-Perot cavity, with different sets of system modes (top: $\lambda = 1$, middle: $\lambda \in \{1, 2\}$, bottom: $\lambda \in \{1, 2, \ldots, 100\}$). In each case, the full (solid blue), input-output (dashed red) and background (dotted orange) transmissivity are shown. For both wave equations, each added system mode transfers a resonance peak from the background to the input-output contribution, such that in the many mode case featuring 100 modes, the input-output result alone agrees with the full transmissivity (bottom panels). For sharp resonance peaks, the input-output result captures the behavior in the relevant energy range, if the corresponding modes are included (top and middle left panels). For overlapping resonances, the background contribution is crucial even in the vicinity of the resonance peak (top and middle right panels).

Chapter 5

Interacting theories: Few-mode expansions

As Chapter 4, this chapter is based on the following publication:

Ab Initio Few-Mode Theory for Quantum Potential Scattering Problems
D. Lentrodt and J. Evers
Physical Review X **10**, 011008 (2020)

The thesis author's role in the paper is that of the sole principle author. The content has been reproduced verbatim with permission of the journal (© 2020 American Physical Society) and coauthors. Sections 5.1, 5.5 have been adapted to suit the format of this thesis. Sec. 5.6 has been added as a perspective on recent results.

5.1 Outline

In the previous chapter, we have shown how to derive ab initio few-mode Hamiltonians for quantum potential scattering problems and how the full scattering information can be reconstructed from such Hamiltonians using the input-output formalism. We have further demonstrated that by choosing certain states in the few-mode basis, the corresponding spectral resonance peaks can be extracted. In this chapter, we employ these results to construct systematic expansion schemes for interacting problems, which addresses further open questions outline in Chapter 1 and 3.

The idea of extracting important degrees of freedom corresponding to the cavity resonances is at the heart of few-mode theory. The concept also naturally leads to a crucial approximation when considering interacting systems, such as atoms coupling to the quantized field, which are often theoretically intractable in their full complexity (see Chapter 3 for a background discussion). The *few-mode approximation* allows to boil down the field continuum to a few relevant degrees of freedom that dominate the interacting dynamics, by neglecting the interaction with other irrelevant modes (see Fig. 5.1). Our ab initio few-mode theory now enables this approximation to be performed rigorously, provides new insight on its range of validity and gives practical advantages for its application. The main step behind this progress is the possibility of choosing the system states at will while still treating the free system exactly, such that one can focus on approximating the interaction.

We note that the few-mode approximation has already been employed extensively in the study of cavity QED [Ber94; Har13; Rit13] and related subjects by using phenomenological few-mode Hamiltonians. Importantly, a large bulk of theoretical tools has been developed to solve and understand the resulting dynamical equations [GZ04; BP02; Car08], which have found applications in a broad quantum optics context, also beyond cavity QED. However, these approaches inherit the limitations of phenomenological few-mode theory discussed in the previous two chapters.

In this chapter, we show how our ab initio few-mode theory can be applied to interacting quantum systems, providing a number of advantages to phenomenological few-mode theory. Firstly, in ab initio few-mode theory, the empty cavity or potential is treated exactly no matter which system modes are chosen such that the interacting case inherits the advantages from the non-interacting one. Secondly, a systematic effective few-mode expansion scheme can now be constructed where only the interaction is approximated. Thirdly, an important aspect of our method is that it connects to the toolbox of phenomenological few-mode theory, such that frequently used techniques do not have to be abandoned. Lastly, this extends the reach of few-mode theory to extreme parameter regimes, such as highly open and multi-mode systems, where previously mentioned aspects of ab initio few-mode theory, such as frequency dependent couplings and background scattering, can be crucial. As

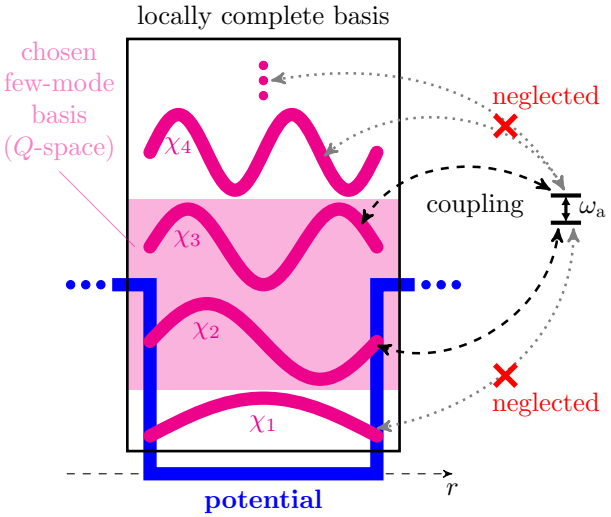

Figure 5.1: Schematic illustrating the results on interacting systems in this chapter, in particular the few-mode approximation and constructive approach to choosing few-mode bases for an ab initio effective few-mode expansion. After introducing system modes and bath modes in the previous chapter (see e.g. Fig. 4.1), the few-mode approximation consists of neglecting the interaction of the interacting subsystem (e.g. a two-level atom located inside the cavity with transition frequency ω_a) with the bath modes. In the figure, an example of a two-mode basis is shown as the states inside the magenta shaded box. Ideally, the set of system modes is chosen exploiting physical insight into the system under study, to facilitate the modeling of the system with as few modes as possible. In the absence of any prior knowledge, a constructive approach can be used to determine a few-mode basis. For this, a locally complete basis (states inside black box) is found as solutions to, for example, the Dirichlet boundary value problem in the potential region, which in general contains infinitely many modes. A few-mode basis is then given by a subset of the locally complete basis. Varying the number of modes in the few-mode basis and performing the few-mode approximation in each case yields a systematic expansion scheme.

outlined in Chapter 3, our method acts as an enabling technique in this context, complementing solution methods for open quantum dynamics and providing access to new approximations.

Fig. 5.1 provides an overview of the results on interacting systems and in particular illustrates the concept of effective few-mode expansions. We use a paradigmatic system from the theory of light-matter interactions, namely a two-level atom inside a cavity, as an example.

In the following, we first outline the construction of ab initio few-mode theory for interacting systems. We then discuss each of the advantages compared to phenomenological few-mode models, and demonstrate them using representative examples.

5.2 Effective few-mode expansions

We outline the construction of ab initio few-mode theory using a paradigmatic model from the field of light-matter interactions: a two-level atom in a cavity.

For clarity and consistency with previous sections, the term ‘system’ is reserved for the cavity in the following, and not used to describe the atom, which is referred to as ‘atom/interaction’.

5.2.1 Interaction Hamiltonian

The Hamiltonian for a Maxwell field interacting with a single two-level atom is [SZ97]

$$\hat{H} = \hat{H}_{\text{field}} + \hat{H}_{\text{atom}} + \hat{H}_{\text{int}}. \tag{5.1}$$

Here, $\hat{H}_{\text{field}}$ is given by the quantization of the dielectric wave equation from Sec. 4.5, and can be expressed in the usual normal mode basis by Eq. (B.79) or equivalently in a few-mode system-bath basis by Eq. (4.56). For a two-level system, the atomic Hamiltonian is given by $\hat{H}_{\text{atom}} = \frac{\omega_a}{2}\hat{\sigma}^z$, where ω_a is the transition frequency and $\hat{\sigma}^{x,y,z,+,-}$ are the Pauli operators. The interaction Hamiltonian can be obtained by the minimal coupling substitution [SZ97; CTDRG08], and in the dipole approximation

can be written as [SZ97; CTDRG08]

$$\hat{H}_{\text{int}} = -i\omega_{\text{a}}(d\hat{\sigma}^{+} - d^{*}\hat{\sigma}^{-})A(r_a), \tag{5.2}$$

where d and r_a are the transition dipole moment and the position of the atom, respectively. Consistently with previous notation, we set $\hbar = m_e = 1$. We note that following the minimal coupling prescription, we use the $p \cdot A$ interaction term here [SZ97; CDG97], since the canonical quantization scheme that we employed works in the Coulomb gauge [GL91], and as a result our system-bath Hamiltonians are also in this gauge. We further neglect the A^2 term in the interaction. This treatment is known to cause problems in the ultra-strong or deep-strong coupling regimes [FK19; FD19], whose resolution has been discussed elsewhere (see, for example, [De 14; GRPD15; MT16; MPT17; DBJR18; DS19; RSH13]). For our purposes, this approach suffices and we also perform the rotating wave approximation in the light-matter coupling. We note that polarization is already absent, since we considered a scalar version of the Maxwell wave equation in Sec. 4.5. As before, we employ these assumptions for simplicity, in order to demonstrate the central ideas of ab initio effective few-mode theories. We expect, however, that the method can be extended to a broad class of Hamiltonians, since it only relies on the few-mode concept and the previously constructed basis transformation for the field, which is exact.

The crucial advantage of the few-mode approach arises when we express the field in terms of a mode expansion. In the standard normal modes basis, the expansion results in an interaction Hamiltonian where the atom couples to a continuum of modes (see Eq. (B.80)). In the few-mode basis, the expansion Eq. (B.86) gives an alternative representation of the interaction Hamiltonian

$$\hat{H}_{\text{int}} = \hat{H}_{\text{atom-cavity}} + \hat{H}_{\text{atom-bath}}\,, \tag{5.3}$$

with [VH03; Kri14]

$$\hat{H}_{\text{atom-cavity}} = \sum_{\lambda} g_{\lambda}\hat{\sigma}^{+}\hat{a}_{\lambda} + h.c.\,, \tag{5.4a}$$

$$\hat{H}_{\text{atom-bath}} = \sum_{m} \int d\omega \tilde{g}_m(\omega)\hat{\sigma}^{+}\hat{b}_m(\omega) + h.c.\,, \tag{5.4b}$$

where the atom-cavity and atom-bath coupling constants are defined analogously to the normal mode case, that is

$$g_{\lambda} = -id\omega_{\text{a}}\sqrt{\frac{1}{2\omega_{\lambda}}}\chi_{\lambda}(r_a)\,, \tag{5.5a}$$

$$\tilde{g}_m(\omega) = -id\omega_{\text{a}}\sqrt{\frac{1}{2\omega}}\tilde{\psi}_m(r_a,\omega)\,. \tag{5.5b}$$

As shown in the previous sections on non-interacting problems, the ab initio few-mode approach allows one to choose the system modes freely without having to approximate the field Hamiltonian $\hat{H}_{\text{field}}$. This enables a systematic few-mode approximation scheme for the interacting theory, which we discuss in detail in the next sections.

5.2.2 Few-mode expansion scheme

We see from Eq. (5.3) that in the system-bath basis, the atom couples to the discrete system (cavity) modes as well as to a continuum of bath modes. While this Hamiltonian has been obtained from the normal modes Hamiltonian without further approximations, there is no clear advantage to the normal modes formulation yet, because the Hamiltonian still involves a continuum part. The *few-mode approximation* consists of only including the atom-cavity interaction,

$$\hat{H}_{\text{int}} \approx \hat{H}_{\text{atom-cavity}}\,, \tag{5.6}$$

such that the continuum part is neglected, where the cavity part includes the chosen system modes. If applicable, this approximation is tremendously useful, since it vastly reduces the complexity of the coupling and the dimension of the coupled system. Phenomenological few-mode theory, encompassing famous models such as the Jaynes-Cummings model [JC63], the Rabi model [Rab36; Bra11] and the Dicke model [Dic54; Kil80], is based on this approximation. Indeed the above interaction

Hamiltonian is exactly of the form of a multi-mode Jaynes-Cummings model, emphasizing the close connection between phenomenological and ab initio few-mode theory. However, we found in the previous sections that phenomenological few-mode theory may lead to incorrect predictions already in the non-interacting case, depending on the system and regime under study.

The key advantage of our ab initio few-mode theory as compared to phenomenological approaches is that the non-interacting system is treated exactly. As a result, we can choose any set of system modes to describe the cavity alone, without affecting the non-interacting part. This allows us to disentangle the few-mode approximation from approximative treatments of the cavity openness.

The few-mode expansion scheme then comprises a systematic variation of the number of system modes, such that the predictions of the approximate interaction Hamiltonian Eq. (5.6) converge to the exact results.

5.2.3 Choice of few-mode basis

From the previous section it is clear that the choice of the few-mode basis is important, and we will find below that it in particular affects the rate of convergence as a function of the number of included system modes. Usually, prior knowledge about the system under study can be used to guide the choice of relevant system modes. In general, this constitutes an optimization problem, where the task is to find the minimal and optimal set of modes with respect to an optimization criterion. What constitutes a good set of relevant modes may also depend on what further approximations one would like to make. For example, if one wants to derive a Markovian master equation by tracing out the bath modes, one should try to limit the frequency dependence of the coupling coefficients (see also Sec. 5.4).

In the absence of any prior knowledge, a constructive approach can be used that allows one to obtain a systematic expansion in the number of included modes. These modes may not be the optimally relevant few-mode basis, but they still provide a non-perturbative series expansion for observables. The method relies on the insight that for strongly confining systems, the perfect cavity eigenstates provide a good few-mode basis. A natural approach, even for weakly confining systems, is thus to solve the Dirichlet boundary value problem in the region of the cavity potential, giving a complete basis set in the region where the atom is located, as illustrated in Fig. 5.1. The few-mode basis is obtained by choosing a subset of these states, according to the energy scales set by the atom inside the cavity. The number of modes can then be varied systematically, and in the limit of infinitely many modes, where the few-mode basis becomes complete in the interaction region, should converge to the full solution of the problem (see Sec. 5.3.3 for a detailed investigation of convergence).

For completeness, we note that the selection of a confinement region with boundary conditions is reminiscent of R-matrix theory [WE47; LT58; Bur77; DB10], a first quantized approach to describe atomic, molecular and nuclear scattering properties, as well as the related exterior complex scaling method [Sim79; RS82; Scr10] in general resonance theory. In relation to shifting environment degrees of freedom of an open quantum system to obtain Markovian master equations we note a recent and very general result [Tam18], generalizing the pseudo-mode approach [Gar97b; Gar97a; DBG01; Maz09] for the spin-boson model.

5.2.4 Few-mode equations of motion

From the effective few-mode Hamiltonian Eq. (5.6), one can derive Heisenberg-Langevin equations of motion, analogously to what has been done in Sec. 4.4 for the free system. The equations of motion for the atomic operators read

$$\dot{\hat{\sigma}}^{+}(t) = i\omega_{\mathrm{a}}\hat{\sigma}^{+}(t) - i\hat{\sigma}^{z}(t)\sum_{\lambda}\hat{a}_{\lambda}^{\dagger}(t)g_{\lambda}^{*}, \tag{5.7a}$$

$$\dot{\hat{\sigma}}^{-}(t) = -i\omega_{\mathrm{a}}\hat{\sigma}^{-}(t) + i\hat{\sigma}^{z}(t)\sum_{\lambda}\hat{a}_{\lambda}(t)g_{\lambda}, \tag{5.7b}$$

$$\dot{\hat{\sigma}}^{z}(t) = -2i\hat{\sigma}^{+}(t)\sum_{\lambda}\hat{a}_{\lambda}(t)g_{\lambda} + 2i\hat{\sigma}^{-}(t)\sum_{\lambda}\hat{a}_{\lambda}^{\dagger}(t)g_{\lambda}^{*}\,. \tag{5.7c}$$

We note that we have not considered additional loss channels here, such as absorption or other electronic processes in the atom. We further note that in dimensions higher than one, it may be advantageous to trace out some of the bath modes and include them as a direct decay term in the

Langevin equations. This can be useful in describing, for example, radiative losses to the side of a Fabry-Perot cavity.

The input-output relation only depends on the system-bath Hamiltonian and hence stays unmodified by the coupling to the atom. Again performing the rotating wave approximation also in the system-bath coupling, we obtain

$$\hat{b}_m^{(\mathrm{out})}(\omega) - \hat{b}_m^{(\mathrm{in})}(\omega) = -i \sum_\lambda \mathcal{W}_{\lambda m}^*(\omega) \hat{a}_\lambda(\omega). \tag{5.8}$$

For the cavity operators, the equations of motion are most easily written in Fourier space analogously to Eq. (4.40) as

$$\hat{a}_\lambda(\omega) = \sum_{\lambda'} \mathcal{D}^{-1}_{\lambda\lambda'}(\omega) \big[2\pi \sum_m \mathcal{W}_{\lambda' m}(\omega) \hat{b}_m^{(\mathrm{in})}(\omega) + g^*_{\lambda'} \hat{\sigma}^-(\omega) \big]. \tag{5.9}$$

We see that by use of the input-output formalism and Heisenberg-Langevin equations, the bath dynamics are completely described by the input-output relation and the driving term in the cavity equation of motion. Therefore the coupled atom-continuum system has been transformed into a driven dissipative few-mode system.

5.3 Linear interacting dynamics

In the following, we demonstrate some specific advantages of ab initio few-mode theory mentioned above using a variety of practically relevant examples. In particular, we study the systematic few-mode expansion scheme for problems involving interactions that is offered by ab initio few-mode theory. To this end, we focus on the linear limit of the interacting system, which allows us to systematically investigate various features of the expansion scheme. The non-linear regime will be discussed in Sec. 5.4.

5.3.1 Scattering in the linear regime

It is well known that for linear systems, the input-output relations can be solved analytically without further approximations [WM08]. However, in obtaining the input-output relation, a Markov approximation [WM08] or an approximate extension of frequency integrals [VH03] is usually performed. Non-Markovian input-output theory [Dió12; Zha13] has been developed on the basis of phenomenological few-mode Hamiltonians. In our approach, neither of these approximations nor the assumption of a model Hamiltonian [GC85; GZ04] are necessary.

Consequently, the linear regime is an ideal candidate to demonstrate the advantages of ab initio few-mode theory.

The example of a two-level atom considered above is non-linear in general, but becomes linear in the weak excitation limit, where $\hat{\sigma}^z(t) \approx -1$, which physically corresponds to a weak field driving the atomic ground state, and is a frequently used approximation in quantum optics [WV06; FKS10]. An alternative way of performing the weak excitation approximation is a Holstein-Primakoff transformation [De 14; DBJR18].

In this limit, the above equations can be solved straightforwardly to give, switching from index to vector-matrix notation,

$$\hat{\underline{b}}^{(\mathrm{out})}(\omega) = \underline{\underline{S}}_{\mathrm{io}}(\omega) \hat{\underline{b}}^{(\mathrm{in})}(\omega), \tag{5.10}$$

with the operator scattering matrix

$$\begin{aligned} \underline{\underline{S}}_{\mathrm{io}}(\omega) &= \underline{\underline{\mathbb{I}}} - 2\pi i \underline{\underline{\mathcal{W}}}^\dagger(\omega) \big[\underline{\underline{\mathcal{D}}}(\omega) - \frac{1}{\omega - \omega_{\mathrm{a}}} \underline{g}^* \underline{g}^T \big]^{-1} \underline{\underline{\mathcal{W}}}(\omega) \\ &= \underline{\underline{S}}^{(\mathrm{free})}_{\mathrm{io}}(\omega) - 2\pi i \frac{\underline{\underline{\mathcal{W}}}^\dagger(\omega) \underline{\underline{\mathcal{D}}}^{-1}(\omega) \underline{g}^* \underline{g}^T \underline{\underline{\mathcal{D}}}^{-1}(\omega) \underline{\underline{\mathcal{W}}}(\omega)}{\omega - \omega_{\mathrm{a}} - \underline{g}^T \underline{\underline{\mathcal{D}}}^{-1}(\omega) \underline{g}^*}. \end{aligned} \tag{5.11}$$

The second formula is particularly useful since one can read off the complex level shift $\underline{g}^T \underline{\underline{\mathcal{D}}}^{-1}(\omega) \underline{g}^*$ and thus extract the Purcell enhanced line width of the atom

$$\gamma_{\mathrm{S}} = -\mathrm{Im}[\underline{g}^T \underline{\underline{\mathcal{D}}}^{-1}(\omega) \underline{g}^*], \tag{5.12}$$

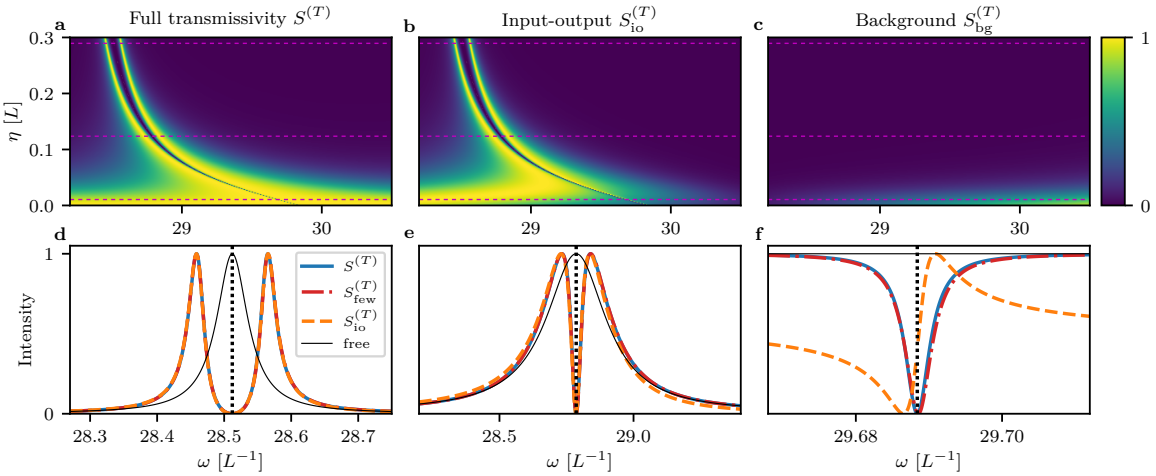

Figure 5.2: Linear transmission spectra of a coupled atom-cavity system. The cavity is chosen as in Fig. 4.4, and the transition frequency of the atom with $d = 0.01$ has been chosen resonant with the 9th empty cavity mode at each mirror quality η. (a) shows the full transmissivity calculated using linear dispersion theory as a reference. (b) shows the input-output part without the background contribution which is shown in (c), each calculated with three system modes ($\Lambda_Q = \{\chi_7, \chi_9, \chi_{11}\}$). Panels (d-f) show slices at $\eta = 0.289,\ 0.124,\ 0.011$, respectively. They correspond to a transition from strong coupling (d) via weak coupling (e) to a regime with negligible cavity confinement (f). In the entire range, the ab initio few-mode result ($S_{\mathrm{few}} = S_{\mathrm{bg}} S_{\mathrm{io}}$, red dash-dotted line) agrees well with the full result from linear dispersion theory (S, blue solid line), with good convergence already found using a single mode χ_9 for (d) and (e), and using three modes Λ_Q for (f). In the weak and strong coupling regimes, the input-output term alone is sufficient to model the interacting system (d,e). But in the regime of strongly overlapping modes and weak confinement, background scattering plays a crucial role (c), such that input-output scattering alone gives a vastly different line shape from the full result (f).

as well as its cavity modified Lamb shift

$$\delta_{\mathrm{LS}} = \mathrm{Re}[\underline{g}^T \underline{\underline{\mathcal{D}}}^{-1}(\omega) \underline{g}^*]. \tag{5.13}$$

These two quantities can thus be directly computed from the cavity geometry using ab initio few-mode theory.

We also see that the effective few-mode theory gives an expansion of the scattering matrix as a sum over the quantum optical coupling constants. As expected, the input-output scattering matrix reduces to the free case Eq. (4.58) in the limit $\underline{g} \to 0$, where the expression is exact up to the rotating wave approximation in the system-bath coupling. For the interacting case, one can systematically include more cavity modes in the projector basis and observe the series' convergence in the many modes limit, where the few-mode basis, if chosen correctly, approaches a complete set in the region of the atom (see Fig. 5.1). The expansion is non-perturbative in the sense that it is not limited to weak atom-mode coupling $\underline{g}$, however due to the rotating wave approximation the above expression does not apply in the ultra-strong coupling regime. Inclusion of the counter-rotating terms would, however, essentially result in additional linearly coupled equations (see also Sec. 4.5.2), which can be solved analogously in the linear regime, as has been shown in detail in [CC06].

To obtain the full scattering matrix between the observable asymptotically free operators, we have to account for the background scattering contribution again. Since it is only responsible for translating the bath operators into asymptotically free operators, the background scattering is independent of the matter coupling and can be computed as in the free theory.

5.3.2 Transition from strong coupling to free space

In Fig. 5.2, we show linear transmission spectra for the Fabry-Perot cavity that has also been investigated in Fig. 4.4, but now containing a single atom at its center, with a dipole moment of $d = 0.01$. The linear regime of this interacting system is ideal to demonstrate the advantages of ab initio few-mode theory, since the resulting equations of motion (5.7) can be solved without a Markov or semi-classical approximation, as shown in Sec. 5.3.1. Thus the effect of frequency dependent system parameters can be investigated. Additionally, linear dispersion theory [BW80; Zhu90] (see Appendix

B.12) can be used as a benchmark for comparison in the linear regime. We note that the results in Fig. 5.2 have been obtained using the constructive approach to choosing a system basis (see Section 5.2.3), without assuming any prior knowledge about the system.

The transmission spectra as a function of the mirror quality η show a transition from the strong coupling regime at high η, via the usual weak coupling regime at intermediate η, to a regime where the resonances overlap significantly until the situation approaches a weakly confined regime at low η, essentially corresponding to free space. The lower panels show slices of the two dimensional spectra in each of these regimes. To explore the potential of the ab initio few mode approach, we compare linear dispersion theory as a reference (S), the results obtained neglecting the background contribution (S_{io}), as well as the full ab initio few-mode result including the background contribution ($S_{\mathrm{few}} = S_{\mathrm{bg}} S_{\mathrm{io}}$).

We see that in the strong and weak coupling regime, all three approaches agree very well. In both cases, we found a single mode to be sufficient for good agreement. This is also illustrated in more detail in panels (d) and (e). However in the overlapping modes regime and at weak confinement, the situation is quite different. Panel (f) clearly shows that excluding the background contribution leads to qualitatively wrong predictions. For example, while S_{io} without the background contribution predicts an asymmetric Fano-like line shape, the full result including the background contribution remains Lorentzian. Consequently, phenomenological input-output theory fails in this regime, since the background and resonant scattering contributions are not distinguished in these models. Thus, the novel aspects of ab initio few-mode theory come into play and it is crucial that the empty cavity is treated exactly due to the strong mode overlap and absence of isolated resonances.

We further note that the ab initio few-mode approach has advantages already in the usual strong and weak coupling regime, even though phenomenological input-output theory is sufficient for a quantitative treatment there. Firstly, a rigorous foundation of the method is given. This also has the practical consequence that the quantum optical coupling constants can now be calculated from the cavity geometry, instead of being obtained by a fitting procedure. The latter may lead to theoretical design opportunities for quantum optical properties of complex structures. Secondly, it can already be seen that the toolbox of interacting few-mode and input-output theory can be applied straightforwardly without additional complexity. After the ab initio Hamiltonian of the non-interacting cavity is obtained, the calculation follows standard methods with minor adjustments (see Sec. 5.2.4).

5.3.3 Convergence of the few-mode expansion

As with any series expansion, an important requirement for the effective few-mode expansion is that it should converge as the number of system modes increases. Demonstrating the convergence of the few-mode expansion is particularly important as multi-mode light-matter coupling models are notorious for their divergent behavior (see, for example, [Kri14; Gel17; SMND18; MPT17]).

In Fig. 5.3, we numerically investigate the dependence of few-mode scattering observables on the number of system modes in the strong coupling and the multi-mode strong coupling regime. We again use the cavity geometry from Fig. 5.2, with $\eta = 0.15$ and $d = 0.03$ (strong coupling) or $d = 0.2$ (multi-mode strong coupling), and $\omega_{\mathrm{a}} = 28.71$ resonant with the ninth cavity mode χ_9. The atom is placed at the center of the cavity, such that only odd Dirichlet modes contribute to the interaction.

The few-mode basis is chosen as described in Sec. 5.2.2 by solving the Dirichlet boundary value problem. The single mode model contains the dominant ninth mode. We then label each few-mode basis in terms of a mode number N_{modes} as follows. We first add the odd modes in steps of two in decreasing order of dominance. A mode number of $N_{\mathrm{modes}} = 3$ then corresponds to $\Lambda_Q \in \{\chi_7, \chi_9, \chi_{11}\}$, $N_{\mathrm{modes}} = 5$ to $\Lambda_Q \in \{\chi_5, \chi_7, \chi_9, \chi_{11}, \chi_{13}\}$ and so on. Since there are no lower lying modes than χ_1, once it is included, we add the remaining higher lying odd modes in steps of one, such that for example $N_{\mathrm{modes}} = 10$ corresponds to $\Lambda_Q \in \{\chi_1, \chi_3, \ldots \chi_{15}, \chi_{17}\}$.

Panels (a,c) in Fig. 5.3 demonstrate that a single mode is already sufficient in the strong coupling regime of this isolated resonance cavity, as is expected from phenomenological few-mode theory. Panels (b,d) show that in the multi-mode strong coupling regime, the convergence is much slower for the chosen generic mode bases. While a single mode can already reproduce the qualitative features of the spectrum, in order to reach quantitative agreement a relatively large number of modes is required. It is further seen that when including more modes symmetrically around the dominant one (see labeling order described above), the spectral peak first shifts away from its final position before it starts to converge, a feature we will explain below.

Panel (e) quantifies the deviation of ab initio few-mode theory from the benchmark provided by linear dispersion theory as a function of the mode number N_{modes}. Note that the x-axis shows

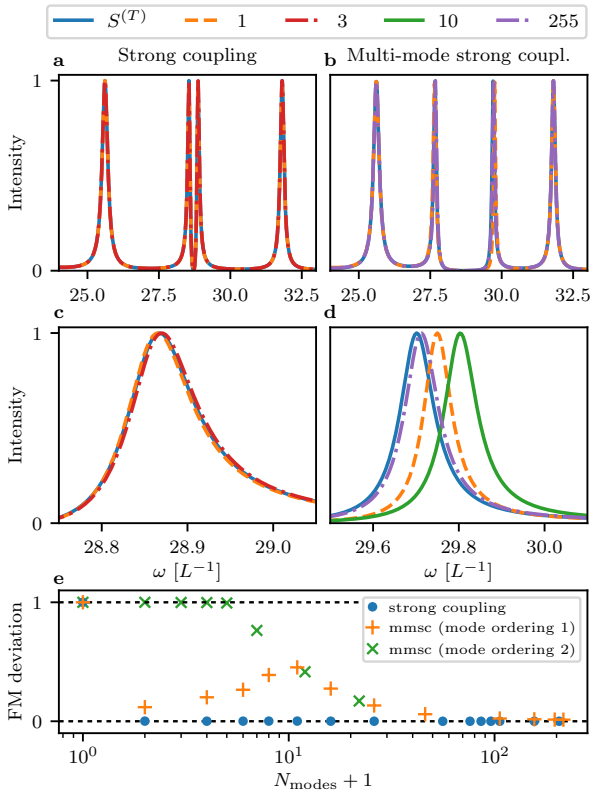

Figure 5.3: Convergence behavior of the few-mode expansion in the strong coupling (a,c) and multi-mode strong coupling (b,d) regime. Panels (a-d) show few-mode spectra at different numbers of system modes ($N_{\mathrm{modes}} \in \{1, 3, 10, 255\}$, see legend). The solid blue line shows linear dispersion spectra as a benchmark ($S^{(T)}$, solid blue). In the strong coupling case, the convergence is fast, with a single mode being sufficient (c), as expected. At multi-mode strong coupling, the qualitative behavior is already captured in a single mode description, but for quantitative agreement more than 100 modes of the generic mode basis are necessary (d). The convergence in the two cases can be quantified by the few-mode (FM) deviation Eq. (5.14). Panel (e) shows this quantity as a function of the mode number ($N_{\mathrm{modes}} + 1$). The strong coupling case (blue dots) shows the expected behavior. In the multi-mode strong coupling case (mmsc, orange crosses, green hatches), the convergence is much slower, and for low mode numbers, the convergence depends on the order in which the modes are added to the few-mode system space, as explained in the main text.

$N_{\mathrm{modes}} + 1$ to allow for a logarithmic representation. The few-mode deviation is defined by

$$\Delta_{\mathrm{few}} = \frac{\sum_\omega |S^{(T)}_{\mathrm{few}}(\omega) - S^{(T)}(\omega)|^2}{\sum_\omega |S^{(T)}_0(\omega) - S^{(T)}(\omega)|^2}, \tag{5.14}$$

where the frequency axis is evaluated on a grid and the superscript (T) indicates the transmission element of the scattering matrix. $S^{(T)}_0(\omega)$ is the zero modes few-mode theory coinciding with the transmission spectrum of the empty cavity. This quantity represents a phase-sensitive χ^2-like deviation metric that is normalized to the zero system modes case. The fast convergence in the strong coupling regime is evident from the sharp deviation drop from zero to a single mode. In the multi-mode strong coupling case, a much slower decline is observed in the generic mode basis, reaching reasonable convergence only at more than 100 modes with the few-mode deviation still decreasing.

Interestingly, a dip in Δ_{few} is found at a single mode, which is related to the above observation that the spectral peak first shifts away from its final position with increasing mode number, before it converges in reverse direction to the correct result. This effect can be understood from the fact that the modes χ_λ with $\lambda < 9$ cause a positive spectral shift of the peak, whereas the modes with higher mode number induce an opposite frequency shift. To verify this interpretation, we also study the convergence using an alternative ordering where the modes are included starting with χ_1 and simply counting up. For example, $N_{\mathrm{modes}} = 2$ corresponds to $\Lambda_Q \in \{\chi_1, \chi_3\}$, $N_{\mathrm{modes}} = 3$ corresponds to $\Lambda_Q \in \{\chi_1, \chi_3, \chi_5\}$ and so on. With this labeling order, a monotonic convergence is found (green crosses), because now the competition between opposite shifts of red-detuned and blue-detuned modes

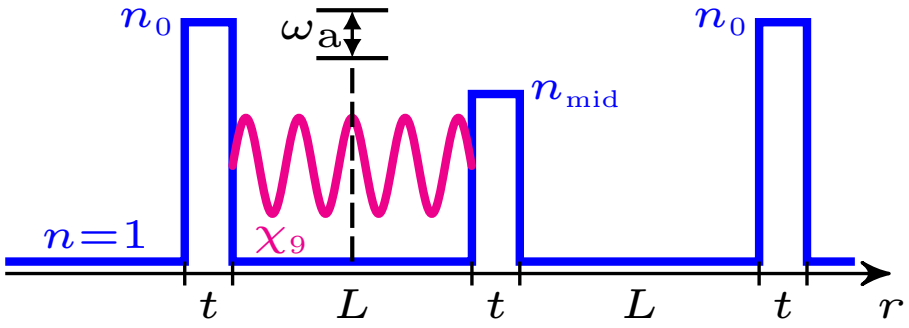

Figure 5.4: One-dimensional double cavity potential. The Q-space basis modes are chosen as solutions of the Dirichlet problem in the left cavity (the figure shows mode χ_9 in magenta as an example). This choice of basis appears particularly suitable for describing local light-matter interactions in the left cavity, but not in the right cavity. An atom is placed at the center of the left cavity, chosen resonant with the ninth cavity mode.

is avoided. These results demonstrate that in particular in the multi-mode strong coupling regime, the convergence properties are affected by the choice of the system basis.

Numerically, it is impossible to show whether the expansion indeed converges in a mathematical sense. In particular for the multi-mode strong coupling results, one may object that Fig. 5.3 does not exclude the possibility that the deviation oscillates very slowly or even diverges in the limit of infinitely many modes. In order to provide justification that this is not the case, we explicitly evaluate the relevant series terms of the few-mode expansion in Appendix B.13 and show that the final result is convergent as for the free cavity. The calculation is restricted to a specific geometry (see Appendix B.13 for details), but applies at any coupling strength within the validity range of the rotating wave approximation. The series expansion is therefore non-perturbative in the atom-cavity coupling strength, in the sense that it does not require a small parameter.

We note that multi-mode convergence of light-matter models has been discussed extensively in the literature, for example in the context of the Rabi and related models at ultra-strong coupling [De 14; Gel17; SMND18; MPT17] as well as in the context of time-dependent problems extending the Wigner-Weisskopf theory of spontaneous emission [Kri14; MPT16]. Divergences can be handled by cutoffs (see, for example, [Kri14] for an explicit account), cutoff-free methods have only been developed more recently by fully accounting for gauge invariance [MPT17]. We note that these discussions are mainly concerned with the complete treatment of the light-matter interaction, which is particularly important at ultra-strong coupling. Ab initio few-mode theory is based on a complete treatment of the cavity-bath interaction in few-mode theory. In our present analysis, we avoided issues arising at ultra-strong coupling by applying the rotating wave approximation. It will therefore be interesting to see if ab initio few-mode theory can be married with ultra-strong coupling theory, where phenomenological few-mode models are also a valuable tool (see, for example, [FK19; FD19; Kir19]).

5.3.4 Quantum optical properties in overlapping modes cavities

One remaining advantage of the ab initio method that we have not demonstrated yet is the effect of frequency-dependent quantum optical couplings in interacting few-mode theory. To this end, we consider the double Fabry-Perot cavity depicted in Fig. 5.4, with a varying refractive index n_{mid} of the central mirror. Unlike before, we choose a finite mirror thickness $t = 0.01$ and outer mirror refractive index $n_0 = 4.0$ in order to demonstrate that our approach is not limited to Ley-Loudon type [LL87] potentials with its unrealistic infinitely thin mirrors.

Such a double cavity geometry is ideal to investigate the transition from an isolated resonance to an overlapping modes regime that still features strong confinement. In this case, the overlap results from the near-degeneracy of modes in each respective cavity, which couple via leakage through the central mirror. Fig. 5.5 shows linear transmission spectra for this cavity as a function of n_{mid}, calculated using ab initio few-mode theory with a single system mode χ_9. The top panel (a) shows the empty cavity spectrum which already displays interesting overlapping modes features, including an avoided

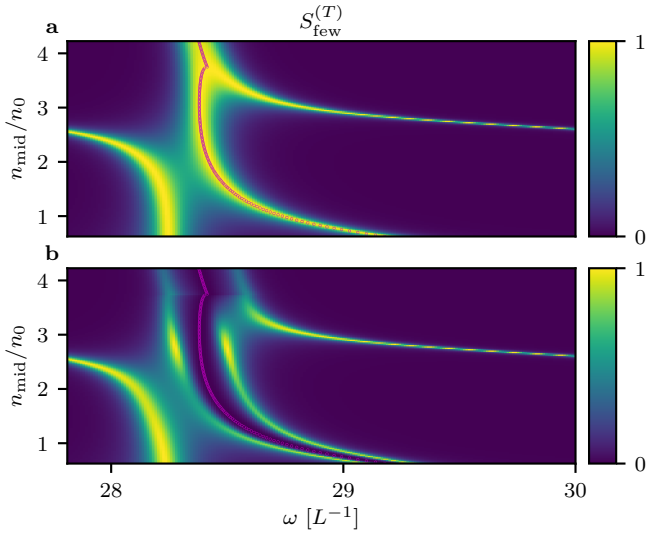

Figure 5.5: Linear transmission spectra for the double Fabry-Perot cavity in Fig. 5.4 as a function of the central mirror refractive index, calculated using ab initio few-mode theory with a single system mode (χ_9). (a) shows the empty cavity without atom. A transition between different regimes featuring an avoided crossing is observed. In (b), results of the interacting system with an atom at the center of the first cavity are shown. The atom's resonance frequency is chosen resonant with the empty cavity spectral peak, indicated by the magenta dots. A splitting of the resonant cavity mode is observed, with interesting features in the transition regions. The shown few-mode results are found to agree well with linear dispersion theory in both cases.

crossing at intermediate n_{mid} as well as a merging of spectral lines at high n_{mid}.

The spectral structure can be understood as follows. At $n_{\mathrm{mid}} \ll n_0$, the separating barrier is insignificant such that the cavity behaves like the single Fabry-Perot case from before with approximately twice the cavity length, showing isolated resonances.

As the central barrier increases, a transition from a single to a double cavity structure occurs. In the latter, a more useful intuitive picture is to think of the system modes in each cavity. Due to their interaction via leakage through the central barrier, the avoided crossing occurs. In this context it is interesting to point out the connection of ab initio few-mode theory to non-Hermitian Hamiltonian formulations [Rot09; Moi11; EG18] that are often used to interpret such scenarios and have also been considered in the context of potential scattering [SSS03; Sha08].

At higher n_{mid}, the central barrier becomes very reflective such that after the avoided crossing two lines merge together. We have thus observed the transition from a single cavity behavior via a double cavity structure with an avoided crossing to a third regime with a strong separating barrier.

The lower spectra include the effect of an atom at the center of the first cavity with $d = 0.03$ and ω_{a} chosen resonant with the cavity peak (magenta dots). We see that when adding the atomic interaction, vacuum Rabi-splitting of the spectral peak is observed, featuring modulations of peak intensity in the regimes of overlapping modes. One of the peaks even disappears completely at high n_{mid}. An interesting aspect is that panel (b) has been computed using only a single "single-cavity" mode (χ_9 in the first cavity, see Fig. 5.4). Nevertheless, this ab initio single mode theory correctly predicts the interacting spectrum across the whole shown range of n_{mid}, with multi-mode deviations from the linear dispersion theory result of less than a few percent at $n_{\mathrm{mid}}/n_0 < 1$ and less than a few permille at $n_{\mathrm{mid}}/n_0 > 1$. In this case, the single mode theory thus provides a good description of the interacting system even in a seemingly multi-mode regime, when the spectral peaks of the empty cavity overlap significantly. In comparison, phenomenological few-mode theory could only reproduce these results by including at least two modes, e.g. χ_9 in each cavity.

To investigate the reason behind this unexpected quality of the ab initio single-mode results in more detail, Fig. 5.6 shows the atom's cavity modified Lamb shift δ_{LS} and Purcell enhanced decay width γ_{S} [Pur46; HE13; KH14] (panels (b) and (c), respectively), along with slices at $n_{\mathrm{mid}} = 2.7,\ 7.0,\ 15.0$ (panels (d-f), respectively). These quantities are directly computed from the cavity geometry (see Appendix 5.3.1 for details) and we observe a varying frequency dependence. At low $n_{\mathrm{mid}} = 2.7$ (panel (d)), we observe two isolated resonance features, each having a frequency dependence as expected from the Lorentzian single-mode contributions in phenomenological few-mode models [WM08]. However, beyond that, the modes overlap significantly at $n_{\mathrm{mid}} = 7.0$ (panel (e)) and $n_{\mathrm{mid}} = 15.0$ (panel

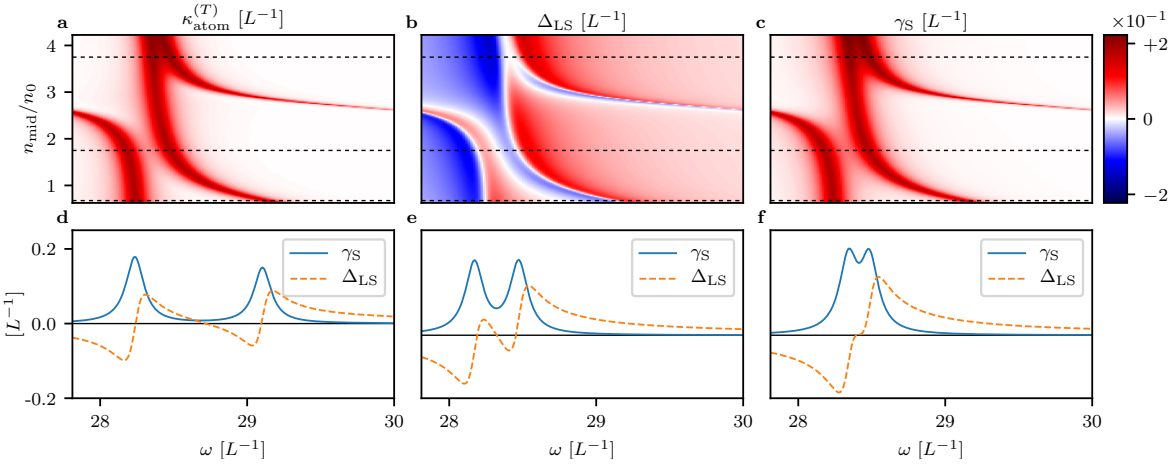

Figure 5.6: Quantum optical quantities corresponding to the atom-cavity spectra in Fig. 5.5. The Purcell enhanced line width γ_{S} of the atom, its cavity modified Lamb shift Δ_{LS} as well as $\kappa^{(T)}_{\mathrm{atom}} = 2\pi|[\underline{\underline{\mathcal{W}}}^{\dagger}(\omega)\underline{\underline{\mathcal{D}}}^{-1}(\omega)\underline{g}^{*}\underline{g}^{T}\underline{\underline{\mathcal{D}}}^{-1}(\omega)\underline{\underline{\mathcal{W}}}(\omega)]_{1,0}|$ are shown. These quantities are the atomic line analogues of the empty cavity couplings shown in Fig. 4.5 and have been computed using ab initio few-mode theory with a single system mode (χ_9). The lower panels (d-f) show slices at $n_{\mathrm{mid}} = 2.7,\ 7.0,\ 15.0$, respectively, demonstrating the transition between different regimes and that even the single mode theory is able to include effects beyond the isolated resonance approximation.

(f)). Still, our ab initio approach is able to account for these non-trivial bath effects in the overlapping modes case as shown in panels (e,f). In the latter cases, the standard result from single mode phenomenological few-mode theory breaks down and the advantage of the frequency dependent couplings in ab initio few-mode theory can be seen. For this reason, we conclude that ab initio few-mode theory can extend the validity range of a single mode description to new regimes by incorporating non-trivial bath effects beyond the isolated resonance approximation into the frequency dependent couplings.

5.4 Non-linear dynamics

In the previous sections, we have demonstrated that ab initio few-mode theory establishes a powerful expansion scheme for problems involving interactions. But so far, we have only considered the linear limit of the interacting system, which has allowed us to systematically investigate various features of the expansion scheme. In the following, we show that the approach can also be applied in the non-linear regime.

As in the linear case, we will again exploit that ab initio few-mode theory gives rise to Hamiltonians of a form similar to those used in phenomenological few-mode and system-bath theory [GZ04; Car08]. This central feature allows us to make use of many existing methods to tackle non-linear open-system dynamics, and to promote these methods to new regimes, by basing them on an ab initio few-mode Hamiltonian instead of on a phenomenological model.

As a concrete example, we extend the previous model of a two-level atom in a cavity to stronger external driving fields. We employ the semi-classical monochromatic drive approximation, which is a textbook example that enables an explicit analytical computation of scattering observables, and which is of significance, for example, in spectroscopy [WM08; Car08]. This model serves to demonstrate the applicability of ab initio few-mode theory in a scattering regime where the precise frequency dependence of the coupling constants matters, and that the resulting few-mode equations can indeed be solved using appropriate methods. In the process, we obtain analytic solutions for non-linear spectra of a two-level atom in an overlapping modes cavity in the form of a few-mode expansion.

5.4.1 Few-mode equations of motion with a semi-classical driving field

In order to show that ab initio few-mode theory can describe non-linear phenomena beyond the isolated resonance case, we employ the semi-classical assumption which is that the operator $\hat{b}^{(\mathrm{in})}_m(\omega)$ can be treated as a commuting classical variable $b^{(\mathrm{in})}_m(\omega) = b^{(\mathrm{in})}_m 2\pi\delta(\omega - \omega_{\mathrm{in}})$, where ω_{in} and $b^{(\mathrm{in})}_m$

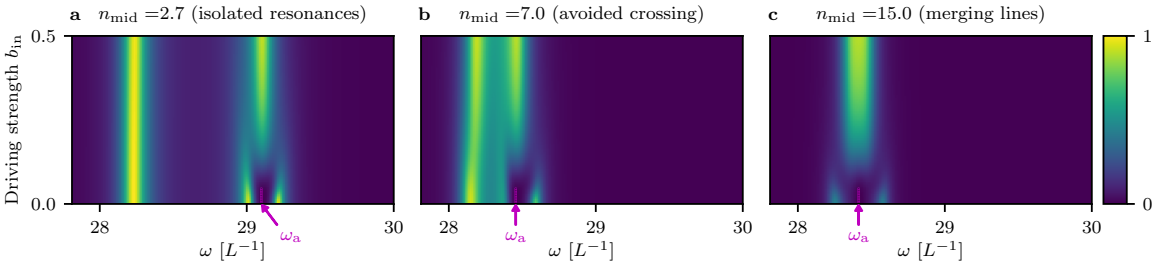

Figure 5.7: Non-linear spectra as a function of driving strength, corresponding to each of the regimes in Fig. 5.6. Panel a-c show results for $n_{\mathrm{mid}} = 2.7,\ 7.0,\ 15.0$, respectively. The cavity is driven from one side, such that $\underline{b}^{(\mathrm{in})} = b_{\mathrm{in}}\binom{1}{0}$, and the corresponding transmission spectra are shown. At $b_{\mathrm{in}} = 0$ the spectrum coincides with the linear interaction spectra shown in Fig. 5.5b at each n_{mid}. At large b_{in} the corresponding empty cavity spectra in Fig. 5.5a are approached due to saturation of the atoms excitation. The atoms resonance frequency for each spectrum has been chosen as before and is indicated by the magenta arrows.

are the driving frequency and amplitude, respectively. In the time domain, one can alternatively write $b_m^{(\mathrm{in})}(t) = b_m^{(\mathrm{in})} e^{-i\omega_{\mathrm{in}} t}$. Physically, this scenario corresponds to the steady-state response of the atom-cavity system for a monochromatic laser input when quantum fluctuations are neglected. The approximation has become a standard tool in quantum optics [CTDRG08; WM08; SZ97; Car99], and can also be interpreted as the calculation of coherent state scattering probabilities [FKS10].

With this driving term, the solution of the few-mode equations of motion is given by the cavity operators and atomic operators all oscillating at a constant frequency, $\hat{a}_\lambda(t) = \hat{a}_\lambda e^{-i\omega_{\mathrm{in}} t}$, $\hat{\sigma}^-(t) = \hat{\sigma}^- e^{-i\omega_{\mathrm{in}} t}$, $\hat{\sigma}^+(t) = \hat{\sigma}^+ e^{+i\omega_{\mathrm{in}} t}$ and $\hat{\sigma}^z(t) = \hat{\sigma}^z$. Substituting into the equations of motion gives

$$0 = i(\omega_a - \omega_{\mathrm{in}})\hat{\sigma}^+ - i\hat{\sigma}^z \sum_\lambda \hat{a}_\lambda^\dagger g_\lambda^*, \tag{5.15a}$$

$$0 = i(\omega_{\mathrm{in}} - \omega_a)\hat{\sigma}^- + i\hat{\sigma}^z \sum_\lambda \hat{a}_\lambda g_\lambda, \tag{5.15b}$$

$$0 = -i\hat{\sigma}^+ \sum_\lambda \hat{a}_\lambda g_\lambda + i\hat{\sigma}^- \sum_\lambda \hat{a}_\lambda^\dagger g_\lambda^*, \tag{5.15c}$$

$$\hat{a}_\lambda = \sum_{\lambda'} \mathcal{D}^{-1}_{\lambda\lambda'}(\omega_{\mathrm{in}}) \big[2\pi \sum_m \mathcal{W}_{\lambda' m}(\omega_{\mathrm{in}}) b_m^{(\mathrm{in})} + g_{\lambda'}^* \hat{\sigma}^- \big]. \tag{5.15d}$$

5.4.2 Steady-state non-linear spectra

Eliminating the cavity mode operator in Eqs. (5.15), we obtain closed equations for the atomic averages in terms of the given semi-classical drive amplitude

$$0 = -i\Delta\langle\hat{\sigma}^+\rangle - i\Omega^*\langle\hat{\sigma}^z\rangle + i\delta^*\langle\hat{\sigma}^+\rangle\,, \tag{5.16a}$$

$$0 = i\Delta\langle\hat{\sigma}^-\rangle + i\Omega\langle\hat{\sigma}^z\rangle - i\delta\langle\hat{\sigma}^-\rangle\,, \tag{5.16b}$$

$$0 = -i\Omega\langle\hat{\sigma}^+\rangle + i\Omega^*\langle\hat{\sigma}^-\rangle + \mathrm{Im}[\delta](\langle\hat{\sigma}^z\rangle + 1)\,, \tag{5.16c}$$

with the parameters

$$\Delta = \omega_{\mathrm{in}} - \omega_{\mathrm{a}}\,, \tag{5.17a}$$

$$\Omega = 2\pi \underline{g}^T \underline{\underline{\mathcal{D}}}^{-1}(\omega_{\mathrm{in}}) \underline{\underline{\mathcal{W}}}(\omega_{\mathrm{in}}) \underline{b}_{\mathrm{in}}\,, \tag{5.17b}$$

$$\delta = \underline{g}^T \underline{\underline{\mathcal{D}}}^{-1}(\omega_{\mathrm{in}}) \underline{g}^*\,. \tag{5.17c}$$

The solution for the atomic operators is given by

$$\langle\hat{\sigma}^-\rangle = \frac{\Omega}{\Delta - \delta + \frac{2|\Omega|^2}{\Delta - \delta^*}}\,, \tag{5.18a}$$

$$\langle\hat{\sigma}^z\rangle = -\frac{\Delta - \delta}{\Delta - \delta + \frac{2|\Omega|^2}{\Delta - \delta^*}}\,, \tag{5.18b}$$

such that the expectation value of the output field $\langle \hat{b}_m^{(\mathrm{out})}(\omega)\rangle = \langle \hat{b}_m^{(\mathrm{out})}\rangle \delta(\omega - \omega_{\mathrm{in}})$ is

$$\langle \hat{\underline{b}}^{(\mathrm{out})}\rangle = \underline{b}^{(\mathrm{in})} - i\underline{\underline{\mathcal{W}}}^{\dagger}(\omega_{\mathrm{in}})\underline{\underline{\mathcal{D}}}^{-1}(\omega_{\mathrm{in}})\big[2\pi\underline{\underline{\mathcal{W}}}(\omega_{\mathrm{in}})\underline{b}^{(\mathrm{in})} + \underline{g}^{*}\langle\hat{\sigma}^{-}\rangle\big]. \tag{5.19}$$

To illustrate the results that can be obtained with this approach, Fig. 5.7 shows non-linear transmission spectra as a function of driving strength for each of the slices that were shown in panels (d-f) of Fig. 5.6. That is the central barrier height is now held fixed at $n_{\mathrm{mid}} = 2.7,\ 7.0,\ 15.0$ corresponding to panels (a-c), respectively, such that non-linear effects in each of the three regimes investigated before can be seen. The atoms resonance frequency is also chosen as before and indicated in the figure for clarity.

At weak driving, that is when $b_{\mathrm{in}} = 0$, the spectra coincide with the linear interaction spectra shown in Fig. 5.5b for each of the depicted n_{mid}. At large b_{in} on the other hand the corresponding empty cavity spectra in Fig. 5.5a are approached, since the atom saturates at high driving strength in steady state. The transition region between these two extremes features rich behavior in the three regimes, all of which are now captured by ab initio few-mode theory with a single system mode.

We have thus demonstrated that ab initio few-mode theory interfaces with an existing method and in particular, that the aspects of the theory which are usually neglected in its phenomenological counterpart, such as frequency dependent couplings and background scattering, can be incorporated fully in the semi-classical monochromatic drive approximation.

5.4.3 Other few-mode solution methods

As outlined in the introduction, our technique connects to various solution methods, extending their reach to new regimes. We have demonstrated this explicitly in the previous sections using two common examples from quantum optics as a proof of principle. In general, to what extent the novel aspects of ab initio few-mode theory can be incorporated into other existing methods will depend on the specific regime and appropriate approximations. A common example is the derivation of a Markovian Master equation for the cavity-atom part of the system by tracing out the bath modes. This method can easily be combined with ab initio few-mode theory in the regime of isolated cavity resonances, where phenomenological few-mode models are expected to apply as well (see also Section 4.7.1). However, in regimes where frequency dependent cavity-bath couplings can not be eliminated by an appropriate choice of system states, the Markov approximation breaks down [GZ04]. On the other hand, non-Markovian Master equations and alternative methods to solve such systems have also been studied extensively in the literature [Car99; BP02; GZ04; dA17], and even non-Markovian input-output theory has been developed [Dió12; Zha13]. This case demonstrates that while ab initio few-mode theory provides a new foundation for existing few-mode methods and allows the underlying Hamiltonian to be applied in extreme regimes, the precise application of each method for computing observables on this basis is regime dependent and should be revisited separately.

5.5 Summary and conclusion

In this and the previous chapter, we introduced the ab initio few-mode theory, a technique to describe quantum dynamics in open and scattering systems. The method and results presented can be understood from different perspectives related to the open problems discussed in Chapters 1 and 3.

From a general point of view, we presented an approach to extract relevant degrees of freedom from a quantum field continuum. The concept exploits that in many physical systems and models, the quantum dynamics are often dominated by resonances or other meta-stable states, such that not the whole continuum participates in the dynamics. For non-interacting theories, we have presented an exact formalism that allows to rewrite the continuum in terms of a chosen set of relevant states. In the presence of interactions, this provides the option of simplifying the dynamics by only considering the interaction with these states. We have presented a systematic way to construct an effective few-mode expansion on this basis.

More specifically in the theory of light-matter interactions, our method closes a gap in the current theoretical description by linking a large existing toolbox based on phenomenological few-mode and input-output models to ab initio theory. This connection is provided by the following set of results. We have firstly presented a systematic approach to derive ab initio few-mode Hamiltonians. As a main result, we have demonstrated how to rigorously reconstruct the entire scattering matrix from such Hamiltonians using an input-output formalism, and have shown its equivalence to standard scattering

theory. In the process, we have found crucial differences to phenomenological few-mode theory, such as a previously unknown background scattering contribution. In the presence of interactions such as atoms coupling to the light field, a systematic expansion scheme has been obtained providing a number of advantages, which are inherited from the exact treatment of the non-interacting theory in the ab initio approach. We have demonstrated each of the advantages explicitly using the paradigmatic situation of a two-level atom in a cavity as an example. In the process, we have shown that ab initio few-mode theory applies in extreme regimes and can be used to compute various observables for linear and non-linear systems.

In conclusion, we have shown that ab initio few-mode theory provides a useful tool for describing a number of physical scenarios in quantum dynamics including extreme regimes, and that due to the generality of its concept, a broad class of systems, ranging from cavity QED to even relativistic scenarios, may be accessible through extensions of the method.

5.6 Afterword

After the submission of the paper which the above results are based on [LE20], further developments in few-mode theory occurred, which deserve to be put into context within the framework of this thesis.

In the way of applications, many of the issues discussed in the motivation in Sec. 3.5 are encountered on related frontiers such as polaritonic chemistry [FGGV18; Rib18] and condensed matter physics [Li20], where ab initio approaches such as quantum-electrodynamical density functional theory [Rug14; SRR18] and extensions of dynamical mean-field theory [GEW19; Aok14] are employed. While the ab initio few-mode theory is mainly concerned with the high openness of cavities and does not address particular questions related to the matter system, the few-mode projection scheme has recently been developed further and connected to the field of cavity-controlled chemistry [MM21], introducing few-mode Hamiltonians for cavity-molecule interactions.

Development on alternative approaches to few-mode theory in various contexts, such as quantized quasi-mode theory [HRK18; Fra19], have already been summarized in Chapter 3 and are discussed further in Chapter 10 and 15. In this afterword, we aim to outline recent progress in relation to and within the few-mode approach.

In particular, [Med21] presents a model approach to few-mode theory which can be applied to arbitrary electromagnetic spectral densities and features a closely analogous structure to the ab initio few-mode theory. The approach essentially uses the inverse basis transformation to the few-mode projection introduced in Chapter 4, i.e. a few-mode Fano diagonalization [Fan61; DBG01] (see Fig. 4.1), which allows to employ the spectral density to fix the model parameters. Importantly, [Med21] imposes that the system-bath coupling is spectrally flat. The latter is further motivated by a recent theorem from open quantum systems theory [Tam18], which proves an equivalence between continuum and discrete mode dynamics for certain correlation functions of such Hamiltonians with flat bath coupling. From the perspective of the ab initio few-mode theory, the method in [Med21] can in principle be seen as the special case of flat system-bath coupling. In particular, the mode coupling terms in [Med21] are essentially a basis transformed version of the cross-mode decay terms in [VH03; LE20]. However, the approach in [Med21] features key advantages. In particular, the difficulty of guessing the few-mode basis satisfying the flat bath condition is eliminated by using the inverse transform in combination with a fitting procedure. Since the projection transformation features matrix elements which can be difficult to calculate numerically, [Med21] thus finally promotes few-mode theory to a general tool that is practically applicable beyond the limitations outlined in Sec. 3.5. We note that we employ the approach of [Med21] for a multi-mode analysis of thin-film x-ray cavities in Chapter 10, where we also point out an interesting connection to Mittag-Leffler expansion as they are used in quasi-mode theory [Lal18].

Beyond quantum optics, our exact version of the input-output formalism constitutes an expansion of the scattering matrix based on the Feshbach projection approach [Dom83]. The question of how to expand the scattering matrix in terms of the alternative quasi-modes has received much recent attention, with multiple methods developed in the last few years [Alp17; Bin20; ZM20; Ben21b], some of which have already been implemented numerically [BBB21]. These approaches feature interesting connections to the input-output expansion. In particular, [ZM20; Ben21b] also use separations into a background and resonant scattering contribution and [Ben21b] further addresses the question of how to truncate the quasi-mode expansion to a finite number of degrees of freedom. Since the quasi-mode approach features an exact correspondence with the response poles, while the few-mode approach is designed to have canonical commutation relations of the underlying operators, uncovering the precise

relation between these different bases is an interesting question for the future (see also Chapter 10 for partial results in this direction).

Chapter 6

Application to x-ray cavity QED

This chapter is based on the following publication:

Ab initio quantum models for thin-film x-ray cavity QED
D. Lentrodt, K. P. Heeg, C. H. Keitel, and J. Evers
Physical Review Research **2**, 023396 (2020)

The thesis author's role in the paper is that of the sole principle author. The content has been reproduced verbatim with permission of the journal (© 2020 American Physical Society) and coauthors. Sec. 6.1 has been adapted to suit the format of this thesis.

6.1 Outline

In this chapter, we present an ab initio theory for thin-film x-ray cavities, based on our general formalism for few-mode theories [LE20] that is described in Chapters 4 and 5 of this thesis. The resulting model presented here is a direct generalization of the phenomenological pXCQED model for thin-film x-ray cavities [HE13; HE15], resolving the first part of the questions raised in Chapters 1 and 2 (see particularly Sec. 2.4).

In Sec. 6.2, we first provide additional details on the general multi-mode multi-ensemble version of the phenomenological pXCQED model [HE13; HE15], a simplified version of which was outlined in Sec. 2.3. As a comparison, we then summarize the structure of the ab initio model in Sec. 6.3. Sec. 6.4 presents the general solution of the resulting equations of motion in the linear regime. Sec. 6.5 gives an analytic expression for the spectroscopic signal, which is exemplified in Sec. 6.6. In Sec. 6.7, the effective level scheme of the nuclear ensembles is derived using adiabatic elimination of the cavity modes [HE15]. Sec. 6.8 considers an analytically solvable example cavity, which is used for benchmarking. In Sec. 6.9, the effects of thick resonant layers in this cavity geometry are considered.

We note that this chapter mainly serves to provide a direct generalization of and justification for the popular phenomenological model for thin-film x-ray cavities [HE13; HE15], and to showcase the ab initio few-mode method. However, the approach presented here is severely limited by the current lack of a numerical scheme that can be applied to general cavities. An orthogonal approach and numerically efficient way to derive the nuclear level scheme using a direct Born-Markov approximation is presented in Part II of this thesis. From a bird's eye perspective, we consider the latter an advantageous method for the quantum optical description of thin-film x-ray cavities with Mössbauer nuclei and defer readers who are interested in practical insights to Chapters 7 and 8. Nevertheless, the few-mode approach developed here also features advantages such as the possibility of analyzing multi-mode effects, which we make use of in Chapter 10.

6.2 Recap of the phenomenological model

In this section, we briefly summarize the essential features of the phenomenological quantum optical model for thin-film cavities developed in [HE13; HE15]. The simpler single-mode single-ensemble version of the model was already summarized in Sec. 2.3. Here, we outline the more general version which is illustrated in Fig. 2.2. For simplicity, we restrict ourselves to the unpolarized and unmagnetized case, which already features the essential ingredients. With polarization and magnetization included, one only obtains additional coupled equations [HE13; HE15].

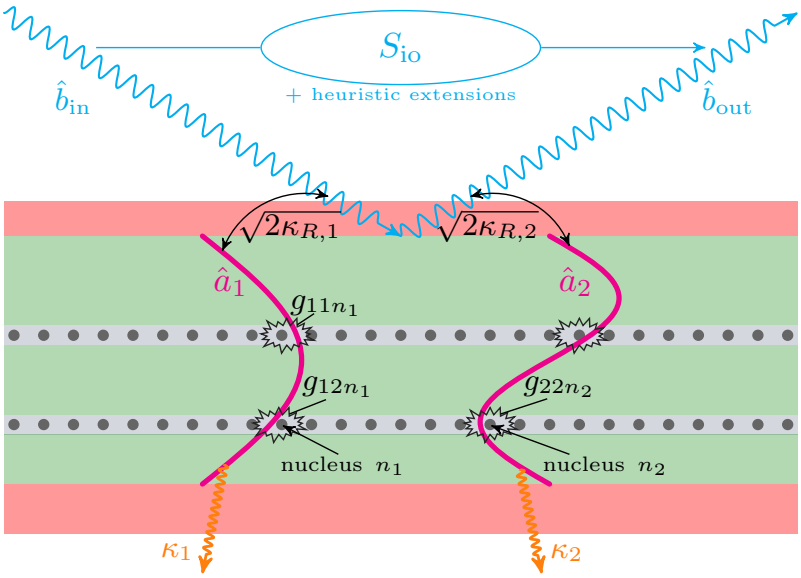

Figure 6.1: Schematic illustration of the phenomenological quantum optical model for cavity QED with Mössbauer nuclei, indicating the relevant processes and their coupling parameters. As an example, two of the system modes (magenta lines, $\hat{a}_\lambda$ for mode $\lambda \in \{1, 2\}$) coupled to the input-drive $\hat{b}_{\mathrm{in}}$ and output field $\hat{b}_{\mathrm{out}}$ (cyan wiggly lines) are shown. The coupling constants in the model include the system-bath coupling ($\sqrt{2\kappa_{R,\lambda}}$), the cavity mode decay constants (κ_λ) and the mode-nucleus coupling ($g_{\lambda l n}$ for nucleus n in ensemble/layer l). See also Table 6.1 for the functional dependencies of each model parameter. The input-output scattering matrix S_{io} describes the scattering process between bath modes via the cavity interacting with the nuclei, and is assumed to provide the full scattering information for x-rays being reflected of the system. For certain cavities, heuristic extensions of the model are necessary to provide more accurate descriptions of the cavity and nuclear response (see text).

The phenomenological model is given by the following equation for the density operator ρ characterizing the cavity and the nuclei [HE15],

$$\dot{\rho} = -i[H, \rho] + \mathcal{L}_{\mathrm{cav}}[\rho] + \mathcal{L}_{\mathrm{SE}}[\rho]\,. \tag{6.1}$$

The Hamiltonian contribution,

$$H = H_{\mathrm{cav}} + H_{\mathrm{nuc}} + H_{\mathrm{int}} + H_{\mathrm{drive}}\,, \tag{6.2}$$

consists of a cavity part H_{cav}, a nuclear part H_{nuc}, their interaction H_{int} and an external driving term H_{drive}. The two Lindblad terms describe the incoherent cavity decay and the spontaneous emission of the nuclei. The model is illustrated in Fig. 6.1. We work in natural units with $\hbar = c = 1$.

The dynamics of the empty cavity in the interaction picture are given by [HE15]

$$H_{\mathrm{cav}} = \sum_{\lambda \in \mathrm{modes}} \Delta_{C,\lambda}(\theta, \omega)\hat{a}_\lambda^\dagger \hat{a}_\lambda\,, \tag{6.3a}$$

$$H_{\mathrm{drive}} = \sum_{\lambda \in \mathrm{modes}} i\sqrt{2\kappa_{R,\lambda}}\hat{b}_{\mathrm{in}}\hat{a}_\lambda^\dagger + h.c.\,, \tag{6.3b}$$

$$\Delta_{C,\lambda}(\theta, \omega) = \omega_{C,\lambda}(\theta, \omega) - \omega = \sqrt{\omega^2 \cos^2(\theta) + \omega_{\mathrm{nuc}}^2 \sin^2(\theta_\lambda)} - \omega\,, \tag{6.3c}$$

where $\hat{a}_\lambda$ is the bosonic cavity mode operator with index λ, $\hat{b}_{\mathrm{in}}$ is an operator characterizing the driving field and $\sqrt{2\kappa_{R,\lambda}}$ is the drive coupling to mode λ. Δ_C is the cavity mode detuning relative to the external field with frequency ω. It depends on the incidence angle θ and is parametrized in terms of the resonance angles θ_λ of the modes at the nuclear resonance frequency ω_{nuc}, which is used as a reference. The detuning dependence on the external driving frequency can usually be neglected [Hee13] since the nuclear line width is typically orders of magnitude smaller than the cavity resonance width (see also Sec. 6.5, where this property is illustrated).

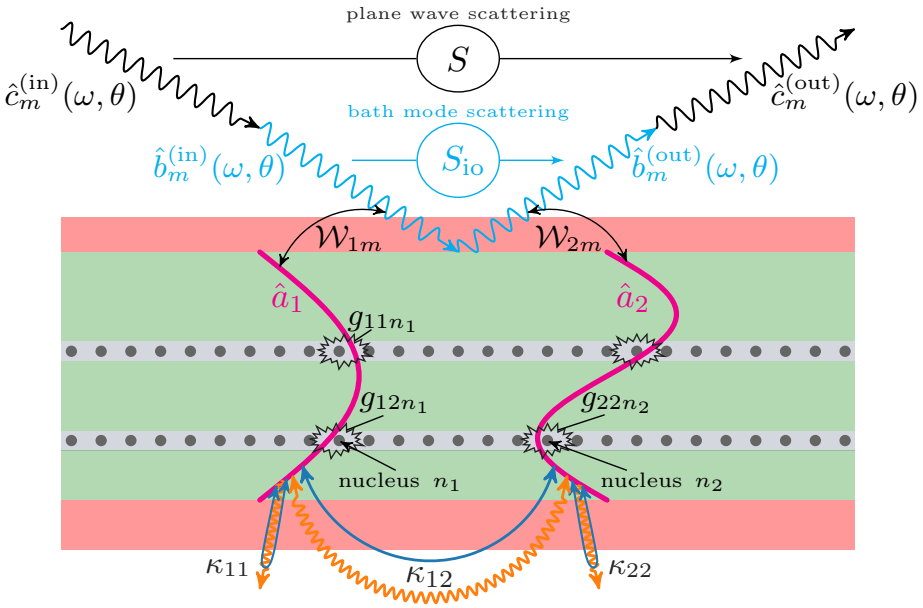

Figure 6.2: Schematic illustration of the ab initio few-mode model for cavity QED with Mössbauer nuclei. In comparison to the phenomenological model depicted in Fig. 6.1, the modes feature additional Lamb shifts (blue arrows at κ_{11}, κ_{22}) and cross-mode couplings (κ_{12}). Instead of a single drive, the bath is now an angle-dependent continuum with system-bath coupling constant $\mathcal{W}_{\lambda m}$ (corresponding to $\sqrt{2\kappa_{R,\lambda}}$ in the phenomenological model). The input-output matrix S_{io} still contains the bath mode scattering information, however, to obtain the plane wave scattering matrix S, one has to employ an additional background scattering contribution (see text). Again, Table 6.1 lists the functional dependencies of each model parameter.

Interactions with nuclei in the cavity are included via the Hamiltonian contributions [HE15]

$$H_{\mathrm{nuc}} = \sum_{\substack{l\in\text{ensembles}\\ n\in 1,2\ldots N_l}} \frac{\omega_{\mathrm{nuc},l}}{2}\hat{\sigma}_{ln}^{z}\,, \tag{6.4a}$$

$$H_{\mathrm{int}} = \sum_{\substack{\lambda\in\text{modes}\\ l\in\text{ensembles}\\ n\in 1,2\ldots N_l}} g_{\lambda ln}\hat{a}_\lambda\hat{\sigma}_{ln}^{+} + h.c.\,, \tag{6.4b}$$

where $\hat{\sigma}^z = |e\rangle\langle e| - |g\rangle\langle g|$, $\hat{\sigma}^+ = |e\rangle\langle g|$, $\hat{\sigma}^- = |g\rangle\langle e|$ are the Pauli operators of a single nucleus, and $|e\rangle$ ($|g\rangle$) is the corresponding excited (ground) state. Further, $\omega_{\mathrm{nuc},l}$ is the nuclear transition frequency of ensemble l. The indices are chosen such that l corresponds to the different resonant layers or ensembles and n runs over all the N_l nuclei within one such layer. $g_{\lambda ln}$ is the coupling constant of a nucleus to the cavity mode. The coupling is assumed to have the form $g_{\lambda ln} = g_{\lambda l}e^{i\phi_n}$ [HE15], including a position dependent phase ϕ_n due to propagation along the waveguide. We note that since the prefactor is independent of the nucleus index n within one layer l, the above form includes the thin-layer approximation. That is it is assumed that the mode profile does not vary significantly across a layer that is considered as one ensemble, such that describing thick resonant layers requires the inclusion of multiple sub-ensembles dividing the thick layer into thinner ones (see Sec. 6.9, Chapter 8 for an illustration and further details).

In addition to these Hamiltonian terms, the model features the incoherent contributions [HE15]

$$\mathcal{L}_{\mathrm{cav}}[\rho] = \sum_{\lambda\in\text{modes}} \kappa_\lambda(2\hat{a}_\lambda\rho\hat{a}_\lambda^\dagger - \{\hat{a}_\lambda^\dagger\hat{a}_\lambda,\,\rho\})\,, \tag{6.5a}$$

$$\mathcal{L}_{\mathrm{SE}}[\rho] = \sum_{\substack{l\in\text{ensembles}\\ n\in 1,2\ldots N_l}} \frac{\gamma}{2}(2\hat{\sigma}_{ln}^{-}\rho\hat{\sigma}_{ln}^{+} - \{\hat{\sigma}_{ln}^{+}\hat{\sigma}_{ln}^{-},\,\rho\})\,, \tag{6.5b}$$

where $\mathcal{L}_{\mathrm{cav}}[\rho]$ describes the cavity decay and $\mathcal{L}_{\mathrm{SE}}[\rho]$ the single nucleus incoherent decay. Here, ρ is the density matrix of the system and $\{\cdot,\cdot\}$ is the anti-commutator. We note that these terms describe inelastic processes only, while the elastic scattering is fully included via the interaction with the cavity modes.

In order to calculate output operators from the driving input and the cavity dynamics, the input-output relation [HE15]

$$\hat{b}_{\mathrm{out}} = -\hat{b}_{\mathrm{in}} + \sum_{\lambda \in \mathrm{modes}} \sqrt{2\kappa_{R,\lambda}}\hat{a}_\lambda \,, \tag{6.6}$$

is invoked. Spectroscopic observables can then be calculated from the output operators, such as the reflection coefficient given by [HE15]

$$r = \frac{\langle \hat{b}_{\mathrm{out}} \rangle}{\langle \hat{b}_{\mathrm{in}} \rangle} = -1 + \sum_\lambda \sqrt{2\kappa_{R,\lambda}} \, \frac{\langle \hat{a}_\lambda \rangle}{\langle \hat{b}_{\mathrm{in}} \rangle} \,. \tag{6.7}$$

Within the adiabatic approximation [HE13; HE15], the mode operator dynamics are given by [HE15]

$$\hat{a}_\lambda = \frac{\sqrt{2\kappa_{R,\lambda}}\hat{b}_{\mathrm{in}} - i\sum_{ln} g_{\lambda ln}\hat{\sigma}^-_{ln}}{\kappa_\lambda + i\Delta_{C,\lambda}} \,. \tag{6.8}$$

The nuclear dynamics can then be obtained from a nuclei-only Master equation obtained by adiabatically eliminating the cavity modes in Eq. (6.1).

The phenomenological few-mode model summarized so far has been employed for the analysis of various experiments in x-ray cavity QED [Hee13; Hee15a; Hee15b; Hab17; Hab19], providing a basis for the quantum mechanical interpretation of the system.

However, for certain cavities, it was found that heuristic extensions to the model are necessary. These include a dispersion as well as an envelope factor resulting in the modified reflection coefficient [HE15]

$$r = \frac{\langle \hat{b}_{\mathrm{out}} \rangle}{\langle \hat{b}_{\mathrm{in}} \rangle} = r_{\mathrm{env}}(\theta) \left[-r_{\mathrm{disp}} + \sum_\lambda \sqrt{2\kappa_{R,\lambda}} \frac{\langle \hat{a}_\lambda \rangle}{\langle \hat{b}_{\mathrm{in}} \rangle} \right] \,, \tag{6.9}$$

where $r_{\mathrm{disp}} = |r_{\mathrm{disp}}|e^{i\phi_C}$ is the dispersion factor that is introduced to account for a dispersion phase ϕ_C as well as for far off-resonant modes and r_{env} is the envelope factor that is introduced to account for total reflection behavior at grazing incidence.

While with these heuristic extensions included, good agreement with the layer formalism and experiment is found in many cases (see e.g. [HE13; Hee13; Hee15a; Hee15b; Hab17; Hab19]), there are still quantitative and even qualitative differences for important setups, such as the EIT cavity [HE15] that is investigated experimentally in [Röh12]. In addition, the heuristic extensions are neither justified nor derived from the quantum mechanical input-output theory [GC85; GZ04], restricting the predictive power of the model. In our analysis below, we will remove these restrictions, clarify the relations between different theoretical approaches, and prove an accurate complete description of the system without the need for heuristic extensions (see Fig. 7.1 for an overview).

We note that our results do not invalidate the phenomenological model, which is intrinsically consistent and which we show to be a good description in many cases. The main improvements of the ab initio theory developed in the following are the extension to the cases of overlapping modes and highly leaky cavities, the unambiguous computation of the quantum couplings in the effective level scheme and the justification of approximations required to obtain the description setting the ground for a predictive theory beyond the linear regime.

6.3 Ab initio few-mode theory for thin-film x-ray cavities

The ab initio few-mode theory for x-ray cavity cases can be written in close analogy to the phenomenological version summarized in Sec. 6.2. The main differences are the functional dependencies of the coupling constants and the treatment of the input-output relation as illustrated in Figs. 6.1, 6.2 and Table 6.1.

In this section, we outline these differences and define the structure of the ab initio theory. A detailed derivation is given in Appendix C.1, together with a functional summary of the concept of the ab initio few-mode theory. For readers who are interested in how to apply the method in practice, we refer to Sec. 6.8, where an explicit example system including analytic formulas for the required coupling constants is presented.

	Pheno model	Ab initio model
Mode resonance	$\Delta_{C,\lambda}(\omega,\theta)$	$\tilde{\Delta}_{C,\lambda}(\omega,\theta)$
Cavity loss	κ_λ	$\kappa_{\lambda\lambda'}(\omega,\theta)$
Bath/drive coupling	$i\sqrt{2\kappa_{R/T,\lambda}}$	$\mathcal{W}_{\lambda m}(\omega,\theta)$
Mode-nucleus coupling	$g_{\lambda l}$	$g_{\lambda l}(\theta)$
Background scattering	-	$S_{\mathrm{bg}}(\omega,\theta)$
Heuristic extensions	r_{disp}, $r_{\mathrm{env}}(\theta)$	-

Table 6.1: Overview of the differences between the phenomenological model for thin-film x-ray cavities [HE13; HE15] and its ab initio counterpart developed in this chapter. The quantum optical parameters (left) and their functional dependencies in each case (middle and right) are shown.

The Hamiltonian governing the dynamics is analogous to the phenomenological version in Eq. (6.2),

$$H = H_{\mathrm{cav}} + H_{\mathrm{nuc}} + H_{\mathrm{int}} + H_{\mathrm{drive}} + H_{\mathrm{field}}\,. \tag{6.10}$$

The empty-cavity dynamics are governed by

$$H_{\mathrm{cav}} = \sum_{\lambda\in\mathrm{modes}} \omega_\lambda(\theta)\hat{a}_\lambda^\dagger\hat{a}_\lambda\,, \tag{6.11a}$$

$$H_{\mathrm{drive}} = \sum_{\substack{m\in\mathrm{channels}\\ \lambda\in\mathrm{modes}}} \int d\omega \mathcal{W}_{\lambda m}(\omega,\theta)\hat{b}_m(\omega)\hat{a}_\lambda^\dagger + h.c.\,, \tag{6.11b}$$

$$H_{\mathrm{field}} = \sum_{m\in\mathrm{channels}} \int d\omega\tilde{\omega}(\omega,\theta)\hat{b}_m^\dagger(\omega)\hat{b}_m(\omega)\,, \tag{6.11c}$$

which generalizes Eqs. (6.3). The cavity mode detuning to a selected bath mode is then given by

$$\tilde{\Delta}_{C,\lambda}(\omega,\theta) = \omega_\lambda(\theta) - \tilde{\omega}(\omega,\theta)\,, \tag{6.12}$$

which replaces $\Delta_{C,\lambda}(\omega,\theta)$ in Eq. (6.3c) from the phenomenological approach. We note that in the ab initio formulation, no explicit driving term is specified on the level of the Hamiltonian. Rather, the coupling to all bath modes $\hat{b}_m(\omega)$ is included, with their free evolution term H_{field}. The external driving field is then specified through expectation values or correlation functions of the input operators corresponding to the bath modes within the input-output formalism [see Eq. (6.17) below]. For this reason, we also do not work in an interaction picture here, but with the bare frequencies such as $\tilde{\omega}(\omega,\theta)$, which is an effective bath mode frequency at a given incidence angle or parallel wave vector (see Appendix C.1 for details). For notational brevity, we omit the parametric angular dependence of the mode operators.

We note that the angular and frequency dependence of the effective mode detuning $\tilde{\Delta}_{C,\lambda}(\omega,\theta)$ may differ from the one assumed in the phenomenological model by $\Delta_{C,\lambda}(\omega,\theta)$ in Eq. (6.3c) (refer to Sec. 6.8 and Fig. 6.4 for an example). Similarly, $\mathcal{W}_{\lambda m}(\omega,\theta)$ extends the in-coupling rate $\sqrt{2\kappa_{R/T,\lambda}}$, where m is an index for the external channels, such as reflection and transmission denoted by R/T in the phenomenological model [Hee13].

Interactions with the nuclei are included via the contributions

$$H_{\mathrm{nuc}} = \sum_{\substack{l\in\mathrm{ensembles}\\ n\in 1,2\ldots N_l}} \frac{\omega_{\mathrm{nuc},l}}{2}\,\hat{\sigma}_{ln}^z\,, \tag{6.13a}$$

$$H_{\mathrm{int}} = \sum_{\substack{\lambda\in\mathrm{modes}\\ l\in\mathrm{ensembles}\\ n\in 1,2\ldots N_l}} g_{\lambda l}(\theta)\,\hat{a}_\lambda\,\hat{\sigma}_{ln}^+ + h.c.\,. \tag{6.13b}$$

which are essentially identical to their phenomenological counterparts Eqs. (6.4), only now the mode-nucleus coupling is dependent on the incidence angle.

The incoherent nuclear decay corresponding to Eq. (6.5) is still given by

$$\mathcal{L}_{\mathrm{SE}}[\rho] = \sum_{\substack{l\in\mathrm{ensembles}\\ n\in 1,2\ldots N_l}} \frac{\gamma}{2}(2\hat{\sigma}_{ln}^-\rho\hat{\sigma}_{ln}^+ - \{\hat{\sigma}_{ln}^+\hat{\sigma}_{ln}^-,\,\rho\})\,. \tag{6.14}$$

As in the phenomenological model, elastic scattering is included via the interaction with the cavity modes.

The density operator fulfills a generalization of the Master equation Eq. (6.1), such that also the radiative bath degrees of freedom are now included, and the Hamiltonian and Lindbladian are modified to comprise Eqs. (6.11-6.14). The decay constant in the spontaneous emission term is the natural linewidth γ, as in the phenomenological case Eq. (6.5b) (see Appendix C.1.5 for details on the decay constant).

The cavity decay term in the phenomenological model $\mathcal{L}_{\text{cav}}[\rho]$, however, has no direct counterpart in the ab initio few-mode theory, since the frequency dependence of the cavity-bath couplings induces non-Markovian dynamics of the cavity modes [HVH02; VH03; Zha13]. In particular for cavities with overlapping modes [LE20], which are realized in standard x-ray cavities as we will show in Sec. 6.8, this effect is not negligible and no Markovian Lindblad term for the cavity modes can be obtained. We note, however, that when tracing out the full cavity as a structured bath for the nuclei, the Markov approximation is applicable for many cavities due to the narrow line width of the nuclear response, which is the basis for the Green's function approach presented in Chapter 7.

In the ab initio few-mode approach, instead of a Lindblad term for the cavity decay, one can write a frequency domain equation for the cavity mode operators [LE20]

$$\hat{a}_\lambda(\omega) = \sum_{\lambda'} \mathcal{D}^{-1}_{\lambda\lambda'}(\omega,\theta)\left[2\pi \sum_m \mathcal{W}_{\lambda' m}(\omega,\theta)\hat{b}^{(\text{in})}_m(\omega) + \sum_{ln} g^*_{\lambda l}\hat{\sigma}^-_{ln}(\omega)\right], \tag{6.15}$$

$$\mathcal{D}_{\lambda\lambda'}(\omega,\theta) = -\tilde{\Delta}_{C,\lambda}(\omega,\theta)\delta_{\lambda\lambda'} + i\kappa_{\lambda\lambda'}(\omega,\theta), \tag{6.16}$$

which is a direct generalization of Eq. (6.8) in the phenomenological approach going beyond the adiabatic and Markov approximations, with the effective mode detuning $\tilde{\Delta}_{C,\lambda}(\omega,\theta)$ defined in Eq. (6.12).

In comparison to the phenomenological model version in Eq. (6.8), the cavity loss rate is now replaced by a frequency and incidence-angle dependent cavity loss matrix $\kappa_{\lambda\lambda'}(\omega,\theta)$, corresponding to $-i\Gamma'_{\lambda\lambda'}(\omega,\theta)$ in [LE20]. It has a matrix structure, as it includes cross-mode coupling terms, going beyond the single-mode cavity decay rates κ_λ in the phenomenological model as illustrated in Figs. 6.1, 6.2.

In order to calculate observables, the exact input-output theory from [LE20] allows one to obtain the frequency-domain input-output relation for the input [output] bath operators $\hat{b}^{(\text{in})}_m(\omega)$ $[\hat{b}^{(\text{out})}_m(\omega)]$ at a given incidence angle,

$$\hat{b}^{(\text{out})}_m(\omega) = \hat{b}^{(\text{in})}_m(\omega) - i\sum_\lambda \mathcal{W}^*_{\lambda m}(\omega,\theta)\hat{a}_\lambda(\omega), \tag{6.17}$$

generalizing Eq. (6.6) in the phenomenological model. In addition to the parametric dependencies of the input-output coupling, solving the input-output relation Eq. (6.17) does not yield the full scattering information, as shown in [LE20]. Instead, an additional background scattering contribution $S_{\text{bg}}(\omega,\theta)$ is necessary to translate the bath-mode scattering into plane-wave scattering (refer to Sec. 6.8 and Fig. 6.5 for an example). This additional contribution is absent in the phenomenological model, but crucial to reproduce the response not only in the vicinity of the studied resonance, but also away from it. Most notably, it accounts for the fact that the empty-cavity response is treated exactly within the ab initio few-mode approach [LE20] independent of the number of included cavity modes.

In summary, we see that the differences between the ab initio and the phenomenological version of the model are a modified frequency and angular dependence of the coupling constants, as well as the cavity decay rate becoming a matrix introducing cross-mode decay terms. We also note that the parameters may in general be complex quantities and a background scattering matrix should be included for accuracy over a large frequency range. The differences between the models are summarized in Table 6.1 and illustrated in Figs. 6.1, 6.2.

6.4 General solution in the linear regime

In this section, we provide a general solution to the multi-mode multi-ensemble ab initio few-mode theory for x-ray cavities with Mössbauer nuclei, which is outlined in the previous section, in the linear regime. By writing the equations in Heisenberg-Langevin form, we find a closed-form solution for the linear scattering observables of systems containing an arbitrary number of modes and layers or

ensembles. By employing the exact input-output formalism [LE20], multi-mode coupling, overlapping modes, non-Markovian, open system and scattering effects are included in the solution method.

For simplicity, we again consider a single polarization and unmagnetized samples. The method, however, can straightforwardly be applied to the full Hamiltonian of x-ray cavities with thin film Mössbauer nuclei, including polarization and magnetization [HE13].

6.4.1 Heisenberg-Langevin equations of motion

The Heisenberg-Langevin equations of motion for the nuclear operators defined by the ab initio model in Sec. 6.3 read [GZ04; KK17a; HE15]

$$\frac{d}{dt}\hat{\sigma}_{ln}^{-}(t) = -(i\omega_{\mathrm{nuc},l} + \frac{\gamma}{2})\hat{\sigma}_{ln}^{-}(t) + i\hat{\sigma}_{ln}^{z}(t)\sum_{\lambda}\hat{a}_{\lambda}(t)g_{l\lambda}, \tag{6.18a}$$

$$\frac{d}{dt}\hat{\sigma}_{ln}^{z}(t) = -2i\hat{\sigma}_{ln}^{+}(t)\sum_{\lambda}\hat{a}_{\lambda}(t)g_{l\lambda} + h.c. - \gamma(\hat{\sigma}_{ln}^{z} + 1)\,. \tag{6.18b}$$

We note that in this form, the equations are particularly simple, in the sense that the individual ensembles only interact with each other via the cavity modes. The many-particle aspect apparent from the nuclear index n can be treated by introducing collective operators [Hee13; HE15] or by working with single particle operators and employing the permutation symmetry of the model [KK17a; Sha18]. The latter can be employed since our Liouvillian is invariant under the relabeling $(l,n) \to (l,n')$ for nuclei within each ensemble l, which is the case due to the coupling and decay constants being independent of n within the single parallel wave vector approximation. We adopt the permutation symmetry in the following, which then allows us to drop the index n on expectation values of single nucleus operators in Eq. (6.18) and to reduce the corresponding sums over nuclei within one ensemble.

The resulting equation for the cavity mode expectation values is given by Eq. (6.15) and now simplifies to [LE20]

$$\langle\hat{a}_{\lambda}(\omega)\rangle = \sum_{\lambda'}\mathcal{D}_{\lambda\lambda'}^{-1}(\omega)\big[2\pi\sum_{m}\mathcal{W}_{\lambda' m}(\omega)\langle\hat{b}_{m}^{(\mathrm{in})}(\omega)\rangle + \sum_{l}N_{l}g_{l\lambda'}^{*}\langle\hat{\sigma}_{l}^{-}(\omega)\rangle\big]\,, \tag{6.19}$$

where we have dropped the parametric angle dependencies for brevity. We note that the number of nuclei N_l in ensemble l appears explicitly in the equations due to the use of the permutation symmetry [KK17a].

The dynamical equations (6.19) are completed by the input-output relation Eq. (6.17).

6.4.2 Solution of the multi-layer multi-mode equations in the linear regime

In [HE15], the linear equations of motion are solved for the phenomenological model within the adiabatic elimination approximation for the special case of a two-layer EIT configuration, which is notably investigated experimentally in [Röh12]. Here, we solve the above ab initio equations in the linear regime without the need for adiabatic elimination, a Markov approximation or a specific mode-ensemble configuration. The adiabatic approximation will, however, be employed a posteriori to gain insight into the final solution and the resulting nuclear line shape.

The crucial approximation to obtain linear spectral observables is the weak excitation approximation, which can conveniently be performed in the Heisenberg-Langevin approach by setting $\langle\hat{\sigma}_{l}^{z}\rangle \approx -1$ [WS10] for all ensembles l (see Sec. 7.3 for further details). This results in the nuclear lowering operator equation of motion becoming linear and independent of the other nuclear operators. Physically, this way of solving the equations of motion corresponds to eliminating the nuclei instead of the modes, which can be done without further approximations in the linear regime (see also Sec. 7.3). An alternative way of performing this approximation is the Holstein-Primakoff method [HP40; DBJR18]. We note that due to this approximation, it is not necessary to trace out the bath modes or the radiative bath of the nuclei. Instead, the linear operator equations of motion can be solved directly.

Within this low-excitation approximation, one obtains three linearly coupled matrix equations in the frequency domain, one for the nuclear lowering operators, one for the cavity modes and one given by the input-output relation. These equations can be solved straightforwardly by linear algebra. For

the nuclear lowering operators we obtain

$$\left(\omega - \omega_{\mathrm{nuc},l} + i\frac{\gamma}{2}\right)\langle\hat{\sigma}_l^-(\omega)\rangle = \sum_\lambda g_{l\lambda}\langle\hat{a}_\lambda(\omega)\rangle\,. \tag{6.20}$$

Substituting Eq. (6.20) into Eq. (6.15), we find

$$\langle\hat{a}_\lambda(\omega)\rangle = 2\pi\sum_{\lambda'}\mathcal{D}^{-1}_{\lambda\lambda'}(\omega)\sum_m \mathcal{W}_{\lambda' m}(\omega)\langle\hat{b}^{(\mathrm{in})}_m(\omega)\rangle\,, \tag{6.21}$$

$$\mathcal{D}_{\lambda\lambda'}(\omega) \to \mathcal{D}^{(\mathrm{int})}_{\lambda\lambda'}(\omega) = \mathcal{D}_{\lambda\lambda'}(\omega) - \sum_l \frac{N_l g^*_{l\lambda} g_{l\lambda'}}{\omega - \omega_{\mathrm{nuc},l} + i\frac{\gamma}{2}}\,. \tag{6.22}$$

Thus, the nuclear ensembles effectively modify the cavity propagator matrix $\underline{\underline{\mathcal{D}}}$. Finally, inserting Eq. (6.21) into the input-output relation Eq. (6.17), we obtain the scattering solution

$$\langle\hat{b}^{(\mathrm{out})}_m(\omega)\rangle - \langle\hat{b}^{(\mathrm{in})}_m(\omega)\rangle = -2\pi i\sum_{\lambda,\lambda',m'}\mathcal{W}^*_{\lambda m}(\omega)[\mathcal{D}^{(\mathrm{int})}]^{-1}_{\lambda\lambda'}(\omega)\mathcal{W}_{\lambda' m'}(\omega)\langle\hat{b}^{(\mathrm{in})}_{m'}(\omega)\rangle. \tag{6.23}$$

The scattering matrix, defined in matrix notation by [LE20]

$$\langle\hat{\underline{b}}^{(\mathrm{out})}(\omega)\rangle = \underline{\underline{S}}_{\mathrm{io}}(\omega)\langle\hat{\underline{b}}^{(\mathrm{in})}(\omega)\rangle, \tag{6.24}$$

thus reads

$$\underline{\underline{S}}_{\mathrm{io}}(\omega) = \underline{\underline{\mathbb{I}}} - 2\pi i\underline{\underline{\mathcal{W}}}^\dagger(\omega)\underline{\underline{\mathcal{D}}}^{-1}_{(\mathrm{int})}(\omega)\underline{\underline{\mathcal{W}}}(\omega)\,. \tag{6.25}$$

As noted before, the input-output scattering is complemented by a background scattering contribution $\underline{\underline{S}}_{\mathrm{bg}}(\omega)$ [LE20], which translates the bath-mode scattering into plane wave scattering via

$$\underline{\underline{S}}(\omega) = \underline{\underline{S}}_{\mathrm{bg}}(\omega)\underline{\underline{S}}_{\mathrm{io}}(\omega)\,. \tag{6.26}$$

Since the background scattering is independent of the nuclear ensembles, it can be computed for the empty cavity and multiplied with the input-output solution without additional effort when solving the interacting system [LE20].

These results provide a general solution for linear scattering observables in the ab initio version of the phenomenological few-mode model for thin-film x-ray cavities with Mössbauer nuclei.

6.5 Separating the contributions of cavity and nuclei

While the above Eq. (6.25) together with the background scattering contribution constitutes a complete solution of the problem, it does not allow to straightforwardly separate the individual contributions of the cavity and the nuclei to the scattering process. To establish this separation, we note that the relevant frequency scale of the nuclei (e.g., ∼neV, quality factor of $Q \sim 10^{12}$ for ^{57}Fe, see also Fig. 2.2) is typically orders of magnitude smaller than that of the cavity (∼keV).

In order to isolate the nuclear contribution, we approximate the frequency response of the cavity as constant on the scale of the nuclear response. If ω_{nuc} is any one of the nuclear transition frequencies, we can then write

$$\mathcal{W}_{\lambda m}(\omega) \approx \mathcal{W}_{\lambda m}(\omega_{\mathrm{nuc}}) \equiv \mathcal{W}_{\lambda m}\,, \tag{6.27}$$

$$\mathcal{D}_{\lambda\lambda'}(\omega) \approx (\omega_{\mathrm{nuc}} - \omega_\lambda)\delta_{\lambda\lambda'} + i\kappa_{\lambda\lambda'}(\omega_{\mathrm{nuc}}) \equiv \mathcal{D}_{\lambda\lambda'}\,. \tag{6.28}$$

That is in Eq. (6.25), the only relevant frequency dependence on the nuclear scale is the ω in the nuclear addition to $\underline{\underline{\mathcal{D}}}^{(\mathrm{int})}$ in Eq. (6.22). This approximation essentially amounts to performing the adiabatic approximation [HE13; HE15] a posteriori on a spectral level and can also be considered as a type of Markov approximation [BP02; GZ04; VH03], since it relies on the cavity's frequency response being flat on the scale of the nuclear response. We refer to Sec. 6.8 and Fig. 6.7 for an explicit demonstration of the validity of this form of the approximation. In the experiments so far [Hee13; Hee15a; Hee15b; Röh10; Röh12; Hab17], the approximation was found to be possible due to the narrow nuclear response. We note, however, that when strong coupling effects are present [Hab17]

or for broader electronic resonances [Hab19], the approximation may break down and it may not be possible to separate the cavity and the nuclear response.

We can now separate the nuclear contribution by employing the Woodbury matrix identity [GVL96; Dom83] to write the inverse of the modified cavity propagator as

$$\underline{\underline{\mathcal{D}}}^{-1}_{(\mathrm{int})}(\omega) = (\underline{\underline{\mathcal{D}}} + \underline{g}^{\dagger}\underline{\underline{\Lambda}}(\omega)\underline{g})^{-1} = \underline{\underline{\mathcal{D}}}^{-1} - \underline{\underline{\mathcal{D}}}^{-1}\underline{g}^{\dagger}(\underline{\underline{\Lambda}}^{-1}(\omega) + \underline{g}\,\underline{\underline{\mathcal{D}}}^{-1}\underline{g}^{\dagger})^{-1}\underline{g}\,\underline{\underline{\mathcal{D}}}^{-1}\,, \tag{6.29}$$

where the first summand is the (inverse) empty cavity propagator $\underline{\underline{\mathcal{D}}}^{-1}$, such that the second term amounts to the nuclear contributions. The matrices appearing in Eq. (6.29) are defined by their components as

$$(\underline{g})_{l\lambda} = \tilde{g}_{\lambda l} = \sqrt{N_l}\, g_{\lambda l}\,, \tag{6.30a}$$

$$(\underline{g}^{\dagger})_{\lambda l} = \tilde{g}^{*}_{\lambda l} = \sqrt{N_l}\, g^{*}_{\lambda l}\,, \tag{6.30b}$$

$$(\underline{\underline{\Lambda}}(\omega))_{ll'} = \Lambda(\omega)_{ll'} = -\frac{1}{\omega - \omega_{\mathrm{nuc},l} + i\frac{\gamma}{2}}\delta_{ll'}\,, \tag{6.30c}$$

$$(\underline{\underline{\Lambda}}^{-1}(\omega))_{ll'} = \Lambda^{-1}(\omega)_{ll'} = -(\omega - \omega_{\mathrm{nuc},l} + i\frac{\gamma}{2})\delta_{ll'}\,, \tag{6.30d}$$

where $\tilde{g}_{\lambda l}$ are the rescaled coupling constants of the collective states [HE15] (see also Appendix C.1.7). Inserting Eq. (6.29) into Eq. (6.25), the scattering matrix then reads

$$\underline{\underline{S}}_{\mathrm{io}}(\omega) = \underline{\underline{S}}^{[\text{no nuclei}]}_{\mathrm{io}}(\omega_{\mathrm{nuc}}) + 2\pi i\underline{\underline{\mathcal{W}}}^{\dagger}\underline{\underline{\mathcal{D}}}^{-1}\underline{g}^{\dagger}(\underline{\underline{\Lambda}}^{-1}(\omega) + \underline{g}\,\underline{\underline{\mathcal{D}}}^{-1}\underline{g}^{\dagger})^{-1}\underline{g}\,\underline{\underline{\mathcal{D}}}^{-1}\underline{\underline{\mathcal{W}}}\,. \tag{6.31}$$

This formula shows the desired separation into the empty-cavity background

$$\underline{\underline{S}}^{[\text{no nuclei}]}_{\mathrm{io}}(\omega_{\mathrm{nuc}}) = \underline{\underline{\mathbb{I}}} - 2\pi i\underline{\underline{\mathcal{W}}}^{\dagger}(\omega)\underline{\underline{\mathcal{D}}}^{-1}(\omega)\underline{\underline{\mathcal{W}}}(\omega) \tag{6.32}$$

and the additional nuclear contribution. The interpretation of the various contributions will become clearer in the following section discussing pertinent example cavities.

6.6 Example: Fano cavities

In this section, we illustrate Eq. (6.31) using standard cavity structures that are known to feature simple, yet relevant, nuclear line shapes in their frequency-dependent response. The basic element contributing to the response can be understood using the single-cavity-mode approximation, in which the inverse $\underline{\underline{\mathcal{D}}}^{-1}$ appearing in Eq. (6.31) can be identified via Eq. (6.28) as a Lorentzian. In the general multi-mode case, since $\underline{g}\,\underline{\underline{\mathcal{D}}}^{-1}\,\underline{g}^{\dagger}$ is a matrix coupling the different transitions, the nuclear contribution therefore is a superposition of coupled Lorentzian resonances interfering with themselves and the flat cavity background. As a result, the nuclear line shape can be rather complex for the general multi-mode multi-ensemble case. It is, however, well known that for certain cavity structures, the response reduces to a single Lorentzian interfering with the cavity background [Hee15a; Hee14], giving rise to Fano line shapes [Hee15a; Fan61; Ott13; Lim17]. In the following, we use such cases to illustrate Eq. (6.31).

6.6.1 Single nuclear ensemble

For a single nuclear ensemble, the index l has only one value, such that $\underline{\underline{\Lambda}}$ reduces to a scalar. Similarly, $\underline{g}$ and, for single channel scattering, $\underline{\underline{\mathcal{W}}}$ reduce to vectors with elements corresponding to the different cavity modes λ. As a result, for the reflection channel, $\underline{\underline{\mathcal{W}}}^{\dagger}\underline{\underline{\mathcal{D}}}^{-1}\underline{g}^{\dagger}$ and $\underline{g}\,\underline{\underline{\mathcal{D}}}^{-1}\underline{\underline{\mathcal{W}}}$ become complex numbers independent of ω, thus characterizing the magnitude of the nuclear contribution as well as its relative phase to the empty-cavity contribution. For the spectral shape, we are therefore left with analyzing

$$(\underline{\underline{\Lambda}}^{-1}(\omega) + \underline{g}\,\underline{\underline{\mathcal{D}}}^{-1}\underline{g}^{\dagger})^{-1} = \frac{-1}{\omega - (\omega_{\mathrm{nuc},l} + \Delta_{\mathrm{LS}}) + i(\gamma + \Gamma_S)/2}\,, \tag{6.33}$$

where we have defined

$$\Delta_{\mathrm{LS}} - \frac{i}{2}\,\Gamma_S = \sum_{\lambda,\lambda'} N\, g_\lambda\, \mathcal{D}^{-1}_{\lambda\lambda'}\, g^*_{\lambda'}\,. \tag{6.34}$$

This is the Lorentzian line shape of a single nucleus, modified by the collective Lamb shift Δ_{LS} and the superradiance Γ_S for the ensemble in the cavity. Due to the interference with the cavity background, this Lorentzian in general becomes a Fano line shape.

Indeed, the above form of the nuclear line shape closely corresponds to what is obtained in the multi-mode phenomenological model (see in particular Eq. (46) in [HE15]). The main difference here is the form of the $\mathcal{D}$-matrix, which is diagonal in the phenomenological case [HE15] and now includes the cross-mode coupling terms in the ab initio generalization (see Table 6.1). In the special case of isolated cavity resonances [LE20], the $\mathcal{D}$-matrix may well be approximated as diagonal, such that the phenomenological assumption can be well justified.

We thus recover the corresponding predictions of the phenomenological model [Hee15a; HE15], at the same time establishing an improved ab initio representation of the complex level shift $\Delta_{\mathrm{LS}} - i\Gamma_S/2$.

6.6.2 Single cavity mode, uniform nuclear ensembles

Another special case where the nuclear contribution is of single Lorentzian form arises when there is only a single mode and, in addition, the $\omega_{\mathrm{nuc},l}$ of all nuclear ensembles are equal [Hee15a; Hee14]. In this case, the index λ is absent, $\underline{\underline{\mathcal{D}}}$ reduces to a scalar, and $\underline{\underline{\mathcal{W}}}$ and $\underline{\underline{g}}$ become column vectors with elements $\mathcal{W}_m$ corresponding to the external channels and g_l to the layers. As a result, we obtain from Eq. (6.25)

$$\underline{\underline{S}}_{\mathrm{io}}(\omega) = \underline{\underline{\mathbb{I}}} + 2\pi i \underline{\mathcal{W}}^* \underline{\mathcal{W}}^T \left(\mathcal{D} - \frac{\sum_l N_l g_l^* g_l}{\omega - \omega_{\mathrm{nuc}} + i\frac{\gamma}{2}} \right)^{-1}. \tag{6.35}$$

Applying the scalar version of the Woodbury formula leads to

$$\underline{\underline{S}}_{\mathrm{io}}(\omega) = \underline{\underline{S}}^{[\text{no nuclei}]}_{\mathrm{io}}(\omega_{\mathrm{nuc}}) - 2\pi i\, \frac{\underline{\mathcal{W}}^* \underline{\mathcal{W}}^T A}{\omega - \omega_{\mathrm{nuc}} + i\gamma/2 - \mathcal{D}^{-1} A}\,, \tag{6.36}$$

where $A = \sum_l \tilde{g}_l^* \tilde{g}_l = \sum_l N_l g_l^* g_l$. Again, the result indeed corresponds to a Fano line shape, recovering the phenomenological result [HE15] with A corresponding to $\mathcal{G}^2$ (Eq. (48) in [HE15]). We note again, that the result is fully expressible in terms of the rescaled couplings $\tilde{g}_l$ (see also Appendix C.1.7).

6.7 Effective few-level scheme realized by the nuclei in the cavity

As shown in [HE13; HE15], one can associate an effective nuclear level scheme to the nuclear cavity QED system, such that the spectroscopic response of the two agree in the low-excitation limit. This way, the spectra of the nuclear cavity QED system can be interpreted in terms of quantum optical phenomena. For instance, a spectral dip in certain two-ensemble x-ray cavities could be interpreted as an EIT phenomenon [Röh12; HE15]. In [HE13; HE15], the effective level scheme is derived using an adiabatic elimination of the cavity modes, giving rise to equations for the nuclear system alone with effective couplings between the ensembles. The parameters of this level scheme are then obtained using fits of the model to numerical calculations of the QED system's response or to experimental data.

In this section, we derive an effective few-level scheme from the ab initio few-mode model given above and generalize it to arbitrary ensemble configurations. While the adiabatic elimination employed here is not necessary to solve the linear scattering problem, it is necessary in order to obtain the effective level scheme. Due to the ab initio character of the theory, this approach further allows us to express the quantum optical level parameters and couplings directly in terms of the cavity geometry. Alleviating the need for parameter fitting not only removes possible ambiguities due to overfitting or degeneracies, but also amplifies the interpretational power in terms of the relevant cavity modes and nuclear ensembles responsible for the observed effects.

As a first step, we write Eq. (6.18) in terms of collective operators [Hee14] $\hat{J}_l^{+/-/z} = \sum_n \hat{\sigma}_{ln}^{+/-/z}$, which gives

$$\frac{d}{dt}\hat{J}_l^-(t) = -(i\omega_{\text{nuc}} + \frac{\gamma}{2})\hat{J}_l^-(t) + i\hat{J}_l^z(t)\underline{g}_l^T\underline{\hat{a}}(t), \tag{6.37a}$$

$$\frac{d}{dt}\hat{J}_l^z(t) = -2i\hat{J}_l^+(t)\underline{g}_l^T\underline{\hat{a}}(t) + h.c. - \gamma(\hat{J}_l^z(t) + N_l)\,. \tag{6.37b}$$

As a next step, we adiabatically eliminate the cavity modes by substituting Eq. (6.15) into Eq. (6.37) and employing the adiabatic approximation [HE13; HE15] on the spectral level Eqs. (6.27, 6.28). The adiabatic solution for the mode operator Eq. (6.15) can then be transformed into the time domain to give

$$\underline{\hat{a}}(t) = \underline{\underline{\mathcal{D}}}^{-1}\left[2\pi\underline{\underline{\mathcal{W}}}\,\underline{\hat{b}}^{(\text{in})}(t) + \sum_l \underline{g}_l^*\hat{J}_l^-(t)\right]. \tag{6.38}$$

Substitution yields

$$\frac{d}{dt}\hat{J}_l^-(t) = -(i\omega_{\text{nuc},l} + \frac{\gamma}{2})\hat{J}_l^-(t) + i\hat{J}_l^z(t)\underline{\Omega}_l^T\underline{\hat{b}}^{(\text{in})}(t) + i\hat{J}_l^z(t)\sum_{l'} G_{ll'}\hat{J}_{l'}^-(t), \tag{6.39a}$$

$$\frac{d}{dt}\hat{J}_l^z(t) = -2i\hat{J}_l^+(t)\underline{\Omega}_l^T\underline{\hat{b}}^{(\text{in})}(t) + h.c. - 2i\hat{J}_l^+(t)\sum_{l'} G_{ll'}\hat{J}_{l'}^-(t) + h.c. - \gamma(\hat{\underline{J}}_l^z(t) + N_l)\,, \tag{6.39b}$$

where the *effective drive coupling matrix* is given by

$$\underline{\Omega}_l^T = \underline{\Omega}_l^T(\omega_{\text{nuc}}) = 2\pi\underline{g}_l^T\underline{\underline{\mathcal{D}}}^{-1}(\omega_{\text{nuc}})\underline{\underline{\mathcal{W}}}(\omega_{\text{nuc}})\,, \tag{6.40}$$

and the *effective level coupling matrix* is

$$G_{ll'} = G_{ll'}(\omega_{\text{nuc}}) = \underline{g}_l^T\underline{\underline{\mathcal{D}}}^{-1}(\omega_{\text{nuc}})\underline{g}_{l'}^*\,. \tag{6.41}$$

These equations can be reformulated in terms of an effective Hamiltonian

$$\hat{H}_{\text{eff}} = \sum_l \frac{\omega_{\text{nuc},l}}{2}\hat{J}_l^z + \sum_{ll'}\hat{J}_l^+\text{Re}[G_{ll'}]\hat{J}_{l'}^- + \sum_l \hat{J}_l^+\underline{\Omega}_l^T\underline{\hat{b}}^{(\text{in})}(t) + h.c.\,, \tag{6.42}$$

and the effective Lindblad operator

$$\mathcal{L}_{\text{eff}}[\rho] = \sum_{ll'} -\text{Im}[G_{ll'}](2\hat{J}_l^-\rho\hat{J}_{l'}^+ - \{\hat{J}_l^+\hat{J}_{l'}^-\,,\,\rho\}) + \mathcal{L}_{\text{SE}}[\rho]\,, \tag{6.43}$$

where $\mathcal{L}_{\text{SE}}[\rho]$ is the local spontaneous emission term defined in Eq. (C.23). This effective level scheme again closely corresponds to the results in the phenomenological model (in particular Eqs. (23-25) in [HE15]), with the aforementioned differences in the ab initio coupling parameters summarized in Sec. 6.3.

Eqs. (6.42) and (6.43) can be interpreted as a system of interacting collective spins. Together, they define an effective level scheme in their low-excitation subspace. Starting from the ground state $|G\rangle$ defined as the state without photons in the cavity and with all nuclei in their ground state, the excited states of this level scheme are collective excitonic states of the many-body QED system, which can be defined as

$$|E_l\rangle = \hat{J}_l^+|G\rangle\,. \tag{6.44}$$

The couplings within this effective level scheme are illustrated in Fig. 6.3. For example, for a single ensemble l the collective Lamb shift and the Purcell enhanced superradiance are given by $\Delta_{\text{LS}} = \text{Re}[G_{ll}]$ and $\gamma_{\text{S}} = -2\text{Im}[G_{ll}]$, respectively. With more than one ensemble, the coherent inter-ensemble couplings are given by $\Delta_{ll'} = \text{Re}[G_{ll'}]$ and incoherent cross-ensemble decay terms with decay rate $\gamma_{ll'} = -2\text{Im}[G_{ll'}]$ are also present. The latter can be shown to yield spontaneously generated coherences in certain cases [Hee13]. The various transitions are driven from an external channel m with the effective Rabi frequency Ω_{lm}.

The spontaneous-emission contribution in Eq. (6.43) requires additional care, because it *a priori* operates on the single-particle level, rather than on the level of the collective transition operators. But

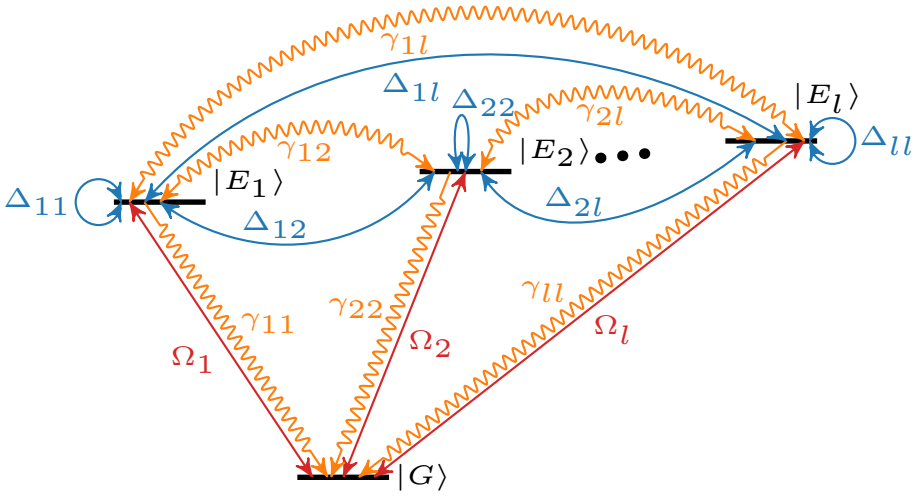

Figure 6.3: Schematic illustration of effective level schemes equivalent to the total system of cavity and nuclei in the linear low-excitation regime. The structure of the level scheme is defined via the couplings given in Eqs. (6.42) and (6.43), with $\Delta_{ll'} = \mathrm{Re}[G_{ll'}]$ and $\gamma_{ll'} = -2\mathrm{Im}[G_{ll}]$. Single nucleus decay terms are not depicted for clarity (see text).

in the low-excitation or the linear regime, it simply adds to the collective decay rate [HE15], such that the system can fully be expressed in terms of collective operators as shown in Eqs. (6.39). However, Eqs. (6.42), (6.43) are also valid beyond the linear regime, where methods based on permutation symmetry [Sha18; KK17a] can be employed to tackle the spontaneous emission term to extend the collective operator treatment in [HKE16]. We note, however, that the non-linear dynamics may break the permutation symmetry by coupling to other parallel wave vector modes.

The effective many-body couplings contain the bare coupling constants $g_{l\lambda}$ instead of the rescaled coupling constants $\tilde{g}_{l\lambda} = \sqrt{N_l}\, g_{l\lambda}$, because the underlying equations contain collective operators defined as sums over single-particle operators. In the linear limit, the former can be replaced by effective single-particle operators, which leads to the appearance of the rescaled coupling constants [HE15; HKE16] (see also Sec. 7.5). In this sense, the linear limit is independent of the number of coherently interacting nuclei, see also Appendix C.1.6, as is also the case in the semi-classical layer formalism [Röh05b], where only the nuclear number density appears as a material parameter. However, beyond the linear excitation regime, the number of coherently interacting nuclei is crucial, since it determines the onset of non-linear effects [HKE16].

We further note that by including the magnetic substructure of the nuclei, more versatile level schemes become accessible [Hee13].

6.8 Analytically solvable example system

In this section, we illustrate the ab initio few-mode approach to nuclear many-body cavity QED using a specific example. We choose the simplest possible layer cavity geometry which features a resonance structure that resembles what is practically investigated in x-ray cavity QED [Röh10; Röh12; Hee13; Hee15a; Hee15b; Hab17], and also has found applications in various contexts, see e.g. [RÖ2; Nie98; Bar94; Röh97; Ślę10]. It furthermore has the advantage that it can be analytically solved within our framework.

We present detailed comparisons to the semi-classical theory and to the phenomenological few-mode theory. In the process, we demonstrate the advantages and the potential of the method, showing differences to previous interpretations and completing the theoretical picture of the few-mode approach. As an application, we generalize the quantum optical model to cavities containing thick resonant layers.

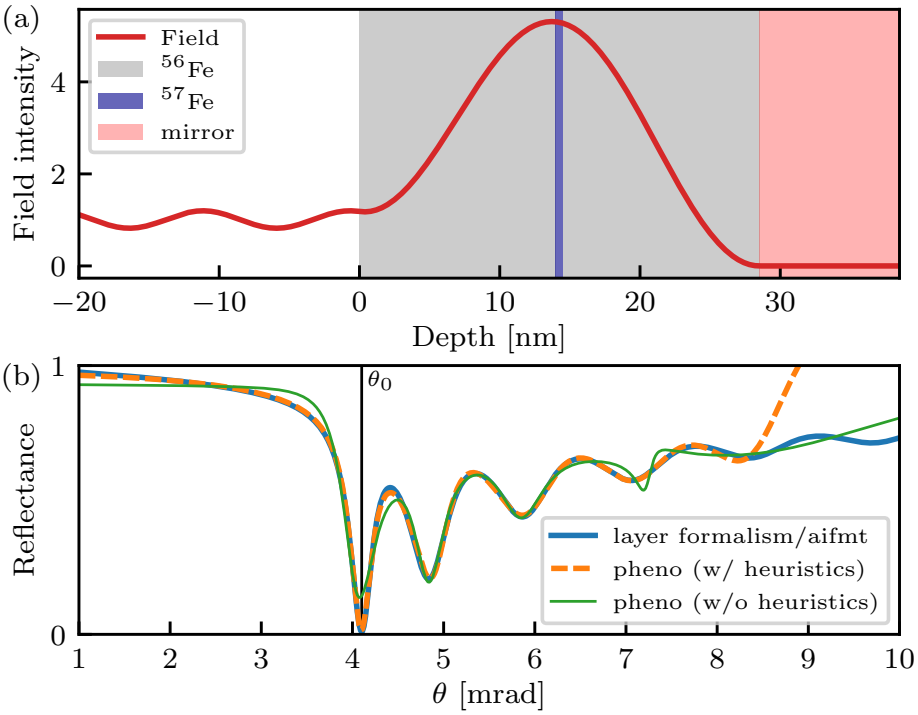

Figure 6.4: Analytically solvable example within the ab initio few-mode theory for x-ray cavities. (a) The structure of the cavity under consideration (materials see legend) and its off-resonant field distribution (red line) at the incidence angle θ_0 corresponding to the first guided mode. The cavity itself (gray ^{56}Fe and blue ^{57}Fe) has a total thickness of 28.5 nm, where the thickness of the resonant ^{57}Fe dopant layer at the center is 0.5 nm (blue). (b) Rocking curve (off-resonant cavity reflectance at 14.4 keV in $\theta-2\theta$ geometry). The position θ_0 of the first guided mode is indicated by the black dashed line at approximately 4 mrad. The panel compares $R^{[\text{no nuclei}]}$ for the ab initio formalism, which equivalently can be obtained using the layer formalism [Röh05b] (solid blue), e.g., implemented in the software package PYNUSS [Hee19], to fits using the phenomenological model. A five-mode model with heuristic extensions (dashed yellow) is necessary for good agreement in the spectral range up to 8 mrad, reproducing the reflectance over the range of four modes. Without heuristic extensions (solid green), the fit is poor already in the first mode and beyond 6 mrad, properly describing only the second and third modes. To fit a larger spectral range, the phenomenological model requires inclusion of more modes. This is a major drawback to the ab initio few-mode theory, where the off-resonant reflectance is always represented exactly for any mode number [LE20].

6.8.1 Cavity layout

The cavity structure considered in the following is depicted in Fig. 6.4. We choose the resonant nucleus ^{57}Fe as the archetype Mössbauer nucleus and practically most used species for nuclear x-ray cavity QED experiments, and consider a single unmagnetized thin resonant layer inside the cavity, where collective Lamb shifts [Röh10] and Fano line shapes [Hee13] can be observed. As the off-resonant dielectric material for the guiding layer, we choose the corresponding isomer ^{56}Fe, which does not feature the nuclear resonance. Choosing two isomers has the advantage that the electronic contribution of the resonant layers is equal to the surrounding cavity material. Consequently, when the resonant layers are placed at varying positions, the electronic scattering properties of the cavity remain the same. This feature allows us to separate resonant effects, such as which modes the nuclear transitions couple to and which effective level scheme is realized, from cavity structure effects, such as which modal environment is realized in the cavity. For the substrate, we choose an idealized material with a high refractive index, which essentially mimics a perfect mirror. This choice is motivated by the fact that a single layer of dielectric alone usually features weak resonances. A reflecting mirror substrate is the simplest way to realize a better resonance structure.

6.8.2 Analytic solution

In order to employ the ab initio few-mode theory, one first has to choose a few-mode basis. While the optimal basis may be difficult to find, one can use a constructive approach by choosing a basis

that becomes locally complete in the region of the interaction if infinitely many discrete modes are considered [LE20]. Note that different choices for the basis vary in the number of modes required to achieve convergence of the results.

Here, we choose Dirichlet modes, that is modes with hard wall boundary conditions at the top and bottom surface of the layer cavity, giving the transverse mode functions [Dom83; LE20; VH04]

$$\tilde{\chi}_\lambda(z) = \sqrt{\frac{2}{L}} \sin\left(\pi\lambda \frac{z}{L}\right) . \tag{6.45}$$

where L is the cavity thickness. The few-mode basis is then constructed as a finite subset of these modes by choosing the relevant set of λ indices. By observing the convergence of the spectral observables, we select the significantly contributing modes.

The corresponding one-dimensional problem for this set of few-mode bases has been solved in [Dom83; LE20], giving the system-bath couplings and few-mode propagator

$$\mathcal{W}_\lambda(\omega,\theta) = \frac{\pi\beta}{L} e^{-i\beta} \frac{1}{\alpha\cot(\alpha) - s - i\beta} \frac{\lambda(-1)^\lambda}{\sqrt{\omega_\lambda}} , \tag{6.46a}$$

$$\mathcal{W}^\dagger_\lambda(\omega,\theta) = \frac{\pi\beta}{L} e^{+i\beta} \frac{1}{\alpha\cot(\alpha) - s + i\beta} \frac{\lambda(-1)^\lambda}{\sqrt{\omega_\lambda}} , \tag{6.46b}$$

$$\mathcal{D}_{\lambda\lambda'}(\omega,\theta) = \frac{\beta^2/L^2 - \omega_\lambda^2}{2\omega_\lambda}\delta_{\lambda\lambda'} + \frac{\pi^2}{L^2} \frac{1}{\alpha\cot(\alpha) - s - i\beta} \frac{\lambda(-1)^\lambda}{\sqrt{\omega_\lambda}} \frac{\lambda'(-1)^{\lambda'}}{\sqrt{\omega_{\lambda'}}} , \tag{6.46c}$$

$$\mathcal{D}^{-1}_{\lambda\lambda'}(\omega,\theta) = \frac{2\omega_\lambda}{\beta^2/L^2 - \omega_\lambda^2}\delta_{\lambda\lambda'} - \frac{\pi^2}{L^2} \frac{1}{\alpha\cot(\alpha) - i\beta} \frac{2\lambda(-1)^\lambda\sqrt{\omega_\lambda}}{\beta^2/L^2 - \omega_\lambda^2} \frac{2\lambda'(-1)^{\lambda'}\sqrt{\omega_{\lambda'}}}{\beta^2/L^2 - \omega_{\lambda'}^2} , \tag{6.46d}$$

where L is the thickness of the cavity layer, $\omega_\lambda^2/2 = (\pi^2\lambda^2)/(2L^2) + \tilde{V}$ defines the system mode frequency, $\tilde{V}(\omega) = (1-n^2)\omega^2/2$ is the energy dependent potential, n is the complex refractive index of the guiding layer material (^{56}Fe), $\beta = \omega L = kL$ is the scaled dimensionless momentum variable [Dom83], k is the wave number in units of m^{-1}, $\alpha = (\beta^2 - 2\tilde{V}L^2)^{1/2}$, $s = \sum_{\lambda\in\Lambda_Q}(2\lambda^2\pi^2)/(\alpha^2 - \lambda^2\pi^2)$, and λ is the system-mode index, which is summed over the chosen few-mode subset Λ_Q of the locally complete Dirichlet basis. Here, we have written the hermitian conjugate of the system-bath coupling $\mathcal{W}$ explicitly, in order to demonstrate which quantities should be excluded from the complex conjugation operation (see Sec. C.1.6 for details). For example, α contains an imaginary part via the complex refractive index, but should not be conjugated within the non-hermitian Hamiltonian prescription.

Due to the perfect mirror substrate, the system reduces to a single-channel problem with reflection only, such that that the system-bath couplings $\mathcal{W}_\lambda(\omega)$ do not depend on a channel index m. The background scattering matrix then reduces to a scalar given by [Dom83]

$$S_{\mathrm{bg}}(\omega,\theta) = e^{-2i\beta} \frac{\alpha\cot(\alpha) + i\beta}{\alpha\cot(\alpha) - i\beta} \frac{\alpha\cot(\alpha) - s - i\beta}{\alpha\cot(\alpha) - s + i\beta} . \tag{6.47}$$

At a given incidence angle or parallel wave vector, this one-dimensional solution can be applied to our three-dimensional x-ray system using

$$n \to n(\theta) = \frac{\sqrt{n^2 - \cos^2(\theta)}}{\sin(\theta)} , \tag{6.48a}$$

$$\beta \to \beta(\theta) = \omega L \sin(\theta) \tag{6.48b}$$

as the index of refraction and scaled momentum variable, respectively, see Appendix C.1.1.

The interaction with the resonant nuclei is governed by the coupling constant

$$g_{\lambda l} = -id\omega_{\mathrm{nuc},l} \sqrt{\frac{f_{\mathrm{LM}}\rho_N t_l}{2\omega_\lambda}} \tilde{\chi}_\lambda(z_l) , \tag{6.49}$$

where we have dropped the dependence on θ for brevity, d is the nuclear dipole moment and f_{LM} is the Lamb-Mössbauer factor. Details on the light-matter coupling constants are summarized in Appendix C.1.7.

6.8.3 A practical guide to calculations in the ab initio few-mode approach

After having derived general results for the ab initio few-mode approach, we now show how to apply these results for practical calculations, that we will use to obtain the numerical results discussed in the following sections. For simplicity, we focus on the linear regime of the example geometry in Fig. 6.4(a), which is a single channel problem, since due to the perfect mirror substrate, only the reflection channel is open. The scattering "matrices" therefore reduce to scalar quantities corresponding to reflection coefficients as a function of incidence angle and frequency. According to Eq. (6.26), the full reflection coefficient is then given by the scalar product

$$r = S = S_{\mathrm{bg}} S_{\mathrm{io}} \,, \tag{6.50}$$

with the reflection intensity, also known as reflectance, given by $R = |r|^2$.

The first step of the calculation is to choose the set of mode indices $\{\lambda\}$ included in the few-mode analysis. The most straightforward approach not requiring any insight into the given problem is to start with the fundamental mode only and then to add higher-order modes successively until convergence of the observables is obtained.

After having chosen the few-mode basis, the coupling constants have to be determined. For the example geometry, analytical results are provided in Eqs. (6.46)-(6.49). For more general geometries, the coupling constants can be obtained by calculating matrix elements between the few-mode, the bath and the scattering states [LE20], using the separable expansion method [Dom83].

Next, the input-output reflection coefficient $r_{\mathrm{io}} = S_{\mathrm{io}}$ defined in Eq. (6.25) can be calculated by substituting the parameters Eqs. (6.46), the nucleus-cavity coupling constant Eq. (6.49), and the modified cavity propagator $\underline{\underline{\mathcal{D}}}^{-1}_{(\mathrm{int})}(\omega)$ containing the matrices in Eqs. (6.30) into Eq. (6.29). We note that in the formulas for the parameters, the three-dimensional geometry substitutions Eqs. (6.48a) have to be used. Alternatively, the input-output scattering matrix can be calculated in the form of Eq. (6.31), where the empty-cavity response is separated out.

Analogously, the empty cavity reflectance $R^{[\text{no nuclei}]}$ evaluated using the scattering matrix $S_{\mathrm{io}}^{[\text{no nuclei}]}$ defined in Eq. (6.32) can readily be calculated. It corresponds to experimental situations in which the reflectance is recorded at x-ray energies detuned away from the nuclear resonance. For this, one may either set the nucleus-cavity coupling Eq. (6.49) in S_{io} to zero, or directly calculate it using Eq. (6.32).

Similarly to the reflectances, the effective level schemes can be calculated. The effective couplings can be evaluated from Eqs. (6.40, 6.41), again with the help of the coupling constants already used for the reflectances.

6.8.4 Empty cavity

We start by analyzing the off-resonant reflectance $R^{[\text{no nuclei}]}$ of the cavity, i.e., in the absence of the nuclear resonances, which represents a property of the empty cavity. In practice, this quantity as function of the incidence angle is also known as the rocking curve and can be measured in a cavity containing resonant nuclei by tuning the incident x-ray beam slightly away from the nuclear resonance, which does not have any influence on the much larger scales of the cavity linewidths. Here, we study the reflectance as a function of incidence angle and photon energy. We compare the results of the ab initio framework to corresponding calculations using the phenomenological input-output theory, and further use the semi-classical layer formalism [Röh05b] implemented in the software package PYNUSS [Hee19] as a reference. The latter is a reimplementation of parts of the CONUSS software package [Stu00] with substantial extensions focused on applications in nuclear quantum optics.

The lower panel of Fig. 6.4 shows results for the rocking curve of the system, i.e. the incidence-angle dependent reflectance observed with incidence angle equal to the exit angle ($\theta - 2\theta$ geometry). We find excellent agreement between the ab initio and the semi-classical approaches. Note that the different cavity mode resonances contributing to the rocking curve overlap strongly. Nevertheless, it is important to note that the ab initio few-mode theory is equivalent to the layer formalism calculation for any set of chosen system modes, a feature which is based on the exact result shown in [LE20] and which can be checked by comparing the analytic formulas given in Sec. 6.8.2 to the layer formalism result for the geometry [Röh05b]. This has the practical advantage that the few-mode approximation only affects the interaction with the nuclei, but not the empty-cavity properties. This way, different approximations are disentangled, contributing to the understanding of the relevant processes. The analytical equivalence implies that the product of the background scattering matrix Eq. (6.47) and

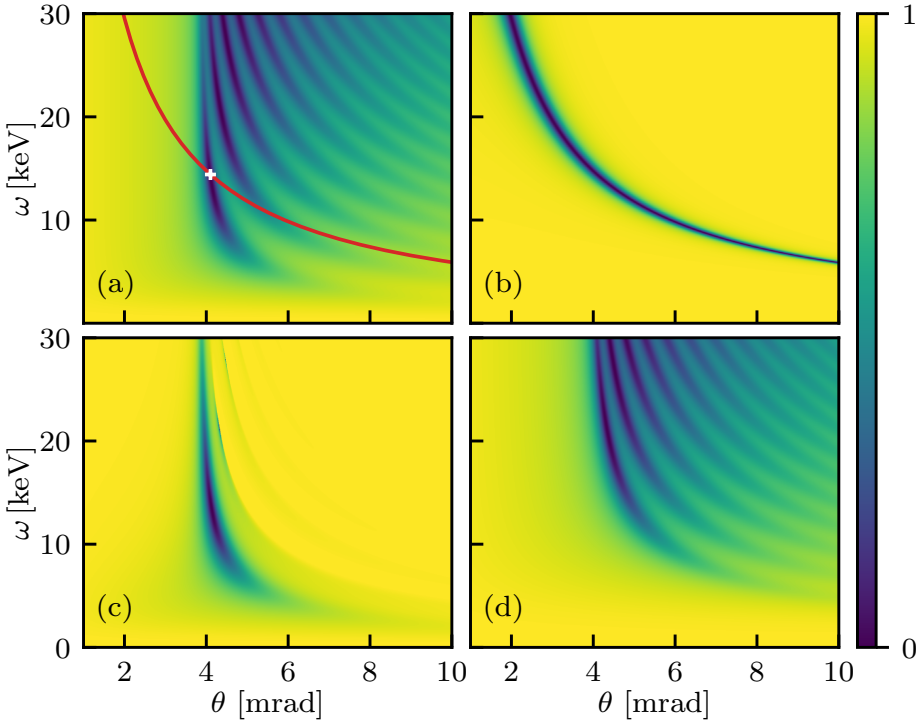

Figure 6.5: Empty-cavity reflectance as a function of the incidence angle and the incident photon energy. (a) shows the full reflectance, which can be calculated via Parratt's formalism or equivalently as $R^{[\text{no nuclei}]}$ via the ab initio few-mode theory. Note that the rocking curve in Fig. 6.4 is a section through this figure at fixed energy. The ab initio approach decomposes the total reflectance into an input-output ($|S_{\text{io}}^{[\text{no nuclei}]}|^2$) and a background reflectance ($|S_{\text{bg}}|^2$), which are shown for a single mode theory ($\lambda = 1$) in panels (c) and (d), respectively. As expected, the input-output contribution extracts the first resonance of the spectrum. The corresponding phenomenological single mode theory (b) does not correctly reproduce the first resonance. This is most clearly visible from the position of the resonance in the phenomenological model, which is shown as a red line in (a) and only coincides at the energy 14.4 keV where the parameters of the model were fitted (white cross).

the empty cavity input-output result $\underline{\underline{S}}_{\text{io}}^{[\text{no nuclei}]}(\omega)$, given by the matrix contractions in Eq. (6.25) of the system-bath couplings Eqs. (6.46), is identical to the Parratt calculation [Röh05b; Hee14]. This mathematically surprising result can indeed be checked for the example geometry by substitution and simplification of the resulting sums in the few-mode case, similarly to what is shown for a Schrödinger equation example in [Dom83].

For the phenomenological few-mode theory on the other hand, no such equivalence is guaranteed. Instead, the model parameters are fitted for a chosen mode number such that the rocking curves agree in a certain angular range. Thus, the few-mode approximation affects the interaction with the nuclei and the empty-cavity response at the same time. The model fits in the bottom panel of Fig. 6.4 show that for a five-mode model with heuristic extensions [dashed yellow] (see Sec. 6.2 for details), the agreement is good in the range of the four lowest resonance dips. Without heuristic extensions [solid green], however, the fit is poor already in the vicinity of the first cavity mode.

These results demonstrate a key advantage of the ab initio few-mode model, that the off-resonant cavity scattering and hence the rocking curve is treated exactly. The model further does not require heuristic extensions and therefore gives a clear picture of the quantum mechanical interpretation of the cavity resonances.

In order to investigate the origin of the difference between the phenomenological and the ab initio theory further, Fig. 6.5 shows a two-dimensional generalization of the rocking curve, where the incidence angle and energy are varied. We note that these spectra are calculated at a fixed off-resonant material refractive index for simplicity. These two-dimensional empty cavity spectra give theoretical insight into the resonance structure of the cavity, which forms the electromagnetic environment for the nuclei. The layer formalism [Röh05b] and the ab initio few-mode theory are again numerically equivalent, only in the latter, the scattering matrix (panel (a), given by $|S|^2$ from Eq. (6.26)) is de-

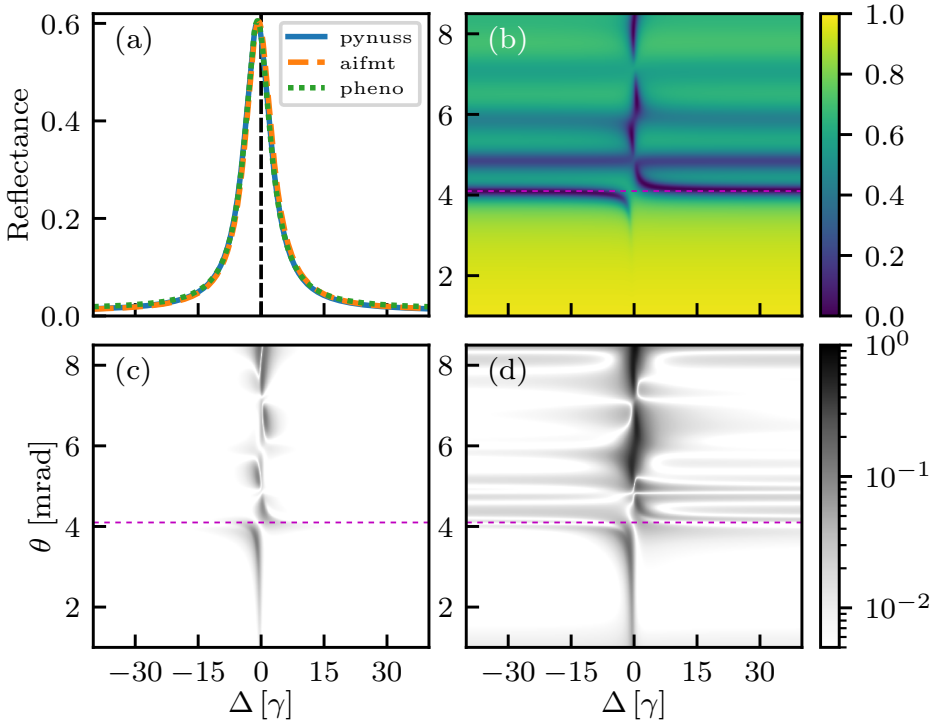

Figure 6.6: (Color online) Nuclear resonance spectra R for the cavity in Fig. 6.4 as a function of incidence angle and detuning. Panel (a) shows spectra at the first cavity resonance $\theta = \theta_0$ obtained from the exact layer formalism, the 5-mode ab initio few-mode theory and a 5-mode phenomenological model, respectively. (b) shows the exact layer formalism results as a function of incidence angle and photon energy. (c) Residual deviation of the 5-mode ab initio few-mode theory results to that of (b). (d) Corresponding results for the 5-mode phenomenological model. The magenta dashed line in (c,d) marks the section at θ_0 shown in (a). On resonance, both the ab initio and the phenomenological approach yield excellent agreement, featuring deviations on the few-percent level and below. At higher incidence angles, however, the ab initio theory agrees significantly better. A more detailed comparison, including different approaches to fitting the phenomenological parameters, is presented in Appendix C.2.

composed into a mode-number dependent input-output (given by $|S_{\mathrm{io}}^{[\text{no nuclei}]}|^2$ from Eq. (6.32)) and a background scattering part (given by $|S_{\mathrm{bg}}|^2$ from Eq. (6.47)). For the single mode results ($\lambda = 1$) shown in the figure [panels (c,d)], we find that the input-output result captures the first resonance line across the whole two-dimensional space, including the total reflection cutoff at low incidence angles. The phenomenological single mode theory in (b), however, does not capture the resonance trajectory, except at 14.4 keV, where the model parameters are fitted to the one-dimensional rocking curve. The reason for this difference is the angular and energy dependence of the quantum optical parameters, in particular $\Delta_C(\theta, \omega)$, which differs between the ab initio and the phenomenological model (see Sec. 6.3). The phenomenological resonance trajectory can also be expressed analytically by solving $\Delta_{C,\lambda}(\theta, \omega) = 0$ using the assumed form of the phenomenological cavity detuning Eq. (6.3c) giving

$$\omega_{\mathrm{res,pheno}}(\theta) = \omega_{\mathrm{nuc}} \frac{\sin(\theta_0)}{\sin(\theta)} \,. \tag{6.51}$$

The comparison of this phenomenological resonance trajectory (shown as a red line in Fig. 6.5) to the actual spectral minimum of the first resonance reveals the difference between the two descriptions.

6.8.5 Nuclear spectra and interacting systems

In Fig. 6.6, we turn to the interacting scattering problem. We consider the nuclear resonance spectrum of the cavity as a function of detuning and incidence angle (panel b), which is accessible experimentally [HE15; Hee15a; Röh10; Röh12; Hee13]. Note that here, the scale of the detuning axis is on the order of neV ($\gamma_{^{57}\mathrm{Fe}} \approx 4.7$ neV), in contrast to the keV scale of the driving radiation, which determines the empty cavity properties investigated in Sec. 6.8.4.

The figure compares the nuclear spectra for the phenomenological and ab initio few-mode approaches to the semi-classical layer formalism [Röh05b], which serves as a well-understood reference in the linear scattering regime. In the phenomenological case, we use a five mode model to fit the nuclear spectra. For comparability, the ab initio few-mode result is also calculated using five cavity modes of the Dirichlet basis ($\lambda \in \{1, 2, 3, 4, 5\}$). The ab initio spectra R are obtained as described in Sec. 6.8.3.

In the fitting procedure for the phenomenological model parameters, we first fit the empty cavity parameters to the rocking curve, yielding the yellow dashed line in Fig. 6.4 as the best fit. This includes the heuristic dispersion phase, which is necessary to obtain a good result already in the empty cavity case (see Fig. 6.4). Due to the absence of a cladding, an envelope factor (see Sec. 6.2) is not necessary for this cavity. The mode-ensemble interaction parameters are then determined by fitting the nuclear spectrum, using the two-dimensional layer formalism result in Fig. 6.6(b) as the fit objective, without prioritizing a certain angular region. We note that other fitting procedures are possible, providing optimized representations for different spectral features. In Appendix C.2, three options, some of which were already suggested in [HE15], are investigated and compared. The above procedure is found to provide the best description of the spectrum across the whole angular range up to 8.5 mrad. In contrast, for the ab initio method, no fit is required, and a single model is adequate for the entire spectrum.

Fig. 6.6(c) and (d) show the residual deviations of the ab initio few-mode result and the phenomenological result obtained using above fitting procedure, both calculated for five cavity modes. The residual deviation is defined as $|R(\theta, \Delta) - R_{\text{reference}}(\theta, \Delta)|$ with the layer formalism result as the reference. We find that while both approaches provide good fits across the whole range, at higher incidence angles the ab initio theory progressively performs better than the phenomenological approach. The excellent agreement of both theories at resonance with the first cavity mode is illustrated by Fig. 6.6(a), where the one-dimensional slice at $\theta = \theta_0$ is shown.

We conclude that both approaches are well suited to model the given cavity, with the ab initio approach yielding a better global description. In comparison to the phenomenological model, it provides the main advantage that due to the absence of a fitting procedure, the quantum optical interpretation is unambiguous. In addition, the model captures the off-resonant properties exactly for any mode number and can be systematically brought to convergence by including larger mode numbers. These features are important in particular when going to more complex cavity structures and nuclear level schemes.

Furthermore, increasing the number of modes provides a systematic way of improving the ab initio results. For 30 or more modes, the relative deviation is below 2% in the entire Fig. 6.6(c) and on this level is dominated by residual effects of the 0.5 nm layer thickness (see also Sec. 6.9). This systematic improvement is not guaranteed in the phenomenological model (see also Appendix C.2).

We note that these results do not invalidate the phenomenological approach, which may still provide numerical advantages for fitting unknown cavity structures, for example in the experiment, where the matrix elements required for the ab initio few-mode theory may be difficult to calculate (see, however, the Green's function approach in Chapter 7 for a numerically efficient alternative). Instead, the applicability of the phenomenological approach is clarified and an upgraded version can be employed when necessary. This progress in the understanding of the approach bears potential in particular for calculations beyond the linear regime [HKE16], where the theoretical models are required to be predictive and hence well understood.

The investigation here is supplemented by a detailed comparison of the phenomenological and ab initio few-mode approaches in Appendix C.2, where we also consider different fitting routines and the convergence at higher mode numbers.

6.8.6 Coupling constants and frequency dependence

In Fig. 6.7, we investigate the parametric dependencies of the coupling constants in the ab initio few-mode theory. In particular, we consider the nuclear complex level shift [Dom83] given by $F = \Delta_{\text{LS}} - i\Gamma_{\text{S}}/2 = \underline{\underline{g}}\,\underline{\underline{\mathcal{D}}}^{-1}\underline{\underline{g}}^{\dagger}$ and the quantity $F_R = -2\pi i \underline{\underline{\mathcal{W}}}^{\dagger}\underline{\underline{\mathcal{D}}}^{-1}\underline{\underline{g}}^{\dagger}\underline{\underline{g}}\,\underline{\underline{\mathcal{D}}}^{-1}\underline{\underline{\mathcal{W}}}$, which quantifies the nuclear resonance peak height in analogy to $2\kappa_R$ for the cavity resonances [HE13]. Together, these two quantities contain the information to calculate the nuclear spectrum in Fig. 6.6 according to Eq. (6.31). Since we consider a single nuclear ensemble in a cavity with only the reflection channel being open, both of these quantities are scalars and can be obtained using the substitution of the analytical formulas described in Sec. 6.8.3.

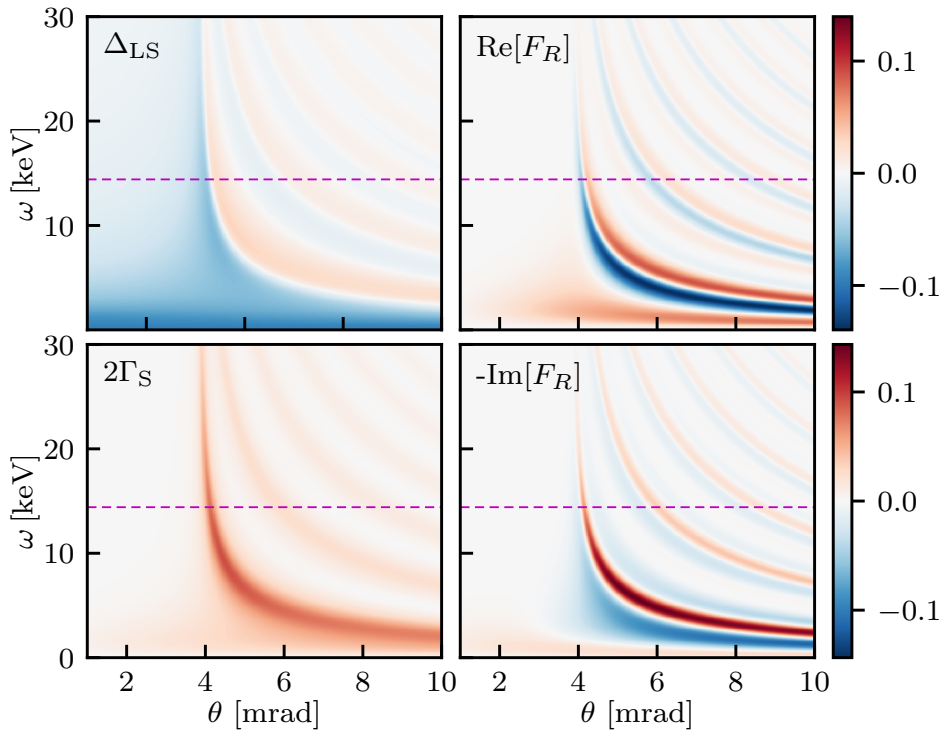

Figure 6.7: (Color online) Quantum optical parameters in the ab initio few-mode theory for the example cavity with a single resonant thin-layer ensemble defined in Fig. 6.4. The results are calculated using the well-converged 20-mode theory and shown as a function of photon frequency and incidence angle. The left panels show the collective Lamb shift Δ_{LS} and superradiance Γ_{S}. The right panels show the real and imaginary parts of F_R as defined in the main text. All parameters vary significantly both along the angular and frequency axis with non-trivial functional dependence. However, in the neV-μeV range around the nuclear resonant energy (magenta dashed line), which is relevant for the nuclear line shape, the variations of the parameters in frequency are negligible.

Results are shown in Fig. 6.7 as a function of photon frequency and incidence angle over the range of the cavity spectrum in Fig. 6.5. We note that all parameters vary significantly in the frequency and angular direction, featuring non-trivial functional dependencies that give rise to the practical differences to the phenomenological model (see Sec. 6.8.5). However, while there are significant variations in the energy direction on the keV scale, the parameters are essentially constant in the neV-μeV range around the nuclear resonant energy. This confirms that the adiabatic approximation performed in Sec. 6.5 is valid for such cavities. The non-trivial angular dependence nevertheless persists. We note that since the cavity parameters are usually obtained by fitting to the rocking curve [HE15], they are particularly susceptible to the differences in the phenomenological description.

6.9 Generalization to thick layers of resonant nuclei

In this section, we develop the quantum optical description for x-ray cavities with thick resonant layers. The case of thick resonant layers is practically relevant as it has been studied extensively in nuclear forward scattering experiments [Hel91; Sch02; Smi07; SVK13] and has been used in grazing incidence, for example, for novel spectroscopy techniques [Röh97] or the study of magnetism in thin films, see, e.g. [Nie98; Śle10]. Placed inside cavities, thick resonant layers are particularly interesting from the theoretical perspective, since they are difficult to describe using a phenomenological approach. The reason is that in the latter, the mode functions are not known, such that one would have to fit a continuum of light-nucleus coupling parameters to describe the spatial variation throughout the thick layer.

Within the ab initio few-mode theory on the other hand, the description is rather straightforward and can be considered as the continuum limit of the general multi-layer solution derived in Sec. 6.4. We further show that the thick layer system can be described as a self-coupled continuum ensemble, rather than the few-level schemes obtained in the thin-layer case.

6.9.1 Theory

With the general solution of multi-mode multi-layer systems available, the case of thick layers can be solved simply by partitioning the layer into finely spaced sub-ensembles and taking the continuum limit of many such sub-ensembles.

The main structure-dependent quantity to compute in order to obtain the scattering matrix is

$$\Delta^{[\mathrm{int}]}_{\lambda\lambda'}(\omega) = \sum_l \frac{N_l g^*_{l\lambda} g_{l\lambda'}}{\omega - \omega_{\mathrm{nuc},l} + i\frac{\gamma}{2}}\,, \tag{6.52}$$

which modifies the intra-cavity propagator according to Eq. (6.22).

For a thick layer of resonant material, adjacent atomic layers of nuclei are usually separated by a distance much less than the variation in the mode profile. Dividing the thick layer into thin sub-ensembles, we can then take the continuum limit of the sub-ensemble sum, such that

$$\Delta^{[\mathrm{int}]}_{\lambda\lambda'}(\omega) \approx \frac{|d|^2 f_{\mathrm{LM}}}{2\sqrt{\omega_\lambda \omega_{\lambda'}}} \int_{z_i}^{z_f} dz \rho_N(z) \frac{\omega^2_{\mathrm{nuc}}(z)\tilde{\chi}^*_\lambda(z)\tilde{\chi}_{\lambda'}(z)}{\omega - \omega_{\mathrm{nuc}}(z) + i\frac{\gamma}{2}}\,, \tag{6.53}$$

where $\omega_{\mathrm{nuc}}(z)$, $\rho_N(z)$ are the position dependent frequency and nuclear number density, respectively. For homogeneous resonant layers the z-dependence of the couplings is mainly determined by the mode profiles. z_i [z_f] is the lower [upper] edge of the thick layer.

Evaluating the integral above gives the necessary quantity to compute scattering observables. Similarly, one can compute a continuum version of the effective level scheme given by the continuum limit of Eqs. (6.42, 6.43)

$$\hat{H}_{\mathrm{eff}} = \int dz \frac{\omega_{\mathrm{nuc}}(z)}{2} \hat{J}^z(z) + \int dz dz' \hat{J}^+(z) \mathrm{Re}[G(z,z')] \hat{J}^-(z') + \int dz \hat{J}^+(z) \underline{\Omega}^T(z) \underline{\hat{b}}^{(\mathrm{in})}(t) + h.c.\,, \tag{6.54}$$

and the effective Lindblad term

$$\mathcal{L}_{\mathrm{eff}}[\rho] = -\int dz dz' \mathrm{Im}[G(z,z')](2\hat{J}^-(z)\rho\hat{J}^+(z') - \{\hat{J}^+(z)\hat{J}^-(z'),\, \rho\}) + \mathcal{L}_{\mathrm{SE}}[\rho]\,.$$

This yields a physical interpretation of the thick layer as a self-coupled continuum ensemble rather than an effective few-level scheme as in the thin layer case.

6.9.2 Thick resonant layer in the example cavity

As a practical example we again use the cavity from Fig. 6.4 and consider a variable thickness of the resonant layer, while keeping it at the center of the cavity.

Since the resonant layer material is homogeneous, the number density of resonant nuclei and the resonance frequency of the nuclear transition do not vary with z. In this case, denoting the thickness of the resonant layer by t_{res}, we can evaluate Eq. (6.53) to obtain

$$\Delta^{[\mathrm{int}]}_{\lambda\lambda'}(\omega) \approx \frac{|d|^2\omega^2_{\mathrm{nuc}}}{2\sqrt{\omega_\lambda\omega_{\lambda'}}} \frac{f_{\mathrm{LM}}\rho_N}{\omega - \omega_{\mathrm{nuc}} + i\frac{\gamma}{2}} \int_{\frac{L-t_{\mathrm{res}}}{2}}^{\frac{L+t_{\mathrm{res}}}{2}} dz \tilde{\chi}^*_\lambda(z)\tilde{\chi}_{\lambda'}(z) = \frac{|d|^2\omega^2_{\mathrm{nuc}}}{2\sqrt{\omega_\lambda\omega_{\lambda'}}} \frac{f_{\mathrm{LM}}\rho_N}{\omega - \omega_{\mathrm{nuc}} + i\frac{\gamma}{2}} \Xi_{\lambda\lambda'}\,, \tag{6.55}$$

where the mode integral for the cavity under consideration is

$$\Xi_{\lambda\lambda'} = \frac{2}{L} \int_{\frac{L-t_{\mathrm{res}}}{2}}^{\frac{L+t_{\mathrm{res}}}{2}} dz \sin\left(\pi\lambda\frac{z}{L}\right) \sin\left(\pi\lambda'\frac{z}{L}\right)\,, \tag{6.56}$$

which can straightforwardly be evaluated analytically.

Fig. 6.8 shows nuclear spectra of the example cavity at different layer thicknesses. The results from the continuum ab initio few-mode theory show excellent agreement with the semi-classical PYNUSS [Hee19] calculation, confirming the validity of our quantum model for cavities with thick resonant layers.

Finally, to interpret the spectra, we note that the self-coupled continuum ensemble features an EIT-like dip effect for thick layers. At layer thicknesses comparable to the cavity thickness, additional distortions are found, indicating the emergence of higher order spectral interferences.

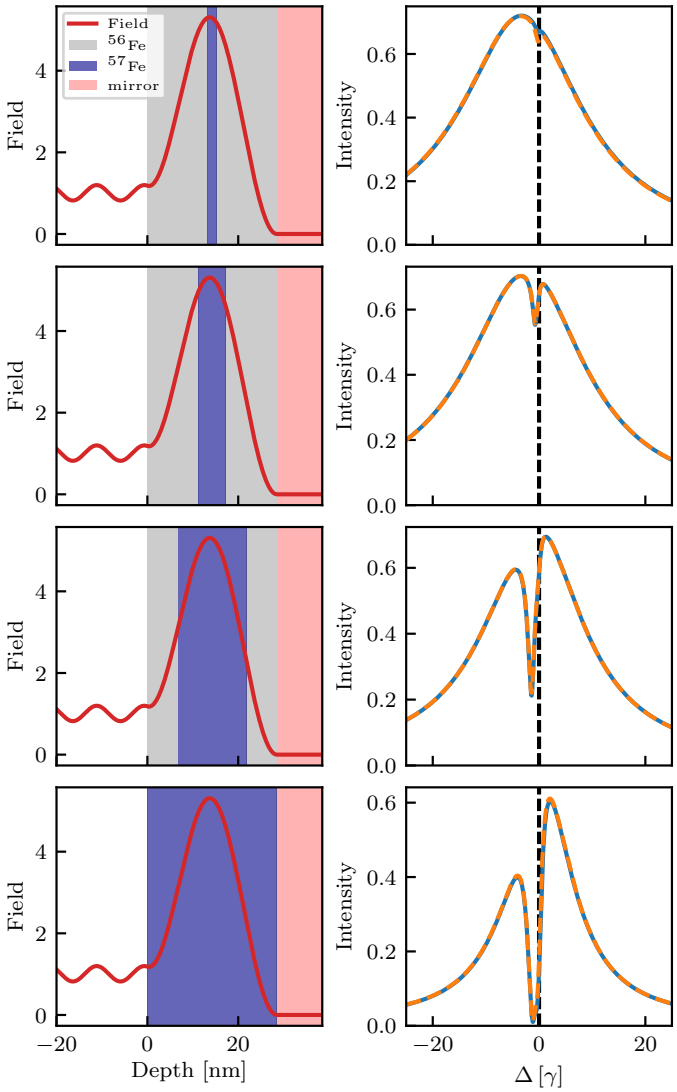

Figure 6.8: Thick resonat layer effects in the nuclear x-ray cavity QED system. The four rows correspond to different thicknesses of the resonant layer. From top to bottom, the thickness of the resonant layer is increased (2.0 nm, 6.0 nm, 15.0 nm, 28.4 nm) while keeping the number of nuclei constant (with the usual enriched abundance of 0.95 at the reference thickness 2.0 nm). The left column shows illustrations of the respective cavity structures. The right column shows corresponding nuclear spectra at the first rocking minima θ_0. We see that as the thickness increases, an EIT-like dip appears in the spectra. The continuum version of the ab initio few-mode theory result (calculated at 15 modes, yellow dashed line) shows excellent agreement with the layer formalism result (solid blue line) in all cases.

Part II

Green's function approach to x-ray cavity QED

Chapter 7

Green's function Master equation and exciton picture

This chapter is based on the following publication:

Ab initio quantum models for thin-film x-ray cavity QED
D. Lentrodt, K. P. Heeg, C. H. Keitel, and J. Evers
Physical Review Research **2**, 023396 (2020)

7.1 Outline

In this chapter, we develop a second ab initio approach to x-ray cavity QED with Mössbauer nuclei. As outlined in Chapter 1, the method involves different approximations and features various advantages compared to the few-mode approach presented in Chapter 6.

The method to be developed directly derives a Born-Markov Master equation for the nuclear ensembles by applying a well-known Green's function technique [GW96; DKW02; SB08; AG17a] to the nuclear x-ray cavity QED system. This approach has the advantage that it is numerically straightforward even for complex planar cavity structures, since the required Green's function is available analytically [Tom95]. As a consequences, the resulting theory resolves the open questions with regards to the pXCQED model [HE13; HE15] outlined in Sec. 2.4, as we discuss in more detail in Sec. 8.5.

Fig. 7.1 shows a schematic overview of the various theoretical approaches to thin-film x-ray cavity QED and how their different approximations fit together.

As a first theoretical result of this chapter, we show that the standard layer formalism [Röh05b] is essentially analogous to an effective propagation equation that can be derived from a Green's function quantization by linear dispersion theory, up to applicable but unnecessary approximations that can be removed. Consequently, in the linear regime, all three ab initio approaches — the layer formalism (see Chapter 2), the ab initio few-mode theory (see Chapter 6) and the Green's function approach in this chapter — are essentially equivalent in that they can be used as alternative methods to calculate linear scattering spectra (see Fig. 7.1). However, each of these methods provides different advantages with regards to the interpretation of the quantum system or the mode structure of the cavity due to the different underlying approximations. In addition, the methods presented here go beyond the semi-classical linear dispersion theory in that they bear the potential for direct application in different sectors beyond the linear scattering and low excitation regimes.

The Green's function technique presented in this chapter most importantly provides a numerically efficient method to calculate effective nuclear level schemes for arbitrary complex layer stacks. It also removes the need for a fitting procedure that is necessary in the phenomenological model in [HE13; HE15], with the main advantage over the ab initio few-mode approach in Sec. 6.7 being the practical applicability even for complex layer geometries. The power of the approach is illustrated for realistic cavity geometries in Chapter 8, resolving previous discrepancies outlined in Sec. 2.4.

For readers who are mainly interested in how to apply the method in practice, we refer to the corresponding guide in Sec. 7.9. In Chapter 8, we further apply the formalism to reveal the role of thick-layer effects in x-ray cavity QED, resolving open questions with importance to a previously observed EIT phenomenon [Röh12; HE15] in such cavities.

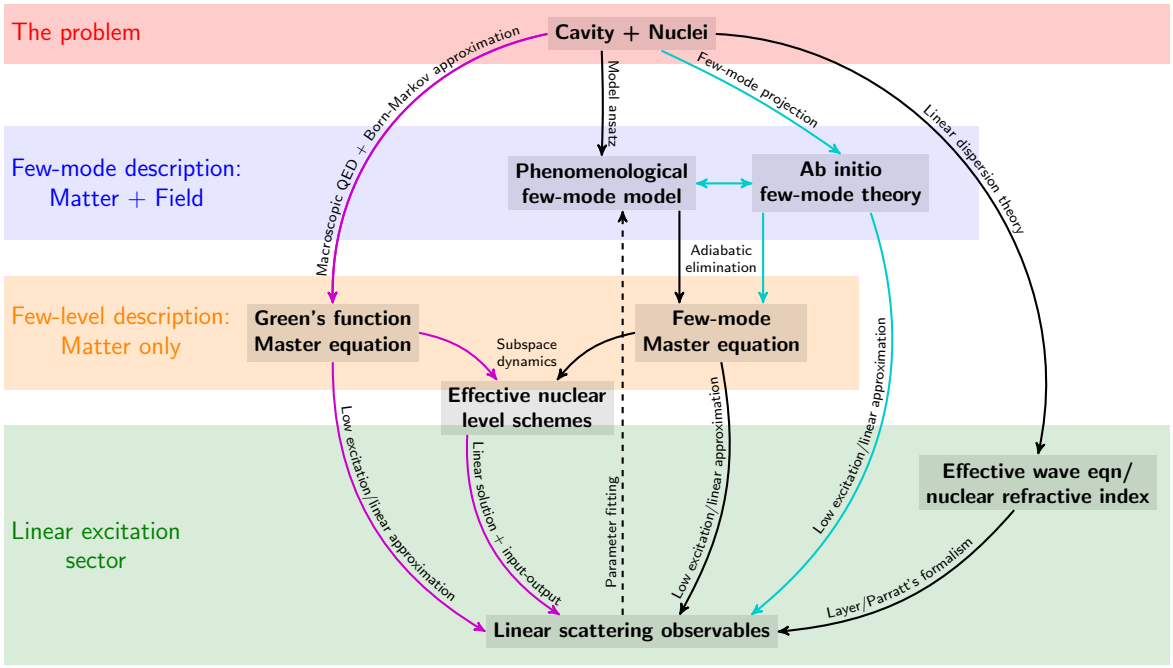

Figure 7.1: Overview of theoretical approaches to thin-film x-ray cavity QED with Mössbauer nuclei, including the standard semi-classical layer formalism [Röh05b], which is based on a variant of linear dispersion theory [Par54; Zhu90; BW80] (see also Chapter 2 for a discussion of related semi-classical approaches), and the successful phenomenological few-mode (pXCQED) model [HE13; HE15], which is based on the quantum input-output formalism of cavity QED [GZ04]. In this thesis, we present two additional ab initio quantum approaches to the problem, including an application of the ab initio few-mode theory [LE20] and of established Green's function techniques [GW96; DKW02; SB08; AG17a] to the layer geometry of the nuclear quantum optics setting. Results presented in this chapter are marked as magenta arrows which establish the Green's function approach as a new method. The connections introduced by the ab initio few-mode approach in Chapter 6 are marked as cyan arrows.

7.2 Green's function and macroscopic QED

The quantization of absorbing dielectrics (see [SB08] for a review) has been studied extensively in the literature (see e.g. [HB92; GW96; DKW02; SB08; BW07; Buh12]). A macroscopic prescription based on the Green's function [DKW02; SB08] gives the Hamiltonian in the dipole approximation [DKW02; Yao09]

$$\hat{H} = \int d^3\mathbf{r} \int_0^\infty d\omega \hbar\omega \hat{\mathbf{f}}^\dagger(\mathbf{r},\omega)\hat{\mathbf{f}}(\mathbf{r},\omega) + \sum_{ln} \frac{\hbar\omega_{\mathrm{nuc},l}}{2}\hat{\sigma}^z_{ln} - \sum_{ln}[\hat{\sigma}^+_{ln}\mathbf{d}^*_l + \hat{\sigma}^-_{ln}\mathbf{d}_l]\cdot\hat{\mathbf{E}}(\mathbf{r}_{ln})\,, \tag{7.1}$$

where $\hat{\mathbf{f}}(\mathbf{r},\omega)$ are bosonic operators, $\hat{\mathbf{E}}$ is the electric field operator and, unlike in the previous chapter, polarization is included. The bosonic operators appearing in the Hamiltonian are related to the field operator by [DKW02]

$$\hat{\mathbf{E}}(\mathbf{r}) = i\sqrt{\frac{\hbar}{\pi\varepsilon_0}}\int_0^\infty d\omega \int d^3\mathbf{r}' \sqrt{\mathrm{Im}[\varepsilon(\mathbf{r}')]}\mathbf{G}(\mathbf{r},\mathbf{r}',\omega)\cdot\hat{\mathbf{f}}(\mathbf{r}',\omega)\,, \tag{7.2}$$

where the Green's tensor is defined via

$$[\nabla\times\nabla\times - \frac{\omega^2}{c^2}\varepsilon(\mathbf{r},\omega)]\mathbf{G}(\mathbf{r},\mathbf{r}',\omega) = \delta(\mathbf{r}-\mathbf{r}')\,, \tag{7.3}$$

and the dielectric permittivity is allowed to be frequency dependent. Approaches based on such Hamiltonians employing the classical electromagnetic Green's function of the system are known as macroscopic QED [SB08], which has been used extensively, for example, for the study of dispersion forces and related phenomena [Buh12], as well as recently for the description of atom-light scattering in nanostructures [AG17a; AG17b] and atomic-waveguide QED [Mas19], for the theory of Bose-Einstein condensation in multi-mode cavities [Ben20] and for inverse design of light-matter interactions in

complex environments [BB19]. The Green's function quantization provides an alternative to the normal modes approach in Appendix C.1.3 that is used as the basis for the ab initio few-mode theory in Sec. 6.3. Besides its numerical efficiency that will be demonstrated later, it has the advantage that absorption is described rigorously without the need for the non-Hermitian Hamiltonian prescription in Appendix C.1.6.

As a drawback, the approach does not offer an interpretation in terms of the modes or resonances of the cavity structure, which are often a driving force for the design of novel and exotic cavity structures, both in the x-ray regime [Hee15a; HKE16; Hab17; Röh12] and at lower wavelengths [RG17]. Instead, all the information about the cavity environment is contained in a single function. In this context, we note that effective modes for the macroscopic QED Hamiltonian have been introduced previously [BW08b] and have recently found applications for cavity interactions of multiple atoms [Esf18; ESB19] and strongly coupled light-matter dynamics in complex environments [SBSF20]. Alternatively, the Green's function can in principle be approximated in terms of mode parameters [AG17a]. For overlapping modes structures, however, such an approximate treatment is non-trivial and results in similar problems as found in the phenomenological model. On the other hand, such techniques provide a route towards direct numerical optimization of cavity structures via the Green's function approach (see e.g. [Dor19; BB19]). These approaches could also be complemented by various decompositions of the Green's function known from resonance theory [Kri14; Tür05; TSC06; Chi98; Lal18; KH14; RG17].

We further note that the macroscopic QED framework, that is treating the material as a refractive index, also has its limitations. Complementary approaches connecting to electronic structure theory [Rug14], quantum chemistry [SRR18] and condensed matter physics [Li20] are available for a variety of parameter regimes and, while often being computationally demanding, allow to fully integrate associated effects.

7.3 Linear dispersion theory and relation to the layer formalism

The equations of motion for the Hamiltonian Eq. (7.1) are all linear, except for the usual non-linear term featuring a product of $\hat{\sigma}^z$ and the field operators (see Eq. (6.18) for the few-mode counterpart of this contribution). In [Yao09], it is shown that analogously to the linear calculation in Sec. 6.4 and the linear dispersion calculation in [Zhu90; LE20], these equations can be tackled by employing the low excitation approximation $\langle \hat{\sigma}^z(t) \rangle \approx -1$ and solving the resulting linearly coupled differential equations. The result can be expressed in frequency space as [Yao09]

$$\langle \hat{\mathbf{E}}(\mathbf{r},\omega) \rangle = \frac{\omega^2}{\varepsilon_0 c^2} \sum_{ln} \mathbf{G}(\mathbf{r},\mathbf{r}_{ln},\omega) \cdot [\mathbf{d}_l^* \langle \hat{\sigma}_{ln}^+(\omega) \rangle + \mathbf{d}_l \langle \sigma_{ln}^-(\omega) \rangle], \tag{7.4}$$

with [Yao09]

$$\langle \hat{\sigma}_{ln}^+(\omega) \rangle = \frac{\mathbf{d}_l \cdot \langle \hat{\mathbf{E}}(\mathbf{r}_{ln},\omega) \rangle}{\hbar(\omega + \omega_{\mathrm{nuc},l})}\,, \tag{7.5}$$

and

$$\langle \hat{\sigma}_{ln}^-(\omega) \rangle = -\frac{\mathbf{d}_l^* \cdot \langle \hat{\mathbf{E}}(\mathbf{r}_{ln},\omega) \rangle}{\hbar(\omega - \omega_{\mathrm{nuc},l})}\,. \tag{7.6}$$

Substitution into Eq. (7.4) and using Eq. (7.3) shows that the electric field obeys the effective wave equation

$$[\nabla \times \nabla \times - \frac{\omega^2}{c^2} \varepsilon(\mathbf{r},\omega)] \langle \hat{\mathbf{E}}(\mathbf{r},\omega) \rangle = -\frac{\omega^2}{\varepsilon_0 c^2} \sum_{ln} \delta(\mathbf{r} - \mathbf{r}_{ln}) \frac{2\omega_{\mathrm{nuc},l} \mathbf{d}_l^T \mathbf{d}_l}{\hbar(\omega^2 - \omega_{\mathrm{nuc},l}^2)} \langle \hat{\mathbf{E}}(\mathbf{r},\omega) \rangle\,, \tag{7.7}$$

where we have assumed real $\mathbf{d}$ for simplicity. The effect of the coupling to the nuclear transitions can thus be interpreted as a modification of the frequency dependent refractive index [LE20; MT16]. We note that in contrast to the formula resulting from the simple model in [LE20], the above approach includes polarization and a rigorous treatment of absorption. On the other hand, a factor of $\frac{\omega_{\mathrm{nuc},l}^2}{\omega^2}$ is

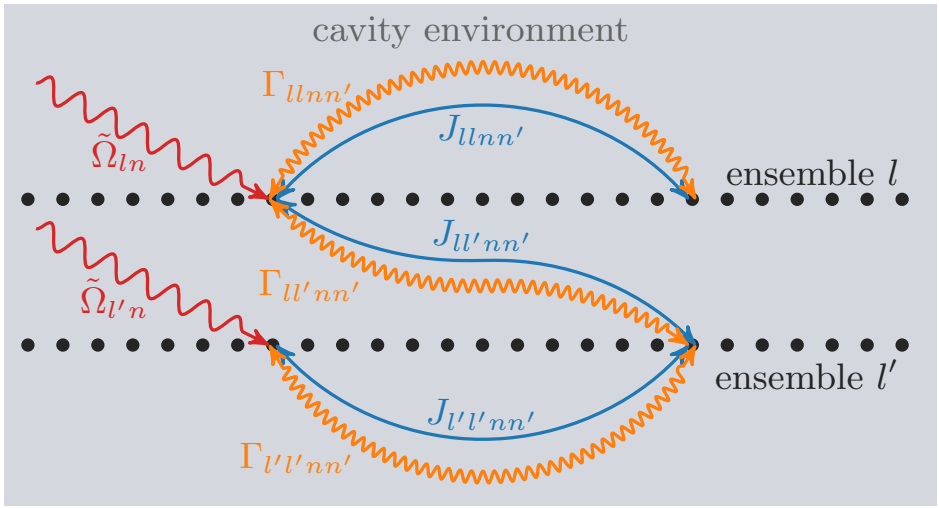

Figure 7.2: Schematic illustration of the effective nuclear Master equation obtained using the Green's function approach. $J_{ll'nn'}$ are couplings between the nuclei, $\Gamma_{ll'nn'}$ decay constants, and $\tilde{\Omega}_{ln}$ the effective driving strengths. The cavity does not appear explicitly, as it is treated as an environment in the Green's function approach.

absent due to the $\mathbf{E}\cdot\mathbf{r}$ gauge that is adopted in [Yao09], which is appropriate for our weak coupling scenario, but has to be adjusted at extreme coupling strengths [MT16; MPT17; Sch19].

We further note that by transforming the above effective wave equation into the time-domain, one can obtain a propagation equation that is of the form of Shvyd'ko's time and space wave equation [Shv99], with the wave equation kernel expressed explicitly for the elastic scattering case considered here.

When one is interested in steady-state scattering properties, the above equation can be solved directly in frequency space using transfer matrices or Parratt's method [Par54], which has been generalized to the layer formalism in the nuclear resonance scattering community [Röh05b; Stu00]. The above derivation thus unveils the connection to the semi-classical theories used in nuclear resonant scattering, clarifying its relation to the full quantum theory of the absorbing dielectric environment interacting with the nuclear transitions. The main insight is that the central approximation in these approaches is the low excitation approximation. In the linear excitation regime, where this approximation applies, the approaches are then analogous. We note that in practice, slight differences in the formulas can be found, since additional convenient approximations are made in the x-ray case, which are well applicable, but unnecessary from a formal perspective. Examples include the rotating wave approximation. We also refer to Appendix C.1.7 for further context.

7.4 Nuclear Master equation in real space

Starting from the macroscopic QED Hamiltonian in the rotating-wave approximation, the Born-Markov approximation can be used to derive an effective Liouvillian for the nuclei interacting with each other via the electromagnetic field [DKW02; AG17a]. Since nuclei and x-rays usually feature very weak coupling and the cavities in use are highly leaky, the Born-Markov approximation is applicable in most cases. Recently, systems featuring collective strong coupling have been reported [Hab16a], where the Born-Markov approximation may break down and the ab initio few-mode theory presented in Sec. 6.3 may be advantageous. Alternatively, effective continuum modes [BW08b] based on the Green's function quantization may prove useful, which have been shown to be tractable via cumulant expansions [SBSF20] in certain parameter regimes.

Following the approach in [AG17a; AG17b] and again excluding polarization effects for simplicity, we can write the effective Hamiltonian in our ensemble notation as

$$\hat{H}_{\mathrm{eff}} = \sum_{ln} \frac{\omega_{\mathrm{nuc},l}}{2} \hat{\sigma}^z_{ln} - \sum_{ln} \sum_{l'n'} J_{ll'nn'} \hat{\sigma}^+_{ln} \hat{\sigma}^-_{l'n'} - \sum_{ln} \left[\mathbf{d}^*_l \cdot \mathbf{E}_{\mathrm{in}}(\mathbf{r}_{ln}) \hat{\sigma}^+_{ln} + h.c. \right] , \tag{7.8}$$

and the Lindblad term as

$$\mathcal{L}_{\text{eff}}[\rho] = \sum_{ln}\sum_{l'n'} \frac{\Gamma_{ll'nn'}}{2}(2\hat{\sigma}^+_{ln}\rho\sigma^-_{l'n'} - \{\hat{\sigma}^+_{ln}\hat{\sigma}^-_{l'n'},\, \rho\}) + \mathcal{L}_{\text{SE}}[\rho]\,, \tag{7.9}$$

where $J_{ll'nn'}$ [$\Gamma_{ll'nn'}$] is the nucleus-nucleus coupling [decay] constant and $\mathbf{E}_{\text{in}}(\mathbf{r}_{ln}) = \langle \mathbf{E}_{\text{in}}(\mathbf{r}_{ln})\rangle$ is the driving field [AG17a] providing a driving strength $\tilde{\Omega}_{ln} = \mathbf{d}^* \cdot \mathbf{E}_{\text{in}}(\mathbf{r}_{ln})$ for the nucleus n in ensemble l. Within the Born-Markov approximation, the nuclei are thus described as driven by the incident cavity field without resonant modification.

The couplings and decay constants can be obtained from the Green's function of the system [AG17a] by

$$J_{ll'nn'} = \frac{\mu_0\omega^2_{\text{nuc},l}}{\hbar}\mathbf{d}^*_l \cdot \text{Re}[\mathbf{G}(\mathbf{r}_{ln}, \mathbf{r}_{l'n'}, \omega_{\text{nuc},l})] \cdot \mathbf{d}_{l'}\,, \tag{7.10}$$

$$\Gamma_{ll'nn'} = 2\frac{\mu_0\omega^2_{\text{nuc},l}}{\hbar}\mathbf{d}^*_l \cdot \text{Im}[\mathbf{G}(\mathbf{r}_{ln}, \mathbf{r}_{l'n'}, \omega_{\text{nuc},l})] \cdot \mathbf{d}_{l'}\,. \tag{7.11}$$

In the above form, the effective nuclear Hamiltonian includes intra-layer couplings between individual nuclei, constituting an effective level scheme beyond the single parallel wave vector approximation employed in Sec. 6.7. The resulting many-body coupling scheme is illustrated in Fig. 7.2.

In order to obtain an ensemble picture as in Fig. 6.3, one can introduce spin-wave operators [Mas19; AG17b; ZLS07] $\hat{\sigma}^\pm_l(\mathbf{k}_\parallel) = \sum_n \hat{\sigma}^\pm_{ln} e^{\pm i\mathbf{k}_\parallel \cdot \mathbf{r}_{\parallel,n}}$, which under the translational invariance assumption diagonalize the effective Hamiltonian [AG17b]. Here, since we are mainly interested in the linear sector, where the parallel wave vector $\mathbf{k}_\parallel$ of a given excitation is conserved, we can then again derive an effective Hamiltonian for the subspace at a single parallel wave vector (see also Appendix C.1.5), as we show in the following. Such an effective level scheme is of interest, since it corresponds directly to the effective level schemes derived in Sec. 6.7 from the ab initio few-mode approach and to the corresponding interpretation of recent experiments [Röh10; Röh12; Hee13; Hee15a; Hee15b; HE15; Hab17; Hab19]. The Green's function approach provides an alternative ab initio method to calculate these level schemes, with different approximations involved bearing the potential for different generalizations. The main advantage of the Green's function approach over the ab initio few-mode theory is its numerically efficiency for calculating effective level schemes in the case of the layered cavity geometry, as we demonstrate in the following sections.

7.5 Effective nuclear level scheme in the spin-wave basis at low excitation

In the low excitation regime, where $\langle \hat{\sigma}^z_{ln}\rangle \approx -1$, the equation of motion for the lowering operator resulting from the Born-Markov Master equation reads

$$\frac{d}{dt}\hat{\sigma}^-_{ln} = -i(\omega_{\text{nuc},l} - i\frac{\gamma}{2})\hat{\sigma}^-_{ln} + i\sum_{l'n'}\mathcal{G}(\mathbf{r}_{ln}, \mathbf{r}_{l'n'})\hat{\sigma}^-_{l'n'} + i\mathbf{d}^*_l \cdot \mathbf{E}_{\text{in}}(\mathbf{r}_{ln})\,, \tag{7.12}$$

where

$$\mathcal{G}(\mathbf{r}_{ln}, \mathbf{r}_{l'n'}) = J_{ll'nn'} + i\frac{\Gamma_{ll'nn'}}{2} = \frac{\mu_0\omega^2_{\text{nuc},l}}{\hbar}\mathbf{d}^*_l \cdot \mathbf{G}(\mathbf{r}_{ln}, \mathbf{r}_{l'n'}, \omega_{\text{nuc},l}) \cdot \mathbf{d}_{l'}\,, \tag{7.13}$$

and we have dropped the expectation value brackets for brevity. Using the approximate in-plane translational invariance of the x-ray cavity, we can write the Green's function as [Tom95]

$$\mathbf{G}(\mathbf{r}_{ln}, \mathbf{r}_{l'n'}, \omega) = \int \frac{d^2\mathbf{k}_\parallel}{(2\pi)^2}\mathbf{G}(z_l, z_{l'}, \mathbf{k}_\parallel, \omega)e^{i\mathbf{k}_\parallel \cdot (\mathbf{r}_{\parallel,n} - \mathbf{r}_{\parallel,n'})}\,, \tag{7.14}$$

where $\mathbf{G}(z_l, z_{l'}, \mathbf{k}_\parallel, \omega)$ is the Fourier transformed Green's function and lattice offsets between the ensembles of less than a lattice constant are neglected. Similarly, we define

$$\mathcal{G}(z_l, z_{l'}, \mathbf{k}_\parallel) = \frac{\mu_0\omega^2_{\text{nuc},l}}{\hbar}\mathbf{d}^*_l \cdot \mathbf{G}(z_l, z_{l'}, \mathbf{k}_\parallel, \omega_{\text{nuc},l}) \cdot \mathbf{d}_{l'}\,. \tag{7.15}$$

Transferring to the spin-wave basis [Mas19], the equations of motion simplify to

$$\frac{d}{dt}\hat{\sigma}_l^-(\mathbf{k}_\parallel) = -i(\omega_{\mathrm{nuc},l} - i\frac{\gamma}{2})\hat{\sigma}_l^-(\mathbf{k}_\parallel) + i\sum_{l'}\frac{N}{A_\parallel}\mathcal{G}(z_l, z_{l'}, \mathbf{k}_\parallel)\hat{\sigma}_{l'}^-(\mathbf{k}_\parallel) + i\frac{N}{A_\parallel}\mathbf{d}_l^* \cdot \mathbf{E}_{\mathrm{in}}(z_l, \mathbf{k}_\parallel)\,, \tag{7.16}$$

where we have used $\sum_n e^{i(\mathbf{k}_\parallel - \mathbf{k}'_\parallel)\cdot\mathbf{r}_{\parallel,n}} = \frac{(2\pi)^2 N}{A_\parallel}\delta(\mathbf{k}_\parallel - \mathbf{k}'_\parallel)$, defined

$$\mathbf{E}_{\mathrm{in}}(z_l, \mathbf{k}_\parallel) = \int d^2\mathbf{r}_{\parallel,n}\mathbf{E}_{\mathrm{in}}(\mathbf{r}_{ln})e^{-i\mathbf{k}_\parallel\cdot\mathbf{r}_{\parallel,n}}\,, \tag{7.17}$$

and used the approximation $\sum_n \mathbf{E}_{\mathrm{in}}(\mathbf{r}_{ln})e^{-i\mathbf{k}_\parallel\cdot\mathbf{r}_{\parallel,ln}} \approx \frac{N}{A_\parallel}\int d^2\mathbf{r}_{\parallel,n}\mathbf{E}_{\mathrm{in}}(\mathbf{r}_{ln})e^{-i\mathbf{k}_\parallel\cdot\mathbf{r}_{\parallel,n}}$, which is valid for grazing incidence illumination, where the phase variation of the illuminating beam is small over the length scale of the lattice parameter, and which effectively neglects Bragg scattering.

Importantly, the driving field and inter-ensemble couplings above are also approximated as independent of n within one ensemble l. If all nuclei are located at the same z_l, this is an exact representation of the ensemble in the considered geometry. Practically, however, one often wishes to interpret a resonant layer of finite thickness as a single ensemble [HE15; Röh12; Röh10]. The ensemble quantities are then approximated as constant over the layer thickness and taken equal to their central value at z_l, which we denote as the thin-layer approximation. We refer to Chapter 8 for a practical discussion of this approximation and its consequences, as well as to the previous discussion of thick layers in the context of the ab initio few-mode theory in Sec. 6.9.

We see that Eq. (7.16) provides a closed set of operator equations at a given parallel wave vector. The effective subspace Liouvillian corresponding to this linear equation of motion is given by

$$\hat{H}_{\mathrm{eff}}(\mathbf{k}_\parallel) = \sum_l \frac{\omega_{\mathrm{nuc},l}}{2}\hat{\sigma}_l^z(\mathbf{k}_\parallel) - \sum_{ll'}\Delta_{ll'}(\mathbf{k}_\parallel)\hat{\sigma}_l^+(\mathbf{k}_\parallel)\hat{\sigma}_{l'}^-(\mathbf{k}_\parallel) - \sum_l \frac{N}{A_\parallel}\left[\mathbf{d}_l^* \cdot \mathbf{E}_{\mathrm{in}}(z_l, \mathbf{k}_\parallel)\hat{\sigma}_l^+(\mathbf{k}_\parallel) + h.c.\right] \tag{7.18}$$

and the Lindblad term as

$$\mathcal{L}_{\mathrm{eff}}[\rho](\mathbf{k}_\parallel) = \sum_{ll'}\frac{\gamma_{ll'}(\mathbf{k}_\parallel)}{2}\Big(2\hat{\sigma}_l^+(\mathbf{k}_\parallel)\rho\sigma_{l'}^-(\mathbf{k}_\parallel) - \{\hat{\sigma}_l^+(\mathbf{k}_\parallel)\hat{\sigma}_{l'}^-(\mathbf{k}_\parallel),\,\rho\}\Big) + \mathcal{L}_{\mathrm{SE}}[\rho]\,, \tag{7.19}$$

where

$$\Delta_{ll'} = \frac{N}{A_\parallel}\frac{\mu_0\omega_{\mathrm{nuc},l}^2}{\hbar}\mathbf{d}_l^* \cdot \mathrm{Re}[\mathbf{G}(z_l, z_{l'}, \mathbf{k}_\parallel, \omega_{\mathrm{nuc},l})] \cdot \mathbf{d}_{l'}\,, \tag{7.20}$$

$$\gamma_{ll'} = 2\frac{N}{A_\parallel}\frac{\mu_0\omega_{\mathrm{nuc},l}^2}{\hbar}\mathbf{d}_l^* \cdot \mathrm{Im}[\mathbf{G}(z_l, z_{l'}, \mathbf{k}_\parallel, \omega_{\mathrm{nuc},l})] \cdot \mathbf{d}_{l'}\,. \tag{7.21}$$

We see that this effective level scheme corresponds in close analogy to the one derived from the few-mode approach in Sec. 6.7 (as depicted in Fig. 6.3), with the driving field being expressed as a channel mode expansion in the few-mode case $\mathbf{d}_l^* \cdot \mathbf{E}_{\mathrm{in}}(z_l, \mathbf{k}_\parallel) = \underline{\Omega}_l^T\hat{\underline{b}}^{(\mathrm{in})}(t)$.

In summary, in the linear regime, the nuclear dynamics for an incident field of a defined parallel wave vector are given by the effective level scheme Eqs. (7.18, 7.19). For an incident field containing multiple parallel wave vectors, the superposition principle applies in the linear regime.

We note that as also observed in the ab initio few-mode theory (see Appendix C.1.7), the effective linear level scheme parameters depend on the dipole moment scaled by $\sqrt{N/A_\parallel}$, such that only the nuclear number density is relevant for linear observables. For a detailed discussion of how to obtain effective dipole moments for arbitrary multi-polar transitions and for how to calculate them for arbitrary hyperfine splitting configurations, we refer to Chapter 9.

7.6 Linear solution in frequency space

Eq. (7.16) can be solved in frequency space to give [AG17a; LE20]

$$\hat{\sigma}_l^-(\mathbf{k}_\parallel, \omega) = -\sum_{l'}(\mathcal{M}^{-1})_{ll'}\tilde{\Omega}_{l'}\,, \tag{7.22}$$

where

$$\mathcal{M}_{ll'} = i(\Delta_{\mathrm{nuc},l} + i\frac{\gamma}{2})\delta_{ll'} + i\frac{N}{A_\parallel}\mathcal{G}(z_l, z_{l'}, \mathbf{k}_\parallel)\,, \tag{7.23}$$

with $\Delta_{\mathrm{nuc},l} = \omega - \omega_{\mathrm{nuc},l}$ and

$$\tilde{\Omega}_l = i\frac{N}{A_\parallel}\mathbf{d}_l^* \cdot \mathbf{E}_{\mathrm{in}}(z_l, \mathbf{k}_\parallel, \omega)\,. \tag{7.24}$$

7.7 Reconstructing spectral observables

The Born-Markov Master equation or the effective nuclear level scheme given above define the dynamics of nuclear observables for a given driving field, which can be solved to obtain, for example, the linear regime solution Eq. (7.22). Scattering observables can be reconstructed using a generalized input-output equation [AG17a], which is also valid beyond the linear sector. At a given parallel wave vector and in frequency space, it reads

$$\hat{\mathbf{E}}(z, \mathbf{k}_\parallel, \omega) = \hat{\mathbf{E}}_{\mathrm{in}}(z, \mathbf{k}_\parallel, \omega) + \mu_0 \sum_l \omega_{\mathrm{nuc},l}^2 \mathbf{G}(z, z_l, \mathbf{k}_\parallel, \omega)\cdot\mathbf{d}_l\, \hat{\sigma}_l^-(\mathbf{k}_\parallel, \omega)\,. \tag{7.25}$$

Substituting the linear frequency space solution for the lowering operator yields

$$\hat{\mathbf{E}}(z, \mathbf{k}_\parallel, \omega) = \hat{\mathbf{E}}_{\mathrm{in}}(z, \mathbf{k}_\parallel, \omega) - \mu_0 \sum_{ll'} \omega_{\mathrm{nuc},l}^2 \mathbf{G}(z, z_l, \mathbf{k}_\parallel, \omega)\cdot\mathbf{d}_l\, (\mathcal{M}^{-1})_{ll'}\tilde{\Omega}_{l'}\,. \tag{7.26}$$

This formula describes the field at position z for a given parallel wave vector $\mathbf{k}_\parallel$ and frequency ω, including the nuclear response. It is thus to be interpreted as a steady state solution for a driving field at frequency ω. $\hat{\mathbf{E}}_{\mathrm{in}}(z, \mathbf{k}_\parallel, \omega)$ is the corresponding field in the absence of the nuclei. It therefore is proportional to the mode profile and a driving amplitude factor α_{in}^q for each polarization, resulting in

$$\hat{\mathbf{E}}_{\mathrm{in}}(z, \mathbf{k}_\parallel, \omega) = \sum_q \alpha_{\mathrm{in}}^q\, \boldsymbol{\mathcal{E}}_q^{0(n)}(z, \mathbf{k}_\parallel, \omega)\,, \tag{7.27}$$

where our notation is chosen close to [Tom95]. The function $\boldsymbol{\mathcal{E}}_q^{0(n)}(z, \mathbf{k}_\parallel, \omega)$ is the mode profile that is normalized to the surface of the cavity from where the radiation is incident [Tom95], with 0 [n] indicating top [bottom] illumination. The polarization index q accounts for s- and p-polarization. For details on the mode functions used to expand the Green's function [Tom95] we refer to Appendix D.

In grazing incidence experiments at synchrotron facilities [Röh05b], a common observable is the reflection spectrum as investigated in Sec. 6.8. In the Green's function approach, such spectra can be obtained by evaluating the total field at the surface of the cavity. For example, for s-polarized incident light and s-polarized detection,

$$r_{\mathrm{green}}(\mathbf{k}_\parallel, \omega) = \frac{\mathbf{e}_s \cdot \hat{\mathbf{E}}(\tilde{z}_0, \mathbf{k}_\parallel, \omega)}{\alpha_{\mathrm{in}}^s} - 1, \tag{7.28}$$

where $\mathbf{e}_s$ is the unit vector in s-direction. Similarly, the transmission can be obtained by

$$t_{\mathrm{green}}(\mathbf{k}_\parallel, \omega) = \frac{\mathbf{e}_s \cdot \hat{\mathbf{E}}(\tilde{z}_n, \mathbf{k}_\parallel, \omega)}{\alpha_{\mathrm{in}}^s}\,, \tag{7.29}$$

where $\tilde{z}_0$ [$\tilde{z}_n$] is the position of the surface boundary of the uppermost [substrate] layer (see Fig. D.1). For substrates with an absorptive character via a non-zero imaginary part of the refractive index, the wave amplitude decays upon propagation through the medium, such that the transmission coefficient characterizes the amplitude ratio at the last layer surface [Tom95].

7.8 Numerical efficiency for the layer geometry

Conveniently, the layered x-ray cavity geometry is one of the few cases [AG17a; Buh12] where the Green's function for the cavity is known analytically [Tom95]. In particular, $\mathbf{G}(z, z', \mathbf{k}_\parallel, \omega)$ can

be expressed algebraically via an analytic recursion formula [Tom95] similar to Parratt's formalism [Par54]. This feature makes the above approach numerically highly efficient. Compared to the ab initio few-mode approach to calculating effective nuclear level schemes presented in Sec. 7.5, this feature poses a major advantage when one is interested in the calculation of effective quantum optical parameters as depicted in Fig. 6.3, and, for example, opens optimization opportunities.

The formula for the Green's function and its practical evaluation, as presented in [Tom95], are summarized in the following section and in Appendix D. In subsequent sections, we employ a numerical implementation thereof in order to benchmark the approach, and to demonstrate its usefulness. As a main result, we provide an ab initio nuclear level scheme for the EIT cavity configuration investigated experimentally in [Röh12], resolving previous discrepancies in the quantum optical description of the system [HE15].

7.9 Practical guide to calculations in the ab initio Green's function approach

Before we present our results for concrete systems, we show how common observables are calculated in the Green's function formalism in practice. This section serves as a recipe to reproduce the calculations discussed in the following sections and to provide clarity on the approach from an algorithmic perspective, in analogy to Sec. 6.8.3 for the few-mode approach.

The first step is to calculate the parallel Fourier transform of the Green's function $\mathbf{G}(z, z_l, \mathbf{k}_\parallel, \omega)$ for the cavity structure under study, which is the basic quantity appearing in the equations of the quantum theory. This is achieved by using the refractive indices of the cavity layers to compute the Fresnel coefficients for neighboring layers given by Eqs. (D.4). The reflection and transmission coefficients for multi-layer stacks of the empty cavity, that is disregarding the nuclear resonances, can then be obtained from the recursion formulas Eqs. (D.3). Substituting these coefficients into Eqs. (D.2) yields the field distributions, which in turn directly give the Green's function using Eq. (D.1). We note that the δ-function term in Eq. (D.1) can be disregarded for calculations of the effective level scheme, since it is identical to the free space term that renormalizes the transition frequency [Mas19]. Since the latter is used as a parameter corresponding to the experimentally observed value, it is already accounted for.

To obtain a nuclear level scheme, one has to specify the nuclear ensembles used in the calculation, corresponding to the summation index l in the formulas. For thin resonant layers with no magnetic or other splittings, it is natural to treat each layer as one ensemble. For thicker layers, the spatial variation of the cavity field across the layer requires a splitting of the thick layer into multiple sub-ensembles for a more accurate treatment, as discussed in more detail in the following chapter.

The coupling constants in the effective low-excitation level scheme can be obtained by evaluating Eq. (7.15) using the effective dipole moments of the nuclear ensembles. The coupling constants then follow by substitution of the latter result and the number density of the resonant material into Eqs. (7.20, 7.21). The effective level scheme Hamiltonian Eq. (7.18) and Lindblad term Eq. (7.19) are then fully determined after the driving term is calculated from the field distributions, where one has to manually specify the polarization state of the incoming field according to Eq. (7.27).

Spectral observables can be computed using the linear scattering solution for the nuclear operators Eq. (7.22). These can be substituted into the input-output relation Eq. (7.25) to obtain the combined field distribution including the nuclear resonance contribution in frequency space Eq. (7.26). For a given external driving field, this quantity encodes the entire output field and therefore the scattering information. However, in the linear regime, the spectral observables can also be computed directly using Parratts formalism, which does not make use of the ensemble interpretation in the effective level scheme. A comparison of the two approaches allows one to evaluate how accurately the effective level scheme describes the scattering process.

Finally, common observables such as reflection coefficients and transmission coefficients can then be computed for defined polarization directions as exemplified by Eqs. (7.28, 7.29).

Chapter 8

Thick layer effects in x-ray EIT cavities

This chapter is based on the following publication:

Ab initio quantum models for thin-film x-ray cavity QED
D. Lentrodt, K. P. Heeg, C. H. Keitel, and J. Evers
Physical Review Research **2**, 023396 (2020)

The thesis author's role in the paper is that of the sole principle author. The content has been reproduced verbatim with permission of the journal (© 2020 American Physical Society) and coauthors. Sec. 8.1 and references to other chapters have been adapted to suit the format of this thesis. Sec. 8.5 has been added as a perspective.

8.1 Outline

Certain x-ray thin-film cavity geometries feature sharp spectral dips in the nuclear reflection spectrum, which have notably been studied experimentally in [Röh12]. These signatures have been shown to correspond to an EIT phenomenon that interestingly does not require a second control field [Röh12]. A corresponding effective level scheme was derived in [HE15] using the phenomenological few-mode theory. Comparison to spectral observables from semi-classical calculations showed that the main EIT feature can be reproduced [HE15] by this approach. However, there are unexplained quantitative and qualitative disagreements [HE15]. In addition, it is unclear to what extent the heuristic extensions of the model that were found to be necessary [HE15] (see also the outline in Chapter 1 and the discussions in Chapters 2 and Sec. 6.2) influence the interpretation in terms of an effective level scheme.

In this chapter, we apply the Green's function approach developed in Chapter 7 to the two cavities studied in [Röh05b; HE15], resolving these open questions. In particular, we show that the qualitative disagreements in the spectra arise due to the relatively thick resonant layers in these cavities, causing the formation of cavity field gradients across the ensembles. The new approach can incorporate such gradients, and thus provides excellent quantitative agreement, improving the previous phenomenological description of the system significantly. In addition, we unambiguously calculate the effective nuclear level schemes using the ab initio method and investigate its quantum optical parameter trends.

8.2 Double resonant layer cavities and spectral benchmarks

The two cavity layer stacks under consideration are depicted in Fig. 8.3 and are identical to the geometries investigated in [HE15] to understand the EIT effect observed in [Röh12]. They consist of platinum cladding layers enclosing a carbon guiding layer that is doped with 3 nm thick resonant ^{57}Fe layers at certain positions. In both cases (cavity 1 and cavity 2), one of the resonant layers is located at the cavity center, where the field distribution in the third cavity mode at incidence angle $\theta = \theta_3$ features an anti-node. As shown in Fig. 8.3, in the EIT cavity (cavity 1, panel a) the second resonant layer is placed in the adjacent field distribution node closer to the cavity surface, while in the non-EIT cavity (cavity 2, panel b), it is placed in the node closer to the bottom of the cavity.

We refer to the two structures as "EIT" ("non-EIT") cavities, because they feature (do not feature) a pronounced spectral dip in the respective nuclear spectra shown in Fig. 8.4 [Röh12]. The two panels compare the spectra obtained using the Green's function approach (computed using Eq. (7.28), see

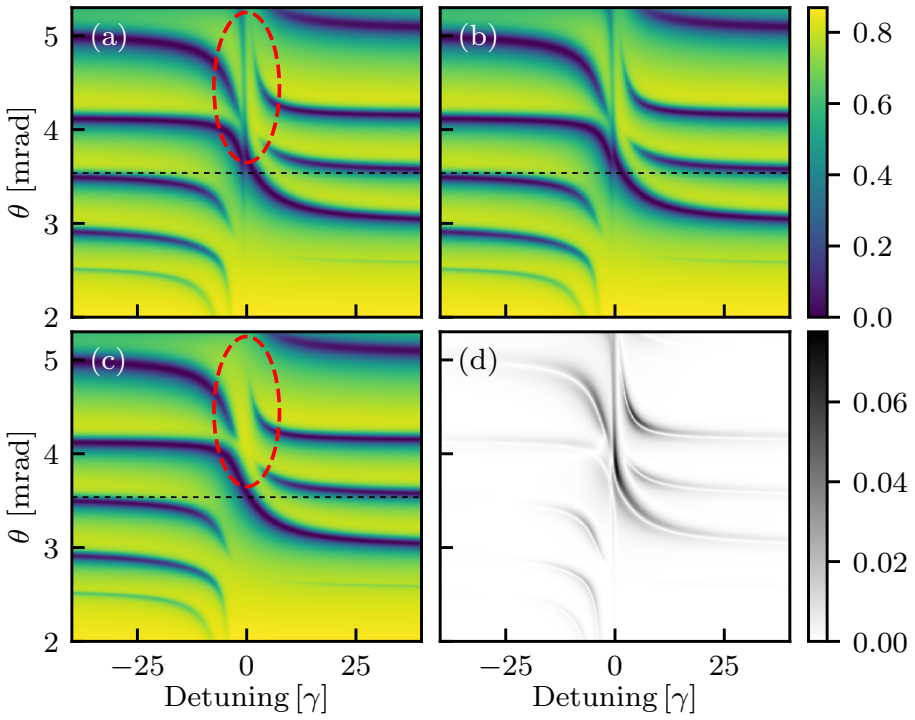

Figure 8.1: Nuclear spectra of the EIT cavity (cavity 1) as a function of incidence angle. The panels show the layer formalism result (a) and the Green's function result with (b) and without (c) sub-ensembles. (d) shows the deviation |(a)−(b)|. The dashed black line indicates the third mode minimum θ_3. The dashed red ellipse marks a region where (a) and (c) differ significantly, while (a) and (b) agree well, indicating that the layer thickness plays a role in particular in the higher modes due to more rapidly varying field distributions.

Sec. 7.9 for a description of the algorithm) to reference spectra calculated using the semi-classical layer formalism [Röh05b; Stu00] implemented in the software package PYNUSS [Hee19]. For the Green's function method, two different curves are shown in each panel. The red line corresponds to a model in which each of the two layers is treated as a single nuclear ensemble, neglecting possible field gradients across the layer. While the qualitative agreement is good and the major spectral features are reproduced, there are quantitative differences, most visible in additional small spectral features shown in the insets. To capture these features, we divide each layer into three sub-layers in our theoretical model (see white dashed lines in Fig. 8.3), to better account for the variation of the field intensity across the layers. The result is shown as the solid yellow line, which essentially agrees perfectly with the semi-classical calculation. The improvement can be understood since in Fig. 8.3 it is clear that the field distribution varies visibly over the thickness of each resonant layer, while it is constant to a good approximation over the thickness of each of the sub-ensembles.

We further note that the agreement between the spectra is much better than in the case of the phenomenological few-mode fits shown in [HE15], even when the sub-ensemble partition is not considered (red line in Fig. 8.4). This general quantitative improvement is due to the absence of heuristic extensions and problems related to the fitting procedure [HE15], which are not needed in the ab initio theories reported here.

8.3 The EIT effect and thick layer sub-ensembles

Next, we extend the discussion to the two-dimensional spectra as a function of detuning and incidence angle, which were also investigated for the two cavities in [HE15] in the context of the phenomenological few-mode model. In this reference, it was found that in addition to the quantitative differences in the one-dimensional spectra (see Fig. 8.4 and the discussion above), there are qualitative features that are not captured by the phenomenologically fitted model even with the heuristic extensions included.

Results are shown in Figs. 8.1 and 8.2 for the EIT- and the non-EIT cavity, respectively. In each figure, panel (a) corresponds to the layer formalism calculation which again serves as a benchmark. Panels (b) and (c) show the Green's function results with and without sub-ensemble partition of the

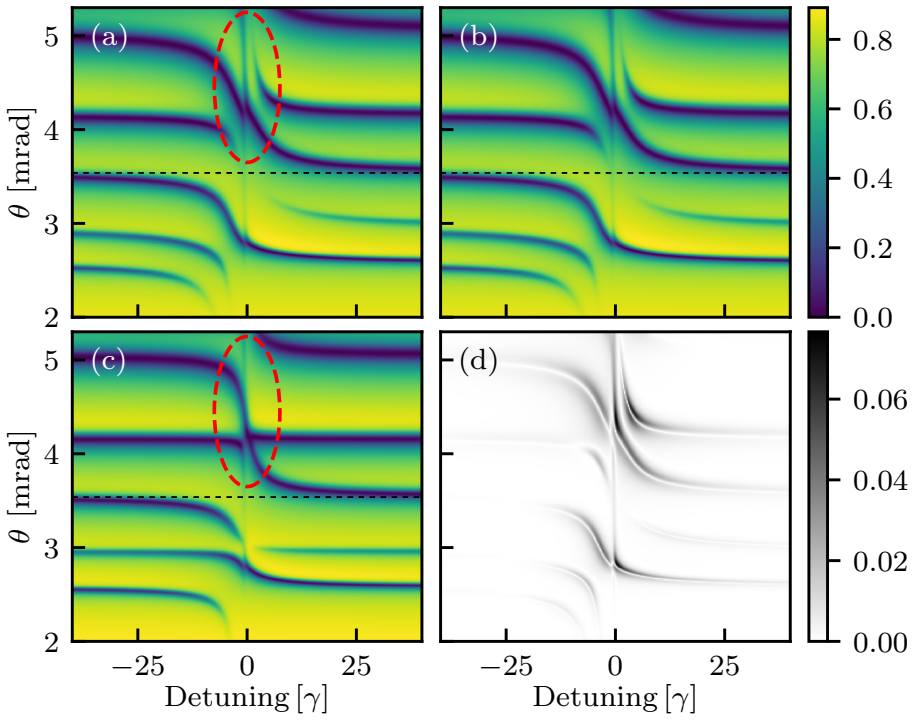

Figure 8.2: Nuclear spectra of the non-EIT cavity (cavity 2), analogous to Fig. 8.1 for the EIT cavity. The additional spectral feature inside the red dashed ellipse is accompanied by changes in the surrounding mode structure, with an avoided crossing in (a) turning into a merging point in (c).

resonant layers, respectively (spectra are computed using Eq. (7.28), see Sec. 7.9 for a description of the algorithm). Finally, panel (d) shows the absolute value of the difference between the results in panels (a) and (b).

We see that while (d) demonstrates excellent agreement of the Green's function description with sub-ensembles to the layer formalism, the corresponding results without sub-ensembles (panel c) are missing a spectral feature as indicated by the red dashed ellipse. Its absence shows that approximating thicker resonant layers as a single thin layer can lead to qualitative differences in the theoretical description.

For the EIT case in Fig. 8.1, we further find that the agreement of the model without sub-ensembles is still rather good close to the third mode minimum $\theta = \theta_3$, justifying the thin-layer approximation at this incidence angle. However, the differences become sizable in the region of the red dashed ellipse, which can be understood by noting that the field distributions vary more rapidly as function of position in the cavity at higher incidence angles. Fig. 8.2 shows analogous results for the non-EIT cavity (cavity 2). In this case, the absence of the spectral feature in the two-ensemble model also causes the surrounding spectral structure to change, with an avoided mode crossing turning into a merging point (see region inside the red dashed ellipse).

8.4 Effective nuclear level schemes

Finally, we discuss the effective level scheme resulting from the Green's function approach to x-ray cavity QED. Fig. 8.5 shows the effective nuclear level scheme and the quantum optical coupling constants for the EIT- and non-EIT cavities in Fig. 8.3 (the couplings are obtained from Eqs. (7.20, 7.21), see Sec. 7.9 for a description of the algorithm used to obtain the level scheme). For simplicity, the case without sub-ensemble partitioning is shown, with the notation adopted from [HE15]. Within the Green's function approach, the couplings and other quantum optical parameters can be calculated directly and unambiguously from the cavity geometry. The resulting parameters at the incidence angle $\theta = \theta_3$ are tabulated in Fig. 8.5.

In Fig. 8.6, we show the quantum optical parameters as a function of incidence angle, revealing the changes of the three level system over the different modes. In particular, the collective Lamb shifts,

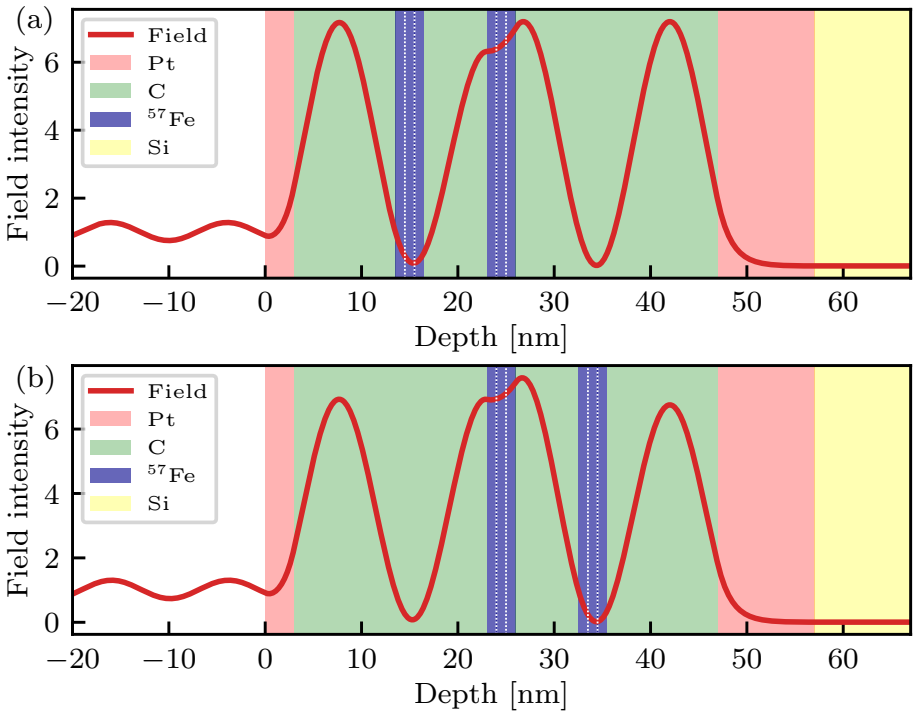

Figure 8.3: X-ray cavities with nuclei in EIT (a) and non-EIT (b) configuration, which were investigated experimentally in [Röh12] and modeled theoretically in [HE15]. (a) and (b) show the cavity structure (for materials, see legend) and off-resonant field distribution for the EIT (a, cavity 1) and non-EIT (b, cavity 2) case, respectively. We note that over the width of the blue resonant layers, the field distribution shows visible variations. The white dashed lines indicate the boundaries of sub-ensembles (see main text) over which the field distribution does not vary significantly.

the superradiant decay rate enhancements and the level couplings between the two ensembles in the EIT cavity (cavity 1) are depicted. Around each mode minimum $(\theta_1, \theta_2, \theta_3)$, the collective Lamb shift and superradiance roughly show the typical behavior of real and imaginary parts of a complex Lorentzian [LKE16; Hee15a]. For the coupling parameters δ_{12} and γ_{12}, similar structures are found. Only in the third mode, where the EIT phenomenon is observed, a different functional dependence and a negative γ_{12} is found.

These results show how complex cavity structures can be unambiguously interpreted in terms of quantum optical models, which paves the way for designing effective nuclear level schemes via tailored mode environments.

As a last consistency check, we show that the collective Lamb shift and superradiance calculated here indeed correspond to what these quantities have been associated with in the nuclear cavity QED literature so far [Hee15a; Röh10]. To this end, we replace the second resonant ^{57}Fe-layer by its off-resonant ^{56}Fe counterpart and fit a generic Fano model [Hee15a; Ott13; Bär10; Zho08] to the resulting line shapes at each incidence angle. The Fano profile fit function for the reflectance spectrum is given by [Hee15a]

$$R(\Delta) = |r(\Delta)|^2 = \sigma_0 \frac{|q + \epsilon(\Delta)|^2}{1 + \epsilon^2(\Delta)}\,, \tag{8.1}$$

where $\epsilon(\Delta) = (\Delta - \delta_1)/(\gamma_1/2)$. The scale factor σ_0, the complex Fano parameter q and δ_1, γ_1 are the fit parameters. This fit provides an alternative way to obtain the collective Lamb shift δ_1 and the superradiance γ_1 from the spectra, which can be compared to the ab initio predictions. Indeed, the fit results (dashed lines in Fig. 8.6b) show excellent agreement with the Green's function calculation, confirming the interpretation of the effective nuclear level scheme derived from the Born-Markov Master equation in Sec. 7.5.

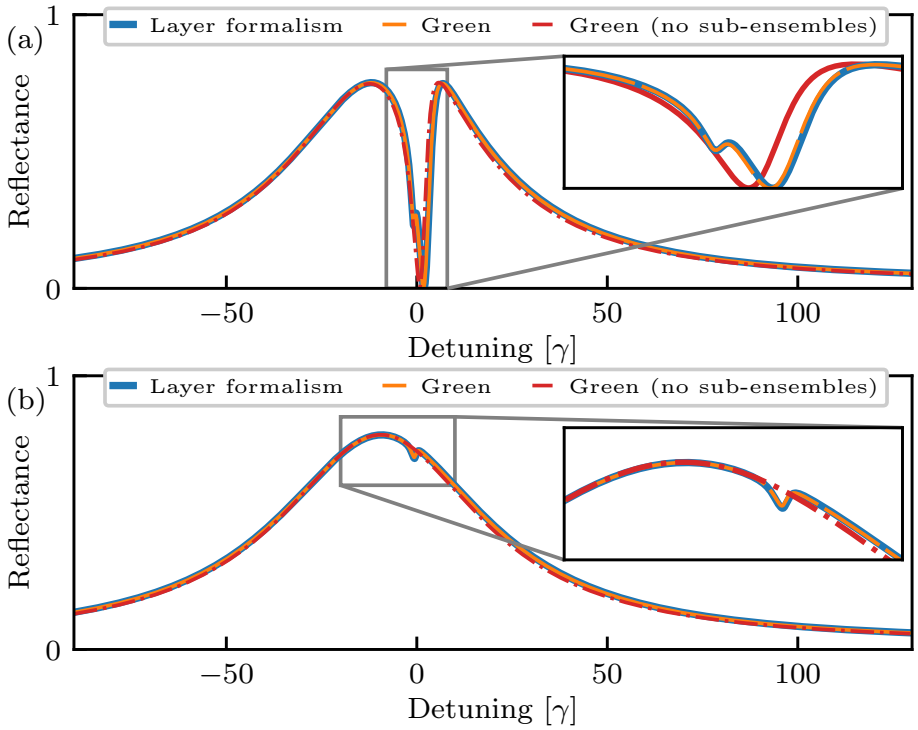

Figure 8.4: Nuclear spectra for the EIT (a) and non-EIT (b) cavities shown in Fig. 8.3. The spectra (yellow, red) are calculated using the Green's function approach for illumination at the third cavity mode, and the well-known layer formalism (blue) is shown for comparison. Without dividing the two nuclear ensembles into sub-ensembles (red), the spectra fit well and reproduce the main spectral features, but fail to reproduce more subtle additional features (see insets). These are captured if each resonant layer is divided into three sub-ensembles (yellow), and therefore can be attributed to the layer thickness resulting in a field gradient across the layer (see also Fig. 8.1).

8.5 Discussion - Green's function versus few-mode approach

In summary, Chapter 7 presented a second ab initio quantum theory to describe thin-film x-ray cavities doped with narrow resonances such as those provided by Mössbauer nuclei. Our results improve the previously introduced pXCQED model [HE13; HE15] for such systems to a numerically efficient ab initio theory, which allows to directly compute the coupling constants in the quantum optical level scheme.

In this chapter, we have used this approach to resolve open questions in the description of recent experiments [Röh12; HE15], which up to now have hindered extensions towards new parameter regimes and cast doubts on the phenomenological model's predictive capabilities at higher intensities [HE15]. On the formal side, this progress to an ab initio and, in the linear regime, essentially exact theory also provides qualitatively new value to quantum optical interpretations in x-ray cavity QED, in the same spirit as recent developments connecting other sectors of quantum optics and ab initio theory [Rug14; Sch19; CS16; TSC06]. On the practical side, it allows for a straightforward calculation of quantum optical parameters from the cavity geometry.

A remaining question to be discussed in this section is: Why are there two different ab initio approaches?

The central reason is that there are two options of approximation hierarchies. One can either directly trace out the cavity environment to obtain a Markovian Master equation for the nuclei, or one can include cavity modes in the description. The latter approach was chosen in the phenomenological model [HE13; HE15], which has had tremendous success in modeling experiments at synchrotron facilities [Hee13; Hee15a; Hee15b; Hab16a; Hab17; Hab19]. For this reason, resolving the connection between the different approaches was an important issue and the topic of Chapter 6.

Since we have now understood the origin of these models and which approximations enter into them, we can comment on which approach is practically preferable. While both may have advantages for particular purposes, the Green's function approach is superior to model nuclear x-ray cavity QED in

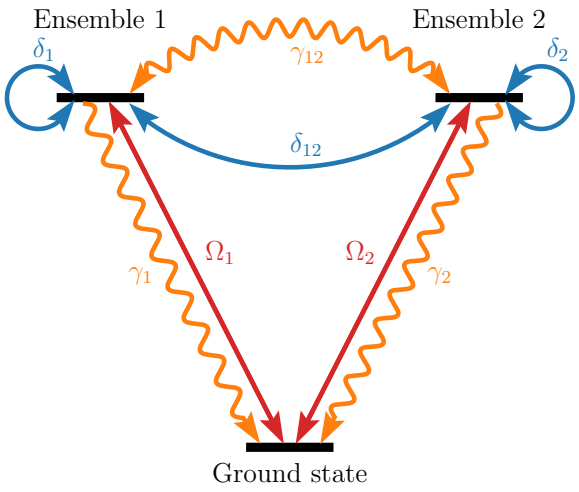

System	Coupling matrix $[\gamma]$	Drive vector
General	$\begin{pmatrix} \delta_1 - i\gamma_1/2 & \delta_{12} - i\gamma_{12}/2 \\ \delta_{12} - i\gamma_{12}/2 & \delta_2 - i\gamma_2/2 \end{pmatrix}$	$\begin{pmatrix} \tilde{\Omega}_1 \\ \tilde{\Omega}_2 \end{pmatrix}$
Cavity 1	$\begin{pmatrix} -0.15 - 0.94i & 6.21 + 2.85i \\ 6.21 + 2.85i & -6.47 - 28.28i \end{pmatrix}$	$\begin{pmatrix} 0.01 + 0.14i \\ -0.85 - 0.51i \end{pmatrix}$
Cavity 2	$\begin{pmatrix} -9.46 - 31.73i & 0.98 - 2.88i \\ 0.98 - 2.88i & -0.45 - 0.64i \end{pmatrix}$	$\begin{pmatrix} -0.82 - 0.57i \\ -0.03 - 0.09i \end{pmatrix}$

Figure 8.5: Nuclear level scheme in the Green's function approach. The figure shows the two-ensemble description of the cavities in Fig. 8.5 as an example. The coupling constants can be calculated directly using the Green's function approach and are shown in the table in matrix form for the EIT (cavity 1) and non-EIT (cavity 2) case. As before, we consider excitation in the third cavity mode ($\theta = \theta_3$). The drive vector has been normalized, since it is proportional to the applied x-ray field amplitude. The corresponding quantities as a function of incidence angle are shown in Fig. 8.6. We note that the layer ensembles are labeled by their position in the cavity from top to bottom, such that the central layer in the anti-node corresponds to index 1 in cavity 1 and to index 2 in cavity 2.

most cases. Due to the extremely weak coupling of nuclei and x-rays, the Born-Markov approximation is well justified and a mode picture is not necessary. Indeed, in the few-mode approach one typically adiabatically eliminates the cavity modes in a second step to obtain the nuclear level scheme [HE13; HE15; Len20]. The latter is essentially the same as a Born-Markov approximation, only the detour via a mode picture complicates the numerical procedure and makes further approximations necessary [Len20] (see Chapter 6).

From the perspective of describing non-linear and correlated quantum dynamics, the Green's function approach also mainly features advantages. The resulting Master equation has a lower number of degrees of freedom than the few-mode Master equation while involving fewer approximations. In addition, the original real space Master equation defined by Eqs. (7.8, 7.9) does not yet involve the linear approximation, which opens the door to investigate non-linear dynamics practically (see Part IV for details).

Besides these conceptual advantages, we showed that the Green's function approach can be implemented in a numerically efficient way, since the parallel wave space Green's function is available analytically for realistic layered cavities. While such analytical results only exist for few cases [BW07; AG17a; SB08] beyond the layer geometry investigated in this thesis, many numerical schemes are available to calculate Green's functions for complex resonator geometries (see e.g. [AG17a; Buh12; NH06] and references therein). Connecting to such electromagnetic solver techniques would enable further

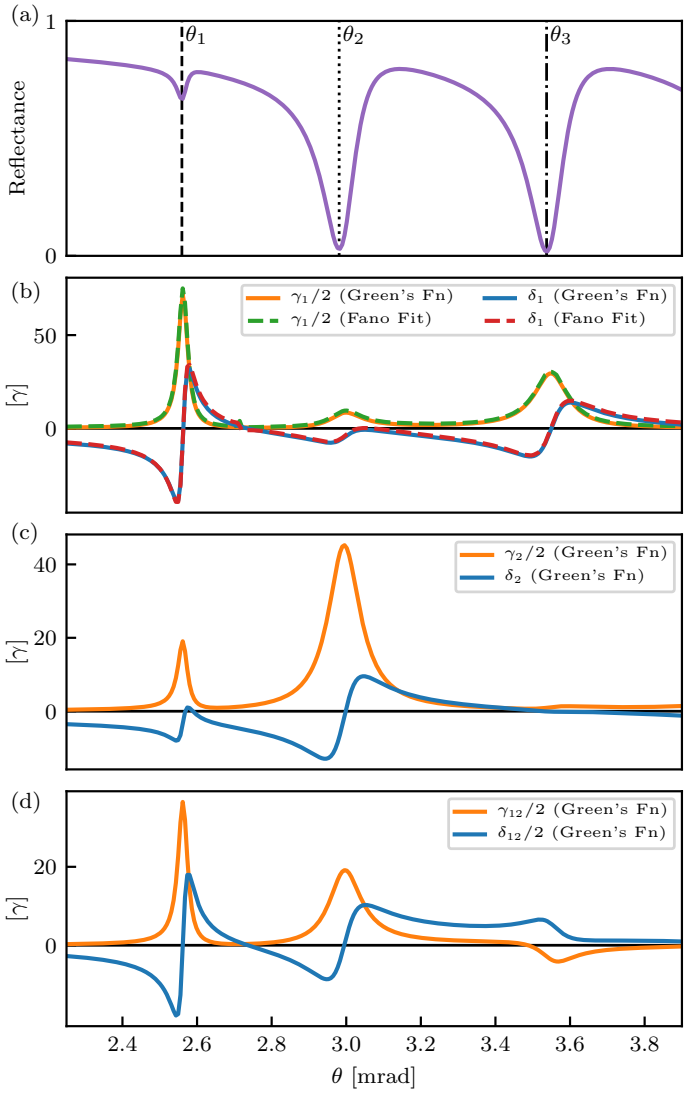

Figure 8.6: Rocking curve (a), collective Lamb shifts and superradiant decay rates of ensemble 1 (b) and ensemble 2 (c), and level couplings (d) in the EIT cavity as a function of incidence angle (solid lines, see legend). The meaning of the quantum optical couplings is illustrated in the effective level scheme Fig. 8.5 and the shown result is calculated using the Green's function approach. As an additional benchmark (see also spectral benchmarks in previous figures), panel (b) shows the superradiance (dashed green) and collective Lamb shift (dashed red) extracted from a Fano fit (details see main text).

investigations of alternative photonic environments for the nuclei. Such structures may become accessible with improving fabrication techniques and already reported examples include waveguides [Pfe02], curved channels [Sal15], nanowires [Che02] and periodically structured surfaces such as nanodots or nanodiscs [Ell12].

We note that, as described in detail in Chapters 4 and 5, the few-mode approach is crucial in other regimes, in particular in the presence of strong coupling. The above discussion is based on the observation that these regimes are rarely relevant for ultra-narrow transitions and cavity QED in the hard x-ray regime.

In addition, there is an aspect with regards to which the few-mode approach is indispensable even at weak coupling. As we will see in Chapter 10, one can encounter multi-mode effects resulting from large losses instead of large coupling strengths. Consequently, while a modal basis is not required for calculations, it may be intrinsically interesting to investigate how the mode environment influences properties of the nuclear ensemble. In Chapter 10, we address this topic and indeed show that a combination of few-mode theory and the Green's function approach can be used to construct a criterion for the appearance of multi-mode effects in lossy resonators, explaining previously observed signatures in x-ray cavity QED [Röh05b] and providing new design options.

Chapter 9

Generalization to multi-pole transitions

9.1 Outline

The Green's function formalism developed in [Len20] and outlined in Chapter 7 is only directly applicable to E1 dipole transitions. For the case of unmagnetized ^{57}Fe, the approach in Chapter 7 assigned an effective dipole moment to the isotope's M1 transition. In this chapter, we extend the effective dipole approach to general multi-polar transitions and provide an algorithm for their numerical calculation from standard nuclear resonance scattering parameters, as they are used, for example, in the layer formalism [Röh05b]. The final algorithm applies to arbitrary hyperfine configurations and can straightforwardly connected to software packages such as PYNUSS [Hee19].

9.2 Multi-polar interaction Hamiltonian

In this section, we first summarize the standard form of the light-matter interaction Hamiltonian for various multi-polarity orders, following the presentation in [Ste19; SB08].

9.2.1 Electric dipole (E1)

In the gauge of the macroscopic QED Hamiltonian [SB08], the dipolar coupling interaction in the long wavelength limit is [Ste19]

$$\hat{H}_{\mathrm{E1}} = -\hat{\mathbf{d}} \cdot \hat{\mathbf{E}}(\mathbf{r}_0)\,. \tag{9.1}$$

where $\mathbf{r}_0$ is the position of the nucleus.

For a system where all charges but a single electron are fixed, the dipole moment operator is given by [Ste19]

$$\hat{\mathbf{d}} := -e\hat{\mathbf{r}}_e\,, \tag{9.2}$$

where $\mathbf{r}_e$ is the position operator for the electron. Since we are interested in nuclei, which may have complicated charge distributions, this relation does not hold. Instead, we can use $\mathbf{d}$ directly and take its matrix elements as the basic parameters of a nuclear transition. In Sec. 9.5, we show that these matrix elements are directly computable via measured nuclear resonance scattering parameters.

9.2.2 Magnetic dipole (M1)

For a magnetic dipole, the interaction Hamiltonian is given by [Ste19]

$$\hat{H}_{\mathrm{M1}} = -\hat{\mathbf{m}} \cdot \hat{\mathbf{B}}(\mathbf{r}_0)\,, \tag{9.3}$$

where $\mathbf{m}$ is the magnetic dipole moment operator of the transition.

9.2.3 General electric multi-pole (En)

In general, the interaction Hamiltonian is a sum over all the electric and magnetic multi-pole contributions, with the dipole terms constituting the leading order. However, Mössbauer nuclei often feature zero E1 dipole moment of the transition, such that the higher order terms up to even E2 can be important [Röh05b].

For the electric case, the sum over the multi-pole orders is given by [Ste19]

$$\hat{H}_{\mathrm{E,multi}} = \underbrace{-\hat{d}_\alpha \hat{E}_\alpha(\mathbf{r}_0)}_{\text{dipole (E1)}} + \underbrace{\hat{Q}_{\alpha\beta}\partial_\alpha \hat{E}_\beta(\mathbf{r}_0)}_{\text{quadrupole (E2)}} - \underbrace{\hat{O}_{\alpha\beta\gamma}\partial_\alpha\partial_\beta \hat{E}_\gamma(\mathbf{r}_0)}_{\text{octupole (E3)}} + \dots\,, \tag{9.4}$$

where we have used vector indices and the Einstein sum convention.

We do not consider higher order magnetic transitions in this work, since they are typically not significant in Mössbauer transitions (see e.g. the parameter tables in [Röh05b]).

9.3 Effective dipole Hamiltonian

In this section, we show how the multi-polar coupling Hamiltonians can be reduced to effective dipole Hamiltonians in the regime studied in this work. We follow the discussion in [Ste19].

9.3.1 Free space consideration

In general, the interaction terms of different multi-polarity are fundamentally different Hamiltonians, since they depend on the field in different ways. This can also be seen from the structure of the electric and magnetic field in quantized form [Ste19], which are

$$\hat{\mathbf{E}}(\mathbf{r},t) = -\int d^3\mathbf{k} \sum_\zeta \sqrt{\frac{\hbar\omega_\mathbf{k}}{2\epsilon_0}} \mathbf{f}_\zeta(\mathbf{k},\mathbf{r}) \hat{a}_\zeta(\mathbf{k},t) + \text{h.c.}\,, \tag{9.5}$$

$$\hat{\mathbf{B}}(\mathbf{r},t) = \int d^3\mathbf{k} \sum_\zeta i\sqrt{\frac{\hbar}{2\epsilon_0\omega_\mathbf{k}}} \nabla \times \mathbf{f}_\zeta(\mathbf{k},\mathbf{r}) \hat{a}_\zeta(\mathbf{k},t) + \text{h.c.}\,, \tag{9.6}$$

respectively, where we consider the free space expressions without a cavity for now.

In free space, the mode functions take the form of plane waves [Ste19]

$$\mathbf{f}_\zeta(\mathbf{k},\mathbf{r}) \propto \hat{\mathbf{e}}_{\mathbf{k},\zeta} e^{i\mathbf{k}\cdot\mathbf{r}}\,, \tag{9.7}$$

such that

$$\nabla \times \mathbf{f}_\zeta(\mathbf{k},\mathbf{r}) = \mathbf{k} \times \mathbf{f}_\zeta(\mathbf{k},\mathbf{r}) \tag{9.8}$$

and consequently

$$\hat{\mathbf{E}}(\mathbf{r},t) = -\int d^3\mathbf{k} \sum_\zeta \sqrt{\frac{\hbar\omega_\mathbf{k}}{2\epsilon_0}} \mathbf{f}_\zeta(\mathbf{k},\mathbf{r}) \hat{a}_\zeta(\mathbf{k},t) + \text{h.c.}\,, \tag{9.9}$$

$$\hat{\mathbf{B}}(\mathbf{r},t) = \int d^3\mathbf{k} \sum_\zeta i\sqrt{\frac{\hbar}{2\epsilon_0\omega_\mathbf{k}}} \mathbf{k} \times \mathbf{f}_\zeta(\mathbf{k},\mathbf{r}) \hat{a}_\zeta(\mathbf{k},t) + \text{h.c.}\,. \tag{9.10}$$

We see that these integrals over the bosonic operators have a different wave vector and frequency dependence. For the higher-order multi-pole moments, similar dependencies arise.

In the regime that we are interested in, the situation can be simplified. In the case of Mössbauer nuclei and modern x-ray sources, we can assume that only a narrow wave vector range participates in the quantum dynamics around the incoming pulse wave vector. For most modern x-ray sources, this approximation holds due the typically narrow-band and highly collimated driving pulses, as well as due to the nuclei's ultra-narrow linewidth. We note, however, that in the absence of driving photons setting a narrow wave vector range, the following treatment will break down.

Within this approximation, we can then write

$$\hat{\mathbf{B}}(\mathbf{r},t) \approx \frac{1}{\omega_{\mathbf{k}_0}} \mathbf{k}_0 \times \hat{\mathbf{E}}(\mathbf{r},t)\,. \tag{9.11}$$

As noted above, this approximation may have to be relaxed in certain cases, such as when full quantum effects become relevant and emission in different directions is possible. However, the approximation certainly applies semi-classically during a strong x-ray drive (see also Chapter 12 for an application). We note that the approximation is implicit in standard treatments of optical Bloch or Maxwell-Bloch equations [Shv99] (see also Chapter 2) and the layer formalism [Röh05b], since the cross-section is also independent of the field's wave components there.

We can also understand this approximation by noting that it is essentially given by the relation

$$-\partial_t \hat{\mathbf{B}} = \nabla \times \hat{\mathbf{E}} \tag{9.12}$$

when applied to a pure plane wave.

A similar approximation can be made for the other derivative terms in the multi-polar coupling Hamiltonian. In the following, we give the resulting effective dipole moment for each case.

Magnetic dipole (M1)

For the M1 case, we then obtain

$$\hat{H}_{\mathrm{M1}} \approx -\frac{1}{\omega_{\mathbf{k}_0}} [\hat{\mathbf{m}} \times \mathbf{k}_0] \cdot \hat{\mathbf{E}}(\mathbf{r}, t)\,, \tag{9.13}$$

where we have used the cyclic identity for the triple product.

This calculation shows that within the plane wave approximation, the M1 Hamiltonian $\hat{H}_{\mathrm{M1}} = -\hat{\mathbf{m}} \cdot \hat{\mathbf{B}}(\mathbf{r}_0)$ can be expressed as an E1 Hamiltonian $\hat{\mathbf{d}}_{\mathrm{eff}}^{(\mathrm{M1})} \cdot \hat{\mathbf{E}}(\mathbf{r}_0)$ with an effective dipole moment

$$\hat{\mathbf{d}}_{\mathrm{eff}}^{(\mathrm{M1})} := -\frac{1}{\omega_{\mathbf{k}_0}} \hat{\mathbf{m}} \times \mathbf{k}_0\,. \tag{9.14}$$

We note that for the M1 case, instead of the approximate method employed here, an alternative exact approach using duality transformations of the field has been used in [AP21], which does not require the assumption of a narrow wave vector range set by a driving field.

Electric multi-pole (En)

An analogous argument can be applied to the derivative terms in the general electric multi-pole expansion.

For the electric quadrupole term, we find that

$$\hat{H}_{\mathrm{E2}} \approx \hat{\mathbf{d}}_{\mathrm{eff}}^{(\mathrm{E2})} \cdot \hat{\mathbf{E}}(\mathbf{r}_0) \tag{9.15}$$

with the effective dipole moment

$$\hat{\mathbf{d}}_{\mathrm{eff}}^{(\mathrm{E2})} = i\hat{Q}_{\alpha\beta} k_\alpha \hat{\mathbf{e}}_\beta\,, \tag{9.16}$$

where $\hat{\mathbf{e}}_\beta$ is the unit vector for the β direction.

Similarly, for the electric octupole term, we find that

$$\hat{H}_{\mathrm{E3}} \approx \hat{\mathbf{d}}_{\mathrm{eff}}^{(\mathrm{E3})} \cdot \hat{\mathbf{E}}(\mathbf{r}_0) \tag{9.17}$$

with the effective dipole moment

$$\hat{\mathbf{d}}_{\mathrm{eff}}^{(\mathrm{E3})} = -\hat{O}_{\alpha\beta\gamma} k_\alpha k_\beta \hat{\mathbf{e}}_\gamma\,. \tag{9.18}$$

9.3.2 Geometry dependence of the effective dipole Hamiltonian

The above investigation considered the electromagnetic field in free space. Since a cavity will in general modify an incident plane wave to a different wave form, the derivative term approximations used above will change. The effective dipole moment is then in general dependent on the cavity geometry. Hence it should be discussed, if a generalization of the effective dipole moment is necessary.

In the x-ray case, we can again simplify the situation without the necessity for a geometry-dependent formulation. Since the refractive index is close unity in the x-ray regime ($n = 1-\delta+i\beta$ with $\delta, \beta < 10^{-3}$ for typical materials and photon energies larger than 5 keV), the total wave vector $\mathbf{k}$ is essentially unchanged in the medium. We can therefore employ the free space effective dipole moment directly.

Let us look at grazing incidence in more detail to understand this approximation. In a planar cavity, the parallel wave vector $\mathbf{k}_\parallel$ is unchanged. In the perpendicular direction, there is a significant deviation from the free wave vector, resulting in enhanced field distributions and the cavity resonances in the reflection coefficient (see also Chapter 2). However, since $\mathbf{k}_\perp \ll \mathbf{k}_\parallel$, their perpendicular contribution to the effective dipole moment can be neglected as a whole. We thus approximate $\mathbf{k} \approx \mathbf{k}_\parallel$.

We further note that this approximation is also implicit in the standard layer formalism [Röh05b], where the transition weight matrices are not geometry dependent either [Stu00; Stu04; Hee19] and the hyperfine configuration is evaluated according to the parallel wave vector [Hee19].

9.4 State expansion and transition Hamiltonian

In the treatment above, the nuclei are represented by the multi-pole operators. In practice, only a finite set of nuclear states are usually relevant for the dynamics. The Hamiltonian is then typically written in terms of transitions between these states and the central parameters become transition moments, which are matrix elements of the multi-pole operators. In the following, we present a general treatment of the translation to a transition picture and outline how the relevant matrix elements for configurations with general hyperfine splittings can be obtained from standard nuclear resonance scattering parameters [Röh05b; Hee19].

To introduce the transition picture, we assume the relevant nuclear states $|\psi_i\rangle$. The identity operator can then be expressed by the approximate completeness relation $\mathbb{I} \approx \sum_i |\psi_i\rangle\langle\psi_i|$. Inserting this expression into the effective dipole Hamiltonian for a general multi-pole transition derived above and using the properties of the transition operators, we obtain

$$\hat{H}_{\mathrm{En/Mn}} \approx \sum_{q \in \mathrm{transitions}} \hat{\sigma}_q^+ \mathbf{d}_{\mathrm{eff,q}}^{(\mathrm{En/Mn})} \cdot \hat{\mathbf{E}}(\mathbf{r}_0) + \mathrm{h.c.}\,, \tag{9.19}$$

where we the q-label runs over all allowed transitions, such that $\mathbf{d}_{\mathrm{eff},q}^{(\mathrm{En/Mn})} = \langle\psi_{i_q}| \hat{\mathbf{d}}_{\mathrm{eff}}^{(\mathrm{En/Mn})} |\psi_{j_q}\rangle$, $\hat{\sigma}_q^+ = |\psi_{i_q}\rangle\langle\psi_{j_q}|$ and $\hat{\sigma}_q^- = |\psi_{j_q}\rangle\langle\psi_{i_q}|$.

This Hamiltonian is then equivalent to the standard dipole interaction that was used in [Len20] and applies to general multi-pole transitions within the specified approximations.

9.5 Dipole moment from resonant scattering parameters

So far, we have not answered the question of how to actually obtain the dipole moment of a single nucleus for a given hyperfine configuration. While the dipole moment is in principle a standard quantity, the nuclear resonance scattering community [Röh05b; HT99; Stu00; Stu04; SBH99; Shv00] is typically concerned with different quantities useful for scattering calculations, such as so called transition weights [Stu00; Hee19].

In the following, we present a general algorithm to extract the nuclear dipole moment from these existing methods. Instead of solving the nuclear eigenvalue problem once more or relying on other spurious approximations, we can then connect to the existing sofware packages CONUSS [Stu00] and PYNUSS [Hee19] to obtain the precise nuclear dipole moment.

We note that previous approaches to calculate dipole moments associated with Mössbauer transitions have been based on reduced interaction matrix elements (see e.g. [Lia13] and references therein). In our approach, we circumvent some of the theoretical complications associated with such calculations by utilizing the existing solutions of the hyperfine interaction problem [Stu00; Hee19]. Group theoretical arguments related to angular momentum are therefore not necessary in the following. Our approach further has the advantage that the scattering observables are usually known rather precisely, at least for commonly used transitions [Röh05b].

9.5.1 Single ground state

The central quantity in the semi-classical scattering theory (see also Chapter 2) is the nuclear forward scattering matrix $\mathbf{f}_n$ [Röh05b; Hee19]. The latter then appears in the expression for the nuclear refractive index [Röh05b] which translates the nuclear scattering process into a semi-classical medium description (see Sec. 2.2.1).

The final result for the nuclear resonant refractive index can be written as [Röh05b; Hee19; Stu00]

$$\mathbf{n}_{\mathrm{nuc}}^{[\mathrm{scatt}]} = \frac{\mathbf{f}_n}{k_0} = -\frac{4\pi^2}{k_0^3} \frac{\rho_N}{(2I_g+1)(1+\alpha)} \sum_{l \in \mathrm{transitions}} \frac{\mathbf{W}_l}{\omega - \omega_0 - \Delta_l + i\gamma/2}\,, \tag{9.20}$$

where k_0 is the resonant wave number, Δ_l the transition detuning, ρ_N is the resonant nuclear density, I_g is the ground state spin, α is the internal conversion coefficient, $\mathbf{W}_l$ is the transition weight matrix and the nuclear refractive index is defined such that the total refractive index is $\mathbf{n}_{\mathrm{tot}} = (1 - \delta + i\beta)\mathbb{I} + \mathbf{n}_{\mathrm{nuc}}$.

In the quantum optical theory based on the effective dipole Hamiltonian and Green's functions (see Chapter 7), the resonant modification of the dielectric permittivity ε is given by [Len20]

$$\varepsilon_{\mathrm{nuc}}(\mathbf{r},\omega) = -\frac{1}{\epsilon_0}\sum_{ln}\delta(\mathbf{r}-\mathbf{r}_{ln})\frac{\mathbf{d}_l^T\mathbf{d}_l^*}{\hbar(\omega-\omega_{\mathrm{nuc},l})+i\gamma/2}\,. \tag{9.21}$$

Making the usual narrow line approximation $\frac{1}{\omega^2}\approx\frac{1}{\omega_{\mathrm{nuc},l}^2}\approx\frac{1}{\omega_0^2}$, approximating $\varepsilon=\mathbf{n}^2=(\mathbb{I}+\Delta\mathbf{n})^2\approx\mathbb{I}+\frac{\Delta\mathbf{n}}{2}$ — note that both of these approximations are also implicit in the layer formalism [Röh05b] — and approximating the sum over individual nuclei as a continuous density, we obtain

$$\mathbf{n}_{\mathrm{nuc}}^{[\mathrm{green}]} \approx -\frac{1}{2\epsilon_0}\rho_N\sum_l\frac{\mathbf{d}_l^T\mathbf{d}_l^*}{\hbar(\omega-\omega_{\mathrm{nuc},l})+i\gamma/2}\,. \tag{9.22}$$

The comparison of Eq. (9.20) and Eq. (9.22) now shows that

$$\frac{4\pi^2}{k_0^3}\frac{\mathbf{W}_l}{(2I_g+1)(1+\alpha)} = \frac{1}{2\epsilon_0\hbar}\sum_{i\in\text{degenerate states}}\mathbf{d}_{l_i}^T\mathbf{d}_{l_i}^*\,. \tag{9.23}$$

We therefore see that the dipole moment vectors can be obtained by employing a singular value decomposition (SVD) of the matrix

$$\tilde{\mathbf{W}}_l = \frac{8\pi^2\epsilon_0\hbar}{k_0^3}\frac{\mathbf{W}_l}{(2I_g+1)(1+\alpha)}\,. \tag{9.24}$$

The singular value decomposition yields

$$\tilde{\mathbf{W}}_l = \sum_i \lambda_{l,i}^{[\mathrm{svd}]}(\mathbf{u}_{l,i}^{[\mathrm{svd}]})^\dagger\mathbf{v}_{l,i}^{[\mathrm{svd}]}\,, \tag{9.25}$$

where $\lambda_{l,i}^{[\mathrm{svd}]}$ are the singular values and $\mathbf{v}_{l,i}^{[\mathrm{svd}]},\mathbf{u}_{l,i}^{[\mathrm{svd}]}$ are the corresponding singular vectors.

We see that the matrices $\tilde{\mathbf{W}}_l$ should therefore have the particular property that $\mathbf{v}_{l,i}^{[\mathrm{svd}]}=\mathbf{u}_{l,i}^{[\mathrm{svd}]}$, which can indeed be verified numerically for practical examples [Hee19]. We can then identify the dipole moment as

$$\mathbf{d}_{l_i} = \sqrt{\lambda_{l,i}^{[\mathrm{svd}]}}(\mathbf{v}_{l,i}^{[\mathrm{svd}]})^*\,, \tag{9.26}$$

where we note that the singular values are real non-negative numbers.

9.5.2 Multiple ground states

An aspect which we have not discussed so far is how to treat multiple ground states. In the following, we briefly point out how this can be included in our theory based on transition operators.

Considering a thermal initial density matrix of the ensembles, a single nucleus is in one of the ground states with a certain classical probability, where we consider any state with a significant initial population as a ground state and all other states as excited states. We therefore have to account for sub-ensembles and their modified number densities when extracting the dipole moment from the transition weight matrices. If we have N_g ground states and a fraction f_{g_l} of nuclei occupying the ground state labeled by g_l associated with transition l, then instead of Eq. (9.22) we have

$$\mathbf{n}_{\mathrm{nuc}}^{[\mathrm{green}]} \approx -\frac{1}{2\epsilon_0\hbar}\sum_l\rho_N f_{g_l}\frac{\mathbf{d}_l^T\mathbf{d}_l^*}{\omega-\omega_{\mathrm{nuc},l}+i\gamma/2}\,. \tag{9.27}$$

Defining

$$\mathbf{W}_l' \equiv \mathbf{W}_l/f_{g_l}\,, \tag{9.28}$$

Eq. (9.24) should then use the primed transition weight matrices according to

$$\tilde{\mathbf{W}}_l = \frac{8\pi^2\epsilon_0\hbar}{k_0^3}\frac{\mathbf{W}_l'}{(2I_g+1)(1+\alpha)} \tag{9.29}$$

to extract the transition dipole moments via the singular value decomposition. We further note that at room temperature, the ground states are typically populated equally [Hee14], such that the population fraction is equal to one over the ground state multiplicity

$$f_{g_l} = \frac{1}{2I_g + 1}\,. \tag{9.30}$$

We note that for the case of degenerate transitions, there may not be a unique set of singular values for the transition weight matrices. A numerical approach is then to take the limiting case of a small magnetic splitting going to zero.

9.5.3 Linear transitions without hyperfine splitting

As a concrete example of practical relevance, let us look at the special case of an unmagnetized sample and in the absence of quadrupole splittings. The effective dipole moment of the linear (π_0) transitions can then be expressed as

$$|\mathbf{d}_{\pi^0}| = \sqrt{\frac{\pi\epsilon_0\hbar c^3}{\omega_0^3}\frac{\gamma}{(1+\alpha)}\frac{2I_e+1}{2I_g+1}}\,. \tag{9.31}$$

Such an explicit formula is particularly useful for excitation of unmagnetized samples by modern x-ray sources, which typically feature linear polarization. This scenario is studied in detail in Chapter 12.

Part III

Multi-mode light-matter interaction in lossy resonators

Chapter 10

Multi-mode effects on the cavity-induced Lamb shift

This chapter is based on the following preprint:

Classifying and harnessing multi-mode light-matter interaction in lossy resonators
D. Lentrodt, O. Diekmann, C. H. Keitel, S. Rotter, and J. Evers
arXiv:2107.11775 [quant-ph]

The thesis author's role in the paper is that of the sole principle author. Content has been reproduced verbatim with permission of the coauthors. The article was restructured to suit the format of this thesis. In particular, main text and supplementary material were merged and additional motivation is provided in the context of this thesis.

10.1 Introduction

10.1.1 Motivation within this thesis

In previous chapters, we have presented theoretical methods to describe multi-mode resonators in the presence of significant losses, as they are used in x-ray cavity QED. We have already explained the origin of heuristic extensions which were required in the phenomenological pXCQED model [HE15] (see Chapter 6) and found that thick layer effects were the reason for previous discrepancies (see Chapter 8).

In this section, we utilize these insights to identify multi-mode effects on the collective Lamb shift, an effect which first observed using x-ray cavities with Mössbauer nuclei in a landmark experiment [Röh10]. There, a non-zero shift was found to occur even at the reflection minimum of the cavity, which was originally not explained by the quantum models [HE13] and one of the reason for the introduction of heuristic extensions [Hee14].

From a broader perspective, x-ray cavity QED can be seen as a platform that uniquely combines the possibility of high-precision spectroscopy at x-ray energies using the extreme Q-values of the involved nuclear resonances with cavities which are restricted to the leaky and absorptive regime due to the low refractive index contrast at hard x-ray energies. As a result, single-mode models fail to quantitatively describe the nuclear spectra [HE15]. For this reason, we pay particular attention to multi-mode effects in this chapter.

A key application of such cavity-nuclei systems is to engineer artificial few-level quantum systems, which are otherwise inaccessible at hard x-ray energies [Röh12; RE21]. As we will show, multi-mode effects can indeed be used to one's advantage by providing a tuning knob to modify the properties of the Mössbauer transitions in the cavity environment.

10.1.2 Motivation within general quantum optics

Besides the motivation within x-ray cavity QED with Mössbauer nuclei, the method developed in this chapter is also relevant with regards to general quantum optics, as we briefly motivate in the following.

In the study of resonators coupled to quantum matter, the concept of a single mode of the light field is an important theoretical [JC63; Kir19] and experimental paradigm [HR06; Kav17], as we have reviewed in Chapter 3. More recently, regimes beyond single mode light-matter interaction have moved into the focus of attention. In particular, multi-mode cavity QED has opened new possibilities in the study of many-body quantum systems [Rit13], for example by enabling the tuning of effective

interactions [Vai18]. Also for single atoms, qualitatively new dynamics can be realized when multiple modes participate, such as in the multi-mode strong coupling regime [Kri14], where the extreme light-matter coupling bridges the free spectral range between the modes [Joh19].

For many platforms, the realization of extreme coupling strengths or the related mode control remains technically challenging. However, multi-mode features may also appear in the opposite regime of open and absorptive resonators, e.g., if the mode widths exceed their frequency spacing [Lal18]. Interestingly, strong losses do not always represent an obstacle, but may instead give rise to interesting physical phenomena, such as for lasers [HVH02; Hod14; Pen14; Mia16] and in the context of non-Hermitian physics [Dit00; FEGG17; Lon17; EG18; MA19], in general.

However, a systematic understanding of multi-mode effects in loss-dominated regimes is currently lacking. For example, in the context of nano-photonics [Bli08; Cha18], where complex mode environments can be engineered [Pen17] and losses are often sizable [Liu17], the question of how to describe quantum dynamics in complex and absorptive electromagnetic environments has sparked recent theoretical interest [Med21; Fra19].

In this context, x-ray cavity QED with ensembles of Mössbauer nuclei [Röh10; HE13] constitutes another example for a platform featuring such loss-dominated regimes. As we have seen in Chapter 6, the properties of the artificial quantum system in this case crucially depend on multi-mode effects, in a way that is still poorly understood. Similar challenges are encountered in the aforementioned nano-photonics platforms, with potential applications ranging from quantum plasmonics [Tam13] to cavity-controlled chemistry [Rib18; FGGV18].

10.1.3 Outline

In this chapter, we develop a framework for identifying, quantifying and interpreting multi-mode quantum effects on light-matter interactions in structured environments featuring strong losses. Our approach is based on relating quantum optical few-mode models to a pole expansion of the classical Green's function characterizing the electromagnetic environment of a quantum emitter. We exemplify the approach using an archetype model comprising a single two-level atom coupled to a cavity. By analyzing the reflectance of the system, we identify three different physical mechanisms that lead to qualitative deviations of the spectral features from standard single-mode predictions, and quantify them for a Fabry-Perot cavity setting. From a practical perspective, on the one hand, these results are indispensable for the interpretation of the spectra of light-matter systems in the loss-dominated regime. On the other hand, they offer a method to engineer the quantum emitter properties by using the loss-induced multi-mode effects to one's advantage. We illustrate both aspects with examples in x-ray cavity QED, and show that the multi-mode effects can be used to invert the sign of a collective cavity-induced nuclear Lamb shift, which was previously measured in [Röh10].

10.2 Single mode case

10.2.1 The open single mode Jaynes-Cummings model revisited

We first review the standard case of a generic single mode cavity [JC63; HR06] containing a two-level system, as schematically illustrated in Fig. 10.1(a). We have already encountered various versions of such model systems throughout this thesis (see Chapters 3, 5 and 6). In the following, we focus on a simple outline aimed at illustrating the locking of certain spectroscopic features in the single mode case. The open single mode Jaynes-Cummings model is given by the Master equation and Hamiltonian [HR06]

$$\dot{\rho} = -i[H;\rho] + \frac{\kappa}{2}\left(2a\rho a^\dagger - a^\dagger a\rho - \rho a^\dagger a\right) , \tag{10.1}$$

$$H = \omega_1 a^\dagger a + \frac{\omega_\mathrm{a}}{2}\sigma^z + \left[g^* a\sigma^+ + h.c.\right] . \tag{10.2}$$

Here, ω_1 is the cavity mode's resonance frequency, κ is its decay rate, ω_a is the transition frequency of the two-level atom, g is the mode-atom coupling strength, and a ($\sigma^{z/-}$) denotes the operator(s) associated with the cavity mode (two-level atom). We note that additional direct loss channels from the atom could easily be added to the model, but we omit them here for simplicity. We use units of $\hbar = 1$ for the Hamiltonian.

The central quantity to be considered in this chapter is the *cavity-induced level shift* of the atom. This quantity is a weak coupling notion, where the cavity acts as a Markovian environment for

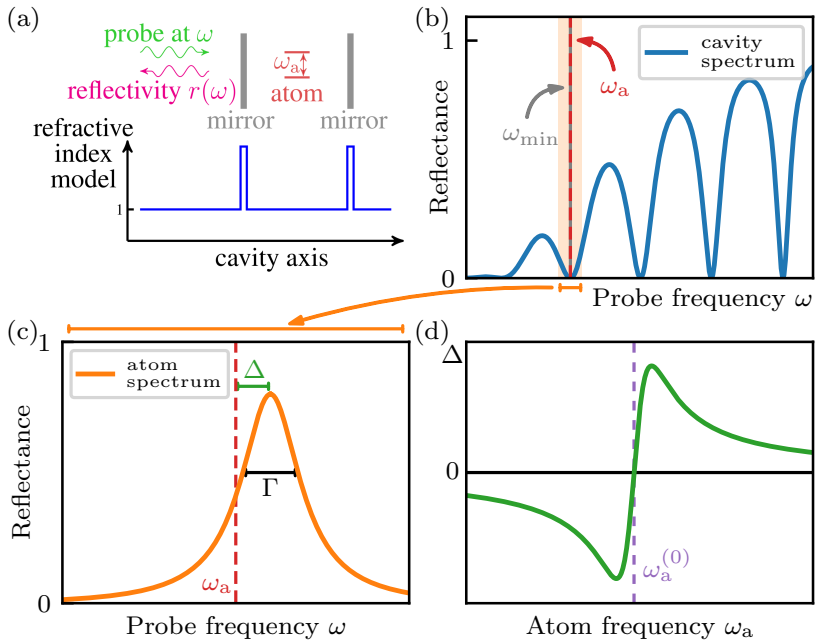

Figure 10.1: Model setup and the spectroscopic quantities considered in the analysis. (a) Model cavity coupled to a two-level atom at its center. The system is probed via its reflectance $|r(\omega)|^2$. (b) Reflectance for the case of spectrally broad cavity modes and a narrow atomic resonance. (c) shows a magnification of (b) around the atomic resonance, from which a frequency shift Δ and a line broadening Γ of the resonance can be extracted. (d) The cavity-induced Lamb shift Δ as a function of the atomic transition frequency ω_a. We denote the location of its zero crossing as $\omega_a^{(0)}$.

the atom. In the above model, we can extract it by adiabatically eliminating the cavity mode (see e.g. [HE13] and Chapter 2). The resulting Master equation for the atom is given by

$$\dot{\rho}_a = -i[H_{\text{adiab}}; \rho_a] + \frac{\Gamma}{2}\left(2\sigma^- \rho_a \hat{\sigma}^+ - \hat{\sigma}^+\hat{\sigma}^-\rho_a - \rho_a\hat{\sigma}^+\hat{\sigma}^-\right), \tag{10.3}$$

$$H_{\text{adiab}} = \frac{1}{2}(\omega_a + \Delta)\sigma^z . \tag{10.4}$$

The cavity-induced frequency shift Δ, often referred to as Lamb shift in the cavity QED literature [Lim17], and the Purcell enhanced line width Γ [Pur46] are then given by

$$\Delta_{\text{lev}} := \Delta - i\frac{\Gamma}{2} = \frac{gg^*}{\omega_a - \omega_1 + i\frac{\kappa}{2}}, \tag{10.5}$$

where we have defined their combination as the complex level shift Δ_{lev}.

In order to derive spectroscopic observables, one typically considers an external bath Hamiltonian [GC85], as discussed in Chapter 4. The Heisenberg-Langevin equations of motion for the above model then read [LE20]

$$\dot{a}(t) = -i\left(\omega_1 - i\frac{\kappa}{2}\right)a(t) - ig\sigma^-(t) - 2\pi i\kappa_R b_{\text{in}}(t), \tag{10.6}$$

$$\dot{\sigma}^-(t) = -i\omega_a\sigma^-(t) + ig^*\sigma^z(t)a(t), \tag{10.7}$$

where κ_R is the mode-bath coupling strength, and $b_{\text{in}}(t)$ the input operator of the bath. The emitted radiation outside the cavity can then be calculated via the input-output relation [GC85]

$$b_{\text{out}}(t) = b_{\text{in}}(t) - i\kappa_R a(t). \tag{10.8}$$

In the linear spectroscopy regime, we can approximate $\langle\sigma^z(t)\rangle \approx -1$ and $\langle\sigma^z(t)a(t)\rangle \approx -\langle a(t)\rangle$, such that the equations of the first order expectation values form a closed system of linear coupled differential equations. The solution for the reflection spectrum defined by $\langle b_{\text{out}}(\omega)\rangle = r(\omega)\langle b_{\text{in}}(\omega)\rangle$ is then obtained as

$$r(\omega) = r_{\text{cav}}(\omega) - 2\pi i\frac{\frac{|\kappa_R g|^2}{(\omega-\omega_1+i\kappa/2)^2}}{\omega - \omega_a - \frac{gg^*}{\omega-\omega_c+i\kappa/2}}, \tag{10.9}$$

where the empty cavity reflection spectrum is

$$r_{\mathrm{cav}}(\omega) = 1 - 2\pi i \frac{|\kappa_R|^2}{\omega - \omega_1 + i\kappa/2} \,. \tag{10.10}$$

An example reflectance (featuring multiple modes) is shown in Fig. 10.1(b). At weak coupling ($\kappa \gg g$) and close to the atomic resonance ($\kappa \gg \omega - \omega_a$), we can approximate the cavity properties as constant on the scale of the light-matter interaction, such that $1/(\omega - \omega_1 + i\kappa/2) \approx 1/(\omega_{\mathrm{a}} - \omega_1 + i\kappa/2)$. The spectrum then separates into a constant cavity background and an atomic line as

$$r(\omega) \approx r_{\mathrm{cav}}(\omega_a) - 2\pi i \frac{|\kappa_R^{(\mathrm{int})}|^2}{\omega - \omega_{\mathrm{a}} - \Delta + i\Gamma/2} \,. \tag{10.11}$$

The resonance modulation depth is given by

$$|\kappa_R^{(\mathrm{int})}|^2 = \frac{|\kappa_R g|^2}{(\omega_{\mathrm{a}} - \omega_1 + i\kappa/2)^2} \,. \tag{10.12}$$

The cavity induced Lamb shift Δ and Purcell enhanced line width Γ can thus be extracted as line shape parameters from the linear reflection spectrum, see Fig. 10.1(c). Subsequently, one can analyze these parameters as a function of ω_a, which in the single-mode case results in a dispersion-like shape Eq. (10.5) for Δ, as shown in Fig. 10.1(d).

10.2.2 Locking of spectroscopic features

In order to analyze properties of the spectroscopic quantities, we introduce ω_{min} as the frequency where $|r_{\mathrm{cav}}(\omega)|^2$ has the resonance minimum of the mode under consideration. We further denote the atomic resonance frequency at which $\Delta(\omega_{\mathrm{a}})$ is zero as $\omega_{\mathrm{a}}^{(0)}$.

By inspection of Eqs. (10.5, 10.10, 10.11), we find that the minimum of the empty cavity reflectance ω_{min}, the zero $\omega_{\mathrm{a}}^{(0)}$ of the frequency shift Δ, the maximum of the line width broadening Γ, and the real part ω_1 of the pole location all coincide at $\omega_{\mathrm{min}} = \omega_{\mathrm{a}}^{(0)} = \omega_1$. This frequency locking of all key spectroscopic features on the one hand renders the interpretation of spectroscopic data straightforward. On the other hand, it severely impedes the design of quantum optical properties of the system. The only control parameters are the detuning between atom and cavity, the cavity loss rate, and the reflection out-coupling. For example, the light-matter coupling rate g simply scales the energy shift and line broadening, as long as one stays at weak coupling. As one consequence, single-mode cavity models do not allow for non-zero shifts Δ at the minimum ω_{min} of the cavity background r_{cav}, which is at odds with experiments in x-ray cavity QED [Röh10].

10.3 Multi-mode case

10.3.1 Few-mode model and expansion of the complex level shift

Next, we generalize the treatment to the multi-mode case. We employ a recently developed few-mode model applicable to general complex and absorptive resonators [Med21] to construct a few-mode expansion of the complex level shift. While the few-mode Hamiltonian used there can in principle be considered a special case of the ab initio few-mode theory [LE20; VH03] developed in Chapters 4 and 5 (see Sec. 5.6 for a discussion), the method in [Med21] is applicable to absorptive systems and has practical advantages in treating complex resonators. For our purposes, the central advantage is that the requirement of choosing an expansion basis is eliminated if independent and spectrally flat baths are imposed. In the following, we provide details on how this feature allows us to directly relate the resulting the resulting few-mode expansion to Green's function techniques similar to the ones discussed in Chapter 7 (see also Sec. 10.4 below).

Following the discussion in [Med21], the few-mode model Hamiltonian is written as

$$H_{\mathrm{cav}} = \sum_{ij} \omega_{ij} \hat{a}_i^\dagger \hat{a}_j \,, \tag{10.13}$$

where the mode interaction parameters ω_{ij} form a real symmetric matrix [Med21] and can also be motivated as a basis-transformed version of cross-mode decay terms [HVH02; VH03; LE20]. The

assumption of spectrally flat and independent baths then results in a Markovian Master equation [Med21]

$$\dot{\rho} = -i[H;\rho] + \sum_i \frac{\kappa_i}{2}\left(2\hat{a}_i\rho\hat{a}_i^\dagger - \hat{a}_i^\dagger\hat{a}_i\rho - \rho\hat{a}_i^\dagger\hat{a}_i\right) , \tag{10.14}$$

with the real bath coupling parameters κ_i. The two-level system inside the cavity is governed by the light-matter interaction Hamiltonian [Med21]

$$H = H_{\mathrm{cav}} + \frac{\omega_{\mathrm{a}}}{2}\hat{\sigma}^z + \sum_i \left[g_i^*\hat{a}_i\hat{\sigma}^+ + h.c.\right] , \tag{10.15}$$

where we used the rotating wave approximation. We note that in [Med21], the g_i are assumed to be real-valued. Here, we consider the option of complex-valued coupling constants, since it provides additional insight into the appearance of multi-mode effects as discussed in Sec. 10.5.2 below.

In the weak coupling limit, upon adiabatic elimination of the cavity modes similarly to the single mode case above, the cavity-induced complex level shift can be written in terms of the mode expansion as [LE20]

$$\Delta_{\mathrm{lev}} = \underline{g}^\dagger \left[\omega_{\mathrm{a}} - \underline{\underline{\omega}}_{\mathrm{cav}} + \frac{i}{2}\underline{\underline{\kappa}}\right]^{-1} \underline{g} , \tag{10.16}$$

where the elements of the vectors and matrices are given by $(\underline{g})_i = g_i$, $(\underline{\underline{\omega}}_{\mathrm{cav}})_{ij} = \omega_{ij}$ and $(\underline{\underline{\kappa}})_{ij} = \kappa_i\delta_{ij}$. We further define the non-Hermitian cavity Hamiltonian [Med21]

$$\underline{\underline{\tilde{H}}}_{\mathrm{cav}} = \underline{\underline{\omega}}_{\mathrm{cav}} - \frac{i}{2}\underline{\underline{\kappa}} , \tag{10.17}$$

and the corresponding propagator

$$\underline{\underline{G}}(\omega_{\mathrm{test}}) = \left[\omega_{\mathrm{test}} - \underline{\underline{\tilde{H}}}_{\mathrm{cav}}\right]^{-1} . \tag{10.18}$$

We note that $\underline{\underline{G}}$ also appears in the expression for the spectral density derived in [Med21], where it was used to fit the model parameters. The spectral density is related to the imaginary part of the level shift. The Lamb shift, whose multi-mode features we mainly investigate in this chapter, is the real part of the level shift.

10.3.2 Green's function expression for the complex level shift

Next to the few-mode expansion, the cavity-induced energy shift and line broadening can alternatively be expressed via the classical electromagnetic Green's tensor $\mathbf{G}$ of the cavity environment as [DKW00; SB08; AG17a]

$$\Delta_{\mathrm{lev}} = -\frac{\mu_0\omega_{\mathrm{a}}^2}{\hbar}\mathbf{d}^* \cdot \mathbf{G}(\mathbf{r}_{\mathrm{a}}, \mathbf{r}_{\mathrm{a}}, \omega_{\mathrm{a}}) \cdot \mathbf{d} , \tag{10.19}$$

where $\mathbf{r}_{\mathrm{a}}$ is the atom's position and $\mathbf{d}$ its transition dipole moment.

This approach, which does not necessitate a modal picture or basis, has been employed in Chapter 7 in the context of x-ray cavities, where its origin and limitations are also discussed. The Green's function expression applies rather generally for dipole transitions in absorptive dielectric environments [SB08], rendering it tremendously useful for a direct prediction of the level shift. However, it does not directly provide insight into the modal structure of the resonator, which is instead encoded in the few-mode expansion Eq. (10.16) [see also the discussion in Sec. 8.5].

10.4 From multi-mode models to pole expansions

So far, we have thus obtained two ways to express the complex level shift — via a mode expansion [Eq. (10.16)] and via the classical electromagnetic Green's function [Eq. (10.19)]. As we will see, the two expressions can be directly related by diagonalizing the mode expansion and performing a Mittag-Leffler expansion of the Green's function.

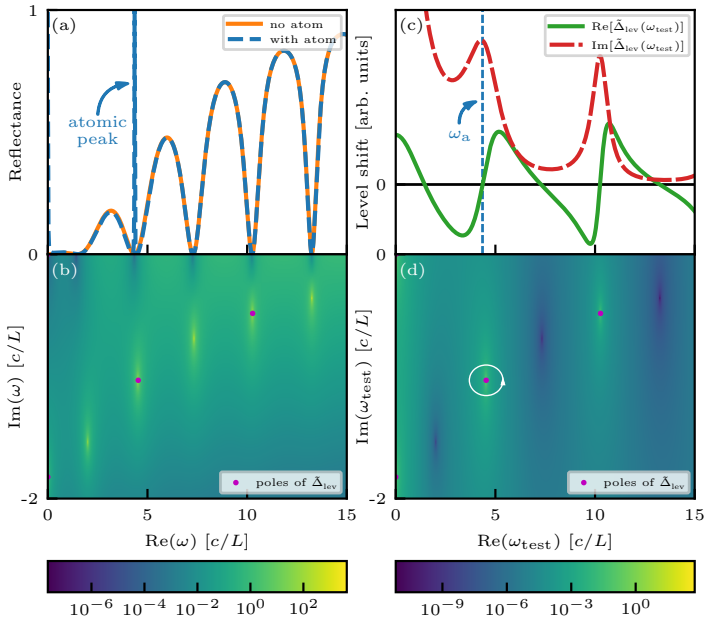

Figure 10.2: Illustration of the Mittag-Leffler expansion via the reflection spectrum and level shift in the complex frequency plane. (a) Reflection spectrum with and without the atom. (b) Corresponding spectrum without the atom in the complex frequency plane. (c) Lamb shift and Purcell enhanced line width as a function of frequency. (d) Absolute value squared of the level shift in the complex frequency plane. Poles are marked in magenta. Note that the reflection has additional poles, which the atom does not couple to due to symmetry. An exemplary contour for the determination of the pole residue is shown in (d) as white circle.

10.4.1 Diagonalization of the mode expansion

First, we introduce a basis transformation to diagonalize the few-mode expansion Eq. (10.16). The interaction matrix $\underline{\underline{\tilde{H}}}_{\mathrm{cav}}$ in the few-mode expansion can be brought to diagonal form via an invertible transformation matrix $\underline{\underline{V}}$. Introducing

$$(\underline{\underline{V}}\,\underline{g})_i = \tilde{g}_i\,, \tag{10.20}$$

$$(\underline{\underline{V}}^{-1}\,\underline{g}^*)_i = \bar{g}_i^*\,, \tag{10.21}$$

$$(\underline{\underline{V}}\,\underline{\underline{\tilde{H}}}_{\mathrm{cav}}\,\underline{\underline{V}}^{-1})_{ij} = (\tilde{\Omega}_i - i\frac{\tilde{\kappa}_i}{2})\delta_{ij}\,, \tag{10.22}$$

the few-mode expansion Eq. (10.16) can be written as

$$\Delta_{\mathrm{lev}} = \underline{g}^{\dagger}\,\underline{\underline{G}}(\omega_{\mathrm{a}})\,\underline{g} = \sum_i \frac{\bar{g}_i^*\tilde{g}_i}{\omega_{\mathrm{a}} - \tilde{\Omega}_i + i\frac{\tilde{\kappa}_i}{2}}\,. \tag{10.23}$$

Note that here, we assumed that the diagonalization exists. A more general treatment is required, e.g., in the presence of exceptional points [MA19; EG18]. The latter assumption enters since otherwise the few-mode interaction matrix $\underline{\underline{\tilde{H}}}_{\mathrm{cav}}$ is not diagonalizable by an invertible matrix. On the pole expansion side in Sec. 10.4.2 below, we will self-consistently incorporate the same assumption by only including single pole terms. Since exceptional points are isolated in parameter space and typically have to be designed by specifically tuning parameters [EG18], the treatment here is still applicable generically. Extensions to the exceptional points case are subject of future work.

We further note that the transformation $\underline{\underline{V}}$ is typically not unitary for the lossy systems that we are considering, such that applying it on an operator level yields modified commutation relations and $\bar{g}_i$ is generally not equal to $\tilde{g}_i$. The ML pole expansion thus corresponds to a non-hermitian diagonal basis, whose associated field operators do not necessarily feature standard bosonic commutation relations (see [Fra19] for the related quantization of quasi-modes).

A central observation is that Eq. (10.23) is now of the same form as a Mittag-Leffler pole expansion [Lal18]

$$\Delta_{\mathrm{lev}} = \sum_i \frac{r_i}{\omega_{\mathrm{a}} - \tilde{\omega}_{\mathrm{pole},i}}\,, \tag{10.24}$$

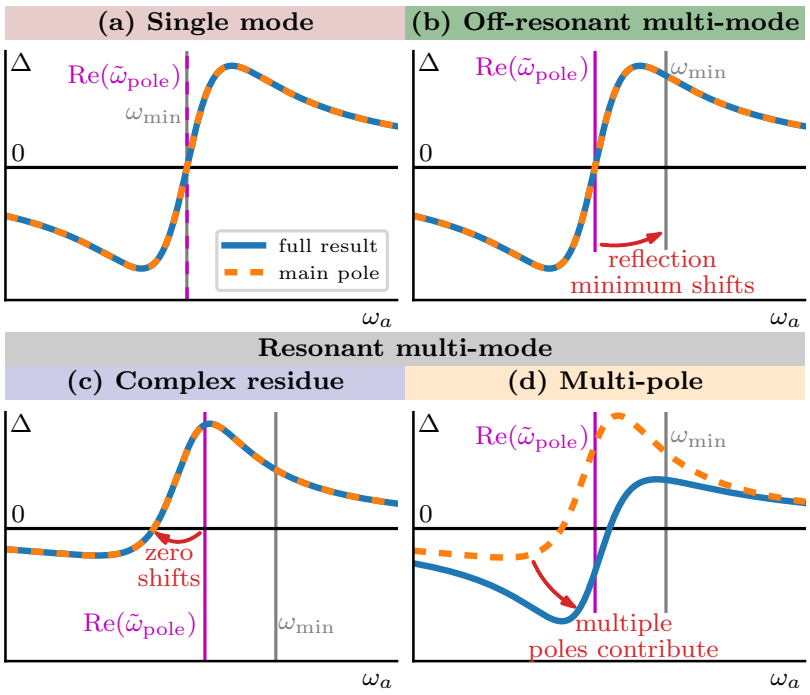

Figure 10.3: Classification of multi-mode effects, illustrated via the energy shift Δ close to the atomic resonance as in Fig. 10.1(d). (a) Single-mode case. The main pole in Eq. (10.23) is sufficient, and the cavity resonance ω_1, the reflectance minimum $\omega_{\rm min}$ and the main pole position $\mathrm{Re}(\omega_{\rm pole})$ coincide. (b) Off-resonant multi-mode effects can appear already in the empty-cavity reflectance, and lift the degeneracy of $\mathrm{Re}(\omega_{\rm pole})$ and $\omega_{\rm min}$. (c, d) Resonant multi-mode effects, which affect the light-matter interaction. (c) In the complex-residue case, the main pole residue has an imaginary contribution, unlike in the single mode case. This shifts the zero $\omega_a^{(0)}$ of Δ from $\omega_{\rm min}$, and modifies the shape of $\Delta(\omega_a)$. (d) In the multi-pole case, more than one pole is required for convergence.

where we can read off the poles and residues in terms of the diagonalized mode frequencies and couplings as

$$\tilde{\omega}_{{\rm pole},i} = \tilde{\Omega}_i - i\frac{\tilde{\kappa}_i}{2}\,, \tag{10.25}$$

$$r_i = \bar{g}^* \tilde{g}_i\,. \tag{10.26}$$

10.4.2 Mittag-Leffler expansion of the complex level shift

The observation that the diagonalized mode expansion is of Mittag-Leffler form is crucial, since it allows us to connect to the Green's function expression Eq. (10.19). The latter is useful in this context as it provides access to the pole expansion without the need for a fitting routine. To this end, we introduce a test frequency $\omega_{\rm test}$ and generalize the complex level shift to a frequency-dependent quantity (indicated by the tilde) as

$$\tilde{\Delta}_{\rm lev}(\omega_{\rm test}) = -\frac{\mu_0 \omega_{\rm a}^2}{\hbar}\mathbf{d}^* \cdot \mathbf{G}(\mathbf{r}_a, \mathbf{r}_a, \omega_{\rm test}) \cdot \mathbf{d}\,. \tag{10.27}$$

Note that the $\omega_{\rm a}^2$ prefactor is kept constant, since we are only interested in characterizing the modal structure encoded in the Green's function. This choice is also important to achieve consistency with the quantum optical few-mode models discussed above, where the g_i-couplings implicitly depend on $\omega_{\rm a}$ in the same fashion [LE20].

This generalization allows us to perform a Mittag-Leffler pole expansion along the frequency axis [Spi09]

$$\tilde{\Delta}_{\rm lev}(\omega_{\rm test}) = \tilde{\Delta}_{\rm lev}(0) + \sum_i \left[\frac{r_i}{\tilde{\omega}_{{\rm pole},i}} + \frac{r_i}{\omega_{\rm test} - \tilde{\omega}_{{\rm pole},i}}\right]\,, \tag{10.28}$$

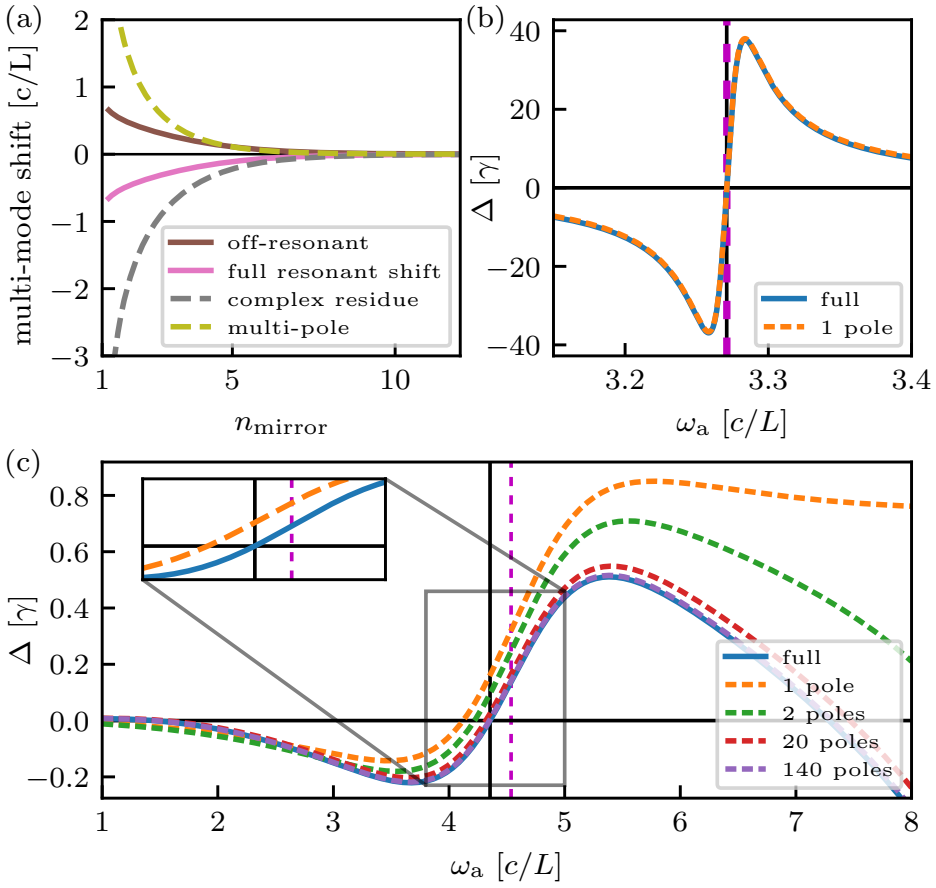

Figure 10.4: Transition from the single-mode to the multi-mode case in Fabry-Perot-like cavities, controlled by the barrier refractive index n_{mirror}. (a) quantifies the resonant multi-mode effects via the displacement of the zero of Δ from the position $\mathrm{Re}(\omega_{\mathrm{pole}})$ of the main pole. Contributions of complex-residue and multi-pole effects are shown separately (see legend). The red line indicates the off-resonant shift $\mathrm{Re}(\omega_{\mathrm{pole}}) - \omega_{\mathrm{min}}$ for comparison. (b) Cavity-induced energy shift Δ in the single-mode limit ($n_{\mathrm{barrier}} = 20$). (c) Corresponding results in a multi-mode case ($n_{\mathrm{barrier}} = 4$), where multiple poles are required to achieve convergence, and even the single-pole line shape differs from the single-mode case due to complex residue effects. In (b,c), the black dotted lines show the minimum ω_{min} of the empty cavity reflectance, while the magenta dashed line shows the position $\mathrm{Re}(\omega_{\mathrm{pole}})$ of the main pole. γ is the free space radiative line width.

where we again assume that the system does not contain exceptional points [MA19; Özd19], such that only single poles are present.

In practice, this expansion can be obtained numerically by finding the poles $\tilde{\omega}_{\mathrm{pole},i}$ of the Green's function in the complex frequency plane and subsequent evaluation of their residue r_i by a line integral around the pole, as illustrated in Fig. 10.2(d) [Spi09]. For the cases considered in this chapter, we find that the constant term converges to zero, such that we can consider the simpler expansion

$$\tilde{\Delta}_{\mathrm{lev}}(\omega_{\mathrm{test}}) = \sum_i \frac{r_i}{\omega_{\mathrm{test}} - \tilde{\omega}_{\mathrm{pole},i}} \,. \tag{10.29}$$

This property can also be understood as a general feature of certain Green's functions [DW20; Lal18].

The physical level shift is then given by

$$\Delta_{\mathrm{lev}} = \tilde{\Delta}_{\mathrm{lev}}(\omega_{\mathrm{a}}) = \sum_i \frac{r_i}{\omega_{\mathrm{a}} - \tilde{\omega}_{\mathrm{pole},i}} \,, \tag{10.30}$$

which is identical to the diagonalized mode expansion Eq. (10.24). We note that in the frequency-dependent generalized level shift $\tilde{\Delta}_{\mathrm{lev}}(\omega_{\mathrm{a}})$, the residues also acquire a dependence on ω_{a}, i.e., $r_i = r_i(\omega_{\mathrm{a}})$.

Importantly, this expansion can be performed numerically by finding the poles of the Green's function and computing their residues. An illustration of the reflection spectrum and the complex level

shift in the complex frequency plane is given in Fig. 10.2, together with a contour line around a pole illustrating the numerical method for finding the Mittag-Leffler expansion. The close correspondence between the poles in the complex level shift and the poles in the complex reflection spectrum is clearly visible. We note that more advanced numerical schemes for computing pole expansions are available and refer to the review in [Lal18] for details.

We further note that such expansion techniques of the Green's function and other observables are widely used in quasi-mode and scattering theory (see e.g. [Bin20; ZM20; Fra19; Alp17; Ben21b; Lal18]). A central novelty of our approach in this context is that it draws connections to the few-mode expansions and the resulting interpretation of quantum optical multi-mode effects to be introduced in the following. In the context of designing the system properties, this connection is particularly useful due to the numerical accessibility of the Green's function, which has already been employed for design of light-matter interactions [BB20; Ben21a]. Our approach connects to such methods by unlocking the quantum optical mode structure of the Green's function [see also the discussion in Sec. 8.5].

10.5 Certifying and classifying multi-mode effects

A key feature of our approach is that the ML expansion is unique and independent of any modal basis choice. Therefore, its truncation to a variable number of poles around ω_a can be used to certify and categorize multi-mode effects via the breakdown of characteristic features in the single-mode case discussed in Sec. 10.2. Furthermore, the ML expansion can be performed without the need for a fitting procedure, such that potential ambiguities related to overfitting and degrees of freedom number are eliminated.

Together, these features allow us to construct a simple criterion to certify and classify multi-mode effects on the complex level shift, as we discuss in this section.

10.5.1 Classification criterion

By comparison to the single mode formula Eq. (10.5), we find that three conditions on the pole expansion Eqs. (10.23, 10.30) have to be fulfilled for the single-mode scenario to be valid. A violation of any of these conditions implies that the single-mode interpretation of the spectra becomes invalid, and in turn leads us to define three different classes of multi-mode effects. We illustrate these effects by their action on the cavity-induced frequency shift Δ as a function of the atomic resonance frequency ω_a in Fig. 10.3. In each panel, the result after inclusion of each effect beyond the single mode case is compared to the corresponding fully converged multi-mode result.

In the single-mode case [Fig. 10.3(a)], already the main pole is sufficient for a quantitative description, with the aforementioned frequency locking $\omega_\mathrm{a}^{(0)} = \mathrm{Re}(\omega_\mathrm{pole}) = \omega_\mathrm{min}$.

The first condition for the single-mode case is that a single main pole has to be sufficient in a relevant frequency range covering the atomic line width to achieve convergence of the ML expansion. The opposite case, where multiple poles are required for good convergence, we will refer to as a *multi-pole effect*, see Fig. 10.3(c).

Second, we also require real-valued residues, since the residue $|g|^2$ in the single-mode case Eq. (10.5) is real. *Complex-residue effects* appear if the main pole $\tilde{\omega}_\mathrm{pole}$ has a non-negligible imaginary part of its residue. Then, already the first pole contribution to the shape of $\Delta(\omega_a)$ is modified and its zero $\omega_\mathrm{a}^{(0)}$ moves away from the pole location $\mathrm{Re}(\omega_\mathrm{pole})$, see Fig. 10.3(b).

Both complex-residue and multi-pole effects are *resonant effects*, since they directly affect the cavity-modified properties Δ and Γ of the atom, and *multi-mode effects*, since the single-mode Jaynes-Cummings model fails to capture them. Interestingly, the latter may even be the case if resonant multi-mode effects are absent, namely if the empty-cavity reflectance (an off-resonant property of the cavity, independent of the atom) is distorted from its single-mode form Eq. (10.10). We will refer to such cases as *off-resonant multi-mode effects*, which typically result in a shift of the zero $\omega_\mathrm{a}^{(0)}$ of Δ away from the minimum ω_min of the empty-cavity reflectance [HE15], see Fig. 10.3(d), or further shape distortions thereof.

From the perspective of the multi-mode model, the expansion Eq. (10.16) provides a clear interpretation for each of these effects. The appearance of complex residues is a direct result of the interaction terms between the relevant modes, when the cavity Hamiltonian is significantly non-diagonal. The multi-pole effect is an even stronger deviation from the single-mode case, amounting to multiple

degrees of freedom in the non-hermitian diagonalized basis contributing significantly. Finally, off-resonant effects correspond to a background scattering contribution independent of the quantum system coupled to the resonator, which results from a difference between bath modes and spectroscopic observables [LE20]. In the following section, we demonstrate how this interpretation of the different multi-mode effects arises from the view-point of the quantum optical few-mode models.

10.5.2 Interpretation in terms of few-mode models

Resonant effects from mode interactions

To see why there are two distinct resonant multi-mode effects, we first specialize Eq. (10.23) to the case of a diagonal interaction matrix ω_{ij}. This case corresponds to the usual multi-mode extensions of the Jaynes-Cummings model [SZ97], which do not consider direct interactions between the modes [Med21] or the analogous cross-mode decay terms in [HVH02; VH03; LE20]. In this case, $\underline{\underline{\tilde{H}}}_{\text{cav}}$ naturally is of diagonal form, and the complex level shift reduces to

$$\tilde{\Delta}_{\text{lev}}^{(\text{diag})}(\omega_{\text{test}}) = \sum_i \frac{\underline{g}_i^\dagger \underline{g}_i}{\omega_{\text{test}} - \omega_{ii} + i\frac{\kappa_i}{2}} \,. \tag{10.31}$$

In this special case, the few-mode expansion is therefore identical to an ML expansion and the residues are *real-valued*. As a result, we can directly attribute the appearance of complex-valued residues in the ML expansion to the non-diagonal elements of the mode coupling matrix ω_{ij} in Eq. (10.17).

A residue with a relevant imaginary contribution may already appear in the case where a single pole is sufficient to achieve convergence of the ML expansion. In terms of the quantum optical few-mode models, this corresponds to the case in which a single cavity degree of freedom (i.e., a single element of the non-hermitian diagonal basis) is sufficient, albeit in the presence of significant interaction between multiple "bare" cavity modes. In Sec. 10.5.1, we denoted this case as the *complex-residue effect*, which is also illustrated in Fig. 10.3. Effectively, it mixes the cavity-induced Lamb shift Δ and the superradiant enhancement of the line width Γ in the complex level shift Δ_{lev}.

Further multi-mode effects may arise if multiple poles are required for the convergence of the ML expansion, which we denote as *multi-pole effects*. In this case, multiple cavity degrees of freedom (i.e., multiple elements of the non-hermitian diagonal basis) are required for convergence.

We again emphasize that both complex-residue and multi-pole effects are *multi-mode effects*, since they require multiple modes in the few-mode expansion and cannot be explained by the standard single mode Jaynes-Cummings model. These results show that the features of the Mittag-Leffler pole expansion indeed certify multi-mode effects in the light-matter interaction. Having shown the connection between the pole and the mode expansions, we have further provided a concrete quantum optical interpretation for the origin of the two types of resonant multi-mode effects.

For completeness, we note that for some systems, poles at negative real frequency contribute to the Mittag-Leffler expansion. On the level of the pole expansion, this feature does not make a difference. On the level of quantum optical models, a fully consistent treatment would be to include counter-rotating terms in the system-bath coupling [CC06; LE20]. This inclusion, however, would not affect the classification and interpretation of the multi-mode effects in terms of the ML expansion discussed above.

Off-resonant effects as background scattering

For the few-mode model in Sec. 10.3.1, one can in principle apply the input-output formalism [GZ04] to obtain spectroscopic observables such as the cavity reflection coefficient with or without the atom. However, the result will not be exact due to the truncation of the mode expansion [LE20]. For isolated resonances, the latter can still be good a good representation of the reflection. For the case of overlapping resonances, however, a background scattering contribution is required, as shown in [LE20]. In particular if a fitting procedure as the one in [Med21] is employed, the bath modes will generally not even be the asymptotic scattering degrees of freedom [LE20].

We note that this does not invalidate the approach for the purpose of computing the system dynamics in the cavity. Indeed, the spectroscopic output can e.g. be calculated via field input-output relations [Med21]. Within the few-mode model, the input-output scattering can be translated to the full scattering result via the background scattering contribution [LE20]. Interestingly, since the latter is an off-resonant cavity property, it can still be significant even if the few-mode expansion of the resonant dynamics is already well converged (see Sec. 10.6 below).

In the present context, the off-resonant multi-mode effects can therefore straightforwardly be identified as arising from non-negligible background scattering contributions. The interpretation as a separate phenomenon to the two resonant multi-mode effects thus also directly maps to quantum optical few-mode models.

10.6 Multi-mode effects in Fabry-Perot-like cavities

Before we turn to an application Sec. 10.7, we explore the relevance of the different multi-mode effects by analyzing a simple model system reminiscent of archetype Fabry-Perot cavities, see Fig. 10.1(a). The cavity of length L is modeled via a piece-wise constant one-dimensional refractive index comprising vacuum with two mirror layers of refractive index n_{mirror} and thickness $t_{\mathrm{mirror}} = L/100$. Note that n_{mirror} here merely acts as a model parameter that may take unrealistically high values, while in practice highly reflecting mirrors are realized, for example, using multi-layer dielectrics [HR06]. This model allows us to study the continuous transition from the single to the multi-mode case by inducing spectral mode overlap via high radiative loss through the mirrors.

Results are shown in Fig. 10.4. Panel (a) quantifies resonant multi-mode effects via the displacement of the zero $\omega_a^{(0)}$ of $\Delta(\omega_a)$ from the main pole position $\mathrm{Re}(\omega_{\mathrm{pole}})$ as a function of n_{mirror}, and off-resonant multi-mode effects via the shift of $\mathrm{Re}(\omega_{\mathrm{pole}})$ from the empty-cavity reflectance ω_{min}. For the single-mode case in high-quality resonators with well-isolated resonances ($n_{\mathrm{mirror}} \gg 1$), all shifts vanish. As expected, towards lower-quality resonators, the multi-mode effects become more and more relevant. Interestingly, we find that in this cavity, the large negative complex-residue shift is partially canceled by the multi-pole and off-resonant shifts. Panels (b,c) show Δ as a function of the atomic transition frequency ω_a for a single-mode (b, $n_{\mathrm{mirror}} = 20$) and a multi-mode (c, $n_{\mathrm{mirror}} = 4$) scenario. As expected, in the single-mode case, one pole is sufficient to model the system, and no zero-shift of Δ appears. In contrast, the multi-mode case in (c) requires many poles for convergence, has a non-vanishing zero-shift of Δ from the pole due to resonant multi-mode effects, and features line-shape modifications due to the complex-residue effect. The single-pole approximation clearly deviates from the full result and has a significantly complex residue. These observations are incompatible with the single-mode model Eqs. (10.5-10.10).

10.7 Multi-mode level shift design in x-ray cavity QED

10.7.1 Level shift inversion at the reflection minimum

Finally, we explore the multi-mode effects outlined above in the concrete platform of thin-film x-ray cavity QED with Mössbauer nuclei, which is the central topic of this thesis. As introduced in detail in Chapter 2, the atom coupled to the resonator is replaced by a thin layer containing an ensemble of Mössbauer nuclei in these cavities. In the experimentally relevant low-excitation regime [Len20], the ensemble can be approximated as a few-level quantum system [HE13], comprising the collective ground state and excitonic single-excitation states coherently spread over the nuclei. Because of the low refractive-index contrast, these structures are probed in grazing incidence, and the parallel wave vector of the incident radiation selects the particular exciton which is driven. The reflectance and level shifts in this setup can then be calculated using similar expressions as the simple example above. Only now, the relevant quantities are evaluated at a given parallel wave vector and the dipole moments are scaled by an area density factor [Len20] (see Chapter 7). Conveniently, the resulting Green's function is available analytically [Tom95] (see Appendix D) and can straightforwardly be evaluated in the complex frequency plane to numerically obtain the Mittag-Leffler expansion.

As discussed in Chapter 1, spectroscopy on such thin-film structures is routinely employed for a variety of applications [Röh05b; YL21]. More specifically, such cavities form a promising platform to implement quantum optical schemes at hard x-ray energies [Röh10; Röh12; Hee13; Hee15b; Hab16a; Hab17]. For the latter purpose, the possibility to design the properties of the exciton resonance is key to implement more advanced quantum optical level schemes [LKE16]. However, the control properties are severely restricted for the lack of suitable x-ray control fields, and since the thin-film cavities inherently suffer from low quality factors and weak light-nucleus coupling, due to the low refractive index contrast and comparably high absorption at hard x-ray energies [Röh05b; VS21].

In Fig. 10.5, we show that instead, the above-developed multi-mode effects provide options for tuning the nuclear exciton properties, such as transition energies, already at weak coupling. The

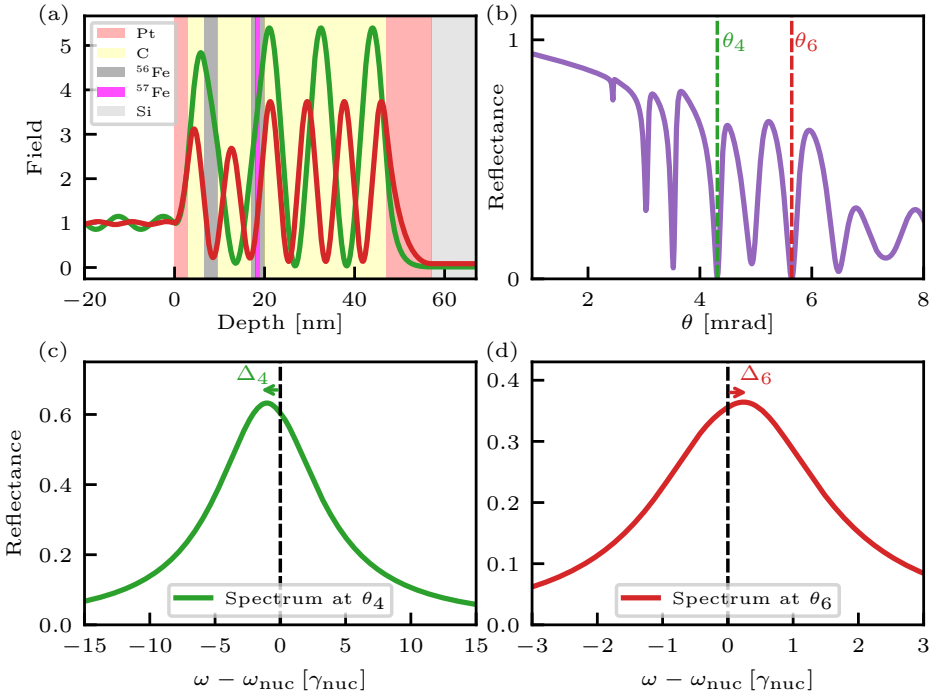

Figure 10.5: Design of multi-mode level shifts. (b) Cavity geometry (materials see legend) and off-resonant field distributions in the fourth (θ_4, green) and sixth (θ_6, red) cavity mode. The cavity structure is Pt (3 nm)/C (3.5 nm)/^{56}Fe (3 nm)/C (7.5 nm)/^{56}Fe (1 nm)/^{57}Fe (1 nm)/^{56}Fe (1 nm)/C (27 nm)/Pt (10 nm)/Si. (b) Off-resonant cavity reflectance as function of incidence angle showing the overlapping modes structure. Both the fourth and the sixth mode are critically coupled. (c,d) Nuclear spectra at θ_4, θ_6, demonstrating the reversed energy shift in the two mode minima.

cavity structure shown in panel (a) features overlapping cavity resonances visible in the off-resonant cavity reflectance shown in (b). Panels (c,d) show the resulting spectra of the nuclear resonances for resonant driving of the two modes θ_4 and θ_6, respectively. The cavity is designed such that both modes are critically coupled, and that the multi-mode effects lead to opposite signs of the respective nuclear Lamb shifts Δ on resonance with the two modes. This observation demonstrates that tuning the multi-mode environment through the cavity geometry allows one to alter the effective level scheme of the nuclear ensemble even qualitatively. A closer analysis (see Sec. 10.7.2 below) reveals that the fourth mode in this cavity mainly features off-resonant multi-mode effects, while the sixth mode is strongly influenced by resonant multi-mode effects.

10.7.2 Detailed analysis

In the previous section, we showed that multi-mode effects can be used to invert the collective Lamb shift in x-ray cavity QED with Mössbauer nuclei. In the following, we illustrate this example further, and in particular show the contributions of the different multi-mode effects to the Lamb shift inversion.

Fig. 10.6 shows results for the cavity considered in Fig. 10.5, with the x-ray angle of incidence chosen such that the reflection minimum of the fourth cavity mode is on resonance with the nuclei. Panel (a) shows the cavity structure together with the resulting field intensity, off-resonance with the nuclei. (b) shows the reflectance, which by design has a minimum at the nuclear resonance. The panel further shows the position of the closest main cavity pole from the ML expansion. Its shift relative to the reflection minimum indicates the presence of off-resonant multi-mode effects. Panels (c,d) show the cavity-induced Lamb shift and the Purcell enhanced line width. It can be seen that the line width is already converged upon inclusion of the single main pole contribution. In contrast, a few poles are required for a converged Lamb shift. We thus find that the cavity also features resonant multi-mode effects, however, with only small line shape modifications, and less pronounced than the off-resonant multi-mode effects.

Fig. 10.7 shows corresponding results for an x-ray incidence angle chosen such that the reflection minimum of the sixth mode is on resonance. In this case, in addition to an off-resonant multi-mode shift, strong resonant multi-mode effects occur. Both, the line width broadening and the cavity Lamb

shift require the summation of multiple poles to achieve convergence. Furthermore, sizeable line-shape distortions appear, indicating the presence of complex-residue and multi-pole effects. The resonant multi-mode effects are strong enough to outweigh the off-resonant multi-mode effects, such that in total a reversed shift is obtained. In particular, the imaginary part of the main pole's residue (sixth pole, orange dashed line) majorly contributes to the inversion. The contributions of higher modes act to reduce the positive shift again, but a significant shift remains at the minimum even when the result is fully converged. This clearly shows that the inversion of the Lamb shift in this configuration can be attributed to resonant multi-mode effects.

10.7.3 Origin of the original collective Lamb shift observation

Finally, Fig. 10.8 summarizes the results of an analogous investigation for the cavity structure considered in the experiment reported in [Röh10]. It can be seen that resonant multi-mode effects are negligible in this case. Instead, the non-zero Lamb shift at the rocking minimum, which is incompatible with single-mode models [HE13], is identified as an off-resonant multi-mode shift.

Our approach is thus able to provide a new interpretation for this seminal experiment [Röh10], identifying the collective Lamb shift as a multi-mode effect. This complements the previous description in terms of semi-classical theory [Röh10] by extending the quantum optical pXCQED model [HE13; HE15] summarized in Chapters 2 and 6.

10.8 Summary

In summary, we have presented a simple method to identify and classify multi-mode effects on the quantum properties of two-level systems inside resonators with strong losses and complex spectra. It relies on a direct relation we derived between a quantum multi-mode model and the Mittag-Leffler pole expansion of the corresponding classical Green's function. We have identified three distinct multi-mode effects, which may appear separately or in combination, depending on the cavity environment. These effects are crucial for the interpretation of spectroscopic observables in the loss-dominated regime. Furthermore, the multi-mode effects open new possibilities for the design of quantum systems by understanding and harnessing loss effects in resonators, connecting quantum optical concepts to recent suggestions from non-Hermitian photonics [EG18], as we illustrated by designing a sign-flipped collective Lamb shift in nuclear x-ray cavity QED. Within the latter platform, the insight on interpretation of the spectra and the novel multi-mode mechanism for tuning the artificial nuclear quantum system provide important progress, as discussed further in Chapter 15.

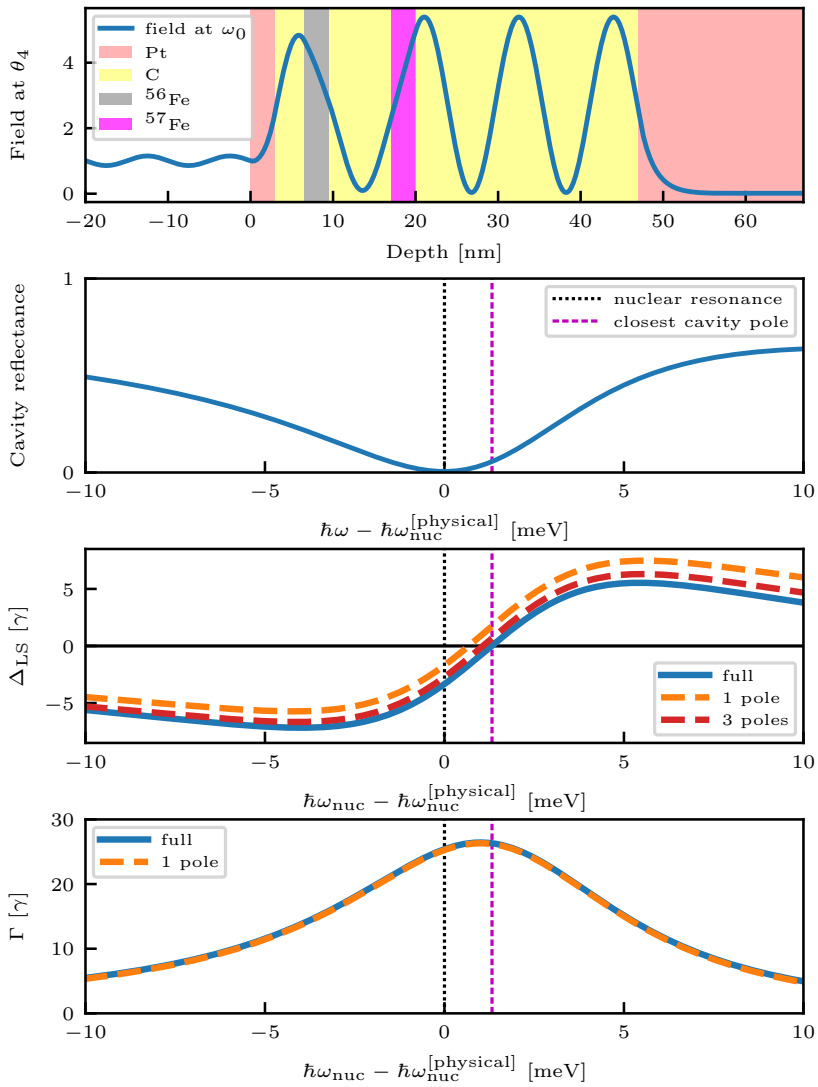

Figure 10.6: Multi-mode effects in the x-ray cavity considered in Fig. 10.5. The x-ray incidence angle is chosen such that the fourth mode minimum lies on resonance. (a) Cavity structure (see legend) and off-resonant cavity-field strength at the resonance frequency $\omega_0 = 14.4$ keV. (b) Cavity reflectance as a function of energy. Note that the incidence angle is chosen such that the first reflection minimum lies on resonance. The real part of the main cavity pole is shifted with respect to the reflection minimum, indicating that this cavity features off-resonant multi-mode effects. (c, d) Cavity induced Lamb shift and Purcell enhanced line width, respectively, as a function of nuclear transition frequency relative to its physical value. We see that a ML expansion containing only the main pole already suffices to reproduce the line width, while few modes are required for convergence in the Lamb shift. Thus, the cavity does feature resonant multi-mode effects, in addition to the off-resonant ones.

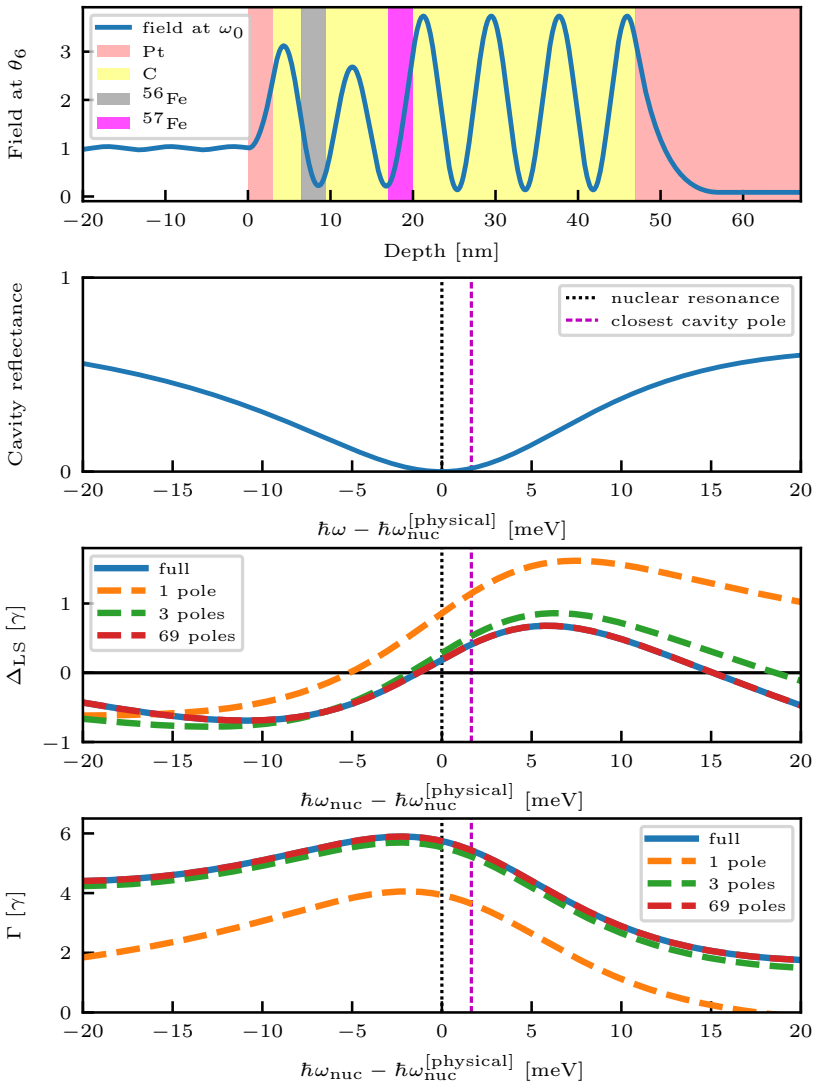

Figure 10.7: This figure is analogous to Fig. 10.6, but with the x-ray incidence angle chosen such that the sixth mode minimum lies on resonance. In this case, we observe strong resonant multi-mode effects for both Δ and Γ, including multi-pole convergence and a significantly complex residue of the main pole. These results show that the inversion of the collective Lamb shift reported in Fig. 10.5 indeed is a resonant multi-mode effect.

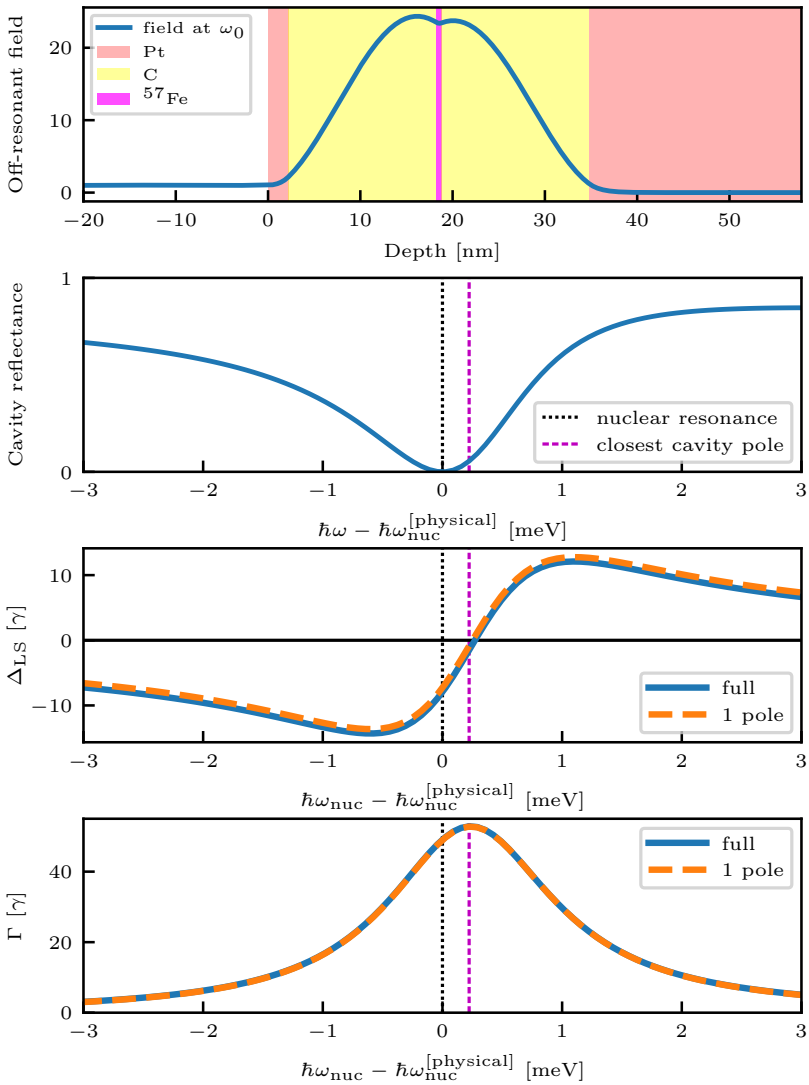

Figure 10.8: This figure is analogous to Fig. 10.6, but for the cavity structure considered in the experiment reported in [Röh10]. We see that resonant multi-mode effects are negligible. The non-zero Lamb shift at the rocking minimum is explained by an off-resonant multi-mode shift.

Chapter 11

Fano cusps in x-ray cavities with overlapping modes

In the previous chapter, we focused on how multiple resonator modes modify the complex level shift, encompassing the Lamb shift and Purcell enhanced linewidth. However, even if we have a two-level system inside the cavity, the resulting reflection spectrum is not fully specified by these parameters. The reason is that the interference of the emitter's spectral line with the cavity background is phase dependent [Hee15a], which in general results in Fano lineshapes [Fan61].

Since Fano resonances are an important phenomenon, which is encountered across the electromagnetic spectrum [Ott13; Lim17], this chapter investigates the influence of multi-mode effects on the Fano interference between an emitter and a cavity. Specifically, we report the theoretical observation of an interesting phenomenon, which we term "Fano cusps".

11.1 Background: Fano profile and q-parameter

Fano interference is a result of phase dependent interference between a resonant scattering channel and a broad background channel [Fan61]. In x-ray cavity QED with Mössbauer nuclei, the former is given by the nuclear resonance and the latter by the electronic scattering off the cavity. In particular, Fano resonances have been used for interferometric phase detection in this system [Hee15a].

The Fano resonance profile is given by [Ott13; Hee15a; Bär10]

$$R(\omega) = |r(\omega)|^2 = |\alpha|^2 \frac{|q+\epsilon|^2}{1+\epsilon^2}\,, \tag{11.1}$$

where q is the Fano parameter characterizing the asymmetry of the line shape and $\epsilon = \frac{\omega-\omega_a}{\Gamma/2}$ is a dimensionless version of the detuning to the transition.

The Fano resonance profile is ubiquitous in various fields of the natural sciences, ranging from optical photonics [Lim17] to time-domain control of atoms [Kal16], and such line shapes have also been shown to feature in general open quantum systems [FS15]. In the hard x-ray regime, in addition to the cavity application, the underlying interference idea has also been employed to control x-ray pulses [Hee17].

The central parameter controlling the lineshape is q, which can in general take complex values [Hee15a; Bär10]. To gain intuition, Fig. 11.1 shows peak-normalized Fano profiles for various q-parameters in the complex plane.

On the real axis, $q = 0$ corresponds to a standard absorption dip and $q \to \pm\infty$ to an emission peak. $q = \pm 1$ is a lineshape that is anti-symmetric around zero detuning and $R = 0.5$.

Away from the real axis, the imaginary part of q essentially allows to describe Fano resonances that do not feature full visibility. For example, the lineshape at $q = \pm i$ is flat and does not feature a visible resonance at all.

Instead of considering complex q, the Fano profile can also be written with real q, if one additionally includes a baseline [Hee15a]. However, the complex q parametrization can be useful [Bär10; Hee15a; Gol21]. Most notably, it was demonstrated in [Bär10] that when varying an additional system property, the trajectory of the q-parameter in the complex plane encodes information about decoherence processes. In particular, it was found that when varying the decoherence strength, dissipative processes result in a linear Fano trajectory while dephasing leads to a circle [Bär10].

Motivated by this work, such Fano trajectories will also be the central observable in this chapter, where we consider the trajectory of the q-parameter for varying detuning between a cavity and an emitter. We first consider the standard single mode case, which we show to also feature a circular trajectory. We then demonstrate that in an x-ray cavity, the Fano trajectory experiences interesting modifications including cusp and loop features in the presence of overlapping modes.

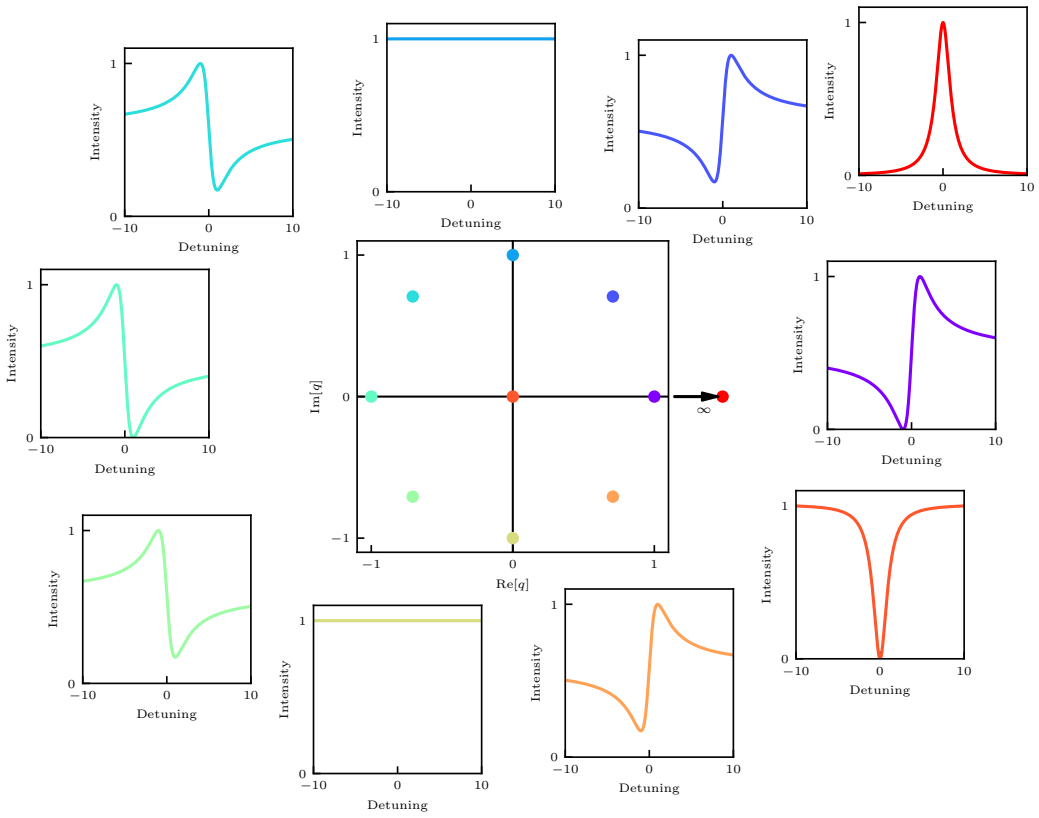

Figure 11.1: Illustration of Fano lineshapes for various Fano q-parameters in the complex frequency plane. The central plot shows the Fano q values to be considered, the outer plots of the corresponding color their lineshapes (maximum normalized to unity). On the real axis, the Fano q controls the asymmetry of the line, with $q = 0$ corresponding to an absorption line, and $q = \pm 1$ corresponding to maximum asymmetry. $q \to \pm\infty$ corresponds to an emission peak (top right corner). At $|q| = 1$, the phase of q essentially controls the visibility of the line shape, with zero visibility at $q = \pm i$.

11.2 Circular Fano trajectories in single mode cavities

For the single cavity case, we can directly reuse the model from Sec. 10.2.1. In particular, the combined cavity-atom reflectance Eq. (10.11) given by

$$r(\omega) = r_{\mathrm{cav}}(\omega_{\mathrm{a}}) - 2\pi i \frac{\frac{|\kappa_R g|^2}{(\omega_{\mathrm{a}} - \omega_1 + i\kappa/2)^2}}{\omega - \omega_{\mathrm{a}} - \frac{gg^*}{\omega_{\mathrm{a}} - \omega_1 + i\kappa/2}} \tag{11.2}$$

can be written in the form of a Fano lineshape [Hee15a]. According to Eq. (11.1), we then find

$$\epsilon = \frac{\omega - \omega_a - \Delta}{\Gamma/2}\,, \tag{11.3}$$

$$\Delta = \mathrm{Re}\Big[\frac{gg^*}{\omega_{\mathrm{a}} - \omega_1 + i\kappa/2}\Big]\,, \tag{11.4}$$

$$\Gamma = -2\,\mathrm{Im}\Big[\frac{gg^*}{\omega_{\mathrm{a}} - \omega_1 + i\kappa/2}\Big]\,, \tag{11.5}$$

$$q = i - \frac{2\pi i}{\alpha\Gamma/2}\frac{|\kappa_R g|^2}{(\omega_{\mathrm{a}} - \omega_1 + i\kappa/2)^2} \tag{11.6}$$

$$\alpha = r_{\mathrm{cav}}(\omega_a)\,. \tag{11.7}$$

The Lamb shift Δ and Purcell enhanced linewidth Γ are identical to the definition in Eq. (10.5).

A Fano trajectory can then be defined by considering the Fano q-parameter as a function of the atom-cavity detuning $\Delta_c = \omega_a - \omega_1$. To see what the resulting trajectory in the complex plane looks

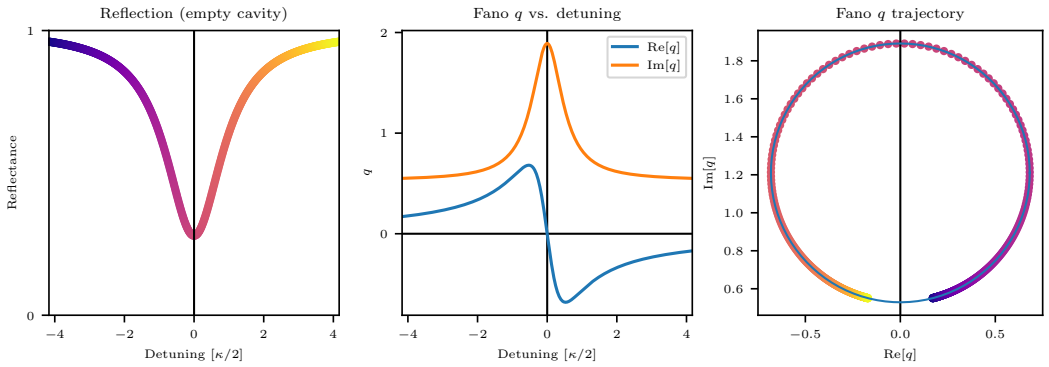

Figure 11.2: Exemplary Fano trajectory for a single mode cavity. Left: Reflectance of the empty cavity as a function of incidence angle. Colors redundantly encode the detuning. Middle: Fano q-parameter as a function of detuning between the atom and the cavity resonance. We see the typical dispersion lineshapes with an offset in the imaginary part, which is a result of the cavity not being critically coupled (see text). Right: Fano trajectory with colors corresponding to the detuning as in the left plot. We see that the trajectory [colored dots, obtained by fitting Fano curves to the spectra] maps out a circle in agreement with the analytical formula Eq. (11.9) for the single mode case [solid blue line].

like, we rewrite Eq. (11.6) similarly to [Bär10] as

$$q(\Delta_c) = i - \frac{2\pi i|\kappa_R|^2}{\gamma}\frac{\Delta_c - i\gamma}{\Delta_c + i\xi}\,, \tag{11.8}$$

where we have defined $\xi = \frac{\kappa}{2} - 2\pi|\kappa_R|^2$. We note that the Fano q-parameter is independent of the light-matter coupling strength, since it quantifies the lineshape instead of the absolute magnitude of its extent.

It can then be checked that this function fulfills the circle equation

$$|q(\Delta_c) - C|^2 = R^2\,, \tag{11.9}$$

where the center and radius are given by

$$C = i - \frac{2\pi i|\kappa_R|^2}{\kappa/2}\frac{\xi - \kappa/2}{2\xi}\,, \tag{11.10}$$

$$R = \frac{2\pi|\kappa_R|^2}{\kappa/2}\frac{\xi + \kappa/2}{2\xi}\,, \tag{11.11}$$

respectively. For a single mode cavity or more generally a single resonance bath, the Fano trajectory as a function of atom-cavity detuning is thus a *circle in the complex plane*. We note that a circle trajectory was also found in [Bär10] for dephasing processes when varying the decoherence strength instead of the detuning as a trajectory parameter.

We firstly note that the center of the circle lies on the imaginary axis. To gain intuition, we consider the special case of a critically coupled cavity mode [Hee14], where the resonance dip in the empty cavity reflectance (see e.g. Fig. 11.2) reaches all the way down to zero. This case corresponds to $\kappa/2 = 2\pi|\kappa_R|^2$, such that $\xi \to 0$. In this case, both the radius and center parameter are divergent. As a result, the Fano trajectory is a line on the real axis, which may be expected from general arguments [Lim17].

As one moves away from critical coupling, a radius of finite extent is observed. An example is shown in Fig. 11.2, where the parameters $\kappa = 2.4$, $\kappa_R = 0.3$ are considered. We see that the circle equation indeed matches the Fano q-parameters obtained from fitting a Fano curve to the atomic spectrum at each detuning.

11.3 Cusps in Fano trajectories of x-ray double cavities

Next, we investigate such Fano trajectories in x-ray cavities doped with Mössbauer nuclei. In particular, we report a geometry where the Fano trajectory deviates qualitatively from the circular shape

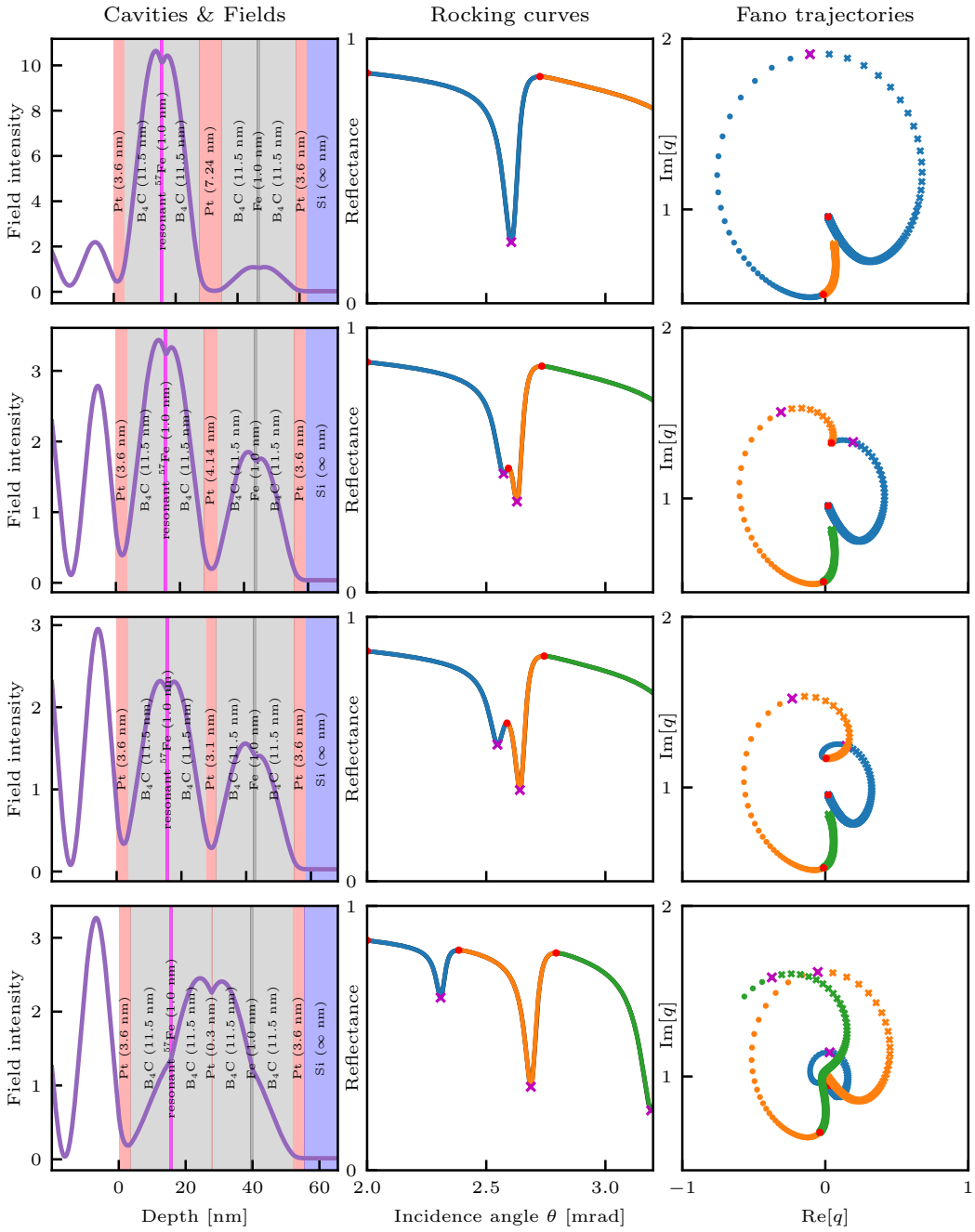

Figure 11.3: Fano cusps in an x-ray cavity with overlapping modes. Left panel column: Cavity structures indicated by vertical color stripes (materials and thicknesses see labels). The field strength at the first rocking curve minimum is shown as a violet line. From top to bottom, the thickness of the central platinum layer separating the two cavities is decreased, leading to an increasing mode coupling. Central panel column: The corresponding rocking curve (reflectance as a function of incidence angle), illustrating the resonance structure in each case. Different segments are colored for visual guidance. Maxima and minima are marked as magenta crossed and red dots, respectively. Right panel column: Fano q-factor trajectory in the complex plane when the incidence angle is scanned. Colors indicate the incidence angles as marked in the rocking curve plot. We see that as the separating layer decreases, the Fano trajectory evolves from a single deformed circle via a Fano cusp and a loop to multiple nested circles (details see text).

in the single case. By considering a near-symmetric double-cavity with significant mode overlap, we find interesting features including cusps and loops in the Fano trajectory.

We consider the thin-film structure Pt (3.6 nm)/B_4C (11.5 nm)/^{57}Fe (1 nm)/B_4C (11.5 nm)/Pt (d_{sep})/B_4C (11.5 nm)/^{56}Fe (1 nm)/B_4C (11.5 nm)/Pt (3.6 nm)/Si. The cavity structure is thus a double cavity version of the usual geometry consisting of a guiding layer surrounded by claddings

[Röh10; Röh12; Hee13; Hee15a; Hee15b]. This results in each of the cavity featuring a mode which couples to a mode in the other cavity [Hab17]. The structure is chosen as close to symmetric as possible, with the low refractive index material Si providing a substrate material to simulate the vacuum on the other side.

d_{sep} is the thickness of the mirror layer separating the two cavities, whose variation allows to control the coupling between the modes in each cavity. We note that in x-ray cavity QED, such double cavity structures have been considered previously [Hab17] in the regime of strong mode coupling. Our design is instead inspired by similar double resonator structures which are frequently employed in non-Hermitian photonics [EG18; Özd19] and aims at achieving overlapping mode effects via intermediate mode coupling [Rot18].

For nuclear resonances in the hard x-ray regime, it is technically infeasible to scan the nuclear transition frequency over a range providing a significant detuning to the cavity mode. Instead, one can effectively tune the cavity mode energy by varying the incidence angle [HE13]. Compared to Sec. 11.2, the latter then replaces the detuning as a scanning parameter.

In order to obtain the Fano trajectory, one can compute a nuclear spectrum at each incidence angle and fit the Fano form Eq. (11.1) to obtain the q-parameter. However, a numerically advantageous method is to instead use the Green's function formalism from Chapter 7 to directly compute the Fano q-parameter without a fitting procedure. From Eq. (7.26), considering s-polarization and the single ensemble case, we can write the reflection spectrum as

$$\begin{aligned} r(\mathbf{k}_\parallel,\omega) &= \frac{\mathbf{e}_s\cdot\hat{\mathbf{E}}_{\mathrm{in}}(\tilde{z}_0,\mathbf{k}_\parallel,\omega)}{\alpha^s_{\mathrm{in}}} - \mu_0\omega^2_{\mathrm{nuc}}\mathbf{e}_s\cdot\mathbf{G}(\tilde{z}_0,z_{\mathrm{nuc}},\mathbf{k}_\parallel,\omega)\cdot\mathbf{d}\,\mathcal{M}^{-1}\frac{\tilde{\Omega}}{\alpha^s_{\mathrm{in}}} \\ &= \frac{\mathbf{e}_s\cdot\hat{\mathbf{E}}_{\mathrm{in}}(\tilde{z}_0,\mathbf{k}_\parallel,\omega)}{\alpha^s_{\mathrm{in}}} - \mu_0\omega^2_{\mathrm{nuc}}\mathbf{e}_s\cdot\mathbf{G}(\tilde{z}_0,z_{\mathrm{nuc}},\mathbf{k}_\parallel,\omega)\cdot\mathbf{d}\,\frac{\frac{N}{A_\parallel}\mathbf{d}^*_l\cdot\mathbf{E}_{\mathrm{in}}(z_l,\mathbf{k}_\parallel,\omega)/\alpha^s_{\mathrm{in}}}{\Delta_{\mathrm{nuc}}+i\frac{\gamma}{2}+\frac{N}{A_\parallel}\mathcal{G}(z_{\mathrm{nuc}},z_{\mathrm{nuc}},\mathbf{k}_\parallel)}\,. \end{aligned}$$

From this form, we obtain

$$q = i - \frac{\zeta}{\alpha\Gamma/2} \tag{11.12}$$

similarly to Eq. (11.6). Only now, we have the parameters

$$\alpha = \frac{\mathbf{e}_s\cdot\hat{\mathbf{E}}_{\mathrm{in}}(\tilde{z}_0,\mathbf{k}_\parallel,\omega)}{\alpha^s_{\mathrm{in}}}\,, \tag{11.13}$$

$$\zeta = \mu_0\omega^2_{\mathrm{nuc}}\mathbf{e}_s\cdot\mathbf{G}(\tilde{z}_0,z_{\mathrm{nuc}},\mathbf{k}_\parallel,\omega)\cdot\mathbf{d}\,\frac{N}{A_\parallel}\mathbf{d}^*_l\cdot\mathbf{E}_{\mathrm{in}}(z_l,\mathbf{k}_\parallel,\omega)/\alpha^s_{\mathrm{in}}\,. \tag{11.14}$$

The superradiance Γ is as defined in Chapter 7. Consequently, the Fano q-parameter can be straightforwardly computed using the algorithm in Chapter 7 without the need for a fitting procedure.

Using this approach, we calculate the Fano trajectories for the aforementioned cavity geometry. Results are shown in Fig. 11.3. The left column shows the cavity structure and field at the first reflectance minimum, the middle column shows the rocking curve (reflectance as a function of incidence angle) around the first minimum and the right column the corresponding Fano trajectory. From top to bottom, we consider four values for the thickness of the separating layer.

The relatively thick $d_{\mathrm{sep}} = 7.24$ nm corresponds to weak coupling between the cavity modes, resulting in the second cavity essentially not participating at all. Consequently, we observe a single resonance dip in the rocking curve. This case is close to a single mode scenario and as expected, we see a roughly circular shape of the Fano trajectory. Deviations compared to the properties derived in Sec. 11.2 include distortions from perfect circularity, which likely result from the grazing incidence setting, and additional bends for large detuning, which are likely a consequence of higher modes.

As we decrease the separating layer thickness, the Fano trajectory qualitatively departs from the roughly circular shape. For $d_{\mathrm{sep}} \approx 4.14$ nm, we observe a cusp feature in the trajectory, whose location coincides with the incidence angle of the rocking curve maximum between the two strongly overlapping modes. For slightly larger mode coupling at $d_{\mathrm{sep}} = 3.1$ nm, the cusp feature turns into a loop.

In the limit of a thin separating layer ($d_{\mathrm{sep}} = 0.3$ nm), we see that the loop unwinds into nested circular features, with a crossing occurring only far off the cavity resonance angle. This behavior can also be understood by noting that this geometry with such a thin separating layer essentially

constitutes a single cavity of doubled thickness. Consequently, the rocking curve features separated resonances again. In the coupled mode picture, the transition from top to bottom can also be regarded as an avoided crossing [Lim17], where the mode coupling is varied from small to large.

The observed transition in the local properties of the Fano trajectory from a cusp to a loop feature is interesting, since it appears to be related to the spectral overlap of the resonances in the regime of *intermediate* mode coupling. The two extreme cases of large and small coupling instead feature roughly circular trajectories, as can be expected from the single mode model.

Beyond theoretical interest, the practical value of the Fano cusp feature is currently unclear. In the context of [Bär10], where it was shown that Fano trajectories allow to distinguish between dephasing and dissipation, the treatment here can be seen as a generalization to structured baths with interesting features in the overlapping modes regime. The latter has close connections to the topic of non-Hermitian photonics [EG18; MA19; Özd19] and potential applications include cavity sensing [GL14]. For example, one could envision that the qualitative difference between a circular and a looped Fano trajectory could be used to identify how many modes effectively participate in the interference. Precise statements on such a relation are subject of future investigation. Within this thesis, the Fano cusps are simply pointed out as an interesting feature beyond single mode cavity physics.

Part IV

Nonlinear quantum dynamics of nuclear ensembles

Chapter 12

Nonlinear excitation dynamics with ultra-short pulse driving

This chapter is based on an article currently in preparation:

Nonlinear excitation of Mössbauer nuclei in thin-film cavities by focussed x-ray pulses
D. Lentrodt, C. H. Keitel, J. Evers, et al.
in preparation

The thesis author's role in the paper is that of the sole principle author. The content is to be submitted for publication in a peer-reviewed journal.

12.1 Outline

In Chapters 7 to 9, we have developed an ab initio approach to x-ray cavity QED with Mössbauer nuclei. In this chapter, we employ the new method to explore nonlinear dynamics in this system as motivated in Chapter 1. In particular, we consider the feasibility of inverting nuclear ensembles in the x-ray cavity QED setup using tightly focused x-ray pulses from currently available XFEL facilities such as the European XFEL [Tsc17; Mad21].

In Sec. 12.2.1, we first give the theoretical background that our calculation is based on, outlining the model for the nuclear quantum dynamics. We then present the resulting solution for the excitation dynamics during an ultra-short x-ray pulse in Sec. 12.3, which allows to predict the nuclear inversion.

In Sec. 12.4, the effect of the cavity is considered in detail. In particular, we introduce an algorithm that allows to calculate the cavity excitation enhancement for a focused x-ray beam beyond the highly collimated limit.

In Sec. 12.5, we provide preliminary numbers for the inversion of nuclear ensembles at the MID and HED instruments at the European XFEL [Mad13; Mad21; Nak14] for a set of example cavities. The results suggest that the inversion of nuclear ensembles or near-inversion nonlinear effects may already be in reach at current photon numbers and focusing strengths.

On the theory side, our approach is based on the Master equation for the nuclear ensemble inside the x-ray cavity introduced in Chapter 7. Besides providing a semi-analytical calculation method for the cavity geometry, we resolve previous questions with regards to the role of collectivity in the excitation dynamics by considering the relevant time scales. During an ultra-short pulse, we show that interaction terms in the Master equation can be neglected, resulting in collective effects being negligible. The latter implies that a Maxwell-Bloch type treatment is valid and can be used for solving the excitation dynamics. However, for the decay dynamics on longer time scales, such approaches or mean-field treatments are not valid and many-body interactions have to be taken into account, as we discuss further in Chapter 13.

12.2 Many-body Master equation and time scales

12.2.1 Nuclear Master equation

As shown in Chapter 7, the nuclear dynamics are well modeled by the many-body Master equation [Len20]

$$\dot{\rho} = -\frac{i}{\hbar}[H_{\text{eff}}, \rho] + \mathcal{L}_{\text{eff}}[\rho]\,, \tag{12.1}$$

where the effective Hamiltonian is

$$\hat{H}_{\text{eff}} = \sum_n \frac{\hbar\omega_{\text{nuc}}}{2}\hat{\sigma}_n^z - \hbar\sum_{nn'} J_{nn'}\hat{\sigma}_n^+\hat{\sigma}_{n'}^- - \sum_n \left[\mathbf{d}^*\cdot\mathbf{E}(\mathbf{r}_n,t)\hat{\sigma}_n^+ + h.c.\right]\,. \tag{12.2}$$

The Lindblad term encoding decay processes is

$$\mathcal{L}_{\text{eff}}[\rho] = \sum_{nn'}\frac{\Gamma_{nn'}}{2}(2\hat{\sigma}_n^-\rho\sigma_{n'}^+ - \{\hat{\sigma}_n^+\hat{\sigma}_{n'}^-,\,\rho\}) + \mathcal{L}_{\text{IC}}[\rho]\,, \tag{12.3}$$

where $\mathcal{L}_{\text{IC}}[\rho] = \sum_n \frac{\gamma_{\text{IC}}}{2}(2\hat{\sigma}_n^-\rho\sigma_n^+ - \{\hat{\sigma}_n^+\hat{\sigma}_n^-,\,\rho\})$ describes the single nucleus loss due to internal conversion. The single nucleus radiative contribution is already included in Γ_{nn} [Len20].

The interaction coefficients can be expressed in terms of the Green's function as [DKW02; SB08; AG17a]

$$J_{nn'} = \frac{\mu_0\omega_{\text{nuc}}^2}{\hbar}\mathbf{d}^*\cdot\text{Re}[\mathbf{G}(\mathbf{r}_n,\mathbf{r}_{n'},\omega_{\text{nuc},l})]\cdot\mathbf{d} \tag{12.4}$$

and

$$\Gamma_{nn'} = 2\frac{\mu_0\omega_{\text{nuc}}^2}{\hbar}\mathbf{d}^*\cdot\text{Im}[\mathbf{G}(\mathbf{r}_n,\mathbf{r}_{n'},\omega_{\text{nuc}})]\cdot\mathbf{d}\,. \tag{12.5}$$

For the layer geometry, the real space Green's function $\mathbf{G}(\mathbf{r}_n,\mathbf{r}_{n'},\omega_{\text{nuc}})$, which enters these coupling and decay terms, can be obtained via Fourier transforming the analytical result available for the parallel wave space Green's function [Tom95] (see also Chapter 7 and Appendix D).

The central approximation used to obtain the above real-space Master equation is the *Born-Markov approximation* [DKW02; BP02; Len20], as outlined in Chapter 7. Since the latter is close to exact at the ultra-weak light-matter coupling of nuclei and x-rays ($\gamma_{\text{rad}} \sim$ neV $\ll \omega_{\text{nuc}} \sim$ keV), the above Master equation is therefore expected to be an excellent model for nonlinear dynamics in most nuclear resonant scattering settings. We emphasize that unlike for the parallel wave space Master equation in Sec. 7.5, a single parallel wave vector or linear approximation is not employed here. In the above form, the Master equation does also not include a semi-classical approximation, such that it captures the quantum and collective character of the dynamics.

12.2.2 The excitation phase

Time scales and interaction terms

While the Master equation has a rather simple form, in general, it poses a difficult quantum many-body problem. The cavity environment may mediate interactions between a large number of nuclei, also facilitated by the high coherence of the nuclear ensembles. While we have seen in Chapters 2 and 7 that various approximations are applicable in the regime of low excitation, a general solution of the *nonlinear* quantum dynamics requires to reconsider the problem starting from the full Master equation.

However, there is still a scenario where the situation can be simplified without employing the linear approximation: the excitation dynamics during an ultra-short pulse, as we explain in the following.

At modern x-ray sources, such as synchrotrons [Röh05b] or x-ray free electron lasers (XFELs) [Bos16; PMR16], the pulse lengths are typically on the picosecond scale or shorter. For high-intensity XFELs such as the European XFEL [Tsc17], the pulse length is even on the level of hundreds of femtoseconds if monochromatized. Such pulses were recently employed in the first nuclear resonant scattering experiment at an XFEL [Chu18], where multiple resonantly scattered photons were observed per shot.

In such an experiment with ultra-narrow transitions, the dynamics can then be divided into two phases. First, the nuclei are strongly driven by the ultra-short x-ray pulse. Subsequently, after the pulse has passed, one observes the decay and collective interaction of the nuclei, resulting in the typical nuclear resonant scattering signatures.

Importantly, these two phases are on completely different time scales, since the nuclear decay dynamics typically occur on the nanosecond scale [HT99; Röh05b] and are therefore slower than the femtosecond pulse length by orders of magnitude. In the following, we refer to the dynamics during the ultra-short pulse as the "excitation phase" and similarly to the subsequent dynamics on longer time scales as the "decay phase".

On the level of the Master equation, the time-scales directly enter in the interaction terms. The collective coupling and decay terms — proportional to $J_{nn'}$ and $\Gamma_{nn'}$, respectively — induce nuclear interaction dynamics on the nanosecond time scale. On the femtosecond scale, however, these interaction terms can be safely neglected. During the ultra-short pulse, the driving term proportional to $\mathbf{d}^* \cdot \mathbf{E}(\mathbf{r}_n, t)$ then dominates the dynamics, forcing teh excitation on short time scale via the large number of photons.

Short pulse approximation

For the excitation phase, we can then neglect the interaction and decay terms such that the equations of motion resulting from the Master equation Eq. (12.1) reduce to

$$\frac{d}{dt}\sigma_n^- = -i\omega_{\mathrm{nuc}}\sigma_n^- - i\Omega_n\hat{\sigma}_n^z\,, \tag{12.6}$$

$$\frac{d}{dt}\sigma_n^+ = +i\omega_{\mathrm{nuc}}\sigma_n^+ + i\Omega_n^*\sigma_n^z\,, \tag{12.7}$$

$$\frac{d}{dt}\sigma_n^z = +2i\Omega_n\sigma_n^+ - 2i\Omega_n^*\sigma_n^-\,, \tag{12.8}$$

where we have defined $\Omega_n(t) = \frac{1}{\hbar}\mathbf{d}^* \cdot \mathbf{E}(\mathbf{r}_n, t)$ and $\mathcal{O} = \langle\hat{\mathcal{O}}\rangle$. Indeed, one can check straightforwardly that this approximation is correct on the pulse time scale using the linear equations of motion or similar models where both the full Master equation and the approximate version can be solved (see Chapter 13).

We see that these equations form closed set already for a single nucleus, since the interactions with the other nuclei have been neglected. This feature means that there are *no significant collective effects* in the excitation phase. The interactions and collective dynamics only become relevant on the longer nanosecond time scales.

We note that Eqs. (12.6–12.8) are essentially of the form of the Maxwell-Bloch equations discussed in Chapter 2. However, our approach provides a clear approximation hierarchy in this context. Importantly, we have not derived these equations using mean-field theory, but instead have taken the route via a quantum optical Master equation and then argued that the interaction terms therein are negligible on certain time scales. This approach allows to clearly identify in which regimes the equations are valid, such that the involved approximations are well under control and can be verified. On longer time scales, Eqs. (12.6-12.8) do not apply and the full Master equation Eq. (12.1) may have to be considered (see Chapter 13 for further discussion).

In the nuclear resonant scattering literature, as discussed in Chapter 2, Maxwell-Bloch type equations have already been used in a number of works [LPK11; JPK12; LPK12; LPK13; KLP14; KP16; LKP16; WL18; Zha19]. In this context, our approach resolves a number of open questions.

First, due to the macroscopic QED and Master equation treatment, our approach allows to describe the effects of cavities, which have previously only been connected heuristically to the Maxwell-Bloch treatment [KP16].

Second, a central insight is that collective effects do not affect the excitation dynamics during an ultra-short driving pulse. The absence of collectivity in the Maxwell-Bloch equations has up to now been seen as a problem of the approach [Che21]. A previous work [JPK12] using the Maxwell-Bloch approach to estimate nuclear inversion in the forward scattering geometry even introduced a heuristic enhancement factor to account for collectivity. The enhancement factor was motivated by the observation that Maxwell-Bloch equations otherwise do not capture the decay dynamics. However, from our approach above, it is clear that the Maxwell-Bloch equations are valid during the ultra-short pulse driving even without an enhancement factor. This feature is not inconsistent with notions of

collectivity in nuclear forward scattering, since these effects appear on longer time-scales where the Maxwell-Bloch equations may break down.

Our approach thus extends the Maxwell-Bloch equation treatment and provides a clear picture of its applicability by introducing an approximation hierarchy. The quantum optical Master equation for the nuclear ensemble is a crucial step in this context, since it allows to systematically include or exclude interaction terms, whose effect can be quantitatively estimated. It also opens the door for investigations of physics physics beyond the mean-field treatment, such as the interacting many-body dynamics on the longer decay time scales (see Chapters 13 and 15).

Low pulse depletion approximation

In addition to the short pulse approximation, we can further simplify the problem by noting that the nuclei's coupling to the radiation field is extremely weak. The excitation dynamics can thus be seen as the nuclei simply absorbing photons from the strong driving field, where a significant rate is achieved due to the large number of photons in the pulse.

With this idea in mind, we can look at the many-nuclei version of the wave equation Eq. (2.45) from the Maxwell-Bloch treatment in Chapter 2, which reads

$$\nabla \times \nabla \times \hat{\mathbf{E}}(\mathbf{r},t) + \frac{\partial^2}{\partial t^2}\hat{\mathbf{E}}(\mathbf{r},t) = \frac{\omega_{\mathrm{nuc}}^2}{\varepsilon_0 \hbar} \sum_n \delta(\mathbf{r}-\mathbf{r}_n)[\mathbf{d}^* \hat{\sigma}_n^+(t) + \mathbf{d}\hat{\sigma}_n^-(t)]\,. \tag{12.9}$$

If we consider the dipole moment $|\mathbf{d}|$ as a small parameter — in the sense that the probability of absorbing a single photon is much less than unity — we see from Eqs. (12.6-12.8) that the nuclear dynamics are first order in $|\mathbf{d}|$ $[\mathcal{O}(|\mathbf{d}|)]$. This in turn means that the source term in the wave equation above is $\mathcal{O}(|\mathbf{d}|^2)$. Consequently, the fractional number of absorbed photons and therefore the correction is typically small, such that the ultra-short pulse is not significantly depleted by the nuclear resonances.

As a result, we can usually approximate the drive term in the optical Bloch equation as

$$\Omega_n(t) = \frac{1}{\hbar}\mathbf{d}^* \cdot \mathbf{E}(\mathbf{r}_n,t) \approx \frac{1}{\hbar}\mathbf{d}^* \cdot \mathbf{E}_{\mathrm{drive}}(\mathbf{r}_n,t)\,, \tag{12.10}$$

where $\mathbf{E}_{\mathrm{drive}}$ is the driving field in absence of the nuclear resonances.

However, there is one pitfall. The above argument applies to a single nucleus, but for high nuclear number density or large propagation depths, the sum over the nuclei in Eq. (12.9) can result in significant pulse depletion. In particular for thick target forward scattering, such effects may have to be taken into account. We note, however, that in such cases, the low pulse depletion approximation results in an overestimation of the driving field. Consequently, to achieve maximum inversion throughout the ensemble, it is experimentally advantageous to stay within the validity region of this approximation by using thin resonant ensembles.

In the context of propagation problems such as thick target forward scattering, the well-known effect of multiple resonant scattering [LHH60; Smi99] is effectively also precluded by this approximation. We note, however, that multiple scattering mainly occurs on longer time scales during the decay phase, which the above approximation does not apply to in the first place.

In this chapter, our focus lies on achieving maximum inversion using thin resonant ensembles in cavities. We will utilize the low pulse depletion approximation for the calculations in the following. Its validity is explicitly confirmed in Appendix E.1.

12.3 Excitation dynamics using the pulse area theorem

In the following, we discuss a simple solution to the above optical Bloch equations, which is practically convenient, and its limitations.

Pulse area theorem

For certain driving fields $\Omega_n(t)$, the above optical Bloch-type equations Eqs. (12.6-12.8) can be solved analytically using the so-called pulse area theorem [MH67; AE87; Ebe98]. For a correct physical solution, it is important to note that the conditions for the pulse area theorem to apply are generally

rather strict [Sho11; Fis17]. Some of these restrictions, such as the absence of interaction and spontaneous emission terms, are already ensured by the time scale separation during the driving phase. However, there are additional conditions on the pulse which have to be confirmed.

In our case, the main condition is a resonant driving field. The pulse area theorem can then be formulated as follows. If the driving field is of the form

$$\Omega_n(t) = |\Omega_n(t)| e^{i\phi_n} e^{-i\omega_{\mathrm{nuc}} t} \tag{12.11}$$

where ϕ_n is a real time-independent constant, the solution for the nuclear expectation values is [Sho11]

$$\sigma_n^z(t) = -\cos(|\Phi_n(t)|)\,, \tag{12.12}$$

$$\sigma_n^-(t) = +\frac{i}{2} e^{i\omega_{\mathrm{nuc}} t} e^{-i\phi_n} \sin(|\Phi_n(t)|)\,, \tag{12.13}$$

$$\sigma_n^+(t) = -\frac{i}{2} e^{-i\omega_{\mathrm{nuc}} t} e^{i\phi_n} \sin(|\Phi_n(t)|)\,, \tag{12.14}$$

where $\Phi_n(t)$ is the pulse area [MH67; AE87] defined by

$$\Phi_n(t) = \int_{t_0}^{t} dt' 2\tilde{\Omega}_n(t')\,, \tag{12.15}$$

$\tilde{\Omega}_n(t) = \Omega_n(t) e^{i\omega_{\mathrm{nuc}} t}$ is the drive in the interaction picture and t_0 is the initial time, where we assume the nucleus to be in its ground state.

The pulse area theorem solution thus applies if the carrier frequency of the driving field is resonant with the nuclear transition and the envelope has a constant phase. For experiments at typical x-ray sources such as synchrotrons and x-ray free electron lasers, these conditions apply as long as the detuning between the nuclear transition and the carrier frequency is smaller than the pulse's spectral bandwidth.

We note that even if the pulse area theorem does not apply, the optical Bloch equations can straightforwardly be solved numerically. However, the pulse area theorem has a useful relation to frequency domain response functions which will be convenient later on. In particular, if we are only interested in the final excitation after the whole pulse has passed, the relevant limit is $t_0 \to -\infty$ and $\Phi_n^{\mathrm{tot}} = \lim_{t\to\infty} \Phi_n(t)$. The pulse area then coincides with the frequency domain Fourier amplitude on resonance, such that

$$\Phi_n^{\mathrm{tot}} = \frac{4\pi}{\hbar} \mathbf{d}^* \cdot \mathbf{E}_{\mathrm{drive}}(\mathbf{r}_n, \omega_{\mathrm{nuc}})\,, \tag{12.16}$$

where

$$\mathbf{E}(\mathbf{r}_n, \omega) = \frac{1}{2\pi} \int dt e^{i\omega t} \mathbf{E}(\mathbf{r}_n, t)\,. \tag{12.17}$$

We will use this property in Sec. 12.4 for a semi-analytical description of nuclear excitation by focused pulses in thin-film cavities without the need for additional approximations.

Beyond the area theorem

We emphasize again that the conditions for the area theorem in the above form to hold are rather strict. In particular, for self-amplified spontaneous emission (SASE) pulses as they are commonly obtain from XFELs [PMR16], one encounters fluctuating phases [Pfe10], such that the area theorem may not apply in the above form. Practically, this aspect does not constitute much of a problem, since Eqs. (12.6-12.8) can instead be straightforwardly solved numerically for the given SASE pulse [HKE16], which can be obtained by the statistical sampling method in [Pfe10].

In the cavity case, we further use the area theorem to justify why only the cavity response at a given frequency is important. However, the exact result obtained via the area theorem can in general also be used approximately, assuming that the spectral width of the pulse is much narrower than the spectral response of the cavity, which is typically the case.

In the following, we ignore the effect of SASE pulses, for simplicity and since its quantitative influence on the inversion has already been considered in [HKE16]. We further note that with the recent demonstration of self-seeding at PAL XFEL [Nam21], Fourier limited pulses may become available at XFEL facilities in the near future.

12.4 Focussed beam driving in the thin-film geometry

According to Eq. (12.16), the central property of the light field which determines the excitation after the pulse is the Fourier amplitude of the field $\mathbf{E}_{\mathrm{drive}}(\mathbf{r}_n, \omega_{\mathrm{nuc}})$. For nuclei in a photonic environment such as thin-film cavities [HE13; Len20], the input field provided by the x-ray source is further modified by off-resonant electronic refraction, which influences the driving field at the location of the nucleus. In the case of a highly collimated beam, the resulting cavity response is well known from Parratt's formalism [Par54] and software packages for its application to nuclear resonance scattering exist [Stu00; Shv00; Hee19].

In this section, we first derive expressions for the free space field's Fourier amplitude in terms of common beam parameters of x-ray sources, which then allows to predict nuclear excitation fractions. We then introduce a numerical scheme to include the cavity response for focussed x-ray pulses beyond the highly collimated case.

12.4.1 Pulsed Gaussian beam in free space

Angular spectrum and real space field

The field from x-ray sources can usually be represented as a pulsed version of the archetype Gaussian beam. The latter can be most concisely represented by its angular spectrum defined by [Nov14]

$$\tilde{\mathbf{E}}(\mathbf{k}_\perp, z, \omega) = \frac{1}{4\pi^2} \int d^2\mathbf{r}_\perp e^{-i\mathbf{k}_\perp \cdot \mathbf{r}_\perp} \tilde{\mathbf{E}}(\mathbf{r}, \omega)\,, \tag{12.18}$$

where z is the spatial coordinate along the beam propagation direction, $\mathbf{r}_\perp$ the vector in the perpendicular plane and $\mathbf{k}_\perp$ its corresponding wave vector. We use the complex phasor notation for the electric field indicated by the tilde.

The Gaussian beam is given by the solution [Nov14]

$$\tilde{\mathbf{E}}(\mathbf{k}_\perp, z, \omega) = \mathbf{A}(\omega) \frac{w_0^2}{2} e^{-\frac{w_0^2}{4}|\mathbf{k}_\perp|^2} e^{ik_z^{(\mathrm{val})} z}\,, \tag{12.19}$$

where w_0 is the beam waist size at the focus and $k_z^{(\mathrm{val})}$ is a function of the frequency and angular wave vector given by $k_z^{(\mathrm{val})} = \sqrt{k^2 - |\mathbf{k}_\perp|^2}$. The beam waist size is further related to the beam divergence θ_{div} by $w_0 = \frac{2}{k\theta_{\mathrm{div}}}$, where we assume full spatial coherence. $\mathbf{A}(\omega)$ is the frequency spectrum of the pulse.

The real-space field can then be obtained by a Fourier transform of the angular spectrum in the perpendicular plane. For the case of a paraxial beam, the real space field can be approximated analytically as [Nov14]

$$\tilde{\mathbf{E}}(\mathbf{r}, \omega) \approx 2\pi \mathbf{A}(\omega) \frac{w_0}{w(z)} e^{ikz} e^{-\frac{|\mathbf{r}_\perp|^2}{w^2(z)}} e^{-i\psi(z)} e^{ik\frac{|\mathbf{r}_\perp|^2}{2R(z)}}\,, \tag{12.20}$$

where the Gaussian beam parameters are the beam size $w(z) = w_0\sqrt{1 + \frac{z^2}{z_R^2}}$, the Gouy phase $\psi(z) = \arctan\left(\frac{z}{z_R}\right)$, the phase curvature radius $R(z) = z(1 + \frac{z_R^2}{z^2})$ and the Rayleigh length $z_R = \frac{kw_0^2}{2}$.

For a frequency spectrum that is narrow compared to the wavelength, we can further assume that only the carrier frequency phase varies significantly with energy. We can then obtain a simple form of a pulsed Gaussian beam in the time domain as

$$\tilde{\mathbf{E}}(\mathbf{r}, t) = 2\pi \mathbf{A}(t - z/c) \frac{w_0}{w(z)} e^{ikz} e^{-\frac{|\mathbf{r}_\perp|^2}{w^2(z)}} e^{-i\psi(z)} e^{ik\frac{|\mathbf{r}_\perp|^2}{2R(z)}}\,, \tag{12.21}$$

where $\tilde{\mathbf{E}}(\mathbf{r}, t) = \int d\omega e^{-i\omega t} \tilde{\mathbf{E}}(\mathbf{r}, \omega)$ and $\mathbf{A}(t) = \int d\omega e^{-i\omega t} \mathbf{A}(\omega)$. We note that due to the complex phasor notation, the physical electric field is given by $\mathbf{E}(\mathbf{r}, t) = \mathrm{Re}[\tilde{\mathbf{E}}(\mathbf{r}, t)]$.

Amplitude normalization

For a Fourier limited pulse, the time domain spectrum has the form $\mathbf{A}(t) = \frac{\mathbf{A}_0}{\tau_{\mathrm{pulse}}\sqrt{2\pi}} e^{-\frac{t^2}{2\tau_{\mathrm{pulse}}^2}} e^{-i\omega_{\mathrm{nuc}} t}$, such that $\mathbf{A}(\omega) = \frac{\mathbf{A}_0}{2\pi} e^{-\frac{\tau_{\mathrm{pulse}}^2}{2}(\omega - \omega_{\mathrm{nuc}})^2}$, where we have chosen the normalization such that $\mathbf{A}_0$ is the peak amplitude of $\tilde{\mathbf{E}}(\mathbf{r}, \omega)$.

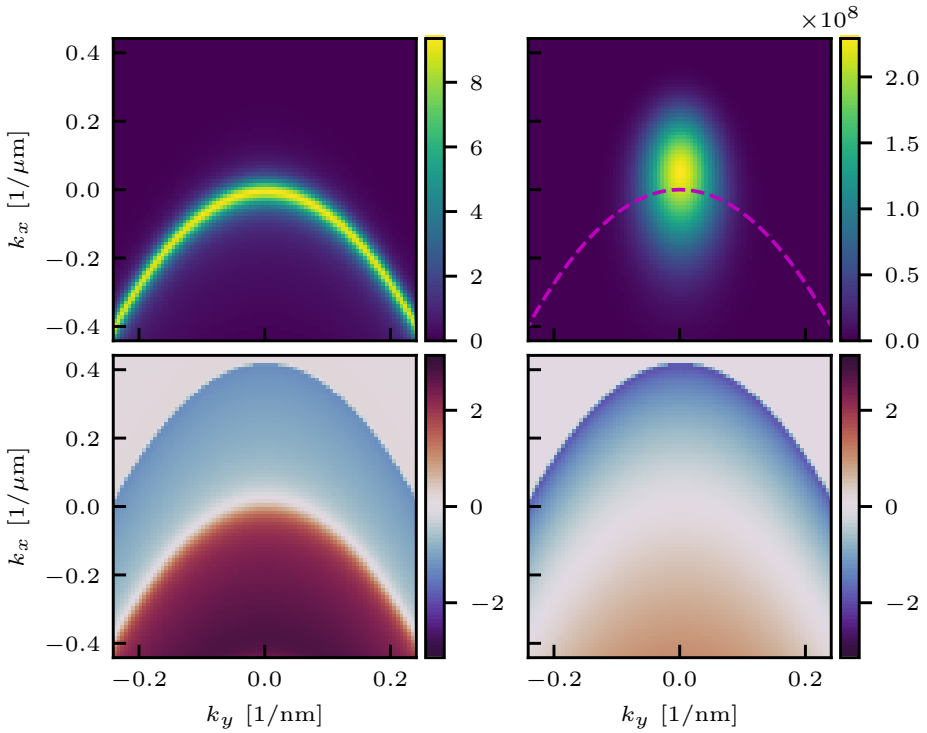

Figure 12.1: Basic quantities used in the Fourier transformation algorithm for the case of the example cavity (see text). The angular spectra are evaluate at the z-position of the nuclear ensemble center. (left; top and bottom) Intensity and phase, respectively, of the cavity response function $\boldsymbol{\mathcal{E}}_s^0(z, \mathbf{k}_\parallel, \omega)$. (right; top and bottom) Intensity and phase, respectively, of the angular spectrum in cavity coordinates $E_{\text{in}}(\mathbf{k}_\parallel, \omega)$ (carrier phases omitted) corresponding to a normalized focused beam with $\theta_{\text{in}} \approx 3.352$ mrad. The dashed magenta line indicates the angular contour corresponding to the incidence angle. The parabola above which the phases are zero corresponds to $k_z^{(\text{val})} = 0$, marking the boundary of the on-shell region.

The amplitude can be fixed via the pulse energy or photon number

$$N_{\text{ph}} \hbar \omega_{\text{nuc}} \approx \frac{\varepsilon_0}{2} \int d^3\mathbf{r} |\tilde{\mathbf{E}}(\mathbf{r}, t)|^2 \,, \tag{12.22}$$

where we have again assumed a narrow frequency spectrum compared to the carrier frequency and neglected the magnetic contribution to the wave energy.

Evaluating the integral for the pulsed Gaussian beam then gives

$$|\mathbf{A}_0| = \sqrt{\frac{2 N_{\text{ph}} \hbar \omega_0 \tau_{\text{pulse}}}{\pi^2 \sqrt{\pi} \varepsilon_0 w_0^2 c}} \,. \tag{12.23}$$

Within the rotating wave approximation $\Omega_n(t) = \frac{1}{\hbar} \mathbf{d}^* \cdot \mathbf{E}_{\text{drive}}(\mathbf{r}_n, t) \approx \frac{1}{2\hbar} \mathbf{d}^* \cdot \tilde{\mathbf{E}}_{\text{drive}}(\mathbf{r}_n, t)$, the pulse area theorem from Sec. 12.3 applies to this pulse and can be used to solve the optical Bloch equations. Using Eq. (12.16) for aligned polarization and dipole transition direction, the peak of the full pulse area is then given by

$$\Phi_{\text{peak}}^{\text{tot}} \approx \frac{2\pi}{\hbar} |\mathbf{d} \cdot \mathbf{A}_0| = \sqrt{\frac{8 N_{\text{ph}} \omega_0 \tau_{\text{pulse}} d^2}{\sqrt{\pi} w_0^2 c \hbar \varepsilon_0}} \,. \tag{12.24}$$

This formula is key in obtaining an absolute scale for the inversion when the parameters of the x-ray source beam, such as from an x-ray free electron laser [Tsc17], are given. Full inversion of the nuclei at the peak intensity location is realized when $\Phi_{\text{peak}}^{\text{tot}} = \pi$ [HKE16].

12.4.2 Cavity field enhancement

Cavity response

When the nuclei are embedded in a cavity, the free space field from the previous section is modified by reflections from and absorption in the cavity material. For a highly collimated monochromatic

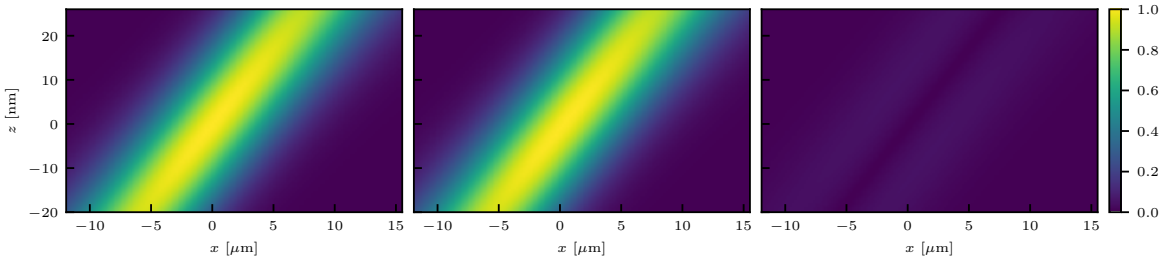

Figure 12.2: Comparison of resonant field intensities $|\mathbf{E}(\mathbf{r},\omega)|^2$ at $y = 0$ in free space for a focused beam with $\theta_{\mathrm{div}} = 1.1$ mrad, $\theta_{\mathrm{in}} \approx 3.352$ mrad. Left: The analytical formula for the Gaussian beam in the paraxial approximation Eq. (12.20). Middle: The result of the numerical Fourier transform of the cavity angular spectrum Eq. (12.28). Right: The intensity of the difference of the two fields.

field, the field distribution can be calculated straightforwardly using the standard Parratt's formalism [Par54] or the extended layer formalism [Röh05b] (see Chapter 2). The effect of the cavity is then given by the mode functions [Tom95] $\boldsymbol{\mathcal{E}}^{0(n)}_{q/p}(z,\mathbf{k}_\parallel,\omega)$ for polarization q/p, depth from the upper cavity boundary z and the wave vector in the cavity plane $\mathbf{k}_\parallel$. 0 (n) signifies an incident field from the top (bottom) of the cavity.

These cavity response functions are available analytically for the planar thin-film geometry (see [Tom95; Len20] and Appendix D), providing a useful basis to expand the field as

$$\mathbf{E}(\mathbf{r},\omega) = \int d^2\mathbf{k}_\parallel e^{i\mathbf{k}_\parallel\cdot\mathbf{r}_\parallel}\boldsymbol{\mathcal{E}}^0_s(z,\mathbf{k}_\parallel,\omega)E_{\mathrm{in}}(\mathbf{k}_\parallel,\omega)\,, \tag{12.25}$$

where we consider the case of a purely s-polarized field incident from the top of the cavity. $E_{\mathrm{in}}(\mathbf{k}_\parallel,\omega)$ are appropriate Fourier coefficients of the incoming field from the x-ray source, which can similarly be expanded as

$$\mathbf{E}_{\mathrm{in}}(\mathbf{r},\omega) = \int d^2\mathbf{k}_\parallel e^{i\mathbf{k}_\parallel\cdot\mathbf{r}_\parallel}e^{ik_z^{(\mathrm{val})}z}E_{\mathrm{in}}(\mathbf{k}_\parallel,\omega)\hat{\mathbf{e}}_s\,, \tag{12.26}$$

such that

$$E_{\mathrm{in}}(\mathbf{k}_\parallel,\omega) = \frac{e^{-ik_z^{(\mathrm{val})}z}}{2\pi}\int d^2\mathbf{r}_\parallel e^{-i\mathbf{k}_\parallel\cdot\mathbf{r}_\parallel}\hat{\mathbf{e}}_s\cdot\mathbf{E}_{\mathrm{in}}(\mathbf{r},\omega)\,. \tag{12.27}$$

Fourier coefficients of the incoming field

Noting that the cavity response functions expansion Eq. (12.25) is an angular spectrum in rotated coordinates, the Fourier coefficients $E_{\mathrm{in}}(\mathbf{k}_\parallel,\omega)$ can indeed be obtained analytically for the Gaussian beam considered in Sec. 12.4.1. The result is derived in Appendix E.1 and reads

$$E_{\mathrm{in}}(\mathbf{k}_\parallel,\omega) = \frac{\hat{\mathbf{e}}_s\cdot\tilde{\mathbf{A}}(\omega)}{2\pi}\tilde{I}\left(k_x,k_y,\sqrt{k^2-k_y^2-k_x^2}\right)F_\delta\left(k_x,k_y,\sqrt{k^2-k_y^2-k_x^2}\right)\Theta(k^2-k_y^2-k_x^2)\,, \tag{12.28}$$

which we refer to as the cavity angular spectrum in the following. Here,

$$\tilde{I}(k_x,k_y,k_z) = \frac{w_0^2}{2}e^{-\frac{w_0^2}{4}\left[k_y^2+k_x^2\sin^2(\theta_{\mathrm{in}})+k_z^2\cos^2(\theta_{\mathrm{in}})-2k_xk_z\cos(\theta_{\mathrm{in}})\sin(\theta_{\mathrm{in}})\right]}\,, \tag{12.29}$$

$$F_\delta\left(k_x,k_y,k_z\right) = \left|\sin(\theta_{\mathrm{in}}) + \frac{k_x\cos(\theta_{\mathrm{in}})}{k_z}\right|\,, \tag{12.30}$$

and θ_{in} is the incidence angle between the Gaussian beam's propagation axis and the cavity plane.

Numerical approach

Once the cavity angular spectrum of the incoming field is known, the field in real space can be obtained by numerically evaluating Eq. (12.25). To this end, we choose a grid in $\mathbf{k}_\parallel$-space and use the SCIPY [Vir20] fast Fourier transform algorithms to perform the integrals.

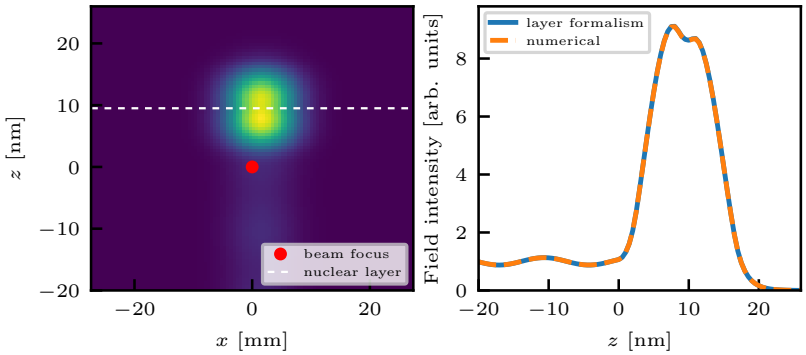

Figure 12.3: Highly collimated limit ($\theta_{\mathrm{div}} = 1$ μrad) of a focused x-ray beam incident on the cavity. Left: Resonant field intensity $|\mathbf{E}(\mathbf{r},\omega)|^2$ at $y = 0$. Right: Slice of the resonant field intensity at $x = y = 0$. The layer formalism result, which analytically evaluates the perfectly collimated result, matches our numerical algorithm in this limit (see legend). Amplitudes were chosen such that the peaks of the two calculations coincide.

In our approach, we mainly use the analytical solution for the Gaussian beam's angular cavity spectrum Eq. (12.28) as an input to the algorithm. For more general spatial beam profiles, the Fourier transform Eq. (12.27) can, however, be performed analogously by numerical means.

For convenience, we then define the cavity field enhancement factor $\xi_{\mathcal{E}}$ as the ratio of the field amplitude in the cavity for a given focusing compared to the ratio of the field amplitude in free space. We can then use the free space result for the nuclear inversion in form of the pulse area Eq. (12.24) multiplied by the $\xi_{\mathcal{E}}$, which can be calculated by the above field propagation formalism for an appropriately normalized input pulse.

12.4.3 Examples and cross-checks

To test and illustrate our approach, we consider an exemplary thin-film cavity which is doped with an ensemble of Mössbauer nuclei at its center. The cavity structure is Pt (2.5 nm)/C (6 nm)/^{57}Fe (2 nm)/C (6 nm)/Pt, such that the first mode is close to critically coupled. The incidence angle is chosen at the first resonance minimum $\theta_{\mathrm{in}} = \theta_{\mathrm{min},1} \approx 3.352$ mrad.

Cavity response and beam angular spectra

Fig. 12.1 shows the cavity response function and angular spectrum in cavity coordinates at $z = 0$ for this setup. We see that the cavity has a peaked response around the incidence angle contour. The incident beam is represented by a distorted Gaussian. We note that due to the coordinate rotation, the wave packet is not only asymmetric in the k_x direction, but also the peak maximum does not coincide with the incidence angle. The latter feature is due to the F_δ-factor in Eq. (12.28) and may influence how optimal settings should be chosen for maximum excitation.

Free space limit

In the free space limit, that is setting all refractive indices of the cavity layers to unity, we can benchmark the numerical Fourier transform by comparison to the analytical formula in the paraxial approximation given by Eq. (12.20). Results for a beam divergence of $\theta_{\mathrm{div}} = 1.1$ mrad are shown in Fig. 12.2, demonstrating excellent agreement. The remaining deviations are due to the finite Fourier grid.

Highly collimated limit

For the highly collimated case, the mode functions $\boldsymbol{\mathcal{E}}_s^0(z, \mathbf{k}_\parallel, \omega)$ are approximately constant over the relevant range of parallel wave vectors set by $E_{\mathrm{in}}(\mathbf{k}_\parallel, \omega)$. One can then factor out the mode functions from the integral, such that

$$\mathbf{E}(\mathbf{r},\omega) \approx \boldsymbol{\mathcal{E}}_s^0(z, \mathbf{k}_\parallel^{(\mathrm{in})}, \omega) \int d^2\mathbf{k}_\parallel e^{i\mathbf{k}_\parallel \cdot \mathbf{r}_\parallel} E_{\mathrm{in}}(\mathbf{k}_\parallel, \omega)\,. \tag{12.31}$$

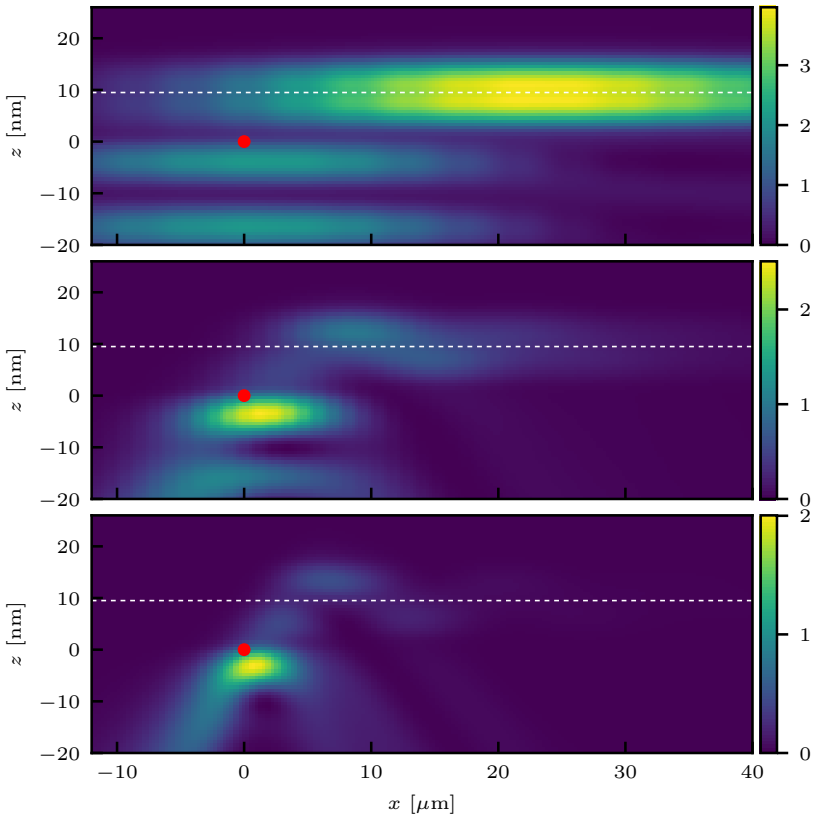

Figure 12.4: Resonant field intensities in and around the example cavity (cladding boundary at $z = 0$) for the beam divergences $\theta_{\text{div}} = 0.3, 1.1$ and 2.0 mrad (top to bottom). The location of the nuclear ensemble is shown as a white dashed line. The red dot indicates the beam focus, which is placed on the surface of the cavity.

The result is thus an envelope in the (x, y)-plane parallel to the cavity with a constant enhancement factor independent of the small beam divergence, which should correspond to the field intensity calculated in the layer formalism [Röh05b; Stu00; Hee19] (see also Chapter 2).

As a test, Fig. 12.3 illustrates the results of our algorithm in this limit for the example cavity. Comparison to the layer formalism [Röh05b; Hee19] shows that our algorithm yields the correct result.

Realistic focused beam

Finally, we apply the algorithm to a realistic focused beam incident on the example cavity, considering beam divergences bigger than the highly collimated case. Results for the beam divergences $\theta_{\text{div}} = 0.3, 1.1$ and 2.0 mrad are shown in Fig. 12.4. We see that as the beam divergence grows, the wavelike steady-state enhancement in the highly collimated limit turns into a more ballistic wavepacket transport. As a consequence, most of the intensity is reflected at the outer cladding for higher beam divergences, due to the varying cavity response over multiple modes. The resulting enhancement at the location of the nuclear ensemble is then much lower. This effect trades off with the decreasing spot size at larger focusing, which results in a higher field intensity of the bare beam.

In order to illustrate this trade-off, Fig. 12.5 shows the cavity enhancement as a function of beam divergence. We see that for low beam divergences up to around 1 mrad, the cavity improves the resonant excitation. At higher focusing, however, the cavity acts to reduce the intensity. While the free space beam intensity keeps scaling quadratically due to the spot size reduction, the cavity modified intensity levels off to a roughly constant value.

These results suggest that cavities may only have limited use at high focusing and the typical geometries used in x-ray cavity QED experiments should instead be thought of as an intensity booster at lower focusing capabilities. The central questions are then whether cavities are useful to increase the nuclear excitation at current focusing capabilities and, if so, whether this boost is sufficient to induce inversion at current photon numbers. We investigate these questions in the following section.

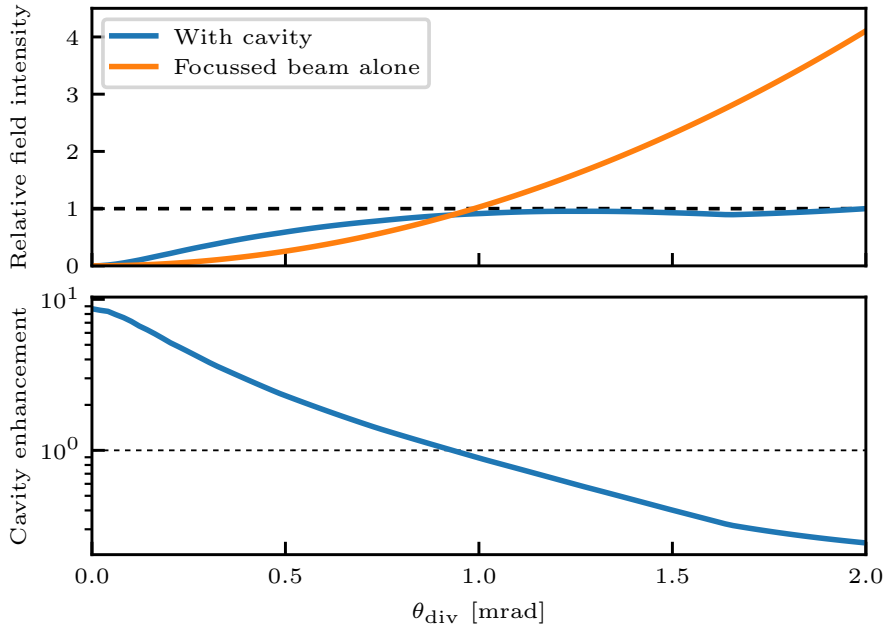

Figure 12.5: Cavity benefit as a function of beam divergence. (a) Peak relative field intensity at the nuclear ensemble position of the cavity modified beam (blue) and of the bare beam in free space (orange), normalized such that the cavity result is unity at a beam divergence of 2 mrad. (b) Corresponding intensity enhancement factor of the cavity. We see that for low beam divergences up to around 1 mrad, the cavity improves the resonant excitation. At higher focusing, however, the cavity acts to reduce the intensity. While the free space beam intensity keeps scaling quadratically due to the spot size reduction, the cavity modified intensity levels off.

12.5 Feasibility of inversion at current facilities

12.5.1 Results for beam parameters at the EuXFEL

In this section, we investigate the feasibility of inverting nuclear ensembles using focused x-ray beams from an XFEL source and thin-film cavities to boost the excitation. Note that this problem has already been considered in [HKE16], where the phenomenological model was used for this calculation. In the following, we use the algorithm introduced above, which is based on the ab initio theory in [Len20].

We consider the cavity structures suggested in [HKE16], one for each of the resonant elements ^{57}Fe, ^{193}Pt, ^{187}Os, ^{169}Tm and ^{119}Sn. Instead of the straightforward dependence on photon number, we investigate the trend of the total pulse area with beam focusing quantified by the spot size, where a value of π corresponds to full inversion [see Sec. 12.4.1].

Results are shown in Fig. 12.6. We consider beam parameters, including pulse lengths and photon numbers, as they are currently available at the EuXFEL, as specified in [Mad13; Nak14; Tsc17; Mad21]. While the inversion and cavity enhancement are plotted as a function of focusing, we indicate currently available values at each energy [Mad13] by vertical dashed lines. We note that the absolute scales of all numbers are preliminary results which are currently still being verified and mainly rely on the constant prefactor in Eq. (12.24). The functional trends and relative cavity enhancements, however, are reliable.

The left panel shows the results for free space, that is without a cavity. This plot is important to get a first idea of what regimes can be reached at current sources using available focusing techniques, and to identify if the cavity is actually advantageous for reaching inversion. We see that the numbers are promising and already at currently available focusing (around 40 nm beam diameter [Mad13; Nak14] for the transition energy of ^{57}Fe, ^{193}Pt, ^{187}Os and ^{169}Tm) and intensities, some of the isotopes can be inverted and others are in a regime where nonlinear effects may already start to kick in. Tighter nm-scale focusing is in principle feasible using Kirkpatrick-Baez mirrors [Dör13] or waveguides [Pfe02; Sal08; Oka12; Che21], however, their implementation at an XFEL is non-trivial. Our results indicate that such tight focusing may not be necessary and that existing setups may already be sufficient to access the nonlinear regime.

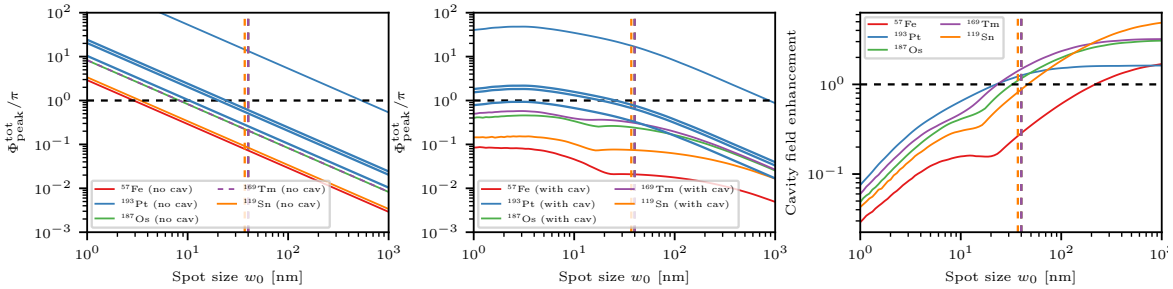

Figure 12.6: Feasibility of inverting nuclear ensembles at photon numbers available at the EuXFEL [Tsc17; Mad21; Mad13; Nak14]. Left: Nuclear pulse area as a function of focusing induced spot size. $\Phi^{\mathrm{tot}}_{\mathrm{peak}} = \pi$ corresponds to full inversion at the beam peak in the nuclear ensemble plane. For ^{193}Pt, multiple values for the internal conversion factor have been reported [HKE16] and are considered separately here. Middle: Corresponding inversion using the cavity structures from [HKE16]. Right: Field enhancement factor $\xi_{\mathcal{E}}$ induced by the cavity. Values bigger than unity indicate an improvement of the excitation by the cavity confinement. Vertical lines indicate currently available focusing strengths at each photon energy, as they are available at the MID or HED instrument of the European XFEL [Mad13; Nak14].

The middle panel shows the results when the ensembles are placed in the cavity structures from [HKE16] and illuminated at the relevant rocking minimum. We see that the magnitude of the pulse area is increased for large spot sizes, but in fact decreased for nanometer scale spot sizes. This observation is consistent with the behavior we observed for the test cavity in Fig. 12.5, where we observed that most of the intensity is reflected at the outer cladding for tightly focused beams [see Fig. 12.4].

The right panel shows the cavity enhancement to further confirm these observations. We see that for ^{187}Os, ^{169}Tm and ^{193}Pt, the considered cavities provide a slight but largely negligible enhancement at the available focusing of around 40 nm. In this context, we note that the cavity structures considered here have not yet been optimized for this purpose. Using optimization schemes currently being developed [Die21], the excitation boost provided by cavities may be further improved and could lead to a significant advantage compared to the free space case (see also the following discussion).

12.5.2 Discussion

In summary, it appears that nuclear inversion or near-inversion nonlinearities may already be within reach of current facilities. Using photon numbers and focusing currently available to users at the EuXFEL [Mad13; Nak14; Tsc17; Mad21], the pulse area is as high as 0.3π (30% of full inversion) for ^{187}Os and ^{169}Tm. For ^{193}Pt, the best case scenario for the internal conversion coefficient [HKE16] even lies significantly above the inversion threshold.

With regards to the role of cavities, the geometries considered here do not significantly boost the inversion at the relevant focusing strengths. However, optimization of the cavity geometry with the goal to boost excitation at 40 nm focusing may lead to further improvement. The current cavities are based on the geometries suggested in [HKE16], which were obtained by a phenomenological model optimization. Since the latter produces rather different results compared to our formalism, especially with regards to focusing [HKE16], a new optimization is expected to lead to a significant improvement. As we saw in Sec. 12.4.3, focused beams are mostly reflected at the outer cladding for tight spot sizes (see Fig. 12.4). This behavior implies that instead of the considered cavities, a geometry without cladding may be beneficial [Die21]. New cavity designs away from the standard cladding/guiding layer/cladding geometry may thus lead to significant further improvement and could potential push some of the considered Mössbauer isotopes over the inversion threshold.

We note that a very recent work theoretically proposes to use tapered waveguides as an alternative way to boost nuclear inversion [Che21]. The resulting tightly focused x-ray beam is shown to achieve spot sizes on the nm-scale. While such waveguide setups may require further development to implement for practical use at XFEL facilities, the inversion numbers in [Che21] are rather promising. The potential use of such tight focusing can also be seen from our calculation in Fig. 12.6, where the waveguide setup is expected to roughly correspond to the free space result at a reported beam radius on the few nm scale [Che21]. The waveguide setup therefore provides a promising alternative to the cavity case. Besides their difference in current implementability, the two approaches can also

be regarded as complementary, since tighter focusing not only leads to a desirable boost in inversion, but also to inverted ensembles with smaller number of nuclei. In addition, the waveguide setup does not provide the option to tune the nuclear level scheme, such that EIT [Röh12] or similar effects as they have been observed in x-ray cavities (see Chapter 2) may not be realizable. Potential avenues in both directions will be interesting to explore in the future, and also alternative nm-scale focusing schemes such as Kirkpatrick-Baez mirrors [Dör13] could prove useful.

Chapter 13

Decay dynamics within the ensemble Master equation

In the previous chapter, we have investigated the dynamics when the nuclear ensemble in the x-ray cavity is driven by an ultra-short pulse, which we called the excitation phase. We showed that due to the time scale set by the pulse length of typical x-ray sources, the quantum dynamical equations of motion of the Master equation developed in Chapter 7 are straightforwardly solved in semi-analytical fashion.

However, the decay dynamics of the nuclear excited state after the initial excitation phase are also of interest, since the experimentally accessible spectroscopic signatures are largely determined by the emitted radiation and its interference. These decay dynamics have previous been studied in [Hee14; HKE16] using the phenomenological XCQED model [HE13; HE15] — see Chapter 2 and Chapter 6 for a summary. As we have shown within the ab initio extensions described in Chapters 6, 7, this model is crucially based on the single parallel wave vector approximation. The investigation in [HKE16] is essentially based on the nuclear ensemble Master equation Eq. (7.18), which we can now derive precisely from ab initio theory, with an analytical algorithm to calculate its parameters.

In this chapter, we further study the nonlinear dynamics of the resulting Master equations within the single parallel wave vector approximation, providing alternative solution methods and extensions to the approach in [HKE16].

In Sec. 13.1, we briefly revisit the general structure of the pXCQED model [HE13; HE15], in particular considering collective operators and the ensemble Master equation beyond the linear regime, both of which are closely analogous to the ab initio version developed in Chapters 6 and 7.

In Sec. 13.2, we show that the solution method in [HKE16] can be extended to include the spontaneous emission terms by using the software package PIQS [Sha18] within the QUTIP ecosystem [JNN12; JNN13], which enables exact diagonalization of such models for relatively large spin numbers by exploiting their permutation symmetry. On the basis of exemplary calculations, we provide further evidence for the validity of the approximations used in Chapter 12 and their breakdown on longer time scales.

In Sec. 13.3, we develop an alternative method based on cumulant expansions [Bon98; KK17a; ZKR19; PHR21], which allows to access larger particle and ensemble numbers. In particular, we implement a PYTHON code which uses SYMPY [Meu17] and SYMPSI [JK] to symbolically derive the correlation function equations of motion for permutation symmetric models, truncated at a given cumulant order. The latter can subsequently be solved using, for example, standard functions within SCIPY [Vir20]. A publication of the code as an open source software package is envisioned, however, development is currently at an early stage. We note that our approach is largely analogous to a recent software package [PHR21] in the JULIA language, with the difference that we focus on the additional feature of exploiting the permutation symmetry.

We note that these methods were initially developed to investigate the nuclear decay dynamics of multi-ensemble systems such as the EIT cavities in [Röh12; HE15]. However, the insights from the ab initio formalism have shown that the single parallel wave vector approximation required to derive the ensemble Master equation [HKE16] may not be valid at nonlinear excitation. An outlook on this limitation and how to go beyond is given in Sec. 13.4.

As a consequence, the results presented in this chapter are largely of methodological nature, providing technical insight for future investigations of nuclear quantum dynamics in x-ray cavities. In addition, the cumulant expansion software in Sec. 13.3 implements a technique which is frequently used in optical quantum dynamics (see e.g. [KR15; KK17a; ZKR19]), complementing software solutions implementing exact diagonalization methods for permutation symmetric systems [GR17; Sha18].

13.1 Background - Structure of the nonlinear pXCQED model

The pXCQED model after adiabatic elimination of the cavity modes results in a Master equation for the nuclei of the form of Eq. (13.1). For a single ensemble, it reads

$$\frac{\mathrm{d}}{\mathrm{d}t}\rho^{(\mathrm{nuc})} = -i[H_{\mathrm{eff}}, \rho] + \mathcal{L}_{\mathrm{eff}}[\rho] \tag{13.1}$$

with [Hee14]

$$H_{\mathrm{eff}} = -\Delta \sum_n \hat{\sigma}_n^+ \hat{\sigma}_n^- - g^2 \delta_{\mathrm{LS}} \sum_{n,m} \hat{\sigma}_n^+ \hat{\sigma}_m^- + \sum_n (\Omega a_{\mathrm{in}} g \hat{\sigma}_n^+ + h.c.) \tag{13.2}$$

and [HE13]

$$\mathcal{L}_{\mathrm{eff}}[\rho] = -\zeta_S g^2 \sum_{n,m} \mathcal{L}[\rho, \hat{\sigma}_n^+, \hat{\sigma}_m^-] - \frac{\gamma}{2} \sum_n \mathcal{L}[\rho, \hat{\sigma}_n^+, \hat{\sigma}_n^-]. \tag{13.3}$$

For the general multi-ensemble case, a closely analogous form is obtained [see Eqs. (7.18, 7.19)].

In [HKE16], it was noted that all of these terms except for $\mathcal{L}_{\mathrm{SE}}[\rho] = -\frac{\gamma}{2}\sum_n \mathcal{L}[\rho, \hat{\sigma}_n^+, \hat{\sigma}_n^-]$ can be expressed using the collective operators [Hee14]

$$\hat{J}^+ = \sum_n \hat{\sigma}_n^+ \,, \tag{13.4}$$

$$\hat{J}^- = \sum_n \hat{\sigma}_n^- \,, \tag{13.5}$$

$$\hat{J}^z = \frac{1}{2}[\hat{J}^+, \hat{J}^-] \,, \tag{13.6}$$

which correspond to the spin wave operators introduced in Chapter 7 upon absorbing the coupling phase into an operator rotation [Hee14]. The Hamiltonian and Lindblad term can then be expressed as [HKE16]

$$\hat{H}_{\mathrm{eff}} = -\Delta \hat{J}^z - g^2 \delta_{\mathrm{LS}} \hat{J}^+ \hat{J}^- - \Omega a_{\mathrm{in}} g \hat{J}^+ + h.c. \,, \tag{13.7}$$

$$\mathcal{L}_{\mathrm{eff}}[\rho] = -g^2 \zeta_S \left(2\hat{J}^- \rho \hat{J}^+ - \{\hat{J}^+ \hat{J}^-, \rho\} \right) + \mathcal{L}_{\mathrm{SE}}[\rho] \,. \tag{13.8}$$

The full multi-ensemble versions given by Eqs. (7.18, 7.19) or Eqs. (6.42, 6.43) again feature an analogous structure with additional sums over the ensembles and their interactions.

In [HKE16], the above model was then solved numerically by neglecting the local spontaneous emission term $\mathcal{L}_{\mathrm{SE}}[\rho]$. This approximation results in the full Master equation only containing collective operators, such that the Hilbert space is restricted to the symmetric Dicke states [HKE16; Sha18]. Consequently, the many-body problem can be solved efficiently for relatively large numbers of nuclei [HKE16].

13.2 Solution using permutation symmetry and QUTIP-PIQS

In subsequent years, various methods which are helpful to extend the solution in [HKE16] were developed for investigations in the optical regime. In particular, the pXCQED model features a permutation symmetry (see [Sha18] and references therein). That is, the Master equation only features all-to-all couplings and decay terms, such that it is invariant under a relabeling $n \to m$ of the nuclear operator indices.

This symmetry results in efficient solution algorithms being directly applicable [GR17; Sha18]. In particular, the PIQS software package [Sha18] within the QUTIP ecosystem [JNN12; JNN13] implements an exact diagonalization method to solve the dynamics of such Master equations. Importantly, it can tackle relatively large numbers of spins and is even able to include the local spontaneous emission term $\mathcal{L}_{\mathrm{SE}}[\rho]$, which couples the symmetric Dicke ladder to other permutation symmetric states [Gar11; Sha18].

In order to illustrate the power of these software packages with regards to solving the Master equation of the pXCQED model, we present exemplary solutions in the following. In addition, one can use this approach to check the approximations used in Chapter 12. In particular, we will verify the time scale separation argument in order to confirm the ab initio solution of the excitation phase dynamics in Chapter 12.

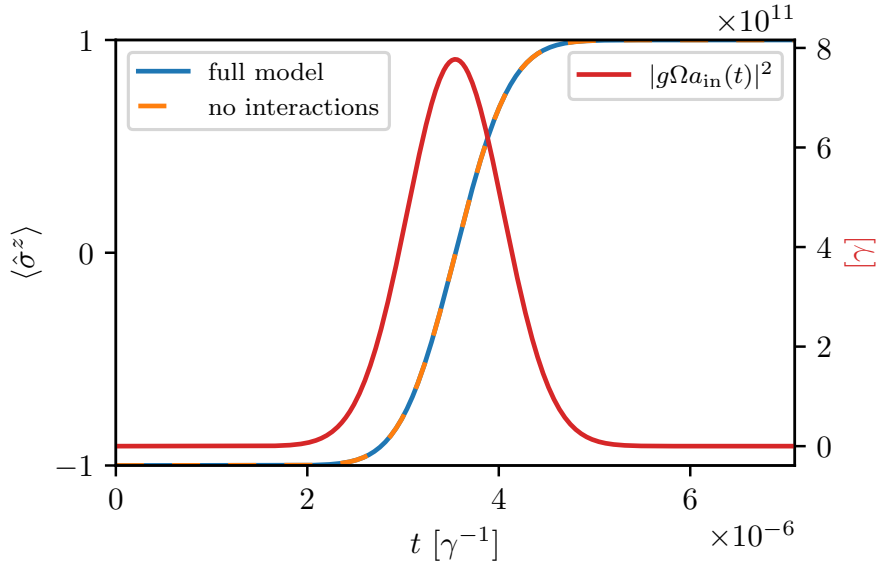

Figure 13.1: Excitation phase solution of the single ensemble pXCQED model (parameters see text). A Gaussian pulse with an amplitude chosen to achieve full inversion is applied (red curve, corresponding to right ordinate). The expectation value of the nuclear $\hat{\sigma}^z$-operator as a function of time is shown. The solid blue line shows the full model, the dashed yellow line corresponds to a calculation neglecting the interaction terms, which results in a single spin calculation analogous to Chapter 12.

As an example, we consider parameter values for $g, \zeta_S, \delta_{\mathrm{LS}}, \Omega$ as they were determined for the cavity geometry in [HE13; HKE16], with the incidence angle chosen to realize the Fano configuration $\Delta_C = \kappa$. We further choose $N = 100$, which is already in the collective regime and can be extrapolated to higher particle numbers using a scaling transformation [HKE16].

13.2.1 Interaction terms in the excitation phase

First, we solve the excitation phase of the model. Starting in the ground state, a Gaussian pulse is applied with the amplitude chosen to achieve full inversion of the ensemble. The resulting excitation dynamics are shown in Fig. 13.1. The solution of the full model given by Eqs. (13.7, 13.8) is shown together with a solution where all interaction terms are neglected ($\delta_{\mathrm{LS}} = \zeta_S = 0$), such that the nuclei are decoupled resulting in a single spin problem. We find that the two solutions agree very well. In Chapter 12, we used an analogous approximation for the real space ab initio version of the model. Since the two Master equations are closely related, both featuring coupled nuclear ensembles with the same interaction time scales, this comparison to a numerically exact solution provides further evidence for the time scale separation argument in Chapter 12. A main difference between the models is the single parallel wave vector approximation, which is, however, not expected to influence the applicability of the short pulse approximation.

13.2.2 Spectrum in the decay phase

As an additional illustration, we consider the dynamics in the decay phase of this model. The QUTIP-PIQS [Sha18] calculation then corresponds to the solution in [HKE16], but provides an extension by allowing to include the spontaneous emission term $\mathcal{L}_{\mathrm{SE}}[\rho]$.

As an observable, we again consider the coherent reflection spectrum [HKE16] (see also Chapter 5). Fig. 13.2 shows results for different degrees of inversion and calculation methods. At low excitation, we find that the full nonlinear solution closely matches the analytic linear result, as expected (see Chapter 6). For a pulse which excites a state close to inversion ($\langle\hat{\sigma}^z\rangle \approx 2/3$), a comparison between the full solution and the method used in [HKE16] neglecting $\mathcal{L}_{\mathrm{SE}}[\rho]$ also shows close agreement, confirming the validity of neglecting this term.

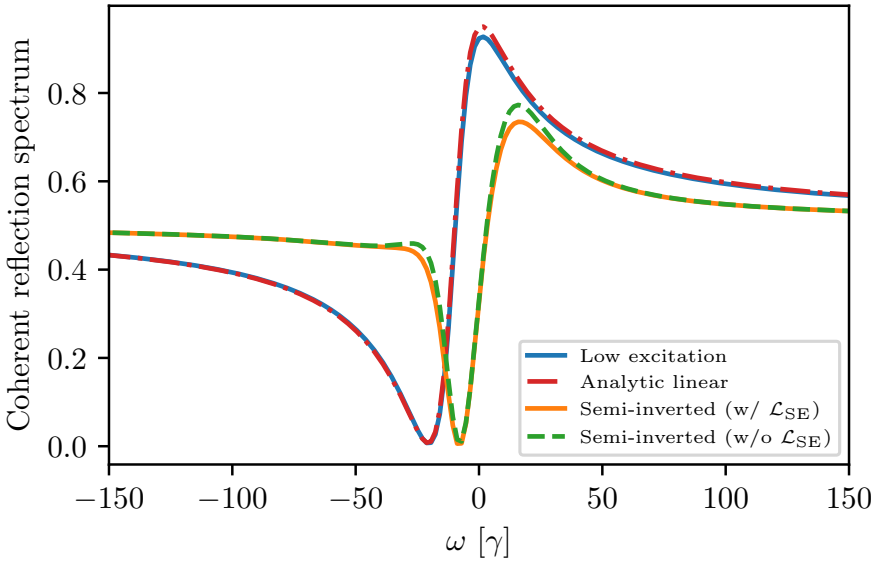

Figure 13.2: Coherent reflection spectra, resulting from the decay dynamics of the pXCQED model [HE13]. The calculation is closely analogous to [HKE16], but uses the permutation symmetric method of QUTIP-PIQS [Sha18] to solve the model. The solid blue line shows the nonlinear solution at low excitation, which closely matches the analytic linear solution (red dash-dotted). The solid yellow line shows the result for a pulse which excites the ensemble up to $\langle \hat{\sigma}^z \rangle \approx 2/3$, close to inversion. For comparison, the green dashed line shows the same scenario with the spontaneous emission term neglected, featuring close agreement with small quantitative deviations.

13.3 Symbolic cumulant expansions for permutation symmetric models

Despite already being able to solve the ensemble Master equation of the pXCQED model [HKE16] via exact diagonalization, there is further demand for alternative methods. For multiple Mössbauer ensembles, the number of nuclei per ensemble that can be feasibly tackled numerically using QUTIP-PIQS [Sha18] rapidly shrinks. In addition, the adiabatic elimination may not be appropriate for ultra-short pulses [HE15] when $\kappa \approx \tau_{\mathrm{pulse}}$ (see Sec. 2.3.2), such that the nuclei-only Master equation Eq. (13.1) may not be valid in the first place.

Both of these limitations can be addressed by considering the pXCQED model without adiabatic elimination, that is a Master equation of the form of Eq. (2.52) or its generalizations discussed in Chapter 6. Such models can be tackled by generalizations of mean-field theory, so-called cumulant expansions [Bon98], as they have been used extensively for investigations in the optical regime, such as in [KR15; KK17a; ZKR19; SBSF20], and recently also at higher energies [BMR19].

13.3.1 Cumulant expansion method

Recently, a software package has been implemented in the JULIA language, which symbolically computes cumulant expansions for general Master equations and solves the resulting nonlinear equations of motion numerically [PHR21]. The approach is similar to our method, which additionally exploits permutation symmetry as outlined in Sec. 13.3.2. In the following, we firstly summarize the general idea of cumulant expansions, largely following the presentation in [ZKR19; PHR21].

Our starting point is a general Master equation

$$\frac{\mathrm{d}}{\mathrm{d}t}\rho = -i[H,\rho] - \sum_i \gamma_i \mathcal{L}[\rho, \mathcal{O}_i^+, \mathcal{O}_i^-]\,, \tag{13.9}$$

where $\mathcal{L}[\rho, \mathcal{O}^+, \mathcal{O}^-] = \mathcal{O}^+\mathcal{O}^-\rho + \rho\mathcal{O}^+\mathcal{O}^- - 2\mathcal{O}^-\rho\mathcal{O}^+$ and the index runs over different loss processes.

The Master equation can alternatively be represented in the Heisenberg picture as [PHR21]

$$\frac{\mathrm{d}}{\mathrm{d}t}\langle\mathcal{O}\rangle = i\langle[H,\rho]\rangle - \sum_i \gamma_i \langle \mathcal{O}_i^+\mathcal{O}_i^-\mathcal{O} + \mathcal{O}\mathcal{O}_i^+\mathcal{O}_i^- - 2\mathcal{O}_i^+\mathcal{O}\mathcal{O}_i^-\rangle \tag{13.10}$$

for a general operator $\mathcal{O}$.

For models such as the pXCQED model, the relevant operators are the spin-operators $\hat{\sigma}^{\pm/z}$ for the nuclei and the mode operators $\hat{a}$, , $\hat{a}^\dagger$. However, one finds that the expectation value equations of motion are not closed at the first operator order [Bon98]. For example, the time derivative of $\langle\hat{\sigma}^z\rangle$ will be related to second-order correlation functions such as $\langle\hat{\sigma}^+\hat{a}\rangle$. The resulting infinite set of coupled correlation functions is known as the BBGKY hierarchy [Bon98].

The commonly used mean-field theory (see also Chapter 2 for the related Maxwell-Bloch approach) then approximates second-order correlation functions as [ZKR19]

$$\langle\mathcal{O}_1\mathcal{O}_2\rangle \approx \langle\mathcal{O}_1\rangle\langle\mathcal{O}_2\rangle\,. \tag{13.11}$$

This idea can be generalized to higher orders by so-called cumulant expansions [Kub62; ZKR19], where in general one approximates the cumulant [ZKR19]

$$\langle\mathcal{O}_1\mathcal{O}_2\rangle_c \approx 0\,. \tag{13.12}$$

This approximation is motivated by the definition of cumulants, which implies that they are zero if the operators are statistically independent [Kub62]. At first order, $\langle\mathcal{O}_1\mathcal{O}_2\rangle_c = \langle\mathcal{O}_1\mathcal{O}_2\rangle - \langle\mathcal{O}_1\rangle\langle\mathcal{O}_2\rangle$ [ZKR19], such that mean-field theory is reproduced. At higher order, the cumulants can be expressed by general formulas [Bon98] to provide an approximation for nth order correlation functions in terms of lower orders [PHR21].

In [PHR21], this approach is implemented in the JULIA language using symbolic algebra to obtain the equations of motion at a given truncation order. In the following, we outline how the resulting equations can be simplified for permutation symmetric models and implement an algorithm for this purpose in PYTHON [VRDJ95].

13.3.2 Permutation symmetric cumulant expansion

An interesting aspect is that the cumulant expansion method interfaces nicely with permutation symmetric models, as has been used for example in [KK17a]. In particular, if a model is permutation symmetric (meaning that both the Master equation and initial state obey the symmetry) over the index s of an operator family $\hat{A}_s$, one finds that

$$\langle\hat{A}_{s_1}\hat{A}_{s_2}\dots\hat{A}_{s_n}\mathcal{O}_1\mathcal{O}_2\dots\rangle = \langle\hat{A}_{\tilde{s}_1}\hat{A}_{\tilde{s}_2}\dots\hat{A}_{\tilde{s}_n}\mathcal{O}_1\mathcal{O}_2\dots\rangle\,, \tag{13.13}$$

for any set of indices $\{\tilde{s}_1,\tilde{s}_2,\dots\tilde{s}_n\}$, as long as $\tilde{s}_i = \tilde{s}_j$ if $s_i = s_j$. Consequently, one can simplify sums over the indices as

$$\sum_{s_1\neq s_2,s_3,\dots s_n} \langle\hat{A}_{s_1}\hat{A}_{s_2}\dots\hat{A}_{s_n}\mathcal{O}_1\mathcal{O}_2\dots\rangle = (N-n+1+m)\langle\hat{A}_{s_1}\hat{A}_{s_2}\dots\hat{A}_{s_n}\mathcal{O}_1\mathcal{O}_2\dots\rangle\,, \tag{13.14}$$

where N is the number of operators in the family $\hat{A}_s$, m is the number of duplicate operators in $\{s_2,s_3,\dots s_n\}$, and $n < N+1$.

This property is useful, since it allows to reduce sums of the above form to a constant times one of the summed observables, which are all equal. For many-particle systems, this results in a tremendous reduction of the size of the cumulant expanded equation system [KK17a]. Since already the cumulant expansion method alone allows to treat spin numbers much larger than by directly solving the Master equation via exact diagonalization [PHR21], the combination with permutation symmetry allows the scaling to only depend on the truncation order and number of permutation symmetric operator families. For such models, this approach thus completely eliminates the scaling with particle number [KK17a].

13.3.3 Symbolic algebra implementation

The approach has been implemented using the symbolic algebra package SYMPY [Meu17] in combination with the operator algebra package SYMPSI [JK]. To be able to symbolically simplify the equations

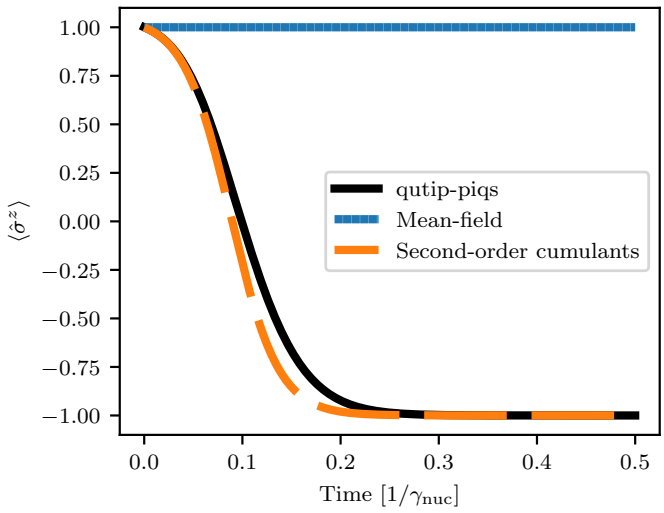

Figure 13.3: Benchmark of the symbolic cumulant expansion method by solving the dynamics of a nuclear ensemble in an x-ray cavity according to the model in [HKE16]. The blue line shows the mean-field result, which features no dynamics for the fully excited state. The orange dashed line shows the second-order cumulant expansion result. The solid black line shows a benchmark obtained using exact diagonalization of the adiabatic version of the model, which is calculated with QUTIP-PIQS [Sha18].

of motion for permutation symmetric models, we defined a sum operator and a correlation operator class with associated algebra rules.

A *sum operator object* contains the following attributes.

- A name as an identifier.
- A list of strings defining the indices which are summed over.
- A correlation operator instance.
- A list of SYMPY symbols defining the number of operators each summed index runs over.
- A truth value to indicate whether the summed indices feature a permutation symmetry or not.

A *correlation operator object* in turn contains the following attributes.

- A name as an identifier.
- A list of strings defining operator indices.
- A list of operators corresponding to each index.
- Another list of strings defining scalar indices.
- A list of symbols for coupling parameters corresponding to each scalar index.

The *algebraic rules* implemented in these objects in particular simplify products of any combination of correlation operators and sum operators. Summed indices and commutation relations of the contained operators are handled separately, with the latter already being implemented in SYMPSI [JK]. If the permutation symmetry option is activated, the rule given by Eq. (13.14) is further applied successively.

An open source publication of the resulting software package is envisioned, however, development is currently at an early stage. In the following, we provide a simple example featuring a code snippet and apply it to solve decay dynamics in the pXCQED model [HE13; HKE16].

13.3.4 Example and benchmark

To demonstrate the working of the algorithm, we provide a simple code example in the following. We consider the simple Hamiltonian

$$H = \sum_{s=1}^{N} \left(g_s \hat{\sigma}_s^- \hat{a}^\dagger + h.c. \right) \tag{13.15}$$

and Lindblad term

$$\mathcal{L}[\rho] = -\kappa \mathcal{L}[\rho, \hat{a}^\dagger, \hat{a}] - \frac{\gamma}{2} \sum_{s=1}^{N} \mathcal{L}[\rho, \hat{\sigma}_s^+, \sigma_s^-] \,, \tag{13.16}$$

which together realize the pXCQED model with $\Delta_C = \Delta = a_{\text{in}} = 0$.

Using the symbolic algorithm, the resulting cumulant equations of motion can be computed automatically using the sum operator [`SumOp()`], correlation operator [`CorrOp()`] classes and a function that symbolically computes the equations of motion [`get_eoms_numeric()`]. For the simple Hamiltonian and Lindblad term above, the following code sample symbolically computes the equations of motion at truncation order two, corresponding to mean-field theory.

```
# Define symbols and operators #
g, κ, γ, t, x, Hsym, N = symbols(r"g, κ, γ, t, x, H, N", positive=True)
t = symbols(r't')
σx, σy, σz, σm, σp = SigmaX(), SigmaY(), SigmaZ(), SigmaMinus(), SigmaPlus()
a = BosonOp("a")

# Hamiltonian #
H = 0
H += SumOp('e1', ['s'], CorrOp('e1', ['s', ''], [σp,  a], ['s'], [g]), [N])
H += SumOp('e1', ['s'], CorrOp('e1', ['s', ''], [σm, Dagger(a)], ['s'], [g]), [N])

# Lindblad terms #
L_ops = [ [σp, σm, 1, γ/2], [Dagger(a), a, 1, κ] ]

# Generate symbolic equations of motion #
obs1 = [CorrOp('e1', ['k'], [σz], [], []),
        CorrOp('e1', ['k'], [σm], [], []),
        CorrOp('e1', [''], [a], [], []),]
params = [ΔC, Δ, κ, N, g, γ, η]
truncation_order = 2
obs, eoms_num, eoms_sym = get_eoms_numeric(H, L_ops, obs1, params, truncation_order)
```

The result is a list of observables and the corresponding nonlinear equations for the time derivates, which can be printed as LaTeX code to give

$$\left[{\sigma_z}^{[s]}, {\sigma_-}^{[s]}, a \right] \tag{13.17}$$

and

$$\left[-2iO_a g \overline{O_m} + 2iO_m g \overline{O_a} - O_z \gamma - \gamma, \, iO_a O_z g - \frac{O_m \gamma}{2}, \, -iNO_m g - O_a \kappa \right] , \tag{13.18}$$

respectively. The notation uses $\langle \hat{\sigma}_s^{-/z} \rangle = {\sigma_{-/z}}^{[s]} = O_{m/z}$, $\overline{O_m} = O_m^* = \langle \hat{\sigma}_s^+ \rangle$, $\langle \hat{a} \rangle = a = O_a$ and $\overline{O_a} = O_a^* = \langle \hat{a}^\dagger \rangle$. Similar expressions can be obtained for arbitrary truncation order and the resulting equations can be parsed into numerical form to be interfaced with, for example, SCIPY solvers [Vir20].

For illustration, we numerically solve the resulting cumulant equations for $N = 40$, $\kappa = 45\xi\gamma_{\text{nuc}}$, $g = 30\xi\gamma_{\text{nuc}}$ and $\gamma = 0$, which corresponds to the values for an x-ray cavity used in [HKE16]. We consider the case without a driving field and an initial state where the nuclear ensemble is fully

excited. This setup corresponds to a variant of the Dicke type model for superradiant decay within the rotating wave approximation [Dic54; Sha18]. As a benchmark, we use QUTIP-PIQS [Sha18] to solve the same model within the adiabatic approximation (see also Sec. 13.2).

The resulting solution for the nuclear $\hat{\sigma}^z$-operator expectation value is shown in Fig. 13.3. We see that the mean-field equations do not capture the dynamics at all, since the fully excited state requires higher-order correlations to start decaying at a finite time in this model [BP70]. The second order cumulant equations, however, provide a reasonable approximation of the QUTIP-PIQS [Sha18] result. We also note that this decay problem is one of the worst-case scenarios for mean-field theory and cumulant expansions, since the fully excited state has highly non-classical properties with regards to the decay dynamics [ZKR19]. For lower-lying states or in the presence of photons from a driving pulse, the cumulant expansion is expected to provide a much better approximation.

We have chosen this particular setting here to illustrate the breakdown of mean-field or Maxwell-Bloch type approaches in the decay phase of nuclear cavity QED, when highly excited states are reached. This investigation provides another perspective on the arguments provided in Chapters 2 and 12.

13.4 Outlook - Beyond the ensemble Master equation

13.4.1 The single parallel wave vector approximation as a limitation

In this chapter, we have developed and applied theoretical methods to solve the nuclear dynamics within the pXCQED model [HE13; HE15; HKE16] or its ab initio version in the form of the ensemble Master equation. While this approach allowed us to confirm the validity of approximations also employed in the ab initio approach in Chapter 12, we have mainly presented methodological progress without direct physical insights into nuclear decay phenomena. The reason is that the ab initio theory in Chapters 7 and 12 suggest that the pXCQED model may not be applicable to describe the decay of highly excited nuclear ensemble states, as we discuss in the following.

In Chapters 6 and 7, we have shown that the central approximation in obtaining the Master equation of the pXCQED model is the single parallel wave vector approximation. The latter can be most straightforwardly applied in two scenarios.

First, we have seen that the approximation is well valid in the linear regime and reproduces the results of the semi-classical layer formalism (see Chapter 8). This agreement was explained by noting that the parallel wave vector is a conserved quantity in the linear regime. Consequently, when a highly collimated beam excites the system, the dynamics are confined to the subspace selected by the incident field (see Chapter 7).

Second, the approximation also applies in the excitation phase if the driving pulse is highly collimated. In this case, the nonlinear dynamics are dominated by the driving field (see Chapter 12 and Sec. 13.2.1), which again only drives the subspace of the nuclear ensemble selected by the parallel wave vector.

In the decay phase and for higher excitation, neither the linear regime is realized nor an ultra-short driving pulse is present. In this case, the single parallel wave vector approximation is likely to break down, as can be seen from the derivation in Chapter 7, where the linear approximation is explicitly necessary to derive the ensemble Master equation. Indeed, this breakdown can also be expected from the structure of the pXCQED model itself. The parameters of the nuclear Master equation Eq. (13.1) depend on the incidence angle [HE13; HKE16] and hence on the parallel wave vector of the incident field. However, if we consider an initial state with a fully excited ensemble and no photons, there is no information about an incident field, since this state has no phase relation across the nuclear ensemble ($\langle\hat{\sigma}^{\pm}\rangle = 0$). Since the fully excited state can in principle be reached using any incidence angle (see Chapter 12), the pXCQED model thus predicts contradicting decay dynamics for the fully excited state of the nuclear ensemble. This inconsistency is a direct consequence of the breakdown of the single parallel wave vector approximation.

In [HKE16], this issue was already partially discussed by noting that the local spontaneous emission term couples the symmetric Dicke ladder to other states. In this language, the above argument and the derivation in Chapter 7 demonstrate that not only the spontaneous emission, but also the Hamiltonian contribution induces such a coupling.

13.4.2 Outlook and possible approaches

The single parallel wave vector approximation therefore potentially imposes limitations on the applicability of the ensemble Master equation to describe nonlinear nuclear quantum dynamics in thin-film cavities during the decay phase. We note that the model may still enable further progress in dynamical sectors where the approximation is applicable, such as for the excitation phase or for the decay phase of few-excitation states [LoE14b]. In particular for the decay dynamics of highly excited states, however, it is expected that alternative approaches will be required.

The real space Master equation Eq. (12.1) outlined in Chapter 12 constitutes an ideal starting point for investigations in this direction, since the main assumption entering it is the Born-Markov approximation, which is well valid for nuclear ensembles. As a first possible approach, the resulting many-body problem may be tractable directly using methods similar to the cumulant expansions discussed in Sec. 13.3 or related techniques from the field of open many-body systems [SBD16; Kir19; Cha18; Dha18; Sca21; RSG21]. Alternatively, multiple parallel wave vectors could be accounted for to generalize the ensemble Master equation Eq. (13.1). Such methods are particularly promising to study the few-excitation sector and results in this direction have already been presented in [LoE14a; LoE14b]. Another potentially directly applicable method is given by a recent study in the context of organic polariton lasing [Arn20], which also considers a two-dimensional layered cavity geometry and provides a parallel wave space solution method that is applicable at higher excitation.

While in this thesis, we have resolved various questions with regards to quantum dynamical models for nuclei in thin-film x-ray cavities, the highly excited sector of nuclear x-ray quantum optics therefore remains largely unexplored. Consequently, there is much more to be discovered and further theoretical development is potentially required to understand upcoming experiments at XFEL facilities [RE21], as we discuss in Chapter 15.

Part V

Experimental aspects

Chapter 14

Bayesian inference for multi-dimensional Mössbauer spectroscopy

This chapter outlines a statistical analysis method developed by the thesis author, which was employed in the following publication:

Coherent X-ray-optical control of nuclear excitons
K. P. Heeg, A. Kaldun, C. Strohm, C. Ott, R. Subramanian, D. Lentrodt, J. Haber, H.-C. Wille, S. Goerttler, R. Rüffer, C. H. Keitel, R. Röhlsberger, T. Pfeifer, and J. Evers
Nature **590**, 401 (2021)

14.1 Background - Synchrotron Mössbauer spectroscopy

In this chapter, we consider an aspect of data analysis in synchrotron Mössbauer experiments, employing Bayesian inference techniques to evaluate how well a particular theory model or parameter set describes given measured spectra.

The most straightforward observable to measure in coherent elastic nuclear resonant scattering is the time spectrum [Röh05b; HT99]. It is obtained by hitting the target with an x-ray pulse and measuring the light intensity $I(t)$ or photon counts $n(t)$ as the nuclear exciton decays [Röh05b]. This observable is already useful for numerous applications and allows access to various material parameters [Röh05b; YL21].

However, due to the inaccessibility of the x-ray phase, the time spectrum does not provide spectral information [Röh05b]. To circumvent this issue, energy spectra are recorded using an analyzer mounted on a so-called Mössbauer drive for a heterodyne detection scheme [Röh05b]. The resonances in the analyzer are then Doppler-shifted by a motion of the drive, which is of constant velocity on the nuclear decay time scale. The target spectrum is then essentially scanned with a spectral "sensing head" [HE20]. Due to practical limitations, typical experiments employing this approach set a finite electronic integration window [Röh05b] to sum up the photon counts in a given time range. The information which is recorded is then only the number of photons in that time range at a given Mössbauer detuning Δ_D, that is $I(\Delta_D) = \int_{t_0}^{t_1} dt I(t, \Delta_D)$ [Hee14]. By appropriately choosing the time range $[t_1; t_2]$, one can obtain pseudo-spectra which can provide good approximations of the target spectrum and have been used extensively in Mössbauer spectroscopy (see [Hee14; Röh05b] and references therein). Due to a time scale separation argument, for broad target spectra, such as cavity samples featuring superradiance, this window is usually chosen at relatively late times, where the signal resulting from scattering off the target only has decayed sufficiently [Hee14], such that the spectral information can ideally be extracted directly. Note that there are various advanced Mössbauer spectroscopy techniques related to this heterodyne detection method [Röh05b; YL21] and alternative [Smi07], which we do not discuss here in detail.

More recently, an event-based detection system has been employed to measure the full spectrum $I(t, \Delta_D)$, with time and energy information as well as overall experimental time stamps recorded for each photon click [Hee15b; Hee17; Hee21]. This two-dimensional spectrum contains the information of a time and a Mössbauer drive spectrum at the same time, rendering it extremely useful for data analysis in complex setups, which has particularly been employed in recent coherent control experiments using piezoelectric actuators [Hee17; Hee21]. An early use of similar spectra is reported in [Cal05].

Access to such multi-dimensional Mössbauer data has sparked interest in how to extract maximum information and observables therefrom. In the context of the two-dimensional event-based detection, the option of setting integration ranges in the time domain [Hee17; Hee14] has been used to obtain multiple one-dimensional pseudo-spectra that could be used for fitting. This approach extends the concept of late-time integration explained above [Röh05b] by allowing a variable integration range [Hee14], which can be optimized. In addition, methods for x-ray phase extraction [HE20] and piezo-motion reconstruction [Hee17; Ger21] based on these or even higher-dimensional spectra have recently sparked interest, extending earlier works in this direction [Cal05]. Direct numerical algorithms to extract such information based on ptychography have also been investigated [Hab16b].

At this stage, most of these methods still involve a fitting routine, comparing the experimental spectra to theoretical calculations in one way or another [Hee17; Hee21; Heu21; Ger21]. Consequently, it is an important question to understand how to statistically evaluate the data in comparison to theory. In this context, we note that the previous methods using multiple or optimized pseudo-spectra for fit evaluation still discard much of the information that is encoded in the two-dimensional spectrum, such that the statistical analysis methods deserve further attention.

In this chapter, we show how statistical inference techniques can be used to employ the entire two-dimensional spectrum in a fitting routine to extract maximum information from the data. Our method is not directly an analysis method for a particular experiment, but rather provides a basic statistical framework for typical analyses which employ fits to such multi-dimensional Mössbauer spectra. In particular, the method allows to calculate a number that indicates how good the theoretical fit of the data is, assuming certain underlying noise processes. The approach is based on the Bayesian maximum likelihood method [Jay03; SS06], which is well studied in the context of counting experiments [HJ01] and which has already been used in nuclear resonance scattering in the context of parameter estimation[Cal05].

14.2 Poisson metric for time-energy spectra

14.2.1 Method

The experimental data set from the two-dimensional spectroscopy is given by the photon count distribution $n_{\mathrm{exp}}(t_i, v_i)$, where the index i labels combined time and energy bins with t_i (v_i) the corresponding time (Mössbauer drive velocity). Typical time resolutions in the experiments performed at synchrotron facilities [Hee17; Hee21] are on the order of 1 ns, limited by the electronics setup. The resolution of the Mössbauer drive velocity v can be adjusted, but is typically given by the required spectral range and limited number of bins in the data acquisition system. For cavity experiments with a superradiant linewidth of around a hundred γ, typical choices are on the order of one γ.

We note that the detection system in [Hee17; Hee21] also records event-based data, such as time stamps of each recorded photon. This information is useful e.g. for dividing the data into total experiment time intervals, which has been used to characterize the interferometric stability of forward scattering setups [Hee21]. In the photon number distribution $n(t_i, v_i)$, this event-based information is not included.

On the theoretical side, one can compute the two-dimensional intensity distribution $I(t, v)$ via Fourier transforms of the target response function [Hee14]. This calculation requires the knowledge of the samples and their parameters. Further information, such as the properties of the analyzer foil, is often required. Such information can be obtained via calibration measurements, where one-dimensional time spectra and standard fitting routines as implemented in CONUSS [Stu00] can usually be employed.

For a typical fitting procedure, one then varies the sample parameters and compares the theoretical spectrum to the experimental data until a best-fit result is found. The method presented in the following constitutes an evaluation strategy to characterize how well the theoretical spectrum represents the data, and can be used for one- or multi-dimensional data sets.

From a statistical perspective, the counts in each bin i are influenced by various statistical and systematic error sources. To name a few, possible fluctuations may include binning errors for each photon, beam variations, experimental backgrounds or dirt effects and many more setup dependent errors.

One important source of fluctuations is the statistical noise associated with photon counting, given by Poissonian shot noise [HJ01]. For the experiments at synchrotron facilities mentioned above

[Hee17; Hee21; Heu21], the latter is expected to be the main source of errors if systematic errors are eliminated.

For Poissonian shot noise, the number of photons in each bin will be distributed according to the conditional likelihood distribution [Hee21]

$$P(n_{\mathrm{exp},i}|n_{\mathrm{theo},i}) \propto (n_{\mathrm{theo},i})^{n_{\mathrm{exp},i}} \frac{e^{-n_{\mathrm{theo},i}}}{n_{\mathrm{exp},i}!} \,. \tag{14.1}$$

That is, if we theoretically predict $n_{\mathrm{theo},i}$ photon counts in bin i, we have a probability $P(n_{\mathrm{exp},i}|n_{\mathrm{theo},i})$ of measuring $n_{\mathrm{exp},i}$ photons in that bin.

Over the whole data set, we can assume each bin to be distributed independently, such that [Hee21]

$$P(\mathrm{exp}|\mathrm{theo}) = \prod_{i \in \mathrm{data\ bins}} P(n_{\mathrm{exp},i}|n_{\mathrm{theo},i}) \,. \tag{14.2}$$

We can then compute the probability $P(\mathrm{exp}|\mathrm{theo})$ of obtaining our experimental data given a theoretical prediction based on the sample parameters.

However, we have the experimental data as a given and instead of calculating their statistical distribution, we would like to evaluate how well the theoretical parameters fit the measured experimental data. To this end, the reversed conditional likelihood can be obtained via Bayes theorem [Jay03]

$$P(\mathrm{theo}|\mathrm{exp}) = P(\mathrm{exp}|\mathrm{theo}) \frac{P(\mathrm{theo})}{P(\mathrm{exp})} \,. \tag{14.3}$$

Assuming uniform priors [SS06], we then have [Hee21]

$$P(\mathrm{theo}|\mathrm{exp}) \propto P(\mathrm{exp}|\mathrm{theo}) \,. \tag{14.4}$$

The uniform prior assumption is a simple way to encode the absence of additional information about the data. However, for problems such as the comparison of models with a different number of parameters, including prior information may be necessary to penalize overfitting [SS06].

A standard way to determine the statistically optimal sample parameters is then to maximize the likelihood $P(\mathrm{theo}|\mathrm{exp})$ [Jay03; SS06]. For our purposes, this quantity constitutes a metric for evaluating how good a particular fit is, which refer to as goodness of fit or fitness in the following. Practically, it can be convenient to consider the logarithm of the likelihood [SS06] in order to avoid the numerical multiplication of small numbers, which turns into a sum when the logarithm is used.

Note that the theory usually predicts intensities $I(t, v)$ instead of photon counts. In order to translate to photon numbers, one can normalize such that the bin integrated theory intensity corresponds to the total number of counts.

14.2.2 Comparison to Gaussian metric and least squares

To provide intuition, we compare the Poisson metric to an analogous Gaussian metric, which is the basis for the more common least squares comparison. The latter assumes that the bin likelihood distribution is given by a Gaussian distribution [Jay03; SS06]

$$P(n_{\mathrm{exp},i}|n_{\mathrm{theo},i}) \propto \exp\left(-\frac{(n_{\mathrm{exp},i} - n_{\mathrm{theo},i})^2}{2\sigma_i^2}\right) , \tag{14.5}$$

where σ_i is the standard deviation for the bin.

Taking the log-likelihood over all bins as previously, we see that the maximum likelihood method corresponds to minimizing the least squares sum [SS06]. A priori, however, it is unclear how to choose the error weights σ_i. In the case of the Poisson distribution, no additional such parameter is necessary. If we choose $\sigma_i = \sqrt{n_{\mathrm{theo},i}}$, which is the standard deviation of the Poisson distribution, the two distributions are approximately identical for large photon numbers. For small photon numbers, however, where the discreteness of the photon counting is statistically relevant, the two distributions differ.

In the case of the two-dimensional Mössbauer spectra, we have the particular feature that the count number exponentially decays along the time axis. This means that at large times, we have much lower statistics than at small times. However, as we know from the standard late-time integration method to determine energy spectra [Röh05b; Hee14] discussed in Sec. 14.1, the late-time region contains

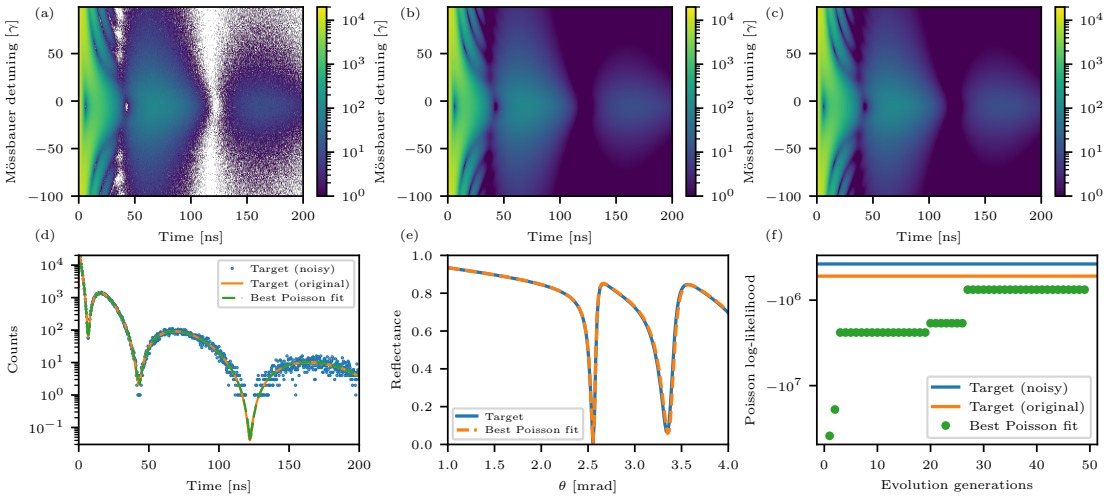

Figure 14.1: Basic benchmarks of the Poisson metric for a cavity target. (a-c) 2D Mössbauer spectra. The color axis shows counts, sampled such that there are $8 \cdot 10^6$ detected photons in total. (a) Simulated data, obtained by Poisson sampling the theoretical spectrum of the target cavity (b). (c) Fitted spectrum, using the evolutionary algorithm from [Hee17; Hee21] in combination with the Poisson metric as a goodness of fit measure. (d) Time slice at zero Mössbauer detuning, showing that the best Poisson fit perfectly captures the target spectrum (see legend). (e) Theoretically calculated rocking curves of the target and of the best fit cavity (see legend). (f) Poisson metric with increasing number of evolution generations. The fit gradually improves, featuring plateaus whenever a generations fails to find a better fit. Two baselines are shown, where the blue line represents the Poisson metric of the noisy target data itself. This value is the best possible value and only obtained if every data point is perfectly predicted by the theory, which is impossible practically due to statistical noise. The orange line corresponds to the Poisson metric of the theoretical target spectrum, which is obtained if the fit finds the perfect cavity parameters. We see that the Poisson metric correctly ranks each case, such that a fit routine can in principle perfectly invert the statistical sampling process (details see text, including a discussion of the insights from this idealized benchmark).

valuable information on the sample-analyzer interference and hence the energy spectrum. For a correct analysis, it is therefore important to weight the early and late-time data correctly, even at low count numbers per bin. If no other noise sources or systematic errors influence the data, the Poisson metric is the correct statistical tool to perform this analysis. While the Gaussian metric often converges to the same fit, it can also overemphasize certain regions of the spectra. In particular for the Allan deviation analysis in [Hee21], the Poisson metric proved advantageous, producing the minimal Allan deviation due to its extraction of maximum information from the data.

14.2.3 Benchmarking

In order to test the working of the Poisson metric, we perform some simple theoretical benchmarks. The central claim to verify is that, in the ideal case where the noise sources are perfectly known, the Poisson metric can indeed be used to fit a 2D Mössbauer spectrum with Poisson noise.

To this end, we consider an exemplary target cavity given by a Pt (2.35 nm)/C (13.5 nm)/^{57}Fe (0.6 nm)/C (13.5 nm)/Pt (13.0 nm)/Si layer stack. We first compute a 2D theory spectrum using PYNUSS [Hee19]. We then generate synthetic photon count data by Poisson sampling the theory spectrum at the first rocking curve minimum on a grid of time-energy bins. That is, each bin i contains n_i photons with a probability of $P(n_i|n_{\mathrm{theo},i})$ according to Eq. 14.1. The theoretical target cavity spectrum and the resulting noisy synthetic data are shown in Fig. 14.1 (b) and (a), respectively. The data then constitutes an idealized synthetic version of what would be obtained in a typical synchrotron experiment (see e.g. [Hee15b]).

For the fitting procedure, we then treat the thickness of each layer as unknown parameters. We use the evolutionary algorithm from [Hee17; Hee21] with 50 generations to fit these parameters to the data. Crucially, the Poisson metric is used to evaluate how good a theoretical spectrum based on random parameters tested during the algorithm fits the synthetic experimental data.

Results are shown in Fig. 14.1 (c-f). The two-dimensional spectrum and a slice at zero Mössbauer detuning show that the best fit provides excellent agreement. Interestingly, also the rocking curve of

the target cavity is perfectly reproduced when calculated from the reconstructed cavity parameters, even though the noisy data only contains information about a single incidence angle. The best-fit cavity was obtained as Pt (2.38 nm)/C (13.47 nm)/^{57}Fe (0.57 nm)/C (13.41 nm)/Pt (13.07 nm)/Si, which agrees with the target cavity on the sub-nanometer level.

Fig. 14.1 (f) shows the Poisson fitness with increasing number of evolution generations. This plot illustrates the working of the metric. With each generation, there is a chance that a better fit is found such that the Poisson metric increases in a plateau-like fashion. In addition, the figure shows two special values of the Poisson metric. The blue line shows the fitness for the noisy data itself as a reference line [Heu21], that is $\log[P(\text{data}|\text{data})]$. The latter constitutes the best possible value, which would be obtained if the theory predicted every single data point perfectly. Due to the statistical noise, this is of course practically impossible. The orange line shows the fitness of the target cavity without noise, that is $\log[P(\text{target}|\text{data})]$. This case corresponds to the ideal parameter fit.

Since we see that $\log[P(\text{data}|\text{data})] > \log[P(\text{target}|\text{data})]$, and that the metric values in the evolutionary fit approach the value $\log[P(\text{target}|\text{data})]$ from below, we conclude that the Poisson metric correctly ranks the different data in the presence of Poisson noise and can be used for evaluating fits.

Of course this idealized data can only serve as a benchmark in a limited sense. There are a variety of assumptions in this scenario which are not necessarily given in an experiment.

On the sample side, assumptions include that the real target is contained in the theory parametrization. Due to sample imperfections such as roughness, unwanted hyperfine splittings and distributions, including the correct sample in the parameter range is practically often challenging [Heu21]. In addition, there may be multiple samples that result in the same 2D spectrum, such that the fit may not be unique. However, both of these issues are systematics in the experimental control and cannot solely be addressed by a statistical analysis.

On the statistical side, the experiment may feature additional noise sources, such as from the detectors, the beam [Chu18] or background processes. While these could be included if their precise nature is known, the Poisson metric can often still provide a good approximate measure, similar to the Gaussian metric.

Beyond these idealized tests, the Poisson metric has been applied to real experimental data in [Hee21; Heu21], which serves as a realistic application benchmark. In particular, the analysis in [Hee21] showed that the result for the Allan deviation differs depending on the fitting procedure, with the Poisson metric analysis yielding a smaller Allan deviation than the Gaussian metric. The extraction of maximum information from the 2D spectrum is therefore of crucial importance for such experiments.

14.3 General metrics and applicability

As outlined above, the Poisson metric analysis was used in [Hee21] and later in [Heu21] to evaluate synchrotron experiment data and found to perform better than the previous approaches based on integrated time ranges, due to the higher information content when using the full two-dimensional information. In particular, the method was crucial for the extraction of the Allan deviation [All66], which was employed to quantify the interferometric stability of the forward scattering setup including the piezo control.

While the method thus already has its use in synchrotron experiments, its roots in Bayesian inference allow it to straightforwardly generalize to include additional noise sources. For multi-photon experiments at x-ray free electron lasers (XFELs), such as the recent work in [Chu18], additional noise sources can be taken into account. At x-ray free electrons in particular, the intensity fluctuations of the source should be taken into account [Chu18]. In addition, binomial statistics resulting from the detection efficiency of the x-ray detectors [Chu18] may influence the results also at synchrotron facilities. Depending on the setup, further error sources associated with the sample control can be important.

If the relevant detection and fluctuation parameters are known, each of these statistical error sources can be included by modifying the bin likelihood distribution $P(n_{\text{exp},i}|n_{\text{theo},i})$ away from a pure Poisson distribution. In principle, the method therefore straightforwardly applies to a general setting. In practice, however, the precise noise distributions or even the relevant error sources may not be known, such that a full statistical analysis of future experiments has to be designed on a case-by-case basis.

Chapter 15

Summary & Outlook

In this chapter, a summary of the thesis results and an outlook on future directions is given. We particularly focus on providing an overarching perspective with regards to nuclear x-ray quantum optics as the main motivation of this thesis. A summary and outlook of the theoretical subtopic of the ab initio few-mode theory is given at the end of Chapter 5.

Brief summary

The main goal of this thesis was to develop a systematic theoretical framework for quantum optical phenomena in x-ray cavity QED with Mössbauer nuclei, which has been an emerging platform and featured many novel experiments in the last decade. The need for an improved quantum theoretical description is especially motivated by the prospect of accessing new regimes using current and upcoming x-ray free electron laser sources.

As a main result, in Chapters 6 to 9, we upgraded a previous phenomenological model for the system to an ab initio theory, developing two separate approaches to obtain quantum optical Master equations for nuclear ensembles in the x-ray cavity environment. The final theory provides a numerically efficient way to directly calculate effective nuclear level schemes, eliminating the need for a fitting procedure, ensuring an unambiguous interpretation of the underlying processes and resolving previous discrepancies compared to semi-classical theory and experiments.

As a prerequisite for this progress, we showed how Jaynes-Cummings type few-mode models for open resonator QED can be derived from first principles, which had been an open question in the general quantum optics literature. The resulting ab initio few-mode theory developed in Chapters 4 and 5 resolves this problem, which is relevant in a broader context beyond x-ray cavity QED, particularly for highly open resonators featuring in other platforms of current experimental importance, where associated theoretical questions have been discussed intensively.

In Chapters 10 and 11, the developed theories were employed to investigate multi-mode light-matter interaction. We introduced a general criterion to identify and classify multi-mode effects in lossy resonators. Within x-ray cavity QED, we showed that a previously observed collective nuclear Lamb shift is a consequence of such effects, and that they can be harnessed to design the properties of the artificial nuclear quantum system by tuning the multi-mode cavity environment. We further reported cusp signatures in Fano interference trajectories of x-ray cavities, which appear in the regime of spectrally overlapping modes.

In Chapters 12 and 13, we returned to the original motivation of describing nuclear quantum dynamics in the nonlinear regime. We explored the feasibility of inverting nuclear ensembles in x-ray cavities using focused pulses from x-ray free electron laser facilities. In particular, an intensity enhancement induced by thin-film cavities was investigated as a function of focusing strength. Our results showed that nuclear ensemble inversion or near-inversion nonlinear effects may already be accessible at current facilities. We further discussed theoretical approaches to the nuclear dynamics on longer time scales than the ultra-short driving pulse lengths, where crucial approximations break down and further theoretical development is required.

In Chapter 14, we considered an aspect of data analysis in synchrotron Mössbauer experiments, providing a statistical method to evaluate multi-dimensional nuclear spectra.

In conclusion, our theoretical framework enables the prediction and interpretation of quantum optical phenomena in lossy resonators. In particular for the platform of x-ray quantum optics with Mössbauer nuclei, it provides a systematic foundation for the exploration of new regimes in upcoming experiments at modern x-ray facilities.

Detailed summary

For readers who are interested in a more detailed outline including technical progress, we provide a second summary of each chapter in the following.

In Chapter 4, we developed an ab initio few-mode theory, which provides a method to derive Jaynes-Cummings-like few-mode models for resonator QED from first principles. We introduced a basis transformation for the resonator light field, which connects such models to fundamental continuum Hamiltonians. As an important feature, the resulting few-mode Hamiltonian for the resonator field is exact for an arbitrary choice of system modes. In addition, we demonstrated an exact equivalence between standard scattering theory applied to the continuum case, and the seminal input-output formalism, which is commonly employed for few-mode models. This connection is enabled by the introduction of a background scattering contribution, which is particularly relevant in the regime of overlapping modes. From a technical perspective, our approach uses Feshbach projections to construct a few-mode operator basis transformation, building on a previous result for the case of infinitely many modes [VH03] and methods from atomic physics [Dom83]. The projection scheme is designed to yield canonical commutation relations of the mode operators, such that the few-mode system-bath Hamiltonian is of Gardiner-Collett form. For overlapping modes or high resonator losses, modifications to standard models such as cross-mode decay terms and frequency-dependent system-bath couplings are found to be necessary.

In Chapter 5, the ab initio few-mode theory is applied to systems featuring interactions with matter, such as a two-level system inside a cavity. Building on the ab initio few-mode Hamiltonian being exact for the free field theory, a few-mode expansion scheme for the interaction is constructed, providing a new perspective on commonly used few-mode models as a systematic truncation of an exact interaction Hamiltonian. For a simple example cavity, we investigated the convergence of this expansion for different regimes of light-matter and resonator-bath coupling strength from weak to multi-mode strong coupling. We discussed the relevance for experimental platforms of current interest and outlined a perspective with regards to alternative methods.

In Chapter 6, the ab initio few-mode theory was applied to the x-ray cavity case, which yields a direct generalization of the previously developed pXCQED model [HE13; HE15], providing a detailed understanding of its origin, structure and necessary modifications. We investigated a simple example geometry, finding essentially perfect agreement with semi-classical theory.

Due to the difficulty of numerically implementing the ab initio few-mode theory for complex cavity geometries, a second orthogonal ab initio approach to x-ray cavity QED with Mössbauer nuclei was developed in Chapter 7. Instead of introducing cavity modes, the method directly traces out the resonator light field to derive a many-body Master equation for the nuclei in the cavity environment. The induced interactions between nuclear ensembles are encoded in the classical electromagnetic Green's function. Since the latter is available analytically even for complex planar cavities, the approach provides a numerically efficient way to calculate the level scheme of nuclear ensembles in the x-ray cavities. The method is benchmarked in Chapter 8, where we also resolve discrepancies in the pXCQED model and provide an ab initio quantum optical interpretation of previously observed EIT signatures [Röh12]. In Chapter 9, we further show how effective transition dipole moments, which are the central parameter in the theory, can be calculated for general multi-pole transitions from standard nuclear resonance scattering parameters.

Based on the two developed ab initio theories, Chapter 10 investigates multi-mode effects on light-matter interaction in lossy resonators. We provided a general criterion to identify and classify such effects, introducing an off-resonant and two distinct resonant categories, which are caused by cross-mode interaction terms in the few-mode Hamiltonian. As an application, we showed that the previously observed collective Lamb shift [Röh10] can indeed be traced back to such multi-mode effects, explaining why there can be a non-zero shift at the reflection minimum of the cavity. We further showed that such multi-mode effects can be harnessed to one's advantage and that they provide a new tuning knob to modify the properties of the artificial nuclear quantum system via the cavity environment. In particular, we designed a cavity geometry where the multi-mode effects cause a flip in the sign of the collective Lamb shift, which illustrates the practical potential. Chapter 10 investigates signatures in Fano interference resulting from similar mechanisms in cavities with overlapping modes. We find that in the regime of intermediate coupling between two modes, trajectories of the Fano q-parameter in the complex plane show cusp and loop features, constituting qualitative deviations from the single mode case.

In Chapters 12 and 13, we returned to one of the original motivations of the theoretical development

by using the derived ab initio Master equations to study nonlinear dynamics of the nuclei in the x-ray cavity environment. In particular, the feasibility of inverting nuclear ensembles by focused x-ray pulses was investigated in Chapter 12. Besides solving the excitation dynamics within systematic and verifiable approximations applicable during an ultra-short driving pulse, we introduced a Fourier-transform algorithm to calculate the effect of the x-ray cavities beyond the highly collimated limit. We analyzed the intensity enhancement provided by the cavities as a function of focusing strength, finding a significant decrease in their effectiveness for low beam divergences. We further provided concrete numbers for the nuclear excitation based on beam parameters at the European XFEL, showing that inversion or near-inversion nonlinear effects may already be accessible at current facilities.

In Chapter 13, methods to study the decay dynamics on longer time scales were discussed. We showed that for the ensemble Master equation within a single parallel wave vector approximation, solutions to the many-body problem can be obtained using existing software packages which exploit a permutation symmetry. In addition, we implemented a symbolic algorithm to compute cumulant expansion equations of motion for such permutation symmetric models to further simplify the complexity. We discussed the single parallel wave vector approximation as a central limitation of such approaches and provided an outlook on potential future avenues.

Chapter 14 presented a standalone result, constituting a Bayesian data analysis method for multi-dimensional Mössbauer spectra. We constructed a simple metric to evaluate how well theoretically predicted spectra fit a given data set. The method proved useful for the analysis of recent experimental data [Hee21].

Outlook and perspective on nuclear x-ray quantum optics

In nuclear x-ray quantum optics, the framework developed in this thesis enables investigations of exciting physics, which were previously not feasible due to theoretical limitations.

Indeed, the step from a phenomenological model [HE13; HE15] to a numerically efficient ab initio theory was previously identified as a long-term goal [Hee14]. In this context, our work in particular will allow to investigate *complex level schemes* in x-ray cavities with multiple resonant ensembles. In the phenomenological description, such systems were difficult to describe, since the fitting procedure and unresolved discrepancies made it difficult to determine the potentially large number of model parameters. In the ab initio theory, we have seen that an application even to continuous ensembles, such as geometries featuring thick resonant layers, is straightforward. With regards to experiments, the approach could be used to construct improved versions or extensions of already implemented multi-level schemes, such as electromagnetically induced transparency [Röh12], spontaneously generated coherences [Hee13] or nuclear optical lattices [Hab16a]. Indeed, our approach has already been employed and developed further in this context [KCP20], including extensions to inhomogeneous ensembles with parameter distributions [AP21].

In the direction of implementing novel level schemes, the ab initio theory also enables an entirely new paradigm. So far, x-ray cavity structures for nuclear quantum optics have been designed mostly by trial and error methods. That is, one usually envisions a level scheme and varies the cavity parameters until the spectral signatures calculated from semi-classical theory [Röh10; Röh12] and fits from phenomenological models [Hee13; HE15] meet the expectations. With the numerically efficient algorithm and unambiguous interpretation of the ab initio theory, it is now possible to apply *inverse design methods* instead. The idea is to specify a level scheme with specific desired parameters and to systematically optimize the cavity geometry afterwards. In addition, one can explore which level schemes are actually feasible within the practically accessible parameter space of cavity geometries. First results in this direction have already been obtained [Die21] and inverse design may enable completely new experimental possibilities in the future. The ab initio formalism is a crucial ingredient for this development, since in order to inverse design cavity geometries from desired level schemes, one first requires a well-understood method to calculate level schemes from cavity geometries.

The multi-mode effects outlined in Chapter 10 further provide a *new tuning mechanism* for the artificial nuclear quantum system. While inverse design methods may be able to harness these effects automatically, a detailed understanding is useful to motivate new directions. For example, moving away from standard structures with claddings and a guiding layer could be useful to realize strong multi-mode effects. Some options in this direction, including double cavities to realize strong ensemble coupling [Hab17] and no-cladding cavities for better in-coupling efficiency [Die21], have already been considered.

To take these ideas one step further, one may also consider the nuclei in *photonic environments beyond the thin-layer cavity geometry*. Various options such as waveguides [Pfe02], curved channels [Sal15], nanowires [Che02] and periodically structured surfaces such as nanodots or nanodiscs [Ell12] are already available and with improving fabrication techniques, even more advanced structures may become accessible in the future. The quantum optical properties of nuclear ensembles in such photonic environments are largely unexplored and in particular the different dimensionality compared to the two-dimensional layer geometry may enable new phenomena. Given the broad use of photonic crystals [Joa08] and other nanostructures for quantum optics at lower energies [LMS15; Cha18], this direction is promising to explore in the future. In this context, the Green's function approach in Chapter 7 could straightforwardly be applied, allowing to interface with electromagnetic solvers and already developed inverse design techniques [BB20; Ben21a] for general geometries.

One of the most exciting frontiers in the field is the envisioned study of *nonlinear quantum dynamics* in Mössbauer ensembles. To this end, we provided a concrete theoretical model in the form of a Master equation, which describes the interactions of nuclei in the cavity environment. From a naive perspective, studying nonlinear phenomena in nuclear ensembles can be seen as the task of solving this model. Practically, however, the latter constitutes a difficult many-body problem. Nevertheless, the introduced Master equation is much simpler than the basic light-matter interaction Hamiltonian and many methods to tackle similar problems are available from the optical regime [SBD16; GRK17; Cha18; Kir19; RSG21; Sca21].

In this context, a central question is which *phenomena beyond the linear regime* can be realized experimentally at modern x-ray facilities in the near future [RE21]. After the first multi-photon nuclear resonance scattering experiment at an XFEL in 2018 [Chu18], the door is now wide open for exciting new physics to be discovered. However, theoretical guidance will be crucial in the upcoming initial period of pioneering experiments. While plenty of setups to implement promising quantum optical schemes exist, concrete predictions and practical considerations for phenomena at higher intensities are still lacking. The excitation phase during an ultra-short pulse has partially been addressed for cavities by our results in Chapter 12, and for waveguides in a recent preprint [Che21]. However, besides the phenomenological model investigation in [HKE16], not much is known about novel observables and dynamical behavior resulting from high excitation of nuclear ensembles. Potential options include Kerr nonlinearities [Röh12], which are typically strong in multi-level schemes as they can be realized in the x-ray cavities, photon correlations [Chu18], and much more [KK17b; RE21]. Since available beamtime at x-ray facilities is limited and the requirements for nuclear resonance scattering are often technically challenging, concrete calculations of expected quantum dynamical phenomena will be paramount. The theory development in this thesis provides a solid foundation for these future investigations and may enable the theoretical guidance of experimental progress.

With regards to a related topic, the results in this thesis also provide insights into the role of *collective effects*. We have shown that in the linear regime, the number of interacting nuclei is indeed not a relevant parameter in the quantum theory. Instead, as in the semi-classical theory, the number density is important and connected to effects such as the collective Lamb shift [Röh10]. This observation is relevant to distinguish what kind of collective effects are at play, connecting to insights from the field of atomic ensembles [GRK17] and theoretical methods therein. As a consequence, it will be interesting to see to what extent collective effects are modified at smaller excitation volumes induced by nanometer scale x-ray beams, as they are available at upcoming facilities [RE21], and how they influence the nonlinear behavior at higher intensities. If these regimes can be realized practically, the x-ray cavity QED platform further promises novel investigations of many-body quantum dynamics in highly coherent spin ensembles to complement studies in the optical domain.

The theoretical development in this thesis therefore connects to various future directions and provides a promising approach to support the upcoming experimental development towards the nonlinear sector of nuclear resonance scattering.

Appendices

Appendix A

Conventions and basics

A.1 Units

We frequently use natural units $\hbar = c = \varepsilon_0 = 1$ and consequently omit these constants in obvious places. However, we often nevertheless include them in certain expressions for clarity, especially when they are used for calculations where the absolute scale is important.

A.2 Commutator relations and operator definitions

In this thesis, we frequently use operators for two-level systems and various photonic degrees of freedom. Unless stated otherwise, we stick with the following conventions.

A.2.1 Two-level operators

For two-level systems with ground state $|g\rangle$ and excited state $|e\rangle$, we use the Pauli operators $\hat{\sigma}^{x/y/z}$ with the convention

$$\hat{\sigma}^x = \frac{|e\rangle\langle g| + |g\rangle\langle e|}{2}\,, \tag{A.1}$$

$$\hat{\sigma}^y = \frac{|e\rangle\langle g| - |g\rangle\langle e|}{2i}\,, \tag{A.2}$$

$$\hat{\sigma}^z = |e\rangle\langle e| - |g\rangle\langle g|\,. \tag{A.3}$$

The corresponding raising and lowering operators are

$$\hat{\sigma}^+ = \hat{\sigma}^x + i\hat{\sigma}^y = |e\rangle\langle g|\,, \tag{A.4}$$

$$\hat{\sigma}^- = \hat{\sigma}^x - i\hat{\sigma}^y = |g\rangle\langle e|\,, \tag{A.5}$$

respectively.

These operators fulfill the commutator relations

$$[\hat{\sigma}^+, \hat{\sigma}^-] = \hat{\sigma}^z\,, \tag{A.6}$$

$$[\hat{\sigma}^z, \hat{\sigma}^+] = 2\hat{\sigma}^+\,, \tag{A.7}$$

$$[\hat{\sigma}^z, \hat{\sigma}^-] = -2\hat{\sigma}^- \tag{A.8}$$

and product relations

$$\hat{\sigma}^z\hat{\sigma}^+ = \hat{\sigma}^+\,, \tag{A.9}$$

$$\hat{\sigma}^z\hat{\sigma}^- = -\hat{\sigma}^-\,, \tag{A.10}$$

$$\hat{\sigma}^+\hat{\sigma}^- = \frac{\mathbb{I} + \hat{\sigma}^z}{2}\,, \tag{A.11}$$

$$\hat{\sigma}^-\hat{\sigma}^+ = \frac{\mathbb{I} - \hat{\sigma}^z}{2}\,. \tag{A.12}$$

Note that the identity in the two-level space can be resolved as

$$\mathbb{I} = |e\rangle\langle e| + |g\rangle\langle g|\,. \tag{A.13}$$

A.2.2 Photon degrees of freedom

We encounter various photon degrees of freedom, which we denote as $\hat{a}_\lambda$, $\hat{b}_m(\omega)$, $\hat{c}(\omega)$ and similar. Unless stated otherwise, their commutator relations are given as

$$[\hat{a}_\lambda, \hat{a}^\dagger_{\lambda'}] = \delta_{\lambda\lambda'}\,, \tag{A.14}$$

$$[\hat{a}_\lambda, \hat{a}_{\lambda'}] = 0\,. \tag{A.15}$$

for the discrete case and

$$[\hat{b}_m(\omega), \hat{b}^\dagger_{m'}(\omega')] = \delta_{mm'}\delta(\omega-\omega')\,, \tag{A.16}$$

$$[\hat{b}_m(\omega), \hat{b}_{m'}(\omega')] = 0 \tag{A.17}$$

in the continuous case.

A.3 Fourier transforms and integrals

For Fourier transforms, we use varying conventions depending on the context and on whether the transformation is between time and frequency or space and wave space. We frequently use the following basic integral identities.

The Fourier resolution of the Dirac delta-function is

$$\int_{-\infty}^{\infty} d\omega e^{i\omega(t-t')} = 2\pi\delta(t-t')\,. \tag{A.18}$$

The Fourier transform of the Gaussian function

$$f(t) = A_0 \exp\left(-\frac{t^2}{2\tau^2}\right) \tag{A.19}$$

is given by

$$\tilde{f}(\omega) = \frac{1}{2\pi}\int_{-\infty}^{\infty} dt f(t) e^{i\omega t} = \frac{A_0\tau}{\sqrt{2\pi}} \exp\left(-\frac{\omega^2\tau^2}{2}\right)\,. \tag{A.20}$$

The normalization of the Gaussian is

$$\int_{-\infty}^{\infty} dt f(t) = \sqrt{2\pi} A_0 \tau\,. \tag{A.21}$$

Appendix B

Technical details on the ab initio few-mode theory

This appendix is based on the following publication:

Ab Initio Few-Mode Theory for Quantum Potential Scattering Problems
D. Lentrodt and J. Evers
Physical Review X **10**, 011008 (2020)

B.1 Canonical quantization of the Schrödinger equation

Eq. (4.1) is an example of a wave equation that can be quantized using the standard canonical quantization procedure [Sch68; YI99], which we recapitulate in the following. The Lagrangian for the system reads

$$L = \int dr[i\psi^\dagger(r,t)\dot{\psi}(r,t) - \frac{1}{2}\frac{\partial}{\partial r}\psi^\dagger(r,t)\frac{\partial}{\partial r}\psi(r,t) - V(r)\psi^\dagger(r,t)\psi(r,t)]\,, \tag{B.1}$$

such that the Euler-Lagrange equations yield Eq. (4.1). The conjugate momentum of $\psi(r,t)$ is then obtained as

$$\pi(r,t) = \frac{\partial}{\partial[\dot{\psi}(r,t)]}L = i\psi^\dagger(r,t)\,. \tag{B.2}$$

For quantization, we promote $\psi(r,t)$ $[\pi(r,t)]$ to operators $\hat{\psi}(r,t)$ $[\hat{\pi}(r,t)]$ and impose the bosonic commutation relations Eq. (4.3).

The second quantized Hamiltonian is then obtained from the Lagrangian as Eq. (4.2). Together with the commutation relations, the Heisenberg equations of motion can be verified to give Eq. (4.1).

B.2 Mode normalization and orthogonality

We choose the normalization of the normal modes such that the orthogonality condition reads

$$\int dr\ \phi^*_{m'}(r,k')\phi_m(r,k) = \delta_{mm'}\,\delta(E(k) - E(k'))\,. \tag{B.3}$$

The normal modes form a complete set in the sense that

$$\sum_m \int dE(k)\ \phi^*_m(r',k)\phi_m(r,k) = \delta(r-r')\,. \tag{B.4}$$

We note that k is simply a relabeling of the energy eigenstates, which we find convenient to introduce. A natural choice is $E(k) = k^2/2$, since k then has a physical interpretation as the wave number.

Similarly, hermicity of the subspace Hamiltonians [Dom83] implies orthogonality of their corresponding eigenstates, the system and bath states. We choose their normalization such that

$$\langle\chi_\lambda|\chi_{\lambda'}\rangle = \delta_{\lambda\lambda'} \tag{B.5}$$

and

$$\left\langle \tilde{\psi}_m(k) \middle| \tilde{\psi}_{m'}(k') \right\rangle = \delta_{mm'}\, \delta\left(E(k) - E(k')\right) . \tag{B.6}$$

Analogously to Eq. (4.11), the bath modes diagonalize the P-space projector via

$$P = \sum_m \int dE(k)\ \left|\tilde{\psi}_m(k)\right\rangle \left\langle \tilde{\psi}_m(k)\right| . \tag{B.7}$$

Since $P = 1 - Q$, the system modes can furthermore be chosen orthogonal to the bath modes [Dom83]

$$\left\langle \chi_\lambda \middle| \tilde{\psi}_m(k) \right\rangle = 0 . \tag{B.8}$$

We note that these orthogonality conditions are crucial for quantization.

B.3 Subspace expansion

Here we summarise the calculation of the matrix elements in the expansion of the full eigenstates Eq. (4.14) as presented by Domcke [Dom83].

We start by writing the Schrödinger equation Eq. (4.1) in Dirac notation

$$H\left|\phi_m(k)\right\rangle = E(k)\left|\phi_m(k)\right\rangle , \tag{B.9}$$

which can be expressed as a pair of coupled equations in the two subspaces [Fes58]

$$H_{PP}\left|\phi_m(k)\right\rangle + H_{PQ}\left|\phi_m(k)\right\rangle = E(k) P\left|\phi_m(k)\right\rangle , \tag{B.10a}$$

$$H_{QP}\left|\phi_m(k)\right\rangle + H_{QQ}\left|\phi_m(k)\right\rangle = E(k) Q\left|\phi_m(k)\right\rangle . \tag{B.10b}$$

The Lippmann-Schwinger equation for the P-space part Eq. (B.10a) reads

$$\begin{aligned} P\left|\phi_m(k)\right\rangle = &\left|\tilde{\psi}_m^{(+)}(k)\right\rangle \\ &+ \left(E(k) - H_{PP} + i\eta\right)^{-1} H_{PQ}\left|\phi_m(k)\right\rangle , \end{aligned} \tag{B.11}$$

where we chose the incoming solution for the homogeneous part. Substitution into Eq. (B.10b) and solving for $Q\left|\phi_m(k)\right\rangle$ gives

$$Q\left|\phi_m(k)\right\rangle = G_{QQ} H_{QP}\left|\tilde{\psi}_m^{(+)}(k)\right\rangle , \tag{B.12}$$

where we have defined

$$G_{QQ} = \left(E(k) - H_{QQ} - H_{QP}\tilde{G}^{(+)} H_{PQ}\right)^{-1} , \tag{B.13a}$$

$$\tilde{G}^{(+)} = \left(E(k) - H_{PP} + i\eta\right)^{-1} . \tag{B.13b}$$

Substitution into Eq. (B.11) gives Eq. (2.11) from [Dom83]

$$P\left|\phi_m(k)\right\rangle = \left|\tilde{\psi}_m^{(+)}(k)\right\rangle + \tilde{G}^{(+)} H_{PQ} G_{QQ} H_{QP}\left|\tilde{\psi}_m^{(+)}(k)\right\rangle . \tag{B.14}$$

Adding Eqs. (B.12) and (B.14) we obtain an expansion for the full eigenstates in terms of the subspace eigenstates

$$\left|\phi_m(k)\right\rangle = Q\left|\phi_m(k)\right\rangle + P\left|\phi_m(k)\right\rangle \tag{B.15}$$

$$= G_{QQ} H_{QP}\left|\tilde{\psi}_m^{(+)}(k)\right\rangle + \left[1 + \tilde{G}^{(+)} H_{PQ} G_{QQ} H_{QP}\right]\left|\tilde{\psi}_m^{(+)}(k)\right\rangle . \tag{B.16}$$

Note that this constitutes a generalization of results obtained in [VH03] to a finite number of system modes and to the Schrödinger equation.

The expansion coefficients in Eq. (4.14) are therefore

$$\left\langle \chi_\lambda \middle| \phi_m(k) \right\rangle = \left\langle \chi_\lambda \right| G_{QQ} H_{QP}\left|\tilde{\psi}_m^{(+)}(k)\right\rangle \tag{B.17}$$

and

$$\left\langle \tilde{\psi}_{m'}^{(+)}(k') \middle| \phi_m(k) \right\rangle = \left\langle \tilde{\psi}_{m'}^{(+)}(k') \right| 1 + \tilde{G}^{(+)} H_{PQ} G_{QQ} H_{QP}\left|\tilde{\psi}_m^{(+)}(k)\right\rangle . \tag{B.18}$$

These expressions can be conveniently evaluated for a certain class of potentials using so-called separable expansions, as has been shown in detail by Domcke [Dom83].

B.4 System-and-bath operators

Here we derive the system-bath expansion and show that the operators associated with the subspace eigenstates naturally fulfill the desired conditions for bosonic system and bath operators as they are used in quantum noise theory [GC85; GZ04; VH03].

Eq. (4.14) can be used to write the field operator Eq. (4.4) as

$$\hat{\psi}(r,t) = \sum_{\lambda\in\Lambda_Q} \hat{a}_\lambda \chi_\lambda(r) + \sum_{m'} \int dE(k')\, \hat{b}_{m'}(k') \tilde{\psi}_{m'}(r,k') \tag{B.19}$$

where we have defined [VH03]

$$\hat{a}_\lambda = \sum_m \int dE(k) \hat{c}_m(k,t) \alpha_{\lambda m}(k)\,, \tag{B.20a}$$

$$\hat{b}_{m'}(k') = \sum_m \int dE(k) \hat{c}_m(k,t) \beta_{mm'}(k,k') \tag{B.20b}$$

as the system and bath operators, respectively. Inverting Eqs. (B.20) by using the coefficient identities in Appendix B.5 gives Eq. (4.16) [VH03].

Using Eqs. (B.20) and the coefficient identities in Appendix B.5, the commutation relations for the system-bath operators are obtained as

$$\left[\hat{a}_\lambda, \hat{a}^\dagger_{\lambda'}\right] = \delta_{\lambda\lambda'}\,, \tag{B.21a}$$

$$\left[\hat{b}_m(k), \hat{b}^\dagger_{m'}(k')\right] = \delta_{mm'}\delta\left(E(k) - E(k')\right)\,, \tag{B.21b}$$

$$\left[\hat{a}_\lambda, \hat{b}^\dagger_m(k)\right] = 0\,, \tag{B.21c}$$

$$\left[\hat{a}_\lambda, \hat{a}_{\lambda'}\right] = \left[\hat{b}_m(k), \hat{b}_{m'}(k')\right] = 0\,, \tag{B.21d}$$

$$\left[\hat{a}^\dagger_\lambda, \hat{a}^\dagger_{\lambda'}\right] = \left[\hat{b}^\dagger_m(k), \hat{b}^\dagger_{m'}(k')\right] = 0\,, \tag{B.21e}$$

which are indeed the desired bosonic commutation relations [VH03].

We note that due to the few-mode projection, the system states do not necessarily form a complete set in the region of the system modes. It is thus necessary to account for the bath state contribution in Eq. (B.19), even when r lies inside this region. This feature is relevant when field-matter interactions are included in the theory, which we discuss in Chapter 5.

B.5 Expansion coefficient identities

Using the completeness relation in full space

$$\mathbb{I} = \sum_m \int dE(k)\ |\phi_m(k)\rangle \langle\phi_m(k)| \tag{B.22}$$

and the orthogonality relations in the subspaces Eqs. (B.5, B.6, B.8) we obtain the coefficient identities

$$\int dE(k) \sum_m \alpha_{\lambda m}(k) \alpha^*_{\lambda' m}(k) = \langle\chi_\lambda|\chi_{\lambda'}\rangle = \delta_{\lambda\lambda'}\,, \tag{B.23a}$$

$$\int dE(k') \sum_{m'} \alpha_{\lambda m'}(k') \beta^*_{m' m}(k',k) = \left\langle \chi_\lambda \middle| \tilde{\psi}^{(+)}_m(k) \right\rangle = 0\,, \tag{B.23b}$$

$$\int dE(k'') \sum_{m''} \beta_{m'' m}(k'',k) \beta^*_{m'' m'}(k'',k') = \left\langle \tilde{\psi}^{(+)}_m(k) \middle| \tilde{\psi}^{(+)}_{m'}(k') \right\rangle = \delta_{mm'}\delta(E(k) - E(k'))\,. \tag{B.23c}$$

Similarly,

$$\int dE(k)E(k)\sum_m \alpha_{\lambda m}(k)\alpha^*_{\lambda' m}(k) = E_\lambda \delta_{\lambda\lambda'}\,, \tag{B.24a}$$

$$\int dE(k'')\sum_{m''} E(k'')\beta_{m''m}(k'',k)\beta^*_{m''m'}(k'',k') = E(k)\delta_{mm'}\delta(E(k)-E(k'))\,, \tag{B.24b}$$

$$\int dE(k')\sum_{m'} E(k')\alpha_{\lambda m'}(k')\beta^*_{m'm}(k',k) = \left\langle \chi_\lambda \middle| H_{QP} \middle| \tilde{\psi}^{(+)}_m(k)\right\rangle =: W_{\lambda m}(k)\,. \tag{B.24c}$$

Note that these relations are analogous to expressions obtained in [VH03] for the dielectric Maxwell equations, but refer to different modes since our few-mode projection scheme differs.

B.6 Scattering matrix in Viviescas-Hackenbroich quantization

In this Appendix, we calculate the scattering matrix for an example cavity using Viviescas&Hackenbroich's Feshbach projection scheme [VH03; VH04].

From Eq. (68) in [VH03] their scattering matrix reads

$$S(\omega) = 1 - 2\pi i \sum_{\lambda,\lambda'=1}^{\infty} \mathcal{W}^\dagger_\lambda(\omega)\left(D^{-1}(\omega)\right)_{\lambda\lambda'}\mathcal{W}_{\lambda'}(\omega)\,. \tag{B.25}$$

Here the matrix D is defined by Eqs. (65, 66) in [VH03] as

$$\left(D(\omega)\right)_{\lambda\lambda'} = (\omega-\omega_\lambda)\delta_{\lambda\lambda'} + \Gamma_{\lambda\lambda'}(\omega)\,, \tag{B.26}$$

with

$$\Gamma_{\lambda\lambda'}(\tilde{\omega}) = \lim_{\epsilon\to 0^+}\int d\omega'\,\frac{\mathcal{W}_\lambda(\omega')\mathcal{W}^*_{\lambda'}(\omega')}{\omega'-\omega-i\epsilon}\,. \tag{B.27}$$

These expressions are similar to our input-output scattering matrix Eq. (4.58), except for the different projection scheme and the infinite number of system modes.

In [VH04], the authors have demonstrated their formalism on the example of a one dimensional cavity with a single homogeneous dielectric layer of thickness d and refractive index n terminated by a perfectly reflecting mirror. In the following we attempt a calculation of the corresponding scattering matrix using the input-output result Eq. (B.25) from their method. The coupling coefficients for Neumann basis states are given by Eq. (46) in [VH04] as

$$\mathcal{W}_\lambda(\omega) = (-1)^\lambda\sqrt{\frac{\omega_\lambda}{\pi\omega d}}\,, \tag{B.28}$$

where the cavity mode frequencies are

$$\omega_\lambda = \frac{c\pi\lambda}{nd} \tag{B.29}$$

with $\lambda\in\{1,2,\dots\}$. We can simply plug this into the Eq. (B.26) above to get

$$\left(D(\omega)\right)_{\lambda\lambda'} = (\omega-\omega_\lambda)\,\delta_{\lambda\lambda'} + \tilde{\Gamma}(\omega)(-1)^{\lambda+\lambda'}\sqrt{\omega_\lambda\omega_{\lambda'}} \tag{B.30}$$

where

$$\tilde{\Gamma}(\omega) = \int d\omega'\,\frac{1}{\omega}\frac{1}{\omega'-\omega-i\epsilon}\,. \tag{B.31}$$

The inverse of this D-matrix can be calculated exactly using the Sherman-Morrison formula [Dom83; GVL96]. Substitution into Eq. (B.25) yields, after a short calculation,

$$S(\omega) = 1 - \frac{2i}{\omega d}\frac{K(\omega)}{1-\tilde{\Gamma}(\omega)K(\omega)}, \tag{B.32}$$

where

$$K(\omega) = \sum_{\lambda=1}^{\infty} \frac{\omega_\lambda}{\omega - \omega_\lambda} \,. \tag{B.33}$$

Substitution of the resonance frequencies Eq. (B.29) gives

$$K(\omega) = \sum_{\lambda=1}^{\infty} \frac{\lambda}{\frac{\omega n d}{c\pi} - \lambda} \,. \tag{B.34}$$

This sum indeed diverges. There is also no well defined notion of taking a limit of λ to infinity, since the projection is performed directly onto infinitely many modes. Similar behavior is observed for other one dimensional examples in [VH04], including a one-sided Ley-Loudon cavity.

We conclude that in Viviescas&Hackenbroich's formalism [VH03], there is no straightforward way to calculate scattering matrices from the input-output formalism due to the convergence behavior of the infinitely many modes included in their projection scheme. For the example cavity investigated above, we have further observed that truncation approximations or cut-off schemes can be used to approximate the spectra around a single resonance for good cavities. For multiple or overlapping modes, however, such approximations fail. In these regimes it is thus crucial to understand how to precisely reconstruct the scattering information in system-bath theory. By using a different projection scheme and few-mode Hamiltonians, the approach presented in this work addresses this topic.

B.7 Domcke's Feshbach projection formalism for potential scattering

In Sec. 4.3.1 we have focused on defining and interpreting the background and resonant scattering matrices. We further have shown how the former corresponds to an asymptotic basis transformation. In this Appendix, we extract the relevant parts of Domcke's [Dom83] derivation of this separation based on Lippmann-Schwinger equations and give his formulae for the T-matrices.

The goal is to expand the P-space projection of the full eigenstate, which contains all the scattering information, in terms of the various subspace eigenstates. During the quantization procedure, we already derived Eq. (B.14), in which we now only have to expand the homogeneous part in terms of free states.

We first write down the Lippmann-Schwinger equation for the bath eigenstates

$$\left|\tilde{\psi}_m^{(\pm)}(k)\right\rangle = \left|k_m\right\rangle + G_0^{(\pm)} H_{PP} \left|\tilde{\psi}_m^{(\pm)}(k)\right\rangle \,, \tag{B.35}$$

where we have defined the free Green function in full space

$$G_0^{(\pm)} = (E(k) - K \pm i\epsilon)^{-1} \tag{B.36}$$

and the free eigenstates

$$K \left|k_m\right\rangle = E(k) \left|k_m\right\rangle . \tag{B.37}$$

Upon substitution into Eq. (B.14) we obtain [Dom83]

$$P \left|\phi_m(k)\right\rangle = \left|k_m\right\rangle + G_0^{(\pm)}(H_{PP} - K) \left|\tilde{\psi}_m^{(\pm)}(k)\right\rangle + \tilde{G}^{(+)} H_{PQ} G_{QQ} H_{QP} \left|\tilde{\psi}_m^{(+)}(k)\right\rangle . \tag{B.38}$$

From there we obtain the separation of the T-matrix [Dom83]

$$T(k) = T_{\mathrm{bg}}(k) + T_{\mathrm{res}}^{(F)}(k), \tag{B.39}$$

where, omitting subscripts for brevity,

$$T_{\mathrm{bg}}(k) \equiv \left\langle k\right| T_{\mathrm{bg}} \left|k\right\rangle = \left\langle k\right| (H_{PP} - K) \left|\tilde{\psi}^{(+)}(k)\right\rangle \tag{B.40}$$

and

$$T_{\mathrm{res}}^{(F)}(k) \equiv \left\langle \tilde{\psi}^{(-)}(k)\right| T_{\mathrm{res}} \left|\tilde{\psi}^{(+)}(k)\right\rangle = \left\langle \tilde{\psi}^{(-)}(k)\right| H_{PQ} G_{QQ} H_{QP} \left|\tilde{\psi}^{(+)}(k)\right\rangle . \tag{B.41}$$

The matrix element from the main text giving the resonant scattering matrix is

$$T_{\rm res}(k) \equiv \left\langle \tilde{\psi}^{(+)}(k) \right| T_{\rm res} \left| \tilde{\psi}^{(+)}(k) \right\rangle = S_{\rm bg}^{-1}\, T_{\rm res}^{(F)}\,. \tag{B.42}$$

Consequently one obtains [Dom83]

$$S(k) = \mathbb{I} - 2\pi i T(k) = S_{\rm bg}(k) S_{\rm res}(k) \tag{B.43}$$

as expected.

B.8 The operator scattering matrix in second quantized potential scattering

In this Appendix we derive the result used in Sec. 4.3.2, that the operator scattering matrix relating asymptotically free in- and out-operators is the same as the conventional on-shell scattering matrix for the corresponding states [New82]. We proceed by solving the operator equations of motions for appropriately defined asymptotically free operators, following Glauber&Lewenstein's method [GL91].

To define the asymptotically free operators one has to adiabatically turn off the interaction in the infinite past and future, such that these operators are actually evolving freely in the corresponding limits. To do so we replace the potential $V(r)$ by a potential $V(r,t)$ slowly varying in time such that

$$\lim_{t\to\pm\infty} V(r,t) \to 0 \tag{B.44}$$

and

$$V(r,0) = V(r). \tag{B.45}$$

Consequently, the normal modes also become time-dependent. In general, they fulfill an explicitly time-dependent form of the wave equation, however in the adiabatic limit they correspond to the time-independent normal modes at each time slice, such that Eq. (4.5) becomes

$$\left(-\frac{1}{2}\frac{\partial^2}{\partial r^2} + V(r,t)\right) \phi_m(r,k,t) = E(k,t)\phi_m(r,k,t)\,. \tag{B.46}$$

The in [out] operators are then defined as the corresponding free interaction picture operators in the infinite past [future], that is

$$\hat{d}_m^{(\rm in)}(k) = \lim_{t\to-\infty} e^{iE(k)t}\, \hat{d}_m(k,t) \tag{B.47}$$

and

$$\hat{d}_m^{(\rm out)}(k) = \lim_{t\to+\infty} e^{iE(k)t}\, \hat{d}_m(k,t). \tag{B.48}$$

In Eq. (4.4) and Eq. (4.31), two separate expansions of the quantum field have been introduced, one in terms for normal modes and one in terms of free states

$$\hat{\psi}(r,t) = \sum_m \int dE(k)\, \phi_m(r,k)\hat{c}_m(k,t) = \sum_m \int dE(k)\, \phi_m^{(\rm free)}(r,k)\hat{d}_m(k,t)\,. \tag{B.49}$$

Using the orthogonality properties of these states one obtains a linear relation between the two operator bases

$$\hat{d}_m(k,t) = \sum_{m'} \int dE(k') \left\langle \phi_m^{(\rm free)}(k) \right| \left. \phi_{m'}(k') \right\rangle \hat{c}_{m'}(k',t). \tag{B.50}$$

The construction of the basis transformation between asymptotically free in- and out-operators proceeds similarly via comparing asymptotic expansions. Let us first asymptotically expand the field in the infinite past in terms of the in-operators using Eq. (B.49) and Eq. (B.47) to get

$$\hat{\psi}(r, t\to-\infty) = \sum_m \int dE(k) \phi_m^{(\rm free)}(r,k)\hat{d}_m^{(\rm in)}(k) e^{-iE(k)t}. \tag{B.51}$$

To obtain a second expansion to compare to let us note that the normal modes are not uniquely defined since we have not specified their boundary conditions. The choice that is relevant in the

infinite past are the states with a controlled incoming state $\left|\phi_m^{(+)}(k,t)\right\rangle$ [New82]. The corresponding expansion reads

$$\hat{\psi}(r,t) = \sum_m \int dE(k)\, \phi_m^{(+)}(r,k,t)\hat{\tilde{c}}_m(k)e^{-iE(k)t}\,, \tag{B.52}$$

where $\hat{\tilde{O}}_m(k,t) = \hat{O}_m(k,t)e^{iE(k)t}$ is the relevant interaction picture operator [GL91], which is independent of t for the normal modes operators. These states by construction have the property that

$$\lim_{t\to-\infty}\left|\phi_m^{(+)}(k,t)\right\rangle = \left|\phi_m^{(\text{free})}(k)\right\rangle\,. \tag{B.53}$$

Comparing Eqs. (B.51) and (B.52), we thus find that

$$\hat{\tilde{c}}_m(k) = \hat{d}_m^{(\text{in})}(k)\,. \tag{B.54}$$

Consequently, since Eq. (B.52) applies at all times, there are now two ways to express the field at the time slice $t = 0$,

$$\hat{\psi}(r,t=0) = \sum_m \int dE(k)\, \phi_m^{(+)}(r,k,t=0)\hat{d}_m^{(\text{in})}(k) \tag{B.55}$$

$$= \sum_m \int dE(k)\, \phi_m^{(\text{free})}(r,k)\hat{\tilde{d}}_m(k,t=0)\,. \tag{B.56}$$

At $t = 0$ our potential has the desired physical value such that $\phi_m^{(+)}(r,k,t=0) = \phi_m^{(+)}(r,k)$, where the latter solves the original mode equation Eq. (4.5).

From Eqs. (B.55, B.56) we can obtain the transformation between asymptotically free operators in the infinite past and free operators at the time slice $t = 0$ as

$$\hat{\tilde{d}}_m(k,t=0) = \sum_{m'} \int dE(k')\left\langle\phi_m^{(\text{free})}(k)\middle|\phi_{m'}^{(+)}(k')\right\rangle\, \hat{d}_{m'}^{(\text{in})}(k')\,. \tag{B.57}$$

Analogously, by expanding in the $\left|\phi_m^{(-)}(k,t)\right\rangle$ basis and performing an asymptotic expansion in the infinite future, we obtain a second expansion

$$\hat{\tilde{d}}_m(k,t=0) = \sum_{m'} \int dE(k')\left\langle\phi_m^{(\text{free})}(k)\middle|\phi_{m'}^{(-)}(k')\right\rangle\, \hat{d}_{m'}^{(\text{out})}(k')\,. \tag{B.58}$$

Upon combining Eqs. (B.57, B.58) and using that the matrix elements vanish off the energy shell, we obtain the operator scattering relation

$$\hat{d}_m^{(\text{out})}(k) = \sum_{m'} \int dE(k')\left\langle\phi_m^{(-)}(k)\middle|\phi_{m'}^{(+)}(k')\right\rangle\, \hat{d}_{m'}^{(\text{in})}(k')\,. \tag{B.59}$$

Indeed, the matrix element in this expression is the scattering matrix [New82]

$$S_{mm'}(k,k') = \left\langle\phi_m^{(-)}(k)\middle|\phi_{m'}^{(+)}(k')\right\rangle\,, \tag{B.60}$$

which is related to the on-shell scattering matrix $S_{mm'}(k)$ used in the main text by [New82]

$$S_{mm'}(k,k') = S_{mm'}(k)\,\delta(E(k) - E(k'))\,. \tag{B.61}$$

We thus obtain the result Eq. (4.32) as

$$\hat{d}_m^{(\text{out})}(k) = \sum_{m'} S_{mm'}(k)\,\hat{d}_{m'}^{(\text{in})}(k). \tag{B.62}$$

B.9 Regularization of Fourier integrals in the input-output formalism

In this Appendix we provide a derivation of Eq. (4.40). In the process we show how the Fourier integrals are regularized in the input-output formalism and how this relates to time-independent scattering theory [New82].

We start by Fourier transforming Eq. (4.33) to get

$$0 = i(E(\tilde{\omega}) - E_\lambda)\hat{a}_\lambda(\tilde{\omega}) - i\sum_m \int dE(k) W_{\lambda m}(k) \int_{-\infty}^{\infty} dt e^{iE(\tilde{\omega})t} \hat{b}_m(k,t)\,. \tag{B.63}$$

Substitution of Eq. (4.35) gives

$$\begin{aligned} 0 = {} & i(E(\tilde{\omega}) - E_\lambda)\hat{a}_\lambda(\tilde{\omega}) - i\sum_m \int dE(k) W_{\lambda m}(k) \int_{-\infty}^{\infty} dt e^{iE(\tilde{\omega})t} \times e^{-iE(k)(t-t_0)} \hat{b}_m(k,t_0) \\ & - \sum_m \int dE(k) W_{\lambda m}(k) \int_{-\infty}^{\infty} dt e^{iE(\tilde{\omega})t} \times \sum_{\lambda' \in \Lambda_Q} W^*_{\lambda' m}(k) \int_{t_0}^{t} dt' e^{-iE(k)(t-t')} \times \\ & \int_{-\infty}^{\infty} dE(\tilde{\omega}') \frac{1}{2\pi} e^{-iE(\tilde{\omega}')t'} \hat{a}_{\lambda'}(\tilde{\omega}')\,. \end{aligned} \tag{B.64}$$

We note that the integration over energies from negative to positive infinity enters via the inverse Fourier transform of Eq. (4.39), where the energy definition range has to be suitably extended beyond the physical spectrum for the inverse Fourier transform to be defined. This does not constitute an approximation, but rather a definition of an energy dispersion beyond the physical spectrum, such that inverse Fourier transforms can be used as a mathematical tool.

The first of the three terms in this Eq. (B.64) is simple enough already, the second can be reduced using the definition of the input operator and the Fourier identity

$$\int_{-\infty}^{\infty} dt e^{i(E(\tilde{\omega}) - E(k))t} = 2\pi\delta(E(\tilde{\omega}) - E(k)). \tag{B.65}$$

The third term can be simplified in the scattering limit $t_0 \to -\infty$. However, we notice that the integral is in fact divergent in this limit. This is a well known feature of time-independent scattering theory and can be dealt with through regularization [New82]. In our case we require a substitution

$$E(k) \to E(k) - i\epsilon \tag{B.66}$$

and taking the limit $\epsilon \to 0^+$ at the end, which regularizes the integral as $t_0 \to -\infty$. Physically this corresponds to solving an initial value problem [New82].

Evaluation of the integrals in Eq. (B.64) then yields Eqs. (4.40-4.42).

B.10 Few-mode Hamiltonian for the scalar Maxwell wave equation

In this Appendix we provide details on the application of our formalism to the dielectric Maxwell wave equation Eq. (4.52), which constitutes a combination of the system-bath formalism by Vivi-escas&Hackenbroich [VH03], the projection scheme by Domcke [Dom83] and the relation of the input-output formalism to scattering theory presented in the main text for the Schrödinger equation.

B.10.1 Canonical quantization

The quantization of the vectorial dielectric Maxwell equation has been presented by Glauber&Lewenstein [GL91]. Here we follow their approach, simplifying the results to the scalar wave equation Eq. (4.52). For simplicity we work with $\hbar = c = 1$. The Lagrangian for the system is [GL91]

$$L = \frac{1}{2}\int dr \left(\varepsilon(r)\dot{A}^2(r) - \left(\frac{\partial A(r)}{\partial r}\right)^2 \right), \tag{B.67}$$

such that the resulting Euler-Lagrange equations can be checked to give Eq. (4.52). The conjugate momentum of $A(r)$ can then be obtained as [GL91]

$$\Pi(r) = \frac{\delta L}{\delta \dot{A}(r)} = \varepsilon(r)\dot{A}(r)\,. \tag{B.68}$$

Therefore, the Hamiltonian reads [GL91]

$$H[A,\Pi] = \int dr\, \Pi(r,t)\dot{A}(r,t) - L = \frac{1}{2}\int dr \left[\frac{\Pi^2(r)}{\varepsilon(r)} + \left(\frac{\partial A(r)}{\partial r}\right)^2\right]. \tag{B.69}$$

This Hamiltonian can now be expressed in its normal mode basis [GL91], as we have done for the Schrödinger equation earlier. To do so we expand the A-field as [GL91]

$$A(r,t) = \sum_m \int d\omega\, \hat{q}_m(\omega,t) f_m(r,\omega)\,, \tag{B.70}$$

and similarly the conjugate momentum via

$$\Pi(r,t) = \sum_m \int d\omega\, \varepsilon(r)\hat{p}_m(\omega,t) f_m^*(r,\omega)\,. \tag{B.71}$$

Here, $\hat{q}_m(\omega,t)$ are coordinate operators and $\hat{p}_m(\omega,t)$ the corresponding momentum operators [GL91], both associated with the normal modes $f_m(r,\omega)$ defined as eigenfunctions of the Fourier transformed equations of motion Eq. (4.53).

The electric field is given by

$$E(r,t) = -\frac{\Pi(r,t)}{\varepsilon(r)} = -\sum_m \int d\omega\, \hat{p}_m(\omega,t) f_m^*(r,\omega). \tag{B.72}$$

We choose the mode normalization such that

$$\int dr\, \epsilon(r)\, f_{m'}^*(r,\omega') f_m(r,\omega) = \delta_{mm'}\delta(\omega-\omega')\,. \tag{B.73}$$

We note that the normalization and energy labeling we have chosen here differ from the choice for the Schrödinger equation, in order to stay close to conventions usually adopted in quantum optics. As a result, care has to be taken to translate between the two cases. Specifically, to go from a Maxwell mode $f_m(r,\omega)$ to a Schrödinger mode $\phi_m(r,k)$ does not only require the substitution of the energy dependent potential $\tilde{V}(r,\omega) \to V(r)$, but also $\omega \to \sqrt{2E(k)}$ and $f_m(r,\omega)/\sqrt{\omega} \to \phi_m(r,k)$. Additionally, we note that unlike the Schrödinger equation, the kinetic term in the scalar Maxwell equation does not have a factor of $1/2$, such that effectively $H \to 2H$. The normalization of the system and bath states as well as their associated operators is modified correspondingly.

Applying the normal mode expansions Eqs. (B.70, B.71) to the Hamiltonian Eq. (B.69) gives [GL91]

$$\hat{H} = \frac{1}{2}\sum_m \int d\omega \left[\hat{p}_m^\dagger(\omega,t)\hat{p}_m(\omega,t) + \omega^2 \hat{q}_m^\dagger(\omega,t)\hat{q}_m(\omega,t)\right]. \tag{B.74}$$

The operators fulfill the equal-time commutation relations [GL91; VH03]

$$\left[\hat{q}_m(\omega,t), \hat{q}_{m'}(\omega',t)\right] = \left[\hat{q}_m(\omega,t), \hat{q}_{m'}^\dagger(\omega',t)\right] = 0\,, \tag{B.75a}$$

$$\left[\hat{p}_m(\omega,t), \hat{p}_{m'}(\omega',t)\right] = \left[\hat{p}_m(\omega,t), \hat{p}_{m'}^\dagger(\omega',t)\right] = 0\,, \tag{B.75b}$$

$$\left[\hat{q}_m(\omega,t), \hat{p}_{m'}(\omega',t)\right] = i\delta_{mn}\delta(\omega-\omega')\,, \tag{B.75c}$$

$$\left[\hat{q}_m(\omega,t), \hat{p}_{m'}^\dagger(\omega',t)\right] = i\mathcal{M}_{mm'}^*(\omega,\omega')\,, \tag{B.75d}$$

where $\mathcal{M}_{mn}(\omega,\omega')$ is defined by

$$\mathcal{M}_{mm'}(\omega,\omega') = \left\langle f_m^*(\omega)\middle| f_{m'}(\omega')\right\rangle = \int dr \varepsilon(r) f_m(r,\omega) f_{m'}(r,\omega')\,. \tag{B.76}$$

We see that the main difference to the single time derivative case is that the Hamiltonian Eq. (B.69) contains momentum operators and therefore the coordinate operators have different commutation relations. One can introduce bosonic normal mode ladder operators $\hat{c}_m(\omega, t)$ and $\hat{c}^\dagger_m(\omega, t)$ via an operator rotation [GL91; VH03]

$$\hat{q}_m(\omega) = \sqrt{\frac{1}{2\omega}}[\hat{c}_m(\omega) + \sum_{m'} \int d\omega' \mathcal{M}^*_{mm'}(\omega, \omega')\hat{c}^\dagger_{m'}(\omega')] \,, \tag{B.77}$$

$$\hat{p}_m(\omega) = i\sqrt{\frac{\omega}{2}}[\hat{c}^\dagger_m(\omega) - \sum_{m'} \int d\omega' \mathcal{M}_{mm'}(\omega, \omega')\hat{c}_{m'}(\omega')] \,, \tag{B.78}$$

where we have omitted each operators time-dependence for brevity. In this basis, the Hamiltonian Eq. (B.74) can then be written as [GL91; VH03]

$$\hat{H} = \sum_m \int d\omega \, \omega \, \hat{c}^\dagger_m(\omega)\hat{c}_m(\omega) + \text{const.} \tag{B.79}$$

and thus is again diagonal. We note, however, the difference in energy dependence to Eq. (B.106), which is a result of the double time derivative. In addition the field expansions Eqs. (B.70-B.72) now contain the coordinate operators instead of the ladder operators. If expanded in terms of ladder operators, the expansions then contain both raising and lowering operators. For example for the electric field we have, dropping time-dependences for brevity,

$$E(r) = i\sum_m \int d\omega \sqrt{\frac{\omega}{2}}[\hat{c}_m(\omega) f_m(r, \omega) - \hat{c}^\dagger_m(\omega) f^*_m(r, \omega)] \,, \tag{B.80}$$

and for the A-field

$$A(r) = \sum_m \int d\omega \sqrt{\frac{1}{2\omega}}[\hat{c}_m(\omega) f_m(r, \omega) + \hat{c}^\dagger_m(\omega) f^*_m(r, \omega)] \,. \tag{B.81}$$

We further note that this canonical quantization scheme works explicitly in the Coulomb gauge [GL91], which is relevant to obtain the correct coupling term in the presence of light-matter interactions (see also Sec. 5.2).

B.10.2 Feshbach projection

Since the mode equation Eq. (4.53) features a wave operator that is Hermitian under the modified inner product Eq. (4.55), we can apply the projection operator formalism analogously to the Schrödinger equation. In particular, we can write similarly to Eq. (4.14), adapting the energy normalization,

$$|f_m(\omega)\rangle = \sum_{\lambda \in \Lambda_Q} |\chi_\lambda\rangle \, \alpha_{\lambda m}(\omega) + \int d\omega' \left|\tilde{\psi}_{m'}(\omega')\right\rangle \beta_{mm'}(\omega, \omega') \,, \tag{B.82}$$

where the coefficients are now

$$\alpha_{\lambda m}(\omega) = \langle \chi_\lambda | f_m(\omega) \rangle \,, \tag{B.83a}$$

$$\beta_{mm'}(\omega, \omega') = \left\langle \tilde{\psi}_{m'}(\omega') \middle| f_m(\omega) \right\rangle \,. \tag{B.83b}$$

The system and bath states each fulfill eigenvalue equations with the energy dependent potential.

To obtain a few-mode Hamiltonian, we now have to apply the resulting operator basis transformation to a different normal mode Hamiltonian given by Eq. (B.74). A related expansion of this form has already been performed by Viviescas&Hackenbroich [VH03]. There are two differences to our case that have to be considered. Firstly, we have a finite number of system modes $|\chi_\lambda\rangle$, while in [VH03] an infinite set of modes has been defined by imposing boundary conditions on a spatial region. Secondly, we use the energy-dependent potential form of the wave equation, while Viviescas&Hackenbroich have performed a variable substitution to obtain a wave equation that is Hermitian under the ordinary inner product. These modifications result in the input-output scattering matrices being well defined, convergent and numerically calculable (see example calculations in Sec. 4.7 and Sec. 5.3.3 for convergence considerations in the interacting case). The reason is that the infinite mode limit has to be

taken with care due to certain coupling contributions that vanish in this limit, but still contribute to the scattering, as has already been noted by Domcke [Dom83].

Apart from these differences, the derivation (see Appendix B.10.3 for details) of the Gardiner-Collett Hamiltonian follows analogously to [VH03], yielding the Hamiltonian Eq. (4.56), where

$$\mathcal{W}_{\lambda m}(\omega) = \frac{1}{2\sqrt{\omega_\lambda \omega}} \left\langle \chi_\lambda \right| H_{QP} \left| \tilde{\psi}_m(\omega) \right\rangle , \tag{B.84a}$$

$$\mathcal{V}_{\lambda m}(\omega) = \frac{1}{2\sqrt{\omega_\lambda \omega}} \left\langle \chi_\lambda^* \right| H_{QP} \left| \tilde{\psi}_m(\omega) \right\rangle . \tag{B.84b}$$

The system and bath operators fulfill the equal time commutation relations

$$\left[\hat{a}_\lambda^\dagger, \hat{a}_{\lambda'}\right] = \delta_{\lambda\lambda'} , \tag{B.85a}$$

$$\left[\hat{b}_m^\dagger(\omega), \hat{b}_{m'}(\omega')\right] = \delta_{mm'}\delta(\omega - \omega') , \tag{B.85b}$$

$$\left[\hat{a}_\lambda^\dagger, \hat{b}_m(\omega)\right] = 0 . \tag{B.85c}$$

The electric field operator Eq. (B.72) can be expanded in this basis as

$$E(r,t) = i\sum_\lambda \sqrt{\frac{\omega_\lambda}{2}}[\hat{a}_\lambda(t)\chi_\lambda(r) - \hat{a}_\lambda^\dagger(t)\chi_\lambda^*(r)] + i\sum_m \int d\omega \sqrt{\frac{\omega}{2}}[\hat{b}_m(\omega,t)\tilde{\psi}_m(\omega,r) - \hat{b}_m^\dagger(\omega,t)\tilde{\psi}_m^*(\omega,r)] . \tag{B.86}$$

We note that, unlike in Viviescas&Hackenbroich's approach [VH03], the external modes contribute to the field even inside the cavity, as has already been noted in Appendix B.4. This feature is crucial when light-matter interactions are included in the theory, which we discuss in Chapter 5.

B.10.3 Details on the system-bath expansion of the Maxwell Hamiltonian

We can apply the system-bath expansion for the normal modes Eq. (B.82) to the Maxwell fields given by Eqs. (B.70, B.71), to get [VH03]

$$A(r,t) = \sum_\lambda \hat{Q}_\lambda \chi_\lambda(r) + \sum_m \int d\omega\, \hat{Q}_m(\omega)\tilde{\psi}_m(r,\omega) , \tag{B.87}$$

and similarly the conjugate momentum [VH03]

$$\Pi(r,t) = \sum_\lambda \varepsilon(r)\hat{P}_\lambda \chi_\lambda^*(r) + \sum_m \int d\omega\, \varepsilon(r)\hat{P}_m(\omega)\tilde{\psi}_m^*(r,\omega) . \tag{B.88}$$

Here we defined the position operators in system space

$$\hat{Q}_\lambda = \int d\omega\, \hat{q}(\omega)\alpha_\lambda(\omega) , \tag{B.89}$$

in bath space

$$\hat{Q}_m(k) = \sum_{m'} \int d\omega'\, \hat{q}_{m'}(\omega')\beta_{mm'}(\omega,\omega') , \tag{B.90}$$

as well as the momentum operators in system space

$$\hat{P}_\lambda = \sum_m \int d\omega\, \hat{p}_m(\omega)\alpha_{\lambda m}^\dagger(\omega) , \tag{B.91}$$

and in bath space

$$\hat{P}_m(k) = \sum_{m'} \int d\omega'\, \hat{p}_{m'}(\omega')\beta_{mm'}^\dagger(\omega,\omega') . \tag{B.92}$$

These relations can again be inverted (cf. Sec. 4.2.3) to give [VH03]

$$\hat{q}_m(\omega) = \sum_{\lambda\in Q} \hat{Q}_\lambda \alpha_{\lambda m}^*(\omega) + \sum_{m'} \int d\omega' \hat{Q}_{m'}(\omega')\beta_{mm'}^*(\omega,\omega') , \tag{B.93}$$

and

$$\hat{p}_m(\omega) = \sum_{\lambda\in Q} \hat{P}_\lambda \alpha_{\lambda m}(\omega) + \sum_{m'} \int d\omega' \hat{P}_{m'}(\omega') \beta_{mm'}(\omega,\omega') \,, \tag{B.94}$$

similarly to Eq. (4.16).

Applying these two expansions to the Maxwell normal mode Hamiltonian Eq. (B.74) and using the coefficient identities analogous to Appendix B.5 gives the system-bath Hamiltonian [VH03]

$$\begin{aligned}\hat{H} = &\frac{1}{2}\sum_{\lambda} [\hat{P}_\lambda^\dagger \hat{P}_\lambda + E_\lambda \hat{Q}_\lambda^\dagger \hat{Q}_\lambda] \\ &+ \frac{1}{2}\sum_{m} \int d\omega [\hat{P}_m^\dagger(\omega)\hat{P}_m(\omega) + \omega^2 \hat{Q}_m^\dagger(\omega)\hat{Q}_m(\omega)] \\ &+ \frac{1}{2}\sum_{\lambda,m} \int d\omega [\tilde{W}_{\lambda m}(\omega)\hat{Q}_\lambda^\dagger \hat{Q}_m(\omega) + h.c.] \,,\end{aligned} \tag{B.95}$$

with the coupling coefficients in Maxwell normalization

$$\tilde{W}_{\lambda m}(\omega) = \left\langle \chi_\lambda \right| H \left| \tilde{\psi}_m(\omega) \right\rangle \,. \tag{B.96}$$

As shown earlier, for the Schrödinger equation this point constitutes the final system-bath Hamiltonian and is of Gardiner-Collett form. However now the operators in the Hamiltonian are not ladder operators, instead the system operators fulfill the commutation relations [VH03]

$$[\hat{Q}_\lambda, \hat{Q}_{\lambda'}] = [\hat{Q}_\lambda, \hat{Q}_{\lambda'}^\dagger] = 0 \,, \tag{B.97a}$$

$$[\hat{P}_\lambda, \hat{P}_{\lambda'}] = [\hat{P}_\lambda, \hat{P}_{\lambda'}^\dagger] = 0 \,, \tag{B.97b}$$

$$[\hat{Q}_\lambda, \hat{P}_{\lambda'}] = i\delta_{\lambda\lambda'} \,, \tag{B.97c}$$

$$[\hat{Q}_\lambda, \hat{P}_{\lambda'}^\dagger] = i\mathcal{N}^*_{\lambda\lambda'} \,, \tag{B.97d}$$

and the bath operators fulfill

$$[\hat{Q}_m(\omega), \hat{Q}_{m'}(\omega')] = [\hat{Q}_m(\omega), \hat{Q}_{m'}^\dagger(\omega')] = 0 \,, \tag{B.98a}$$

$$[\hat{P}_m(\omega), \hat{P}_{m'}(\omega')] = [\hat{P}_m(\omega), \hat{P}_{m'}^\dagger(\omega')] = 0 \,, \tag{B.98b}$$

$$[\hat{Q}_m(\omega), \hat{P}_{m'}(\omega')] = i\delta_{mm'}\delta(\omega-\omega') \,, \tag{B.98c}$$

$$[\hat{Q}_m(\omega), \hat{P}_{m'}^\dagger(\omega')] = i\mathcal{N}^*_{mm'}(\omega,\omega') \,. \tag{B.98d}$$

To obtain a Gardiner-Collett Hamiltonian in terms of ladder operators, we have to perform an operator rotation on the system operators

$$\hat{Q}_\lambda = \sqrt{\frac{1}{2\omega_\lambda}} [\hat{a}_\lambda + \sum_{\lambda'} \mathcal{N}^*_{\lambda\lambda'} \hat{a}_{\lambda'}^\dagger] \,, \tag{B.99}$$

$$\hat{P}_\lambda = i\sqrt{\frac{\omega_\lambda}{2}} [\hat{a}_\lambda^\dagger - \sum_{\lambda'} \mathcal{N}_{\lambda\lambda'} \hat{a}_{\lambda'}] \,, \tag{B.100}$$

and on the bath operators

$$\hat{Q}_m(\omega) = \sqrt{\frac{1}{2\omega}} [\hat{b}_m(\omega) + \sum_{m'} \int d\omega' \mathcal{N}^*_{mm'}(\omega,\omega') \hat{b}_{m'}^\dagger(\omega')] \,, \tag{B.101}$$

$$\hat{P}_m(\omega) = i\sqrt{\frac{\omega}{2}} [\hat{b}_m^\dagger(\omega) - \sum_{m'} \int d\omega' \mathcal{N}_{mm'}(\omega,\omega') \hat{b}_{m'}(\omega')] \,. \tag{B.102}$$

Here, we have defined the overlap matrices [GL91]

$$\mathcal{N}_{\lambda\lambda'} = \left\langle \chi_\lambda^* \middle| \chi_{\lambda'} \right\rangle = \int dr\, \varepsilon(r)\, \chi_\lambda(r) \chi_{\lambda'}(r) \,, \tag{B.103}$$

$$\mathcal{N}_{mm'}(\omega,\omega') = \left\langle \tilde{\psi}_m^*(\omega) \middle| \tilde{\psi}_{m'}(\omega') \right\rangle = \int dr\, \varepsilon(r)\, \tilde{\psi}_m(r,\omega) \tilde{\psi}_{m'}(r,\omega') \,. \tag{B.104}$$

Substitution into the Hamiltonian Eq. (B.95) gives the Gardiner-Collett Hamiltonian Eq. (4.56) for Maxwell's equations. The associated ladder operator commutation relations Eq. (B.85) can be obtained from substitution of the operator rotation into Eqs. (B.97a, B.98a).

B.11 Maxwell scattering in the slowly varying envelope approximation

The rotating wave approximation employed in Sec. 4.5.1 simplifies the second quantized Hamiltonian by omitting counter-rotating terms. Recognizing that these terms arise due to a double time derivative in the wave equation, we may consider a modified wave equation with a single time derivative

$$-\frac{1}{2}\frac{\partial^2}{\partial r^2}\psi(r,t) = i\varepsilon(r)\frac{\partial}{\partial t}\psi(r,t)\,. \tag{B.105}$$

This can be regarded as a variant of the slowly-varying envelope approximation of Eq. (4.52).

B.11.1 Canonical quantization

For this wave equation, the canonical quantization is completely analogous to the Schrödinger case in Sec. 4.2.1. We again get a Hamiltonian

$$\hat{H} = \sum_m \int dE(k)\, E(k)\, \hat{c}_m^\dagger(k,t)\hat{c}_m(k,t)\,, \tag{B.106}$$

only now, the mode operators $\hat{c}_m(k,t)$ are associated with states $\phi_m(r,k)$ defined by the eigenvalue equation

$$-\frac{1}{2}\frac{\partial^2}{\partial r^2}\phi_m(r,k) = \varepsilon(r)E(k)\phi_m(r,k)\,. \tag{B.107}$$

B.11.2 Feshbach projection

To reveal its similarity with the Schrödinger equation [RG17], we rewrite Eq. (B.107) in the form

$$[-\frac{1}{2}\frac{\partial^2}{\partial r^2} + \tilde{V}(r,k)]\phi_m(r,k) = E(k)\phi_m(r,k)\,. \tag{B.108}$$

It is thus convenient to use the normalization and energy labeling that we used for the Schrödinger equation, such that the energy-dependent potential is given by

$$\tilde{V}(r,\omega) = [1-\varepsilon(r)]\, E(k)\,. \tag{B.109}$$

Again accounting for the modified inner product, the system-bath separation via projection operators in Sec. 4.2.3 can be performed identically to yield the same ab initio Gardiner-Collett Hamiltonian as in Sec. 4.2.4, namely

$$\hat{H} = \sum_{\lambda\in\Lambda_Q} E_\lambda \hat{a}_\lambda^\dagger \hat{a}_\lambda + \sum_m \int dE(k)\, E(k)\hat{b}_m^\dagger(k)\hat{b}_m(k) + \sum_{\lambda\in\Lambda_Q}\sum_m \int dE(k)\, \left[W_{\lambda m}(k)\hat{a}_\lambda^\dagger \hat{b}_m(k) + \text{h.c.}\right], \tag{B.110}$$

with

$$W_{\lambda m}(k) := \left\langle \chi_\lambda \right| H \left| \tilde{\psi}_m(k) \right\rangle . \tag{B.111}$$

The only differences are now the changed inner product in the couplings definition and that the system and bath states are defined by the eigenvalue equation Eq. (B.108) with an energy dependence of the potential.

Therefore, the equivalence between input-output formalism and scattering theory follows analogously to Sec. 4.4.2. This wave equation serves as a useful intermediate between the Schrödinger and Maxwell case, since it already features the modified inner product while no counter-rotating terms appear.

B.12 Linear dispersion theory

Linear dispersion theory is a method that allows to translate atoms whose transitions couple to the light field into a linear refractive index. The main assumption is that all of the transitions are weakly excited, such that a linear effective medium description can be used.

Historically, this approach was developed in the early days of quantum mechanics (see [Lax51] for a review) and can be employed for a variety of systems (see for example [Lax51; BW80; Röh05b]). Later it was realized, that even strong coupling effects such as vacuum Rabi-splitting can be described [Zhu90] by it. For us, linear dispersion theory can thus serve as an ideal practical benchmark, since it has been extensively tested experimentally and its limitations are well understood. In addition, due to the effective medium description, the concept of a mode is not necessary, that is linear dispersion theory can be understood as a basis-free method. This independence of a mode description makes linear dispersion theory also a perfect conceptual benchmark for our few-mode theory.

For completeness, we provide a slightly unusual derivation for the single transition case in the following. In particular it is shown that, apart from the weak excitation as well as the dipole approximation, no further assumptions are necessary.

The derivation is inspired by a similar account in [MT16], which focused on the consequences of the A^2-term in cavity and circuit QED.

From Eq. (5.2), the atom-field interaction Hamiltonian reads

$$\hat{H}_{\mathrm{int}} = -i\omega_{\mathrm{a}}(d\hat{\sigma}^{+} - d^{*}\hat{\sigma}^{-})A(r_a) + c_A A^2(r_a). \tag{B.112}$$

We have now also included the A^2-term, introducing an additional constant c_A, which depends on the physical realization of the two-level system [MT16].

The Heisenberg equations of motion for the atomic lowering operator then read, applying the weak excitation approximation $\hat{\sigma}^{z}(t) \approx -1$,

$$\dot{\hat{\sigma}}^{-}(t) = -i\omega_{\mathrm{a}}\hat{\sigma}^{-}(t) - \omega_{\mathrm{a}} dA(r_a, t). \tag{B.113}$$

The solution of this equation can be written as

$$\hat{\sigma}^{-}(t) = \int_{-\infty}^{\infty} \frac{d\omega}{2\pi} e^{-i\omega t} \frac{i\omega_{\mathrm{a}} dA(r_a,\omega)}{\omega_{\mathrm{a}} - \omega}, \tag{B.114}$$

where $A(r_a, \omega)$ is the Fourier transformed field operator. Similarly, for the raising operator one obtains

$$\hat{\sigma}^{+}(t) = \int_{-\infty}^{\infty} \frac{d\omega}{2\pi} e^{-i\omega t} \frac{-i\omega_{\mathrm{a}} d^{*} A(r_a,\omega)}{\omega_{\mathrm{a}} + \omega}. \tag{B.115}$$

The field equations of motion for the coupled system are

$$\varepsilon(r)\frac{\partial^2}{\partial t^2}A(r,t) = \frac{\partial^2}{\partial r^2}A(r,t) + c_A A(r,t)\delta(r-r_a) + i\omega_{\mathrm{a}}\big(d\hat{\sigma}^{+}(t) - d^{*}\hat{\sigma}^{-}(t)\big)\delta(r-r_a). \tag{B.116}$$

Substituting the solutions for the atomic operators and moving to the frequency domain, we obtain an effective Maxwell equation

$$\frac{\partial^2}{\partial r^2}A(r,\omega) = -\omega^2\varepsilon(r)A(r,\omega) + c_A\delta(r-r_a)A(r,\omega) + \frac{2\omega_{\mathrm{a}}^3|d|^2}{\omega^2-\omega_{\mathrm{a}}^2}\delta(r-r_a)A(r,\omega). \tag{B.117}$$

As a result, we can write an effective energy dependent permittivity for the two-level system as

$$\varepsilon'(r) = \varepsilon(r) - \left(\frac{\omega_{\mathrm{a}}^2}{\omega^2}\frac{2\omega_{\mathrm{a}}|d|^2}{\omega^2-\omega_{\mathrm{a}}^2} + \frac{c_A}{\omega^2}\right)\delta(r-r_a). \tag{B.118}$$

We note that for an atomic medium of number density ρ sufficiently large compared to the wavelength, the more standard expression

$$\varepsilon'(r) = \varepsilon(r) - \frac{|d|^2}{\omega-\omega_{\mathrm{a}}}\rho(r) \tag{B.119}$$

can be obtained in the weak coupling regime, where the rotating wave approximation $\omega^2 - \omega_{\mathrm{a}}^2 \approx 2\omega_{\mathrm{a}}(\omega-\omega_{\mathrm{a}})$ as well as $\omega_{\mathrm{a}}^2/\omega^2 \approx 1$, and $c_A \approx 0$ are assumed. Usually, a decay rate γ is also included

to account for additional decay channels. In our case, this contribution does not appear, since we only consider radiative losses which are already accounted for by the dipole coupling.

We further note that in one dimension and for layered systems, the scattering solutions of these modified Maxwell equations can be found efficiently using a transfer matrix formalism [Par54; Röh05b], which we employ to perform the calculations for the examples shown in the main text. For simplicity, we also neglect the A^2-term contribution by setting $c_A = 0$. The formula Eq. (B.118) nevertheless includes the contribution from counter-rotating terms, such that the applicability of the rotating wave approximation in both the cavity-bath and the atom-cavity coupling that were performed for the linear scattering calculation in ab initio few-mode theory can be tested.

B.13 Analytical convergence

In this Appendix, we show the convergence of the effective few-mode expansion for an analytically solvable example cavity. We choose the cavity geometry depicted in Fig. B.1 and the Dirichlet basis states for Q-space with $\omega_\lambda^2 = \lambda^2\pi^2/L^2 + 2\tilde{V}_0(\omega)$. This configuration is particularly convenient since the exact solution for the Schrödinger potential analogue of its free theory has been given by Domcke [Dom83]. Adapting the expression from [Dom83] to the Maxwell case gives

$$\mathcal{W}_\lambda(\omega) = \frac{w}{\alpha\cot\alpha - s - i\beta}\frac{\lambda(-1)^\lambda}{\sqrt{\omega_\lambda}}, \tag{B.120}$$

where α, β and w are constants in the sense that they do not depend on the mode index or number of chosen modes, but they may for example depend on frequency. s is the sum

$$s = \sum_{\lambda\in\Lambda_Q}\frac{2\lambda^2\pi^2}{\alpha^2 - \lambda^2\pi^2}, \tag{B.121}$$

it therefore does not explicitly depend on the mode index, however it does depend on which modes are included in the few-mode basis. The latter is important if we want to take the limit of infinitely many system modes in the end, where the effective few-mode expansion should converge and become exact. We note that s by itself does not converge on its own in this limit, however any observables quantities will in the end. This non-trivial convergence behavior has already been pointed out by Domcke [Dom83] and will be encountered again multiple times in the following. Note that one consequence is that all system-bath couplings approach zero in this limit. We note that this poses no problem for practical calculations since any relevant observables, such as the scattering matrices, should converge. Furthermore, the couplings are finite at any finite mode number, such that numerical calculations can be performed and yield the correct observables as shown in the main text.

For the free scattering matrix this convergence has already been shown by Domcke [Dom83] for the Schrödinger case. The same derivation in essence also applies to the Maxwell case by invoking the result from Sec. 4.5.1.

In the following we will show the convergence in the linear interacting case to confirm the validity of the effective few-mode expansion scheme.

From Eq. (4.59) the $\mathcal{D}$-matrix is

$$\mathcal{D}_{\lambda\lambda'}(\omega) = (\omega - \omega_\lambda)\delta_{\lambda\lambda'} + \Gamma'_{\lambda\lambda'}(\omega). \tag{B.122}$$

For consistency with the rotating wave approximation, as outlined in Sec. 4.5, we employ

$$\mathcal{D}_{\lambda\lambda'}(\omega) \approx \frac{\omega^2 - \omega_\lambda^2}{2\omega_\lambda}\delta_{\lambda\lambda'} + \frac{\Gamma_{\lambda\lambda'}(\omega)}{\sqrt{\omega_\lambda\omega_{\lambda'}}}. \tag{B.123}$$

This approximation is also convenient for the contour integral in the level shift matrix to be computable via Domcke's separable expansion method [Dom83], resulting in the expression

$$\frac{\Gamma_{\lambda\lambda'}(\omega)}{\sqrt{\omega_\lambda\omega_{\lambda'}}} = \frac{\tilde{\gamma}}{\alpha\cot\alpha - s - i\beta}\frac{\lambda(-1)^\lambda}{\sqrt{\omega_\lambda}}\frac{\lambda'(-1)^{\lambda'}}{\sqrt{\omega_{\lambda'}}} \tag{B.124}$$

where $\tilde{\gamma} = \pi^2/L^2$ is a constant. We further note that it is crucial to approximate the diagonal and level shift term consistently within the rotating wave approximation in order to obtain a converging series expansion in the rotating wave approximation (see also Sec. 4.5).

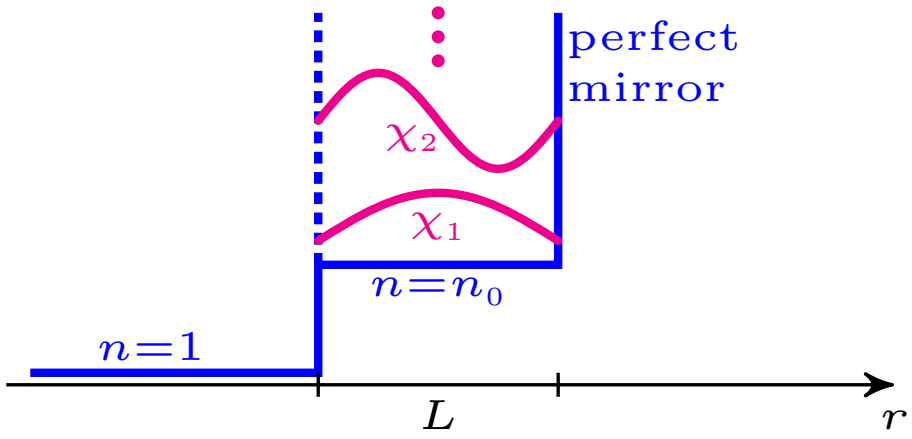

Figure B.1: A cavity geometry whose Schrödinger analogue has been solved exactly by Domcke [Dom83] using the Feshbach projection formalism.

Inverting the $\mathcal{D}$-matrix via the Sherman-Morrison formula [Dom83; GVL96] gives

$$\mathcal{D}^{-1}_{\lambda\lambda'}(\omega) = \frac{2\omega_\lambda \delta_{\lambda\lambda'}}{\omega^2-\omega_\lambda^2} - \frac{\tilde{\gamma}}{\alpha\cot\alpha - i\beta - s + \tilde{\gamma}b}\frac{2\lambda(-1)^\lambda\sqrt{\omega_\lambda}}{\omega^2-\omega_\lambda^2}\frac{2\lambda'(-1)^{\lambda'}\sqrt{\omega_{\lambda'}}}{\omega^2-\omega_{\lambda'}^2}, \tag{B.125}$$

where

$$b = \frac{L}{\pi}\sum_{\lambda\in\Lambda_Q}\frac{2\pi^2\lambda^2}{\alpha^2-\pi^2\lambda^2} = \frac{s}{\tilde{\gamma}}. \tag{B.126}$$

We then have

$$\mathcal{D}^{-1}_{\lambda\lambda'}(\omega) = \frac{2\omega_\lambda \delta_{\lambda\lambda'}}{\omega^2-\omega_\lambda^2} - \frac{\tilde{\gamma}}{\alpha\cot\alpha - i\beta}\frac{2\lambda(-1)^\lambda\sqrt{\omega_\lambda}}{\omega^2-\omega_\lambda^2}\frac{2\lambda'(-1)^{\lambda'}\sqrt{\omega_{\lambda'}}}{\omega^2-\omega_{\lambda'}^2}.$$

The coupling constants in this basis are

$$g_\lambda = \tilde{g}\frac{\sin\left(\frac{\pi\lambda}{L}r_\mathrm{a}\right)}{\sqrt{\omega_\lambda}}, \tag{B.127}$$

where $\tilde{g}$ is a constant containing d and ω_a. r_a is the atom's position, which we take to be $r_\mathrm{a} = \frac{L}{2}$, such that the atom is located at the cavity center. We are now in a position to check the convergence of the interaction sums appearing in Eq. (5.11). We can write

$$\underline{g}^T\underline{\underline{\mathcal{D}}}^{-1}(\omega)\underline{g}^* = G_1 - \frac{4|\tilde{g}|^2L^2}{\alpha\cot\alpha - i\beta}(G_2)^2, \tag{B.128}$$

where the sums

$$G_1 = 2|\tilde{g}|^2L^2\sum_{\lambda\in\Lambda_Q^\mathrm{odd}}\frac{1}{\alpha^2-\pi^2\lambda^2} \tag{B.129}$$

and

$$G_2 = \sum_{\lambda\in\Lambda_Q}\sin\left(\frac{\pi\lambda}{2}\right)(-1)^\lambda\frac{\pi\lambda}{\alpha^2-\pi^2\lambda^2}. \tag{B.130}$$

In the limit of infinite number of system modes, that is $\Lambda_Q = \{\chi_1, \chi_2, ..., \chi_N\}$ with $N\to\infty$ one obtains

$$G_1 \to -\frac{|\tilde{g}|^2L^2}{2\alpha}\tan\frac{\alpha}{2}, \tag{B.131}$$

and G_2 can be expressed in terms of beta, gamma and hypergeometric functions. Therefore $\underline{g}^T\underline{\underline{\mathcal{D}}}^{-1}(\omega)\underline{g}^*$ converges individually in this limit, only containing isolated poles at certain energies.

Similarly,

$$\underline{g}^T \underline{\underline{\mathcal{D}}}^{-1}(\omega) \underline{\underline{\mathcal{W}}}(\omega) = \frac{w/\pi}{\alpha \cot \alpha - s - i\beta} \left[2\tilde{g} L^2 G_2 - \frac{2\tilde{g} L^2}{\alpha \cot \alpha - i\beta} G_2 s \right], \tag{B.132}$$

and

$$\underline{\underline{\mathcal{W}}}^\dagger(\omega) \underline{\underline{\mathcal{D}}}^{-1}(\omega) \underline{g}^* = \left[\frac{w/\pi}{\alpha \cot \alpha - s - i\beta} \right]^* \left[2\tilde{g}^* L^2 G_2 - \frac{2\tilde{g}^* L^2}{\alpha \cot \alpha - i\beta} G_2 s \right]. \tag{B.133}$$

These terms contain the s-sum, which diverges in the limit $N \to \infty$. They can be understood by comparing to the empty cavity term

$$\underline{\underline{\mathcal{W}}}^\dagger(\omega) \underline{\underline{\mathcal{D}}}^{-1}(\omega) \underline{\underline{\mathcal{W}}}(\omega) = \left| \frac{w}{\alpha \cot \alpha - s - i\beta} \right|^2 \left[\frac{L}{\pi} s - \frac{L/\pi}{\alpha \cot \alpha - i\beta} s^2 \right], \tag{B.134}$$

which, as already shown by Domcke [Dom83], is convergent and yields a well defined resonant scattering matrix. The non-convergent s-terms furthermore completely cancel when the result is multiplied by the background scattering matrix [Dom83].

We have thus shown the convergence of the few-mode expansion in the infinite mode limit for a special case. We note that in order to obtain this converging series, there are two crucial factors. Firstly, for gauge consistency we require the $p \cdot A$ interaction term, leading to a $1/\sqrt{\omega_\lambda}$ dependence in the couplings. Secondly, the rotating wave approximation in the system-bath coupling has to be applied consistently (see also Sec. 4.5). The latter is already necessary in the non-interacting case and thus a feature of the system-bath interaction, rather than of the light-matter coupling.

Appendix C

Technical details on the x-ray ab initio few-mode theory

This appendix is based on the following publication:

Ab initio quantum models for thin-film x-ray cavity QED
D. Lentrodt, K. P. Heeg, C. H. Keitel, and J. Evers
Physical Review Research **2**, 023396 (2020)

C.1 Detailed derivation of the x-ray ab initio few-mode theory

In Sec. 6.3, we explained how the phenomenological few-mode model for thin-film x-ray cavities with Mössbauer nuclei [HE13; HE15] can be modified to comply with ab initio theory. We focused on differences to the established model [HE13; HE15], which has been used extensively for interpreting experiments [Hee13; Hee15a; Hee15b; HE15; Hab17; Hab19], and on what advantages the ab initio version can provide practically, which we illustrated extensively for example systems.

In this appendix, we provide a detailed derivation of the improved ab initio model. We outline which approximations are necessary to obtain such a description and provide a clear physical interpretation of the model parameters and operator degrees of freedom.

C.1.1 Classical wave equation for the layered geometry

The thin-film x-ray cavities under consideration are made up of a dieletric cavity structure (see Fig. 2.2 for an illustration), which acts as an off-resonant background confining the electromagnetic field. Before quantizing the system in order to describe the field-nucleus interaction, we consider the classical wave propagation in this geometry in the absence of the resonant nuclei, that is for the "empty cavity". The system can then be described by Maxwell's equations with a spatially varying dielectric permittivity [Röh05b; RG17].

Again omitting polarization degrees of freedom, the scalar Maxwell mode equation for a homogeneous isotropic medium [SB08; Buh12] in frequency space reads [RG17; GL91]

$$\nabla^2 f_m(\mathbf{r},\omega) + \varepsilon(\mathbf{r})\omega^2 f_m(\mathbf{r},\omega) = 0\,, \tag{C.1}$$

where $f_m(\mathbf{r},\omega)$ are the normal modes for the scattering problem. The index m encodes all additional necessary degrees of freedom. We note that we neglect the frequency dependence of the dielectric permittivity $\varepsilon(\mathbf{r})$ of the off-resonant cavity material here, which is typically irrelevant for the nuclear dynamics due to the narrow resonances, but can be important if electronic resonances [Hab19] or collective strong coupling [Hab16a] are considered.

In the case of thin-film x-ray cavities, the system is approximately translation invariant in two directions, such that the dielectric index only depends on the transverse coordinate, $\varepsilon(\mathbf{r}) = \varepsilon(z)$. As can be seen by a product ansatz, the normal modes then take the form

$$f_m(\mathbf{r},\omega,\mathbf{k}_\parallel) = C\, e^{i\mathbf{k}_\parallel\cdot\mathbf{r}_\parallel} \tilde{f}_m(z,k_\perp,\theta)\,, \tag{C.2}$$

where $\mathbf{r}_\parallel$ is a displacement vector in the layer plane, $\mathbf{k}_\parallel$ is the corresponding parallel wave vector, C is a normalization factor for the parallel mode component, and $\tilde{f}_m(z, k_\perp, \theta)$ is an effective one-dimensional mode function at incidence angle θ. The latter fulfills the effective one-dimensional mode equation

$$\frac{d^2}{dz^2}\tilde{f}_m(z, k_\perp, \theta) + \tilde{\varepsilon}(z, \theta)k_\perp^2 \tilde{f}_m(z, k_\perp, \theta) = 0\,, \tag{C.3}$$

where

$$\tilde{\varepsilon}(z, \theta) = \frac{\varepsilon(z) - \cos^2(\theta)}{\sin^2(\theta)}\,. \tag{C.4}$$

The perpendicular wave component can be obtained from the mode energy via $k_\perp = \omega \sin(\theta)$ and is to be understood as a scattering boundary condition, that is the incoming perpendicular wave vector in the far field (see Fig. 2.2 for an illustration).

In summary, the classical three dimensional problem for the layer geometry can be reduced to an effective one-dimensional problem with an effective dielectric constant

$$\varepsilon(r) \to \tilde{\varepsilon}(r, \theta) = \frac{\varepsilon(r) - \cos^2(\theta)}{\sin^2(\theta)}\,, \tag{C.5}$$

and wave energy

$$\omega \to k_\perp(\omega, \theta) = \omega \sin(\theta)\,. \tag{C.6}$$

These substitutions are employed in the analytical calculation in Sec. 6.8.

C.1.2 Recap of the ab initio few-mode construction

Before we turn to applying the effective few-mode theory to the three-dimensional wave equation above, we first briefly summarize its concept as presented in [LE20]. For brevity, we focus on the basic principles that are necessary to understand the more detailed derivation for the layered geometry in the following section.

The starting point of the few-mode scheme is a continuum theory, that is an open or scattering problem with a continuum Hamiltonian, which can, for example, be obtained from canonically quantizing a wave equation such as Eq. (C.1). In quantum optical scenarios, the wave equation can, for example, describe the electromagnetic field inside and around a cavity. The considered Hamiltonian is typically of the form

$$H_{\text{field}} = \sum_m \int d\omega \omega \hat{b}_m^\dagger(\omega)\hat{b}_m(\omega)\,. \tag{C.7}$$

In three dimensions, the index m can also include continuous parameters such as the propagation direction of a wave.

The central feature of this Hamiltonian is that it comprises a continuum of frequencies, as is typical for an open quantum system. When coupling the field to a two-level system within the dipole approximation, one obtains a field-matter Hamiltonian that is well-known in the theory of light-matter interactions in free space [SZ97] or cavities [GL91; Kri14; MPT17].

However, the continuum Hamiltonian conceals the resonance structure of the cavity, which is encoded in the frequency-dependence of the light-matter coupling [Kri14; MPT17; BP02]. For this reason, phenomenological few-mode Hamiltonians and input-output theory [GC85; GZ04] are common tools to describe light-matter interaction in structured environments such as cavities. The few-mode model for thin-film X-ray cavity QED with Mössbauer nuclei by Heeg & Evers [HE13; HE15] is based on the latter approach.

The ab initio few-mode theory [LE20] provides a connection between the two sides and allows to systematically construct few-mode Hamiltonians from the continuum description. Most importantly, the ab initio construction allows to generalize the approach such that overlapping modes and bad cavities can be described accurately. It is the latter feature which is particularly valuable in the X-ray case, where the cavities in use are highly leaky, feature overlapping modes and are doped with nuclear resonances boasting high spectral resolution.

In the ab initio few-mode theory, the first step is a basis transformation, splitting the continuum modes into a discrete part (the "system") and an interacting continuum (the "bath"). The few modes that are included in the system part can be chosen arbitrarily and the resulting theory for the free field remains exact. In particular, an exact version of the input-output formalism can be obtained. For scattering observables, the latter allows to compute an input-output scattering matrix $S_{\mathrm{io}}(\omega)$ analogously to the phenomenological case, which describes the scattering between bath modes. The full scattering matrix is then obtained by translating the bath modes into the asymptotically free modes [GL91; Dom83] via

$$S(\omega) = S_{\mathrm{bg}}(\omega) S_{\mathrm{io}}(\omega)\,, \tag{C.8}$$

with the so-called background scattering matrix $S_{\mathrm{bg}}(\omega)$.

While in the free theory, the few-mode construction is exact independently of the choice of modes, for the interacting case it is useful to choose the few-mode basis such that the relevant resonances of the system are well approximated [LE20]. The advantage is that if a sufficient number of modes are included in the few-mode basis, the so called few-mode approximation can be applied: the direct interaction between the external bath modes and the atom or matter degrees of freedom can be neglected, such that the latter only couple directly to the few system modes. This feature, in turn, allows for various existing solution methods to be applied [GZ04; Bre16; dA17; Car93]. For example, a Markovian Master equation can often be derived for a strongly coupled light-matter system if the strongly coupled modes are included in the system and only the remaining weakly coupled bath modes are traced out, which is reminiscent of an input-output version of the pseudo-modes theory [Gar97a; Tam18].

We note that the few-mode construction results in a converging expansion scheme in the mode number [LE20], such that the validity of the few-mode approximation can be ensured by including more modes.

The form of the resulting ab initio Hamiltonian [VH03; LE20] is very close to the one used in the phenomenological model for thin-film X-ray cavity QED [HE13; HE15], such that the ab initio few-mode theory can provide new insights into the system by directly connecting to and extending an existing and well established model. In [LE20], only one-dimensional special cases are considered. The thin-film geometry and the extreme parameter regimes encountered in the hard X-ray and nuclear resonance case require additional consideration. The precise derivation of the relevant few-mode Hamiltonian and an outline of its limitations are given in the following section.

As a last remark on the basics of the ab initio few-mode theory, we note that from a computational perspective, the main step to obtain the few-mode Hamiltonian and its coupling constants is to calculate matrix elements between the few-mode, bath and scattering states [LE20; Dom83]. While the resulting formulas in [LE20] are general, the explicit computation for the one-dimensional example systems relies on separable expansions of the cavity structure [Dom83]. In this thesis, the same approach is applied to simple cases of the three-dimensional layered geometry. More general cavity structures may become accessible using related methods from quantum chemistry [BD84; Dom83].

C.1.3 Application to the layered geometry

The wave equation Eq. (C.1) can be quantized canonically [GL91], resulting in the Hamiltonian

$$H_{\mathrm{cav}} = \sum_m \int d^2\mathbf{k}_\parallel dk_\perp \omega(\mathbf{k}_\parallel, k_\perp) \hat{c}_m^\dagger(\mathbf{k}_\parallel, k_\perp) \hat{c}_m(\mathbf{k}_\parallel, k_\perp), \tag{C.9}$$

where $\hat{c}_m(\mathbf{k}_\parallel, k_\perp)$ are bosonic operators at a given parallel and perpendicular wave vector, with $\omega(\mathbf{k}_\parallel, k_\perp)$ representing their corresponding frequency. The operator equations of motion for this Hamiltonian are equivalent to the Maxwell wave equation [GL91]. The advantage of the quantized formalism is that we can treat interactions with resonant nuclei (see Sec. C.1.4) beyond mean-field Maxwell-Bloch [Shv99; LPK12] or semi-classical scattering treatments [Röh99a; Röh05b]. We note that the canonical normal modes quantization is valid for real refractive indices. To account for complex refractive indices, which are relevant in the hard x-ray regime, we employ a non-hermitian Hamiltonian prescription, which allows the above Hamiltonian to be used directly (see Appendix C.1.6 for details). For a complete treatment of absorptive processes within the framework of macroscopic QED see Chapter 7, where an alternative approach is developed.

The Hamiltonian Eq. (C.9) features the typical normal mode continuum of open scattering systems [GL91; LE20]. In order to connect to the successful phenomenological model [HE13; HE15] for thin-film x-ray cavities with Mössbauer nuclei, the notion of a few resonant modes has to be introduced. To perform this step systematically without a model or fitting prescription, we employ the ab initio few-mode theory [LE20], whose concept is summarized in the previous section.

Following this approach, we can partition the cavity Hamiltonian given above into a few-mode part and an external bath. If we choose the few mode basis to respect the translation symmetry, the full Hamiltonian can be written as

$$H_{\mathrm{cav}} = H_{\mathrm{few}} + H_{\mathrm{ext}}\,, \tag{C.10}$$

where

$$H_{\mathrm{few}} = \int d^2\mathbf{k}_\parallel \sum_{\lambda\in\mathrm{modes}} \omega_\lambda(\mathbf{k}_\parallel)\hat{a}^\dagger_\lambda(\mathbf{k}_\parallel)\hat{a}_\lambda(\mathbf{k}_\parallel)\,, \tag{C.11}$$

$$\begin{aligned} H_{\mathrm{ext}} = &\sum_{m\in\mathrm{channels}} \int d\omega d^2\mathbf{k}_\parallel \tilde{\omega}(\omega,\mathbf{k}_\parallel)\hat{b}^\dagger_m(\omega,\mathbf{k}_\parallel)\hat{b}_m(\omega,\mathbf{k}_\parallel) \\ &+ \sum_{\substack{m\in\mathrm{channels}\\ \lambda\in\mathrm{modes}}} \int d\omega d^2\mathbf{k}_\parallel \mathcal{W}_{\lambda m}(\omega,\mathbf{k}_\parallel)\hat{b}_m(\omega,\mathbf{k}_\parallel)\hat{a}^\dagger_\lambda(\mathbf{k}_\parallel) \\ &+ h.c.\,, \end{aligned} \tag{C.12}$$

where we have employed the relabeling from Appendix C.1.1 and $\hat{a}_\lambda(\mathbf{k}_\parallel)$ are bosonic few-mode operators at each parallel wave vector, which have frequency $\omega_\lambda(\mathbf{k}_\parallel)$. Similarly, $\hat{b}_m(\omega,\mathbf{k}_\parallel)$ are the external bath operators, which couple to the few-mode operators with coupling strength $\mathcal{W}_{\lambda m}(\omega,\mathbf{k}_\parallel)$.

We see that the Hamiltonian is a linear combination of one-dimensional few-mode terms at each parallel wave vector $\mathbf{k}_\parallel$. The parallel direction thus still features a continuum. Since there is no confinement or resonance structure in the parallel direction, this continuum can not easily be removed by another few-mode projection.

C.1.4 Nuclear resonant interaction

The interaction with nuclear transitions can be described within the dipole and rotating wave approximation by the Hamiltonian

$$H = H_{\mathrm{cav}} + H_{\mathrm{nuc}} + H_{\mathrm{int}}\,, \tag{C.13}$$

where

$$H_{\mathrm{nuc}} = \sum_{\substack{l\in\mathrm{ensembles}\\ n\in 1,2\ldots N_l}} \frac{\omega_{\mathrm{nuc},l}}{2}\hat{\sigma}^z_{ln}\,, \tag{C.14}$$

$$\begin{aligned} H_{\mathrm{int}} = &\int d^2\mathbf{k}_\parallel \sum_{\substack{\lambda\in\mathrm{modes}\\ l\in\mathrm{ensembles}\\ n\in 1,2\ldots N_l}} g_{\lambda ln}(\mathbf{k}_\parallel)\hat{a}_\lambda(\mathbf{k}_\parallel)\hat{\sigma}^+_{ln} + h.c. \\ &+ \int d\omega d^2\mathbf{k}_\parallel \sum_{\substack{m\in\mathrm{channels}\\ l\in\mathrm{ensembles}\\ n\in 1,2\ldots N_l}} \tilde{g}_{mln}(\omega,\mathbf{k}_\parallel)\hat{b}_m(\omega,\mathbf{k}_\parallel)\hat{\sigma}^+_{ln} + h.c.\,, \end{aligned} \tag{C.15}$$

and $\hat{\sigma}^{+,-,z}$ are the Pauli operators for the nuclear transitions. We have included the effect of multiple ensembles (indexed by l), each of which contains N_l individual nuclei (indexed by n) and couples to the system modes (indexed by λ) with coupling constant $g_{\lambda ln}(\mathbf{k}_\parallel)$ as well as to the bath modes with coupling constant $\tilde{g}_{mln}(\omega,\mathbf{k}_\parallel)$. These coupling constants can be calculated from nuclear transition and material parameters (see Appendix C.1.7 for details), which are also used in the layer formalism [Röh05b].

We note that if a sufficient number of system modes is chosen, the few-mode approximation can be performed [LE20], that is the direct interaction of the nuclei with the bath modes can be neglected, as explained in Appendix C.1.2.

We further note that in addition to these Hamiltonian terms which arise from the nucleus-light coupling, nuclear transitions can feature additional incoherent decay channels, such as internal conversion [Röh05b; Stu04; HT99]. For example for ^{57}Fe where the α-factor is 8.56 [Röh05b], internal conversion makes up the majority of the incoherent decay rate (see Appendix C.1.7 for details). In our prescription, this effect can be accounted for by a Lindblad term [Hee13]

$$\mathcal{L}_{\mathrm{IC}}[\rho] = \sum_{\substack{l\in\text{ensembles}\\ n\in 1,2\dots N_l}} \frac{\gamma_{\mathrm{IC}}}{2}(2\hat{\sigma}^-_{ln}\rho\hat{\sigma}^+_{ln} - \{\hat{\sigma}^+_{ln}\hat{\sigma}^-_{ln},\, \rho\})\,, \tag{C.16}$$

where γ_{IC} is the internal conversion decay constant.

We note that since the field continuum is still present in the theory, radiative incoherent losses are already included in the light-nucleus interaction Hamiltonian and should not be added as an additional incoherent Lindblad term. If the few-mode approximation is performed, a small residual decay contribution is added to the incoherent decay rate to account for the weak interaction with the removed bath modes, which tends to zero at large system mode numbers.

Within the dipole, rotating-wave and non-hermitian field Hamiltonian approximations (see also Appendices C.1.6, C.1.7), the Hamiltonian derived above is a fully general description in few-mode form, with the translational invariance of the system explicitly implemented.

C.1.5 Effective one-dimensional problem

We see that the derived few-mode Hamiltonian is already very similar to the phenomenological model [HE13; HE15], with the main difference being the continuum of parallel wave vectors. In order to complete the connection, we derive an effective one-dimensional description in this section, which is well applicable in the linear excitation regime.

We first note that in practice, the nuclear cavity QED system is often studied spectroscopically. That is the system is excited by a collimated and highly monochromatic[1] beam from a modern low-emittance x-ray facility such as a synchrotron or an x-ray free electron laser in conjunction with a high-resolution monochromator. At anticipated light sources such as x-ray free electron laser oscillators [Ada19], similar setups are to be expected.

In such a setup, the exciting light defines a narrow range of incidence angles and consequently a narrow range of parallel wave vectors. Due to the assumed translational invariance of the system in the layer plane, the parallel wave vector is a conserved quantity in the low-excitation regime (see Sec. 7.5 for details, and [LoE14b] for a related discussion of higher excitations), such that each parallel wave vector forms an isolated subspace of the dynamics. Therein, we can then obtain the effective one-dimensional Hamiltonian

$$H^{\mathrm{1D}}(\mathbf{k}_\parallel^{(\mathrm{in})}) = H^{\mathrm{1D}}_{\mathrm{cav}}(\mathbf{k}_\parallel^{(\mathrm{in})}) + H_{\mathrm{nuc}} + H^{\mathrm{1D}}_{\mathrm{int}}(\mathbf{k}_\parallel^{(\mathrm{in})})\,, \tag{C.17}$$

where

$$H^{\mathrm{1D}}_{\mathrm{cav}}(\mathbf{k}_\parallel^{(\mathrm{in})}) = H^{\mathrm{1D}}_{\mathrm{few}}(\mathbf{k}_\parallel^{(\mathrm{in})}) + H^{\mathrm{1D}}_{\mathrm{ext}}(\mathbf{k}_\parallel^{(\mathrm{in})})\,, \tag{C.18}$$

with

$$H^{\mathrm{1D}}_{\mathrm{few}}(\mathbf{k}_\parallel^{(\mathrm{in})}) = \sum_{\lambda\in\text{modes}} \omega_\lambda(\mathbf{k}_\parallel^{(\mathrm{in})})\hat{a}^\dagger_\lambda(\mathbf{k}_\parallel^{(\mathrm{in})})\hat{a}_\lambda(\mathbf{k}_\parallel^{(\mathrm{in})})\,, \tag{C.19}$$

$$\begin{aligned} H^{\mathrm{1D}}_{\mathrm{ext}}(\mathbf{k}_\parallel^{(\mathrm{in})}) = &\sum_{m\in\text{channels}} \int d\omega\tilde{\omega}(\omega,\theta)\hat{b}^\dagger_m(\omega,\mathbf{k}_\parallel^{(\mathrm{in})})\hat{b}_m(\omega,\mathbf{k}_\parallel^{(\mathrm{in})}) \\ &+ \sum_{\substack{m\in\text{channels}\\ \lambda\in\text{modes}}} \int d\omega\mathcal{W}_{\lambda m}(\omega,\mathbf{k}_\parallel^{(\mathrm{in})})\hat{b}_m(\omega,\mathbf{k}_\parallel^{(\mathrm{in})})\hat{a}^\dagger_\lambda(\mathbf{k}_\parallel^{(\mathrm{in})}) \\ &+ h.c.\,, \end{aligned} \tag{C.20}$$

[1] On the spectral scale of the cavity, the beams are monochromatic. On the scale of the nuclei on the other hand, the exciting radiation has a broad spectrum.

and

$$H_{\mathrm{int}}^{\mathrm{1D}}(\mathbf{k}_{\parallel}^{(\mathrm{in})}) = \sum_{\substack{\lambda\in\text{modes}\\ l\in\text{ensembles}\\ n\in 1,2\ldots N_l}} g_{\lambda ln}(\mathbf{k}_{\parallel}^{(\mathrm{in})})\hat{a}_{\lambda}(\mathbf{k}_{\parallel}^{(\mathrm{in})})\hat{\sigma}_{ln}^{+} + h.c.\,. \tag{C.21}$$

In addition to the internal conversion Lindblad term, we obtain a radiative contribution to the incoherent decay

$$\mathcal{L}_{\mathrm{rad}}[\rho] = \sum_{\substack{l\in\text{ensembles}\\ n\in 1,2\ldots N_l}} \frac{\gamma_{\mathrm{rad}}}{2}(2\hat{\sigma}_{ln}^{-}\rho\sigma_{ln}^{+} - \{\hat{\sigma}_{ln}^{+}\hat{\sigma}_{ln}^{-},\,\rho\})\,, \tag{C.22}$$

where γ_{rad} is the spontaneous emission rate of the nuclear transition in the cavity environment. The two incoherent terms can be combined to

$$\mathcal{L}_{\mathrm{SE}}[\rho] = \sum_{\substack{l\in\text{ensembles}\\ n\in 1,2\ldots N_l}} \frac{\gamma}{2}(2\hat{\sigma}_{ln}^{-}\rho\sigma_{ln}^{+} - \{\hat{\sigma}_{ln}^{+}\hat{\sigma}_{ln}^{-},\,\rho\})\,, \tag{C.23}$$

which is the single-transition version of the term used in [HE13]. We note that $\gamma = \gamma_{\mathrm{IC}} + \gamma_{\mathrm{rad}}$ can in principle differ slightly from the natural linewidth since the cavity modes are retained in the Hamiltonian, but is essentially equal for all practical purposes.

Noting that $\mathbf{k}_{\parallel}^{(\mathrm{in})}$ appears only as a parametric dependence now, we see that the above description provides the improved input-output model summarized in Sec. 6.3, where the parallel wave vector dependence is rewritten in terms of the incidence angle and the frequency of the transition energy.

We have thus provided an ab initio generalization of the successful phenomenological model [HE13; HE15] for thin-film x-ray cavities with Mössbauer nuclei and clarified its origin as well as the involved approximations. The basic structure and its relation to the original phenomenological version [HE13; HE15] are summarized in Sec. 6.3.

In the Chapter 6, we show that the improved model provides a number of qualitative advantages, allowing the quantum optical description to be applied to new systems and featuring essentially exact predictions in the linear regime. The ab initio character of the theory further provides a solid foundation, which, as a main motivation beyond the quantum interpretation of linear scattering experiments, will allow the method to be applied as a predictive tool in the non-linear and correlated quantum dynamics regime.

C.1.6 Complex refractive index in the ab initio few-mode theory

In the treatment presented in Appendix C.1.3 and also in the original development of the ab initio few-mode theory [LE20], a real refractive index is considered. X-ray cavities, however, feature significant material absorption and as a result a complex refractive index should be accounted for.

A rigorous treatment of material absorption and the resulting effective quantum theory can be obtained in various ways (see [SB08; Buh12] for a review as well as [Fra19] for a recent advance). In general, the resulting light-matter Hamiltonian is highly complex even if the resonant quantum interaction is not included.

Here, we resort to a simple approach, which is also employed in the standard nuclear resonant scattering literature including the semi-classical scattering theory [Röh99a; Röh05b]. In the latter approach, the Maxwell wave equation is directly coupled to the resonant nuclei or atoms, while neglecting quantization effects of the light field. For a real refractive index, the generalization to the quantum level is given by the canonical quantization scheme (see Appendix C.1.3). We then include the absorptive character of the material by using the complex refractive index to obtain a non-Hermitian Hamiltonian. Since this approximation is also included in the standard semi-classical x-ray scattering theory [Röh99a; Röh05b], previous experiments substantiate its validity at least for intensity observables at low driving fields. The approach can be complemented by the quantum jump formalism [Min19; Car99; Car08], similarly to recent work using Green's function techniques [Mas19], where the absorptive bath is treated rigorously from the outset (see Chapter 7 for a detailed comparison of the approaches).

Practically, the non-Hermitian few-mode Hamiltonian approach is implemented by performing calculations as for a real refractive index, and then transferring to the non-Hermitian theory by substitution of the complex refractive index. We note that for numerical implementations, one has to ensure that complex conjugation operations, as they are used for example in the quantum scattering theory [Dom83] underlying the projection scheme, are not applied to the refractive index.

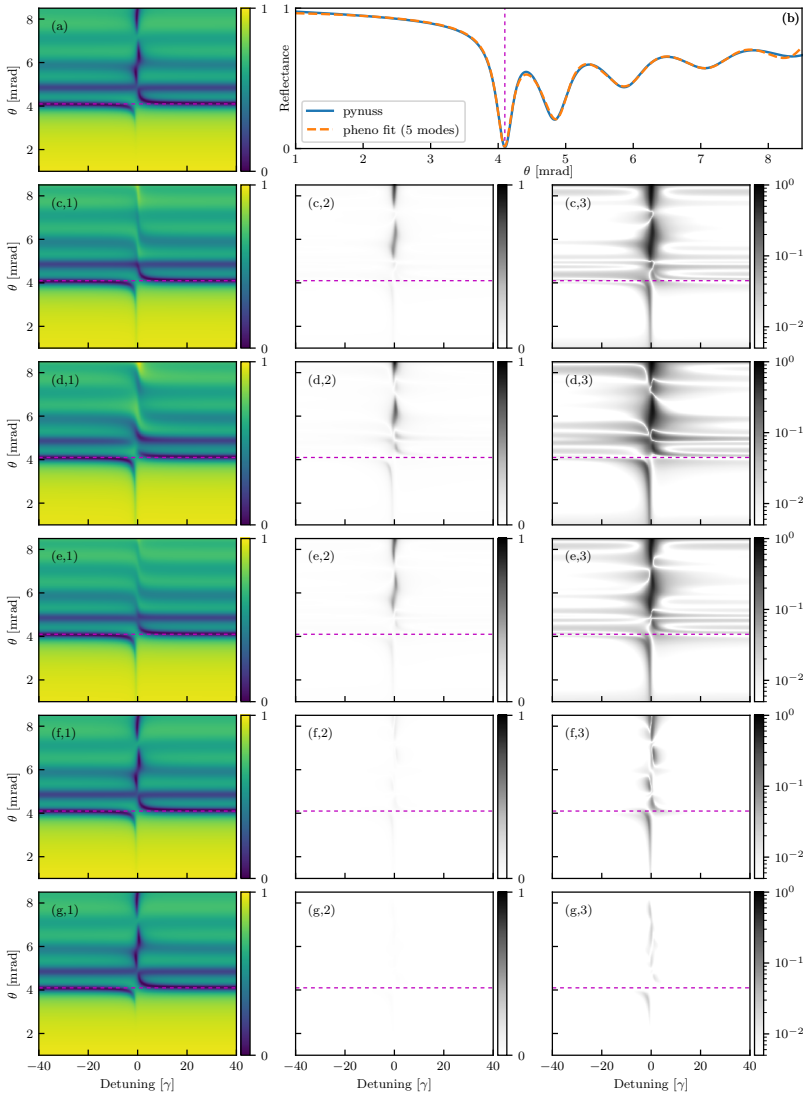

Figure C.1: (Color online) Comparison of the ab initio few-mode model with corresponding phenomenological approaches. (a) Reference spectrum obtained using a semi-classical calculation. Panel (b) shows the best phenomenological model fit (five modes, yellow dashed) of the rocking curve (solid blue), which is used to constrain the cavity parameters $(\kappa_\lambda, \kappa_{R,\lambda}, \theta_\lambda)$ in the phenomenological models. Panels (c)-(g) show results for different few-mode approaches, with (c)-(e) comprising the phenomenological model with different parameter fitting procedures (fit method 1, 2 and 3, respectively, definition see text) and (f), (g) being the ab initio few-mode theory with 5 and 20 modes, respectively. Panels (c-g,1) show the model spectrum in each case, while panels (c-g,2) and (c-g,3) show the residual deviation on a linear and logarithmic scale, respectively.

C.1.7 Coupling constant in the ab initio few-mode theory

In this appendix, we derive the mode-nucleus coupling in terms of known nuclear resonance and material parameters.

Mode coupling and quantization area

The few-mode coupling in our approach can be written as [LE20]

$$g_{\lambda l n}(\mathbf{k}_\parallel) = -\frac{i d \omega_{\mathrm{nuc},l}}{\sqrt{2\omega_\lambda(\mathbf{k}_\parallel)}} \chi_\lambda(z_l, \mathbf{r}_\parallel, \mathbf{k}_\parallel)\,, \tag{C.24}$$

where $\chi_\lambda(z, \mathbf{r}_\parallel, \mathbf{k}_\parallel)$ is the three-dimensional system mode from Eq. C.15 and z_l the vertical position of the nuclei, which is by construction independent of n within the thin-layer approximation. If z_l varies within one ensemble, the latter should be divided into multiple sub-ensembles (see also the

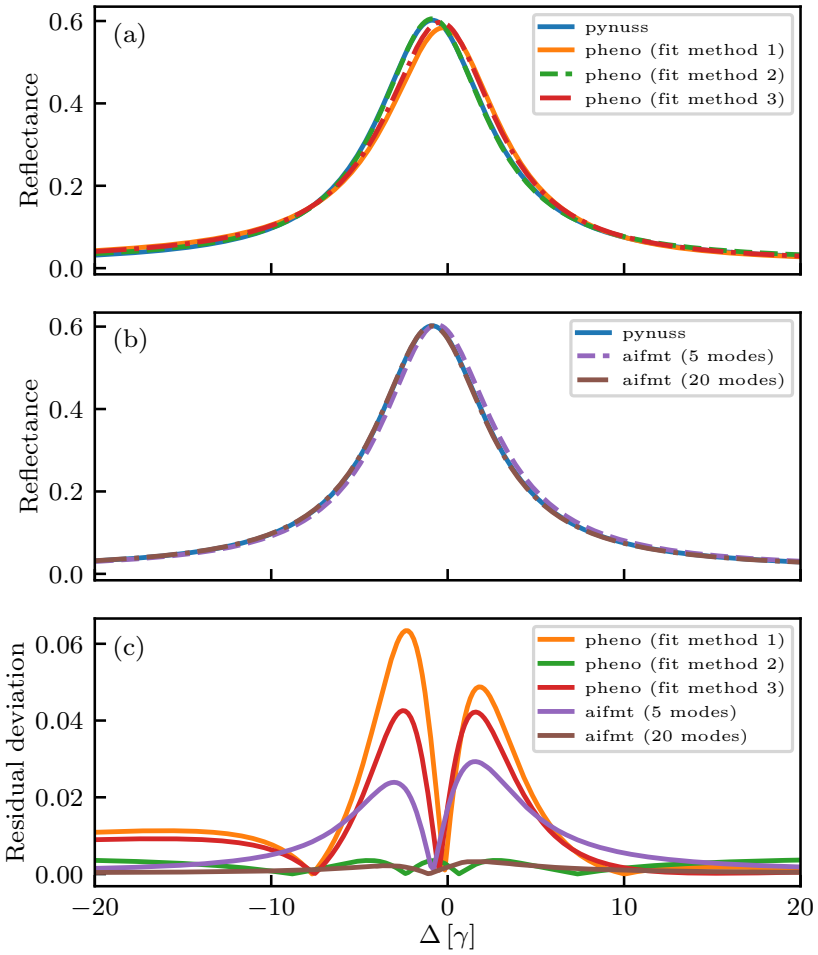

Figure C.2: (Color online) One dimensional slices at the first cavity resonance $\theta = \theta_0$ of the spectra in Fig. C.1 resulting from the different models. Panel (a) compares the various phenomenological fits (see legend) to the semi-classical reference (solid blue). Panel (b) compares the ab initio few-mode result for 5 and 20 modes (see legend). In panel (c), the residual deviations are shown.

thick layer treatment in Sec. 6.9). Since the system modes themselves also fulfill the translational invariance, we have

$$\chi_\lambda(z_l, \mathbf{r}_\parallel, \mathbf{k}_\parallel) = C\, e^{i\mathbf{k}_\parallel \cdot \mathbf{r}_\parallel} \tilde{\chi}_\lambda(z_l)\,, \tag{C.25}$$

where $\tilde{\chi}_\lambda(z_l)$ is the effective one-dimensional mode function evaluated at the nuclear layer position z_l and C is a normalization factor. We therefore see that the mode normalization constant is important to determine the value of the coupling. In order to obtain the constant, we resort to the usual box quantization procedure [SZ97] for the parallel direction. We require that

$$\int_{A_\parallel} d^2\mathbf{k}_\parallel \int dz \chi_\lambda(z, \mathbf{r}_\parallel, \mathbf{k}_\parallel) = 1\,, \tag{C.26}$$

where $A_\parallel$ is a parallel quantization area, such that we obtain

$$C = \frac{1}{\sqrt{A_\parallel}}\,. \tag{C.27}$$

Consequently, the coupling constant is given by

$$g_{\lambda l n}(\mathbf{k}_\parallel) = -\frac{i d\omega_{\mathrm{nuc},l}}{\sqrt{2A_\parallel \omega_\lambda(\mathbf{k}_\parallel)}} e^{i\mathbf{k}_\parallel \cdot \mathbf{r}_{\parallel,ln}} \tilde{\chi}_\lambda(z_l)\,. \tag{C.28}$$

The phase factor $e^{i\mathbf{k}_\parallel \cdot \mathbf{r}_{\parallel,ln}}$ can be absorbed into an algebra preserving redefinition of the $\hat{\sigma}$-operators in the effective one-dimensional Hamiltonian [Hee14], amounting to a basis change that affects the

nuclear dipole moment by a phase. The coupling is thus independent of the nuclear index n within one ensemble, such that we have

$$g_{\lambda l}(\mathbf{k}_\parallel) = -\frac{id\omega_{\mathrm{nuc},l}}{\sqrt{2A_\parallel \omega_\lambda(\mathbf{k}_\parallel)}}\tilde{\chi}_\lambda(z_l)\,. \tag{C.29}$$

We see that the coupling remains dependent on the quantization area $A_\parallel$. While this feature may initially seem unphysical, it is to be expected, since the number of nuclei N_l participating in the dynamics also depends on this area. As is also noted in the phenomenological model [HE13], in the linear regime the collective coupling constant

$$\tilde{g}_{l\lambda} = \sqrt{N_l} g_{l\lambda} = -\frac{id\omega_{\mathrm{nuc},l}}{\sqrt{2\omega_\lambda}}\sqrt{\frac{N_l}{A_\parallel}}\tilde{\chi}_\lambda(z_l) \tag{C.30}$$

$$= -id\omega_{\mathrm{nuc},l}\sqrt{\frac{f_{\mathrm{LM}}\rho_N t_l}{2\omega_\lambda}}\tilde{\chi}_\lambda(z_l) \tag{C.31}$$

is the relevant quantity, where ρ_N is the number density of the resonant nuclei and f_{LM} is the Lamb-Mössbauer factor encoding the fraction of nuclei which participate in the recoil free scattering or decay process [Röh05b; HT99]. t_l is the thickness of the ensemble layer l and we assume the thin layer limit for a single ensemble by taking z_l to be independent of the nuclear index n. We further drop the parametric parallel wave vector dependence for brevity. In the linear limit, the properties of the system thus only depend on the number density and not on the absolute number of nuclei participating in the dynamics, which is consistent with the semi-classical layer formalism [Röh05b; Hee14; HT99].

Beyond the linear limit, however, the absolute number of nuclei and the quantization area become important and do not reduce to the number density in the equations. This feature can be understood by recognizing that in a fully translation invariant system, the number of nuclei is necessarily infinite. Physically, however, only a finite number participates in the dynamics due to a limited coherence volume and a limited size of the excitation beam. The quantization area $A_\parallel$ should therefore be chosen to capture these physical features. We further note that the translationally invariant description essentially neglects finite excitation size effects and excitation spreading at the edge of the excitation region. A phenomenological argument to include such contributions is given in [HKE16].

Effective nuclear dipole moment

A remaining question is how to compute the effective single nucleus transition matrix element d from tabulated resonance parameters. The connection to quantities that are conventionally used for example in the layer formalism [Röh05b] can be obtained by a simple comparison of physical scattering observables. Note that a more general framework for extracting nuclear dipole moments in the case of electric or magnetic multi-pole transitions and for arbitrary hyperfine field configurations is given in Chapter 9. This appendix provides intuition for the simplest case.

The formula for the resonant contribution to the refractive index of a resonant nuclear medium is [Hee14]

$$n_{^{57}\mathrm{Fe}} - n_{^{56}\mathrm{Fe}} = -2\pi\frac{\rho_N}{k_0^3}\frac{f_{\mathrm{LM}}}{2(1+\alpha)}\frac{2I_e+1}{2I_g+1}\frac{1}{2\Delta/\gamma + i}\,, \tag{C.32}$$

where we have taken ^{57}Fe as an example, and "magnetic splitting and polarization dependence" [Hee14] have been neglected [Hee14; SBH99]. The quantities here are defined as in [Hee14], including the Lamb-Mössbauer factor f_{LM}, the resonant wave number k_0, the spins for the ground (excited) state I_g (I_e) and the internal conversion factor α.

A formula for the resonant contribution to the refractive index in the linear regime can alternatively be obtained from our effective transition theory, for example via a linear dispersion theory [LE20] calculation, which gives

$$\varepsilon_{\mathrm{res}}(r) = -\frac{|d|^2}{\omega - \omega_{\mathrm{nuc}} + i\frac{\gamma}{2}} f_{\mathrm{LM}}\rho_N\,. \tag{C.33}$$

where we have neglected the A^2-term contribution, assumed a dense lattice, which for example results in Bragg scattering being neglected, and performed the rotating wave approximation by setting

$\omega^2 - \omega_{\mathrm{nuc}}^2 \approx 2\omega_{\mathrm{nuc}}(\omega - \omega_{\mathrm{nuc}})$ as well as $\frac{\omega_{\mathrm{nuc}}^2}{\omega^2} \approx 1$ [LE20]. We note that all of these approximations are already implicit in the nuclear refractive index formula Eq. (C.32), with more general treatments including lattice effects and other scattering processes being available [HT99]. The Lamb-Mössbauer factor f_{LM} encodes the fraction of nuclei that participate in the recoil free scattering process [Röh05b; HT99] and therefore modifies the nuclear number density.

A further approximation which is commonly performed in nuclear resonant scattering and which is implicit in Eq. (C.32) is the small response approximation $n = \sqrt{\varepsilon} = \sqrt{1+\chi} \approx 1 + \chi/2$. Performing this approximation also in the linear dispersion theory case we obtain

$$n - n_{\mathrm{electronic}} \approx -\frac{|d|^2}{\omega - \omega_{\mathrm{nuc}} + i\frac{\gamma}{2}} \frac{f_{\mathrm{LM}}\rho_N}{2} \,. \tag{C.34}$$

In order to obtain the effective nuclear transition matrix element d, we can therefore straightforwardly compare Eq. (C.34) to Eq. (C.32), which gives

$$|d_{^{57}\mathrm{Fe}}|^2 \approx \frac{2\pi\gamma}{k_0^3} \frac{1}{2(1+\alpha)} \frac{2I_e+1}{2I_g+1} \,. \tag{C.35}$$

We recall that as our previous calculations this formula is given in natural units with $\hbar = c = \varepsilon_0 = 1$.

This calculation also clarifies the connection to the semi-classical layer formalism [Röh05b], which is a standard tool for describing resonant x-ray scattering experiments [Röh05b; Stu00] and can be used to include various experimental imperfections in the description [Röh05b; Stu00]. In this context, we note that our quantum optical approach is based on nuclear *transitions*, whose properties are assumed to be known, as the starting point. In the established perturbative scattering theory [HT99; SBH99], the transition structure of the nuclei is investigated in detail and effects such as interaction with the lattice are included. Related approaches such as Shvyd'ko's time and space picture [Shv99] allow for the inclusion of additional effects such as inelastic scattering [Shv00]. For further details on the relation between the formalisms refer to Sec. 7.3 and Fig. 7.1.

C.2 Detailed comparison of the ab initio and phenomenological few-mode approaches

In Sec. 6.8.5, we presented a comparison of the phenomenological and ab initio few-mode approaches with regards to their capability to model nuclear spectra of the example cavity. However, this comparison is not unique, because the phenomenological models are based on fits of their parameters to predictions from semi-classical theories, and the fits can be obtained using different fit objectives, i.e., different approaches to quantify the differences between the model and the references. Note that these differences are often not of practical relevance close to the resonance at which the parameters are fitted, but deviations between different parameter sets are expected further away from the resonance. In contrast, the parameters of the ab initio model are unique, as they are calculated from the cavity structure without a fitting procedure.

Because of the ambiguity in the phenomenological parameters, in this appendix, we provide additional detail on this comparison to support our conclusions. In particular, we consider multiple ways of fitting the phenomenological model parameters. Fig. C.1(a) shows the layer formalism spectrum used as a reference for this analysis. In order to obtain such a spectrum from the phenomenological model, in all cases, the empty cavity parameters are first fitted to the rocking curve as described in Sec. 6.8.5, yielding the best fit shown in Fig. C.1(b). Next, we employ three fitting procedures for the mode-ensemble interaction parameters.

C.2.1 Fit method 1

In this method, we only fit one global interaction parameter. This method was already employed successfully in [HE15] for the EIT-scenario and uses an extraction of the individual mode parameters. The latter is achieved by decomposing the coupling constants as [HE15]

$$\sqrt{N_l} g_{\lambda l} = \tilde{\mathcal{E}}_{\lambda l} (\sqrt{N_l} g_l) \,, \tag{C.36}$$

where $\tilde{\mathcal{E}}_{\lambda l}$ is taken as the mode amplitude at the location of ensemble l when illuminated at the rocking minimum corresponding to mode λ [HE15]. For our single ensemble case, $\sqrt{N_l} g_l$ is then a single global scale that is fitted to the two-dimensional spectrum.

C.2.2 Fit method 2

In this approach we replace the mode parameter extraction prescription of fit method 1 and instead fit the $\sqrt{N_l} g_{\lambda l}$ parameters for each mode. As a fit objective, we use the one-dimensional spectrum at resonance with the first cavity mode, that is at $\theta = \theta_0$.

C.2.3 Fit method 3

Here, we proceed as in fit method 2, only that agreement to the full two-dimensional spectrum (see Fig. C.1) is used as a fit objective.

The results from the three methods are shown in Fig. C.1. Panels (c,1)-(g,1) show the two-dimensional spectra calculated using the phenomenological model with the model parameters extracted from the respective fitting methods. The remaining panels show the corresponding residual deviation to the layer formalism result in panel (a), both on a linear scale in panels (c,2)-(g,2) and on a log scale in panels (c,3)-(g,3).

We find that all models capture the behavior well, in particular at low incidence angles. At higher incidence angles, that is going towards the edge of the fitting range for the cavity parameters, the deviations become more significant. The agreement at higher incidence angles can be improved by including a larger set of modes, resulting in more fitting parameters. We further see that the various fitting procedures result in deviations due to the emphasis on different regions of the spectrum, but yield the same qualitative spectral features and the same overall quantitative level of agreement.

In comparison, Fig. C.1(f) shows analogous results for the ab initio few-mode theory with 5 cavity modes. We see that the performance is similar to the phenomenological cases around the first resonance, but better at higher incidence angles. Panel (g) shows the corresponding 20 modes result, illustrating the systematic convergence when including more cavity modes. In the latter case, the residual deviations are mainly due to the thin layer approximation, with higher modes only having a tiny contribution.

In Fig. C.2, we focus on the slice at the first mode resonance ($\theta = \theta_0$). To illustrate the excellent level of agreement of all approaches, the nuclear spectra are plotted on top of the semi-classical reference (panels a,b). The residual deviations are shown in panel (c). We find that the ab initio result at 20 modes is well converged. Indeed, the phenomenological result gives a comparable level of agreement with only 5 modes for the case of fit method 2, illustrating that the phenomenological model can yield very good agreement if one focuses on a particular spectral region. However, it is not known *a priori* which phenomenological fit works best for a given problem. The remaining fitting methods and the 5-mode ab initio theory show similar deviations, which are structurally comparable, with already a good quantitative agreement on the level of a few percent deviation.

Appendix D

Analytic formula for the layer stack Green's function

This appendix is based on the following publication:

Ab initio quantum models for thin-film x-ray cavity QED
D. Lentrodt, K. P. Heeg, C. H. Keitel, and J. Evers
Physical Review Research **2**, 023396 (2020)

In this appendix, we summarize the analytical form of the Green's function and its efficient numerical calculation as presented in [Tom95]. The appendix is structured to allow for a convenient numerical implementation of the formulas.

As shown in [Tom95], the in-plane Fourier transformed Green's function is given by

$$\mathbf{G}(z\in j, z'\in j', \mathbf{k}_\parallel, \omega) = -\frac{1}{k_j^2}\hat{\mathbf{z}}\hat{\mathbf{z}}\delta(z-z') + \frac{i}{2\beta_n}\sum_{q\in p,s}\frac{\xi_q}{t^q_{0/n}}\Big[\boldsymbol{\mathcal{E}}^0_q(z,\mathbf{k}_\parallel,\omega)\boldsymbol{\mathcal{E}}^n_q(z',-\mathbf{k}_\parallel,\omega)\Theta(z-z') + \boldsymbol{\mathcal{E}}^n_q(z,\mathbf{k}_\parallel,\omega)\boldsymbol{\mathcal{E}}^0_q(z',-\mathbf{k}_\parallel,\omega)\Theta(z'-z)\Big], \tag{D.1}$$

where Θ is the step function, $\xi_{p(s)} = +(-)1$, $\hat{\mathbf{z}}$ is the unit vector in z-direction and $z\in j$ denotes that the position in z-direction lies in the jth layer of the cavity stack (see Fig. D.1 for details on the notation, which is adapted from [Tom95]). $k_j = \sqrt{\varepsilon_j(\omega)}\omega/c$ is the in-medium wave number and $\beta_j = \sqrt{k_j^2 - k_\parallel^2}$ is its z-component [Tom95].

The information about the spatial dependence of the Green's function is given by the mode profiles, which are given explicitly by [Tom95]

$$\boldsymbol{\mathcal{E}}^{n(0)}_p(z\in j,\mathbf{k}_\parallel,\omega) = \frac{t^p_{n(0)/j}e^{i\beta_j d_j}}{D_{pj}}\left[\pm\frac{\beta_j}{k_j}(e^{-i\beta_j z^\mp} - r^p_{j/0(n)}e^{i\beta_j z^\mp})\hat{\mathbf{k}} + \frac{k_\parallel}{k_j}(e^{-i\beta_j z^\mp} + r^p_{j/0(n)}e^{i\beta_j z^\mp})\hat{\mathbf{z}}\right], \tag{D.2a}$$

$$\boldsymbol{\mathcal{E}}^{n(0)}_s(z\in j,\mathbf{k}_\parallel,\omega) = \frac{t^s_{n(0)/j}e^{i\beta_j d_j}}{D_{sj}}\left[(e^{-i\beta_j z^\mp} + r^s_{j/0(n)}e^{i\beta_j z^\mp})\hat{\mathbf{k}}\times\hat{\mathbf{z}}\right], \tag{D.2b}$$

where $D_{qj} = 1 - r^q_{j/0}r^q_{j/n}e^{2i\beta_j d_j}$, $z^+ = d_j - (z-\tilde{z}_j)$ and $z^- = z - \tilde{z}_j$ with $\tilde{z}_j$ being the position of the surface of layer j and d_j its thickness as shown in Fig. D.1. $\hat{\mathbf{k}}$ is the unit vector in direction of the parallel wave vector. We note that in the case of grazing incidence, the p- and s-polarization mode profiles have approximately identical magnitude [Par54; Hee14].

The result is expressed in terms of the coefficients $t_{i/j}$ and $r_{i/j}$, which are defined as the transmission and reflection coefficients, respectively, from layer i into layer j [Tom95]. They can be calculated via a recursion formula [Tom95] analogous to Parratt's formalism [Par54]. Specifically, the i/k coefficients

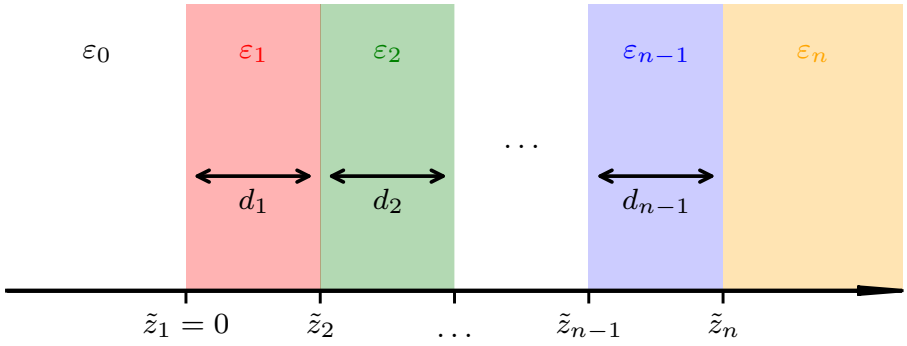

Figure D.1: Setup of the cavity layer stack and notation for the analytical Green's function formula, adapted from [Tom95]. The first (last) layer with $j = 0$ ($j = n$) extends infinitely to the left (right).

can be expressed in terms of i/j, j/k coefficients for any in-between j by [Tom95]

$$r^q_{i/k} = r^q_{i/j/k} = \frac{r^q_{i/j} + (t^q_{i/j} t^q_{j/i} - r^q_{i/j} r^q_{j/i}) r^q_{j/k} e^{2i\beta_j d_j}}{D^{(ik)}_{qj}}\,, \tag{D.3a}$$

$$t^q_{i/k} = t^q_{i/j/k} = \frac{1}{D^{(ik)}_{qj}} t^q_{i/j} t^q_{j/k} e^{i\beta_j d_j}\,, \tag{D.3b}$$

where $D^{(ik)}_{qj} = 1 - r^q_{ji} r^q_{jk} e^{2i\beta_j d_j}$.

If the coefficient i/k is required, the conversion is conveniently started by choosing $j = i + 1$ for $i < k$ or $j = i - 1$ for $i > k$, and terminated by the Fresnel coefficients for adjacent layers [Tom95]

$$r^q_{ij} = \frac{\beta_i - \gamma^q_{ij} \beta_j}{\beta_i + \gamma^q_{ij} \beta_j}\,, \tag{D.4a}$$

$$t^q_{ij} = \sqrt{\gamma^q_{ij}} (1 + r^q_{ij})\,, \tag{D.4b}$$

where the absence of a slash indicates that the layers are adjacent and $\gamma^p_{ij} = \varepsilon_i(\omega)/\varepsilon_j(\omega)$ as well as $\gamma^s_{ij} = 1$.

Together, the results from [Tom95] summarized here provide a recursively analytic and hence numerically efficient way to calculate the Green's function at a given parallel wave vector for the layer cavities, which is the central quantity appearing in the effective nuclear level scheme described in the Chapter 7.

Appendix E

Details on the non-linear excitation calculation

This appendix is based on an article currently in preparation:

Non-linear excitation of Mössbauer nuclei in thin-film cavities by focussed x-ray pulses
D. Lentrodt, C. H. Keitel, J. Evers, et al.
in preparation

The content is to be submitted for publication in a peer-reviewed journal.

E.1 Gaussian beam angular spectrum in cavity coordinates

E.1.1 Coordinate rotation in wave space

In the following we will rotate the Gaussian beam field intensity to cavity coordinates. For the angular spectrum, a rotation is not possible directly since x and z mix in this transformation. However, the x-direction is Fourier transformed in the angular spectrum, such that we have a k_x functionality. Instead, we take the Fourier transform along the z-direction, then rotate in full wave space (k_x, k_y, k_z) and Fourier transform back to an angular spectrum afterwards.

The z-direction Fourier transform of the angular pulse spectrum Eq. (12.19) is

$$\mathbf{E}_{\text{pulse}}(\mathbf{k}^{(\text{pulse})},\omega) = \frac{\tilde{\mathbf{A}}(\omega)}{\sqrt{2\pi}}\frac{w_0^2}{2}e^{-\frac{w_0^2}{4}|\mathbf{k}_\parallel^{(\text{pulse})}|^2}\delta(k_z^{(\text{pulse})}-k_z^{(\text{val})})\,, \tag{E.1}$$

where $k_z^{(\text{val})} = \sqrt{k^2-|\mathbf{k}_\parallel^{(\text{pulse})}|^2}$ is the on-shell wave number in the propagation direction.

The wave space spectrum in cavity coordinates is then simply given by

$$\mathbf{E}_{\text{cav}}(\mathbf{k},\omega) = \mathbf{E}_{\text{pulse}}(\mathbf{k}^{(\text{pulse})}(\mathbf{k}),\omega)\,, \tag{E.2}$$

where the pulse wave vector in terms of cavity coordinates is given by a rotation

$$\mathbf{k}^{(\text{pulse})}(\mathbf{k}) = \begin{pmatrix} k_x\sin(\theta)-k_z\cos(\theta) \\ k_y \\ k_x\cos(\theta)+k_z\sin(\theta)\end{pmatrix}\,. \tag{E.3}$$

Note that the rotation is rather unusual, since the x- and z-component swap roles in addition to the small θ-rotation.

To obtain the angular spectrum in cavity coordinates, we have to perform the inverse Fourier transform along the cavity z-direction

$$\mathbf{E}_{\text{cav}}(\mathbf{k}_\parallel,z,\omega) = \frac{1}{\sqrt{2\pi}}\int dk_z e^{ik_z z}\mathbf{E}_{\text{cav}}(\mathbf{k},\omega)\,. \tag{E.4}$$

E.1.2 Analytical evaluation for the Gaussian beam

In the following, we calculate the above integral analytically for the case of the Gaussian beam from Sec. 12.4.1. The integral is of the form

$$\mathbf{E}_{\text{cav}}(\mathbf{k}_\parallel,z,\omega) = \frac{\tilde{\mathbf{A}}(\omega)}{2\pi}\frac{w_0^2}{2}\int dk_z e^{ik_z z}e^{-\frac{w_0^2}{4}|\mathbf{k}_\parallel^{(\text{pulse})}(\mathbf{k})|^2}\delta(f_{k_x,k_y}(k_z))\,, \tag{E.5}$$

where

$$f_{k_x,k_y}(k_z) = \sqrt{k^2 - k_y^2 - [k_x \sin(\theta_{\text{in}}) - k_z \cos(\theta_{\text{in}})]^2} - k_x \cos(\theta_{\text{in}}) - k_z \sin(\theta_{\text{in}})\,. \tag{E.6}$$

This function has two roots at

$$k_z^{\pm} = \pm\sqrt{k^2 - k_y^2 - k_x^2}\,. \tag{E.7}$$

As expected, the roots are therefore on-shell as in the unrotated case. We can then express the δ-function in Eq. (E.5) as

$$\delta\left(f_{k_x,k_y}(k_z)\right) = \sum_{\pm} \frac{\delta\left(k_z - k_z^{\pm}\right)}{|f'_{k_x,k_y}(k_z^{\pm})|}\,, \tag{E.8}$$

where the prime indicates a derivative along k_z. Since our x-ray beam is incident from the top of the cavity and the already small contribution impinging from the bottom due to the angular spread is typically absorbed by sample holders or the side of the cavity in practice, we can perform a single root approximation

$$\delta\left(f_{k_x,k_y}(k_z)\right) \approx \frac{\delta\left(k_z - k_z^{+}\right)}{|f'_{k_x,k_y}(k_z^{+})|}\,. \tag{E.9}$$

The derivative can be evaluated as

$$f'_{k_x,k_y}(k_z^{+}) = \frac{-1}{\sin(\theta_{\text{in}}) + \frac{k_x}{\sqrt{k^2 - k_y^2 - k_x^2}} \cos(\theta_{\text{in}})}\,. \tag{E.10}$$

Substitution into Eq. (E.5) then yields the result for the Gaussian beam's cavity angular spectrum Eq. (12.28). We note that this form assumes that the focus is at $z = 0$. If the focus is moved relative to the cavity, one can either shift the coordinate system accordingly or add an additional phase for the offset.

E.2 Confirming the low pulse depletion approximation

In Chapter 12, we have used an approximation that results in neglecting the effect of nuclear excitation during the ultra-short pulse on the pulse profile. In this appendix, we confirm the validity of this approximation for the considered cavity targets.

To this end, we calculate the number of photons required for fully inverting the nuclear ensemble according to Eq. 12.24. Requiring $\Phi_{\text{peak}}^{\text{tot}} = \pi$ and solving for the photon number gives

$$N_{\text{ph}}^{[\text{required}]} = \frac{\sqrt{\pi} c \varepsilon_0 \hbar}{32 \omega_0 d} \frac{w_0^2}{\tau_{\text{pulse}}} \tag{E.11}$$

This number should then be compared to the number of absorbed excitations after the pulse has passed, which can be estimated as the number of nuclei N_{nuc} in the pulse volume. Since we have used the peak inversion above, a conservative estimate can be obtained via the illuminated volume as

$$N_{\text{nuc}}^{[\text{absorbed}]} \approx \pi w_0^2 \frac{t_{\text{res}} \rho_{\text{nuc,res}}}{\sin(\theta_{\text{in}})}\,, \tag{E.12}$$

where t_{res} is the thickness of the resonant layer and $\rho_{\text{nuc,res}}$ the number density of resonant nuclei. If the Rayleigh length of the pulse is smaller than $\frac{t_{\text{res}}}{\sin(\theta_{\text{in}})}$, the number of excited nuclei will be even smaller.

The low pulse depletion approximation is then valid even at full inversion if

$$\frac{N_{\text{ph}}^{[\text{required}]}}{N_{\text{nuc}}^{[\text{absorbed}]}} = \frac{c \varepsilon_0 \hbar}{32 \sqrt{\pi} \omega_0 d} \frac{\sin(\theta_{\text{in}})}{\tau_{\text{pulse}} t_{\text{res}} \rho_{\text{nuc,res}}} \gg 1\,. \tag{E.13}$$

Fig. E.1 shows this fraction for the free space scenario considered in Fig. 12.6. We see that for all five isotopes and across typical pulse durations available at XFELs [HKE16], the low pulse depletion approximation is well valid in this setup. Also note that for the case of ^{193} Pt, the worst case scenario of the internal conversion coefficient is shown ($\alpha = 3.5$).

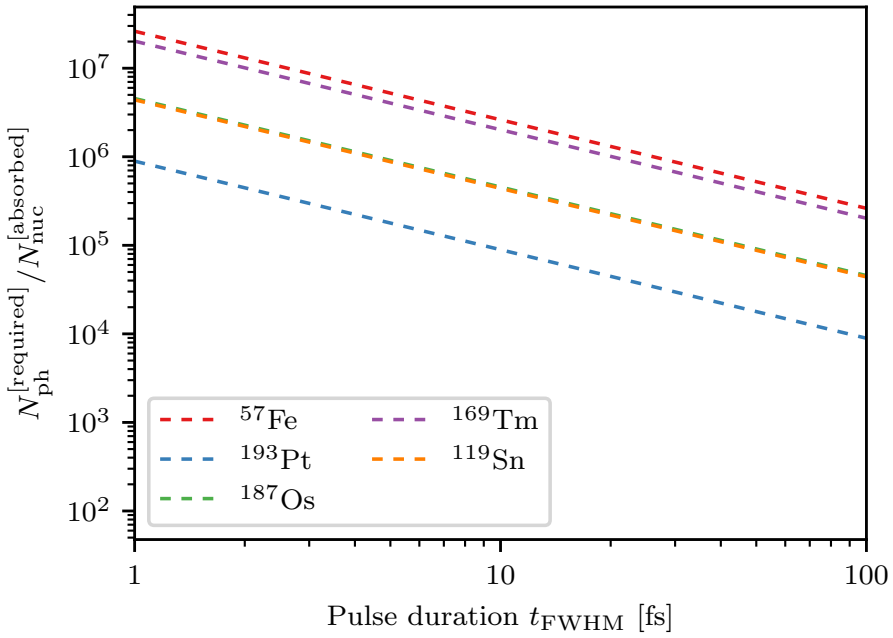

Figure E.1: Pulse depletion ratio as a function of pulse duration for the isotopes considered in the main text, illustrating the validity of the low pulse depletion approximation.

Bibliography

[Abe50] Abelès. In: *Ann. de Physique* **5**, 603 (1950).

[Ada03] B. Adams. "Nonlinear Optics, Quantum Optics, and Ultrafast Phenomena with X-Rays: Physics with X-Ray Free-Electron Lasers". Springer (2003).

[Ada09] B. W. Adams. "Nuclear γ-ray superradiance". In: *Journal of Modern Optics* **56**, 1974–1984 (2009). DOI: 10.1080/09500340903199921.

[Ada13] Bernhard W. Adams et al. "X-ray quantum optics". In: *Journal of Modern Optics* **60**, 2–21 (2013). DOI: 10.1080/09500340.2012.752113. eprint: https://doi.org/10.1080/09500340.2012.752113.

[Ada19] Bernhard Adams et al. *Scientific Opportunities with an X-ray Free-Electron Laser Oscillator*. 2019. arXiv: 1903.09317 [physics.ins-det].

[AE87] L. Allen and J.H. Eberly. "Optical Resonance and Two-level Atoms". Dover books on physics and chemistry. Dover (1987).

[AG17a] A. Asenjo-Garcia et al. "Atom-light interactions in quasi-one-dimensional nanostructures: A Green's-function perspective". In: *Phys. Rev. A* **95**, 033818 (2017). DOI: 10.1103/PhysRevA.95.033818.

[AG17b] A. Asenjo-Garcia et al. "Exponential Improvement in Photon Storage Fidelities Using Subradiance and "Selective Radiance" in Atomic Arrays". In: *Phys. Rev. X* **7**, 031024 (2017). DOI: 10.1103/PhysRevX.7.031024.

[Aga12] Girish S. Agarwal. "Quantum Optics". Cambridge University Press (2012). DOI: 10.1017/CBO9781139035170.

[Aga85] G. S. Agarwal. "Vacuum-field Rabi oscillations of atoms in a cavity". In: *J. Opt. Soc. Am. B* **2**, 480–485 (1985). DOI: 10.1364/JOSAB.2.000480.

[AK64] A. M. Afanas'ev and Yu. Kagan. "Theory of Hyperfine Structure of the Mössbauer Line in Paramagnetic Substances". In: *Sov. Phys. JETP* **18**, 1139 (1964).

[All66] D.W. Allan. "Statistics of atomic frequency standards". In: *Proc. IEEE* **54**, 221–230 (1966). DOI: 10.1109/PROC.1966.4634.

[Alp17] Filippo Alpeggiani et al. "Quasinormal-Mode Expansion of the Scattering Matrix". In: *Phys. Rev. X* **7**, 021035 (2017). DOI: 10.1103/PhysRevX.7.021035.

[ANM01] J. Als-Nielsen and D. McMorrow. "Elements of Modern X-ray Physics". John Wiley & Sons (2001). DOI: 10.1002/9781119998365.

[Aok14] Hideo Aoki et al. "Nonequilibrium dynamical mean-field theory and its applications". In: *Rev. Mod. Phys.* **86**, 779–837 (2014). DOI: 10.1103/RevModPhys.86.779.

[AP21] Petar Andrejić and Adriana Pálffy. *Superradiance and anomalous hyperfine splitting in inhomogeneous ensembles*. 2021. arXiv: 2102.11183 [quant-ph].

[Arn20] Kristin B. Arnardottir et al. "Multimode Organic Polariton Lasing". In: *Phys. Rev. Lett.* **125**, 233603 (2020). DOI: 10.1103/PhysRevLett.125.233603.

[Aru19] Frank Arute et al. "Quantum supremacy using a programmable superconducting processor". In: *Nature* **574**, 505–510 (2019). DOI: 10.1038/s41586-019-1666-5.

[Ash97] Arthur Ashkin. "Optical trapping and manipulation of neutral particles using lasers". In: *Proceedings of the National Academy of Sciences* **94**, 4853–4860 (1997). DOI: 10.1073/pnas.94.10.4853. eprint: https://www.pnas.org/content/94/10/4853.full.pdf.

[Bal86] G. Baldwin et al. "MÖSSBAUER-BORRMANN SUPERRADIANCE". In: *Journal de Physique Colloques* **47**, C6–299–C6–308 (1986). DOI: 10.1051/jphyscol:1986637.

[BAN11] Iulia Buluta, Sahel Ashhab, and Franco Nori. "Natural and artificial atoms for quantum computation". In: *Reports on Progress in Physics* **74**, 104401 (2011). DOI: 10.1088/0034-4885/74/10/104401.

[Bar00] Alfred Q. R. Baron. "Detectors for nuclear resonant scattering experiments". In: *Hyperfine Interactions* **125**, 29–42 (2000). DOI: 10.1023/A:1012625418707.

[Bar06] Alfred Q. R. Baron et al. "Silicon avalanche photodiodes for direct detection of X-rays". In: *Journal of Synchrotron Radiation* **13**, 131–142 (2006). DOI: 10.1107/S090904950503431X.

[Bar94] A. Q. R. Baron et al. "Angular dependence of specular resonant nuclear scattering of x rays". In: *Phys. Rev. B* **50**, 10354–10357 (1994). DOI: 10.1103/PhysRevB.50.10354.

[BB00] Ya. M. Blanter and M. Büttiker. "Shot noise in mesoscopic conductors". In: *Phys. Rep.* **336**, 1 –166 (2000). DOI: https://doi.org/10.1016/S0370-1573(99)00123-4.

[BB19] Robert Bennett and Stefan Yoshi Buhmann. *Inverse design of light-matter interactions*. 2019. arXiv: 1910.00389 [quant-ph].

[BB20] Robert Bennett and Stefan Yoshi Buhmann. "Inverse design of light-matter interactions in macroscopic QED". In: *New Journal of Physics* **22**, 093014 (2020). DOI: 10.1088/1367-2630/abac3a.

[BBB21] Fridtjof Betz, Felix Binkowski, and Sven Burger. "RPExpand: Software for Riesz projection expansion of resonance phenomena". In: *SoftwareX* **15**, 100763 (2021). DOI: https://doi.org/10.1016/j.softx.2021.100763.

[BCS57] J. Bardeen, L. N. Cooper, and J. R. Schrieffer. "Theory of Superconductivity". In: *Phys. Rev.* **108**, 1175–1204 (1957). DOI: 10.1103/PhysRev.108.1175.

[BD84] Michael Berman and Wolfgang Domcke. "Projection-operator calculations for shape resonances: A new method based on the many-body optical-potential approach". In: *Phys. Rev. A* **29**, 2485–2496 (1984). DOI: 10.1103/PhysRevA.29.2485.

[Bee97] C. W. J. Beenakker. "Random-matrix theory of quantum transport". In: *Rev. Mod. Phys.* **69**, 731–808 (1997). DOI: 10.1103/RevModPhys.69.731.

[BEK06] Thomas J. Bürvenich, Jörg Evers, and Christoph H. Keitel. "Nuclear Quantum Optics with X-Ray Laser Pulses". In: *Phys. Rev. Lett.* **96**, 142501 (2006). DOI: 10.1103/PhysRevLett.96.142501.

[Ben20] Robert Bennett et al. "Symmetry Breaking in a Condensate of Light and its Use as a Quantum Sensor". In: *Phys. Rev. Applied* **13**, 044031 (2020). DOI: 10.1103/PhysRevApplied.13.044031.

[Ben21a] Robert Bennett. "Inverse design of environment-induced coherence". In: *Phys. Rev. A* **103**, 013706 (2021). DOI: 10.1103/PhysRevA.103.013706.

[Ben21b] Mohammed Benzaouia et al. *Quasi-normal mode theory enforcing fundamental constraints for truncated expansions*. 2021. arXiv: 2105.01749 [physics.app-ph].

[Ber12] S. Bernitt et al. "An unexpectedly low oscillator strength as the origin of the Fe xvii emission problem". In: *Nature* **492**, 225–228 (2012). DOI: 10.1038/nature11627.

[Ber19] Klaas Bergmann et al. “Roadmap on STIRAP applications”. In: *Journal of Physics B: Atomic, Molecular and Optical Physics* **52**, 202001 (2019). DOI: 10.1088/1361-6455/ab3995.

[Ber94] P. Berman, ed. “Cavity quantum electrodynamics”. Academic Press, San Diego (1994).

[Bet16] Robert J. Bettles. “Cooperative Interactions in Lattices of Atomic Dipoles”. PhD thesis. Durham University, Department of Physics (2016).

[Bin20] Felix Binkowski et al. “Quasinormal mode expansion of optical far-field quantities”. In: *Phys. Rev. B* **102**, 035432 (2020). DOI: 10.1103/PhysRevB.102.035432.

[Bli08] Konstantin Y. Bliokh et al. “Colloquium: Unusual resonators: Plasmonics, metamaterials, and random media”. In: *Rev. Mod. Phys.* **80**, 1201–1213 (2008). DOI: 10.1103/RevModPhys.80.1201.

[Blo08] Immanuel Bloch. “Quantum coherence and entanglement with ultracold atoms in optical lattices”. In: *Nature* **453**, 1016–1022 (2008). DOI: 10.1038/nature07126.

[BM88] J. Georg Bednorz and K. Alex Müller. “Perovskite-type oxides—The new approach to high-T_c superconductivity”. In: *Rev. Mod. Phys.* **60**, 585–600 (1988). DOI: 10.1103/RevModPhys.60.585.

[BMR19] Andrei Benediktovitch, Vinay P. Majety, and Nina Rohringer. “Quantum theory of superfluorescence based on two-point correlation functions”. In: *Phys. Rev. A* **99**, 013839 (2019). DOI: 10.1103/PhysRevA.99.013839.

[BO13] Motoaki Bamba and Tetsuo Ogawa. “System-environment coupling derived by Maxwell’s boundary conditions from the weak to the ultrastrong light-matter-coupling regime”. In: *Phys. Rev. A* **88**, 013814 (2013). DOI: 10.1103/PhysRevA.88.013814.

[BO14] Motoaki Bamba and Tetsuo Ogawa. “Recipe for the Hamiltonian of system-environment coupling applicable to the ultrastrong-light-matter-interaction regime”. In: *Phys. Rev. A* **89**, 023817 (2014). DOI: 10.1103/PhysRevA.89.023817.

[Boc21] Lars Bocklage et al. “Coherent control of collective nuclear quantum states via transient magnons”. In: *Science Advances* **7** (2021). DOI: 10.1126/sciadv.abc3991. eprint: https://advances.sciencemag.org/content/7/5/eabc3991.full.pdf.

[Bon98] M. Bonitz. “Quantum Kinetic Theory”. Springer, Cham (1998). DOI: 10.1007/978-3-319-24121-0.

[Bor26] Max Born. “Quantenmechanik der Stoßvorgänge”. In: *Zeitschrift für Physik* **38**, 803–827 (1926). DOI: 10.1007/BF01397184.

[Bos16] Christoph Bostedt et al. “Linac Coherent Light Source: The first five years”. In: *Rev. Mod. Phys.* **88**, 015007 (2016). DOI: 10.1103/RevModPhys.88.015007.

[Boy03] Robert W Boyd. “Nonlinear optics; 2nd ed.” Amsterdam: Academic Press (2003).

[BP02] H. P. Breuer and F. Petruccione. “The Theory of Open Quantum Systems”. Oxford University Press (2002).

[BP70] Rodolfo Bonifacio and Giuliano Preparata. “Coherent Spontaneous Emission”. In: *Phys. Rev. A* **2**, 336–347 (1970). DOI: 10.1103/PhysRevA.2.336.

[BR88] S. M. Barnett and P. M. Radmore. “Quantum theory of cavity quasimodes”. In: *Opt. Comm.* **68**, 364–368 (1988). DOI: https://doi.org/10.1016/0030-4018(88)90233-7.

[Bra11] D. Braak. "Integrability of the Rabi Model". In: *Phys. Rev. Lett.* **107**, 100401 (2011). DOI: 10.1103/PhysRevLett.107.100401.

[Bra18] Daniel Braun et al. "Quantum-enhanced measurements without entanglement". In: *Rev. Mod. Phys.* **90**, 035006 (2018). DOI: 10.1103/RevModPhys.90.035006.

[Bre16] Heinz-Peter Breuer et al. "Colloquium: Non-Markovian dynamics in open quantum systems". In: *Rev. Mod. Phys.* **88**, 021002 (2016). DOI: 10.1103/RevModPhys.88.021002.

[BRM97] A.Q.R. Baron, R. Rüffer, and J. Metge. "A fast, convenient, X-ray detector". In: *Nuclear Instruments and Methods in Physics Research Section A: Accelerators, Spectrometers, Detectors and Associated Equipment* **400**, 124 –132 (1997). DOI: https://doi.org/10.1016/S0168-9002(97)00936-4.

[Bro19] Michael Brooks. "Beyond quantum supremacy: the hunt for useful quantum computers". In: *Nature* **574**, 19–21 (2019). DOI: 10.1038/d41586-019-02936-3.

[Bru19] Colin D. Bruzewicz et al. "Trapped-ion quantum computing: Progress and challenges". In: *Applied Physics Reviews* **6**, 021314 (2019). DOI: 10.1063/1.5088164.

[BS97] George C. Baldwin and Johndale C. Solem. "Recoilless gamma-ray lasers". In: *Rev. Mod. Phys.* **69**, 1085–1118 (1997). DOI: 10.1103/RevModPhys.69.1085.

[Buh12] Stefan Yoshi Buhmann. "Dispersion Forces I". Springer, Berlin, Heidelberg (2012). DOI: 10.1007/978-3-642-32484-0.

[Bur65] P. G. Burke. "Resonances in electron scattering and photon absorption". In: *Adv. Phys.* **14**, 521–567 (1965). DOI: 10.1080/00018736500101121.

[Bur77] P. G. Burke. "R-Matrix Theory of Atomic and Molecular Processes". In: *Atomic Physics 5*. Ed. by Richard Marrus, Michael Prior, and Howard Shugart. Boston, MA: Springer US, 1977, 293–311.

[BW07] Stefan Yoshi Buhmann and Dirk-Gunnar Welsch. "Dispersion forces in macroscopic quantum electrodynamics". In: *Progress in Quantum Electronics* **31**, 51 –130 (2007). DOI: https://doi.org/10.1016/j.pquantelec.2007.03.001.

[BW08a] Rainer Blatt and David Wineland. "Entangled states of trapped atomic ions". In: *Nature* **453**, 1008–1015 (2008). DOI: 10.1038/nature07125.

[BW08b] Stefan Yoshi Buhmann and Dirk-Gunnar Welsch. "Casimir-Polder forces on excited atoms in the strong atom-field coupling regime". In: *Phys. Rev. A* **77**, 012110 (2008). DOI: 10.1103/PhysRevA.77.012110.

[BW80] Max Born and Emil Wolf. "Principles of optics". Pergamon Press (1980), 808.

[Bär10] Andreas Bärnthaler et al. "Probing Decoherence through Fano Resonances". In: *Phys. Rev. Lett.* **105**, 056801 (2010). DOI: 10.1103/PhysRevLett.105.056801.

[Bür92] U. van Bürck et al. "Nuclear forward scattering of synchrotron radiation". In: *Phys. Rev. B* **46**, 6207–6211 (1992). DOI: 10.1103/PhysRevB.46.6207.

[Bür99] U. van Bürck. "Coherent pulse propagation through resonant media". In: *Hyperfine Interactions* **123**, 483–509 (1999). DOI: 10.1023/A:1017080008712.

[Cal05] R. Callens et al. "Phase determination in nuclear resonant scattering using a velocity drive as an interferometer and phase shifter". In: *Phys. Rev. B* **72**, 081402 (2005). DOI: 10.1103/PhysRevB.72.081402.

[Can15] Tommaso Caneva et al. “Quantum dynamics of propagating photons with strong interactions: a generalized input-output formalism”. In: *New J. Phys.* **17**, 113001 (2015).

[Car08] Howard J. Carmichael. “Statistical Methods in Quantum Optics 2”. Berlin, Heidelberg: Springer (2008). DOI: 10.1007/978-3-540-71320-3.

[Car93] Howard J. Carmichael. “An Open Systems Approach to Quantum Optics”. Vol. 18. Lecture Notes in Physics Monographs. Berlin, Heidelberg: Springer (1993). DOI: 10.1007/978-3-540-47620-7.

[Car99] Howard J. Carmichael. “Statistical Methods in Quantum Optics 1”. Berlin, Heidelberg: Springer (1999). DOI: 10.1007/978-3-662-03875-8.

[CBC05] Cristiano Ciuti, Gérald Bastard, and Iacopo Carusotto. “Quantum vacuum properties of the intersubband cavity polariton field”. In: *Phys. Rev. B* **72**, 115303 (2005). DOI: 10.1103/PhysRevB.72.115303.

[CC06] Cristiano Ciuti and Iacopo Carusotto. “Input-output theory of cavities in the ultrastrong coupling regime: The case of time-independent cavity parameters”. In: *Phys. Rev. A* **74**, 033811 (2006). DOI: 10.1103/PhysRevA.74.033811.

[CDG97] C. Cohen-Tannoudji, J. Dupont-Roc, and G. Grynberg. “Photons and Atoms - Introduction to Quantum Electrodynamics”. New York: John Wiley (1997).

[Cha11] Henry N. Chapman et al. “Femtosecond X-ray protein nanocrystallography”. In: *Nature* **470**, 73–77 (2011). DOI: 10.1038/nature09750.

[Cha18] D. E. Chang et al. “Colloquium: Quantum matter built from nanoscopic lattices of atoms and photons”. In: *Rev. Mod. Phys.* **90**, 031002 (2018). DOI: 10.1103/RevModPhys.90.031002.

[Che02] Ziyu Chen et al. “Mössbauer study of Fe-Co nanowires”. In: *Journal of Physics: Condensed Matter* **14**, 613–620 (2002). DOI: 10.1088/0953-8984/14/3/328.

[Che21] Yu-Hsueh Chen et al. *Transient nuclear inversion by X-Ray Free Electron Laser in a tapered x-ray waveguid*. 2021. arXiv: 2104.09624 [physics.optics].

[Chi98] E. S. C. Ching et al. “Quasinormal-mode expansion for waves in open systems”. In: *Rev. Mod. Phys.* **70**, 1545–1554 (1998). DOI: 10.1103/RevModPhys.70.1545.

[Chu18] Aleksandr I. Chumakov et al. “Superradiance of an ensemble of nuclei excited by a free electron laser”. In: *Nat. Phys.* **14**, 261–264 (2018). DOI: 10.1038/s41567-017-0001-z.

[Chu91] Steven Chu. “Laser Manipulation of Atoms and Particles”. In: *Science* **253**, 861–866 (1991). DOI: 10.1126/science.253.5022.861. eprint: https://science.sciencemag.org/content/253/5022/861.full.pdf.

[Cla17] Anton Classen et al. “Incoherent Diffractive Imaging via Intensity Correlations of Hard X Rays”. In: *Phys. Rev. Lett.* **119**, 053401 (2017). DOI: 10.1103/PhysRevLett.119.053401.

[Cla79] R. Clausius. “Die Mechanische Behandlung der Electricität”. Vieweg+Teubner Verlag, Wiesbaden (1879). DOI: https://doi.org/10.1007/978-3-663-20232-5.

[Cou02] R. Coussement et al. “Controlling Absorption of Gamma Radiation via Nuclear Level Anticrossing”. In: *Phys. Rev. Lett.* **89**, 107601 (2002). DOI: 10.1103/PhysRevLett.89.107601.

[CS16] Alexander Cerjan and A Douglas Stone. “Why the laser linewidth is so narrow: a modern perspective”. In: *Phys. Scr.* **91**, 013003 (2016).

[CTDRG08] Claude Cohen-Tannoudji, Jacques Dupont-Roc, and Gilbert Grynberg. "Atom-Photon Interactions: Basic Processes and Applications". Wiley-VCH (2008).

[CVL14] Darrick E. Chang, Vladan Vuletić, and Mikhail D. Lukin. "Quantum nonlinear optics — photon by photon". In: *Nature Photonics* **8**, 685–694 (2014). DOI: 10.1038/nphoton.2014.192.

[CZ00] J. I. Cirac and P. Zoller. "A scalable quantum computer with ions in an array of microtraps". In: *Nature* **404**, 579–581 (2000). DOI: 10.1038/35007021.

[dA17] Inés de Vega and Daniel Alonso. "Dynamics of non-Markovian open quantum systems". In: *Rev. Mod. Phys.* **89**, 015001 (2017). DOI: 10.1103/RevModPhys.89.015001.

[Dat97] Supriyo Datta. "Electronic Transport in Mesoscopic Systems". Cambridge University Press, Cambridge, England (1997). DOI: 10.1017/CBO9780511805776.

[Day08] Barak Dayan et al. "A Photon Turnstile Dynamically Regulated by One Atom". In: *Science* **319**, 1062–1065 (2008). DOI: 10.1126/science.1152261.

[DB10] P. Descouvemont and D. Baye. "The R-matrix theory". In: *Reports on Progress in Physics* **73**, 036301 (2010). DOI: 10.1088/0034-4885/73/3/036301.

[DBG01] B. J. Dalton, Stephen M. Barnett, and B. M. Garraway. "Theory of pseudomodes in quantum optical processes". In: *Phys. Rev. A* **64**, 053813 (2001). DOI: 10.1103/PhysRevA.64.053813.

[DBJR18] Daniele De Bernardis, Tuomas Jaako, and Peter Rabl. "Cavity quantum electrodynamics in the nonperturbative regime". In: *Phys. Rev. A* **97**, 043820 (2018). DOI: 10.1103/PhysRevA.97.043820.

[DBK99] B. J. Dalton, Stephen M. Barnett, and P. L. Knight. "Quasi mode theory of macroscopic canonical quantization in quantum optics and cavity quantum electrodynamics". In: *J. Mod. Opt.* **46**, 1315–1341 (1999). DOI: 10.1080/09500349908231338.

[Dha18] Himadri Shekhar Dhar et al. "Variational Renormalization Group for Dissipative Spin-Cavity Systems: Periodic Pulses of Nonclassical Photons from Mesoscopic Spin Ensembles". In: *Phys. Rev. Lett.* **121**, 133601 (2018). DOI: 10.1103/PhysRevLett.121.133601.

[Dic54] R. H. Dicke. "Coherence in Spontaneous Radiation Processes". In: *Phys. Rev.* **93**, 99–110 (1954). DOI: 10.1103/PhysRev.93.99.

[Die21] O. Diekmann et al. "Inverse design of artificial two-level systems with Mössbauer nuclei in thin-film cavities". In: *to be submitted*.

[Dir27a] P. A. M. Dirac. "The Quantum Theory of Dispersion". In: *Proceedings of the Royal Society of London A: Mathematical, Physical and Engineering Sciences* **114**, 710–728 (1927). DOI: 10.1098/rspa.1927.0071. eprint: http://rspa.royalsocietypublishing.org/content/114/769/710.full.pdf.

[Dir27b] P. A. M. Dirac. "The Quantum Theory of the Emission and Absorption of Radiation". In: *Proceedings of the Royal Society of London A: Mathematical, Physical and Engineering Sciences* **114**, 243–265 (1927). DOI: 10.1098/rspa.1927.0039. eprint: http://rspa.royalsocietypublishing.org/content/114/767/243.full.pdf.

[Dit00] Frank-Michael Dittes. "The decay of quantum systems with a small number of open channels". In: *Phys. Rep.* **339**, 215 –316 (2000). DOI: https://doi.org/10.1016/S0370-1573(00)00065-X.

[Dió12] Lajos Diósi. "Non-Markovian open quantum systems: Input-output fields, memory, and monitoring". In: *Phys. Rev. A* **85**, 034101 (2012). DOI: 10.1103/PhysRevA.85.034101.

[DKW00] Ho Trung Dung, Ludwig Knöll, and Dirk-Gunnar Welsch. "Spontaneous decay in the presence of dispersing and absorbing bodies: General theory and application to a spherical cavity". In: *Phys. Rev. A* **62**, 053804 (2000). DOI: 10.1103/PhysRevA.62.053804.

[DKW02] Ho Trung Dung, Ludwig Knöll, and Dirk-Gunnar Welsch. "Resonant dipole-dipole interaction in the presence of dispersing and absorbing surroundings". In: *Phys. Rev. A* **66**, 063810 (2002). DOI: 10.1103/PhysRevA.66.063810.

[DM03] Jonathan P. Dowling and Gerard J. Milburn. "Quantum technology: the second quantum revolution". In: *Phil. Trans. R. Soc. A* **361**, 1655–1674 (2003). DOI: 10.1098/rsta.2003.1227.

[DN00a] S. M. Dutra and G. Nienhuis. "Derivation of a Hamiltonian for photon decay in a cavity". In: *J. Opt. B* **2**, 584 (2000).

[DN00b] S. M. Dutra and G. Nienhuis. "Quantized mode of a leaky cavity". In: *Phys. Rev. A* **62**, 063805 (2000). DOI: 10.1103/PhysRevA.62.063805.

[DN01] S. M. Dutra and G. Nienhuis. "What Is a Quantized Mode of a Leaky Cavity?" In: *Modern Challenges in Quantum Optics*. Ed. by M. Orszag and J. C. Retama. Vol. 575. Lecture Notes in Physics. Springer, Berlin, 2001, 338.

[Dom83] W. Domcke. "Projection-operator approach to potential scattering". In: *Phys. Rev. A* **28**, 2777–2791 (1983). DOI: 10.1103/PhysRevA.28.2777.

[Dor19] Constantin Dory et al. "Inverse-designed diamond photonics". In: *Nature Communications* **10**, 3309 (2019). DOI: 10.1038/s41467-019-11343-1.

[Dou11] G. Doumy et al. "Nonlinear Atomic Response to Intense Ultrashort X Rays". In: *Phys. Rev. Lett.* **106**, 083002 (2011). DOI: 10.1103/PhysRevLett.106.083002.

[DRC17] C. L. Degen, F. Reinhard, and P. Cappellaro. "Quantum sensing". In: *Rev. Mod. Phys.* **89**, 035002 (2017). DOI: 10.1103/RevModPhys.89.035002.

[DS19] Omar Di Stefano et al. "Resolution of gauge ambiguities in ultrastrong-coupling cavity quantum electrodynamics". In: *Nature Physics* **15**, 803–808 (2019). DOI: 10.1038/s41567-019-0534-4.

[DSM16] Konstantin E. Dorfman, Frank Schlawin, and Shaul Mukamel. "Nonlinear optical signals and spectroscopy with quantum light". In: *Rev. Mod. Phys.* **88**, 045008 (2016). DOI: 10.1103/RevModPhys.88.045008.

[DW20] J. Defrance and T. Weiss. "On the pole expansion of electromagnetic fields". In: *Opt. Express* **28**, 32363–32376 (2020). DOI: 10.1364/OE.403948.

[Dör13] F. Döring et al. "Sub-5 nm hard x-ray point focusing by a combined Kirkpatrick-Baez mirror and multilayer zone plate". In: *Opt. Express* **21**, 19311–19323 (2013). DOI: 10.1364/OE.21.019311.

[Ebe98] J.H. Eberly. "Area Theorem rederived". In: *Opt. Express* **2**, 173–176 (1998). DOI: 10.1364/OE.2.000173.

[EG18] Ramy El-Ganainy et al. "Non-Hermitian physics and PT symmetry". In: *Nat. Phys.* **14**, 11 (2018).

[Ell12] J. Ellrich et al. "Mössbauer spectroscopy and magnetization of ordered arrays of ultrathin FePt nanodisks with perpendicular magnetisation". In: *Hyperfine Interactions* **211**, 135–145 (2012). DOI: 10.1007/s10751-012-0590-y.

[EM71] P. Eisenberger and S. L. McCall. "X-Ray Parametric Conversion". In: *Phys. Rev. Lett.* **26**, 684–688 (1971). DOI: 10.1103/PhysRevLett.26.684.

[Emm10] P. Emma et al. “First lasing and operation of an ångstrom-wavelength free-electron laser”. In: *Nature Photonics* **4**, 641–647 (2010). DOI: 10.1038/nphoton.2010.176.

[Eri16] M. Eriksson et al. “Commissioning of the MAX IV Light Source”. In: *Proc. of International Particle Accelerator Conference (IPAC'16), Busan, Korea, May 8-13, 2016* (Busan, Korea). International Particle Accelerator Conference 7. doi:10.18429/JACoW-IPAC2016-MOYAA01. Geneva, Switzerland: JACoW, 2016, 11–15. DOI: doi:10.18429/JACoW-IPAC2016-MOYAA01.

[ESB19] Saeideh Esfandiarpour, Hassan Safari, and Stefan Yoshi Buhmann. “Cavity-QED interactions of several atoms”. In: *Journal of Physics B: Atomic, Molecular and Optical Physics* **52**, 085503 (2019). DOI: 10.1088/1361-6455/aaf6d7.

[Esf18] Saeideh Esfandiarpour et al. “Cavity-QED interactions of two correlated atoms”. In: *J. Phys. B* **51**, 094004 (2018).

[Eve20] J. Evers. personal communication. 2020.

[Fan61] U. Fano. “Effects of Configuration Interaction on Intensities and Phase Shifts”. In: *Phys. Rev.* **124**, 1866–1878 (1961). DOI: 10.1103/PhysRev.124.1866.

[FD19] P. Forn-Díaz et al. “Ultrastrong coupling regimes of light-matter interaction”. In: *Rev. Mod. Phys.* **91**, 025005 (2019). DOI: 10.1103/RevModPhys.91.025005.

[FDBM18] Antonio I. Fernández-Domínguez, Sergey I. Bozhevolnyi, and N. Asger Mortensen. “Plasmon-Enhanced Generation of Nonclassical Light”. In: *ACS Photonics* **5**, 3447–3451 (2018). DOI: 10.1021/acsphotonics.8b00852.

[FEGG17] Liang Feng, Ramy El-Ganainy, and Li Ge. “Non-Hermitian photonics based on parity–time symmetry”. In: *Nature Photonics* **11**, 752–762 (2017). DOI: 10.1038/s41566-017-0031-1.

[Fel97] J. Feldhaus et al. “Possible application of X-ray optical elements for reducing the spectral bandwidth of an X-ray SASE FEL”. In: *Optics Communications* **140**, 341–352 (1997). DOI: https://doi.org/10.1016/S0030-4018(97)00163-6.

[Fes58] Herman Feshbach. “Unified theory of nuclear reactions”. In: *Ann. Phys. (N. Y.)* **5**, 357–390 (1958).

[Fes62] Herman Feshbach. “A unified theory of nuclear reactions. II”. In: *Ann. Phys. (N. Y.)* **19**, 287–313 (1962). DOI: 10.1016/0003-4916(62)90221-X.

[Fes67] Herman Feshbach. “The unified theory of nuclear reactions: III. Overlapping resonances”. In: *Ann. Phys. (N. Y.)* **43**, 410–420 (1967).

[Fey82] Richard P. Feynman. “Simulating physics with computers”. In: *International Journal of Theoretical Physics* **21**, 467–488 (1982). DOI: 10.1007/BF02650179.

[FGGV18] Johannes Feist, Javier Galego, and Francisco J. Garcia-Vidal. “Polaritonic Chemistry with Organic Molecules”. In: *ACS Photonics* **5**, 205–216 (2018). DOI: 10.1021/acsphotonics.7b00680. eprint: https://doi.org/10.1021/acsphotonics.7b00680.

[FHM73] R. Friedberg, S. R. Hartmann, and J. T. Manassah. “Frequency shifts in emission and absorption by resonant systems ot two-level atoms”. In: *Physics Reports* **7**, 101–179 (1973). DOI: https://doi.org/10.1016/0370-1573(73)90001-X.

[FIM05] Michael Fleischhauer, Atac Imamoglu, and Jonathan P. Marangos. “Electromagnetically induced transparency: Optics in coherent media”. In: *Rev. Mod. Phys.* **77**, 633–673 (2005). DOI: 10.1103/RevModPhys.77.633.

[Fin08] J. M. Fink et al. “Climbing the Jaynes–Cummings ladder and observing its nonlinearity in a cavity QED system”. In: *Nature* **454**, 315–318 (2008). DOI: 10.1038/nature07112.

[Fis17] Kevin A Fischer et al. “Pulsed Rabi oscillations in quantum two-level systems: beyond the area theorem”. In: *Quantum Science and Technology* **3**, 014006 (2017). DOI: 10.1088/2058-9565/aa9269.

[FK19] Anton Frisk Kockum et al. “Ultrastrong coupling between light and matter”. In: *Nature Reviews Physics* **1**, 19–40 (2019). DOI: 10.1038/s42254-018-0006-2.

[FKS10] Shanhui Fan, Şükrü Ekin Kocabaş, and Jung-Tsung Shen. “Input-output formalism for few-photon transport in one-dimensional nanophotonic waveguides coupled to a qubit”. In: *Phys. Rev. A* **82**, 063821 (2010). DOI: 10.1103/PhysRevA.82.063821.

[FL61] A. G. Fox and Tingye Li. “Resonant Modes in a Maser Interferometer”. In: *Bell Syst. Tech. J.* **40**, 453–488 (1961). DOI: 10.1002/j.1538-7305.1961.tb01625.x.

[Fle99] Michael Fleischhauer. “Spontaneous emission and level shifts in absorbing disordered dielectrics and dense atomic gases: A Green’s-function approach”. In: *Phys. Rev. A* **60**, 2534–2539 (1999). DOI: 10.1103/PhysRevA.60.2534.

[Fli17] Johannes Flick et al. “Atoms and molecules in cavities, from weak to strong coupling in quantum-electrodynamics (QED) chemistry”. In: *Proceedings of the National Academy of Sciences* **114**, 3026–3034 (2017). DOI: 10.1073/pnas.1615509114. eprint: https://www.pnas.org/content/114/12/3026.full.pdf.

[FR18] Yisheng Fang and Zhichao Ruan. “Temporal Coupled-Mode Theory for Light Scattering and Absorption by Nanostructures”. In: *Fano Resonances in Optics and Microwaves: Physics and Applications*. Ed. by Eugene Kamenetskii, Almas Sadreev, and Andrey Miroshnichenko. Cham: Springer International Publishing, 2018, 157–183. DOI: 10.1007/978-3-319-99731-5_7.

[Fra19] Sebastian Franke et al. “Quantization of Quasinormal Modes for Open Cavities and Plasmonic Cavity Quantum Electrodynamics”. In: *Phys. Rev. Lett.* **122**, 213901 (2019). DOI: 10.1103/PhysRevLett.122.213901.

[Fra20a] Sebastian Franke et al. “Fluctuation-dissipation theorem and fundamental photon commutation relations in lossy nanostructures using quasinormal modes”. In: *Phys. Rev. Research* **2**, 033332 (2020). DOI: 10.1103/PhysRevResearch.2.033332.

[Fra20b] Sebastian Franke et al. “Quantized quasinormal-mode description of nonlinear cavity-QED effects from coupled resonators with a Fano-like resonance”. In: *Phys. Rev. Research* **2**, 033456 (2020). DOI: 10.1103/PhysRevResearch.2.033456.

[Fra21] Sebastian Franke et al. “Fermi’s Golden Rule for Spontaneous Emission in Absorptive and Amplifying Media”. In: *Phys. Rev. Lett.* **127**, 013602 (2021). DOI: 10.1103/PhysRevLett.127.013602.

[Fri07] D. M. Fritz et al. “Ultrafast Bond Softening in Bismuth: Mapping a Solid’s Interatomic Potential with X-rays”. In: *Science* **315**, 633–636 (2007). DOI: 10.1126/science.1135009. eprint: https://science.sciencemag.org/content/315/5812/633.full.pdf.

[FS05] Z. Ficek and S. Swain. “Quantum interference and coherence: theory and experiments”. Springer series in optical sciences. Heidelberg: Springer (2005).

[FS15] Daniel Finkelstein-Shapiro et al. “Fano-Liouville Spectral Signatures in Open Quantum Systems”. In: *Phys. Rev. Lett.* **115**, 113006 (2015). DOI: 10.1103/PhysRevLett.115.113006.

[FSJ03] Shanhui Fan, Wonjoo Suh, and J. D. Joannopoulos. "Temporal coupled-mode theory for the Fano resonance in optical resonators". In: *J. Opt. Soc. Am. A* **20**, 569–572 (2003). DOI: 10.1364/JOSAA.20.000569.

[FY99] Michael Fleischhauer and Susanne F. Yelin. "Radiative atom-atom interactions in optically dense media: Quantum corrections to the Lorentz-Lorenz formula". In: *Phys. Rev. A* **59**, 2427–2441 (1999). DOI: 10.1103/PhysRevA.59.2427.

[Gal19] Javier Galego et al. "Cavity Casimir-Polder Forces and Their Effects in Ground-State Chemical Reactivity". In: *Phys. Rev. X* **9**, 021057 (2019). DOI: 10.1103/PhysRevX.9.021057.

[Gam28] G. Gamow. "Zur Quantentheorie des Atomkernes". In: *Z. Phys.* **51**, 204–212 (1928). DOI: 10.1007/BF01343196.

[GAN14] I. M. Georgescu, S. Ashhab, and Franco Nori. "Quantum simulation". In: *Rev. Mod. Phys.* **86**, 153–185 (2014). DOI: 10.1103/RevModPhys.86.153.

[Gar04] C. W. Gardiner. "Input and output in damped quantum systems III: formulation of damped systems driven by Fermion fields". In: *Opt. Commun.* **243**, 57–80 (2004).

[Gar11] B. M. Garraway. "The Dicke model in quantum optics: Dicke model revisited". In: *Philosophical Transactions of the Royal Society A: Mathematical, Physical and Engineering Sciences* **369** (2011). DOI: 10.1098/rsta.2010.0333.

[Gar90] W. R. Garrett et al. "Large multiple collective line shifts observed in three-photon excitations of Xe". In: *Phys. Rev. Lett.* **64**, 1717–1720 (1990). DOI: 10.1103/PhysRevLett.64.1717.

[Gar97a] B. M. Garraway. "Decay of an atom coupled strongly to a reservoir". In: *Phys. Rev. A* **55**, 4636–4639 (1997). DOI: 10.1103/PhysRevA.55.4636.

[Gar97b] B. M. Garraway. "Nonperturbative decay of an atomic system in a cavity". In: *Phys. Rev. A* **55**, 2290–2303 (1997). DOI: 10.1103/PhysRevA.55.2290.

[GBT11] Philipp Gütlich, Eckhard Bill, and Alfred X. Trautwein. "Mössbauer Spectroscopy and Transition Metal Chemistry". (2011). DOI: 10.1007/978-3-540-88428-6.

[GC07] K. J. Gaffney and H. N. Chapman. "Imaging Atomic Structure and Dynamics with Ultrafast X-ray Scattering". In: *Science* **316**, 1444–1448 (2007). DOI: 10.1126/science.1135923. eprint: https://science.sciencemag.org/content/316/5830/1444.full.pdf.

[GC85] C. W. Gardiner and M. J. Collett. "Input and output in damped quantum systems: Quantum stochastic differential equations and the master equation". In: *Phys. Rev. A* **31**, 3761–3774 (1985). DOI: 10.1103/PhysRevA.31.3761.

[Gel17] Mario F. Gely et al. "Convergence of the multimode quantum Rabi model of circuit quantum electrodynamics". In: *Phys. Rev. B* **95**, 245115 (2017). DOI: 10.1103/PhysRevB.95.245115.

[Ger21] M. Gerharz et al. to be published. 2021.

[Ger21] M. Gerharz. personal communication. 2021.

[Ger94] E. Gerdau. "Developments in time domain Mössbauer spectroscopy". In: *Hyperfine Interactions* **90**, 301–312 (1994). DOI: 10.1007/BF02069134.

[GEW19] Denis Golež, Martin Eckstein, and Philipp Werner. "Multiband nonequilibrium GW + EDMFT formalism for correlated insulators". In: *Phys. Rev. B* **100**, 235117 (2019). DOI: 10.1103/PhysRevB.100.235117.

[Gib19] Elizabeth Gibney. "Quantum gold rush: the private funding pouring into quantum start-ups". In: *Nature* **574**, 22–24 (2019). DOI: 10.1038/d41586-019-02935-4.

[Gib20] Elizabeth Gibney. "Quantum computer race intensifies as alternative technology gains steam". In: *Nature* **587**, 342–343 (2020). DOI: 10.1038/d41586-020-03237-w.

[GL14] Gianluca Gagliardi and Hans-Peter Loock. "Cavity-Enhanced Spectroscopy and Sensing". Springer, Berlin, Heidelberg (2014). DOI: 10.1007/978-3-642-40003-2.

[GL91] Roy J. Glauber and M. Lewenstein. "Quantum optics of dielectric media". In: *Phys. Rev. A* **43**, 467–491 (1991). DOI: 10.1103/PhysRevA.43.467.

[GLM11] Vittorio Giovannetti, Seth Lloyd, and Lorenzo Maccone. "Advances in quantum metrology". In: *Nature Photonics* **5**, 222–229 (2011). DOI: 10.1038/nphoton.2011.35.

[Glo12] T. E. Glover et al. "X-ray and optical wave mixing". In: *Nature* **488**, 603–608 (2012). DOI: 10.1038/nature11340.

[Gol21] Jakob Gollwitzer et al. "Connecting Fano interference and the Jaynes-Cummings model in cavity magnonics". In: *npj Quantum Information* **7**, 114 (2021). DOI: 10.1038/s41534-021-00445-8.

[GR17] Michael Gegg and Marten Richter. "PsiQuaSP–A library for efficient computation of symmetric open quantum systems". In: *Scientific Reports* **7**, 16304 (2017). DOI: 10.1038/s41598-017-16178-8.

[Gri20] Dominic Gribben et al. "Exact quantum dynamics in structured environments". In: *Phys. Rev. Research* **2**, 013265 (2020). DOI: 10.1103/PhysRevResearch.2.013265.

[GRK17] W. Guerin, M.T. Rouabah, and R. Kaiser. "Light interacting with atomic ensembles: collective, cooperative and mesoscopic effects". In: *Journal of Modern Optics* **64**, 895–907 (2017). DOI: 10.1080/09500340.2016.1215564. eprint: https://doi.org/10.1080/09500340.2016.1215564.

[GRPD15] J. J. García-Ripoll, B. Peropadre, and S. De Liberato. "Light-matter decoupling and A2 term detection in superconducting circuits". In: *Scientific Reports* **5**, 16055 EP –. Article (2015).

[Gu21a] Bing Gu et al. "Manipulating Core Excitations in Molecules by X-Ray Cavities". In: *Phys. Rev. Lett.* **126**, 053201 (2021). DOI: 10.1103/PhysRevLett.126.053201.

[Gu21b] Bing Gu et al. "Manipulating valence and core electronic excitations of a transition-metal complex using UV/Vis and X-ray cavities". In: *Chem. Sci.* **12**, 8088–8095 (2021). DOI: 10.1039/D1SC01774H.

[GVB94] E. Gerdau and U. Van Bürck. In: *Resonant Anomalous X-Ray Scattering*. Ed. by G. Materlik, C. J. Sparks, and K. Fischer. Amsterdam: North-Holland, 1994, 589.

[GVL96] Gene H. Golub and Charles F. Van Loan. "Matrix Computations (3rd Ed.)" Baltimore, MD, USA: Johns Hopkins University Press (1996).

[GW96] T. Gruner and D.-G. Welsch. "Green-function approach to the radiation-field quantization for homogeneous and inhomogeneous Kramers-Kronig dielectrics". In: *Phys. Rev. A* **53**, 1818–1829 (1996). DOI: 10.1103/PhysRevA.53.1818.

[GZ04] C. W. Gardiner and P. Zoller. "Quantum noise". Heidelberg: Springer (2004).

[Hab16a] Johann Haber et al. "Collective strong coupling of X-rays and nuclei in a nuclear optical lattice". In: *Nat. Phot.* **10**, 445 EP – (2016).

[Hab16b] Johann F. A. Haber. “Hard X-ray quantum optics in thin-film nanostructures”. PhD thesis. (2016).

[Hab17] Johann Haber et al. “Rabi oscillations of X-ray radiation between two nuclear ensembles”. In: *Nat. Phot.* **11**, 720–725 (2017). DOI: 10.1038/s41566-017-0013-3.

[Hab19] Johann Haber et al. “Spectral Control of an X-Ray L-Edge Transition via a Thin-Film Cavity”. In: *Phys. Rev. Lett.* **122**, 123608 (2019). DOI: 10.1103/PhysRevLett.122.123608.

[Hak70] H. Haken. “The Semiclassical and Quantum Theory of the Laser”. In: *Quantum Optics*. Ed. by S. M. Kay and A. Maitland. Academic Press, New York, 1970, 201.

[Han07] R. Hanson et al. “Spins in few-electron quantum dots”. In: *Rev. Mod. Phys.* **79**, 1217–1265 (2007). DOI: 10.1103/RevModPhys.79.1217.

[Har07] Serge Haroche. “A Short History of Cavity Quantum Electrodynamics”. In: *Conference on Coherence and Quantum Optics*. Optical Society of America, 2007, CTuF2. DOI: 10.1364/CQO.2007.CTuF2.

[Har13] Serge Haroche. “Nobel Lecture: Controlling photons in a box and exploring the quantum to classical boundary”. In: *Rev. Mod. Phys.* **85**, 1083–1102 (2013). DOI: 10.1103/RevModPhys.85.1083.

[Hau12] Philipp Hauke et al. “Can one trust quantum simulators?” In: *Reports on Progress in Physics* **75**, 082401 (2012). DOI: 10.1088/0034-4885/75/8/082401.

[Hau84] H. A. Haus. “Waves and Fields in Optoelectronics”. Prentice-Hall, Englewood Cliffs, N.J. (1984).

[HB92] Bruno Huttner and Stephen M. Barnett. “Quantization of the electromagnetic field in dielectrics”. In: *Phys. Rev. A* **46**, 4306–4322 (1992). DOI: 10.1103/PhysRevA.46.4306.

[HE13] Kilian P. Heeg and Jörg Evers. “X-ray quantum optics with Mössbauer nuclei embedded in thin-film cavities”. In: *Phys. Rev. A* **88**, 043828 (2013). DOI: 10.1103/PhysRevA.88.043828.

[HE15] Kilian P. Heeg and Jörg Evers. “Collective effects between multiple nuclear ensembles in an x-ray cavity-QED setup”. In: *Phys. Rev. A* **91**, 063803 (2015). DOI: 10.1103/PhysRevA.91.063803.

[HE20] Benedikt Herkommer and Jörg Evers. “Phase-sensitive nuclear target spectroscopy”. In: *Phys. Rev. Research* **2**, 023397 (2020). DOI: 10.1103/PhysRevResearch.2.023397.

[Hee13] Kilian P. Heeg et al. “Vacuum-Assisted Generation and Control of Atomic Coherences at X-Ray Energies”. In: *Phys. Rev. Lett.* **111**, 073601 (2013). DOI: 10.1103/PhysRevLett.111.073601.

[Hee14] Kilian Peter Heeg. “X-Ray quantum optics with Mössbauer nuclei in thin-film cavities”. PhD thesis. Ruprecht-Karls-Universität, Heidelberg (2014). DOI: 10.11588/heidok.00017869.

[Hee15a] K. P. Heeg et al. “Interferometric phase detection at x-ray energies via Fano resonance control”. In: *Phys. Rev. Lett.* **114**, 207401 (2015). DOI: 10.1103/PhysRevLett.114.207401.

[Hee15b] Kilian P. Heeg et al. “Tunable Subluminal Propagation of Narrow-band X-Ray Pulses”. In: *Phys. Rev. Lett.* **114**, 203601 (2015). DOI: 10.1103/PhysRevLett.114.203601.

[Hee17] K. P. Heeg et al. “Spectral narrowing of x-ray pulses for precision spectroscopy with nuclear resonances”. In: *Science* **357**, 375–378 (2017). DOI: 10.1126/science.aan3512.

[Hee19] K. P. Heeg. *Software package* PYNUSS. unpublished. 2019.

[Hee20] K. P. Heeg et al. "Coherent x-ray-optical control of nuclear excitons with zeptosecond phase-stability". In: (2020). arXiv: 2003.03755 [quant-ph].

[Hee21] Kilian P. Heeg et al. "Coherent X-ray-optical control of nuclear excitons". In: *Nature* **590**, 401–404 (2021). DOI: 10.1038/s41586-021-03276-x.

[Hel91] P. Helistö et al. "Gamma echo". In: *Phys. Rev. Lett.* **66**, 2037–2040 (1991). DOI: 10.1103/PhysRevLett.66.2037.

[Hen96] Klaus Hentschel. "Measurements of gravitational redshift between 1959 and 1971". In: *Annals of Science* **53**, 269–295 (1996). DOI: 10.1080/00033799600200211.

[Heu21] P. H. van den Heuvel. "Arbitrary phase control of X-ray pulses with zeptosecond phase stability". Master Thesis. Ruprecht-Karls-Universität, Heidelberg (2021).

[HJ01] T. Hauschild and M. Jentschel. "Comparison of maximum likelihood estimation and chi-square statistics applied to counting experiments". In: *Nuclear Instruments and Methods in Physics Research Section A: Accelerators, Spectrometers, Detectors and Associated Equipment* **457**, 384–401 (2001). DOI: https://doi.org/10.1016/S0168-9002(00)00756-7.

[HKE16] K. P. Heeg, C. H. Keitel, and J. Evers. "Inducing and detecting collective population inversions of Mössbauer nuclei". In: (2016). arXiv: 1607.04116 [quant-ph].

[Hod14] Hossein Hodaei et al. "Parity-time–symmetric microring lasers". In: *Science* **346**, 975–978 (2014). DOI: 10.1126/science.1258480.

[HP40] T. Holstein and H. Primakoff. "Field Dependence of the Intrinsic Domain Magnetization of a Ferromagnet". In: *Phys. Rev.* **58**, 1098–1113 (1940). DOI: 10.1103/PhysRev.58.1098.

[HR06] Serge Haroche and Jean Michel Raimond. "Exploring the Quantum: Atoms, Cavities, and Photons". Oxford: Oxford Univ. Press (2006). DOI: 10.1093/acprof:oso/9780198509141.001.0001.

[HRK18] Stephen Hughes, Marten Richter, and Andreas Knorr. "Quantized pseudomodes for plasmonic cavity QED". In: *Opt. Lett.* **43**, 1834–1837 (2018). DOI: 10.1364/OL.43.001834.

[HSP10] Klemens Hammerer, Anders S. Sørensen, and Eugene S. Polzik. "Quantum interface between light and atomic ensembles". In: *Rev. Mod. Phys.* **82**, 1041–1093 (2010). DOI: 10.1103/RevModPhys.82.1041.

[HT68] J. P. Hannon and G. T. Trammell. "Mössbauer Diffraction. I. Quantum Theory of Gamma-Ray and X-Ray Optics". In: *Phys. Rev.* **169**, 315–329 (1968). DOI: 10.1103/PhysRev.169.315.

[HT69] J. P. Hannon and G. T. Trammell. "Mössbauer Diffraction. II. Dynamical Theory of Mössbauer Optics". In: *Phys. Rev.* **186**, 306–325 (1969). DOI: 10.1103/PhysRev.186.306.

[HT99] J. P. Hannon and G. T. Trammell. "Coherent γ-ray optics". In: *Hyperfine Interactions* **123**, 127–274 (1999). DOI: 10.1023/A:1017011621007.

[Hua17] Xin-Chao Huang et al. "Field redistribution inside an X-ray cavity-QED setup". In: *Opt. Express* **25**, 31337–31346 (2017). DOI: 10.1364/OE.25.031337.

[Hua21] Xin-Chao Huang et al. "Controlling core-hole lifetime through an x-ray planar cavity". In: *Phys. Rev. Research* **3**, 033063 (2021). DOI: 10.1103/PhysRevResearch.3.033063.

[HVH02] Gregor Hackenbroich, Carlos Viviescas, and Fritz Haake. "Field Quantization for Chaotic Resonators with Overlapping Modes". In: *Phys. Rev. Lett.* **89**, 083902 (2002). DOI: 10.1103/PhysRevLett.89.083902.

[Ish12] Tetsuya Ishikawa et al. "A compact X-ray free-electron laser emitting in the sub-ångström region". In: *Nature Photonics* **6**, 540–544 (2012). DOI: 10.1038/nphoton.2012.141.

[Jac75] John David Jackson. "Classical electrodynamics; 2nd ed." New York, NY: Wiley (1975).

[Jay03] E. T. Jaynes. "Probability Theory: The Logic of Science". Ed. by G. Larry Bretthorst. Cambridge University Press (2003). DOI: 10.1017/CBO9780511790423.

[JC63] E. T. Jaynes and F. W. Cummings. "Comparison of quantum and semiclassical radiation theories with application to the beam maser". In: *Proc. IEEE* **51**, 89–109 (1963). DOI: 10.1109/PROC.1963.1664.

[JK] R. Johansson and E. Kim. *Sympsi - Symbolic Quantum Mechanics with Python and SymPy*. https://github.com/sympsi/sympsi.

[JNN12] J.R. Johansson, P.D. Nation, and Franco Nori. "QuTiP: An open-source Python framework for the dynamics of open quantum systems". In: *Computer Physics Communications* **183**, 1760–1772 (2012). DOI: 10.1016/j.cpc.2012.02.021.

[JNN13] J.R. Johansson, P.D. Nation, and Franco Nori. "QuTiP 2: A Python framework for the dynamics of open quantum systems". In: *Computer Physics Communications* **184**, 1234–1240 (2013). DOI: 10.1016/j.cpc.2012.11.019.

[Joa08] John D. Joannopoulos et al. "Photonic Crystals: Molding the Flow of Light". Princeton University Press (2008).

[Joh19] Aisling Johnson et al. "Observation of Collective Superstrong Coupling of Cold Atoms to a 30-m Long Optical Resonator". In: *Phys. Rev. Lett.* **123**, 243602 (2019). DOI: 10.1103/PhysRevLett.123.243602.

[JPK12] André Junker, Adriana Pálffy, and Christoph H Keitel. "Cooperative effects in nuclear excitation with coherent x-ray light". In: *New Journal of Physics* **14**, 085025 (2012). DOI: 10.1088/1367-2630/14/8/085025.

[Kal16] A. Kaldun et al. "Observing the ultrafast buildup of a Fano resonance in the time domain". In: *Science* **354**, 738–741 (2016). DOI: 10.1126/science.aah6972. eprint: https://science.sciencemag.org/content/354/6313/738.full.pdf.

[Kan17] Heung-Sik Kang et al. "Hard X-ray free-electron laser with femtosecond-scale timing jitter". In: *Nature Photonics* **11**, 708–713 (2017). DOI: 10.1038/s41566-017-0029-8.

[KAP67] Yu. Kagan, A. M. Afanas'ev, and I.P. Perstnev. "Theory of Resonance Bragg Scattering of γ Quanta by Regular Crystals". In: *Sov. Phys. JETP* **27**, 819 (1967).

[Kav17] Alexey Kavokin et al. "Microcavities". Oxford University Press (2017).

[KCP20] Xiangjin Kong, Darrick E. Chang, and Adriana Pálffy. "Green's-function formalism for resonant interaction of x rays with nuclei in structured media". In: *Phys. Rev. A* **102**, 033710 (2020). DOI: 10.1103/PhysRevA.102.033710.

[Kea12] J. Keaveney et al. "Cooperative Lamb Shift in an Atomic Vapor Layer of Nanometer Thickness". In: *Phys. Rev. Lett.* **108**, 173601 (2012). DOI: 10.1103/PhysRevLett.108.173601.

[KH14] Philip Trøst Kristensen and Stephen Hughes. "Modes and Mode Volumes of Leaky Optical Cavities and Plasmonic Nanoresonators". In: *ACS Photonics* **1**, 2–10 (2014). DOI: 10.1021/ph400114e.

[KH25] H. A. Kramers and W. Heisenberg. "Über die Streuung von Strahlung durch Atome". In: *Zeitschrift für Physik* **31**, 681–708 (1925). DOI: 10.1007/BF02980624.

[Kha05] M. Khanbekyan et al. "QED of lossy cavities: Operator and quantum-state input-output relations". In: *Phys. Rev. A* **72**, 053813 (2005). DOI: 10.1103/PhysRevA.72.053813.

[Kif10] Martin Kiffner et al. "Vacuum-induced processes in multi-level atoms". In: *Progress in Optics*. Vol. 55. Burlington: Elsevier Science (2010), pp. 85–197.

[Kil80] S. Kilin. "Collective effects in resonance fluorescence". In: *Sov. Phys. JETP* **55**, 38 (1980).

[Kir19] Peter Kirton et al. "Introduction to the Dicke Model: From Equilibrium to Nonequilibrium, and Vice Versa". In: *Advanced Quantum Technologies* **2**, 1800043 (2019). DOI: https://doi.org/10.1002/qute.201800043.

[Kja20] Morten Kjaergaard et al. "Superconducting Qubits: Current State of Play". In: *Annual Review of Condensed Matter Physics* **11**, 369–395 (2020). DOI: 10.1146/annurev-conmatphys-031119-050605.

[KK12] G. Kalvius and P. Kienle, eds. Berlin, Heidelberg: Springer-Verlag (2012).

[KK17a] Peter Kirton and Jonathan Keeling. "Suppressing and Restoring the Dicke Superradiance Transition by Dephasing and Decay". In: *Phys. Rev. Lett.* **118**, 123602 (2017). DOI: 10.1103/PhysRevLett.118.123602.

[KK17b] Elena Kuznetsova and Olga Kocharovskaya. "Quantum optics with X-rays". In: *Nature Photonics* **11**, 685–686 (2017). DOI: 10.1038/s41566-017-0034-y.

[KKR99] Olga Kocharovskaya, Roman Kolesov, and Yuri Rostovtsev. "Coherent Optical Control of Mössbauer Spectra". In: *Phys. Rev. Lett.* **82**, 3593–3596 (1999). DOI: 10.1103/PhysRevLett.82.3593.

[Kli04] G. Klingelhöfer et al. "Jarosite and Hematite at Meridiani Planum from Opportunity's Mössbauer Spectrometer". In: *Science* **306**, 1740–1745 (2004). DOI: 10.1126/science.1104653. eprint: https://science.sciencemag.org/content/306/5702/1740.full.pdf.

[KLM01] E. Knill, R. Laflamme, and G. J. Milburn. "A scheme for efficient quantum computation with linear optics". In: *Nature* **409**, 46–52 (2001). DOI: 10.1038/35051009.

[KLP14] Xiangjin Kong, Wen-Te Liao, and Adriana Pálffy. "Field control of single x-ray photons in nuclear forward scattering". In: *New Journal of Physics* **16**, 013049 (2014). DOI: 10.1088/1367-2630/16/1/013049.

[KO21] Norimichi Kojima and Atsushi Okazawa. "Molecular Magnetism of Metal Complexes and Light-Induced Phase Transitions". In: *Modern Mössbauer Spectroscopy: New Challenges Based on Cutting-Edge Techniques*. Ed. by Yutaka Yoshida and Guido Langouche. Singapore: Springer Singapore, 2021, 267–317. DOI: 10.1007/978-981-15-9422-9_6.

[Koe10] A. F. Koenderink. "On the use of Purcell factors for plasmon antennas". In: *Opt. Lett.* **35**, 4208–4210 (2010). DOI: 10.1364/OL.35.004208.

[Kok07] Pieter Kok et al. "Linear optical quantum computing with photonic qubits". In: *Rev. Mod. Phys.* **79**, 135–174 (2007). DOI: 10.1103/RevModPhys.79.135.

[KP16] Xiangjin Kong and Adriana Pálffy. "Stopping Narrow-Band X-Ray Pulses in Nuclear Media". In: *Phys. Rev. Lett.* **116**, 197402 (2016). DOI: 10.1103/PhysRevLett.116.197402.

[KR15] Sebastian Krämer and Helmut Ritsch. "Generalized mean-field approach to simulate the dynamics of large open spin ensembles with long range interactions". In: *The European Physical Journal D* **69**, 282 (2015). DOI: 10.1140/epjd/e2015-60266-5.

[KR76] L.A. Kroger and C.W. Reich. "Features of the low-energy level scheme of 229Th as observed in the alpha-decay of 233U". In: *Nuclear Physics A* **259**, 29–60 (1976). DOI: https://doi.org/10.1016/0375-9474(76)90494-2.

[Kra19] P. Krantz et al. "A quantum engineer's guide to superconducting qubits". In: *Applied Physics Reviews* **6**, 021318 (2019). DOI: 10.1063/1.5089550.

[Kri14] Dmitry O. Krimer et al. "Route from spontaneous decay to complex multimode dynamics in cavity QED". In: *Phys. Rev. A* **89**, 033820 (2014). DOI: 10.1103/PhysRevA.89.033820.

[KSR08] Kwang-Je Kim, Yuri Shvyd'ko, and Sven Reiche. "A Proposal for an X-Ray Free-Electron Laser Oscillator with an Energy-Recovery Linac". In: *Phys. Rev. Lett.* **100**, 244802 (2008). DOI: 10.1103/PhysRevLett.100.244802.

[Kub62] Ryogo Kubo. "Generalized Cumulant Expansion Method". In: *Journal of the Physical Society of Japan* **17**, 1100–1120 (1962). DOI: 10.1143/JPSJ.17.1100.

[LA15] Wen-Te Liao and Sven Ahrens. "Gravitational and relativistic deflection of X-ray superradiance". In: *Nature Photonics* **9**, 169–173 (2015). DOI: 10.1038/nphoton.2015.7.

[Lab12] D. E. Laban et al. "Extreme Ultraviolet Interferometer Using High-Order Harmonic Generation from Successive Sources". In: *Phys. Rev. Lett.* **109**, 263902 (2012). DOI: 10.1103/PhysRevLett.109.263902.

[Lad10] T. D. Ladd et al. "Quantum computers". In: *Nature* **464**, 45–53 (2010). DOI: 10.1038/nature08812.

[Lal18] Philippe Lalanne et al. "Light Interaction with Photonic and Plasmonic Resonances". In: *Laser & Photonics Reviews* **12**, 1700113 (2018). DOI: 10.1002/lpor.201700113.

[Lax51] Melvin Lax. "Multiple Scattering of Waves". In: *Rev. Mod. Phys.* **23**, 287–310 (1951). DOI: 10.1103/RevModPhys.23.287.

[LE20] Dominik Lentrodt and Jörg Evers. "Ab Initio Few-Mode Theory for Quantum Potential Scattering Problems". In: *Phys. Rev. X* **10**, 011008 (2020). DOI: 10.1103/PhysRevX.10.011008.

[Le21p] D. Lentrodt et al. "Non-linear excitation of Mössbauer nuclei in thin-film cavities by focussed x-ray beams". In: *in preparation* (2021).

[Len20] Dominik Lentrodt et al. "Ab initio quantum models for thin-film x-ray cavity QED". In: *Phys. Rev. Research* **2**, 023396 (2020). DOI: 10.1103/PhysRevResearch.2.023396.

[Len21] Dominik Lentrodt et al. *Classifying and harnessing multi-mode light-matter interaction in lossy resonators*. 2021. arXiv: 2107.11775 [quant-ph].

[LHH60] F. J. Lynch, R. E. Holland, and M. Hamermesh. "Time Dependence of Resonantly Filtered Gamma Rays from Fe^{57}". In: *Phys. Rev.* **120**, 513–520 (1960). DOI: 10.1103/PhysRev.120.513.

[Li20] Jiajun Li et al. “Electromagnetic coupling in tight-binding models for strongly correlated light and matter”. In: *Phys. Rev. B* **101**, 205140 (2020). DOI: 10.1103/PhysRevB.101.205140.

[Lia13] Wen-Te Liao. “Coherent Control of Nuclei and X-Rays”. Springer Theses. Springer (2013). DOI: https://doi.org/10.1007/978-3-319-02120-1.

[Lim17] Mikhail F. Limonov et al. “Fano resonances in photonics”. In: *Nat. Phot.* **11**, 543 EP –. Review Article (2017).

[Lin76] G. Lindblad. “On the generators of quantum dynamical semigroups”. In: *Comm. Math. Phys.* **48**, 119–130 (1976).

[Lip21] Pierre-Emmanuel Lippens. “Application of Mössbauer Spectroscopy to Li-Ion and Na-Ion Batteries”. In: *Modern Mössbauer Spectroscopy: New Challenges Based on Cutting-Edge Techniques*. Ed. by Yutaka Yoshida and Guido Langouche. Singapore: Springer Singapore, 2021, 319–379. DOI: 10.1007/978-981-15-9422-9_7.

[Liu16] S.M. Liuzzo et al. “Updates on Lattice Modeling and Tuning for the ESRF-EBS Lattice.” In: *Proc. of International Particle Accelerator Conference (IPAC'16), Busan, Korea, May 8-13, 2016* (Busan, Korea). International Particle Accelerator Conference 7. doi:10.18429/JACoW-IPAC2016-WEPOW005. Geneva, Switzerland: JACoW, 2016, 2818–2821. DOI: doi:10.18429/JACoW-IPAC2016-WEPOW005.

[Liu17] Renming Liu et al. “Strong Light-Matter Interactions in Single Open Plasmonic Nanocavities at the Quantum Optics Limit”. In: *Phys. Rev. Lett.* **118**, 237401 (2017). DOI: 10.1103/PhysRevLett.118.237401.

[LKE16] Paolo Longo, Christoph H. Keitel, and Jörg Evers. “Tailoring superradiance to design artificial quantum systems”. In: *Scientific Reports* **6**, 23628 (2016). DOI: 10.1038/srep23628.

[LKP16] Wen-Te Liao, Christoph H. Keitel, and Adriana Pálffy. “X-ray-generated heralded macroscopical quantum entanglement of two nuclear ensembles”. In: *Scientific Reports* **6**, 33361 (2016). DOI: 10.1038/srep33361.

[LL87] M. Ley and R. Loudon. “Quantum Theory of High-resolution Length Measurement with a Fabry-Perot Interferometer”. In: *J. Mod. Opt.* **34**, 227–255 (1987). DOI: 10.1080/09500348714550251.

[LMS15] Peter Lodahl, Sahand Mahmoodian, and Søren Stobbe. “Interfacing single photons and single quantum dots with photonic nanostructures”. In: *Rev. Mod. Phys.* **87**, 347–400 (2015). DOI: 10.1103/RevModPhys.87.347.

[LoE14a] Paolo Longo and Jörg Evers. “Far-Field Signatures of a Two-Body Bound State in Collective Emission from Interacting Two-Level Atoms on a Lattice”. In: *Phys. Rev. Lett.* **112**, 193601 (2014). DOI: 10.1103/PhysRevLett.112.193601.

[LoE14b] Paolo Longo and Jörg Evers. “Probing few-excitation eigenstates of interacting atoms on a lattice by observing their collective light emission in the far field”. In: *Phys. Rev. A* **90**, 063834 (2014). DOI: 10.1103/PhysRevA.90.063834.

[Lon17] Stefano Longhi. “Parity-time symmetry meets photonics: A new twist in non-Hermitian optics”. In: *EPL (Europhysics Letters)* **120**, 64001 (2017). DOI: 10.1209/0295-5075/120/64001.

[Lor80] H. A. Lorentz. In: *Wiedem. Ann.* **9**, 641 (1880).

[Lor81] L. Lorenz. In: *Wiedem. Ann.* **11**, 70 (1881).

[LP17] Wen-Te Liao and Adriana Pálffy. "Optomechanically induced transparency of x-rays via optical control". In: *Scientific Reports* **7**, 321 (2017). DOI: 10.1038/s41598-017-00428-w.

[LPK11] Wen-Te Liao, Adriana Pálffy, and Christoph H. Keitel. "Nuclear coherent population transfer with X-ray laser pulses". In: *Physics Letters B* **705**, 134–138 (2011). DOI: https://doi.org/10.1016/j.physletb.2011.09.107.

[LPK12] Wen-Te Liao, Adriana Pálffy, and Christoph H. Keitel. "Coherent Storage and Phase Modulation of Single Hard-X-Ray Photons Using Nuclear Excitons". In: *Phys. Rev. Lett.* **109**, 197403 (2012). DOI: 10.1103/PhysRevLett.109.197403.

[LPK13] Wen-Te Liao, Adriana Pálffy, and Christoph H. Keitel. "Three-beam setup for coherently controlling nuclear-state population". In: *Phys. Rev. C* **87**, 054609 (2013). DOI: 10.1103/PhysRevC.87.054609.

[LR99] Claus Lamprecht and Helmut Ritsch. "Quantized Atom-Field Dynamics in Unstable Cavities". In: *Phys. Rev. Lett.* **82**, 3787–3790 (1999). DOI: 10.1103/PhysRevLett.82.3787.

[LSL73] Roy Lang, Marlan O. Scully, and Willis E. Lamb. "Why is the Laser Line So Narrow? A Theory of Single-Quasimode Laser Operation". In: *Phys. Rev. A* **7**, 1788–1797 (1973). DOI: 10.1103/PhysRevA.7.1788.

[LT58] A. M. Lane and R. G. Thomas. "R-Matrix Theory of Nuclear Reactions". In: *Rev. Mod. Phys.* **30**, 257–353 (1958). DOI: 10.1103/RevModPhys.30.257.

[Lud15] Andrew D. Ludlow et al. "Optical atomic clocks". In: *Rev. Mod. Phys.* **87**, 637–701 (2015). DOI: 10.1103/RevModPhys.87.637.

[MA19] Mohammad-Ali Miri and Andrea Alù. "Exceptional points in optics and photonics". In: *Science* **363** (2019). DOI: 10.1126/science.aar7709.

[Mad13] A. Madsen et al. *Technical Design Report - Scientific Instrument MID*. https://www.xfel.eu/sites/sites_custom/site_xfel/content/e35165/e46561/e46883/e46942/e46945/xfel_file46946/TR-2013-005_TDR_MID_eng.pdf. Accessed: 2021-07-25. 2013.

[Mad21] A. Madsen et al. "Materials Imaging and Dynamics (MID) instrument at the European X-ray Free-Electron Laser Facility". In: *Journal of Synchrotron Radiation* **28**, 637–649 (2021). DOI: 10.1107/S1600577521001302.

[MAG20] Stuart J. Masson and Ana Asenjo-Garcia. "Atomic-waveguide quantum electrodynamics". In: *Phys. Rev. Research* **2**, 043213 (2020). DOI: 10.1103/PhysRevResearch.2.043213.

[Mar16] Esteban A. Martinez et al. "Real-time dynamics of lattice gauge theories with a few-qubit quantum computer". In: *Nature* **534**, 516–519 (2016). DOI: 10.1038/nature18318.

[Mas19] A. Masson S. J. Asenjo-Garcia. "Atomic-Waveguide Quantum Electrodynamics". In: (2019). arXiv: 1912.06234 [quant-ph].

[Maz09] L. Mazzola et al. "Pseudomodes as an effective description of memory: Non-Markovian dynamics of two-state systems in structured reservoirs". In: *Phys. Rev. A* **80**, 012104 (2009). DOI: 10.1103/PhysRevA.80.012104.

[McC21] Catherine McCammon. "Mössbauer Spectroscopy with High Spatial Resolution: Spotlight on Geoscience". In: *Modern Mössbauer Spectroscopy: New Challenges Based on Cutting-Edge Techniques*. Ed. by Yutaka Yoshida and Guido Langouche. Singapore: Springer Singapore, 2021, 221–266. DOI: 10.1007/978-981-15-9422-9_5.

[Med21] Ivan Medina et al. “Few-Mode Field Quantization of Arbitrary Electromagnetic Spectral Densities”. In: *Phys. Rev. Lett.* **126**, 093601 (2021). DOI: 10.1103/PhysRevLett.126.093601.

[Meu17] Aaron Meurer et al. “SymPy: symbolic computing in Python”. In: *PeerJ Computer Science* **3**, e103 (2017). DOI: 10.7717/peerj-cs.103.

[Mey21a] Pierre Meystre. “Quantum Optics: Taming the Quantum”. Cham: Springer International Publishing (2021). DOI: 10.1007/978-3-030-76183-7.

[Mey21b] Pierre Meystre. “Tailoring the Environment—Cavity QED”. In: *Quantum Optics: Taming the Quantum*. Cham: Springer International Publishing, 2021, 187–228. DOI: 10.1007/978-3-030-76183-7_7.

[MH67] S. L. McCall and E. L. Hahn. “Self-Induced Transparency by Pulsed Coherent Light”. In: *Phys. Rev. Lett.* **18**, 908–911 (1967). DOI: 10.1103/PhysRevLett.18.908.

[Mia16] Pei Miao et al. “Orbital angular momentum microlaser”. In: *Science* **353**, 464–467 (2016). DOI: 10.1126/science.aaf8533.

[Mil17] Christopher J. Milne et al. “SwissFEL: The Swiss X-ray Free Electron Laser”. In: *Applied Sciences* **7** (2017). DOI: 10.3390/app7070720.

[Min18] Lorenzo Mino et al. “Materials characterization by synchrotron x-ray microprobes and nanoprobes”. In: *Rev. Mod. Phys.* **90**, 025007 (2018). DOI: 10.1103/RevModPhys.90.025007.

[Min19] Fabrizio Minganti et al. “Quantum exceptional points of non-Hermitian Hamiltonians and Liouvillians: The effects of quantum jumps”. In: *Phys. Rev. A* **100**, 062131 (2019). DOI: 10.1103/PhysRevA.100.062131.

[MM21] L. A. Martínez-Martínez. “Photophysics of Organic Molecules under the Polariton regime”. PhD thesis. UC San Diego (2021).

[MO33] W. Meissner and R. Ochsenfeld. “Ein neuer Effekt bei Eintritt der Supraleitfähigkeit”. In: *Naturwissenschaften* **21**, 787–788 (1933). DOI: 10.1007/BF01504252.

[Moi11] Nimrod Moiseyev. “Non-Hermitian Quantum Mechanics”. Cambridge: Cambridge University Press (2011). DOI: 10.1017/CBO9780511976186.

[Mos50] O. F. Mossotti. “Discussione analitica sull’influenza che l’azione di un mezzo dielettrico ha sulla distribuzione dell’elettricità alla superficie di più corpi elettrici disseminati in esso”. In: *Mem. di mathem. e fisica in Modena* **24**, 49–74 (1850).

[MPT16] Moein Malekakhlagh, Alexandru Petrescu, and Hakan E. Türeci. “Non-Markovian dynamics of a superconducting qubit in an open multimode resonator”. In: *Phys. Rev. A* **94**, 063848 (2016). DOI: 10.1103/PhysRevA.94.063848.

[MPT17] Moein Malekakhlagh, Alexandru Petrescu, and Hakan E. Türeci. “Cutoff-Free Circuit Quantum Electrodynamics”. In: *Phys. Rev. Lett.* **119**, 073601 (2017). DOI: 10.1103/PhysRevLett.119.073601.

[MRW10] G. E. Mitchell, A. Richter, and H. A. Weidenmüller. “Random matrices and chaos in nuclear physics: Nuclear reactions”. In: *Rev. Mod. Phys.* **82**, 2845–2901 (2010). DOI: 10.1103/RevModPhys.82.2845.

[MS08] P. Markoš and C. M. Soukoulis. “Wave Propagation”. Princeton University Press (2008). DOI: 10.1515/9781400835676.

[MT10] Brian W. J. McNeil and Neil R. Thompson. “X-ray free-electron lasers”. In: *Nature Photonics* **4**, 814–821 (2010). DOI: 10.1038/nphoton.2010.239.

[MT16] Moein Malekakhlagh and Hakan E. Türeci. "Origin and implications of an A^2-like contribution in the quantization of circuit-QED systems". In: *Phys. Rev. A* **93**, 012120 (2016). DOI: 10.1103/PhysRevA.93.012120.

[MW69] C. Mahaux and H. A. Weidenmüller. "Shell-model approach to nuclear reactions." North-Holland Pub. Co., London (1969).

[Mös58] Rudolf L. Mössbauer. "Kernresonanzfluoreszenz von Gammastrahlung in Ir191". In: *Zeitschrift für Physik* **151**, 124–143 (1958). DOI: 10.1007/BF01344210.

[Mös62] Rudolf L. Mössbauer. "Recoilless Nuclear Resonance Absorption of Gamma Radiation". In: *Science* **137**, 731–738 (1962). DOI: 10.1126/science.137.3532.731. eprint: https://science.sciencemag.org/content/137/3532/731.full.pdf.

[Nak14] M. Nakatsutsumi et al. *Technical Design Report - Scientific Instrument HED*. https://www.xfel.eu/sites/sites_custom/site_xfel/content/e35165/e46561/e46886/e46954/e46959/xfel_file46960/TR-2014-001_TDR_HED_eng.pdf. Accessed: 2021-07-25. 2014.

[Nam21] Inhyuk Nam et al. "High-brightness self-seeded X-ray free-electron laser covering the 3.5 keV to 14.6 keV range". In: *Nature Photonics* **15**, 435–441 (2021). DOI: 10.1038/s41566-021-00777-z.

[New82] Roger G. Newton. "Scattering Theory of Waves and Particles". Springer-Verlag, New York (1982).

[NH06] Lukas Novotny and Bert Hecht. "Principles of Nano-Optics". Cambridge University Press (2006). DOI: 10.1017/CBO9780511813535.

[Nie98] L. Niesen et al. "Magnetic behavior of probe layers of ^{57}Fe in thin Fe films observed by means of nuclear resonant scattering of synchrotron radiation". In: *Phys. Rev. B* **58**, 8590–8595 (1998). DOI: 10.1103/PhysRevB.58.8590.

[Nov14] Lukas Novotny. *Physical Optics II*. https://www.photonics.ethz.ch/fileadmin/user_upload/Courses/PhysicalOpticsII/notes13.pdf. Accessed 19/02/2021. 2014.

[Ode10] J. Odeurs et al. "Towards more relaxed conditions for a gamma-ray laser: Methods to realize induced transparency for nuclear resonant gamma radiation". In: *Laser & Photonics Reviews* **4**, 1–20 (2010). DOI: https://doi.org/10.1002/lpor.200810068. eprint: https://onlinelibrary.wiley.com/doi/pdf/10.1002/lpor.200810068.

[Oka12] K. Okamoto et al. "X-ray Waveguide Mode in Resonance with a Periodic Structure". In: *Phys. Rev. Lett.* **109**, 233907 (2012). DOI: 10.1103/PhysRevLett.109.233907.

[Ott13] Christian Ott et al. "Lorentz Meets Fano in Spectral Line Shapes: A Universal Phase and Its Laser Control". In: *Science* **340**, 716–720 (2013). DOI: 10.1126/science.1234407.

[Par54] L. G. Parratt. "Surface Studies of Solids by Total Reflection of X-Rays". In: *Phys. Rev.* **95**, 359–369 (1954). DOI: 10.1103/PhysRev.95.359.

[Pei21] E Peik et al. "Nuclear clocks for testing fundamental physics". In: *Quantum Science and Technology* **6**, 034002 (2021). DOI: 10.1088/2058-9565/abe9c2.

[Pen14] B. Peng et al. "Loss-induced suppression and revival of lasing". In: *Science* **346**, 328–332 (2014). DOI: 10.1126/science.1258004.

[Pen17] Pai Peng et al. "Enhancing Coherent Light-Matter Interactions through Microcavity-Engineered Plasmonic Resonances". In: *Phys. Rev. Lett.* **119**, 233901 (2017). DOI: 10.1103/PhysRevLett.119.233901.

[Pet79] K. Petermann. "Calculated spontaneous emission factor for double-heterostructure injection lasers with gain-induced waveguiding". In: *IEEE J. Quantum Electron.* **15**, 566–570 (1979). DOI: 10.1109/JQE.1979.1070064.

[Pez18] Luca Pezzè et al. "Quantum metrology with nonclassical states of atomic ensembles". In: *Rev. Mod. Phys.* **90**, 035005 (2018). DOI: 10.1103/RevModPhys.90.035005.

[Pfe02] F. Pfeiffer et al. "Two-Dimensional X-ray Waveguides and Point Sources". In: *Science* **297**, 230–234 (2002). DOI: 10.1126/science.1071994. eprint: https://science.sciencemag.org/content/297/5579/230.full.pdf.

[Pfe10] Thomas Pfeifer et al. "Partial-coherence method to model experimental free-electron laser pulse statistics". In: *Opt. Lett.* **35**, 3441–3443 (2010). DOI: 10.1364/OL.35.003441.

[PGP20] Graeme Pleasance, Barry M. Garraway, and Francesco Petruccione. "Generalized theory of pseudomodes for exact descriptions of non-Markovian quantum processes". In: *Phys. Rev. Research* **2**, 043058 (2020). DOI: 10.1103/PhysRevResearch.2.043058.

[PHR21] David Plankensteiner, Christoph Hotter, and Helmut Ritsch. *QuantumCumulants.jl: A Julia framework for generalized mean-field equations in open quantum systems*. 2021. arXiv: 2105.01657 [quant-ph].

[PKE09] Adriana Pálffy, Christoph H. Keitel, and Jörg Evers. "Single-Photon Entanglement in the keV Regime via Coherent Control of Nuclear Forward Scattering". In: *Phys. Rev. Lett.* **103**, 017401 (2009). DOI: 10.1103/PhysRevLett.103.017401.

[PMR16] C. Pellegrini, A. Marinelli, and S. Reiche. "The physics of x-ray free-electron lasers". In: *Rev. Mod. Phys.* **88**, 015006 (2016). DOI: 10.1103/RevModPhys.88.015006.

[PR59] R. V. Pound and G. A. Rebka. "Gravitational Red-Shift in Nuclear Resonance". In: *Phys. Rev. Lett.* **3**, 439–441 (1959). DOI: 10.1103/PhysRevLett.3.439.

[PR60] R. V. Pound and G. A. Rebka. "Apparent Weight of Photons". In: *Phys. Rev. Lett.* **4**, 337–341 (1960). DOI: 10.1103/PhysRevLett.4.337.

[Pre18] John Preskill. "Quantum Computing in the NISQ era and beyond". In: *Quantum* **2**, 79 (2018). DOI: 10.22331/q-2018-08-06-79.

[Pur46] E. M. Purcell. "Spontaneous emission probabilities at radio frequencies". In: *Phys. Rev.* **69**, 681 (1946).

[Pál08] Adriana Pálffy. "A systematic study of nuclear photoexcitation with X-ray laser fields". In: *Journal of Modern Optics* **55**, 2603–2615 (2008). DOI: 10.1080/09500340802213666.

[RÖ02] R. Röhlsberger et al. "Imaging the Magnetic Spin Structure of Exchange-Coupled Thin Films". In: *Phys. Rev. Lett.* **89**, 237201 (2002). DOI: 10.1103/PhysRevLett.89.237201.

[Rab36] I. I. Rabi. "On the Process of Space Quantization". In: *Phys. Rev.* **49**, 324–328 (1936). DOI: 10.1103/PhysRev.49.324.

[RC21] Rudolf Rüffer and Aleksandr I. Chumakov. "Historical Developments and Future Perspectives in Nuclear Resonance Scattering". In: *Modern Mössbauer Spectroscopy: New Challenges Based on Cutting-Edge Techniques*. Ed. by Yutaka Yoshida and Guido Langouche. Singapore: Springer Singapore, 2021, 1–55. DOI: 10.1007/978-981-15-9422-9_1.

[RE21] Ralf Röhlsberger and Jörg Evers. "Quantum Optical Phenomena in Nuclear Resonant Scattering". In: *Modern Mössbauer Spectroscopy: New Challenges Based on Cutting-Edge Techniques*. Ed. by Yutaka Yoshida and Guido Langouche. Singapore: Springer Singapore, 2021, 105–171. DOI: 10.1007/978-981-15-9422-9_3.

[RES14] Ralf Röhlsberger, Jörg Evers, and Sharon Shwartz. "Quantum and Nonlinear Optics with Hard X-Rays". In: *Synchrotron Light Sources and Free-Electron Lasers: Accelerator Physics, Instrumentation and Science Applications*. Ed. by Eberhard Jaeschke et al. Cham: Springer International Publishing, 2014, 1–28. DOI: 10.1007/978-3-319-04507-8_32-1.

[RG17] Stefan Rotter and Sylvain Gigan. "Light fields in complex media: Mesoscopic scattering meets wave control". In: *Rev. Mod. Phys.* **89**, 015005 (2017). DOI: 10.1103/RevModPhys.89.015005.

[Rib18] Raphael F. Ribeiro et al. "Polariton chemistry: controlling molecular dynamics with optical cavities". In: *Chem. Sci.* **9**, 6325–6339 (2018). DOI: 10.1039/C8SC01043A.

[Rit13] Helmut Ritsch et al. "Cold atoms in cavity-generated dynamical optical potentials". In: *Rev. Mod. Phys.* **85**, 553–601 (2013). DOI: 10.1103/RevModPhys.85.553.

[Roh12] Nina Rohringer et al. "Atomic inner-shell X-ray laser at 1.46 nanometres pumped by an X-ray free-electron laser". In: *Nature* **481**, 488–491 (2012). DOI: 10.1038/nature10721.

[Ros17] Daniel Z. Rossatto et al. "Spectral classification of coupling regimes in the quantum Rabi model". In: *Phys. Rev. A* **96**, 013849 (2017). DOI: 10.1103/PhysRevA.96.013849.

[Rot09] Ingrid Rotter. "A non-Hermitian Hamilton operator and the physics of open quantum systems". In: *J. Phys. A* **42**, 153001 (2009).

[Rot18] S. Rotter. personal communication. 2018.

[RR15] Andreas Reiserer and Gerhard Rempe. "Cavity-based quantum networks with single atoms and optical photons". In: *Rev. Mod. Phys.* **87**, 1379–1418 (2015). DOI: 10.1103/RevModPhys.87.1379.

[RS82] M. Reed and B. Simon. "Methods of Modern Mathematical Physics". Academic, New York (1982).

[RSG21] Michael Reitz, Christian Sommer, and Claudiu Genes. *Cooperative quantum phenomena*. 2021. arXiv: 2107.02674 [quant-ph].

[RSH13] A. Ridolfo, S. Savasta, and M. J. Hartmann. "Nonclassical Radiation from Thermal Cavities in the Ultrastrong Coupling Regime". In: *Phys. Rev. Lett.* **110**, 163601 (2013). DOI: 10.1103/PhysRevLett.110.163601.

[Rub74] S. L. Ruby. "Mössbauer experiments without conventional sources". In: *J. Phys. Colloques* **35**, C6–209–C6–211 (1974). DOI: 10.1051/jphyscol:1974623.

[Rug14] Michael Ruggenthaler et al. "Quantum-electrodynamical density-functional theory: Bridging quantum optics and electronic-structure theory". In: *Phys. Rev. A* **90**, 012508 (2014). DOI: 10.1103/PhysRevA.90.012508.

[Röh10] Ralf Röhlsberger et al. "Collective Lamb Shift in Single-Photon Superradiance". In: *Science* **328**, 1248–1251 (2010). DOI: 10.1126/science.1187770.

[Röh97] R. Röhlsberger et al. "X-ray optics for μeV-resolved spectroscopy". In: *Nuclear Instruments and Methods in Physics Research Section A: Accelerators, Spectrometers, Detectors and Associated Equipment* **394**, 251 –255 (1997). DOI: https://doi.org/10.1016/S0168-9002(97)00710-9.

[Röh99a] R. Röhlsberger. "Theory of X-ray grazing incidence reflection in the presence of nuclear resonance excitation". In: *Hyperfine Interactions* **123**, 301–325 (1999). DOI: 10.1023/A:1017063605078.

[Röh99b] R. Röhlsberger. "Theory of X-ray grazing incidence reflection in the presence of nuclear resonance excitation". In: *Hyperfine Interactions* **123**, 301–325 (1999). DOI: 10.1023/A:1017063605078.

[Röh05a] R. Röhlsberger et al. "Accelerating the Spontaneous Emission of X Rays from Atoms in a Cavity". In: *Phys. Rev. Lett.* **95**, 097601 (2005). DOI: 10.1103/PhysRevLett.95.097601.

[Röh05b] Ralf Röhlsberger. "Nuclear Condensed Matter Physics with Synchrotron Radiation". Vol. 208. Springer Tracts in Modern Physics. Berlin, Heidelberg: Springer (2005). DOI: 10.1007/b86125.

[Röh12] Ralf Röhlsberger et al. "Electromagnetically induced transparency with resonant nuclei in a cavity". In: *Nature* **482**, 199–203 (2012). DOI: 10.1038/nature10741.

[Saf18] M. S. Safronova et al. "Search for new physics with atoms and molecules". In: *Rev. Mod. Phys.* **90**, 025008 (2018). DOI: 10.1103/RevModPhys.90.025008.

[Sak17] S. Sakshath et al. "Optical pump - nuclear resonance probe experiments on spin crossover complexes". In: *Hyperfine Interactions* **238**, 89 (2017). DOI: 10.1007/s10751-017-1461-3.

[Sal01] E.L. Saldin et al. "X-ray FEL with a meV bandwidth". In: *Nuclear Instruments and Methods in Physics Research Section A: Accelerators, Spectrometers, Detectors and Associated Equipment* **475**, 357–362. FEL2000: Proc. 22nd Int. Free Electron Laser Conference and 7th F EL Users Workshop (2001). DOI: https://doi.org/10.1016/S0168-9002(01)01539-X.

[Sal08] T. Salditt et al. "High-Transmission Planar X-Ray Waveguides". In: *Phys. Rev. Lett.* **100**, 184801 (2008). DOI: 10.1103/PhysRevLett.100.184801.

[Sal15] T. Salditt et al. "X-Ray Optics on a Chip: Guiding X Rays in Curved Channels". In: *Phys. Rev. Lett.* **115**, 203902 (2015). DOI: 10.1103/PhysRevLett.115.203902.

[Sav12] Kevin J. Savage et al. "Revealing the quantum regime in tunnelling plasmonics". In: *Nature* **491**, 574 (2012).

[SB08] S. Scheel and S. Y. Buhmann. "Macroscopic quantum electrodynamics - concepts and applications". In: *Acta Phys. Slovaca* **58**, 675 (2008).

[SBD16] L M Sieberer, M Buchhold, and S Diehl. "Keldysh field theory for driven open quantum systems". In: *Reports on Progress in Physics* **79**, 096001 (2016). DOI: 10.1088/0034-4885/79/9/096001.

[SBH99] D. P. Siddons, U. Bergmann, and J. B. Hastings. "Polarization effects in resonant nuclear scattering". In: *Hyperfine Interactions* **123**, 681–719 (1999). DOI: 10.1023/A:1017096512347.

[SBSF20] M. Sánchez-Barquilla, R. E. F. Silva, and J. Feist. "Cumulant expansion for the treatment of light–matter interactions in arbitrary material structures". In: *The Journal of Chemical Physics* **152**, 034108 (2020). DOI: 10.1063/1.5138937.

[SC95] D. Sayre and H. N. Chapman. "X-ray microscopy". In: *Acta Crystallographica Section A* **51**, 237–252 (1995). DOI: https://doi.org/10.1107/S0108767394011803. eprint: https://onlinelibrary.wiley.com/doi/pdf/10.1107/S0108767394011803.

[Sca21] Orazio Scarlatella et al. "Dynamical Mean-Field Theory for Markovian Open Quantum Many-Body Systems". In: *Phys. Rev. X* **11**, 031018 (2021). DOI: 10.1103/PhysRevX.11.031018.

[Sch02] P. Schindelmann et al. “Radiative decoupling and coupling of nuclear oscillators by stepwise Doppler-energy shifts”. In: *Phys. Rev. A* **65**, 023804 (2002). DOI: 10.1103/PhysRevA.65.023804.

[Sch18a] Raimund Schneider et al. “Quantum imaging with incoherently scattered light from a free-electron laser”. In: *Nature Physics* **14**, 126–129 (2018). DOI: 10.1038/nphys4301.

[Sch18b] Christian G. Schroer et al. “PETRA IV: the ultralow-emittance source project at DESY”. In: *Journal of Synchrotron Radiation* **25**, 1277–1290 (2018). DOI: https://doi.org/10.1107/S1600577518008858. eprint: https://onlinelibrary.wiley.com/doi/pdf/10.1107/S1600577518008858.

[Sch19] Christian Schäfer et al. “Relevance of the quadratic diamagnetic and self-polarization terms in cavity quantum electrodynamics”. In: (2019). arXiv: 1911.08427 [quant-ph].

[Sch21] Volker Schünemann. “From Small Molecules to Complex Systems: A Survey of Chemical and Biological Applications of the Mössbauer Effect”. In: *Modern Mössbauer Spectroscopy: New Challenges Based on Cutting-Edge Techniques*. Ed. by Yutaka Yoshida and Guido Langouche. Singapore: Springer Singapore, 2021, 173–219. DOI: 10.1007/978-981-15-9422-9_4.

[Sch35] E. Schrödinger. “Die gegenwärtige Situation in der Quantenmechanik”. In: *Naturwissenschaften* **23**, 807–812 (1935). DOI: 10.1007/BF01491891.

[Sch68] L. I. Schiff. “Quantum Mechanics”. McGraw Hill (1968).

[Scr10] Armin Scrinzi. “Infinite-range exterior complex scaling as a perfect absorber in time-dependent problems”. In: *Phys. Rev. A* **81**, 053845 (2010). DOI: 10.1103/PhysRevA.81.053845.

[Scu09] Marlan O. Scully. “Collective Lamb Shift in Single Photon Dicke Superradiance”. In: *Phys. Rev. Lett.* **102**, 143601 (2009). DOI: 10.1103/PhysRevLett.102.143601.

[Sea02] C. P. Search et al. “Input-output theory for fermions in an atom cavity”. In: *Phys. Rev. A* **66**, 043616 (2002). DOI: 10.1103/PhysRevA.66.043616.

[Sei19] Benedict Seiferle et al. “Energy of the 229Th nuclear clock transition”. In: *Nature* **573**, 243–246 (2019). DOI: 10.1038/s41586-019-1533-4.

[SG94] W. Sturhahn and E. Gerdau. “Evaluation of time-differential measurements of nuclear-resonance scattering of x rays”. In: *Phys. Rev. B* **49**, 9285–9294 (1994). DOI: 10.1103/PhysRevB.49.9285.

[SH88] Olev Sild and Kristjan Haller. “Zero-Phonon Lines and Spectral Hole Burning in Spectroscopy and Photochemistry”. Springer (1988). DOI: 10.1007/978-3-642-73638-4.

[Sha08] Varvara V. Shamshutdinova et al. “Feshbach projection-operator formalism applied to resonance scattering on Bargmann-type potentials”. In: *Phys. Rev. A* **78**, 062712 (2008). DOI: 10.1103/PhysRevA.78.062712.

[Sha18] Nathan Shammah et al. “Open quantum systems with local and collective incoherent processes: Efficient numerical simulations using permutational invariance”. In: *Phys. Rev. A* **98**, 063815 (2018). DOI: 10.1103/PhysRevA.98.063815.

[Sho11] Bruce W. Shore. “Manipulating Quantum Structures Using Laser Pulses”. Cambridge University Press (2011). DOI: 10.1017/CBO9780511675713.

[Shv00] Yuri V. Shvyd’ko. “MOTIF: Evaluation of time spectra for nuclear forward scattering”. In: *Hyperfine Interactions* **125**, 173–188 (2000). DOI: 10.1023/A:1012633620524.

[Shv96] Yu. V. Shvyd'ko et al. "Storage of Nuclear Excitation Energy through Magnetic Switching". In: *Phys. Rev. Lett.* **77**, 3232–3235 (1996). DOI: 10.1103/PhysRevLett.77.3232.

[Shv99] Yuri V. Shvyd'ko. "Nuclear resonant forward scattering of x rays: Time and space picture". In: *Phys. Rev. B* **59**, 9132–9143 (1999). DOI: 10.1103/PhysRevB.59.9132.

[Sie86] A. E. Siegman. "Lasers". University Science Books (1986), 1283.

[Sim79] B. Simon. "The definition of molecular resonance curves by the method of exterior complex scaling". In: *Physics Letters A* **71**, 211 –214 (1979). DOI: https://doi.org/10.1016/0375-9601(79)90165-8.

[Smi07] G. V. Smirnov et al. "Currents and fields reveal the propagation of nuclear polaritons through a resonant target". In: *Phys. Rev. A* **76**, 043811 (2007). DOI: 10.1103/PhysRevA.76.043811.

[Smi66] Kenneth Smith. "Resonant scattering of electrons by atomic systems". In: *Rep. Prog. Phys.* **29**, 373 (1966).

[Smi86] G. V. Smirnov. "Coherent effects in resonant diffraction: experiment". In: *Hyperfine Interactions* **27**, 203–218 (1986). DOI: 10.1007/BF02354756.

[Smi99] G. V. Smirnov. "General properties of nuclear resonant scattering". In: *Hyperfine Interactions* **123**, 31–77 (1999). DOI: 10.1023/A:1017007520099.

[SMND18] Carlos Sánchez Muñoz, Franco Nori, and Simone De Liberato. "Resolution of superluminal signalling in non-perturbative cavity quantum electrodynamics". In: *Nature Communications* **9**, 1924 (2018). DOI: 10.1038/s41467-018-04339-w.

[SN21] Adam Stokes and Ahsan Nazir. *Implications of gauge-freedom for nonrelativistic quantum electrodynamics*. 2021. arXiv: 2009.10662 [quant-ph].

[Sof19] S. Sofer et al. "Quantum Enhanced X-ray Detection". In: *Phys. Rev. X* **9**, 031033 (2019). DOI: 10.1103/PhysRevX.9.031033.

[Spi09] M. R. Spiegel et al. "Schaum's Outline of Complex Variables, 2ed". Schaum's Outline Series. McGraw-Hill Education (2009).

[SR08] G. K. Shenoy and R. Röhlsberger. "Scientific opportunities in nuclear resonance spectroscopy from source-driven revolution". In: *Hyperfine Interactions* **182**, 157–172 (2008). DOI: 10.1007/s10751-008-9720-y.

[SRR18] Christian Schäfer, Michael Ruggenthaler, and Angel Rubio. "Ab initio nonrelativistic quantum electrodynamics: Bridging quantum chemistry and quantum optics from weak to strong coupling". In: *Phys. Rev. A* **98**, 043801 (2018). DOI: 10.1103/PhysRevA.98.043801.

[SS06] D. S. Sivia and J. Skilling. "Data analysis: A Bayesian tutorial". Oxford University Press (2006).

[SSS03] Dmitry V. Savin, Valentin V. Sokolov, and Hans-Jürgen Sommers. "Is the concept of the non-Hermitian effective Hamiltonian relevant in the case of potential scattering?" In: *Phys. Rev. E* **67**, 026215 (2003). DOI: 10.1103/PhysRevE.67.026215.

[ST58] A. L. Schawlow and C. H. Townes. "Infrared and Optical Masers". In: *Phys. Rev.* **112**, 1940–1949 (1958). DOI: 10.1103/PhysRev.112.1940.

[Ste14] J. Steinbeck. "The Grapes of Wrath". Penguin Books (2014).

[Ste19] Daniel A. Steck. "Quantum and Atom Optics". revision 0.12.6, available online at http://steck.us/teaching. (2019).

[Sto18] Mark I Stockman et al. “Roadmap on plasmonics”. In: *Journal of Optics* **20**, 043001 (2018). DOI: 10.1088/2040-8986/aaa114.

[Str18] A. Strathearn et al. “Efficient non-Markovian quantum dynamics using time-evolving matrix product operators”. In: *Nature Communications* **9**, 3322 (2018). DOI: 10.1038/s41467-018-05617-3.

[Stu00] W. Sturhahn. “CONUSS and PHOENIX: Evaluation of nuclear resonant scattering data”. In: *Hyperfine Interactions* **125**, 149–172 (2000). DOI: 10.1023/A:1012681503686.

[Stu04] Wolfgang Sturhahn. “Nuclear resonant spectroscopy”. In: *Journal of Physics: Condensed Matter* **16**, S497–S530 (2004). DOI: 10.1088/0953-8984/16/5/009.

[SVG20] R. N. Shakhmuratov, F. G. Vagizov, and V. Ya. Gaiduk. “Methods of Coherent Control of Spectral and Temporal Properties of Gamma Photons and Their Potential Applications”. In: *Crystallography Reports* **65**, 409–411 (2020). DOI: 10.1134/S1063774520030311.

[SVK13] R. N. Shakhmuratov, F. Vagizov, and O. Kocharovskaya. “Single gamma-photon revival from sandwich absorbers”. In: *Phys. Rev. A* **87**, 013807 (2013). DOI: 10.1103/PhysRevA.87.013807.

[SWM10] M. Saffman, T. G. Walker, and K. Mølmer. “Quantum information with Rydberg atoms”. In: *Rev. Mod. Phys.* **82**, 2313–2363 (2010). DOI: 10.1103/RevModPhys.82.2313.

[SZ97] Marlan O. Scully and M. Suhail Zubairy. “Quantum Optics”. Cambridge University Press (1997). DOI: 10.1017/CBO9780511813993.

[Tam13] M. S. Tame et al. “Quantum plasmonics”. In: *Nature Physics* **9**, 329 (2013).

[Tam14] Kenji Tamasaku et al. “X-ray two-photon absorption competing against single and sequential multiphoton processes”. In: *Nature Photonics* **8**, 313–316 (2014). DOI: 10.1038/nphoton.2014.10.

[Tam18] D. Tamascelli et al. “Nonperturbative Treatment of non-Markovian Dynamics of Open Quantum Systems”. In: *Phys. Rev. Lett.* **120**, 030402 (2018). DOI: 10.1103/PhysRevLett.120.030402.

[Tay20] Michael A. D. Taylor et al. “Resolution of Gauge Ambiguities in Molecular Cavity Quantum Electrodynamics”. In: *Phys. Rev. Lett.* **125**, 123602 (2020). DOI: 10.1103/PhysRevLett.125.123602.

[TC69] MICHAEL TAVIS and FREDERICK W. CUMMINGS. “Approximate Solutions for an N-Molecule-Radiation-Field Hamiltonian”. In: *Phys. Rev.* **188**, 692–695 (1969). DOI: 10.1103/PhysRev.188.692.

[TH78] G. T. Trammell and J. P. Hannon. “Quantum beats from nuclei excited by synchrotron pulses”. In: *Phys. Rev. B* **18**, 165–172 (1978). DOI: 10.1103/PhysRevB.18.165.

[Tho13] D.J. Thouless. “The Quantum Mechanics of Many-Body Systems: Second Edition”. Dover Books on Physics. Dover Publications (2013).

[Tom95] M. S. Tomaš. “Green function for multilayers: Light scattering in planar cavities”. In: *Phys. Rev. A* **51**, 2545–2559 (1995). DOI: 10.1103/PhysRevA.51.2545.

[Tri18] Rahul Trivedi et al. “Few-photon scattering and emission from low-dimensional quantum systems”. In: *Phys. Rev. B* **98**, 144112 (2018). DOI: 10.1103/PhysRevB.98.144112.

[TSC06] Hakan E. Türeci, A. Douglas Stone, and B. Collier. "Self-consistent multimode lasing theory for complex or random lasing media". In: *Phys. Rev. A* **74**, 043822 (2006). DOI: 10.1103/PhysRevA.74.043822.

[Tsc17] Thomas Tschentscher et al. "Photon Beam Transport and Scientific Instruments at the European XFEL". In: *Applied Sciences* **7** (2017). DOI: 10.3390/app7060592.

[Tür05] H. E. Türeci et al. "Modes of wave-chaotic dielectric resonators". In: *Prog. Opt.* **47**, 75. Ed. by E. Wolf (2005). DOI: https://doi.org/10.1016/S0079-6638(05)47002-X.

[Tür08] Hakan E. Türeci et al. "Strong Interactions in Multimode Random Lasers". In: *Science* **320**, 643–646 (2008). DOI: 10.1126/science.1155311.

[Vag14] Farit Vagizov et al. "Coherent control of the waveforms of recoilless g-ray photons". In: *Nature* **508**, 80–83 (2014). DOI: 10.1038/nature13018.

[Vag90] F. G. Vagizov. "The splitting of hyperfine lines of57Fe nuclei in RF magnetic field". In: *Hyperfine Interactions* **61**, 1359–1362 (1990). DOI: 10.1007/BF02407625.

[Vah03] Kerry J. Vahala. "Optical microcavities". In: *Nature* **424**, 839–846 (2003). DOI: 10.1038/nature01939.

[Vai18] Varun D. Vaidya et al. "Tunable-Range, Photon-Mediated Atomic Interactions in Multimode Cavity QED". In: *Phys. Rev. X* **8**, 011002 (2018). DOI: 10.1103/PhysRevX.8.011002.

[VB86] U. Van Bürck. "Coherent effects in resonant diffraction: theory". In: *Hyperfine Interactions* **27**, 219–230 (1986). DOI: 10.1007/BF02354757.

[Vel21] S. Velten et al. In: *unpublished*.

[VH03] Carlos Viviescas and Gregor Hackenbroich. "Field quantization for open optical cavities". In: *Phys. Rev. A* **67**, 013805 (2003). DOI: 10.1103/PhysRevA.67.013805.

[VH04] C Viviescas and G Hackenbroich. "Quantum theory of multimode fields: applications to optical resonators". In: *J. Opt. B* **6**, 211 (2004).

[Vir20] Pauli Virtanen et al. "SciPy 1.0: Fundamental Algorithms for Scientific Computing in Python". In: *Nature Methods* **17**, 261–272 (2020). DOI: 10.1038/s41592-019-0686-2.

[VRDJ95] Guido Van Rossum and Fred L Drake Jr. "Python reference manual". Centrum voor Wiskunde en Informatica Amsterdam (1995).

[VS21] Malte Vassholz and Tim Salditt. "Observation of electron-induced characteristic x-ray and bremsstrahlung radiation from a waveguide cavity". In: *Science Advances* **7** (2021). DOI: 10.1126/sciadv.abd5677.

[Wal06] Herbert Walther et al. "Cavity quantum electrodynamics". In: *Rep. Prog. Phys.* **69**, 1325 (2006).

[WE47] E. P. Wigner and L. Eisenbud. "Higher Angular Momenta and Long Range Interaction in Resonance Reactions". In: *Phys. Rev.* **72**, 29–41 (1947). DOI: 10.1103/PhysRev.72.29.

[Web10] J. R. Weber et al. "Quantum computing with defects". In: *Proceedings of the National Academy of Sciences* **107**, 8513–8518 (2010). DOI: 10.1073/pnas.1003052107. eprint: https://www.pnas.org/content/107/19/8513.full.pdf.

[Wei33] V. Weisskopf. "Die Streuung des Lichts an angeregten Atomen". In: *Z. Phys.* **85**, 451–481 (1933). DOI: 10.1007/BF01330970.

[Wen16] Lars von der Wense et al. “Direct detection of the 229Th nuclear clock transition”. In: *Nature* **533**, 47–51 (2016). DOI: 10.1038/nature17669.

[Win13] David J. Wineland. “Nobel Lecture: Superposition, entanglement, and raising Schrödinger’s cat”. In: *Rev. Mod. Phys.* **85**, 1103–1114 (2013). DOI: 10.1103/RevModPhys.85.1103.

[Wit69] Ludwig Wittgenstein. “On Certainty (Ed. Anscombe and von Wright)”. Harper Torchbooks (1969).

[WK04] F. E. Wagner and A. Kyek. “Mössbauer Spectroscopy in Archaeology: Introduction and Experimental Considerations”. In: *Hyperfine Interactions* **154**, 5–33 (2004). DOI: 10.1023/B:HYPE.0000032112.94624.95.

[WL18] Guan-Ying Wang and Wen-Te Liao. “Generation of Short Hard-X-Ray Pulses of Tailored Duration Using a Mössbauer Source”. In: *Phys. Rev. Applied* **10**, 014003 (2018). DOI: 10.1103/PhysRevApplied.10.014003.

[WM08] D.F. Walls and Gerard J. Milburn, eds. “Quantum Optics”. Berlin, Heidelberg: Springer (2008). DOI: 10.1007/978-3-540-28574-8.

[WS10] Edo Waks and Deepak Sridharan. “Cavity QED treatment of interactions between a metal nanoparticle and a dipole emitter”. In: *Phys. Rev. A* **82**, 043845 (2010). DOI: 10.1103/PhysRevA.82.043845.

[WV06] Edo Waks and Jelena Vučković. “Dipole Induced Transparency in Drop-Filter Cavity-Waveguide Systems”. In: *Phys. Rev. Lett.* **96**, 153601 (2006). DOI: 10.1103/PhysRevLett.96.153601.

[XF15] Shanshan Xu and Shanhui Fan. “Input-output formalism for few-photon transport: A systematic treatment beyond two photons”. In: *Phys. Rev. A* **91**, 043845 (2015). DOI: 10.1103/PhysRevA.91.043845.

[XF17] Shanshan Xu and Shanhui Fan. “Input-Output Formalism for Few-Photon Transport”. In: *Quantum Plasmonics*. Ed. by Sergey I. Bozhevolnyi, Luis Martin-Moreno, and Francisco Garcia-Vidal. Cham: Springer International Publishing, 2017, 1–23. DOI: 10.1007/978-3-319-45820-5_1.

[Xia13] Ze-Liang Xiang et al. “Hybrid quantum circuits: Superconducting circuits interacting with other quantum systems”. In: *Rev. Mod. Phys.* **85**, 623–653 (2013). DOI: 10.1103/RevModPhys.85.623.

[Yao09] Peijun Yao et al. “Ultrahigh Purcell factors and Lamb shifts in slow-light metamaterial waveguides”. In: *Phys. Rev. B* **80**, 195106 (2009). DOI: 10.1103/PhysRevB.80.195106.

[YF97] S. F. Yelin and M. Fleischhauer. “Modification of local field effects in two level systems due to quantum corrections”. In: *Opt. Express* **1**, 160–168 (1997). DOI: 10.1364/OE.1.000160.

[YI99] Y. Yamamoto and A. Imamoglu. “Mesoscopic Quantum Optics”. New York: John Wiley (1999).

[YL21] Yutaka Yoshida and Guido Langouche, eds. “Modern Mössbauer Spectroscopy: New Challenges Based on Cutting-Edge Techniques”. Singapore: Springer Singapore (2021). DOI: 10.1007/978-981-15-9422-9.

[Yod98] Y. Yoda et al. “X-ray parametric scattering by a diamond crystal”. In: *Journal of Synchrotron Radiation* **5**, 980–982 (1998). DOI: 10.1107/S0909049597020232.

[Yos21] Yutaka Yoshida. “Mössbauer Spectroscopic Studies on Atomic Diffusion in Materials”. In: *Modern Mössbauer Spectroscopy: New Challenges Based on Cutting-Edge Tech-*

niques. Ed. by Yutaka Yoshida and Guido Langouche. Singapore: Springer Singapore, 2021, 445–515. DOI: 10.1007/978-981-15-9422-9_9.

[You10] L. Young et al. "Femtosecond electronic response of atoms to ultra-intense X-rays". In: *Nature* **466**, 56–61 (2010). DOI: 10.1038/nature09177.

[YTI15] Makina Yabashi, Hitoshi Tanaka, and Tetsuya Ishikawa. "Overview of the SACLA facility". eng. In: *Journal of synchrotron radiation* **22**, 477–484 (2015). DOI: 10.1107/S1600577515004658.

[Yur04] B. Yurke. "Input-Output Theory". In: *Quantum Squeezing*. Ed. by P. D. Drummond and Z. Ficek. Springer, Heidelberg (2004), pp.

[ZD10] Oleg Zaitsev and Lev Deych. "Recent developments in the theory of multimode random lasers". In: *J. Opt.* **12**, 024001 (2010).

[Zha13] Jing Zhang et al. "Non-Markovian quantum input-output networks". In: *Phys. Rev. A* **87**, 032117 (2013). DOI: 10.1103/PhysRevA.87.032117.

[Zha19] Xiwen Zhang et al. "Nuclear Quantum Memory and Time Sequencing of a Single γ Photon". In: *Phys. Rev. Lett.* **123**, 250504 (2019). DOI: 10.1103/PhysRevLett.123.250504.

[Zho08] Lan Zhou et al. "Controllable Scattering of a Single Photon inside a One-Dimensional Resonator Waveguide". In: *Phys. Rev. Lett.* **101**, 100501 (2008). DOI: 10.1103/PhysRevLett.101.100501.

[Zho20] Han-Sen Zhong et al. "Quantum computational advantage using photons". In: *Science* **370**, 1460–1463 (2020). DOI: 10.1126/science.abe8770. eprint: https://science.sciencemag.org/content/370/6523/1460.full.pdf.

[Zhu90] Yifu Zhu et al. "Vacuum Rabi splitting as a feature of linear-dispersion theory: Analysis and experimental observations". In: *Phys. Rev. Lett.* **64**, 2499–2502 (1990). DOI: 10.1103/PhysRevLett.64.2499.

[ZKR19] Matthias Zens, Dmitry O. Krimer, and Stefan Rotter. "Critical phenomena and nonlinear dynamics in a spin ensemble strongly coupled to a cavity. II. Semiclassical-to-quantum boundary". In: *Phys. Rev. A* **100**, 013856 (2019). DOI: 10.1103/PhysRevA.100.013856.

[ZLS07] Lan Zhou, Jing Lu, and C. P. Sun. "Coherent control of photon transmission: Slowing light in a coupled resonator waveguide doped with $\mathbf{\Lambda}$ atoms". In: *Phys. Rev. A* **76**, 012313 (2007). DOI: 10.1103/PhysRevA.76.012313.

[ZM20] Hanwen Zhang and Owen D. Miller. *Quasinormal Coupled Mode Theory*. 2020. arXiv: 2010.08650 [physics.optics].

[Zsc18] Lin Zschiedrich et al. "Riesz-projection-based theory of light-matter interaction in dispersive nanoresonators". In: *Phys. Rev. A* **98**, 043806 (2018). DOI: 10.1103/PhysRevA.98.043806.

[De 14] Simone De Liberato. "Light-Matter Decoupling in the Deep Strong Coupling Regime: The Breakdown of the Purcell Effect". In: *Phys. Rev. Lett.* **112**, 016401 (2014). DOI: 10.1103/PhysRevLett.112.016401.

[Di 12] A. Di Piazza et al. "Extremely high-intensity laser interactions with fundamental quantum systems". In: *Rev. Mod. Phys.* **84**, 1177–1228 (2012). DOI: 10.1103/RevModPhys.84.1177.

[Özd19] S. K. Özdemir et al. "Parity-time symmetry and exceptional points in photonics". In: *Nature Materials* **18**, 783–798 (2019). DOI: 10.1038/s41563-019-0304-9.

[Ślę10] T Ślęzak et al. “Magnetism of ultra-thin iron films seen by the nuclear resonant scattering of synchrotron radiation”. In: *Journal of Physics: Conference Series* **217**, 012090 (2010). DOI: 10.1088/1742-6596/217/1/012090.

Acknowledgements

"Knowledge is in the end based on acknowledgement."
– Ludwig Wittgenstein, *On certainty* [Wit69]

With the above quote, I would like to start by thanking my PhD supervisor Jörg Evers, to whom I owe most of the knowledge I have today about physics. Anecdotally, the two courses I had not attended during my Master's degree syllabus included "Atomic, Molecular and Optical Physics" and "Quantum and Nonlinear Optics" — possibly not the wisest choice for starting a PhD in nuclear quantum optics. Nevertheless, thanks to Jörg's guidance, patience and support, my PhD journey and the work in his group have been as much enjoyable as they have been productive. I am particularly grateful for his unique way of finding a balance between being an advisor, a mentor, a supervisor and a friend, and for encouraging me to develop and pursue my own ideas. Besides his expertise in physics, he has shared with me an invaluable perspective on and taught me how to do research, which has formed me as a scientist and improved me as a person.

I would like to thank Christoph H. Keitel for providing a wonderful work environment in his theory division at the Max Planck Institute for Nuclear Physics in Heidelberg, which I had the pleasure of being a part of during the last years. I am also grateful for discussions, his advice and support, and for enabling numerous trips to conferences and synchrotron experiments.

Another important figure during my PhD project has been Kilian P. Heeg, whom I would like to thank for his advice, help and patience with my frequent questions on the theoretical and experimental aspects of nuclear quantum optics. At times, he was essentially a second supervisor to me, who was conveniently sitting only a chair roll away. I have learned an incredible amount from him and also had much fun during the office times, group lunches and beamtimes together.

I would like to thank Ralf Röhlsberger and Thomas Pfeifer for their mentorship and support, in particular through discussions during beamtimes and the writing of reference letters.

I would also like to thank all the colleagues who have enabled our experiments at synchrotron facilities and taught me about various aspects of nuclear resonant scattering, including Petar Andrejić, Lars Bocklage, Johann Haber, Olaf Leupold, Christian Ott, Adriana Pálffy, Rudolf Rüffer, Kai Schlage, Ilya Sergueev, René Steinbrügge, Kai S. Schulze and Sven Velten. I thank Petar Andrejić, Adriana Pálffy, Sven Velten, Lars Bocklage and Ralf Röhlsberger for allowing me to contribute to their experiments, during which I gained invaluable experience. I would like to thank Christian Ott for discussions and for sharing his insights on Fano interference.

I am grateful for inspiring visits in Vienna, Warsaw, Freiburg and Hamburg; and would like to thank Giulio Amato, Robert Bennett, Andreas Buchleitner, Stefan Y. Buhmann, Adam Buraczewski, Himadri Shekhar Dhar, Monika Mycroft, Stefan Rotter, Michael Ruggenthaler, Faruk Salihbegovic, Alexander Schumer, Vyacheslav N. Shatokhin, Magdalena Stobińska, Giacomo Sorelli, Thomas Sturges and Matthias Zens for their hospitality, fruitful discussions and invaluable insights. I thank Stefan Rotter for crucial discussions and inputs, which led to the multi-mode project in this thesis.

I am indebted to the RACIRI initiative and the XXV International Summer School 'Nicolás Cabrera' for the inspiring research schools and associated funding. I would particularly like to thank Johannes Feist for fruitful discussions and later correspondence.

I would like to thank the IMPRS-QD and HGSFP for the research environment with many exciting events, including annual meetings and winter schools. I thank Ákos, Jeanette, Martin, Ralf and Tim for the fun times during the organization of the winter school, along with all the other great people I have met there and at other HGSFP events.

I would like to thank Sergey Bragin, Oliver Diekmann, Miriam Gerharz, Piet-Hein van den Heuvel and Lukas Wolff for proof-reading of and valuable feedback on this thesis. I further thank Oliver Diekmann for productive collaboration on the multi-mode project as well as for being an avid spotter of formula mistakes, and Miriam Gerharz for the exciting beamtimes with fruitful discussions.

I would further like to express my gratitude to Prof. Maurits W. Haverkort for serving as a referee for this thesis, as well as to Prof. Markus Oberthaler and Prof. Werner Aeschbach for complementing my thesis committee.

Besides scientific companions, I am thankful for the friends that have made my PhD journey more enjoyable, including my fellow PhD students in the division Archana, Daniel, Halil, Kamil, Michael, Petar, Sergei and Sergey; my office and group mates Benedikt, Fabian, Kilian, Lukas, Miriam, Oliver, Paul, Pim and Salvatore; and Austen, Binaya, Gonzalo, Jakub, Lennard, Long, Marta, Matt, Michel, Niklas, Ross, Tim F. and Tim S. Thank you for keeping me sane, especially during the pandemic!

"All we got is the family unbroke."
– John Steinbeck, *The Grapes of Wrath* [Ste14]

Zu guter Letzt möchte ich mich bei meiner liebevollen Familie bedanken, die mich auf dem Weg der Doktorarbeit und auch auf allen anderen Lebenswegen immer tatkräftig begleitet, unterstützt und ermutigt haben. Mama, Papa, Constantin, Selina und Oma, danke für alles! Ohne Euch würde es diese Arbeit nicht geben und meine Welt wäre auch nicht dieselbe.